Université de Paris VII-Denis Diderot

HABILITATION À DIRIGER LES RECHERCHES

présentée par

Dr. Allan Sacha BRUN

Spécialité: Physique

Convection, Turbulence, Rotation et Magnétisme dans les Étoiles

Soutenue le 21 Octobre 2005
à l'amphithéâtre Claude Bloch
devant la commission d'examen composée de:

Dr. Bérengère Dubrulle	**rapporteur**
Prof. Jacques Le Bourlot	**Président et rapporteur interne**
Prof. Michel Rieutord	**rapporteur**
Dr. Sylvaine Turck-Chièze	**examinatrice**
Dr. Jean-Paul Zahn	**examinateur**

Service d'Astrophysique
DSM/DAPNIA/CEA-Saclay
UMR AIM n° 7158
CEA - CNRS - Université de Paris 7
sacha.brun@cea.fr

À mes "A"-mours, Ambre, Aster, Agnès,
Ariane et Allan...

Remerciements

Je tiens à remercier les membres du jury en commençant par le président Jacques Le Bourlot, qui m'a lancé dans la modélisation en astrophysique en créant à Paris 7 une filière de 2^{eme} cycle de physique fondamentale et simulations numériques, totalement nouvelle et avant gardiste! La grande qualité et originalité des cours enseignés et la très bonne ambiance qui régnait au CCRE (ex CICRP) de Jussieu avec mes camarades du groupe modélisation, m'ont ouvert une voie royale vers la recherche. Je tiens également à remercier mes rapporteurs Bérengère Dubrulle et Michel Rieutord, pour leur bienveillance vis à vis des mes travaux scientifiques et leurs remarques toujours judicieuses, qui m'ont fait murir dans le métier difficile qu'est celui de chercheur et de dynamicien des fluides. L'école de Cargèse en Dynamique des Fluides Astrophysiques qu'ils ont organisée en Mai 2005, restera un grand souvenir et en appelle d'autres! Enfin je tiens à remercier Sylvaine Turck-Chièze et Jean-Paul Zahn qui me suivent depuis mes débuts en astrophysique et ont été d'un soutien permanent et sans faille. Leur complémentarité a été un grand atout et m'a permis de trouver ma voie en tant que chercheur. Sylvaine par ses encouragements, ses questions et sa connaissance de la physique microscopique m'a appris comment fonctionne une étoile et m'a fait comprendre le sens du mot rigueur tellement nécessaire pour être un bon chercheur. Jean-Paul, par sa gentillesse, sa disponibilité et sa compréhension profonde de la dynamique des fluides en rotation magnétisés, m'a appris comment fonctionne dynamiquement une étoile et m'a incité à être persévérant devant les difficultés, autre atout très important pour un jeune chercheur. Ils ont finalement joué le rôle de père et de mère scientifique! Cette image ne serait donc pas complète sans un oncle d'Amérique!!! Je tiens donc à remercier tout particulièrement Juri Toomre qui par son acceuil exceptionnel à Boulder dans son groupe a joué un rôle crucial dans ma carrière en me permettant de m'épanouir comme jeune chercheur et en m'apprenant à attaquer les problèmes de dynamique des fluides directement sur des ordinateurs massivement parallèles. À eux trois, Sylvaine, Jean-Paul et Juri m'ont permis de continuer avec passion cette grande aventure (difficile) de la recherche fondamentale et je leur en suis très reconnaissant.
Ces remerciements ne seraient pas complets sans que je remercie mes nombreux collègues en France, en Europe ou aux USA entre autre, N. Brummell, M. Miesch, T. Foglizzo, R. Garcia, J.-P. Chièze, R. Teyssier, E. Audit, R. Lehouq, H. Triou, D. Gough, J. Leibacher, J. Christensen-Dalsgaard, M. Thompson, P. Gilman, S. Kosovichev, P. Charbonneau, R. Grappin, J. Léorat, S. Bonnazzola, A. Pouquet, A. Brandenburg, G. Rudiger ...et tant d'autres (pardonnez moi) avec qui j'ai régulièrement des discussions très intéressantes.

Je tiens aussi à remercier le chef du Service d'Astrophysique du CEA-Saclay, P.-O. Lagage et son adjoint M. Talvard pour leur accueil chaleureux et leur soutien/encouragement pour l'activité simulation des plasmas astrophysiques, sans oublier les secrétaires du service, Christine, Dominique, Elisabeth, Laetitia et Pascale, sans qui il serait difficile de mener à bien notre recherche.
Finalement je tiens à remercier ma femme, Agnès pour ses preuves d'amour et pour supporter l'invasion de mon travail dans notre vie quotidienne, mes enfants Ambre et Aster qui sont une source de joie permanente et qui me permettent de relativiser bien des choses, ma famille, surtout ma mère Ariane, mon père, Allan et ma soeur Sandy pour leurs attentions et leur tendresse ainsi que mes amis proches, Louis-Jacques, Nicolas, Jérémy, Hélios, Noré, Lure, Chat, Seb, Alexis, Hugo, Françoise, Sophie, Marlène, etc... avec qui il fait bon de profiter et de philosopher sur la vie.
Un Grand Merci à Vous Tous.

Saint-Cyr l'École, le 15 Novembre 2005

Originalité des Travaux de Recherches

L'originalité de mes travaux de recherche réside dans l'approche *tridimensionnelle, non linéaire, magnétohydrodynamique* (MHD) et *dépendante du temps*, que j'ai adopté pour décrire les processus dynamiques multiples et variés observés dans et autour du Soleil et des étoiles, tels que la convection thermique, la turbulence, la rotation et l'activité magnétique. Elle repose sur des simulations numériques globales à très haute résolution (jusqu'à 1200^3) en coordonnées sphériques, particulièrement bien adaptées pour les étoiles, utilisant le code Anelastic Spherical Harmonic (ASH), fruit d'une collaboration franco-américaine dans laquelle j'ai joué un rôle moteur. Cette approche numérique lourde est tout à fait originale et d'actualité, tant il est vrai que l'avancée simultanée sans précédent des moyens informatiques, comme les super-calculateurs massivement parallèles, et des moyens observationnels au sol (Thémis, Solar Swedish Telescope, Espadons, VLTi, GONG, GOLF-NG) et dans l'espace (SoHO, Trace, Cluster, Corot, SDO, XMM) permettent de réaliser un saut qualitatif et quantitatif sans précédent dans notre compréhension et description de la dynamique des étoiles. Encadré par un travail théorique et d'analyse de fond, les simulations numériques multidimensionnelles nous permettent d'étudier d'un coté, les processus dynamiques non linéaires nécessaires pour calculer la structure interne et l'évolution des étoiles de façon détaillée, et de l'autre, la nature des relations Soleil-Terre en partie liées à l'activité magnétique intense que connaît notre étoile. Cette approche unificatrice consistant à lier les différents aspects internes et externes du magnétisme solaire (et stellaire) commence à se mettre en place, encouragée en cela par les organismes de recherche comme le CEA et le CNRS et par les programmes nationaux de Physique Stellaire (PNPS), Soleil-Terre (PNST) et l'action spécifique en Simulations Numériques en Astrophysique (ASSNA). Assembler tout ou partie de ces éléments en une vue cohérente et globalisante des processus dynamiques présents dans le Soleil, les étoiles et leur environnement spatial immédiat est le but premier des travaux présentés dans ce manuscrit qui en propose en quelque sorte un premier rapport d'étape.

Table des matières

Chapitre 1

Préambule

L'étude des étoiles, de leur intérieur, de leur structure, de leur composition chimique et de leur dynamique interne et externe est cruciale pour notre compréhension de l'univers, car elles en constituent les briques fondamentales. La théorie de la structure interne et de l'évolution stellaire a été développée depuis fort longtemps (Eddington 1926, Chandrasekhar 1939) et depuis sans cesse améliorée (Cox & Giuli 1968, Clayton 1968, Schatzman & Praderie 1990, Kippenhahn & Weigert 1991, Hansen & Kawaler 1995 etc...). Au milieu du siècle dernier, l'avènement des premiers calculateurs a permis la résolution numérique, à une dimension, des équations de la structure interne pour élaborer des modèles des différents types d'étoiles. De par sa proximité, le Soleil a de tout temps joué un rôle particulier en astrophysique et d'autant plus en évolution stellaire puisque tous les autres modèles d'étoiles sont calibrés par rapport au modèle du Soleil, dit "modèle standard" (voir par exemple Turck-Chièze et al. 1993, Christensen-Dalsgaard et al. 1996, Brun, Turck-Chièze et Zahn 1999, Brun et al. 2002). Les équations de la structure interne des étoiles sont déduites des équations du mouvement d'un fluide, en considérant des hypothèses simplificatrices telles que l'équilibre hydrostatique, l'absence de rotation [1] ou de champ magnétique ou la stricte égalité entre l'énergie produite par réaction nucléaire au centre et celle rayonnée à la surface par l'étoile (Schatzman & Praderie 1990, Kippenhahn & Weigert 1991, Hansen & Kawaler 1995). Pour décrire le mode de transport de l'énergie, outre l'approximation de diffusion pour le transfert du rayonnement dans les couches optiquement épaisses (Mihalas & Mihalas), le modèle "standard" s'appuie sur la théorie de la longueur de mélange (MLT) (Bohm-Vitense 1958) pour traiter, à une dimension, les zones convec-

1. il faut noter cependant que beaucoup d'efforts ces dernières années ont été fait pour inclure les effets de la rotation dans le calcul monodimensionnel de l'évolution et de la structure interne des étoiles (voir par exemple Maeder et Meynet 2001, Mathis et Zahn 2003), mais ces modèles ne sont pas encore considérés comme "standard"

tives. Ces zones apparaissent là où la stratification (ou le gradient de température) de l'étoile est instable, ce qui déclenche des mouvements macroscopiques ascendants (ou courants convectifs) qui transportent vers la surface la chaleur générée au centre par les réactions nucléaires. Bien évidemment la nature hautement turbulente de la convection thermique, avec un nombre de Reynolds typique de 10^{15} (voir Appendice 2.2) n'est que très grossièrement représentée par la MLT. Cependant la montée en puissance continue des (super)calculateurs fait qu'il est maintenant possible de s'attaquer à la modélisation multidimensionnelle (2-D ou 3-D) des étoiles, et de leurs zones convectives en particulier. L'observation multi-longueur d'onde, le diagnostic sismique (hélio ou astérosismologie) et même la détection des neutrinos produits dans le coeur nucléaire, fournissent autant de données de plus en plus nombreuses et de plus en plus précises permettant de contraindre les caractéristiques physiques du Soleil et des étoiles. Progressivement les modèles quasi-statiques laissent place à des modèles dynamiques basés sur les équations de l'hydrodynamique (HD) couplés à une description microscopique de plus en plus réaliste du plasma stellaire (opacités, équation d'état, atmosphère, etc.), voir Cattaneo et al. (1991), Brummell et al. (1996), (1998), Stein & Nordlund (1998), (2000), Rincon et al. (2005) etc.... Dès lors cette approche dynamique permet d'étudier un autre aspect intéressant et fondamental pour notre compréhension du fonctionnement des étoiles dans les différentes phases de leur évolution: leur magnétisme. En résolvant l'équation d'induction couplée aux équations de l'hydrodynamique modifiées pour inclure la force de Laplace et la dissipation ohmique, i.e. les équations de la magnétohydrodynamique (MHD) (voir chapitre 3), on peut décrire l'interaction complexe existant dans les étoiles entre turbulence, convection, rotation et champ magnétique (voir par exemple, Weiss & Galloway 1981, Gilman & Miller 1981, Hurlburt et al. 1986., Glatzmaier 1987, Brandenburg et al. 1996, Tobias et al. 2001, Proctor 2004, Brun, Miesch et Toomre 2004, Brun, Browning et Toomre 2005). Des programmes numériques performants ont été et sont développés, utilisant le C++ ou le Fortran90/95 et MPI (Message passing interface), afin de résoudre ce système complexe d'équations magnétohydrodynamiques couplées sur des ordinateurs massivement parallèles et pouvoir analyser et décortiquer les interactions non linéaires présentes dans les étoiles [2].

Nous proposons ici de présenter l'effort personnel de plusieurs années de recherche dans le domaine de la dynamique des fluides stellaires effectué au Service d'Astrophysique du DAPNIA au CEA-Saclay, au Laboratoire de l'Univers et de ses théories de l'Observatoire de Paris et au laboratoire de Dynamique Computationelle à l'Univer-

2. des techniques similaires sont également utilisées pour d'autres objets célestes, tels que la Terre, les planètes géantes, les galaxies.

sité du Colorado dans le cadre d'une collaboration franco-américaine. Cette recherche a consisté à étudier en détail à partir d'expériences numériques 3-D MHD bien identifiées, le fonctionnement et les interactions subtiles de la convection, de la turbulence, de la rotation et de l'activité magnétique dans les étoiles.

Dans la première partie du manuscrit nous discutons au chapitre 2, les nombreuses évidences observationelles des phénomènes dynamiques présents dans les étoiles et servant de guide à notre recherche. Au chapitre 3, nous introduisons succinctement les équations de la magnétohydrodynamique servant de fondement théorique à l'étude des processus dynamiques dans les étoiles et nous présentons les évidences numériques et expérimentales de l'effet dynamo et comment ce concept peut être efficacement étendu aux étoiles.

Puis dans la deuxième partie, nous présentons dans le détail nos travaux originaux sur la magnétohydrodynamique stellaire (le lecteur pourra également y trouver les articles majeurs concernant ce travail). Dans un premier temps nous nous sommes plus particulièrement intéressés au Soleil afin de valider notre approche sur notre étoile dont la qualité des observations contraignent fortement nos simulations. Suite au résultats encourageants obtenus dans le cas solaire (cf. chapitre 4 & 5), nous nous sommes intéressés aux étoiles A (deux fois plus massives) possédant une convection centrale (donc différente de la convection de surface solaire), comme une première étape vers la modélisation de la gamme la plus large possible d'étoiles (cf. chapitre 6). Finalement nous présentons les nombreuses perspectives et extensions possibles de ce travail dans le chapitre 7.

Nous complétons la présente introduction par une première présentation générale de la convection, de la rotation, du champ magnétique et de l'effet dynamo. Il est conseillé au lecteur avisé de directement se rendre au chapitre 2.

1.1 Convection

La convection joue un rôle très important dans la structure et l'évolution des étoiles ainsi que dans notre vie de tous les jours. C'est le processus de transport de l'énergie thermique par le mouvement généralement ascendant d'un fluide. Ce qui est localement plus chaud (donc léger) que le milieu environnant monte et ce qui est localement plus froid (donc dense) descend créant ainsi un courant (cf. Figure 1.1).

Ces mouvements à grande échelle, sous la forme de rouleaux convectifs, tendent à réduire la différence de température existant dans le système étudié et créés des couches limites thermiques aux bord du domaine. De ces couches limites chaudes et froides, se détachent des panaches, ou tubes de vorticité intense, très étroits qui se dirigent vers la

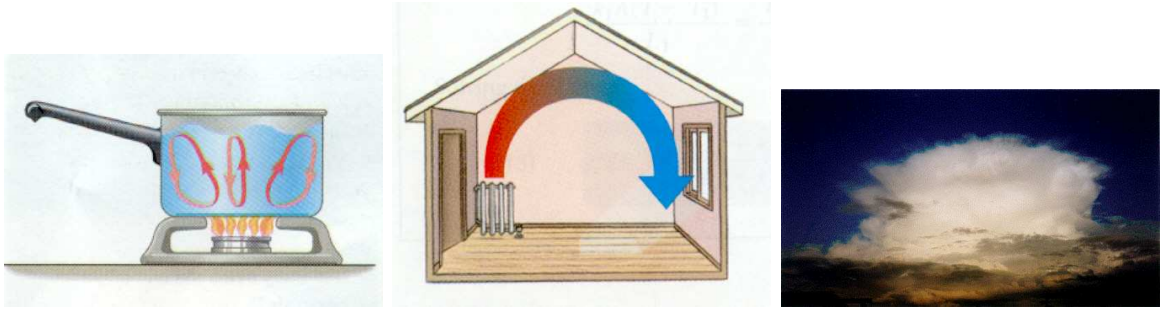

FIG. 1.1 – *Mouvements de convection dans a) une casserole d'eau, b) une maison et c) un nuage de convection (type cumulonimbus) proche de se transformer en orage.*

limite opposée (si la stratification est faible sinon seulement les panaches descendants sont fortement concentrés et traversent a priori le domaine convectif)[3].

Un paramètre clé pour caractériser l'existence et l'intensité de la convection est le nombre sans dimension de Rayleigh Ra (cf. Appendice 2.2). C'est le rapport entre le processus à l'origine du mouvement (ici la poussée d'Archimède) et les processus résistants (diffusion de chaleur et frottements visqueux, si seule la viscosité est considérée on obtient le nombre de Grashof). Lorsque ce nombre sans dimension est inférieur à une valeur critique Ra_c de l'ordre de 660 en laboratoire (cas surface libre en géométrie plane, Chandrasekhar 1961), l'énergie transmise au système est insuffisante pour déclencher l'instabilité: le fluide demeure immobile. Mais lorsque Ra est supérieur à la valeur critique Ra_c, le fluide convecte.

La seule étude du nombre de Rayleigh permet donc de caractériser la dynamique d'un système. Dans le Soleil, ce nombre de Rayleigh est de l'ordre de $Ra \sim 10^{12}$, très largement supérieur à la valeur critique trouvée en laboratoire, elle même confirmée par l'étude de stabilité linéaire (Chandrasekhar 1961). Ce nombre très élevé indique que la convection solaire est certainement dans un régime convectif turbulent ayant des propriétés de transport de la chaleur particuliers. Il est intéressant de remarquer que la convection naturelle comme dans le Soleil diffère de celle trouvée en laboratoire, où l'on impose une différence de température entre des plaques contrairement aux étoiles ou c'est le flux qui est imposé. Cela implique que les considérations d'efficacité de transport d'énergie cruciales dans les expériences de laboratoire et formalisées par des relations entre les nombres de Nusselt (cf. Appendice) et de Rayleigh ($Nu \propto Ra^{\beta}$ avec $\beta \geq 2/7$, Castaing et al. 1990, Dubrulle 2002), ont moins de pertinence

3. dans la nature le transport de l'énergie thermique peut également se faire par conduction (contact direct entre un corps chaud et un corps froid) ou par rayonnement (énergie transportée par les photons/la lumière), le premier étant négligeable dans les étoiles.

dans les étoiles. Une expérience de convection en géométrie sphérique, a été menée en apesanteur sur la navette spatiale Columbia (expérience spacelab 3, Hart t al. 1986), en utilisant la force centrifuge comme substitution de la gravité radiale et en imposant un contraste de température inversé entre la surface et le centre de la demi-sphère. Cet appareillage expérimental, reproduit raisonnablement bien les conditions présentes dans les planètes et les étoiles. Dans cette expérience, on observe l'apparition simultanée de colonnes tiltées et d'une rotation différentielle en latitude, semblables aux simulations numériques de convection Boussinesq (et laminaire) en coquille sphérique (voir chapitre 4).

Dans le cas des étoiles, les mouvements convectifs servent à évacuer l'énergie thermonucléaire créée en leur centre, il est donc crucial de bien décrire ce processus physique. La localisation des zones de convection dépend fortement de la masse des étoiles (mais aussi de leur métallicité), les plus massives ayant une convection centrale (cf. chapitre 2). Quand il y a une forte variation de la densité (comme dans les enveloppes convectives de type solaire), le profil de température mais surtout celui de l'entropie du fluide s'ajuste en fonction de l'efficacité de la convection, une convection très efficace étant quasi-adiabatique (sans perte de chaleur durant l'ascension). De plus dans ce cas, il y a une forte asymétrie entre les panaches descendants (contenant beaucoup de vorticité) et les structures montantes significativement plus larges et lentes. Les simulations numériques sont un outil idéal pour étudier ce processus de transport dans le contexte stellaire. De récents progrès ont été réalisés pour modéliser et décrire la convection turbulente compressible dans les étoiles (Brummell et al. 1996, Stein & Nordlund 1998, Rincon et al. 2005 et chapitres 4 et 6).

1.2 Rotation

La rotation (symbole $\mathbf{\Omega}$) est présente partout dans l'Univers (planètes, systèmes planétaires, étoiles, galaxies, etc...). Son effet sur un système donné (objet, fluide, etc...) dépend de l'amplitude relative entre force centrifuge et force de Coriolis:

$$\mathbf{F}_{Ce} = -\rho\,\mathbf{\Omega_0}\times(\mathbf{\Omega_0}\times\mathbf{r}) \text{ et } \mathbf{F}_{Co} = -2\rho\,\mathbf{\Omega_0}\times\mathbf{v}.$$

La force centrifuge a plusieurs influences sur un objet comme les étoiles, elle peut modifier l'équilibre hydrodynamique, modifier sa forme et rompre l'équilibre thermique dans les zones radiatives. Par exemple, plus le système considéré tournera vite, plus la force centrifuge dominera, jusqu'à éparpiller complètement l'objet si son amplitude dépasse la/les forces de cohésion interne(s) de celui-ci (qui sont par exemple pour un

objet solide, les forces électrostatiques entre atomes et pour une masse de fluide comme une étoile, la force de gravité). Le Soleil tourne plutôt lentement (1 tour / 28 jours), si on le compare par exemple, à la période de rotation de 10 heures de Jupiter, ou même aux autres étoiles dont certaines tournent sur elles même en moins d'un jour voire dans le cas le plus extrême de certains pulsars, dans la gamme des millisecondes. Ses mouvements convectifs sont donc surtout influencés par la force de Coriolis, dont l'effet premier est d'écarter un objet/projectile ou une masse d'air/fluide d'une trajectoire purement rectiligne, en la déviant sur la droite dans l'hémisphère nord et sur la gauche dans l'hémisphère sud.

L'effet le plus frappant de la force de Coriolis est sans aucun doute la création dans l'atmosphère terrestre de cyclones (cf. Figures 1.2 a,b). Il y a alors un faible déséquilibre entre le gradient de pression horizontal et la force de Coriolis et on parle d'écart à équilibre géostrophique (voir Appendice 3.1).

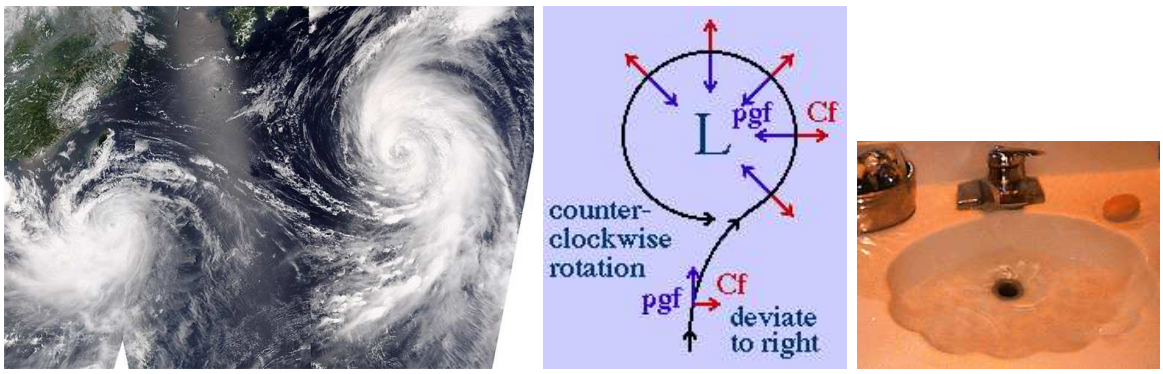

FIG. 1.2 – *Effets de la force de Coriolis dans a) une paire de cyclones dans l'hémisphère nord de la Terre. b) Schéma permettant de comprendre pourquoi alors que la force Coriolis dans l'hémisphère nord fait dévier une masse vers la droite, les cyclones tournent autour d'une dépression contre le sens des aiguilles d'une montre (cf. le site web de A. Fraser: Bad Meteorology), c) un lavabo ce vidant dans le sens des aiguilles d'une montre dans l'hémisphère nord confirmant la petitesse de la force de Coriolis à cette échelle spatiale.*

Dans les étoiles de tels phénomènes "météorologique" existent également, mais, comme sur la Terre (où les cyclones ont toujours un rayon supérieur à environ 100 km), il n'apparaissent pour une vitesse donnée qu'à partir d'une certaine extension spatiale (appelée rayon de Rossby). Dans la zone convective du Soleil, ce rayon est de l'ordre de 30000 Km pour une vitesse de 100 m/s, ce qui permet de distinguer les mouvements ressentant les effets de la rotation (plutôt grandes échelles spatiales) de ceux ne les ressentant pas (plutôt de petites échelles). Bien sûr, la nature turbulente des

mouvements convectifs dans les étoiles altère cet équilibre, et par exemple la circulation méridienne observée dans le Soleil provient d'un tel écart à la géostrophie. Pour les étoiles tournant plus rapidement, la force centrifuge devient importante et elle tend alors à aplatir l'étoile aux pôles, la faisant passer d'une forme sphérique à une forme aplatie (Rieutord 1997).

1.3 Champs Magnétiques

Le mot *magnétisme* vient de Magnes, mot originaire de la ville grecque Magnesia où fut trouvée la pierre d'aimant. Le magnétisme s'intéresse aux phénomènes magnétiques dont la manifestation physique la plus courante se retrouve dans les aimants (cf. Fig 1.3a).

L'Univers étant constitué principalement de gaz sous la forme de plasma ($4^{\text{ème}}$ état de la matière), il s'en suit que l'on retrouve les effets du champ magnétique dans la plupart des objets célestes. En effet, par définition le plasma représente *tout gaz conducteur (ionisé) dans lequel des courants électriques sont libres de circuler*. Dès lors la présence de champs magnétiques est incontournable dans un objet parcouru par des courants, comme Oersted, Faraday et Ampère l'ont démontré expérimentalement au début du $19^{\text{ème}}$ siècle, et Maxwell, quelques décennies plus tard, l'a si élégamment formalisé mathématiquement. Par exemple sur Terre, c'est le champ dit 'géomagnétique' qui agit sur l'aiguille des boussoles et l'oriente vers le nord (cf. Fig 1.3b). Ce champ géomagnétique est certainement dû au cœur liquide de fer au centre de la Terre générant un champ par effet dynamo (cf. §1.4, Glatzmaier & Roberts 1995, Roberts & Glatzmaier 2000). Dans le Soleil, le champ magnétique est plus de 1000 fois plus intense, prenant tour à tour la forme de taches solaires, éruptions, protubérances, points brillants, etc... (voir chapitre 2). Ici il prend son origine dans deux types de dynamo (petites et grandes échelles) au travers des mouvements convectifs et de la forte rotation différentielle présente dans le Soleil (voir §1.4 et chapitre 4). De plus la présence d'un vent et d'un cycle d'activité magnétique dans le Soleil et les étoiles de type solaire, rend particulièrement intéressante l'étude des interactions entre le Soleil et la Terre, notamment avec la magnétosphère. D'ailleurs l'étude de l'interaction magnétique entre deux structures cosmiques magnétisées comme par exemple un système d'étoiles doubles ou une proto étoile et son disque, constitue une autre extension prometteuse du rôle potentiellement joué par le champ magnétique dans la structuration et l'évolution des objets célestes peuplant l'Univers.

Comme l'écrit le grand spécialiste E.N. Parker dans son livre Cosmic Magnetic Fields en 1989:

"Sous plusieurs aspects l'Univers a atteint un âge mûr, sa phase juvénile violente étant derrière lui et ses phases finales de sénilité heureusement encore loin devant lui... Il est donc surprenant, dès lors, que l'examen de l'Univers à certaines échelles révèle tant d'activité. Après 10 milliards d'années, de nouvelles étoiles sont toujours en train d'être créées. Après 5 milliards d'années, le Soleil convecte et éjecte toujours, incapable de se retrouver dans cet âge mûr et tranquille auquel on pourrait s'attendre.[...] Il semble que l'élément responsable pour un aspect si peu calme de notre Univers soit le champ magnétique[4]. Les champs magnétiques sont communs dans les laboratoires, et même dans les maisons, où leurs propriétés sont bien connues; ils sont facilement contrôlables, et utilisés à volonté. Avec les grandes échelles présentes dans l'Univers, cependant, le champ magnétique joue un rôle particulier, assez différent de celui qu'il joue dans les laboratoires. Le champ magnétique se comporte dans l'Univers comme un "organisme", se nourrissant des mouvements créés par les étoiles et galaxies. La présence d'un champ faible résulte dans le fait qu'une petite quantité d'énergie est détournée pour générer plus de champ magnétique, et cette petite diversion est responsable pour l'activité incessante du système solaire, des galaxies, et de l'Univers en général. Sur des échelles astronomiques le champ magnétique possède des caractéristiques qui ne sont pas présentes dans les laboratoires[5]. Le cosmos devient dès lors le laboratoire, dans lequel nous pouvons découvrir et comprendre le champ magnétique et appréhender ses conséquences."

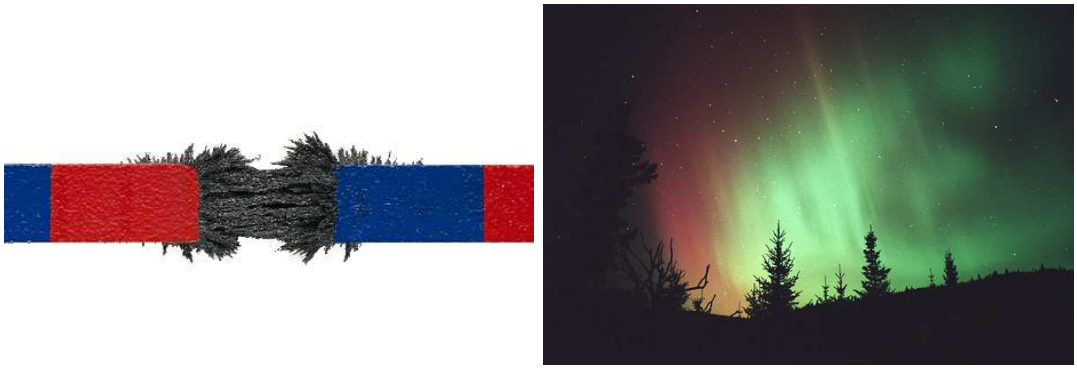

FIG. 1.3 – *a) barreaux d'aimant permanent s'attirant mutuellement, les lignes de champs étant visualisées grâce à de la limaille de fer. b) Aurore boréales dans le cercle polaire, évidence colorée de la présence d'un champ géomagnétique.*

4. bien que la rotation et la turbulence jouent également un grand rôle pour déterminer les propriétés dynamiques des structures cosmiques

Comme le dit si bien Parker, à cause de l'énorme taille caractéristique des conducteurs cosmiques, les courants électriques qu'ils contiennent sont déterminés par auto-induction plutôt que par la résistance électrique. À cause des longs temps présents dans les problèmes cosmiques, les forces mécaniques d'origine électromagnétique, bien que petites, sont capables de produire des effets importants. Pour ces deux raisons, les idées (intuitions) déduites d'expériences traditionnelles[5] sont plutôt trompeuses pour les problèmes s'attachant à comprendre le champ magnétique et son rôle dans l'Univers.

A la présence d'un champ magnétique est associée la force de Laplace qui agit sur les mouvements du plasma:

$$\mathbf{F}_L = \frac{1}{c}\mathbf{j}\times\mathbf{B} = \frac{1}{4\pi}(\boldsymbol{\nabla}\times\mathbf{B})\times\mathbf{B} = \frac{1}{4\pi}\left(-\frac{1}{2}\boldsymbol{\nabla}\mathbf{B}^2 + (\mathbf{B}\cdot\boldsymbol{\nabla})\mathbf{B}\right)$$

On peut décomposer l'effet de cette force en une composante reliée à un gradient de pression magnétique perpendiculairement aux lignes de force et une autre reliée à la tension des lignes de champ magnétique, le long desquelles les ondes d'Alfvén se propagent. Comme dans le cas de la rotation, il est possible de trouver des états d'équilibre entre gradient de pression et champ magnétique, voire avec la force de Coriolis dans le cas d'un système tournant comme le Soleil. On parle alors d'équilibre magnétostrophique (voir Appendice 2.2). Cependant le fort degré de turbulence présent dans les couches externes du Soleil, modifie cette vue quelque peu simplifiée de la magnétohydrodynamique solaire.

1.4 Effet Dynamo

Il est plutôt banal de trouver une dynamo sur un vélo, celle-ci convertissant l'énergie mécanique fournie par la personne en train de pédaler en énergie électrique utile pour allumer l'ampoule du phare. Pour les objets célestes un principe équivalent de transfert d'énergie cinétique en énergie magnétique existe mais il est lié au mouvement du plasma les composant: c'est l'effet dynamo (fluide). Cet effet est vraisemblablement à l'origine du magnétisme de la Terre, de Jupiter, du Soleil, de certaines étoiles et des galaxies (Zeldovich et al. 1983, Parker 1989). Une définition simple peut être: *la propriété qu'un fluide conducteur en mouvement a de pouvoir générer par induction et d'entretenir un champ magnétique contre sa diffusion ohmique.* S'il n'est pas entretenu,

5. il faut cependant noter que beaucoup d'efforts depuis une dizaine d'années ont été dépensé afin de reproduire certains de ces phénomènes magnétiques dans des appareillages expérimentaux d'un nouveau type, tel que les expériences Von-Karman Sodium (VKS) au CEA-Cadarache ou Derviche Tourneur Sodium (DTS) au LGIT à Grenoble (voir chapitre 3).

le champ magnétique diffuse et décroît. Il s'avère que seuls certains écoulements ont la capacité d'amplifier et d'entretenir un champ magnétique, ceci est par exemple le cas des mouvements turbulents convectifs présents dans le Soleil et les étoiles. En effet, la convection turbulente associée à la forte rotation différentielle en latitude et profondeur, présente dans la plupart des étoiles, possède toutes les propriétés d'étirement, de cisaillement, de repliement et d'enroulement des lignes de champ magnétique nécessaires au développement d'un effet dynamo.

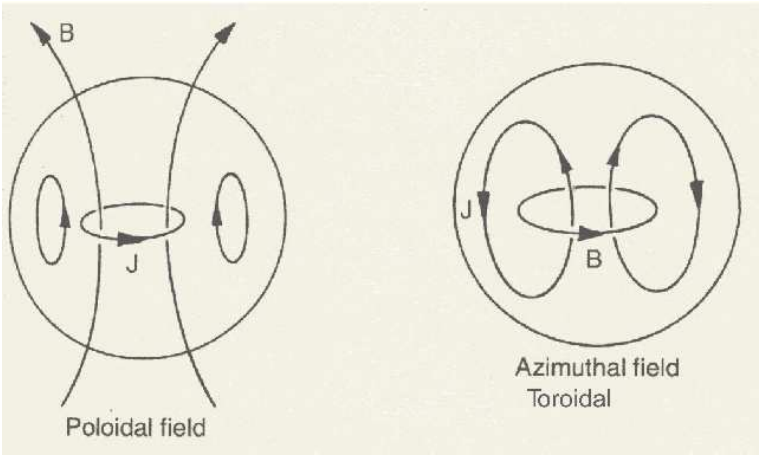

FIG. 1.4 – *Configurations poloidales et toroidales simples du champ magnétique* $\mathbf{B} = \boldsymbol{\nabla}\times(A\hat{\mathbf{e}}_\phi) + B_\phi\hat{\mathbf{e}}_\phi$ *et du courant associé* $\mathbf{J}$ *dans le cas axisymétrique (adaptée de Davidson 2001).*

Dans l'approche classique du champ moyen (Moffatt 1978, Krause & Radler 1980, Parker 1989) deux effets sont principalement invoqués pour expliquer la génération du champ poloidal (i.e le long des méridiens dans une sphère, voir Fig. 1.4) en champ toroidal (i.e le long de parallèles dans une sphère) et vice et versa; ce sont les effets α et ω (voir Fig. 1.5):

- effet α: un coude est produit sur un champ aligné $\mathbf{B}$ suivi d'une rotation créant une "boucle" au travers duquel un courant $\mathbf{J}$ est induit. Cela permet de créer un champ radial à partir d'un champ toroidal $B_{tor} \rightarrow B_{pol}$, mais également un champ toroidal à partir d'un champ poloidal $B_{pol} \rightarrow B_{tor}$.
- effet ω: cisaillement causé par une rotation différentielle génère une composante dans la direction du cisaillement, et convertit le champ poloidal en champ toroidal, $B_{pol} \rightarrow B_{tor}$

L'effet dynamo est essentiellement un effet tridimensionnel, et l'effet α particulièrement. Cowling a même établi un théorème anti-dynamo dans le cas où le champ de vitesse et

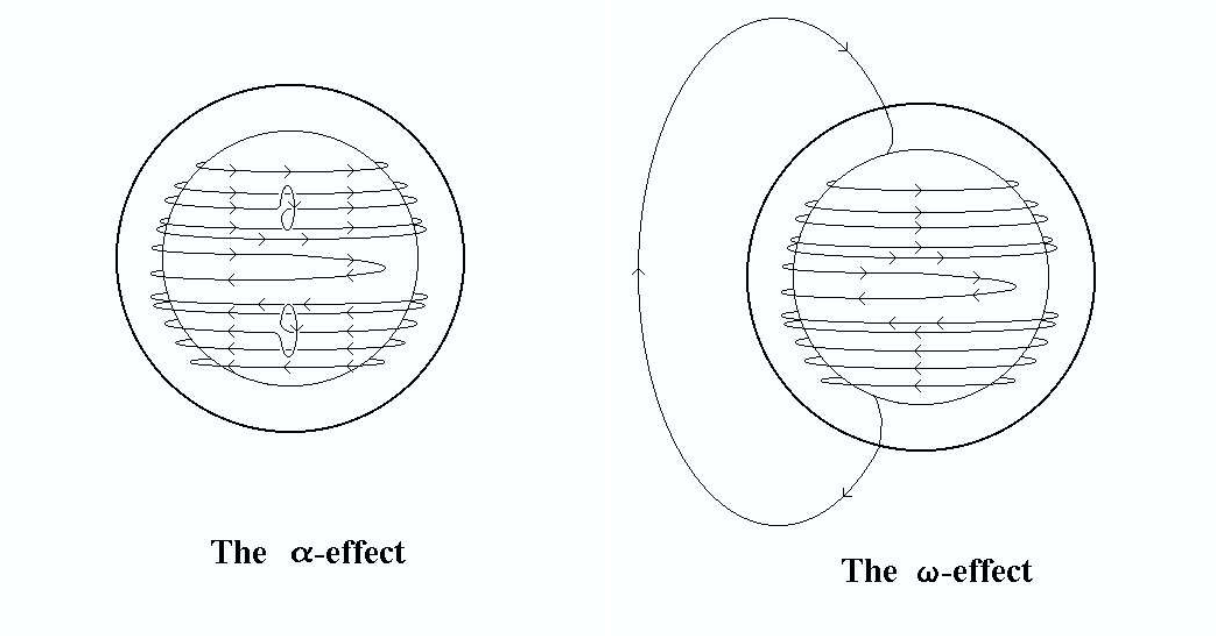

FIG. 1.5 – *Schéma représentant les effets α et ω assurant respectivement la conversion du champ magnétique* $\mathbf{B}$ *de toroidal en poloidal et de poloidal en toroidal (voir Krause & Radler 1981). Notons cependant que l'effet α peut également convertir un champ poloidal en toroidal. C'est le rapport d'amplitude entre l'effet ω et l'effet α à générer un champ toroidal à partir d'un champ poloidal qui désigne en théorie des champs moyens de l'effet dynamo si la dynamo est de type α^2 (petit effet ω) ou $\alpha - \omega$ (crédit Nasa).*

le champ magnétique sont purement axisymétriques. Car l'effet dynamo est plus que l'amplification d'une composante soit toroidale soit poloidale du champ magnétique. En effet il est possible de trouver des écoulements qui amplifieront par exemple B_{tor} via un effet ω mais ne laisseront inchangée la composante poloidale du champ, qui par conséquence décroîtra ohmiquement jusqu'à disparaître. Dès lors l'effet ω ne peut plus s'appliquer au champ magnétique poloidal ce qui résulte en la décroissance de B_{tor} et donc la disparition du champ magnétique. À l'inverse quand il y a régénération des deux composantes du champ (poloidale et toroidale), il y a effet dynamo car les deux composantes du champ magnétique sont entretenues contre l'action dissipative de la diffusion ohmique. Un nombre utile pour caractériser l'efficacité d'un flot à générer un effet dynamo est le nombre de Reynolds magnétique (voir appendice et chapitres 4 et 6). L'amplitude relative entre l'effet ω et l'effet α pour générer un champ toroidal à partir d'un champ poloidal, est ce qui permet de classifier en théorie des champs moyens les dynamos en tant que $\alpha - \omega$, α^2 ou $\alpha^2 - \omega$. On remarque qu'il n'y a pas

de dynamo ω^2, car seul l'effet α permet de régénérer un champ poloidal à partir d'un champ toroidal, dès lors il n'y pas de dynamo possible (à moins d'invoquer un autre effet[6]) sans effet α. Cet effet a largement été étudié dans la littérature spécialisée, et sa définition est très stricte. Dès lors certains des phénomènes de génération de champ magnétique observés dans les simulations non linéaires multidimensionnelles de l'effet dynamo sont difficilement descriptibles dans le vocabulaire de la théorie des champs moyens. Au chapitre 4 et 6 nous reviendrons sur l'existence de différences subtiles pour décrire la génération et le transport de champ magnétique entre les modèles de dynamo reposant sur l'approche champ moyen et ceux reposant sur des simulations numériques non linéaires.

Dans les étoiles, l'activité magnétique est vraisemblablement fonction du type spectral considéré. Cette activité provient certainement de plusieurs types de dynamos (par exemple $\alpha-\omega$ ou α^2 ou turbulente), voire est peut être seulement due à la présence d'un champ fossile. Les conditions permettant d'avoir tel ou tel type d'activité sont vraisemblablement fonction de la répartition en profondeur des zones radiatives et convectives et donc de la masse et de la métallicité de l'étoile considérée (cf. chapitres 2 et 3).

Dans ce manuscrit nous nous efforcerons d'éclaircir à partir de simulations numériques non linéaires et tridimensionnelles le rôle respectif que la convection, la turbulence, la rotation et le champ magnétique jouent pour obtenir la grande diversité de phénomènes (magnétohydro-)dynamiques observés dans les étoiles. Ces simulations numériques de la (magnéto)hydrodynamique des étoiles ont été effectuées dans plusieurs centres de calculs français (CEA-CCRT à Bruyère le Chatel, CNRS-IDRIS à Orsay) et américains (centres NPACI de SanDiego, Pittsburg & Urbana-Champaign) et représentent plusieurs millions d'heures de calculs sur ces machines massivement parallèles.

1.5 Articulation du Manuscrit

• dans la première partie nous situons le travail de recherche dans son contexte scientifique. Nous présentons section 2 un panorama rapide des phénomènes dynamiques observés dans les étoiles, tel que la convection, la rotation et le champ magnétique grâce à la diversité des techniques d'observations utilisées de nos jours, telles que (liste non exhaustive) l'émission X, effets Zeeman et Hanle, imagerie Dopler, rayonnement non thermique. Puis section 3 nous posons le contexte théorique, la théorie des fluides conducteurs ou magnétohydrodynamique, et discutons les évidences numériques

6. comme par exemple celui utilisé dans les dynamos de type transport de flux autrement appelées Babcock-Leigthon (Dikpati & Charbonneau 1999), ou c'est la dissipation des régions actives tiltées à la surface du Soleil qui est la source du champ poloidal, remplaçant ainsi l'effet α classique

et expérimentales de l'existence d'un effet dynamo, afin d'appliquer ce concept aux étoiles. En particulier nous discutons les avantages et inconvénients des modèles de dynamos stellaires déduits de la théorie des champs moyens et de l'intérêt de développer des modèles tridimensionnels et non linéaires comme ceux discuter en deuxième partie pour aller au-delà.

• dans la deuxième partie, nous présentons les travaux de recherche théoriques et numériques effectués depuis des années en dynamique des plasmas stellaires afin de préciser et améliorer notre compréhension des phénomènes dynamiques observés dans les étoiles. Dans la section 4, nous présentons notre étude de la convection solaire, de sa rotation différentielle, de sa circulation méridienne, ainsi que les conditions nécessaires à l'obtention d'un effet dynamo et le retour non linéaire du magnétisme sur l'hydrodynamique. Section 5 nous nous concentrons sur la zone stable radiative du Soleil et principalement sur la tachocline, site présumé de la dynamo solaire globale. Section 6 nous étudions la convection centrale et le magnétisme d'une étoile A, afin d'étendre notre modélisation multidimensionnelle à d'autres étoiles que le Soleil, et analyser les points communs et les différences. Section 7 nous synthétisons les progrès que notre étude nous a permis d'obtenir sur le comportement dynamique des étoiles et discutons les perspectives et les nouvelles pistes à explorer.

Le manuscrit est complété de deux appendices présentant le code anelastic spherical harmonic (ASH) et l'équation du vent thermique dans le cas MHD. Dans les annexes suivantes les pièces complémentaires nécessaires à l'obtention de l'habilitation à diriger les recherches sont présentées.

Première partie

(MagnétoHydro-)Dynamique Stellaire et Effet Dynamo

Chapitre 2

Phénomènes Dynamiques dans les Étoiles

Dans ce chapitre nous allons récapituler brièvement les caractéristiques et propriétés des phénomènes dynamiques observés dans les étoiles, en particulier leur convection, leur profil de rotation et leurs champs magnétiques, avec une attention particulière portée au Soleil. Nous commençons par une description succincte de la structure interne des étoiles et nous exposons les raisons pour lesquelles il est nécessaire de passer à une approche multidimensionnelle.

2.1 Structure Interne des Étoiles

Les étoiles ont une vie riche en événements, de leur naissance dans les nuages moléculaires, en passant par leur phase active sur la séquence principale et jusqu'à la fin de leur vie qui peut parfois être cataclysmique comme dans le cas des supernovae, un large éventail de processus physiques, souvent dynamiques, entre en jeu. Durant ces différentes phases, les étoiles verront leur masse, rayon, luminosité, température, composition chimique, etc... évoluer, et parcourir le célèbre diagramme de Herztsrung-Russell. Afin de décrire les grandes étapes de ce trajet évolutif et comprendre l'intérieur des étoiles, la théorie de la structure interne et d'évolution des étoiles a été développée et exposée dans série d'ouvrages de référence (Eddington 1926, Chandrasekhar 1939, Cox & Giuli 1968, Clayton 1968, Schatzman & Praderie 1990, Kippenhahn & Weiler 1991, Hansen & Kawaler 1995 etc...). Cette théorie repose sur les équations dite de la structure interne, qui caractérise l'équilibre mécanique et thermique de l'étoile en fonction de plusieurs paramètres (voir Appendice 2 pour un résumé des principales équations). En particulier sur la séquence principale (SP) la structure interne des étoiles dépend principalement de leur masse et de leur composition chimique, c'est le "théorème" de

Vogt-Russell qui stipule:

Pour une masse et une composition chimique données la structure interne d'une étoile est unique.

Sur la SP on peut également montrer qu'il existe des relations simples entre la masse et le rayon de l'étoile ($R \sim M^{0.8}$) et sa masse et sa luminosité ($L \sim M^{3.5}$). La séquence principale dure pour les étoiles les plus massives quelques dizaines de millions d'années (étoiles O) et jusqu'à plus de 10 milliards d'années pour les étoiles moins massives (type spectral G et plus tardif). La source principale d'énergie des étoiles sur la SP est le brûlage de l'hydrogène en hélium, soit via les chaînes pp pour les étoiles inférieures à environ 1.3 $M_\odot$, soit via les cycles CNO pour les autres (Clayton 1968). Cette énergie qui doit être transportée vers la surface de l'étoile ne peut le faire efficacement que par rayonnement ou par mouvements macroscopiques (i.e. la convection, cf. §1), la conduction jouant un rôle négligeable dans les intérieurs stellaires.

Figure 2.1 et Table 2.1 nous représente et indique la localisation des zones convectives (et par complémentarité les zones radiatives) en fonction de la masse et du type spectral de l'étoile. Nous voyons que les étoiles de faible masse possèdent toutes une région convective à leur surface s'étendant de plus en plus profondément jusqu'à devenir complètement convective au delà du type spectral M3 ($M \lesssim 0.3 M_\odot$). Cette enveloppe convective est vraisemblablement à l'origine de leur activité magnétique (ou du moins en expliquer une partie), via l'existence d'un effet dynamo (cf. §1.3 et chapitre 4). Dans le cas particulier du Soleil, le rayonnement est dominant du centre jusqu'à $r < 0.713$ $R_\odot$ et la convection entre 0.713 et 1 $R_\odot$ mais ne représente que 2% de la masse de l'étoile (cf. Fig. 2.1). Pour les étoiles intermédiaires comme les étoiles A tardives et F, la surface et le cœur sont convectifs, avec même parfois plusieurs zones très fines en surface (Richard et al. 2001).

$M/M_\odot$	q_c	q_{env}
30	0.56	0
2	0.13	$< 10^{-7}$
1.5	0.07	$< 10^{-5}$
1	0	0.02
0.3	0	1

TAB. 2.1 – *Modèles d'étoiles sur la ZAMS:* 1^{ere} *colonne: masse de l'étoile normalisée à celle du Soleil,* 2^{eme} *col.* q_c *est la fraction de masse contenue dans le coeur convectif,* 3^{eme} *col.* q_{env} *est la masse contenue dans l'enveloppe convective.*

Vu la diversité de la distribution relative des zones convectives ou radiatives dans

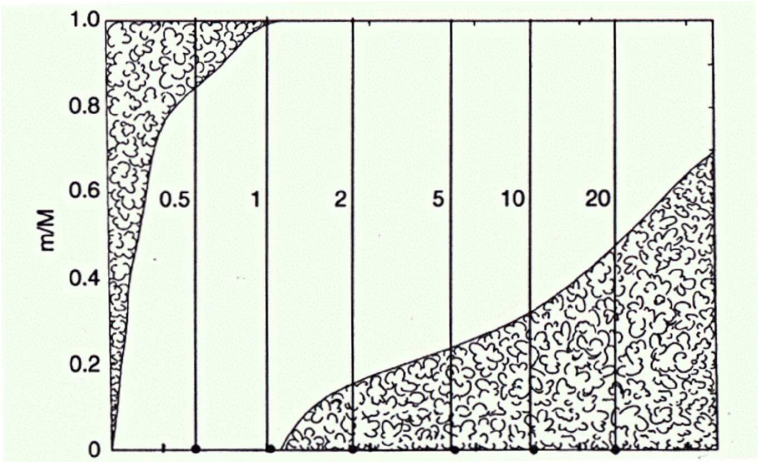

FIG. 2.1 – *Localisation des zones de convection en fonction de la masse des étoiles (adapté de Hansen & Kawaler 1995)*

les étoiles, il est naturel de penser que celle-ci va avoir un impact direct sur le type et la localisation des circulations et/ou instabilités présentes dans les étoiles. Ces processus macroscopiques introduisent des corrections dynamiques, parfois importantes, qu'il faut prendre en compte pour améliorer la description quasi-statique sur laquelle repose le modèle standard de la structure interne des étoiles et dont le théorème de Vogt-Russell dérive.

2.2 Avantages et Limitations de la Modélisation 1-D des Étoiles

L'approche traditionnelle de la théorie de la structure interne basée sur l'équilibre thermique et mécanique (quasi-statique) des étoiles est très utile, et encore pour l'instant incontournable, pour suivre l'évolution longue d'une étoile. Des théorèmes comme celui de Vogt-Russell ou les relations sur le rayon et la luminosité en fonction de la masse discutés précédemment, sont pratiques pour peindre un premier tableau des étoiles et de leur diversité. La précision avec laquelle le modèle standard du Soleil reproduit la structure radiale déduite des inversions héliosismiques (voir par exemple Turck-Chièze et al. 1993, Christensen-Dalsgaard et al. 1996, Brun et al. 1998), tout comme la qualité des prédictions d'isochrones et de tracés évolutifs pour les amas d'étoiles, confirme sans aucun doute le bien fondé de cette théorie. Cependant cette description "quasi-statique" montre des limites quand il s'agit de décrire plus en détails les processus dynamiques présents dans les étoiles. Par exemple les propriétés dyna-

miques parfois hautement turbulentes des étoiles de la séquence principale ne sont pas décrites précisément. Un exemple typique vient des étoiles de masse supérieure à 1.3 M pour lesquelles le mode de production d'énergie sur la SP provient du cycle CNO (Clayton 1968). La forte dépendance en température des taux de réactions nucléaires de ce cycle impose la présence d'un cœur convectif car le rayonnement seul ne parvient pas à évacuer l'énergie produite. Actuellement la description physique du cœur convectif repose sur l'approximation de la longueur de mélange ou MLT à une dimension. Il parait clair que cette approche locale peut être mise en difficulté s'il s'agit par exemple de décrire précisément les mouvements convectifs turbulents et non-locaux, et comment ils pénètrent dans les zones radiatives avoisinantes (cf. chapitre 6). Or de tels mélanges peuvent alimenter en hydrogène "frais" le cœur nucléaire et ainsi en modifier sa composition et son évolution et donc la structure et l'évolution de l'étoile tout entière. De plus les équations de la structure interne ne peuvent être utilisées efficacement, en tout cas dans leur version la plus simpliste, sur les autres phases de la vie d'une étoile comme sa formation et son évolution vers la phase géante ou super géante, car d'autres paramètres importants rentrent en jeu pour déterminer l'état final atteint, comme la quantité de perte de masse, le couplage à un disque, l'influence du champ magnétique ou de la rotation de l'étoile etc...

Nous voyons donc qu'afin de progresser dans notre description des étoiles il faut développer des modèles permettant de prendre en compte de tels phénomènes dynamiques. Plusieurs approches ont été menées. Par exemple, de réels progrès ont été effectués pour inclure à travers soit de prescriptions analytiques, soit par l'ajout d'équations supplémentaires aux équations de la structure interne, l'effet de la rotation, des mélanges qu'elle induit, ou la présence d'une tachocline, dans les modèles d'évolution des étoiles (Zahn 1992, Pinsonneault 1997, Richard et al. 1996, Talon 1997, Maeder & Zahn 1998, Brun, Turck-Chièze et Zahn 1999, Meynet & Maeder 1997, Mathis & Zahn 2004). En particulier, le rôle crucial joué par les mélanges macroscopiques pour expliquer la sous abondance du lithium (^{7}Li) observée dans les atmosphères des étoiles a été démontrée de façon convaincante (Brun et al. 1999, Cayrel 1998). Les modèles 1-D commencent également à considérer certains effets liés au champ magnétique (Maeder & Meynet 2003, Couvidat, Turck-Chièze & Kosovichev 2003, et Mathis & Zahn 2005). Une autre approche repose sur la simulation numérique multidimensionnelle. Cette approche ambitieuse permet soit de fournir des recettes/prescriptions rendant ainsi plus fidèlement compte du phénomène considéré dans les modèle d'évolution 1-D, soit d'étudier le processus physique directement, comme par exemple l'effet dynamo ou la convection (cf. chapitres 3 à 6).

Bien évidemment la communauté scientifique veut développer à terme des modèles

2-D et 3-D suivant l'évolution dynamique des étoiles sur des temps longs. Pour réaliser ce saut conceptuel entre une description monodimensionnelle d'une étoile et une vision multidimensionnelle et magnétohydrodynamique, nous sommes aidés et guidés par la mise à notre disposition simultanée d'une part d'observations de très haute qualité et résolution tant spectrale, que photométrique (permettant d'appliquer des méthodes d'astérosismologie), et d'autre part par l'accès à des ordinateurs de plus en plus performants, dit massivement parallèles. En particulier l'héliosismologie, qui étudie les ondes acoustiques du Soleil (i.e les oscillations de 5 min), depuis maintenant plus de 20 ans, impose de fortes contraintes non seulement sur la dynamique de la surface du Soleil mais aussi sur son intérieur comme la base de la zone convective ou le profil de rotation (Gough & Toomre 1991, Thompson et al. 2003, Couvidat et al. 2003). Vu le succès de l'héliosismologie pour contraindre la dynamique solaire (voir plus bas), de grandes attentes reposent sur l'astérosismologie et le satellite Corot (Baglin 2003).

Le calcul tridimensionnel de l'évolution (sur des échelles de temps aussi courte que la minute) et de la structure interne des étoiles incluant l'aspect dynamique, turbulent et dépendant du temps présent dans les étoiles, est un problème difficile, dit numériquement *raide*, vu les nombreuses décades d'échelles spatiales et temporelles que cela représente, et de tels calculs restent pour l'instant encore hors de portée. Des codes magnétohydrodynamiques globaux comme le code ASH présenté ici peuvent servir de soutien à l'effort consistant à développer de tels codes, en précisant les propriétés statistiques par exemple de la turbulence MHD des zones convectives afin qu'elles soient incorporées dans des codes d'évolution multidimensionnels à travers une version simplifiée des équations de la magnétohydrodynamique permettant de s'affranchir de pas de temps trop courts ou de la modélisation d'échelles trop petites. Des premiers efforts dans ce sens ont vu le jour ces dernières années comme le projet ESTER en France (Rieutord et al. 2004) ou DJEHUTY aux USA (Bazán et al. 2003, Eggleton et al. 2003).

2.3 Convection, Rotation et Activité Magnétique

L'observation multi-longueur d'onde de la surface du Soleil a toujours révélé nombre de phénomènes variables et dépendant du temps, surtout liés à sa granulation, à son activité magnétique et à sa rotation, fournissant autant de contraintes pour le physicien solaire. De nos jours, de tels observations commencent à apparaître pour d'autres étoiles, notamment dans les rayons X et l'ultra violet lointain, grâce entre autres aux satellites Einstein, ROSAT et EUVE, cette gamme de fréquences électromagnétiques représentant un bon marqueur de l'activité magnétique (Schmitt 2004 et sections sui-

vantes). Il est également possible de déduire le profil de rotation des étoiles, par l'utilisation de techniques comme l'imagerie Doppler ou la spectroscopie haute résolution et dans un futur proche l'astérosismologie. Nous proposons ici de faire un rapide panorama sur les connaissances actuelles des processus dynamiques présents dans le Soleil et les étoiles. Plusieurs conférences ont eu lieu ces dernières années sur ce thème et les relations/connections Soleil-Étoiles (liste non exhaustive): XIIth cool stars meeting, Magnetic fields across the H-R diagram, IAU Symposium 215 on stellar rotation, IAU Symposium 219 on stars as suns: activity, evolution and planets, Magnetism and activity of the sun and stars, SoHO14/GONG04 helio- and asteroseismology: towards a golden future ..., démontrant ainsi le dynamisme de ce champ de recherche. Les papiers suivants permettent de faire une bonne synthèse de nos connaissances actuelles sur la dynamique et l'activité des étoiles: Mestel 2001, Basri 2003, Dupree 2003, Mathys 2003, Donati 2003, Landstreet 2003, Strassmaier 2004 et Schmitt 2004.

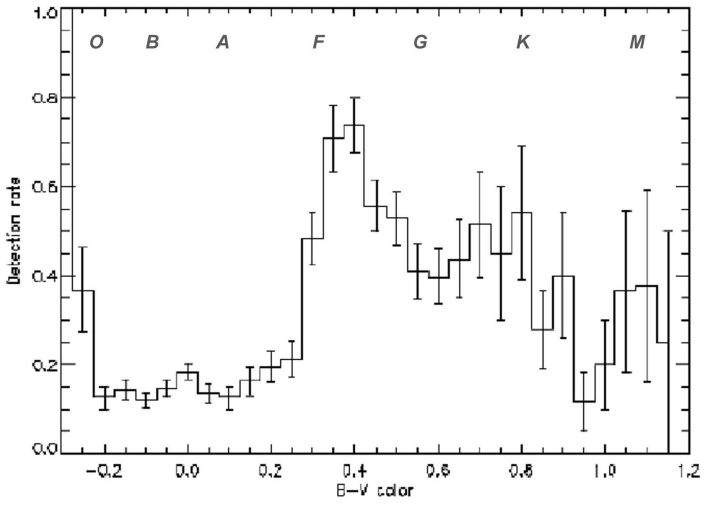

FIG. 2.2 – *Pourcentage de détection dans la gamme des rayons X "mous" en fonction de l'indice de couleurs B-V et du type spectral (approximatif) (adapté de Schmitt 2004)*

Sur la figure 2.2 nous représentons le taux de détection dans la fréquence des rayons X mous de l'activité stellaire en fonction de l'indice de couleur (B-V), auquel j'ai ajouté le type spectral (Schmitt 2004). Le taux de détection varie de 100% dans les étoiles O, à 10-20% pour les étoiles B-A, 70% pour les étoiles F et ensuite cela devient de plus en plus difficile vers les types spectraux plus rouges. La première chose qui frappe à la vue de cette figure, c'est effectivement l'absence presque totale de détection dans la gamme d'étoile de type spectral B et A. Cette particularité s'appelle le "trous des étoiles A", et son origine est certainement liée à l'absence de zone convective de surface

dans ces étoiles. En effet comme nous l'avons vu plus haut, la répartition des zones radiatives et convectives est modifiée entre autres choses par la masse et la métallicité de l'étoile, or il s'avère que c'est justement aux alentours de cette masse ($\sim 1.5 M_{\odot}$) que les étoiles perdent leur enveloppe convective tout en ayant un cœur convectif de plus en plus important. Dès lors l'absence d'une zone convective de surface prive l'étoile d'une source potentielle de magnétisme et d'activité liée à l'effet dynamo qu'une telle turbulence de surface peut générer. À l'inverse les étoiles de type F tardif jusqu'à M en passant par les étoiles de type solaire montrent une forte activité X, et possèdent toutes une convection de surface. La lente décroissance du taux de détection du type G au type M est due à l'effet cumulé d'une taille de plus en plus petite des étoiles observées et du niveau limité de sensibilité du détecteur sur ROSAT, et non pas à cause de l'absence de magnétisme comme pour les étoiles A. Il semble donc se dégager une première classification pour l'existence de phénomènes dynamiques intenses à la surface des étoiles de la séquence principale entre les étoiles possédant une zone convective de surface et celles n'en possédant pas. Dans les sections suivantes nous détaillons un peu plus en fonction du type et de la phase d'évolution des étoiles nos connaissances actuelles sur leurs processus dynamiques.

2.3.1 Le Soleil et les Étoiles de Type Solaire

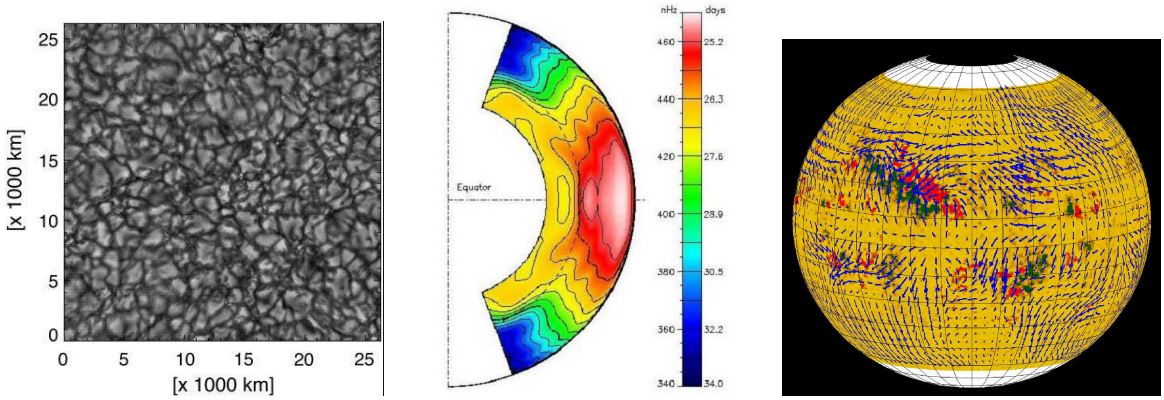

FIG. 2.3 – *Granulation (observation pic du midi), rotation différentielle de surface (inversion héliosismique réseau GONG, Harvey et al. 1996) et mouvements de surface (SubSurface Weather, SSW) solaire (Haber et al. 2002)*

La proximité du Soleil nous a permis d'accumuler beaucoup d'informations sur sa convection, son profil de rotation et sur les différentes facettes de son magnétisme. A sa surface le Soleil possède une zone convective hautement turbulente, avec un nombre

de Reynolds $Re \sim 10^{15}$, avec toute une large gamme d'échelles spatiales et temporelles parcourant plus de 6 ordres de grandeurs (cf. Table 2.2). En particulier sa surface est couverte de motifs convectifs (de taille 1 Mm), appelés granules qui ont un temps de retournement de 5-10 minutes (cf. Figure 2.3), et qui sont vraisemblablement à l'origine des ondes sonores (également appelés modes p) utilisées par l'héliosismologie pour sonder la structure et la dynamique interne du Soleil (Gough & Toomre 1991).

Description	L	τ
Éruptions, trous coronaux, CMEs:	200+ Mm	varies entre qqles jours et qqles mois
Cellules géantes?:	100-200 Mm	10-20 jours
Supergranulation:	30-50 Mm	20 heures
Mésogranulation??:	7-10 Mm	2 heures
Granulation:	1-2 Mm	5-10 mins
Lignes intergranulaires, points magnétiques brillants, diffusion:	$< 10^3$ km	varies entre qqles minutes et qqles heures

TAB. 2.2 – *Taille et durée de vie caractéristiques des processus dynamiques à la surface du Soleil (Rast 2003, Roudier et al. 2003, Stix 2002). Le nombre de points d'interrogation indique le degré d'incertitude sur l'existence réelle dans la convection solaire de cette échelle.*

La puissance du diagnostic héliosismique a permis de faire de grandes avancées dans notre compréhension de l'intérieur du Soleil. Figure 2.3b nous représentons la rotation différentielle en fonction de la latitude et du rayon dans le plan méridien obtenue par inversion des données héliosismiques du réseau sol GONG (modes p globaux, Harvey 1996). On constate deux choses: 1) la rotation est différentielle en surface, avec un contraste $\Delta\Omega/\Omega_0$ de 30%, l'équateur tournant plus vite que les pôles, et dépend peu du rayon à moyenne latitude, et 2) la rotation devient rigide à l'intérieur jusqu'à 0.2 R (Thompson et al. 2003, Couvidat et al. 2003), tournant en moyenne en 28 jours. La transition d'un mode de rotation à l'autre se fait dans une couche mince de fort cisaillement radial en vitesse appelée tachocline (Spiegel & Zahn 1992 et chapitre 5).

Ce profil de rotation, dès sa version la plus rudimentaire obtenue vers la fin des années 1980, a révolutionné les modèles de dynamo solaire de l'époque; ceux-ci reposés sur un modèle de rotation différentielle au profil cylindrique qui ne correspond pas à la réalité excepté à l'équateur. Très tôt on a su que le Soleil tournait différentiellement à sa surface grâce au suivi des taches solaires au cours du temps (voir plus loin), mais aucune information sur la rotation interne du Soleil n'était disponible, et donc les théoriciens avaient choisi le profil à priori le plus intuitif. Cette "révolution" a totalement relancé

la problématique de la dynamo solaire et forcé la communauté à repenser le modèle en particulier en prenant en compte l'existence d'une tachocline (voir chapitre 3 et 4 et Brun, Miesch & Toomre 2004).

Le développement rapide de techniques sismiques locales (temps-distance, diagramme en anneaux, etc) et la mise en service en 2008 du satellite SDO devrait permettre de progresser encore plus. Nous montrons en Figure 2.3c les courants de surface solaire déduits grâce à une méthode locale dite de diagramme en anneaux à partir de données MDI (Haber et al. 2002). Ces méthodes locales (diagrammes en anneaux, temps-distance, holographie) permettent de déterminer la circulation méridienne (de l'ordre de 25 m/s) ou l'impact du champ magnétique sur les courants jusqu'à une profondeur de 20-30 Mm. Elles confirment l'interaction permanente qui existe entre mouvements moyens, fluctuants et le champ magnétique. Durant le dernier cycle d'activité (numéro 23), Haber et al. (2002), ont mis en évidence l'apparition d'une deuxième cellule dans l'hémisphère nord pendant la période de maximum. L'image d'une seule cellule méridienne parcourant toute la zone convective est quelque peu écornée, ce qui peut poser des problèmes à certains modèles de dynamo (cf. chapitre 3 et Dikpati et al. 2004).

En effet, accompagnant cette convection de surface turbulente et la forte rotation différentielle, l'activité magnétique du Soleil est très intense et variée, comme ses taches solaires, sa couronne, ses éjections de masse coronale (CME),... (Figure 2.4). Dans la liste suivante nous avons récapitulé la plupart des points importants (ainsi que Table 2.2):

- Un cycle total de 22 ans (dit de Schwabe), 11 ans pour les taches solaires, une modulation sur l'amplitude des cycles de 90-100 ans (Gleissberg) et l'existence de grand minima d'activité tous les 200 ans (Maunder, Sporer),
- Dynamo grandes et petites échelles, avec pour cette dernière la présence de points brillants et de tout un réseau intergranulaire de flux magnétique,
- Diagramme papillon du champ toroidal (des taches solaires/ régions actives) restreint dans une bande équatoriale $\pm 35°$, avec semble-t-il des longitudes actives séparées de 180 deg, sites privilégiés d'émergence des nouvelles régions actives,
- Tilt de $10°$ ($4°$) des régions bipolaires à $35°$ ($10°$) (loi de Joy) par rapport à une direction est-ouest, polarité inversée entre hémisphères nord et sud pour le champ toroidal et pour la tache qui précède son groupe dipolaire (loi de Hale)
- Un champ poloidal migrant des moyennes latitudes aux pôles
- Un déphasage (quadrature) entre le champ de surface aux pôles avec le champ toroidal en profondeur, de sorte que le champ polaire se renverse ($- \rightarrow +$) quand Btor est maximal ($+$)

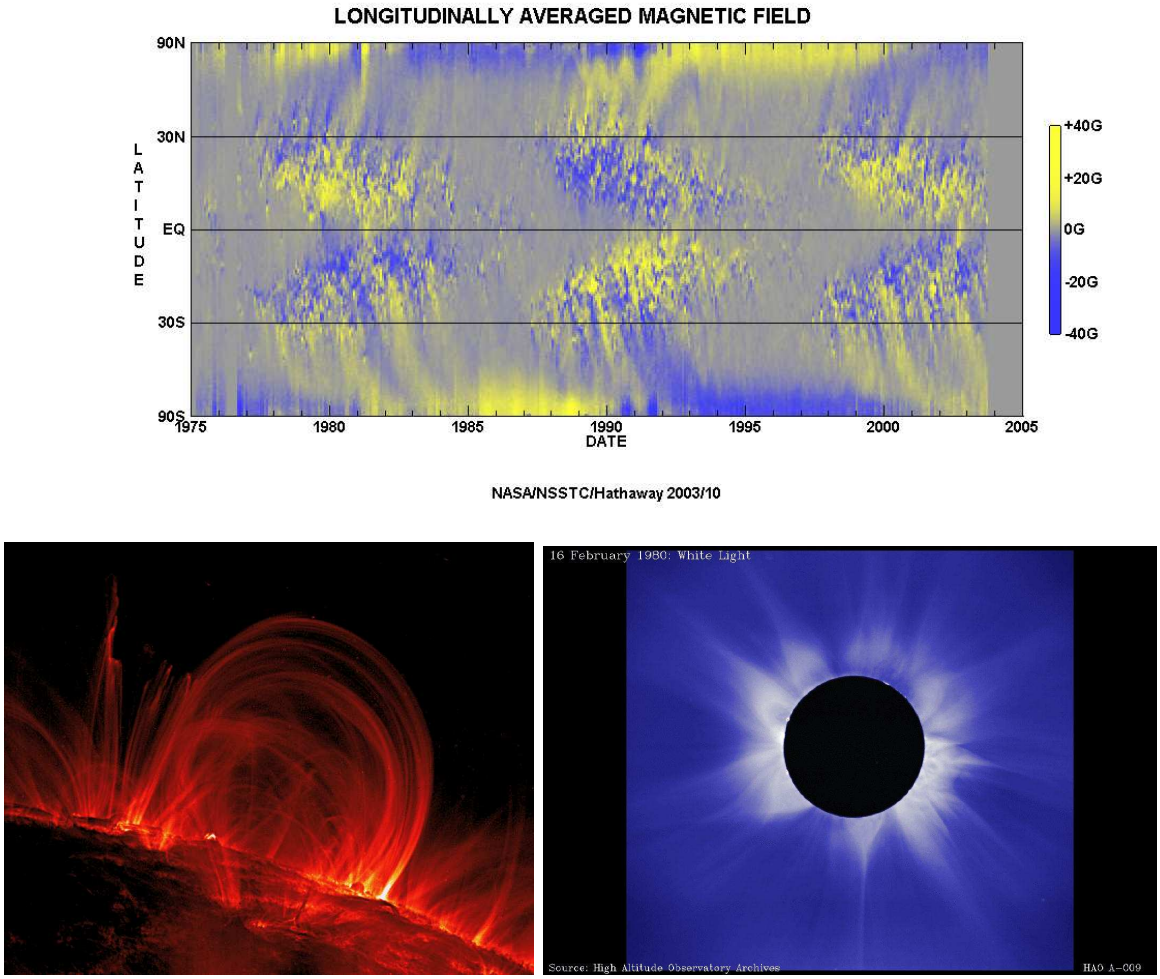

FIG. 2.4 – *Différentes manifestations du magnétisme solaire: Diagramme papillon des taches solaires entre* $\pm 35^{\mathrm{deg}}$ *de latitude (Hathaway, NASA), boucles magnétiques (satellite Trace), couronne solaire lors d'une éclipse totale en 1980 (NCAR/HAO)*

- Btor $3\,10^3$ G observé dans l'ombre des taches solaires (évaluer indirectement à $10^4 - 10^5$ G dans la tachocline),
- Bpol 10 G aux pôles en surface
- une couronne chaude ($\sim 1 - 2\,10^6 K$) étendue se transformant en vent solaire lent ou rapide (au dessus des trous coronaux), le tout délimitant l'héliosphère.

Notre connaissance de l'existence de phénomènes ou d'irrégularités à la surface du Soleil remonte à Galilée (début du 17^{eme} siècle), mais leur description en tant que manifestation visible d'un champ magnétique interne que beaucoup plus récemment. L'identification d'un cycle de 11 ans des taches solaires, s'accompagnant d'un ren-

versement de la polarité du champ magnétique, et se propageant vers l'équateur, le tout constituant un cycle de 22 ans remonte aux années 1850-1930 (Hale, Sporer). Grâce à l'analyse du carbone ^{14}C dans les arbres et du béryllium ^{10}Be dans les carrotages profonds de glace, Beer (1998) a pu reconstruire l'activité magnétique solaire sur $\sim$10000 ans, confirmant l'existence de cycles sur une longue période et même durant les grands minima d'activité comme celui de Maunder en 1650-1715 et Sporer (1420-1530). D'après les observations, il semble donc que dans le Soleil il y ait deux types d'activité magnétique, une globale et cyclique, et une locale et irrégulière. Pour expliquer cet aspect double de l'activité solaire, il semble qu'il faille considérer deux types de dynamo, une aux grandes échelles (pour le cycle de 22 ans, le diagramme papillon) et une aux petites échelles (points brillants, flux magnétique petites échelles[7], voir par exemple Cattaneo & Hughes (1996, 2001), Judge (2003), Brun et al. (2004), §3.3 et chapitre 4. Il semble assez clair qu'une grande partie de l'activité magnétique intense de surface du Soleil (ses éruptions, et autres CMEs) est dûe à l'effet déstabilisant de la convection et est fortement liée à l'organisation interne du champ. Il y a par exemple typiquement plus de CME dans la phase de maximum d'activité qu'en période de minimum. L'existence d'un vent solaire permanent, accompagné de bouffées explosives (les CMEs) en période de maximum (une sorte de tempête dans un vent), fait que la Terre est directement affectée par le Soleil. On parle des relations Soleil-Terre, et il est crucial de comprendre la dynamo interne afin d'expliquer et d'anticiper les phénomènes éruptifs solaires les plus violents. Intégrer dans une vue globale l'aspect interne et externe de la dynamique solaire et plus tard stellaire constitue certainement un des défis des années à venir.

Comparée au Soleil, notre connaissance observationnelle des processus dynamiques présents dans les autres étoiles peut paraître rudimentaire, mais elle renferme en fait beaucoup d'informations utiles qui permettent de prendre du recul par rapport à l'énorme quantité et complexité des observation solaires. On sait par exemple qu'il existe des taches stellaires, que celles-ci peuvent couvrir une large fraction de la surface de l'étoile (bien au delà de la couverture maximale de 1% atteinte durant le maximum d'activité solaire) et être présentes aux pôles, atteignant même vraisemblablement une couverture quasi totale. Cet extrême recouvrement est fortement relié à la vitesse de rotation et peut même se traduire par une saturation des principaux indicateurs du magnétisme stellaire (comme l'émission X).

O.C. Wilson a commencé dans les années 70 un programme systématique d'observations d'étoiles solaires au sens large comprises entre le type spectral F2 et M2,

7. ce flux pourrait être bien plus important pour structurer le champ coronal qu'initialement pensé (Schrijver & Title 2003)

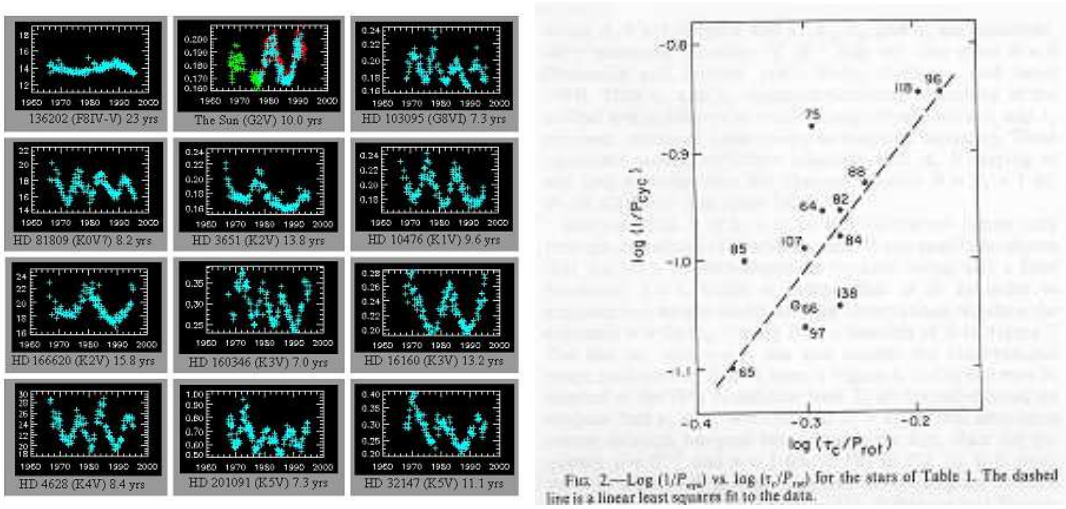

FIG. 2.5 – *a) Échantillon d'étoiles observées dans le programme HK au mont Wilson (USA), commencé dans les années 70 par Wilson (1978) et continué par Baliunas et al. (1995). Plus de 111 étoiles ont été observées allant du type F2 au type M2. b) Forte corrélation entre la période du cycle des étoiles de type solaire avec le nombre de Rossby pondéré du temps de retournement convectif à la base de la zone convective.*

dénommé HK, en référence aux deux raies du calcium une fois ionisé CaII, très bons traceurs de l'activité magnétique des étoiles (Wilson 1978). En 1995, Baliunas et collaborateurs, ont analysé et comparé les 111 étoiles de ce programme plus le Soleil (voir Figure 2.5a). Il ressort de cette étude que parmi les 111 étoiles, 31 possèdent un signal plat ou linéaire, 29 une activité variable irrégulière, et 51 plus le Soleil un cycle magnétique, variant entre 7 et 15 ans. Il a été montré par Noyes et al (1984) que dans ces étoiles lactivité dépend de la rotation et du temps convectif à la base de la zone convective, τ, via le nombre de Rossby (stellaire) $R_{os} = P_{rot}/\tau$, alors l'indicateur $< R_{HK} >= \tau/P_{rot}$ (voir Figure 2.5b). Une telle corrélation avait été proposée par Durney et Latour (1978) à partir de considérations théoriques sur le modèle de dynamo $\alpha - \omega$ (voir chapitre 3). Cette relation traduit que le nombre dynamo $D = R_\alpha R_\omega$, où $R_\alpha = \alpha_0 L/\nu$ et $R_\omega = \Omega_0 L/\nu$ sont les nombres de Reynolds associés aux effets α et ω (cf. chapitre 3), soit inversement proportionnel à R_{os}^2.

Plus récemment une base observationnelle en rayons X, Nexxus (Schmitt 2004), a collecté plus de 1333 étoiles, dans une zone autour du Soleil s'étendant respectivement à 14, 12 et 6 pc, dans les gammes spectrales F, G, K, et M. Près de 95% des étoiles F, G, K et M qui ont été observées possèdent une activité et toutes possèdent une couronne chaude (pouvant atteindre des températures bien supérieures à celle du Soleil 10^7 vs 2 $10^6 K$). On constate une saturation de l'émission X au delà d'une vitesse de rotation,

celle ci étant égale à 35 km/s pour les étoiles G et de 10 km/s pour les étoiles K. Toutes les étoiles analogues au Soleil émettent en X, il n'y a pas de soleils X sombres, du moins dans notre voisinage proche. Je désire d'ailleurs faire un aparté sur la possible existence d'étoiles réellement identiques au Soleil, des vraies "jumelles" en quelque sorte. Dans notre galaxie la Voie Lactée, il y a environ 2.6 milliards d'étoiles de type spectral G sur un total de 400 milliards, dont 1 milliard d'étoiles G2V (Strassmaier 2004). Cependant en pratique il y a très peu d'analogues/jumeaux solaires dans un rayon de 25 pc alors que cela devrait être le contraire! Les deux meilleurs candidats sont $18Sco$ et $51Peg$, il semble donc que le Soleil soit tout de même un peu particulier...

La présence de ce fort magnétisme organisé à grande échelle pour la plupart des étoiles de type solaire, implique que le champ magnétique exerce un fort freinage via le vent stellaire au rayon d'Alfvén (de l'ordre de $10R_*$), quand les particules composant le vent (principalement des protons, des électrons et des noyaux α) se désolidarisent des lignes de champ. Cela résulte en une dépendance temporelle du taux de rotation $\Omega_0 \propto t^{-1/2}$, pour $t > 600$ Mans sur la SP (Skumanich 1972). Le profil de rotation de surface, déduit soit par le suivi des taches stellaires, soit par la spectropolarimétrie, indique un certain degré de rotation différentielle (Donati 2003, Reiners & Schmitt 2003). Donahue et al. 1996 ont même mis en évidence une relation entre $\Delta\Omega$ et Ω_0 ($\Delta\Omega \propto \Omega_0^{0.7}$), mais tout le monde ne semble pas d'accord avec la robustesse de cette relation car plusieurs types d'étoile (de F à K) auraient été mélangés pour déduire la loi. Il semble en fait ressortir d'une étude plus récente que $\Delta\Omega$ dépend du type spectral de l'étoile, et est d'autant plus grand que l'enveloppe convective est étroite (que l'étoile est chaude jusqu'à la frontière en masse $\lesssim 2M_\odot$ ou l'enveloppe convective disparait, cf. Barnes et al. 2005, Reiners 2005). De cette étude sur un échantillon de 10 étoiles dont on distingue le type spectral la relation suivante apparaît: $\Delta\Omega \propto \Omega_0^{0.15}$. Il est vraisemblable que cette relation s'affinera dans les années à venir car pour l'instant les observations manquent encore de cohérence entre les différents groupes. Une autre caractéristique de la rotation différentielle de ces étoiles est qu'elle est plus faible en présence de magnétisme ce qui semble être aussi le cas du Soleil (Eddy et al. 1976, Ambroz 2002, 2005) et les simulations numériques (voir chapitre 4 et Brun 2004). Comme dans le cas de la dynamo la plus simple, dite $\alpha - \omega$, il est nécessaire d'avoir une forte rotation différentielle, on comprend bien qu'il doit y avoir une interaction non linéaire subtile entre rotation, convection et champ magnétique. Finalement un autre élément important de la dynamique interne des étoiles ayant des conséquences directes sur leur activité externe, est leur circulation moyenne. En effet elle peut naturellement réguler le cycle magnétique en imposant le temps de recirculation (ventilation) du flux magnétique dans la zone convective.

2.3.2 Étoiles Massives

Par massives, on entend les étoiles possédant un cœur convectif développé, donc pour des masses supérieures à $\sim 1.5 M_{\odot}$. Comme nous l'avons déjà discuté précédemment, l'absence d'une enveloppe convective de surface pour ce type spectral d'étoiles (excepté pour les étoiles A tardives) implique qu'elles sont différentes des étoiles de type solaire du point de vue observationel et dynamique.

Étoiles B & A

On les appelle étoiles du milieu de la séquence principale depuis plus d'un siècle vu leur position dans le diagramme HR, leur masse étant comprise entre 1.5 et 10 $M_{\odot}$. Ces étoiles ont été beaucoup étudiées, notamment les rares ($\sim 15\%$) qui possèdent un champ magnétique. Souvent ces étoiles possèdent également des anomalies d'abondances et on les regroupe dans la classe des étoiles CP (chemically peculiar, Moss 2001). Le champ magnétique de ses étoiles est généralement stable sur de longues périodes mais présente souvent une forte modulation. Il est probable qu'un champ oblique par rapport à l'axe de rotation puisse reproduire cette modulation (Mestel 1999, 2001), cependant il faut dès lors expliquer l'origine de cette oblicité. La structure du champ magnétique de ces étoiles est plutôt dipolaire, bien que la composante quadrupolaire et certains multipoles plus élevés peuvent aussi être importants (Landstreet & Mathys 2000). L'amplitude du champ est de l'ordre du kG voire au delà. Un panorama de la diversité et des énigmes entourant les étoiles A peut être trouvé dans Wolff (1983). Récemment, Landstreet (2003) a montré que les étoiles A avec champ magnétique tournent plus lentement en général mais il y a des exceptions. Hubrig et al. (2000) semblent trouver une corrélation entre apparition d'activité magnétique et âge de l'étoile, les étoiles plus âgées étant généralement plus actives, mais à nouveau il y a des exceptions et cet effet de sélection par l'âge est loin d'être systématique ou démontré (Pöhnl et al. 2005). Auriere al. (2003) en utilisant l'instrument Musicos, ont pu déduire les 4 paramètres de Stokes (I, Q, U, V) et ainsi dériver la topologie complexe du champ B (au delà du dipole) des étoiles Ap/Bp. En considérant l'intensité de la convection présente dans les cœurs de ses étoiles, on peut légitimement s'attendre à ce qu'il y ait un effet dynamo dans ceux ci. La raison pour laquelle nous ne voyons pas de champ magnétique dans toutes les étoiles A (puisqu'elles possèdent toutes un cœur convectif), peut être dûe, soit à un biais observationnel (sensibilité), mais c'est peu probable, soit alors à la difficulté que le champ magnétique interne généré dans le cœur émerge à la surface (cf. chapitre 6, MacGregor & Cassinelli 2003, et Brun et al. 2005). Il n'est pas clair si ces étoiles possèdent une couronne, mais certaines étoiles B tardives et A pourraient

connaître des éruptions (voir aussi sous section suivante). Actuellement l'explication la plus probable pour expliquer le magnétisme est l'existence d'un champ fossile dans l'enveloppe radiative (Moss 2003), mais la possibilité d'avoir un effet dynamo dans cette enveloppe est aussi invoquée (Spruit 2002, McDonald & Mulan 2004). Une dernière alternative, serait liée à l'existence d'un compagnion actif de plus faible masse autour de ces étoiles, ce qui dès lors pourrait également expliquer le faible taux de détection (d'une activité), puisque toutes ces étoiles n'en posséderaient pas.

Étoiles O

Ces étoiles font plus de 10 $M_\odot$ et ont une durée de vie très courte. Elles sont dans une classe à part car leur luminosité X est déjà très supérieure à celle des autres étoiles, expliquant ainsi pourquoi on constate sur la figure 2.2 une remontée du taux de détection pour ce type d'étoiles. On pense généralement qu'une partie de l'activité observée vient des reconnections dans le fort vent radiatif que possèdent ces étoiles, comme θ^1 Ori C (Babel & Montmerle 1997).

2.3.3 Étoiles de Très Faible Masse

Les étoiles de type plus tardif que M3 ($M \lesssim 0.3 M_\odot$), sont certainement complètement convectives et possèdent une activité magnétique variable (Hawley 1993, 2000; Basri 2003). Leur luminosité X, L_x, décroit de $\sim 10^{29}\, erg/s$ dans les étoiles de type solaire à seulement $\sim 10^{26}\, erg/s$ les rendant difficilement détectables. Ceci est dû à leur petitesse, car leur flux X est bien du même ordre que dans les étoiles G, ce qui laisse à penser que du point de vue de ce marqueur de l'activité l'existence ou non d'une zone radiative intérieur n'est pas significative. Par contre il est clair que la modulation régulière du signal, indication probable d'un cycle d'activité, permet de distinguer la présence ou non d'une zone radiative (et donc d'une tachocline). Une telle modulation n'est pas observée dans ces étoiles, qui possèdent une activité irrégulière, plus proche du magnétisme qu'une dynamo turbulente génère que de celui d'un dynamo type $\alpha - \omega$ (cf. chapitre 3). Ces étoiles connaissent des éruptions et ont certainement une couronne subissant des reconnections comme dans le Soleil. Le phénomène de saturation de X déjà discutée pour les étoiles de type solaire, semble s'effectuer pour cette classe d'étoiles à des vitesses de l'ordre de 5 km/s. Ces étoiles ralentissent plutôt lentement, car il semble que le processus de frein magnétique exercé par un champ magnétique grande échelle n'opère pas aussi efficacement que dans les étoiles de type solaire, peut être en partie à cause de la faible amplitude de celui-ci. Nous notons au passage que la présence d'un champ magnétique a également été détectée dans certaines naines

brunes (Hawley 2000).

2.3.4 Étoiles Jeunes

Par jeunes étoiles nous sous entendons les étoiles depuis leur phase de formation ou descente d'Hayashi (dans le diagramme H-R), jusqu'à leur arrivée sur la séquence principale, on dénomme cette phase de la vie des étoiles la pré-séquence principale (PMS). On peut classifier en différentes phases ce parcours évolutif sur des critères observationels, en partant de la classe 0 (proto étoile) à la classe 3 (étoiles T-Tauri faibles), pour les étoiles de types solaires, voir André et al. 1993. Pour les étoiles de masse intermédiaire on parle d'étoiles de Herbig. À cette phase de leur vie, les étoiles sont souvent complètement convectives jusqu'à ce que n'apparaisse une partie centrale radiative. Pour le Soleil la PMS dure de l'ordre de 50 Mans, et le cœur radiatif apparaît vers 2-3 Mans. Ces étoiles sont très actives magnétiquement et la présence d'une surface convective turbulente n'y est encore une fois pas étranger. Le champ magnétique joue donc certainement lors des phases initiales un rôle crucial dans le processus de formation des étoiles, car il permet entre autre de stabiliser les cœurs denses, d'imposer l'échelle de temps par diffusion ambipolaire lors de l'effondrement des cœurs et de transférer du moment cinétique de la proto-étoile à son environnement. L'interaction du corps central avec son enveloppe ou plus tard son disque d'accrétion est cruciale pour déterminer la vitesse de rotation de l'étoile lors de son arrivée sur la SP. Plus le couplage durera longtemps plus l'étoile tournera lentement (Bouvier et al. 1997). Pour cette raison la loi de Skumanich (1972) prévoyant le ralentissement par frein magnétique des étoiles ne s'applique pas aux étoiles jeunes. Chaque amas jeune a une évolution initiale propre ne permettant pas de dégager des tendances claires et ce jusqu'à ce qu'il évolue suffisamment longtemps sur la séquence principale. On observe alors que pour les amas de l'âge des Hyades (700 Mans) ou plus âgés, une moindre dispersion des vitesse de rotation, comme si la mémoire des phases initiales de formation commençait à s'estomper. Utilisant des observations du satellite Chandra dans la gamme des rayons X, Feigelson (2004) a étudié plus d'un millier d'étoiles, et une faible corrélation entre activité et taux de rotation (contrairement à Noyes et al. 1984 pour les étoiles de la MS), excepté pour les taux de rotation élevés où il observe une saturation de l'émission, suggérant un processus dynamo de nature différente que dans le Soleil, certainement turbulente. De récents progrès ont été faits pour dériver le profil de rotation de surface de ces étoiles. En particulier, Donati et al. (2003) ont observé de jeunes étoiles G & K, et en ont conclu que le contraste de rotation différentielle absolu $\Delta\Omega$ varie peu par rapport à celui actuel du Soleil, malgré la grande différence de taux

de rotation.

En pratique, peu de choses sont connues entre la phase nuage et la phase T-Tauri où le champ magnétique (ré)apparait. Son amplitude passe de quelques μG-mG dans les nuages à quelques kG dans les T-Tauri. L'application directe de la conservation du flux magnétique résulte en un champ magnétique trop fort dans la phase TT. Il doit donc y avoir des processus de perte de flux magnétique lors de la formation de l'étoile. Faire le lien entre les différentes phases dynamiques du parcourt évolutif des étoiles est certainement un des défis majeurs des décennies à venir.

2.3.5 Étoiles Évoluées

Quand le brûlage de l'hydrogène en hélium s'arrête dans le cœur des étoiles, celles-ci s'écartent de la SP (perpendiculairement dans un diagramme H-R) pour aller sur la branche des géantes, puis la branche asymptotique où elles traversent la zone d'instabilité des céphéides, puis la phase du brûlage d'hélium (sans ou avec flash selon si elles sont massives ou pas) pour enfin finir soit en naines blanches après avoir soufflé leur enveloppe d'hydrogène sous la forme d'une nébuleuse planétaire, soit en étoiles à neutron ou en trous noirs après avoir explosé sous forme de supernovae (Kippenhahn & Weigert 1995 et §2.2.6). Il est naturel de se demander, sachant que sur la SP beaucoup d'étoiles possèdent une certaine activité magnétique, si l'on observe un champ magnétique dans ces étoiles évoluées et quel est leur taux de rotation. Comme ces étoiles se dilatent, l'enveloppe s'ajustant au changement de conditions thermodynamiques dans les parties centrales de l'étoile, elles tournent généralement très lentement comparées à leurs plus jeunes équivalents sur la SP. Peu de choses sont connues sur leur magnétisme, il semblerait cependant que leur activité décroisse lors de leur évolution sur la branche des géantes, l'amplitude du champ magnétique B étant inférieure ou égale à 1 G. Dans la gamme des rayons X, Schmitt (2004) a mis en évidence une ligne séparatrice (X dividing line ou XDL) entre les étoiles possédant une activité et celles n'en possédant pas (ou étant inférieure à la sensibilité instrumentale). Pour les étoiles plus chaudes que le type spectral K3, le champ B est observé. On trouve une réelle activité dans les étoiles géantes G ($L_x \sim 10^{30}$ erg/s), mais elle devient de plus en plus faible dans les géantes K voire inexistante dans les géantes M. Certains auteurs ne croient pas en l'existence d'une XDL, et pensent plutôt que cette séparation est liée au parcourt évolutif de l'étoile, les étoiles ayant une masse supérieure à 1.25 $M_\odot$ possédant toutes un champ magnétique.

Récemment on aurait observé une résurgence d'activité dans les étoiles en phase de brûlage de l'hélium, grâce à l'identification des raies du calcium CaII H& K dans

quelques étoiles (Dupree 2003), ce qui pourrait suggérer le redémarrage d'une dynamo dans des phases plus avancées.

2.3.6 Étoiles Dégénérées

La vie des étoiles se termine en donnant naissance à trois types d'objet, en fonction de la masse avec laquelle elles atteignent la SP: les naines blanches ($M < 8M_\odot$), les étoiles à neutrons ($8 < M < 25M_\odot$) et les trous noirs ($M > 25M_\odot$). Il se pourrait qu'au delà d'une certaine masse ($M > 50M_\odot$?), les étoiles perdent tellement de masse sur la ZAMS au travers de leur vent, que celles-ci pourraient terminer leur évolution non pas en trous noirs mais en étoiles à neutrons.

De l'ordre de 10% des naines blanches observées grâce à l'effet Zeeman ou la polarisation de la lumière, possèdent un champ magnétique dont l'amplitude varie entre $10^6 - 10^8$ G (Mestel 2001). Ce champ est plutôt uniforme variant peu d'une naine à l'autre. La simple conservation du flux magnétique, $4\pi R_1^2 F_1 = 4\pi R_2^2 F_2$, où R_1, F_1, R_2 et F_2 sont respectivement le rayon et le flux magnétique pendant la SP puis dans l'état final dégénéré, permet d'expliquer en grande partie l'augmentation par plusieurs ordres de grandeurs de l'intensité du champ. En effet le rayon typique d'une naine blanche est de l'ordre de quelques 10^3 Km ce qui est petit comparé aux 10^6 Km des étoiles de type solaire. L'explication d'une origine fossile du champ de certaines naines blanches est donc plausible et ne nécessite pas le recours à un effet dynamo. Il faut cependant noter que la structure interne des étoiles A et G différent totalement durant leur vie sur la SP, les deux finissant cependant en naines blanches. On sait que les étoiles de type solaire donnent plutôt des naines blanches de 0.6 $M_\odot$ alors que les étoiles plus massives, comme les A et B tardives, forment plutôt des naines blanches proche de la masse de Chandrasekhar $M = 1.4M_\odot$. Il serait intéressant de voir si les naines blanches actives sont plutôt massives, ce qui indiquerait qu'elles aient conservé le champ magnétique généré dans leur cœur convectif pendant la SP, certaines indications semblent soutenir cet argument (Rudiger & Hollerbach 2004).

Pour les étoiles à neutron, l'intensité du champ magnétique est gigantesque, typiquement $10^9 - 10^{12}$ G (Mestel 2001). Là aussi la seule conservation du flux magnétique, permet de comprendre les ordres de grandeur, vu que le rayon typique d'une étoile à neutrons est 10 km. La manifestation la plus flagrante d'un tel magnétisme est certainement l'existence de pulsars et l'émission synchotron (donc détection in situ et directe de B) qu'ils émettent. Récemment quelques étoiles avec des champs magnétiques de l'ordre de 10^{15} G ont été observées, on les appelle les magnéstars. L'existence d'un cœur convectif magnétisé dans les étoiles massives donnant naissance à ces étoiles pourrait

peut être expliquer l'amplitude encore plus grande du champ dans celles-ci. Cependant comme pour les étoiles CP, il faut expliquer dès lors pourquoi toutes les étoiles à neutron ne sont pas des magnéstars. Il est clair que le parcours individuel de chaque étoile peut influencer sur le champ magnétique résultant. Une forte corrélation semble exister entre l'amplitude de B et l'âge de l'étoile à neutron, les plus âgées ayant un champ faible et tournant rapidement (pulsar millisecondes $B \sim 10^{7-8}$). La décroissance du champ est donc en soit un problème à comprendre, l'effet Hall pourrait expliquer en partie cette corrélation entre âge et amplitude (Rudiger & Hollerbach 2004).

Peu de choses sont connus sur les trous noirs concernant leur magnétisme, il est cependant possible de trouver une solution des équations d'Einstein pour un trou noir incluant rotation (TN de Kerr) et champ magnétique. Le disque d'accrétion orbitant autour des trous noirs peut lui aussi posséder un champ magnétique, mais le gros de l'émission X vient des particules accélérées spiralant (tombant) vers l'horizon du trou noir plutôt que de la reconnection des lignes de champ magnétique dans le disque. Que ce soit les naines blanches, les étoiles à neutron, ou les trous noirs ces objets nécessitent un traitement à part, devant inclure les effets relativistes et quantiques. La théorie magnétohydrodynamique discutée chapitre 3 et utilisée section 2, n'est pas adaptée à de telles conditions sans des modifications importantes. Il est nécessaire de considérer des équations d'état pour la matière dégénérée voire relativiste (Cox & Guili 1968) et de faire un développement au moins post-newtonien (en $O(v^3/c^3)$), voire de résoudre les équations d'Einstein avec le tenseur électromagnétique pour l'aspect dynamique stellaire (Battaner 1996, Bonazzola et al. 1998), ce qui sort du champ d'investigation de notre étude.

Chapitre 3

Magnétohydrodynamique et Effet Dynamo

Dans ce chapitre nous allons présenter de manière succincte la théorie développée pour comprendre et décrire l'interaction complexe et subtile qui existe entre les mouvements et les champs magnétiques d'un fluide conducteur, comme les plasmas rencontrés en astrophysique. Cette théorie repose sur les équation de l'electromagnétisme de Maxwell et celles de la mécanique des fluides ou équations hydrodynamiques. De très bons livres existent pour aborder ce sujet, notamment les livres de Cowling 1957, Moffatt 1978, Krause & Radler 1980, Zeldovich et al. 1983, Parker 1989, Pedlosky 1989, Biskamp 1993, Sturrock 1994, Childress & Gilbert 1995, Battaner 1996, Rieutord 1997, Chouduri 1998, Mestel 1999, Davidson 2001, Kundu, Rudiger & Hollerbach 2004, etc..., il n'est donc pas ici question de rentrer dans les détails mais juste de préciser le modèle et les hypothèses de cette étude.

3.1 Contexte Général

Comme nous l'avons vu chapitre 1, le fait que les gaz en astrophysique sont souvent ionisés implique que des courants électriques et donc des champs magnétiques sont présents dans ceux-ci. Afin de caractériser le comportement de tel gaz subissant souvent l'influence simultanée des forces de gravité, Coriolis et Laplace, il est nécessaire d'avoir un jeu d'équations rendant compte du mouvement mécanique et des propriétés thermodynamiques du fluide et permettant un traitement dynamique de ses interactions et couplages: Les équations du mouvement aussi appelées équations de Navier-Stokes doivent être couplées aux équations de continuité du flux de masse et d'énergie. Dans le cas où les forces électromagnétiques jouent un rôle, on adjoint à ces équations, outre la force de Laplace et le chauffage ohmique, une équation déduite des équations de Max-

well, appelée équation d'induction. Dans ce chapitre nous allons préciser sous quelle forme le code ASH intègre ce système d'équations (voir aussi Appendice) et avec quelles hypothèses simplificatrices. Une conséquence importante de l'existence de courant et de champ magnétique dans un plasma, est qu'il est possible que l'écoulement auquel se plasma est soumis, par exemple grâce à un forçage mécanique aux grandes échelles, puisse entretenir les champs magnétiques contre leur dissipation ohmique: c'est l'effet dynamo vu au chapitre 1. Nous voulons ici également récapituler les expériences dans lesquelles cet effet dynamo a été observé et comment ce concept se prolonge naturellement au magnétisme et à l'activité stellaire, sujet principal de cette HDR.

3.2 Les Équations de la Dynamique des Fluides et des Plasmas

Avant de décrire les équations de la (magnéto)-hydrodynamique, il est naturel de se demander si ces équations sont appropriées pour l'étude des étoiles et de leurs processus dynamiques. Une étoile est un gaz auto-gravitant composé d'un très grand nombre N d'atomes neutres, d'ions et d'électrons. Du point de vue le plus fondamental le comportement d'un tel système devrait être décrit par l'équation d'onde de Schrödinger appliquée à une superposition de N paquets d'ondes décrivant le comportement quantique de N particules. Cette description, au delà de sa complexité intrinsèque et de son impractibilité, est bien loin de l'approche fluide utilisée en hydrodynamique qui suppose que l'on puisse identifier une particule fluide dans un continuum représentant le système étudié de particules individuelles. Comment dès lors pouvons nous passer de la description quantique du plasma stellaire à sa description magnétohydrodynamique? Il suffit en fait de procéder par approximations successives et de constater que le plasma stellaire est, à part pour quelques corrections non-idéales, un gaz parfait. En supposant que la longueur de Broglie de chaque particule est petite devant la séparation moyenne entre particules, ce qui est vrai dans le cas d'un gaz non dégénéré[8], nous déduisons que les paquets d'onde des particules ne se superposent pas et l'approximation classique permet alors de décrire ce gaz comme la collection d'un ensemble de particules classiques suivant les équations d'Hamilton et les lois de Newton. Pour pouvoir passer de cette description microscopique individuelle de chaque particule à une description

8. donc typiquement pour les étoiles dans leurs phases PMS et SP, mais pas pas en fin de vie ou c'est la pression de dégénérescence du gaz d'électrons ou de neutrons qui maintien l'étoile en équilibre. Cependant même pour ses étoiles il est possible de se ramener à une approche fluide (Battaner 1996, Bonazzola et al. 1998)

basée sur des fonctions de distribution $f(\mathbf{x},\mathbf{v},t)$ dépendant seulement de la position et de la vitesse de ces mêmes particules à un instant donné, il faut pouvoir définir la limite $\lim_{\delta V \to 0^+} \delta N/\delta V$. Si cette limite a un sens alors l'équation de Boltzmann (déduite elle même de l'équation de Liouville) permet de suivre l'évolution des fonctions de distributions f, et ainsi de décrire la dynamique du gaz grâce à une approche statistique (Chouduri 1998). Finalement la possibilité de décrire ce gaz comme un continuum, i.e. un fluide, et donc d'utiliser les équations de la mécanique des fluides présentées dans ce chapitre, suppose que les particules ont un libre parcours moyen petit devant la taille du système (mais grand devant la taille des particules) et que le gaz est proche de l'équilibre thermodynamique et donc les particules d'une distribution maxwellienne/gaussienne[9] (cf. Chouduri 1995, Diu et al. 1989). Il suffit alors de connaître deux variables thermodynamiques, par exemple la densité $\rho(\mathbf{x})$ et la température $\mathrm{T}(\mathbf{x})$ en plus de la vitesse $\mathbf{v}(\mathbf{x})$ à un instant donné pour suivre l'évolution du système.

3.2.1 Cas Hydrodynamique

Nous considérons le cas d'un objet composé d'un fluide compressible possédant un champ de pesanteur et un mouvement de rotation Ω_0. Les équations de continuité de la masse, du mouvement et de l'énergie formant les équations de la mécanique des fluides, s'écrivent alors:

$$\begin{aligned}
\frac{\partial \rho}{\partial t} + \boldsymbol{\nabla} \cdot (\rho \mathbf{v}) &= 0, && (3.1)\\
\rho \left(\frac{\partial \mathbf{v}}{\partial t} + (\mathbf{v} \cdot \boldsymbol{\nabla}) \mathbf{v} \right) &= -\boldsymbol{\nabla} P + \rho \mathbf{g} - 2\rho \boldsymbol{\Omega}_\mathbf{o} \times \mathbf{v} - \boldsymbol{\nabla} \cdot \boldsymbol{\mathcal{D}}, && (3.2)\\
\rho T \frac{\partial S}{\partial t} + \rho T (\mathbf{v} \cdot \boldsymbol{\nabla}) S &= \boldsymbol{\nabla} \cdot (\kappa_r \rho c_p \boldsymbol{\nabla} T) \\
&+ 2\bar{\rho}\nu \left[e_{ij} e_{ij} - 1/3 (\boldsymbol{\nabla} \cdot \mathbf{v})^2 \right] + \rho \epsilon, && (3.3)
\end{aligned}$$

avec $\mathbf{v} = (v_r, v_\theta, v_\phi)$ la vitesse locale en coordonnées sphériques dans le repère en rotation à la vitesse angulaire $\boldsymbol{\Omega}_\mathbf{o}$, $\mathbf{g}$ l'accélération gravitationelle, c_p la chaleur spécifique à pression constante, κ_r la diffusivité radiative, et $\mathcal{D}$ le tenseur des contraintes visqueuses, ayant pour composantes

$$\mathcal{D}_{ij} = -2\rho\nu [e_{ij} - 1/3 (\boldsymbol{\nabla} \cdot \mathbf{v}) \delta_{ij}], \qquad (3.4)$$

avec e_{ij} le tenseur du taux de déformation, et ν la viscosité cinématique. Un terme de chauffage volumique $\rho\epsilon$ est également inclus dans ces équations pour complétude mais il

9. car sous l'action systématique des collisions entre particules un gaz évolue de lui-même vers une distribution de particules normale

est négligeable dans l'enveloppe convective solaire. Par contre quand nous appliquons notre modèle à d'autres étoiles, comme les cœurs convectifs des étoiles de type A (Browning et al. 2004, Brun et al. 2005 et chapitre 6), ce terme représente la génération d'énergie par réactions nucléaires. Pour compléter ce jeu d'équations, nous utilisons l'équation d'état suivante:

$$P = \frac{\mathcal{R}\rho T}{\mu} \tag{3.5}$$

avec $\mathcal{R}$ la constante des gaz et μ le poids moléculaire moyen.

3.2.2 Cas MagnétoHydrodynamique

Le cas d'un plasma est encore plus compliqué qu'un gaz neutre, car entre chaque collision les particules chargées peuvent ressentir l'effet longue distance des forces électromagnétiques [10]. De plus les collisions ions-neutres ou des particules chargées entre elles peuvent différer significativement de celles de neutres entre eux. Il se trouve cependant que pour un gaz suffisamment dilué un effet d'écrantage des charges électriques se produit qui est bien utile pour simplifier l'étude de ce système complexe. Il est alors possible de considérer l'effet collectif des particules environnantes sur une particule test. La distance typique de cet écrantage est la longueur de Debye $\lambda_D = (k_B T/8\pi n e^2)^{1/2}$. Comme pour un gaz neutre, il est possible de ramener la description du plasma à celle de fonctions de distribution f caractérisant les différentes charges présentes. Cette fonction f est alors solution d'une équation dynamique dite de Vlasov (Sturrock 1994, Chouduri 1998). Pour pouvoir utiliser l'approximation mono fluide, qui ne distingue pas les neutres des particules chargées, donc la séparation des charges, il est nécessaire de s'assurer que les phénomènes étudiés ont des échelles temporelles et spatiales respectivement plus longues que l'inverse de la fréquence plasma $\omega_p = |q|B/mc$ et plus grande que la longueur de Debye. Ces conditions sont réalisées pour le plasma des étoiles de la SP.

Dans un conducteur stationnaire la loi d'Ohm s'écrit simplement $\mathbf{J} = \sigma\mathbf{E}$. Pour un fluide conducteur en mouvement comme dans les zones convectives des étoiles, le champ électrique doit être évalué dans le repère $\mathcal{R}'$ se déplaçant à la vitesse du fluide $\mathbf{v}$, le champ électrique $\mathbf{E}'$ s'écrit: $\mathbf{E}' = \mathbf{E} + (\mathbf{v} \times \mathbf{B})/c$, et comme $\mathbf{J}' = \mathbf{J}$ la loi d'Ohm devient alors:

10. dans le cas d'un gaz composé de particules neutres, la force de gravité n'a qu'un faible effet comparée à l'agitation thermique sur la trajectoire des particules, qui est rectiligne entre chaque collision

$$\mathbf{J} = \sigma \left(\mathbf{E} + \frac{\mathbf{v} \times \mathbf{B}}{\mathbf{c}} \right),$$

En ajoutant l'hypothèse que la vitesse de l'écoulement du plasma est faible devant celle de la lumière (ce qui revient à négliger le courant de déplacement) [11] on peut dériver des équations de Maxwell, l'équation d'induction permettant de suivre l'évolution spatio-temporelle du champ magnétique:

$$\frac{\partial \mathbf{B}}{\partial t} = \boldsymbol{\nabla} \times (\mathbf{v} \times \mathbf{B}) - \boldsymbol{\nabla} \times (\eta \boldsymbol{\nabla} \times \mathbf{B}), \tag{3.6}$$

avec $\eta = c^2/4\pi\sigma$ la diffusivité magnétique. Si celle-ci est constante, alors l'équation d'induction se simplifie:

$$\frac{\partial \mathbf{B}}{\partial t} = \boldsymbol{\nabla} \times (\mathbf{v} \times \mathbf{B}) + \eta \Delta \mathbf{B}. \tag{3.7}$$

En adjoignant l'équation d'induction aux équations de l'hydrodynamique (cf. §3.1.2) on obtient les équations de la magnétohydrodynamique auxquelles nous devons ajouter deux termes (la force de Laplace dans l'équation du mouvement et la dissipation Ohmique dans l'équation de l'énergie):

$$\begin{aligned}
\boldsymbol{\nabla} \cdot \mathbf{B} &= 0, && (3.8)\\
\frac{\partial \rho}{\partial t} + \boldsymbol{\nabla} \cdot (\rho \mathbf{v}) &= 0, && (3.9)\\
\rho \left(\frac{\partial \mathbf{v}}{\partial t} + (\mathbf{v} \cdot \boldsymbol{\nabla}) \mathbf{v} \right) &= -\boldsymbol{\nabla} P + \rho \mathbf{g} - 2\rho \boldsymbol{\Omega_0} \times \mathbf{v} \\
&+ \frac{1}{4\pi} (\boldsymbol{\nabla} \times \mathbf{B}) \times \mathbf{B} - \boldsymbol{\nabla} \cdot \boldsymbol{\mathcal{D}}, && (3.10)\\
\rho T \frac{\partial S}{\partial t} + \rho T \mathbf{v} \cdot \boldsymbol{\nabla} S &= \boldsymbol{\nabla} \cdot (\kappa_r \rho c_p \boldsymbol{\nabla} T) \\
&+ 2\rho\nu \left[e_{ij} e_{ij} - 1/3 (\boldsymbol{\nabla} \cdot \mathbf{v})^2 \right] + \frac{4\pi\eta}{c^2} \mathbf{J^2} + \rho\epsilon, && (3.11)\\
\frac{\partial \mathbf{B}}{\partial t} &= \boldsymbol{\nabla} \times (\mathbf{v} \times \mathbf{B}) - \boldsymbol{\nabla} \times (\eta \boldsymbol{\nabla} \times \mathbf{B}), && (3.12)
\end{aligned}$$

Il suffit alors de connaître deux variables thermodynamiques, par exemple la densité $\rho(\mathbf{x})$ et la température $\mathrm{T}(\mathbf{x})$ en plus de la vitesse $\mathbf{v}(\mathbf{x})$ et du champ magnétique $\mathbf{B}(\mathbf{x})$ [12]

11. l'équation d'Ampère devient alors $\mathbf{J} = c/4\pi\,(\boldsymbol{\nabla} \times \mathbf{B})$,

12. Il n'est pas nécessaire de suivre le champ électrique $\mathbf{E}(\mathbf{x})$, car à l'intérieur des conducteurs, le champ électrique est nul, ce qui pour un plasma signifie que les champs électriques disparaissent par la réorganisation rapide des charges. Il n'est pas toujours justifié de faire cette hypothèse de non séparation des charges, ce qui est le cas avec la magnétosphère terrestre, ou l'approche bi-fluide (i.e neutres + particules chargées) est plus appropriée.

à un instant donné pour suivre l'évolution du système MHD considéré. Nous avons reporté dans l'Appendice 1, la description du code ASH et du jeu d'équations MHD qu'il résout. En particulier, l'approche LES-SGS choisie avec le code ASH pour intégrer les équations nous impose la présence d'un terme supplémentaire de transport de l'énergie proportionnel au gradient d'entropie $d\bar{S}/dr$ (voir Clune et al. 1999).

3.3 Effet Dynamo

Nous avons vu chapitre 1, qu'un gaz ionisé ou plasma, peut développer un effet dynamo s'il possède certaines propriétés d'étirement, de torsion et de repliage du champ magnétique (dénommés effets ω et α en théorie des champs moyens, Krause & Radler 1980, voir aussi Childress & Gilbert 1995), de sorte que ces mouvements simultanés et continus tendent à s'opposer à la décroissance ohmique du champ magnétique (Moffatt 1978). On peut dès lors se demander quelles doivent être les propriétés de l'écoulement du plasma pour que cela se produise. Il se trouve que cette question est hautement non triviale, et aucun théorème d'existence de l'effet dynamo n'a pu être établi à ce jour alors que foules de théorèmes anti-dynamo existent. Cependant un nombre bien utile peut être formé pour comparer les termes de génération de champ magnétique avec ceux de dissipation dans l'équation d'induction: le nombre de Reynolds magnétique $Rm = VL/\eta$, où V et L sont une vitesse et une échelle caractéristiques du mouvement. Si dans un écoulement tridimensionnel ce nombre Rm est plus grand que 1, alors l'amplification du champ l'emporte, sinon le champ décroît. On peut donc parler de l'existence d'un seuil pour obtenir un effet dynamo[13]. Vu les très grands nombres de Reynolds cinétiques et magnétiques caractérisant les étoiles, en particulier dans leurs zones convectives, on peut s'attendre à ce que ce seuil soit atteint voire largement dépassé. Dans les sous sections suivantes nous allons discuter rapidement dans quel cas un effet dynamo a été observé par les chercheurs à partir soit de simulations numériques, soit d'appareillages expérimentaux et pourquoi il est probable que ce phénomène soit aussi présent dans les étoiles.

Il est intéressant de noter, que dans l'espace de paramètres portant le nombre de Reynolds magnétique en abscisse et le nombre de Prandtl magnétique $Pm = \nu/\eta$ en ordonnée, il n'y a aucun recouvrement des zones représentant les simulations numériques, les expériences et les étoiles et de manière plus générale les dynamos naturelles (voir Figure 3.1). En effet les étoiles ont un grand Rm ($> 10^{10}$) et un petit Pm ($\leq 10^{-2}$), les

13. nous tenons encore ici à rappeler qu'amplification du champ magnétique ne signifie pas forcément effet dynamo car si par exemple seule une composante est amplifiée et régénérée, le cycle $B_{pol} \rightarrow B_{tor} \rightarrow B_{pol}$ n'est alors pas complet et à long terme la dynamo échouera, voir chapitre 1

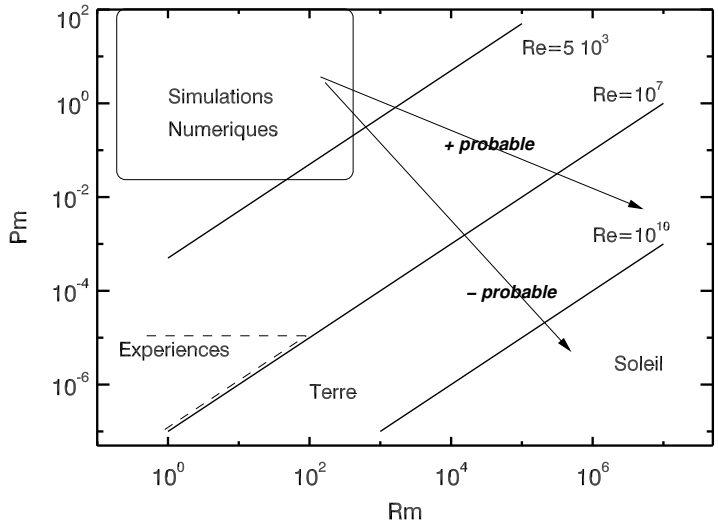

FIG. 3.1 – *Espace de paramètres Pm-Rm pour les simulations numériques, les expériences dynamos et les objets naturels (adapté de Fauve 2004). Nous représentons également par les flèches différents scénari (du plus probables au moins probables) sur l'évolution future des simulations numériques. Si il est effectivement confirmé qu'à partir de* $Pm = 10^{-2}$ *l'effet dynamo devient indépendant de Pm, alors les conditions solaires seront plus rapidement atteintes par les calculs tridimensionnels.*

expériences ont un petit Rm ($\sim 10 - 100$) et un très petit Pm (10^{-5}) et les simulations ont un Rm modéré ($\sim 10^{3-4}$) et un Pm de l'ordre de l'unité et au mieux de 0.1. Il faut donc être prudent avant d'étendre des résultats expérimentaux et numériques aux étoiles. Des efforts théoriques et numériques récents ont essayé de déterminer si le seuil dynamo (c'est à dire le nombre de Reynolds magnétique critique) dépendait fortement de Pm. Il semblerait qu'en dessous de $Pm < 0.01$, le nombre de Reynolds magnétique critique asymptote vers une valeur finie (Ponty et al. 2004). Ceci en soit est une très bonne nouvelle pour les simulations numériques 3-D MHD, dont la faiblesse est d'avoir des nombres Pm un peu trop grands. On peut alors pousser dans un premier temps les nombres de Reynolds cinétiques et magnétiques, pour élever le degré de turbulence, plutôt que d'essayer en réduisant la diffusivité magnétique vis a vis de la viscosité cinétique de réaliser le faible Pm caractérisant les fluides expérimentaux et les plasmas stellaires. Si effectivement au delà de 0.01, l'influence du nombre de Pm sur l'existence et les propriétés de la dynamo est réduite, on peut alors s'attendre à ce que des simulations numériques à très larges Re et Rm (mais avec $Pm \sim 0.1$) puissent reproduire suffisamment fidèlement les observations.

3.3.1 Évidences Numériques

Si on met de côté la difficulté pour ne pas dire l'impossibilité de réaliser les conditions dynamiques présentes dans les étoiles, les simulations numériques sont un outil très performant pour analyser un ou plusieurs processus physiques et ainsi valider notre compréhension de ce(s) phénomène(s). La mise en évidence d'un effet dynamo dans les simulations numériques et la caractérisation des propriétés physiques le permettant se prêtent donc bien à une approche numérique. Cet effet a d'abord été très étudié dans le contexte de la géodynamo (Cuong & Busse 1981, voir aussi Christensen et al. 1999, Roberts & Glatzmaier 2000, Busse 2000 pour une discussion plus récente) et de la dynamo solaire (Gilman & Miller 1981, Glatzmaier 1987, voir aussi Brun et al. 2004). Plus récemment il a été étendu aux autres planètes (Jupiter, Saturne) (Sun & Schubert 1995, Fearn 1998), aux étoiles (massives, jeunes, géantes, Dorch 2004, Brun, Browning & Toomre 2005) et aux galaxies (Otmianowska-Mazur, K. & Elstner, D. 2003, Elstner 2005, voir aussi Stix 1975, Beck et al. 1996, Weiss 2002). Pour modéliser l'effet dynamo il y a principalement deux approches:

L'approche cinématique, qui consiste à se donner un écoulement et à intégrer en fonction du temps et de l'espace l'équation d'induction afin de tester si cet écoulement développe un effet dynamo. Si c'est le cas, alors il y a croissance exponentielle de l'énergie magnétique, et la dynamo est accomplie. Les principaux désavantages de cette approche sont d'une part qu'il n'y a pas rétroaction de la force de Laplace sur le champ de vitesse imposée, donc pas de processus de saturation non linéaire et d'autre part que les processus comme les effets α, ω et la vitesse poloidale ne sont pas déduits de manière auto-consistante en résolvant l'équation de Navier-Stokes, et sont donc un peu *ad hoc*. Cette méthode a surtout été utilisée pour modéliser la dynamo globale du Soleil afin d'expliquer par exemple le diagramme papillon (voir §3.3.3 pour plus de détail).

L'autre approche est dynamique, elle consiste à intégrer le jeu complet des équations de la MHD en 3-D et donc de prendre en compte toutes les non linéarités. Vu la difficulté d'une telle tâche plusieurs degrés de simplification peuvent être utilisés, Boussinesq, anélastique, mixte 2D-3D, approche locale ou LES, etc... Mettre en évidence un effet dynamo dans une simulation numérique est devenu fréquent avec la grande avancée des moyens informatiques. Cependant il est prudent de calculer ces solutions sur plusieurs temps ohmiques car il peut y avoir des surprises, et des dynamos transitoires. Cette approche s'attache à la fois à comprendre l'effet dynamo en tant que processus physique et à modéliser le magnétisme des objets naturels comme la Terre ou les étoiles. Pour se faire, les simulations multidimensionnelles reposent soit sur une étude locale, à très haute résolution atteignant des nombres Re, Rm et Ra (dans le cas d'une dynamo

convective) élevés, soit une approche globale à géométrie sphérique permettant d'atteindre des degrés de turbulence plus modérés mais incluant les bons effets de géométrie et autorisant l'établissement de courants et champs moyens à grande échelle comme ceux observés. Vu la très vaste littérature publiée sur ce sujet, il n'est pas question ici d'en donner une liste exhaustive, cependant dans le contexte de la dynamo stellaire on pourra considérer entre autres les travaux de Galloway & Weiss (1981), Gilman et Miller (1981), Ménéguzzi et al. 1981, Gilman 1983, Hurlburt et al. 1986, Glatzmaier 1987, Cattaneo et al. 1991, Nordlund et al. 1992, Brandenburg et al. 1996, Cattaneo 1999, Tobias et al. 2001, Cattaneo, Emonet & Weiss 2003 (et les nombreuses références citées dans ces mêmes articles).

3.3.2 Évidences Expérimentales

Les premières dynamos expérimentales mettaient en jeu des matériaux solides. Beaucoup de tentatives ont été entreprises afin de réussir à obtenir un effet dynamo avec des fluides[14], mais sans succès. Il a fallu attendre les années 90 pour observer les premières dynamos fluides expérimentales réussies et convaincantes mais en écoulement contraint: Riga avec la dynamo de Ponomarenko et Karlsruhe à partir de l'écoulement de Roberts. A chaque fois les expérimentateurs ont cherché à reproduire un modèle analytique bien maîtrisé. Les résultats montrent clairement l'amplification à un niveau élevé puis la saturation de toutes les composantes du champ magnétique. Il semble que les parois et donc la conductivité de l'enceinte de l'appareillage jouent un grand rôle dans la maintenance du champ par l'écoulement contraint. Afin de s'abstraire d'un mouvement contraint peu réaliste dans le contexte géo et astrophysique, une nouvelle génération d'expériences voit le jour en ce moment. Cette deuxième génération d'expériences dynamos s'intéresse aux écoulements libres et dans la plupart des cas à des écoulements turbulents (vu le faible nombre Pm des fluides utilisés). Deux géométries sont privilégiées, la sphère et le cylindre (cf. expériences de Maryland (projets dynamoIII et sphère 3 m), du Wisconsin (Madison Dynamo Experiment), DTS à Grenoble et VKS I & II à Cadarache). La présence de turbulence dans ces nouvelles expériences résulte en ce que le champ magnétique amplifié est hautement fluctuant avec des fluctuations qui peuvent atteindre la moyenne, i.e $f/\bar{f} \sim 0.5-1$, alors que dans la première génération d'expériences, l'écoulement était plutôt laminaire et $f/\bar{f} \sim 0.1$. Il n'est pas encore clair si la turbulence est un allié ou un "empêcheur de tourner en rond" dans les expériences (Leprovost 2004).

14. souvent avec du sodium (particulièrement dangereux) ou du gallium (très onéreux)

3.3.3 Effet Dynamo dans le Soleil et les Étoiles

Les étoiles possèdent tous les ingrédients a priori nécessaires au développement d'un effet dynamo (Weiss 1994). La présence de cisaillements à grandes échelles (ou rotation différentielle), de mouvements turbulents (principalement dans leurs zones convectives), d'hélicité (grâce à la rotation et la force de Coriolis) et d'une faible diffusivité sont autant de propriétés favorables à l'émergence d'un champ magnétique. L'observation dans le Soleil et la plupart des étoiles de phénomènes clairement associés à la présence d'un champ magnétique (voir chapitre 2), amène naturellement à considérer que ce magnétisme vient d'un effet dynamo[15]. Cependant nous avons vu que l'activité magnétique des étoiles se manifeste sous une multitude de facettes (irrégulière, modulée, cyclique), indiquant certainement la présence de plusieurs types de dynamo ou de magnétisme. Jusqu'à l'avènement récent de super ordinateurs, les astrophysiciens se sont surtout intéressés à la dynamo cyclique et grande échelle, en développant des modèles simplifiés reposant sur la théorie des champs moyens et les incontournables effets α et ω (Krause & Radler 1980).

Cette théorie consiste à séparer le champ magnétique (et la vitesse) en deux parties, une représentant le champ moyen à grande échelle dont on veut suivre l'évolution, et l'autre le champ fluctuant à petite échelle que l'on désire approximer, i.e:

$$\mathbf{B} = < \mathbf{B} > + \mathbf{b}' \text{ avec } < \mathbf{b}' > = 0\,,$$
$$\mathbf{v} = < \mathbf{V} > + \mathbf{v}' \text{ avec } < \mathbf{v}' > = 0$$

où $< >$ représente une moyenne d'ensemble. En introduisant cette décomposition dans l'équation d'induction (3.6) et en appliquant l'opérateur moyenne, on obtient l'équation pour $< \mathbf{B} >$:

$$\frac{\partial < \mathbf{B} >}{\partial t} = \boldsymbol{\nabla} \times (< \mathbf{V} > \times < \mathbf{B} > + < \mathcal{E} > - \eta \boldsymbol{\nabla} \times < \mathbf{B} >) \tag{3.13}$$

où $< \mathcal{E} > = < \mathbf{v}' \times \mathbf{b}' >$ représente la "force" électromotrice moyenne. Cette équation est l'équation d'induction pour le champ moyen, seulement elle dépend du champ fluctuant ce qui nécessite de suivre l'évolution d'une variable supplémentaire et donc de posséder une équation le permettant. On obtient cette équation pour $\mathbf{b}'$, en soustrayant l'équation (3.13) de l'équation (3.6):

15. on peut distinguer deux types de dynamo, soit rapide (d'autant plus intense que Rm croit) soit lente (Childress & Gilbert 1995). Cette dernière décroît si Rm devient trop grand, car elle repose sur la diffusion et la reconnection des lignes de champs pour fonctionner. Il est clair que pour les étoiles la dynamo rapide correspond mieux (Cattaneo, Hughes & Weiss 1991). Il est cependant difficile de démontrer par simulation numérique qu'une dynamo est rapide

$$\frac{\partial \mathbf{b}'}{\partial t} = \boldsymbol{\nabla} \times (< \mathbf{V} > \times \mathbf{b}' + \mathbf{v}' \times < \mathbf{B} > + \mathbf{G} - \eta \boldsymbol{\nabla} \times \mathbf{b}') \tag{3.14}$$

où le courant $\mathbf{G} = \mathbf{v}' \times \mathbf{b}' - < \mathbf{v}' \times \mathbf{b}' >$. Cette équation possède plusieurs termes impliquant les composantes fluctuantes du champ de vitesse et magnétique. Il serait utile de pouvoir se ramener uniquement à l'étude des champs moyens en appliquant une procédure de fermeture reliant la partie fluctuante à la partie moyenne du champ. L'approche la plus simple pour atteindre cet objectif, dénommée *first order smoothing approximation* (FOSA), consiste à considérer que le courant $\mathbf{G}$ est négligeable. On déduit alors de l'équation (3.14), que $\mathbf{b}' = \mathcal{F}(< \mathbf{B} >)$, où $\mathcal{F}$ est une fonctionnelle dépendant linéairement de $< \mathbf{B} >$, et donc il en va de même pour $< \mathcal{E} > = \mathcal{G}(< \mathbf{B} >)$. En appliquant un développement de Taylor autour de $< \mathbf{B} >$ pour $< \mathcal{E} >$, nous obtenons:

$$\mathcal{E}_i = \alpha_{ij} < B_j > + \beta_{ijk} \frac{\partial < B_j >}{\partial x_k} + \dots .$$

En analysant ce terme on remarque qu'il y a un terme proportionnel au champ moyen, impliquant le pseudo-tenseur α_{ij} qui peut être identifié à l'effet α (voir chapitre 1 et Krause & Radler 1981), et un terme de diffusion effective plus standard. En reportant cette expression dans l'équation (3.13), on peut alors obtenir une équation ne dépendant que de $< \mathbf{B} >$:

$$\frac{\partial < \mathbf{B} >}{\partial t} = \boldsymbol{\nabla} \times (< \mathbf{V} > \times < \mathbf{B} > + \alpha < \mathbf{B} > - (\eta + \beta) \boldsymbol{\nabla} \times < \mathbf{B} >) \tag{3.15}$$

où nous avons considéré le cas isotrope et homogène pour les coefficients $\alpha_{ij} = \alpha \delta_{ij}$ et $\beta_{ijk} = \beta \epsilon_{ijk}$. Le premier terme correspond au transport et à l'étirement du champ $< \mathbf{B} >$ par les mouvements à grande échelle (circulation méridienne et effet ω), le deuxième à l'effet α et le dernier à la diffusion ohmique augmentée d'une diffusion effective β (souvent supérieure à η de sorte que $\beta + \eta \sim \beta$). On peut alors comprendre que selon l'amplitude respective des deux effets α et ω pour amplifier le champ toroidal, on parle soit de dynamo α^2, $\alpha - \omega$ ou $\alpha^2 - \omega$. Pour savoir si dans un cas particulier de profils de rotation différentielle ω et d'effet α, il y a croissance ou décroissance de l'énergie magnétique et donc effet dynamo, le produit des nombres de Reynolds R_α et R_α définis respectivement à partir de l'amplitude caractéristique de l'effet α, α_0 et de l'effet ω doit dépasser une certaine amplitude (seuil). Ce seuil est également sensible à la polarité du champ magnétique initial (famille dipolaire ou quadrupolaire, voir par exemple Krause & Radler 1981).

Cette méthode a été souvent appliquée afin d'étudier les différents type de dynamos ($\alpha - \omega$ ou α^2) dans le cas du Soleil (Roberts 1972, Stix 1976) et des étoiles. Une question en particulier a attiré beaucoup d'attention dans la littérature spécialisée est

celle de savoir pourquoi et comment un système aussi turbulent que le Soleil possède un cycle magnétique aussi régulier de 22 ans? En effet, le rapport élevé (~ 300) entre la période du cycle magnétique et le temps de retournements convectifs, nous suggère que leur relation n'est pas simple à caractériser (Rudiger & Hollerbach 2004). La solution préférée jusqu'au milieu des années 80 est celle d'une dynamo $\alpha - \omega$ distribuée dans la zone convective solaire (voir cependant Brandenburg 2005 pour une version revisitée de la dynamo distribuée). Il n'est cependant pas question ici de faire l'historique des différents modèles publiés dans la littérature car l'héliosismologie va totalement modifier notre compréhension de la dynamo solaire. En effet l'inversion vers la fin des années 80 d'un profil interne de rotation du Soleil complètement différent de celui utilisé dans les modèles de type champs moyens, car très peu cylindrique et possédant un gradient radial de rotation différentielle proche de zéro, ce qui a forcé la communauté à reconsidérer le modèle simple $\alpha - \omega$ de la dynamo solaire.

Actuellement afin d'expliquer la dynamo solaire grande échelle tout en intégrant les contraintes venant de l'héliosismologie, les modèles cinématiques de la dynamo solaire reposent sur la dynamo dite interfaciale (Parker 1993). La tachocline y joue un rôle dominant pour concentrer l'effet ω à la base de la zone convective, où le champ toroidal peut être amplifié et stocké efficacement sur plusieurs années (résolvant de manière élégante le problème du grand rapport entre les échelles temporelles de la convection et du cycle). Il y a par contre deux approches différentes pour convertir le champ toroidal en champ poloidal, l'effet α usuel (dynamo α-ω, Charbonneau & McGregor 1997) ou la dynamo de type transport de flux. Dans cette dernière, c'est la diffusion ohmique des taches solaires, qui par leur inclinaison par rapport à la direction est-ouest d'un angle de 4-10 deg (Loi de Joy, chapitre 2), possèdent une composante poloidale qui fournit la source du champ poloidal. Celui ci peut être ensuite transporté vers la base de la zone convective par la circulation méridienne pour y être transformé en champ toroidal (dynamo Babcock-Leighton ou transport de flux, Babcock (1961), Leighton (1969), voir aussi Chouduri et al. 1995, Durney 1997, Dikpati et al. 2004 et Ossendrijver 2003 pour une revue récente). Actuellement il semble que les modèles hybrides incorporant toutes les sources de champ poloidal, sont ceux qui donnent les résultats les plus probants (Dikpati et al. 2004). Nous remarquons qu'il est crucial de progresser sur la détection et la modélisation de la circulation méridienne (voir chapitre 4 et Brun & Toomre 2002), vu le grand rôle que joue la circulation méridienne dans les dynamos du type transport de flux.

Les conclusions déduites de l'approche des champs moyens pour décrire l'activité magnétique du Soleil sont à considérer avec une certaine prudence car cette théorie moyenne ne s'intéresse qu'aux grandes échelles et possèdent beaucoup de paramètres

libres. Nous savons que les simulations 3D MHD sont une alternative de choix pour comprendre le magnétisme des étoiles et du Soleil en particulier. Le paradigme actuel, déduit des simulations non linéaires 3-D MHD (voir par exemple Cattaneo 1999, Cattaneo & Hughes 2001, Brun et al. 2004), est de considérer qu'il y a en fait deux dynamos différentes dans le Soleil: une à petite échelle associée aux mouvements turbulents convectifs expliquant l'activité magnétique irrégulière, et l'autre à grande échelle certainement localisée à la base de la zone convective solaire dans la tachocline (cf. chapitre 5), expliquant l'éruption régulière des taches solaires (ou diagramme papillon) et le renversement tous les 11 ans de la polarité du champ poloidal et toroidal solaire moyen. Réaliser l'équivalent d'un diagramme papillon à l'aide d'un modèle auto-consistant 3D MHD constitue un des défis majeurs des années à venir.

En ce qui concerne les autres type d'étoiles, la bonne corrélation entre rotation et activité obtenus par Noyes et al. (1984), Durney et Latour (1986), Baliunas et al. (1996), Saar & Brandenburg (1999) renforce l'idée de la présence d'une dynamo globale de type interfaciale dans les étoiles de type solaire. En étendant ce concept de dynamo aux autres type spectral ($F- > M$), il semblerait qu'une transition du type de dynamo depuis $\alpha - \omega$+transport de flux, vers une dynamo α^2 et enfin une dynamo turbulente (comme avec la dynamo de surface de Cattaneo (1999)) s'opère.

Il est cependant utile de rappeler que magnétisme stellaire n'implique pas forcément effet dynamo. Par exemple pour les étoiles Ap, l'effet dynamo n'est peut être pas nécessaire pour expliquer leur magnétisme très rare, un champ fossile en est peut être la cause (voir Moss 2001, 2003, mais aussi chapitre 6 et Spruit 2002).

Après cette longue introduction présentant la thématique de ce travail de recherche, nous allons maintenant dans la partie 2, discuter en détail notre contribution originale au vaste sujet de la magnétohydrodynamique stellaire.

Deuxième partie

Simulations 3-D en Magnétohydrodynamique Stellaire

Chapitre 4

Convection, Rotation et Magnétisme dans le Soleil

Dans ce chapitre nous allons nous intéresser aux propriétés dynamiques globales du Soleil en étudiant sa convection, le profil de rotation de ses couches superficielles et son activité magnétique interne. Pour se faire nous allons utiliser le code ASH (voir Appendice 1) et modéliser numériquement, tridimensionnellement, non linéairement et en fonction du temps sa zone convective. Vu le haut degré de turbulence de la zone convective solaire, caractérisé par un nombre de Reynolds de l'ordre de 10^{15} et plus de 10 ordres de grandeur séparant les petites échelles spatiales (où l'énergie est dissipée) des grandes échelles (typiquement l'épaisseur de la zone convective), une telle tache est toujours actuellement impossible sans hypothèses simplificatrices [16]. Notre approche consiste donc à modéliser en géométrie sphérique le plus correctement possible les grandes échelles de la convection solaire et de faire du mieux possible pour traiter les petites échelles; c'est ce que l'on appelle des simulations de types LES (Large Eddy Simulations)-SGS (SubGrid Scale) (cf. Lessieur 1999, Pope 2003). L'avantage d'une telle approche est que la convection se développe dans la bonne géométrie et aucune périodicité spatiale *ad-hoc* n'est présupposée comme dans beaucoup des approches locales utilisant la géométrie cartésienne (Galloway & Weiss 1981, Hurlburt et al. 1986, Cattaneo et al. 1991, Brandenburg et al. 1996, Brummell et al. 1996, 1998, Cattaneo 1999, Stein & Nordlund 1998, Robinson & Chan 2003, Proctor 2004, Rincon et al. 2005). Ces modèles locaux permettent cependant d'atteindre des degrés de turbulence plus élevés que les simulations globales, voire d'étudier la granulation solaire avec un très bon réalisme (dans ce cas la taille maximale de la boite correspond à la supergranulation) et constituent donc un effort numérique nécessaire et complémentaire des

16. même sur les ordinateurs massivement parallèles disponibles dans les centres de calculs centralisés tel le CCRT au CEA, l'IDRIS en France ou les centres NPACI américains

simulations globales discutées dans ce manuscrit.

L'étude de la physique des couches supérieures du Soleil (chromosphère, couronne, vent) est un vaste sujet en lui-même et ne sera pas abordée dans ce manuscrit (voir cependant les perspectives (chapitre 7) et les efforts en cours dans la communauté pour coupler l'interieur solaire à son atmosphère étendue). Il semble cependant clair qu'une grande partie des phénomènes magnétiques observés à la surface (CME's, protubérances, etc...) est dûe à l'activité magnétique interne soit via l'apparition/génération continue de flux, soit via l'émergence de régions actives et leur interaction permanente avec la convection turbulente. Ainsi comprendre le fonctionnement de la dynamo interne du Soleil, permet de mettre en place le premier bloc d'un modèle du Soleil intégrant le couplage dynamique interne-externe. Le passage de la transition de $\beta = p_{gaz}/p_{mag}$ fort à l'intérieur à β faible à l'extérieur constitue déjà un difficile problème qui commence à être sérieusement étudié (Amari et al. 2004).

4.1 Contexte Général

Les premiers calculs de convection non linéaire en coquille sphérique sous l'influence de la rotation étaient basés sur l'approximation Boussinesq (Cuong & Busse (1981), dans le cas de la convection terrestre et Gilman (1979), dans le cas solaire), l'analyse linéaire ayant été extensivement traitée par Chandrasekhar (1961) en axisymétrique et par Roberts (1968), Busse (1970), Gilman (1975) et Busse & Cuong (1977) dans le cas général. Dans ces simulations pionières à faibles nombres de Rayleigh et Reynolds, la convection est caractérisée par des structures dominées par des cellules convectives en forme de colonnes alignées le long de l'axe nord-sud (i.e. cellules bananes). Ces structures convectives se déplacent plus rapidement que l'écoulement moyen local (on parle de sur rotation), en accord avec l'analyse linéaire (Busse 1970). Gilman et Miller (1981) et Gilman (1983), sont les premiers à étudier la dynamo solaire en couplant l'équation d'induction aux équations hydrodynamiques dans l'approximation Boussinesq. Ils ont démontré que dans un espace de paramètres restreint, une dynamo cyclique entièrement localisée dans la zone convective solaire est possible (dynamo distribuée) mais sa période est trop courte (1.5 ans) comparée aux 11 ans du cycle solaire. Dès 1985, Glatzmaier entreprit de prendre en compte de façon plus réaliste la forte stratification présente dans les enveloppes convectives stellaires (Glatzmaier 1985a,b, 1987). Il confirme l'existence d'une dynamo cyclique mais trouve que le champ magnétique migre vers les pôles plutôt que vers l'équateur. L'ajout d'une zone stable semble ralentir le cycle de la dynamo mais ne modifie pas le sens de propagation du champ magnétique. Dans tous ces modèles, la rotation différentielle de la zone convective est

plutôt cylindrique, profil qui était également utilisé par les modèles de champ moyen (Stix 1976). Or nous avons vu au chapitre 2, que l'héliosismologie va révolutionner les modèles de dynamo solaire en révélant que le profil de rotation différentielle du Soleil est plutôt indépendant de r (Libbrecht 1989, Thompson et al. 2003).

Notre étude sur la convection et l'activité magnétique solaire s'inscrit dans la continuité des travaux de Gilman et Glatzmaier; elle consiste à étudier la rotation différentielle et la dynamo solaire à partir d'une code MHD tridimensionnel, mais à beaucoup plus haute résolution ($\ell_{max} \sim 340$ vs 24 ou 32) et un plus haut degré de turbulence. Le code ASH utilisé pour notre étude est un code moderne écrit en Fortran 90, utilisant une méthode pseudo-spectrale basée sur les harmoniques sphériques et les polynômes de Chebyshev développée originalement par G. Glatzmaier (1984) pour résoudre les équations magnétohydrodynamiques dans l'approximation anélastique (cf. Chapitre 3 et Appendice A). Cependant ce code a été complètement revu depuis zéro en intégrant des commandes MPI (Message Passing Interface) afin d'être exécuté sur des ordinateurs massivement parallèles de dernière génération (Clune et al. 1999).

Dans cette étude, nous désirons ainsi réexaminer à haute résolution, certains aspects de la dynamo interfaciale (à la Parker 1993) en procédant pas étapes successives, et ainsi progresser vers un modèle global de la dynamo solaire. Nous avons donc décidé de discuter nos travaux sur la convection et son interaction avec la rotation et les champs magnétiques obtenus avec le code ASH, en distinguant les effets les uns après les autres puis de les considérer tous ensemble. Nous avons été inspirés en cela par le livre de Chandrasekhar (1961) qui a magistralement étudié la stabilité linéaire de ce problème dans l'approche Boussinesq et construit en quelque sorte les fondements de la dynamique des fluides astrophysiques sur lesquels reposent cette étude. Sans avoir la prétention d'être aussi exhaustif que Chandrasekhar, nous nous sommes surtout intéressés à l'aspect non linéaire du couplage entre ces processus physiques et voulons en particulier insister sur certains points comme les motifs de convection obtenus, la forme du spectre de l'énergie cinétique et magnétique (si présente), l'existence d'écoulements moyens et/ou d'un effet dynamo dans de tels systèmes dynamiques.

4.2 Le Modèle Numérique

Le modèle consiste à résoudre à trois dimensions en coordonnées sphériques (r, θ, ϕ), les équations de la MHD pour un gaz parfait contenu dans une coquille sphérique de r=0.7 à 0.96 R, avec $\theta = [0,\pi]$ et $\phi = [0,2\pi]$ (voir Figure 4.1). Il repose sur une description simplifiée de la zone convective solaire: le flux de chaleur F imposé à la base du domaine, la vitesse angulaire Ω_0 (dans les cas avec rotation), la masse M et le rayon

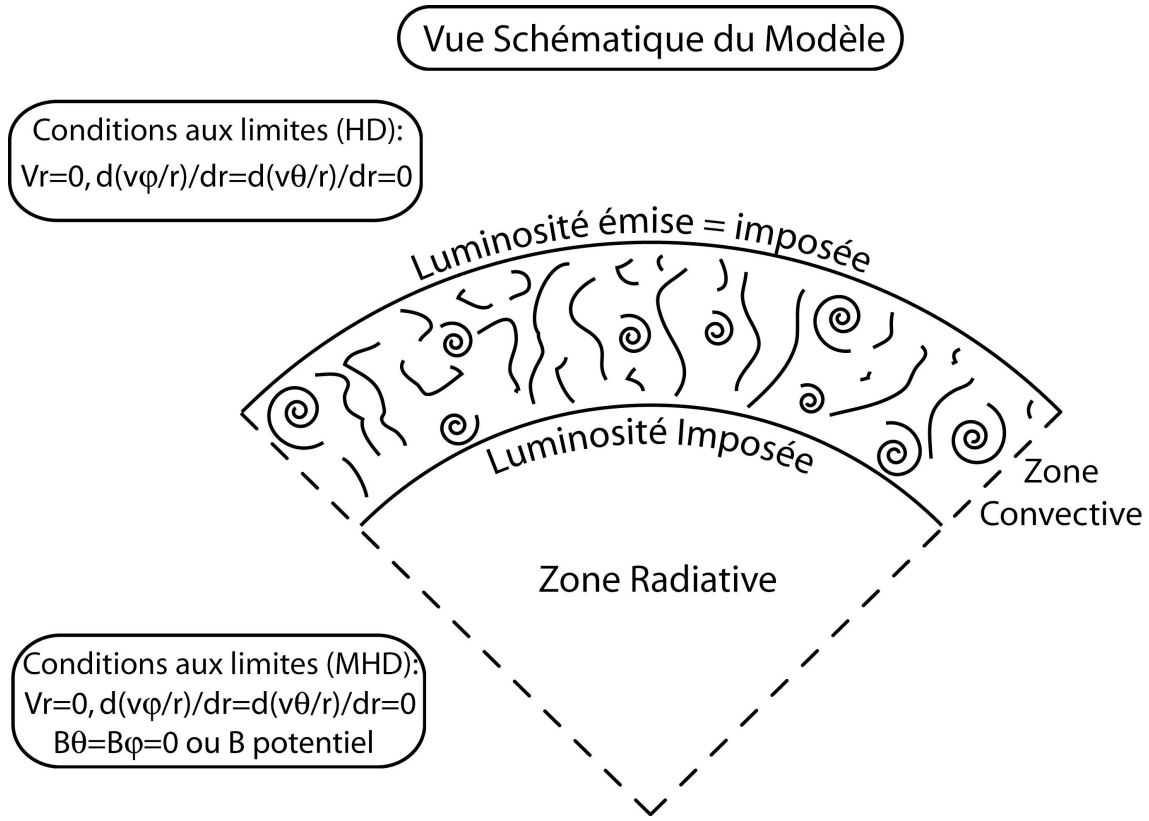

FIG. 4.1 – *Vue schématique du modèle numérique (plan équatorial $r - \phi$ tronqué en longitude)*

R, correspondent aux valeurs solaires. Nous avons calculé quatre cas qui tour à tour incorporent de plus en plus d'ingrédients physiques et ce, afin de se rapprocher le plus possible d'un modèle réaliste de l'enveloppe convective du Soleil (cf. Table 4.1). Les couches les plus externes du Soleil, où le gaz est partiellement ionisé et où la granulation est présente sont encore hors de portée ($\ell_{max} = 4000$) des simulations sphériques globales comme celles calculées avec ASH, mais on s'en rapproche petit à petit. Dans les quatre cas présentés ici, qui possèdent tous une condition aux limites inférieure impénétrable, nous ne prenons pas en compte l'effet de la pénétration convective[17].

17. on pourra cependant lire Miesch et al. (2000) pour une première approche en géométrie sphérique et purement hydrodynamique du problème. Des efforts sont en cours pour inclure un champ magnétique dans ces cas pénétratifs au sein de notre collaboration franco-américaine.

Cas	1	2	3	4
Rotation	F	V	F	V
Champ Magnétique	F	F	V	V
Ω_0 (rad s^{-1})	0	2.6×10^{-6}	0	2.6×10^{-6}
N_r,N_θ,N_ϕ	128, 256, 512	64, 256, 512	128, 512, 1024	128, 512, 1024
R_a	6.1 $\times 10^4$	8.1 $\times 10^4$	6.1 $\times 10^4$	8.1 $\times 10^4$
P_m	-	-	2.9	4
R_c	-	0.73	-	0.73
ν (cm^2 s^{-1})	1.9×10^{12}	1.4×10^{12}	1.9×10^{12}	1.4×10^{12}
κ (cm^2 s^{-1})	1.5×10^{13}	1.1×10^{13}	1.5×10^{13}	1.1×10^{13}
η (cm^2 s^{-1})	-	-	6.4×10^{11}	3.5×10^{11}
τ_η (jours)	-	-	540	990
R_e	151	136	145	121
R_m	-	-	448	486
Λ	-	-	-	20
P_e	19	17	18	15
R_o	-	0.12	-	0.11

TAB. 4.1 – *Paramètres des modèles de convection solaire, avec N_r,N_θ,N_ϕ, le nombre de points de grille radiaux, latitudinaux et longitudinaux. Toutes les simulations possèdent un rayon interne $r_{bot} = 5.0 \times 10^{10}$ cm et un rayon externe $r_{top} = 6.72 \times 10^{10}$ cm et toutes les quantitiés listées dans cette table ont été évaluées au milieu du domaine de la simulation. Pour tous les cas, le nombre de Prandtl $P_r = \nu/\kappa = 0.125$. Pour les cas (2 & 4) avec rotation le nombre de Taylor vaut $T_a = 4\Omega_0^2 L^4/\nu^2 = 1.2 \times 10^6$, avec $L = r_{top} - r_{bot}$. Nous utilisons la vitesse rms $\tilde{v}'$ et le champ magnétique rms $\tilde{B_r}'$ pour évaluer les nombres sans dimension de Reynolds R_e, Reynolds magnétique R_m, Elsasser Λ, Péclet P_e et Rossby R_o (cf. Table 4.3 et Appendice 2.2 pour leur définition). Un nombre de Reynolds basé sur la vitesse maximale au milieu du domaine serait de l'ordre de 5 fois plus grand.*

4.3 Convection Turbulente ($\mathbf{\Omega_0 = B = 0}$)

Le cas numéro 1 est le plus académique car il étudie uniquement la convection en géométrie sphérique sans l'effet ni de la rotation (omniprésente dans les étoiles) ni du champ magnétique. Sur la Figure 4.2, nous représentons un instantané de la vitesse radiale, des fluctuations de température et du logarithme de l'enstrophie (le carré de la vorticité $\omega = \boldsymbol{\nabla} \times \mathbf{v}$) réalisé dans la simulation 1. La solution a mûri plus de 2000 jours

(ou 70 temps de retournement convectif) et a atteint un équilibre statistiquement stationnaire après être passée par une phase de croissance exponentielle puis la saturation non linéaire de l'instabilité de convection.

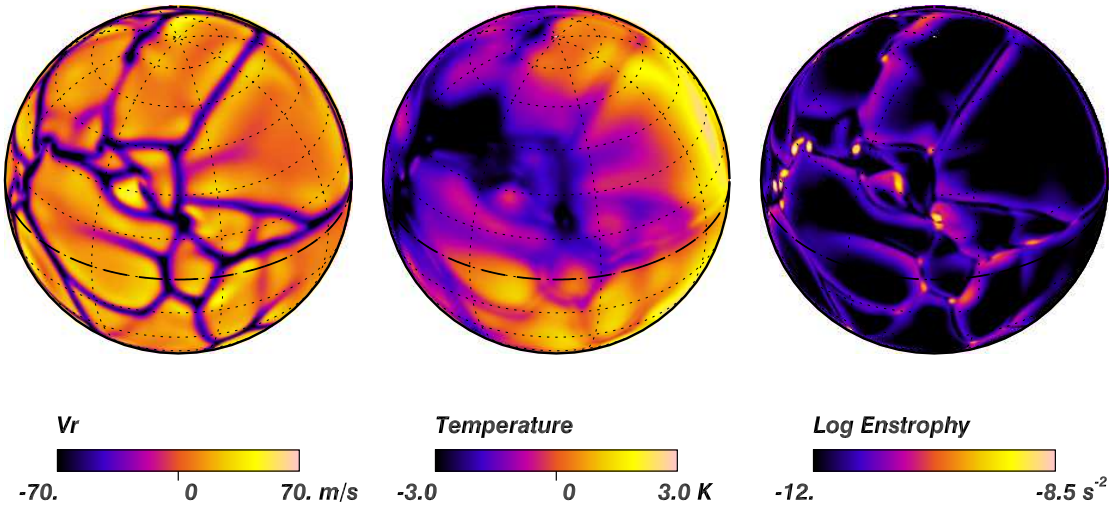

FIG. 4.2 – *Instantanés de la vitesse radiale, des fluctuations de température et du logarithme de l'enstrophie dans le cas 1.*

La première chose que nous constatons est que les motifs convectifs sont distribués sur toute la sphère. Il est en particulier frappant de voir la grande taille des cellules convectives montantes comparée à la finesse du réseau de flots descendants. Nous voyons que tout comme les cellules montantes chaudes, le réseau des flots descendants est fortement corrélé avec les fluctuations (ici négatives) de la température, ce à quoi on pouvait s'attendre vu que cela correspond à la présence d'un flux d'enthalpie (convectif) dirigé vers l'extérieur. De façon encore plus remarquable, on s'apercoît qu'il y a un dipôle dominant dans le champ de température avec la partie froide (négative) orienté face devant dans la Figure. Ce dipole convectif est une solution naturelle de la convection sans rotation dans une géométrie sphérique. Il possède le seuil de croissance le moins élevé dans le cas d'une sphère pleine et devient de plus en plus stable avec la réduction de l'épaisseur de la coquille sphérique de sorte que les modes $\ell = 6 - 8$ sont les plus instables dans le cas solaire (i.e pour un rapport $r_{bot}/r_{top} = 0.6 - 0.7$ et des conditions aux limites rigides, voir Chandrasekhar 1961, Busse 1982). Ce fort dipole en température est dû à une circulation à grande échelle des mouvements convectifs ascendants et descendants, séparant ainsi la coquille sphérique en deux hémisphères "virtuels" centrés sur les deux zones diamétralement opposées de forte convergence ($T_{dipole} < 0$) et de forte divergence ($T_{dipole} > 0$) de l'écoulement. Cependant le nombre

de Rayleigh atteint dans cette simulation numérique est suffisamment supercritique pour que tous les modes deviennent instables, de sorte que le dipole se retrouve excité et interagit avec les autres modes convectifs. Cela se traduit par un mouvement complexe ou selon la zone où les structures convectives se forment elle peuvent être pour le même contraste de température montantes ou descendantes, le tout dépendant de leur signe relatif au dipole. Les motifs convectifs ne possèdent pas un aspect très enroulés, l'enstrophie étant surtout intense le long des lignes de flots descendants ou les fortes zones de cisaillement se concentrent.

Nous indiquons dans la Table 4.2, la quantité d'énergie cinétique contenue dans la coquille convective et la séparons en ses composantes toroidales (DRKE), poloidales moyennes (MCKE) et non axisymétriques (i.e convectives CKE). Nous voyons que le gros de l'énergie est contenu dans les mouvements non-axisymétriques[18], démontrant l'aspect fondamentalement 3-D de la simulation. L'énergie contenue dans les mouvements poloidaux est de l'ordre de 2 fois plus importante que dans les mouvements longitudinaux, en accord raisonnable avec une distribution égale de l'énergie moyenne entre chacune des trois composantes de vitesse. Nous indiquons dans la Table 4.3, l'amplitude de la vitesse rms $\tilde{v}$ et des fluctuations $\tilde{v}'$ au milieu du domaine ainsi que des composantes individuelles. Nous voyons que la partie moyenne est très faible vu que la vitesse totale et ses fluctuations sont du même ordre, et que chaque composante de vitesse a la même amplitude, confirmation directe que les mouvements associés aux vitesses totales sont isotropes. La prise en compte de la rotation et la brisure de symétrie qu'elle impose devrait modifier cela.

4.4 Effets de la Rotation ($\mathbf{\Omega_0 \neq 0}$, $\mathbf{B = 0}$)

Le cas numéro 2 discuté dans cette sous section, représente un premier effort pour modéliser la convection sous l'effet de la rotation afin d'étudier l'établissement de la rotation différentielle et de la circulation méridienne dans le Soleil. Il fait partie d'une série de calculs publiés dans Brun & Toomre (2002), joint à ce manuscrit. Il est dans la continuité, mais à plus haute résolution ($\sim$ 10 fois supérieure), des efforts entrepris par Gilman et Glatzmaier dans les années 80 pour comprendre la rotation différentielle du Soleil (voir bibliographie).

Afin de pouvoir évaluer l'effet de la rotation sur la convection nous avons représenté

18. vis à vis d'un repère tournant virtuel alignés le long de l'axe z comme pour les cas 2 & 4. Une définition plus générale reposant sur la décomposition poloidale/toroidale (cf. équation A.9 et A.10) peut être utilisée (voir Busse 2000), mais nous ne pensons pas que les conclusions sur la dominance des mouvements fluctuants seraient différentes

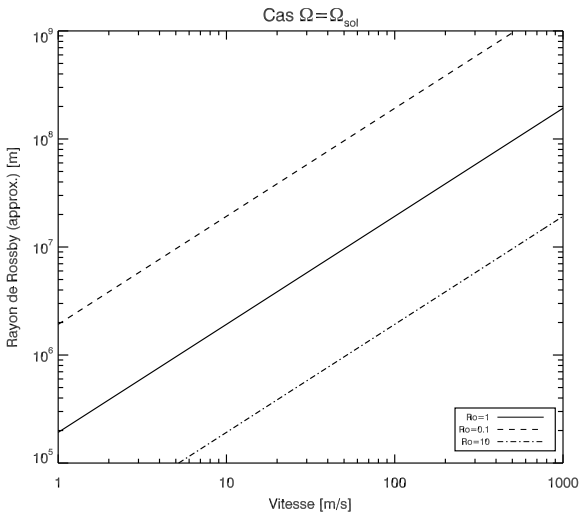

FIG. 4.3 – *Le rayon de Rossby défini comme* $L = V/(2\Omega_0 Ro)$ *évalué pour le taux de rotation solaire. La courbe* $Ro = 1$ *délimite pour une vitesse donnée le rayon* L *minimum pour lequel la rotation domine.*

plusieurs variables du modèle sur la Figure 4.4, dont notamment les composantes radiale et longitudinale de la vitesse, les fluctuations de température et de pression, la vorticité radiale et le logarithme de l'enstrophie. On remarque tout de suite un aspect moins isotrope des mouvements convectifs surtout dans la bande équatoriale, où il y a une tendance à l'alignement avec l'axe de rotation des lignes de flots descendants. Celles-ci sont toujours plus concentrées que les cellules montantes. À l'interstice du réseau de flots descendants on trouve les sites de plus forte vorticité, enstrophie et fluctuation négative de la pression et de la température. Cela confirme plusieurs choses: 1) il y a toujours une bonne corrélation entre champ de vitesse radiale et température pour transporter l'énergie vers l'extérieur, 2) la convection n'est pas très éloignée d'un équilibre géostrophique, vu qu'autour des dépressions dans l'hémisphère nord, la vorticité radiale est positive (i.e dirigé vers l'extérieur) ce qui correspond à un mouvement contre-horaire, i.e cyclonique. Le cas 2 possède d'ailleurs un degré de cyclonicité nettement supérieur au cas 1, avec des valeurs maximales de l'ordre de 10 fois plus élevées. On remarque que la température ne possède plus ce fort dipole en arrière plan, et donc les structures possédant une fluctuation de température négative sont bien plus majoritairement descendantes que dans le cas 1. Par contre, à la surface, la température possède trois bandes alignées de l'équateur aux pôles, respectivement tièdes, froides et chaudes. Cette variation en latitude est accompagnée de gradients de pression et d'entropie complémentaires. Nous constatons également que l'entropie est à l'origine d'un vent thermique brisant en partie la cylindricité du profil de rotation réalisé dans

le cas 2 (voir Appendices 4.2 et Brun & Toomre 2002).

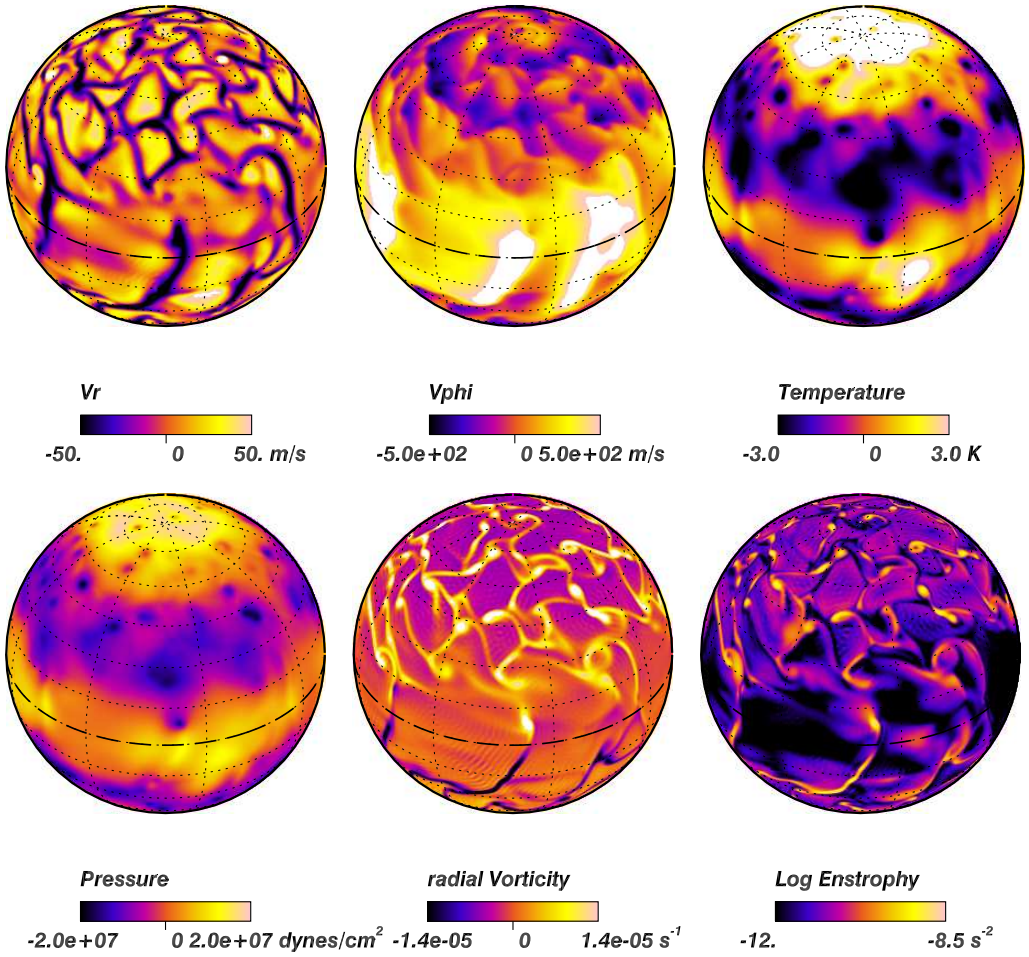

FIG. 4.4 – *Instantanés des composantes radiales et longitudinales de la vitesse, des fluctuations de température et de pression, de la composante radiale de la vorticité et du logarithme de l'enstrophie dans le cas 2.*

Nous avons également listé Table 4.2, l'énergie cinétique et sa décomposition en ces différentes composantes. La différence avec le cas 1 est claire, plus de 50% de l'énergie contenue dans les mouvements non-axisymétriques (fluctuants) se retrouve dans la rotation différentielle, de sorte que maintenant DRKE domine. Alors que dans le cas 1, CKE et DRKE état du même ordre de grandeur, ce n'est maintenant plus le cas. Dans la Table 4.3, nous indiquons également les vitesses rms et leurs contreparties fluctuantes. Ici encore, nous pouvons constater la différence nette avec le cas 1, $\tilde{v}$, $\tilde{v}_\phi$ sont de l'ordre du double de $\tilde{v}'$ et $\tilde{v}'_\phi$, preuve de la présence d'une fort vent zonal axisymétrique (i.e la rotation différentielle).

Les profils de rotation différentielle obtenus dans nos simulations, en particulier dans

le cas AB (voir Brun & Toomre 2002), sont en accord raisonnable avec l'héliosismologie (Thompson et al 2003): Elles présentent un contraste $\Delta\Omega/\Omega_0$ de 30% (cf. Table 4.2, une certaine constance le long des lignes radiales à moyenne latitude et un fort ralentissement de la rotation des régions polaires. Il faut reconnaître cependant que la contrainte de Taylor qui tend à faire que les fluides en rotation deviennent quasi 2-D et alignés le long de l'axe de rotation est dur à briser. Plusieurs effets peuvent y parvenir dans le cas HD, la baroclinicité (non alignement des gradients de densité et pression), les tenseurs de Reynolds, voire la viscosité (mais ce n'est pas très pertinent pour le Soleil) (voir Appendice 3). Dans notre cas, il semble que cela soit l'effet cumulé d'un vent thermique et des tenseurs de Reynolds associés aux fortes plumes convectives perçant tout le domaine convectif qui soit à l'origine de l'établissement de la rotation différentielle (Brummell et al. 1998, Miesch et al. 2000). De récents travaux par Robinson (2004), Rempel (2005) et Rudiger & Kitchatinov (2005) semblent privilégier le vent thermique comme le principal terme à l'origine de la rotation conique du Soleil. Ce vent serait établi, soit par diffusion thermique depuis la tachocline vers la zone convective, soit par transport anisotrope en latitude dans la zone convective comme observé dans le cas 2 simulé ici. Comme le montre l'équation du vent thermique générale (cf. Appendice 4.2 et Durney 1999), il n'y a pas que ce terme barocline qui rentre en jeu, mais aussi les tenseurs de Reynolds et Maxwell. Quel poids respectif possèdent ces différents termes l'un envers l'autre dans l'établissement de la rotation différentielle solaire reste encore sujet à débat. Des travaux sont en cours pour essayer de caractériser encore plus précisément et systématiquement cela. Notamment un récent papier par notre collaboration franco-américaine, Miesch, Brun & Toomre (2006) a montré qu'il est en effet possible de rendre les profils de rotation de nos simulations plus coniques si nous prenions en compte l'influence de la tachocline, via une condition aux limites thermiques modifiée correspondant à une variation en latitude de l'entropie.

La circulation méridienne possède comme on l'a vu une amplitude plus faible (de l'ordre de 20 m/s) que la rotation différentielle (i.e MCKE << DRKE), ce qui est en plutôt bon accord avec les observations (Chapitre 2 et Haber et al. 2002). La présence de plusieurs cellules méridiennes, tant en latitude, qu'en profondeur, n'avait pas été anticipée. Cependant, de premières évidences de l'existence de plusieurs cellules en latitude sont apparues lors du pic d'activité magnétique du Soleil en 2001 (Haber et al. 2002). Ces cellules traversent-elles toutes la zone convective, comme certains modèles de dynamo de type Babcock-Leigthon le suggèrent, ou se bouclent-elles au milieu de la zone convective, comme dans nos simulations? Répondre à cette question est clairement un des défis à venir avec des satellites comme SDO.

TAB. 4.2 – *Energies, et Rotation Différentielle Typiques*

Cas	1	2	3	4
Volume Average				
KE	8.32×10^6	9.01×10^6	7.79×10^6	5.26×10^6
DRKE/KE	2.1%	59.3%	2.5%	49.5%
MCKE/KE	5.6%	0.3%	7.8%	0.5%
CKE/KE	92.3%	40.4%	89.7%	50.0%
ME	-	-	3.45×10^5	3.47×10^5
ME/KE	-	-	4.4%	6.6%
MTE/ME	-	-	1.5%	1.5%
MPE/ME	-	-	1.1%	0.5%
FME/ME	-	-	97.4%	98%
$\Delta\Omega/\Omega_o$	-	34%	-	24%

Pour chaque simulation nous indiquons la densité d'énergie cinétique KE ($1/2\ \bar{\rho}v^2$), moyennée sur le volume et en temps, accompagnée des contributions relatives venant de la convection non-axisymétrique (CKE) et de la rotation différentielle axisymétrique (DRKE) et de la circulation méridienne (MCKE). Nous listons également, pour les cas appropriés, la moyenne de la densité d'énergie magnétique ME ($B^2/8\pi$) accompagnée des contributions relatives venant de ses composantes fluctuantes (non-axisymétriques) FME et moyennes (axisymétriques) toroidal et poloidal MTE et MPE. Le contraste relatif en latitude de la rotation différentielle, $\Delta\Omega/\Omega_o$, entre latitudes 0° et 60° près du haut du domaine, complète le tableau (moyenne des deux hémisphères).

4.5 Effets du Champ Magnétique ($\mathbf{\Omega_0 = 0}$, $\mathbf{B \neq 0}$)

L'ajout d'un champ magnétique dans nos simulations de convection turbulente peut nous permettre d'aborder certains aspects du problème de la dynamo solaire. Nous ne considérons pour le cas 3 qu'une coquille convective magnétisée sans l'influence de la rotation et de la brisure d'isotropie (supplémentaire par rapport à la direction radiale) et de la réflection miroir qui en résulte pour les flots convectifs (Parker 1955). On peut ainsi s'attaquer au problème de la dynamo convective turbulente en géométrie sphérique[19].

Sur la Figure 4.5a, nous représentons l'évolution temporelle de l'énergie magnétique

19. ce problème a reçu plus d'attention en géométrie cartésienne avec des conditions aux limites horizontales périodiques (voir par exemple Cattaneo (1999), Proctor (2003)).

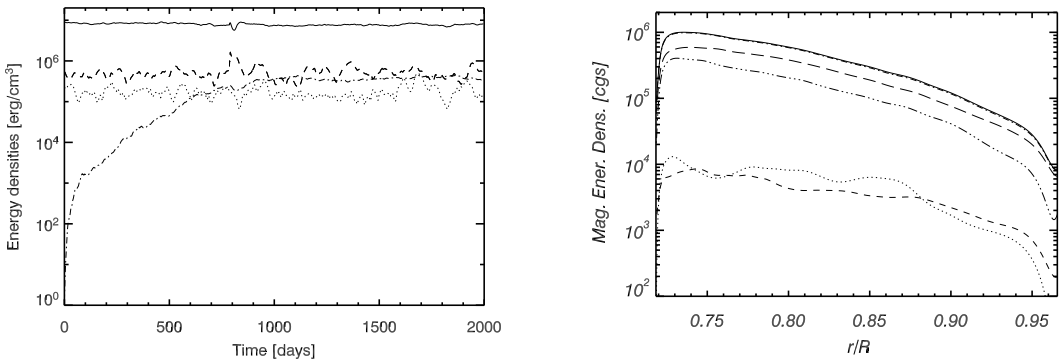

FIG. 4.5 – *(panneau gauche) Énergies cinétiques (KE, solide) et magnétiques (ME, tiret-point) en fonction du temps, accompagnées de MCKE (tiret) et DRKE (point) dans le cas non-rotatif. (panneau droit) Distribution en fonction du rayon de l'énergie magnétique (ME, solide) et des composantes moyennes toroidales (MTE, point) et poloidales (MPE, tiret), et fluctuantes (FME, indistinguable de la courbe ME), fluctuantes poloidales (FPE, grand tiret) et fluctuantes toroidales (FTE, tiret-3 points) dans le cas 3.*

(ME), depuis l'introduction dans le cas 1, dans sa phase mûre, d'une graine dipolaire de champ magnétique d'amplitude infinitésimale ($ME_0/KE < 10^{-6}$). L'énergie magnétique commence d'abord par une croissance exponentielle durant les 700 premiers jours, puis sature non linéairement et se maintient sur plusieurs temps ohmiques τ_η (cf. Table 4.1) à un niveau élevé, représentant de l'ordre de 4.5% de l'énergie cinétique (KE) (cf. Table 4.2). Cette croissance ajoutée à la maintenance du champ magnétique est un bon indicateur pour la présence d'un effet dynamo dans cette simulation de convection car dans le cas présent les composantes poloidales (MPE) et toroidales (MTE) sont bien amplifiées (avec MTE $\sim$ MTE) et non pas seulement l'une d'entre elle (cf. Figure 4.5). Cela suppose que les mouvements convectifs aient des trajectoires suffisamment chaotiques et tridimensionnelles pour amplifier le champ davantage qu'il n'est diffusé, autrement dit $Rm > Rm_{crit}$. Nous évaluons ce seuil à $Rm_{crit} \sim 250$. Ceci est très intéressant car on obtient un effet dynamo alors qu'il n'y a pas a priori de processus d'amplification comme l'effet α lié à la présence d'une hélicité cinétique globale (au moins par hémisphère), confirmant ainsi les résultats obtenus en géométrie cartésienne dans l'approximation Boussinesq par Cattaneo (1999) sur l'existence d'une dynamo non hélicitaire, ou turbulente (dans le jargon habituel).

On constate en analysant les Tables 4.2 et 4.3, que les composantes moyennes du champ magnétique sont faibles comparées aux champs fluctuants, qui représentent près

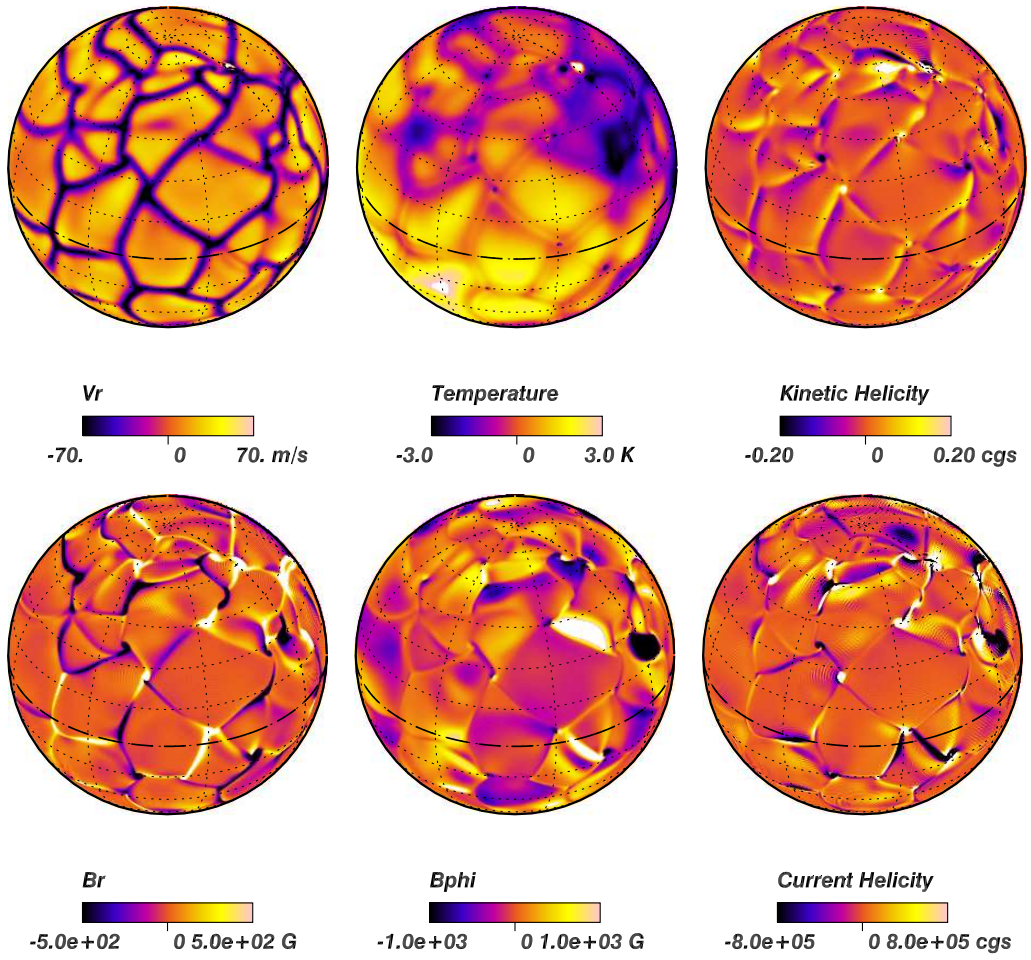

FIG. 4.6 – *Instantanés de la vitesse radiale, des fluctuations de température, de l'hélicité cinétique, des composantes radiales et longitudinales du champ magnétique et de l'hélicité de courant dans le cas 3.*

de 97.4% de ME. L'interaction entre la convection et le champ magnétique s'opère donc sur tout un spectre d'échelles spatiales turbulentes et pas uniquement à grande échelle avec les composantes moyennes (axisymétriques). L'amplitude typique des champs magnétiques entretenus est de l'ordre de 1000 G. Figure 4.5b nous représentons la distribution d'énergie en fonction du rayon. On constate que l'énergie pique vers le bas du domaine, une indication probable de pompage turbulent par les flots étroits et descendants du champ magnétique comme observé par Tobias et al. (2001). Nous voyons que pour ce qui est du champ fluctuant, la majorité de l'énergie (66%) est concentrée dans la composante poloidale (FPE) du champ, ce qui se traduit par une redistribution égale d'un tiers de FME à chaque composante de $\mathbf{B}$.

La croissance de ME, se produit au détriment de KE et CKE qui voient leur ampli-

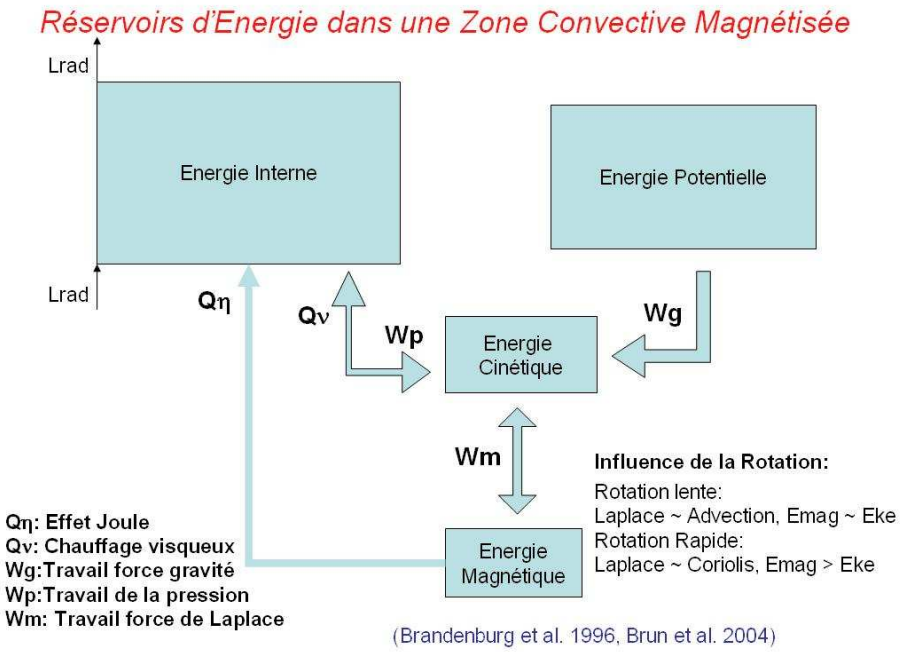

FIG. 4.7 – *Représentation shématique des différents réservoirs d'énergie présents en convection magnétisée et des processus physiques les reliant*

tude diminuer d'environ 8%. Il est clair que l'énergie magnétique n'est que le produit final d'une séquence complexe d'interactions entre les différents réservoirs d'énergie présents dans le système que sont l'énergie thermique (ET) et potentielle (EP) et dans une moindre mesure KE (qui sont des ordres de grandeurs plus petites que ET et EP, voir figure 4.7, Brandenburg et al. 1996 et Brun et al. 2004). L'amplitude de l'énergie cinétique est fonction du flux d'énergie imposée à la base de la zone convective (ici un flux radiatif venant chauffer la base de la ZC et alimentant le réservoir d'énergie thermique). L'échange entre l'énergie cinétique et ET et EP se fait via les mouvements générés par le travail de la pression et par la flottaison. Dès lors, comme l'énergie cinétique est l'intermédiaire unique pour convertir en énergie magnétique l'énergie contenue dans les réservoirs, cela se traduit en la modification/ralentissement des mouvements et donc à une baisse de KE, une fois que l'amplitude de B, et donc de la force de Laplace, est devenue suffisante. On peut identifier ce phénomène comme un des processus non linéaires permettant la saturation de l'énergie magnétique dans nos simulations. Nous trouvons que ce processus de saturation apparaît quand ME/KE$\sim$0.005.

Dans la Figure 4.6, nous représentons la vitesse radiale, les fluctuations de température, l'hélicité cinétique, les composantes radiales et longitudinales du champ magnétique et l'hélicité de courant pour le cas 3. Nous remarquons que la présence de champ magnétique n'élimine pas le dipole en température comme l'a fait la rotation dans

le cas 2. Le champ magnétique radial après avoir été balayé du centre des cellules convectives se retrouve concentré le long des lignes de flots descendants avec un fort gradient de polarité de part et d'autre de celles-ci, alors que le champ magnétique longitudinal est lui plus allongé et se retrouve souvent sous forme de zones étendues de mono-polarité couvrant toute une cellule convective. Les motifs convectifs semblent avoir une taille caractéristique plus petite que dans le cas 1, sans doute à cause de l'effet de la pression magnétique qu'exercent les champs sur les mouvements. Cependant cet effet n'est pas trop fort car ME ne représente que 5% de KE[20]. Les hélicités cinétiques et magnétiques ne présentent pas de structures particulières, confirmant ainsi l'absence dans les simulations sans rotation d'un signe préférentiel par hémisphère pour ces quantités physiques.

TAB. 4.3 – *Amplitudes des Vitesses et Champs Magnétiques*

Milieu de la Zone Convective												
Cas	$\tilde{v}_r$	$\tilde{v}_\theta$	$\tilde{v}_\phi$	$\tilde{v}'_\phi$	$\tilde{v}$	$\tilde{v}'$	$\tilde{B}_r$	$\tilde{B}_\theta$	$\tilde{B}_\phi$	$\tilde{B}'_\phi$	$\tilde{B}$	$\tilde{B}'$
1	99	100	98	95	172	167	-	-	-	-	-	-
2	61	63	137	68	163	111	-	-	-	-	-	-
3	94	97	93	91	165	160	1857	2052	2021	1975	3427	3381
4	58	54	104	59	131	99	1752	1855	2277	2239	3420	3386

Reportées pour chaque simulation sont: l'amplitude rms de la vitesse $\tilde{v}$ et de chacune de ses composantes, $\tilde{v}_r$, $\tilde{v}_\theta$, et $\tilde{v}_\phi$, moyennée sur un intervalle de temps ($\sim$ 100 jours) et sur une surface située au milieu de la zone convective. Aussi reportées sont les amplitudes rms des vitesses totales et longitudinales fluctuantes, $\tilde{v}'$, et $\tilde{v}'_\phi$, obtenues après avoir soustrait la moyenne temporelle et azimutale. Pour les simulations magnétiques, nous avons inclu les amplitudes rms correspondantes pour le champ magnétique et ses composantes, $\tilde{B}$, $\tilde{B}_r$, $\tilde{B}_\theta$, $\tilde{B}_\phi$, $\tilde{B}'$, et $\tilde{B}'_\phi$. Les vitesses sont exprimées en m s^{-1} et les champs magnétiques en G.

20. Des expériences numériques récentes avec un champ magnétique externe imposé d'intensité variable (Cattaneo et al. 2003), ont montré qu'au delà d'un certaine amplitude du champ la taille des cellules convectives rétrécit jusqu'à devenir figée

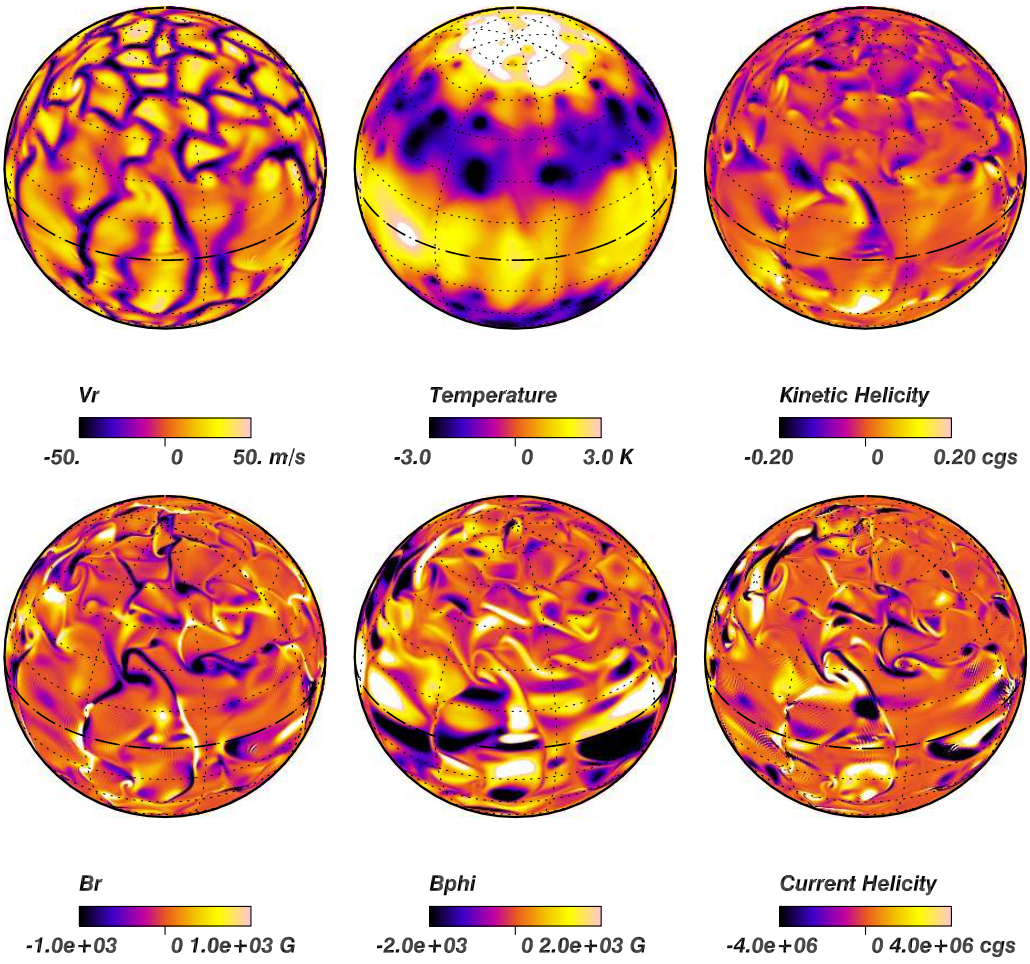

FIG. 4.8 – *Instantanés de la vitesse radiale, des fluctuations de température, de l'hélicité cinétique, des composantes radiales et longitudinales du champ magnétique et de l'hélicité de courant dans le cas 4.*

4.6 Effets Couplés de la Rotation et du Champ Magnétique ($\mathbf{\Omega_0 \neq 0}$, $\mathbf{B \neq 0}$)

Le cas numéro 4, représente un premier effort majeur pour modéliser la convection sous l'effet de la rotation et du champ magnétique à haute résolution numérique afin d'étudier l'établissement de la rotation différentielle, de la circulation méridienne, d'un effet dynamo, voire d'un cycle magnétique et de l'effet de retour de la force de Laplace sur la rotation et la convection dans le Soleil. Il fait partie d'une série de calculs publiés dans Brun, Miesch & Toomre (2004), joint à ce manuscrit. C'est certainement actuellement le cas le plus réaliste pour étudier non linéairement et en géométrie sphérique l'effet cumulé de la rotation différentielle et de l'effet dynamo. Il est, comme le cas 2,

dans la continuité, mais à beaucoup plus haute résolution ($\sim$ 10 fois supérieure), des efforts entrepris par Gilman et Glatzmaier dans les années 80 pour étudier la dynamo solaire (voir bibliographie).

Nous voulons ici juste récapituler les principaux résultats publiés dans notre article et les commenter en prenant en compte les résultats des 3 autres cas présentés dans ce chapitre.

Tout d'abord comme pour le cas 3 nous confirmons que la dynamo est possible du moment que le nombre de Reynolds magnétique est supérieur à un certaine valeur, ici évaluée à $Rm \sim 300$. Cette valeur critique est semble t-il plus élevée que dans le cas sans rotation mais nous n'avons pas fait une étude précise du seuil dans le cas sans rotation. Contrairement aux calculs de Gilman et Glatzmaier obtenus au milieu des années 80, notre dynamo est à petite échelle car nettement plus turbulente (Brun 2004). Cette simulation possède des propriétés très proches de celles trouvées dans le cas 3 sans l'effet de la rotation. Les différences principales viennent de la façon dont les énergies cinétiques et magnétiques sont réparties sur les différentes composantes (voir Table 4.2). Avec rotation, MTE est trois fois plus importante que MPE, ce qui n'était pas le cas avec la simulation 3, suggérant alors pour le cas 4, l'action d'un effet ω amplifiant MTE. L'énergie dans la circulation méridienne est beaucoup plus faible que dans le cas sans rotation, le gros de l'énergie étant dans CKE. Cela diffère du cas 2, où DRKE domine. Cette différence est dûe à la rétroaction du champ magnétique sur la rotation différentielle, qui résulte en ce que CKE $>$ DRKE. Les cas 3 et 4 différent également dans la répartition de l'énergie entre les parties fluctuantes, la présence de rotation amplifiant FTE, de sorte que FTE $\sim$ FPE.

Sur la figure 4.8, nous représentons les mêmes variables que sur la Figure 4.6. Les motifs convectifs et la topologie du champ magnétique (toroidal) sont clairement affectés par la présence de rotation. En particulier le champ toroidal est beaucoup plus allongé et enroulé autour de l'axe de rotation. En effet dans le cas 3, les zones larges composées d'une seule polarité de champ magnétique toroidal sont distribuées sans direction préférentielle, et ne présentent aucuns enroulements. Par contre pour le champ radial il n'y a pas de différence entre le cas 3 et 4, Br étant systématiquement entraîné par les mouvements horizontaux divergeants au centre des cellules montantes (balayés en quelque sorte) vers le réseau de flots descendants en périphérie. Comme pour B_r, l'hélicité de courant n'est pas trop modifiée par la rotation, bien qu'elle présente un aspect plus enroulé. Par contre, pour l'hélicité cinétique, variable cruciale dans la théorie du champ moyen puisque l'effet α lui est associé, le changement est significatif. En effet cette variable possède maintenant un signe dominant par hémisphère (négatif dans l'hémisphère nord) contrairement au cas 3. Pour confirmer cette propriété importante

pour la dynamo solaire, nous représentons figure 4.9, le profil radial de l'hélicité dans trois des cas discutés dans ce chapitre, cas 2, 3 et 4. On y remarque clairement que le cas 3 possède une hélicité négligeable sans signe préférentiel. À l'inverse les 2 cas avec rotation, possèdent une forte hélicité cinétique ayant le même signe en fonction de r (négatif en haut du domaine et positif en bas). La principale différence est que le cas 2 contient un degré supérieur d'hélicité, cela étant dû au fait que le champ magnétique dans le cas 4 tend à supprimer les zones de vorticité intense en s'opposant localement au cisaillement. Nous désirons ici insister sur le fait que dans les cas 3 & 4, l'absence ou la présence d'hélicité magnétique ne semble pas modifier de façon importante le rapport entre les champs magnétiques axi et non axisymétriques. Pour les deux modèles les champs non axisymétriques dominent et la rotation ne semble pas favoriser le développement d'une composante grande échelle axisymmétrique du champ. La relation entre l'effet α et l'hélicité cinétique, $\alpha = \tau/3(v \cdot (\boldsymbol{\nabla} \times v))$, ne semble donc pas simplement réalisée dans nos simulations. Il est fort probable cependant que l'hélicité magnétique ou de courant joue un rôle important dans l'établissement des propriétés globales des dynamos (Brandenburg 2005). De plus il est nécessaire d'étudier le rôle du champ initial introduit dans la simulation, car il se pourrait que notre choix d'un champ dipolaire axisymétrique, ne permette pas de différencier les cas avec ou sans rotation.

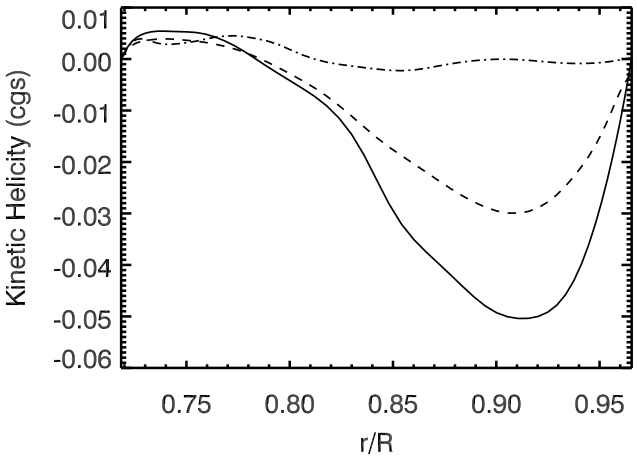

FIG. 4.9 – *Profil radial de l'hélicité cinétique en fonction de r et moyenné sur l'hémisphère nord dans les cas 2 (solid), 3 (tiret-point) & 4 (tiret).*

Le profil de rotation différentielle dans le cas 4 possède un plus faible contraste que celui réalisé dans le cas 2 (voir Figure 3 de Brun 2004). Ceci est dû à la croissance

de l'énergie magnétique qui se fait au détriment principalement de l'énergie contenue dans la rotation différentielle. Brun (2004) a montré en se basant sur les travaux de Eddy et al. (1976) que durant le minimum de Maunder il semblerait que le Soleil ait eu une rotation différentielle plus intense, et il a évalué qu'un rapport ME/KE de l'ordre de 0.05 serait suffisant dans le Soleil actuel pour reproduire cette différence d'amplitude de la rotation différentielle. Ambroz (2005) retrouve cette tendance dans le cycle solaire actuel, avec une rotation différentielle légèrement plus forte lors d'un minimum d'activité solaire (voir aussi Gilman & Howard 1984). Il est alors tentant de parler plutôt d'un "ω-quenching" plutôt que d'un α-quenching (Cattaneo & Hughes 1996) dans ce modèle incluant des écoulements moyens, et on peut se demander si les simulations dynamo en géométrie cartésienne n'incluant pas de rotation différentielle ne sont pas un peu académique. Il est également intéressant de remarquer que la présence de champ magnétique réduit significativement la contrainte de Taylor-Proudman et l'établissement d'un vent thermique en introduisant une brisure supplémentaire de la cylindricité dans le problème (voir Appendice 4.2).

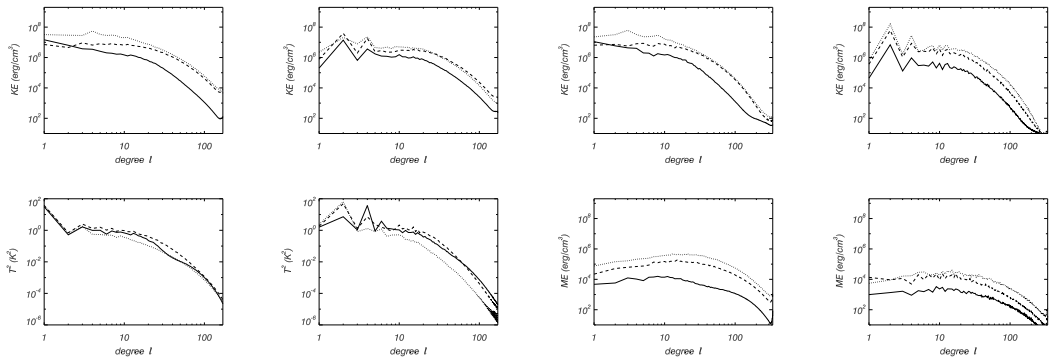

FIG. 4.10 – *Spectres d'énergie cinétique, magnétique et des fluctuations de températures en fonction du degré ℓ pour les cas 1 (panneaux haut et bas de gauche), 2 (2eme colonne), 3 (3eme colonne), & 4 (panneaux droits). Les spectres sont calculés à trois profondeurs, $r = 0.95R$ (ligne pleine), $r = 0.86R$ (tiret) et $r = 0.73R$ (pointillée).*

Finalement nous représentons Figure 4.10, différents spectres pour les quatres modèles afin de voir comment ceux ci sont modifiés par l'influence de la rotation et du champ magnétique. Il est connu qu'un fluide incompressible, turbulent, homogène et isotrope possède un spectre d'énergie cinétique dans sa partie inertielle dit de Kolmogorov $E_k \propto k^{-5/3}$ (Frisch 1999, Pope 2000). Cependant, dans le cas d'un gaz stratifié, Bolgiano (1959) a démontré que ce spectre est modifié en $E_k \propto k^{-11/5}$ et $E_T \propto k^{-7/5}$, pour les échelles de la convection ressentant les effets de flottaison (et donc d'accélération locale) via l'action d'un champ de température dynamique (voir aussi Chillà et al. 1993,

Benzi et al. 1998). Grappin et al (1983) ont démontré qu'une turbulence MHD possède un spectre différent $E_k = E_M \propto k^{-3/2}$. La rotation peut aussi modifier ces spectres pour les échelles plus grandes que le rayon de Rossby (Dubrulle & Valdetarro 1992). Nous voyons donc, que dans notre série de simulations, nous pouvons légitimement nous attendre à obtenir une variété de spectres, et éventuellement nous demander si une échelle de Bolgiano magnétique n'existe pas. Dans les simulations de convection, l'intervalle d'échelles où il y a injection de l'énergie est large, ce qui tend à rendre la zone inertielle petite. Malgré la résolution utilisée dans cette étude, nous ne retrouvons aucune des lois d'échelles énoncées plus haut dans les spectres présentés Figure 4.10, car leur régime inertiel est trop étroit. De tous les spectres, c'est celui de l'énergie magnétique qui est le moins éloigné des prédictions phénoménologiques (voir Brun et al. 2004).

Ces lois d'échelles misent à part, on remarque que pour le spectre de la température l'absence de rotation favorise l'émergence d'un fort dipole (cas 1 et 3) totalement absent dans le cas rotatif. Pareillement pour l'énergie cinétique, la présence d'une forte rotation différentielle (cas 2 et 4), modifie le spectre à grande échelle et déplace le pic vers les ℓ plus élevés. Par contre, pour l'énergie magnétique rien de tel n'est apparent, les spectres de ME étant presque identiques avec ou sans rotation, confirmant la nature proche des dynamos établies dans les cas 3 et 4. Ces deux dynamos sont plutôt de petites échelles (dominées par la convection turbulente) malgré la géométrie sphérique globale et la présence dans le cas 4 d'une rotation différentielle. Nos simulations de convection n'indiquent pas de façon claire qu'il existe une échelle supplémentaire entre les cas avec ou sans champ magnétique, les spectres d'énergie cinétique sont proches dans le cas 1 et 3, et 2 et 4. Nous notons par contre que la rotation modifie de façon plus radicale les spectres d'énergie cinétique, avec l'apparition à grande échelle de la forte composante $m = 0$ de la rotation différentielle (cf. spectres KE des cas 1 et 2). Cela pouvait être anticipé vu la brisure de symétrie que la rotation impose. Par contre la rotation n'influence pas le spectre d'énergie magnétique, ce qui est plus surprenant. En effet on pourrait s'attendre à ce que l'effet ω associé à la forte rotation différentielle présente dans le cas 4, modifie le spectre de l'énergie magnétique obtenu avec le cas 3, en générant un champ toroidal à grande échelle (au delà du Rayon de Rossby). Bien que l'énergie contenue dans MTE pour le cas 4 soit supérieure à celle contenue dans le cas 3 (cf. Table 4.2), la nature très non axisymétrique de nos solutions dynamos ne met pas en évidence cette différence. Il semble que la création de champs moyens grandes échelles plus intenses par cisaillement soit requise pour voir une modification du spectre d'énergie magnétique par la rotation. La nature instable de la convection ne permet pas d'amplifier des champs moyens suffisamment intenses, il semble que la

tachocline à la base de la zone convective soit plus propice à la génération d'un fort champ toroidal.

L'action cumulée de la rotation et du champ magnétique résulte en une dynamique plus complexe qui peut parfois amener la convection à devenir sous-critique (i.e se déclencher à une valeur plus basse que dans le cas purement magnétique ou rotationnel, cf. Chandrasekhar 1961), et ainsi modifier le seuil où la dynamo est réalisée ou l'aspect des motifs convectifs et les propriétés de la turbulence. Nous avons l'intention d'explorer encore plus en détails cette problématique en calculant par exemple les différentes échelles caractéristiques de nos simulations (échelle intégrale, de Bolgiano, visqueuse, voir par exemple Rincon 2005) et comment elles sont modifiées par la rotation et le champ magnétique.

4.7 Article publiés

4.7.1 Turbulent convection under the influence of rotation: sustaining a strong differential rotation

par Brun & Toomre 2002, ApJ, 570, 865

The Astrophysical Journal, 570:865–885, 2002 May 10

TURBULENT CONVECTION UNDER THE INFLUENCE OF ROTATION: SUSTAINING A STRONG DIFFERENTIAL ROTATION

Allan Sacha Brun and Juri Toomre
JILA and Department of Astrophysical and Planetary Sciences, University of Colorado, Boulder, CO 80309-0440;
sabrun@solarz.colorado.edu, jtoomre@jila.colorado.edu
Received 2001 June 8; accepted 2001 December 14

ABSTRACT

The intense turbulence present in the solar convection zone is a major challenge to both theory and simulation as one tries to understand the origins of the striking differential rotation profile with radius and latitude that has been revealed by helioseismology. The differential rotation must be an essential element in the operation of the solar magnetic dynamo and its cycles of activity, yet there are many aspects of the interplay between convection, rotation, and magnetic fields that are still unclear. We have here carried out a series of three-dimensional numerical simulations of turbulent convection within deep spherical shells using our anelastic spherical harmonic (ASH) code on massively parallel supercomputers. These studies of the global dynamics of the solar convection zone concentrate on how the differential rotation and meridional circulation are established. We have addressed two issues raised by previous simulations with ASH. First, can solutions be obtained that possess the apparent solar property that the angular velocity Ω continues to decrease significantly with latitude as the pole is approached? Prior simulations had most of their rotational slowing with latitude confined to the interval from the equator to about 45°. Second, can a strong latitudinal angular velocity contrast $\Delta\Omega$ be sustained as the convection becomes increasingly more complex and turbulent? There was a tendency for $\Delta\Omega$ to diminish in some of the turbulent solutions that also required the emerging energy flux to be invariant with latitude. In responding to these questions, five cases of increasingly turbulent convection coupled with rotation have been studied along two paths in parameter space. We have achieved in one case the slow pole behavior comparable to that deduced from helioseismology and have retained in our more turbulent simulations a consistently strong $\Delta\Omega$. We have analyzed the transport of angular momentum in establishing such differential rotation and clarified the roles played by Reynolds stresses and the meridional circulation in this process. We have found that the Reynolds stresses are crucial in transporting angular momentum toward the equator. The effects of baroclinicity (thermal wind) have been found to have a modest role in the resulting mean zonal flows. The simulations have produced differential rotation profiles within the bulk of the convection zone that make reasonable contact with ones inferred from helioseismic inversions, namely, possessing a fast equator, an angular velocity difference of about 30% from equator to pole, and some constancy along radial lines at midlatitudes. Future studies must address the implications of the tachocline at the base of the convection zone, and the near-surface shear layer, on that differential rotation.

Subject headings: convection — hydrodynamics — methods: numerical — Sun: interior — Sun: rotation — turbulence

1. INTRODUCTION

The solar turbulent convection zone has striking dynamical properties that continue to challenge basic theory. The most fundamental issues involve the solar rotation profile with latitude and depth and the manner in which the 22 yr cycles of solar magnetic activity are achieved. These two issues are closely interrelated since the global dynamo action is likely to be very sensitive to the angular velocity Ω profiles realized by convection redistributing angular momentum within the deep zone. Both dynamical topics touch on the seeming inconsistency that turbulence can be both highly intermittent and chaotic on smaller spatial and temporal scales yet exhibit large-scale ordered behavior (e.g. Brummell, Cattaneo, & Toomre 1995). The differential rotation profile established by the turbulent convection, although strong in contrast, is remarkably smooth; the global-scale magnetic activity is orderly, involving sunspot eruptions with very well-defined rules for field parity and emergence latitudes as the cycle evolves. The wide range of dynamical scales of turbulence present in the solar convection zone yield severe challenges to both theory and simulation: the discernible structures range from granules ($\sim 10^3$ km or 1 Mm in horizontal size), to supergranules ($\sim$30 Mm), to possible patterns of giant cells comparable to the overall depth of that zone ($\sim$200 Mm, or nearly 30% by radius). Given that the dissipation scales are on the order of 0.1 km or smaller, the solar turbulence encompasses at least 6 orders of magnitude for each of the three physical dimensions. The largest current three-dimensional turbulence simulations can resolve about 3 orders of magnitude in each dimension. Yet, despite the vast difference in the range of scales dynamically active in the Sun and those accessible to simulations, the latter have begun to reveal basic self-ordering dynamical processes yielding coherent structures that appear to play a crucial role in the global differential rotation and magnetic dynamo activity realized in the Sun.

It has long been known by tracking surface features that the surface of the Sun rotates differentially (e.g., Ward 1966; Schüssler 1987): there is a smooth poleward decline in the angular velocity Ω, the rotation period being about 25 days in equatorial regions and about 33 days near the poles. Helioseismology, which involves the study of the acoustic *p*-mode oscillations of the solar interior (e.g., Gough &

Toomre 1991), has provided a remarkable new window for studying dynamical processes deep within the Sun. This has been enabled by nearly continuous helioseismic observations provided from the *Solar and Heliospheric Observatory* with the high-resolution Michelson Doppler Imager (SOI-MDI; Scherrer et al. 1995) and from the ground-based Global Oscillation Network Group (GONG) set of six related instruments (Harvey et al. 1996). The helioseismic findings about differential rotation deeper within the Sun have turned out to be revolutionary since they are unlike any anticipated by convection theory prior to such probing of the interior of a star. Helioseismology has revealed that the rotation profiles obtained by inversion of frequency splittings of the *p* modes (e.g., Libbrecht 1989; Thompson et al. 1996; Schou et al. 1998; Howe et al. 2000b) have the striking behavior shown in Figure 1. The variation of angular velocity Ω observed near the surface, where the rotation is considerably faster at the equator than near the poles, extends through much of the convection zone with relatively little radial dependence. Thus, at midlatitudes Ω is nearly constant on radial lines, in sharp contrast to early numerical simulations of rotating convection in spherical shells (e.g., Gilman & Miller 1986; Glatzmaier 1987) that suggested that Ω should be nearly constant on cylinders aligned with the rotation axis and decreasing inward on the equatorial plane. Another striking feature is the region of strong shear at the base of the convection zone, now known as the tachocline, where Ω adjusts to apparent solid body rotation in the deeper radiative interior. Whereas the convection zone exhibits prominent differential rotation, the deeper radiative interior does not; these two regions are joined by the complex shear of the tachocline. There is further a thin shear boundary layer near the surface in which Ω increases with depth at intermediate and high latitudes.

The tachocline has been one of the most surprising discoveries of helioseismology, especially since its strong rotational shear affords a promising site for the solar global dynamo. Such a tachocline was not anticipated, and current theoretical approaches to explain its presence are still only innovative sketches (Spiegel & Zahn 1992; Gough & McIntyre 1998; Charbonneau, Dikpati, & Gilman 1999). Helioseismology has also recently detected prominent variations in the rotation rate near the base of the convective envelope, with a period of 1.3 yr evident at low latitudes (Howe et al. 2000a; Toomre et al. 2000). These are the first indications of dynamical changes close to the presumed site of the global dynamo as the cycle advances. Such a succession of developments from helioseismology provides both a challenge and a stimulus to theoretical work on solar convection zone dynamics.

Seeking to understand solar differential rotation and magnetism requires three-dimensional simulations of convection in the correct full spherical geometry. However, the global nature of such solutions represents a major computational problem given that the largest scale is pinned, and only 3 orders of magnitude smaller in scale can be represented. Much of the small-scale dynamics in the Sun dealing with supergranulation and granulation are, by necessity, then largely omitted. The alternative is to reduce the fixed maximum scale by studying smaller localized domains within the full shell and utilizing the 3 orders of magnitude to encompass the dynamical range of turbulent scales. There are clear trade-offs: the global models operate in the correct geometry yet struggle to encompass enough of a dynamical range to admit fully turbulent solutions, whereas the local models are able to study intensely turbulent convection but only within a particular limited portion of the full domain. Both approaches are needed, and the efforts are complementary, as reviewed in detail by Gilman (2000) and Miesch (2000). Highly turbulent but localized three-dimensional portions of a convecting spherical shell are being studied to assess transport properties and topologies of dynamical structures (e.g., Brandenburg et al. 1996; Brummell, Hurlburt, & Toomre 1996, 1998; Porter & Woodward 2000; Robinson & Chan 2001), penetration into stable domains below (Brummell, Clune, & Toomre 2002)

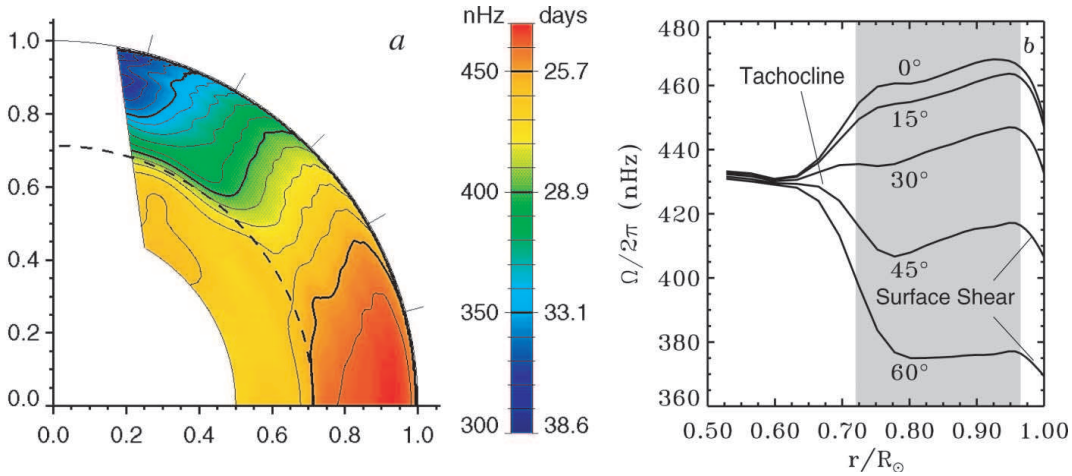

FIG. 1.— (*a*) Angular velocity profile $\Omega/2\pi$ with radius and latitude as deduced from helioseismology using SOI-MDI data, with red tones indicating fast rotation and blue-green the slowest rotation (adapted from Schou et al. 1998). (*b*) Time-averaged rotation rates from 5 years of GONG helioseismic data, plotted against radius at different latitudes. The surface shear layer and the tachocline at the base of the convective zone are indicated as well as the zone covered by our computational domain (*gray area*) (adapted from Howe et al. 2000b).

effects of realistic near-surface physics on granulation and supergranulation (e.g., Stein & Nordlund 1998), and dynamo processes and magnetic transport by the convection (e.g., Cattaneo 1999; Tobias et al. 2001). Without recourse to direct simulations, the angular momentum and energy transport properties of turbulent convection have also been considered using mean-field approaches to derive second-order correlations (the Reynolds stresses and anisotropic heat transport) under the assumption of the separability of scales. Although such procedures involve major uncertainties, the resulting angular momentum transport, which is described by mechanisms such as the so-called Λ effect, have served to reproduce the solar meridional circulation (e.g., Durney 1999, 2000) and differential rotation (e.g., Kichatinov & Rüdiger 1995). Various other states can be achieved by adjusting parameters.

Initial studies of convection in full spherical shells to assess effects of rotation with correct accounts of geometry (e.g., Gilman & Miller 1986; Glatzmaier & Gilman 1982; Glatzmaier 1985, 1987; Sun & Schubert 1995) have set the stage for our efforts to study more turbulent flows using new numerical codes designed for the massively parallel computer architectures that are enabling such major simulations. We here report on our continuing studies with the anelastic spherical harmonic (ASH) code (Clune et al. 1999) to examine the Ω profiles established within the bulk of the solar convection zone by turbulent convection, building on the progenitor work by Miesch et al. (2000), Elliott, Miesch, & Toomre (2000), and Brun & Toomre (2001). We also recognize the recent modeling of convection in spherical shells by Takehiro & Hayashi (1999) and Grote & Busse (2001).

The simulations reported in Miesch et al. (2000) and Elliott et al. (2000) have revealed the richness and complexity of compressible convection achieved in rotating spherical shells. Most of the resulting angular velocity profiles in the seven simulations considered have begun to make substantial contact with the helioseismic deductions within the bulk of the solar convection zone. These possess fast equatorial rotation (prograde), substantial Ω contrasts with latitude, and reduced tendencies for rotation to be constant on cylinders. The simulations with ASH have not yet sought to deal with questions of the near-surface rotational shear layer nor with the formation of a tachocline near the base of the convection zone. These studies have revealed that to achieve fast equators, it is essential that parameter ranges be considered in which the convection senses strongly the effects of rotation, which translates into having a convective Rossby number less than unity for large Taylor numbers. Such rotationally constrained convection exhibits downflowing plumes that are tilted away from the local radial direction, resulting in velocity correlations and thus Reynolds stresses that are found to have a significant role in the redistribution of angular momentum. This seems to provide paths to realize solar-like Ω profiles. Further, it is desirable to impose thermal boundary conditions at the top of the domain that enforce the constancy of emerging flux with latitude in order to be consistent with what appears to be observed.

We wish to focus on two outstanding issues raised by the prior simulations with ASH that need particular attention concerning the differential rotation established within the bulk of the solar convection zone. As *issue 1*, the helioseismic inferences in Figure 1 emphasize that Ω in the Sun appears to decrease significantly with latitude even at mid- and high latitudes, a property that has been difficult to attain in the prior seven simulations. The substantial latitudinal decrease in angular velocity, say $\Delta\Omega$, in the models is primarily achieved in going from the equator to about 45°, with little further decrease in Ω achieved at higher latitudes in most of the cases. Whereas the overall latitudinal contrasts from equator to pole in the models and the Sun are roughly of the same order, the angular velocity in the Sun continues to slow down much more as the pole is approached. Two models, designated as *LAM* (in Miesch et al. 2000) and *L3* (in Elliott et al. 2000), do exhibit Ω that decrease at high latitudes, but *LAM* involves an emerging heat flux that varies too much with latitude because of the choice of boundary conditions, and *L3* has an overall $\Delta\Omega$ that is only two-thirds of the helioseismic value. Thus, in confronting issue 1, we will search in parameter space for solutions that can achieve Ω profiles in which the decrease with latitude does not taper off at midlatitudes and for which the contrast $\Delta\Omega$ is at least comparable to the helioseismic findings.

As *issue 2*, with the convection becoming more turbulent, achieved by decreasing either the thermal or viscous diffusivities, there is a tendency for the latitudinal contrast $\Delta\Omega$ in the solutions to diminish or even decrease very prominently, thus being at variance with $\Delta\Omega$ deduced from helioseismology. This behavior appears to arise from increasing complexity leading to a weakening of nonlinear velocity correlations that have a crucial role in angular momentum redistribution. These Reynolds stress terms are strong in the laminar solutions that involve tilted columnar convection cells ("banana cells") aligned with the rotation axis; they weaken as the flows become more intricate but would be expected to become again significant once coherent structures develop at higher levels of turbulence. For example, the model *TUR* (in Miesch et al. 2000) exhibits the emergence of downflow networks involving fairly persistent plumes that possess some of the expected attributes of the coherent structure seen in localized domains of highly turbulent convection (e.g., Brummell et al. 1998). As a result, *TUR* has a fairly interesting angular momentum transport attributed to the nonlinear correlations that sustain a level of differential rotation slightly weaker than *LAM*, but it too has a considerable variation of heat flux with latitude. The model *T2* (in Elliott et al. 2000) sought to correct the latter by using modified thermal boundary conditions but appears to not have attained high enough turbulence levels to realize strong coherent structures. Absent those features, *T2* yielded Ω profiles with a small $\Delta\Omega$ and even a slightly slower equatorial rotation rate than that in the midlatitudes. Thus, in confronting issue 2, we seek turbulent solutions that possess Ω profiles with fast equators and strong latitudinal contrasts $\Delta\Omega$ and emerging heat fluxes that vary little with latitude. To achieve this, we have considered two paths in parameter space that yield more turbulent solutions by either varying the Prandtl number or keeping it fixed while maintaining the same rotational constraint as measured by a convective Rossby number.

We describe briefly in § 2 the ASH code and the set of parameters used for the simulations studied here. In § 3 we discuss the properties of rotating turbulent convection and the resulting differential rotation and meridional circulation for the five cases A, AB, B, C, and D. In § 4 we analyze the transport of angular momentum by several processes and the influence of baroclinic effects in establishing the mean

flows. In § 5 we reflect on the significance of our findings, especially in terms of dealing with the two issues raised by the prior simulations with ASH.

2. FORMULATING THE MODEL

Our numerical models are intended to be a faithful if highly simplified descriptions of the solar convection zone. In brief overview, solar values are taken for the heat flux, rotation rate, mass, and radius, and a perfect gas is assumed since the upper boundary of the shell lies below the H and He ionization zones; contact is made with a real solar structure model for the radial stratification being considered. The computational domain extends from about 0.72 to 0.96 $R_\odot$, where $R_\odot$ is solar radius, with such shells having an overall density contrast in radius of about 25, and as a consequence compressibility effects are substantial. Thus, we are concerned only with the central portion of the convection zone, dealing with neither the penetrative convection below that zone nor the two shear layers present at the top and bottom of it. Given the computational resources available, we prefer to concentrate our effort on processes that establish the primary differential rotation in the bulk of the convection zone and in future studies will seek to incorporate the other regions. We have as well softened the effects of the very steep entropy gradient close to the surface that would otherwise favor the driving of very small granular and mesogranular scales of convection, with these requiring a spatial resolution at least 10 times greater than presently available.

The ASH code solves the three-dimensional anelastic equations of motion in a rotating spherical shell geometry using a pseudospectral semi-implicit approach (Clune et al. 1999). As discussed in detail in Miesch et al. (2000), these equations are fully nonlinear in velocity variables and linearized in thermodynamic variables with respect to a spherically symmetric mean state having a density $\bar{\rho}$, pressure $\bar{P}$, temperature $\bar{T}$, specific entropy $\bar{S}$, and perturbations about this mean state of ρ, P, T, and S. The conservation of mass, momentum, and energy (or entropy) in a rotating reference frame is thus expressed as

$$\boldsymbol{\nabla}\cdot(\bar{\rho}\boldsymbol{v}) = 0\ , \tag{1}$$

$$\bar{\rho}\left[\frac{\partial \boldsymbol{v}}{\partial t} + (\boldsymbol{v}\cdot\boldsymbol{\nabla})\boldsymbol{v} + 2\boldsymbol{\Omega}_0\times\boldsymbol{v}\right] = -\boldsymbol{\nabla}P + \rho\boldsymbol{g} - \boldsymbol{\nabla}\cdot\mathscr{D} - [\boldsymbol{\nabla}\bar{P} - \bar{\rho}\boldsymbol{g}]\ , \tag{2}$$

$$\bar{\rho}\bar{T}\frac{\partial S}{\partial t} = \boldsymbol{\nabla}\cdot[\kappa_r\bar{\rho}c_p\boldsymbol{\nabla}(\bar{T}+T) + \kappa\bar{\rho}\bar{T}\boldsymbol{\nabla}(\bar{S}+S)] - \bar{\rho}\bar{T}\boldsymbol{v}\cdot\boldsymbol{\nabla}(\bar{S}+S) + 2\bar{\rho}\nu\left[e_{ij}e_{ij} - \tfrac{1}{3}(\boldsymbol{\nabla}\cdot\boldsymbol{v})^2\right]\ , \tag{3}$$

where c_p is the specific heat at constant pressure, $\boldsymbol{v} = (v_r, v_\theta, v_\phi)$ is the local velocity in spherical geometry in the rotating frame of constant angular velocity $\boldsymbol{\Omega}_0$, $\boldsymbol{g}$ the gravitational acceleration, κ_r the radiative diffusivity, and $\mathscr{D}$ the viscous stress tensor, with components

$$\mathscr{D}_{ij} = -2\bar{\rho}\nu\left[e_{ij} - \tfrac{1}{3}(\boldsymbol{\nabla}\cdot\boldsymbol{v})\delta_{ij}\right]\ , \tag{4}$$

where e_{ij} is the strain rate tensor. Here ν and κ are effective eddy diffusivities for vorticity and entropy. To close the set of equations, the linearized relations for the thermodynamic fluctuations are

$$\frac{\rho}{\bar{\rho}} = \frac{P}{\bar{P}} - \frac{T}{\bar{T}} = \frac{P}{\gamma\bar{P}} - \frac{S}{c_p}\ , \tag{5}$$

assuming the ideal gas law

$$\bar{P} = \mathscr{R}\bar{\rho}\bar{T}\ , \tag{6}$$

where $\mathscr{R}$ is the gas constant. The bracketed term in the second line of equation (2), $\boldsymbol{\nabla}\bar{P} - \bar{\rho}\boldsymbol{g}$, vanishes initially because the mean state begins in hydrostatic balance from a one-dimensional radial solar model (Brun, Turck-Chièze, & Zahn 1999), but as the convection becomes established this term becomes nonzero through effects of turbulent pressure. It is essential to take into account effects of compressibility on the convection since the solar convection zone spans many density scale heights. To accommodate this, we use the anelastic approximation (Gough 1969) to filter out the sound waves and therefore permit bigger time steps for the temporal evolution. The latter is allowed since the Courant, Friedrichs, & Lewy numerical stability condition now applies to the smaller convective velocities rather than the sound speed c_s.

Because of the small solar molecular viscosity, direct numerical simulations of the full scale range of motions present in stellar convection zones are currently not feasible. We seek to resolve the largest scales of convective motion that we believe are the main drivers of the solar differential rotation, doing so within a large-eddy simulation (LES) formulation where ν and κ are assumed to be an effective eddy viscosity and eddy diffusivity, respectively, that represent unresolved subgrid-scale (SGS) processes, chosen to suitably truncate the nonlinear energy cascade. For simplicity, both are here taken to be functions of radius alone and are chosen to scale as the inverse of mean density. Other forms that may be determined from the properties of the large-scale flows according to one of many prescriptions (e.g., Lesieur 1997; Canuto 1999) will be considered in the future. We have also introduced an unresolved enthalpy flux proportional to the mean entropy gradient in equation (3) in order to account for transport by small-scale convective structures near the top of our domain (Miesch et al. 2000). We utilize the same radial profile for that mean eddy diffusivity in our five cases in order to minimize the impact of our SGS treatment on the main properties of our solutions. We emphasize that currently tractable simulations are still many decades away in parameter space from the intensely turbulent conditions encountered in the Sun, and thus these large-eddy simulations must be viewed as training tools for developing our dynamical intuition of what might be proceeding within the solar convection zone.

Within the ASH code, the mass flux is imposed to be divergence-free by using poloidal W and toroidal Z functions. The thermodynamic variables P and S and W and Z are expanded in spherical harmonics $Y_\ell^m(\theta, \phi)$ to resolve their horizontal structures and in Chebyshev polynomials $T_n(r)$ to resolve their radial structures. This approach has the distinct advantage that the spatial resolution is uniform everywhere on a sphere when a complete set of spherical harmonics is used in degree ℓ (retaining all azimuthal orders m). We expand up to degree $\ell = \ell_{\max}$ [depending on the number of latitudinal mesh points N_θ, e.g., $\ell_{\max} = (2N_\theta - 1)/3$], utilize as longitudinal mesh points $N_\phi = 2N_\theta$, and employ N_r collocation points in projecting on the Che-

TABLE 1
PARAMETERS FOR THE FIVE SIMULATIONS

Case	A	AB	B	C	D
N_r, N_θ, N_ϕ.....	64, 128, 256	64, 128, 256	64, 256, 512	192, 256, 512	192, 512, 1024
R_a.....	3.1×10^4	3.4×10^4	1.4×10^5	3.1×10^5	6.5×10^5
T_a.....	7.7×10^4	3.1×10^5	1.2×10^6	5.4×10^6	6.5×10^6
P_r.....	1	0.25	0.25	0.125	0.25
R_{oc}	0.645	0.662	0.673	0.682	0.633
ν.....	5.5×10^{12}	2.8×10^{12}	1.4×10^{12}	6.8×10^{11}	6.0×10^{11}
κ	5.5×10^{12}	1.1×10^{13}	5.5×10^{12}	5.5×10^{12}	2.4×10^{12}
$\tilde{R}_e$	28	85	170	385	410
$\tilde{R}_o$	0.10	0.16	0.15	0.17	0.16
$\tilde{P}_e$.....	28	21	43	48	103

NOTE.—All simulations have an inner radius $r_{\rm bot} = 5.0 \times 10^{10}$ cm, an outer radius $r_{\rm top} = 6.72 \times 10^{10}$ cm, with $L = 1.72 \times 10^{10}$ cm the thickness of the computational domain. The number of radial, latitudinal and longitudinal mesh points are N_r, N_θ, and N_ϕ, respectively. Here evaluated at midlayer depth are the Rayleigh number $R_a = (-\partial\rho/\partial S)\Delta S g L^3/\rho\nu\kappa$, the Taylor number $T_a = 4\Omega^2 L^4/\nu^2$, the Prandtl number $P_r = \nu/\kappa$, the convective Rossby number $R_{oc} = (R_a/T_a P_r)^{1/2}$, the rms Reynolds number $\tilde{R}_e = \tilde{v}L/\nu$, the rms Péclet number $\tilde{P}_e = \tilde{R}_e P_r = \tilde{v}L/\kappa$, and the rms Rossby number $\tilde{R}_o = \tilde{\omega}/2\Omega \sim \tilde{v}/2\Omega L$, where $\tilde{v}$ is a representative rms convective velocity. A Reynolds number based on the peak velocity at middepth would be about a factor 4 larger. The eddy viscosity ν and eddy conductivity κ at middepth are quoted in $\mathrm{cm}^2\ \mathrm{s}^{-1}$.

byshev polynomials. In this study the highest resolution used has $\ell_{\max} = 340$ and $N_r = 193$. The time evolution is carried out using an implicit, second-order Crank-Nicholson scheme for the linear terms and an explicit, second-order Adams-Bashforth scheme for the advective and Coriolis terms.

Within ASH, all spectral transformations are applied to data local to each processor, with interprocessor transposes performed when necessary to arrange for the transformation dimension to be local. The triangular truncation in spectral space precludes any simple distribution of the data and work load among the nodes. For very large problems, the Legendre transformations dominate the work load, and as a result, great care has been taken to optimize their performance on cache-based architectures. Arrays and loops have been structured to operate on blocks that minimize cache misses. The ASH code is extremely flexible and has demonstrated excellent scalability on massively parallel supercomputers such as the Cray T3E, IBM SP-3, and Origin 2000.

As boundary conditions, we impose impenetrable and stress-free conditions for the velocity field and constant flux (i.e., constant entropy gradient) at both the inner and outer boundaries. We seek solutions with an emerging flux at the top that is invariant with latitude (issue 2). As initial conditions, we have started some simulations (cases A and B) from quiescent conditions of uniform rotation and others (cases AB, C, and D) from evolved solutions in which we modify certain diffusivities. This leads to changes in the effective Rayleigh number R_a, the Prandtl number P_r, the Péclet number P_e, the Reynolds number R_e, and the Taylor number T_a, while keeping constant the convective Rossby number R_{oc}, all of which are defined in Table 1. We also summarize there the parameters of the five simulation cases.

3. PROPERTIES OF TURBULENT COMPRESSIBLE CONVECTION

We have conducted five simulations involving increasingly nonlinear flows that are achieved by reducing the viscous and entropy diffusivities in the manner outlined in Table 1. We have followed two paths in parameter space in obtaining more complex convective flows. On *path 1* in going from case A to case C via case B, we incrementally decreased the eddy viscosity ν while keeping the eddy diffusivity κ constant, thereby reducing the Prandtl number P_r by a factor of 8. In particular, the laminar case A has P_r of unity; reducing the viscosity by a factor of 4 leads to the mildly turbulent case B with $P_r = 0.25$, or by reducing it a factor of 8 leads to the more turbulent case C with $P_r = 0.125$. This serves to increase the Reynolds number R_e while only mildly increasing the Péclet number P_e. *Path 2* kept the Prandtl number fixed at $P_r = 0.25$ since the complexity of the flows was increased by reducing both diffusivities. Starting from case AB, we go to case B by decreasing both diffusivities ν and κ by a factor of 2 and then to our most turbulent case D by further reducing both by a factor of 2 relative to case B. This path 2 in going from case AB to case D via case B results in both R_e and P_e increasing comparably. All our models possess a convective Rossby number R_{oc} on the order of $\frac{2}{3}$, thus maintaining a strong rotational constraint on the convection.

As we shall describe in some detail, the resulting vigorous convection influenced by rotation in all these cases is intricate and richly time-dependent, similar to that found in Miesch et al. (2000) and Elliott et al. (2000). It is characterized by networks of strong downflow at the periphery of the convection cells and weaker upflows in their middle, both of which are a consequence of the effects of compressibility since we consider flows that can span multiple density scale heights in the vertical. Indeed, we consistently observe that the downflows are able to extend over the full depth of the unstable layer, appearing as twisted sheets of downflow near the top and more distinctive plumes deeper in the layer. These downflow networks essentially represent coherent structures amidst the turbulence, and they are found to have a most significant role in the nonlinear transport of angular momentum by yielding correlations between different velocity components that form Reynolds stress terms. We find that the convection in all cases studied here is able to redis-

tribute angular momentum in such a manner that substantial differential rotation profiles are established, the properties of which are the major focus of this work.

3.1. *Complex Evolution of Convective Patterns*

The time dependence in our most turbulent simulation (case D) is shown in Figure 2, which displays two sequences of images of the radial velocity on spherical surfaces over the course of one full rotation. The upper sequence with views near the top of the layer involves simpler downflow networks (shown in darker tones) that are easier to intercompare from frame to frame, whereas the lower ones with views in the middle of the convecting layer are more difficult to track because of increased complexity of the patterns in the more turbulent flows there. The vantage point is in the uniformly rotating frame used in our modeling, and some of the pattern evolution results from the prograde zonal flows at low latitudes and retrograde ones at high latitudes associated with the differential rotation relative to this frame. There is further melding and shearing of particular downflow lanes as the convection cells evolve over a broad range of timescales, some of which are comparable to the rotation period. This is particularly evident in some of the downflow structures identified near the equatorial region in the upper sequence, with features labeled "1" and "2" illustrating the merging of two downflow lanes and feature "3" the typical distortion of a lane that also involves both a site of cyclonic swirl in the northern hemisphere and another that is appropriately anticyclonic in the southern hemisphere. The behavior at higher latitudes that involves retrograde displacement of the downflow networks is somewhat more intricate, partly because the convection cells are of smaller scale and exhibit the frequent formation of new downflow lanes (as in feature 4) that can serve to cleave existing cells. Figure 2 emphasizes that the overall pattern of these global cells is sufficiently modified during the course of one rotation period so that it would be difficult to identify particular structures (relative to our uniformly rotating vantage point) when viewed in a subsequent rotation. This would suggest that giant cells possibly present within the solar convection zone may also loose their identity from one Carrington rotation to the next. This comes about because of both advection and distortion of the cells by the mean zonal flows associated with the differential rotation (here at the equator leading to relative angular displacements in longitude of about 70° over one rotation period) and fairly rapid evolution and some propagation in their individual downflow patterns.

3.2. *Downflow Networks and Variation with Depth*

The convective structures as delineated by the downflow networks show distinctive changes as the level of turbulence is increased in going from case A to case D. Figure 3 provides an overview of radial velocity snapshots in our five simulations at three depths (near the top, middle, and bottom) accompanied by the fluctuating temperature fields at middepth. The upper surface in all our cases involves a connected network of downflows surrounding broad upflows, but such smoothness can disguise far more turbulent flows below. The seemingly cellular motions near the surface result from the expansion of fluid elements rising through the rapidly decreasing density stratification near the upper boundary, aided also by our increasing viscous and thermal diffusivities there. As viewed near the top, the tendency of the convection in our laminar case A to be organized into "banana cells" nearly aligned with the rotation axis at low latitudes is progressively disrupted by increasing the level of complexity in going in turn to cases AB, B, C, and D. There is still some semblance of north-south alignment in the downflows even in our most turbulent case D, but the latitudinal span of this alignment is confined to a narrow interval around the equator. Clearly, the downflow lanes become more wiggly and exhibit more pronounced vortical features and curvature in this sequence of cases. The downflow networks as well involve more frequent branching points and smaller horizontal scales for the convective patterns, especially at higher latitudes. Given the three simultaneous views of the radial velocity, one can clearly identify downflow lanes near the top in all our cases that turn into distinctive plumes at greater depths, showing that organized flows extend over multiple scale heights. Indeed, the strongest downflows occur at the interstices of the upper network and are able to pierce through the interior turbulence, thus spanning the full depth range of the domain.

The plumes in the more turbulent cases C and D represent coherent structures that are embedded within less ordered flows that surround them. They are able to maintain their identity, although with some distortion and mobility, over significant intervals of time. Although these downflowing plumes are primarily directed radially inward, they show some tilt both toward the rotation axis and out of the meridional plane. This yields correlated velocity components and thus Reynolds stresses that are a key ingredient in the redistribution of angular momentum within the shell. Such tilting away from the local radial direction in coherent downflows has been seen in high-resolution local *f*-plane simulations of rotating compressible convection (Brummell et al. 1998), and their presence has a dominant role in establishing the mean zonal and meridional flows. We also refer to Rieutord & Zahn (1995) and Zahn (2000) for an analytical study of the transport properties and correlations present in such strong vortex structures and on their potential dynamical role in the solar convection zone.

The strong downflows shown in Figure 3 accentuate the asymmetries that are characteristic of compressible convection, with typical peak amplitudes in these downflows at midlayer being as much as twofold greater than that in the upflows. As might be expected, the overall rms radial velocities listed in Table 2 increase with complexity in the flow fields in going from case A to case D. The asymmetries between upflows and downflows have the consequence that the kinetic energy flux in such compressible convection is directed radially inward, in contrast to the enthalpy and radiative fluxes that are directed outward in transporting the solar flux (see Fig. 10*a*).

That enthalpy flux involves correlations between radial velocities and temperature fluctuations, and these are evidently strong, as seen when inspecting the temperature and velocity fields shown at midlayer in Figure 3. Buoyancy driving within our thermal convection involves downflows that are cooler and thus denser and upflows that are warmer and lighter than the mean; there are systematic asymmetries in those temperature fluctuations, much as in the radial velocities. Further, in comparing the temperature maps with those of radial velocity in the middle of the layer, some of the temperature patterns are evidently smoother, which is a consequence of the greater thermal diffusivities than viscos-

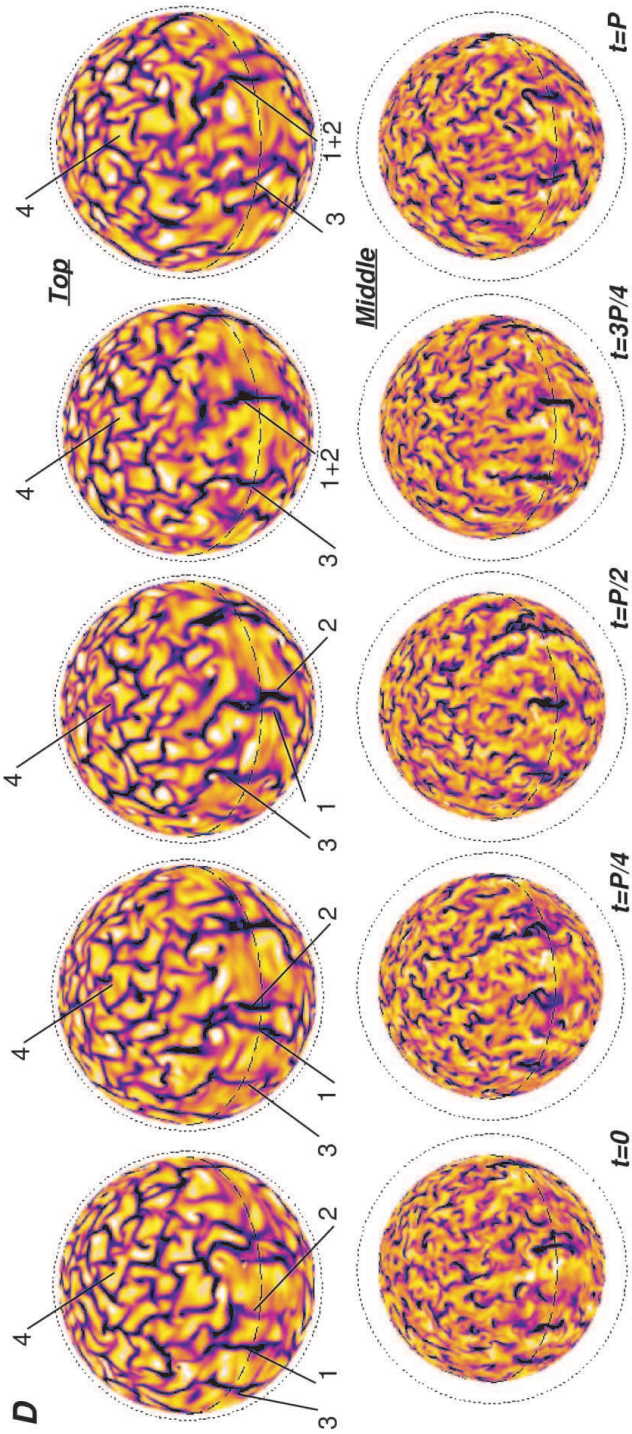

FIG. 2.—Evolution of the convection throughout one solar rotation, showing the radial velocity of case D near the top and at the middle of the domain. The time interval between each successive image is about 7 days. Features 1 and 2 exhibit the merging of the downflow lanes, feature 3 the shearing action of the differential rotation present in the shell, and feature 4 the appearance and deformation of a convective cell at higher latitudes.

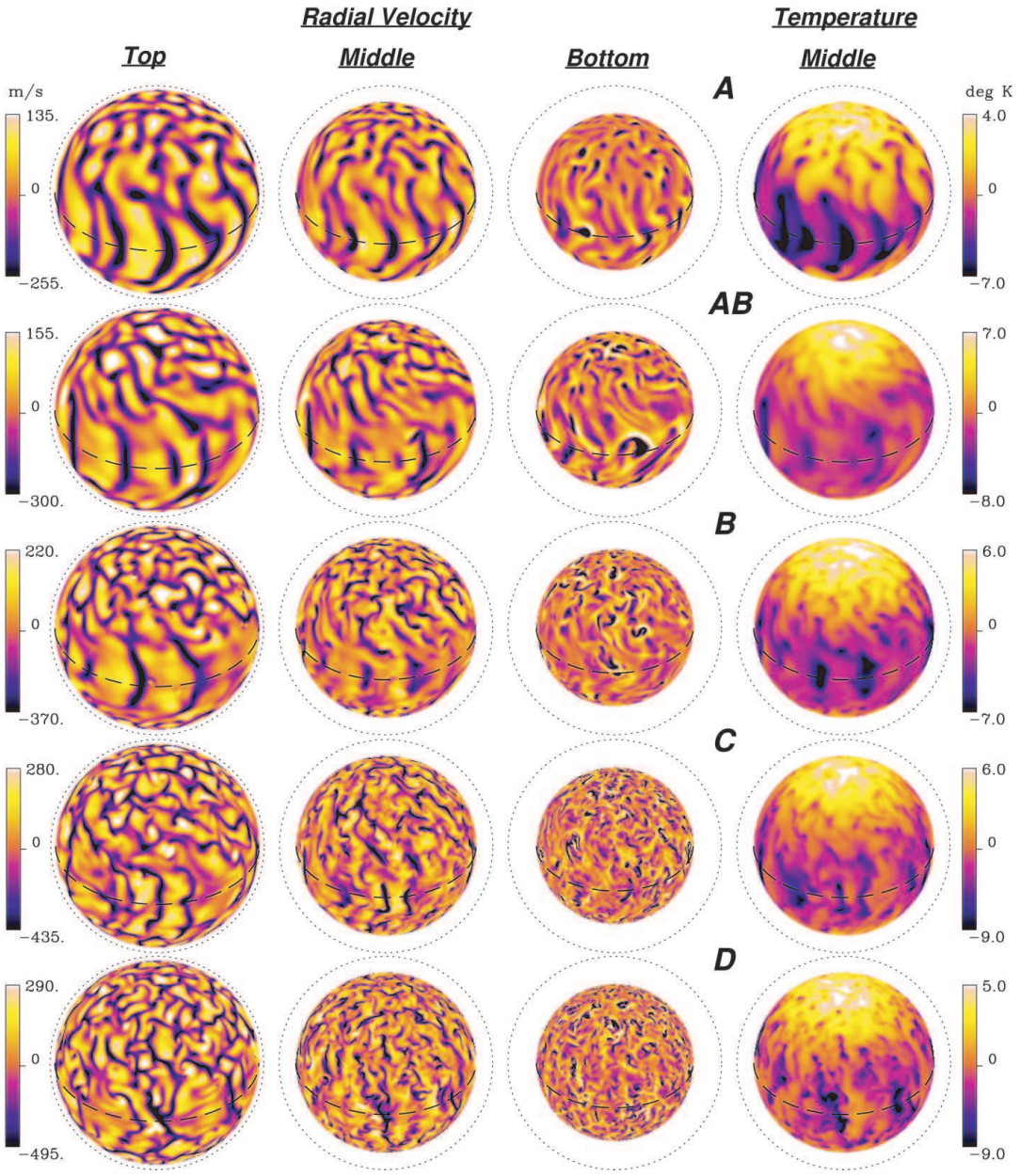

FIG. 3.—Convective patterns for the five cases A, AB, B, C, and D as increasingly turbulent flows are attained. The radial velocity snapshots are shown at three different depths (0.95, 0.84, and 0.73 $R_\odot$). Downflows are represented in dark purple tones and upflows in bright orange tones, with dynamic ranges indicated. The dotted circle is positioned at radius $R_\odot$, and the equator is indicated by the dashed curve. The convective structures become more complex in this progression of cases, with the banana-like convective cells giving way to stronger and more frequent vortex sites. The strongest downflow lanes extend over the full depth range. The fluctuating temperature fields at middepth are shown on the right, emphasizing that downflows are relatively cool and that the polar regions are on average warm.

TABLE 2
REPRESENTATIVE VELOCITIES, ENERGIES, AND DIFFERENTIAL ROTATION

	MIDCONVECTIVE ZONE						VOLUME AVERAGE				
CASE	$\tilde{v}_r$	$\tilde{v}_\theta$	$\tilde{v}_\phi$	$\tilde{v}'_\phi$	$\tilde{v}$	$\tilde{v}'$	KE	DRKE	CKE	MCKE	$\Delta\Omega / \Omega_0$ (%)
A	46	40	69	44	92	74	2.7×10^6	8.2×10^5(30%)	1.9×10^6 (70%)	1.0×10^4 (0.37%)	12
AB	50	47	124	53	142	87	6.5×10^6	4.2×10^6(64%)	2.3×10^6 (36%)	2.1×10^4 (0.32%)	33
B	57	56	115	59	140	99	6.5×10^6	3.4×10^6(52%)	3.1×10^6 (48%)	2.5×10^4 (0.38%)	28
C	68	67	122	70	155	117	7.9×10^6	3.6×10^6(46%)	4.3×10^6 (54%)	3.3×10^4 (0.42%)	30
D	72	67	108	64	146	111	6.5×10^6	2.3×10^6(35%)	4.2×10^6 (65%)	3.0×10^4 (0.46%)	25

NOTE.—In the five cases, temporal averages at midlayer depth in the convection zone of rms components of velocity $\tilde{v}_r$, $\tilde{v}_\theta$, $\tilde{v}_\phi$, of speed $\tilde{v}$, and of fluctuating velocities $\tilde{v}'_\phi$ and $\tilde{v}'$ (with the temporal and azimuthal means subtracted) are expressed, all in units of m s^{-1}. Also listed are the time averages over the full domain of the total kinetic energy KE and that associated with the (axisymmetric) differential rotation DRKE, the (axisymmetric) meridional circulation MRKE, and the nonaxisymmetric convection itself CKE, all in units of ergs cm^{-3}. The relative latitudnal contrast of angular velocity $\Delta\Omega/\Omega_0$ between 0° and 60° near the top of the domain are stated.

ities for cases with Prandtl numbers less than unity. A striking property shared by all these temperature fields is that the polar regions are consistently warmer than the lower latitudes, a feature that we will find to be consistent with a fast or prograde equatorial rotation.

3.3. *Driving Strong Differential Rotation*

The differential rotation profiles with radius and latitude that result from the angular momentum redistribution by the vigorous convection in our five simulations are presented in Figure 4. In order to simplify comparison of our results with deductions drawn from helioseismology (Fig. 1), we have converted our mean longitudinal velocities $\tilde{v}_\phi$ (with the hat denoting averaging in longitude and time) into a sidereal angular velocity Ω with radius and latitude and note that our reference frame rotation rate $\Omega_0/2\pi$ is 414 nHz (or a period of 28 days). The angular velocity in all our cases exhibits substantial variations in time, and thus long time averages must be formed to deduce the time mean profiles of Ω shown in Figure 4. The layout of the five cases in Figure 4 reflects the two paths we have taken in increasing the complexity or turbulence level in the solutions: Path 1, in going from case A to case C via case B while decreasing the Prandtl number, takes us from upper left to lower right, and path 2, in going from case AB to case D via case B while keeping the Prandtl number fixed at $P_r = \frac{1}{4}$, takes us from upper right to lower left. Complexity in the convective flows increases in going down the page.

All five simulations yield angular velocity Ω profiles that involve fast (prograde) equatorial regions and slow (retrograde) high-latitude regions. The variation of Ω with radius and latitude may be best judged in the color contour plots in Figure 4, which are scaled independently for each of the cases; the reference frame rate is also indicated. The immediate polar regions are omitted in these plots because it is difficult to obtain stable mean Ω values at very high latitudes since the averaging domain there becomes very small, whereas the temporal fluctuations in the flows remain substantial. The contour plots reveal that there are some differences in the Ω realized in the northern and southern hemispheres, although such symmetry breaking is modest and probably will diminish with longer averaging. The convection itself is not symmetric about the equator, and thus the mean zonal flows that accompany such convection, and which are manifest as differential rotation, can be expected to have variations in the two hemispheres. In cases B, C, and D, there is some alignment of the Ω contours at the lower latitudes with the rotation axis, thus showing a tendency for Ω to be somewhat constant on cylinders. Further, in these cases almost all the decrease in Ω with latitude occurs in going from the equator to about 45° or thus is confined to the region outside the tangent cylinder to the inner boundary (which intersects the outer boundary in our shell configuration at 42°). In contrast, cases A and AB show far less alignment of Ω contours with cylinders at the lower latitudes, and at midlatitudes the contours are nearly aligned with radial lines, more in the spirit of the helioseismic inferences.

Case AB in Figure 4 is unique in having the monotonic decrease of Ω with latitude continue onward to high latitudes, which is also the trend deduced from helioseismic measurements. Thus, issue 1 concerned with achieving a consistently decreasing Ω at high latitudes is resolved with case AB. This is significant in showing that such behavior can be realized in our modeling of convection in deep shells, although it is not a common property in our other cases. It would be most desirable to understand how such high-latitude variation in Ω is achieved in case AB, and we will address this in § 4.

The accompanying radial cuts of Ω at six fixed latitudes in Figure 4 permit us to readily quantify the Ω contrasts with latitude achieved in these solutions and to judge the functional variation with radius in each case. We use a common scaling for all these line plots to make an intercomparison between the cases most convenient; the radial cuts for Ω have been averaged between the northern and southern hemispheres. Near the top of the convection zone at radius 0.96 R. the laminar convection in case A produces a differential rotation with a contrast in angular velocity, or $\Delta\Omega/2\pi$, of about 50 nHz between the equator and 60° or 12% relative to the frame rotation rate (also quoted in Table 2). Continuing on path 1 in parameter space to the more turbulent cases B and C, we find that the latitudinal contrast in angular velocity has increased substantially, becoming 115 and 125 nHz in the two cases, respectively. These correspond in turn to a 28% and a 30% variation of the rotation rate, respectively. These values are of interest since the helioseismic inferences (Thompson et al. 1996; Schou et al. 1998; Howe et al. 2000b) have a contrast of about 92 nHz at a similar depth between the equator and 60° or a variation of about 22% in rotation rate, which further increases to about 32% in going to 75°. The pronounced differential rotation in cases B and C is accompanied by the Ω profiles becoming

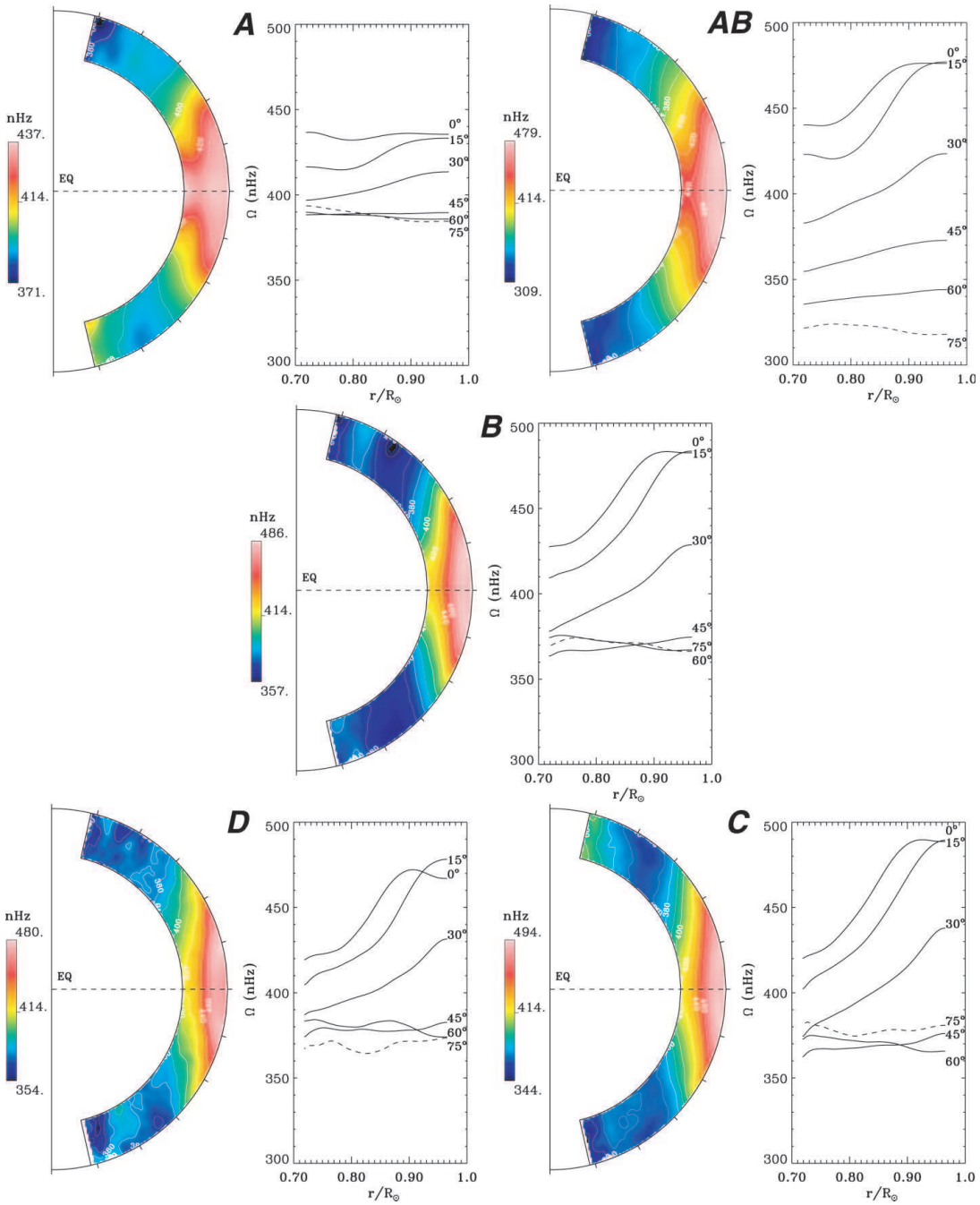

FIG. 4.—Temporal and longitudinal averages of the angular velocity profiles achieved in cases A, AB, B, C, and D, formed over intervals in turn of 295, 275, 275, 175, and 35 days. The contour plots for $\Omega/2\pi$ on the left of each panel are independently scaled, whereas the radial cuts at the indicated latitudes share the same scaling to accentuate the overall behavior of the five cases. The crossed layout of the five cases emphasizes the two different paths followed to reach more turbulent states, mainly by lowering P_r on path 1 (A → B → C) and by lowering diffusivities while keeping P_r constant on path 2 (AB → B → D). All cases exhibit a prograde equatorial rotation and a strong contrast $\Delta\Omega$ from equator to pole. Case AB possesses a high latitude region of particularly slow rotation.

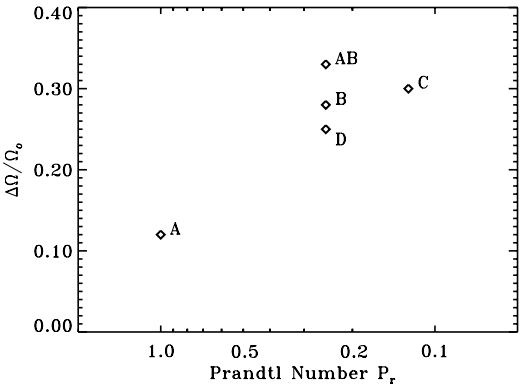

FIG. 5.—Parameter space diagram for relative latitudinal angular velocity contrast $\Delta\Omega/\Omega_0$ as a function of the Prandtl number P_r for the five cases. The two paths toward higher levels of turbulence either reduce P_r (A → B → C) or maintain a constant P_r (AB → B → D).

somewhat more aligned with the rotation axis, resulting in steeper slopes in the radial cuts at low and midlatitudes. These two turbulent cases achieve their larger $\Delta\Omega$ by both faster equatorial rotation rates and slower rates at higher latitudes. Thus, path 1 has been able to resolve issue 2, concerned with retaining a strong contrast $\Delta\Omega$ and a fast equator, as the solution becomes more complex and turbulent.

Turning to path 2 in parameter space, case AB shows a contrast of about 135 nHz between the equator and 60°, or a 33% variation of rotation rate, which further increases to about 160 nHz or 39% in going to 75°. The pivotal case B has a somewhat reduced contrast $\Delta\Omega/2\pi$ of 115 nHz or 28% variation between the equator and 60°, with little further variation at higher latitudes. The most turbulent case D has a $\Delta\Omega/2\pi$ of about 105 nHz or a 25% variation between the equator and 60°. Thus, path 2 leads to a slight reduction in $\Delta\Omega$ with increasing complexity, unlike the behavior of path 1. However, even this path yields a turbulent solution case D whose $\Delta\Omega$ is still close to the helioseismic contrast, thus largely resolving issue 2. This is reemphasized in Figure 5, which summarizes the variation of $\Delta\Omega$ with P_r for our five cases.

Most of our cases possess overall latitudinal contrasts in Ω that are in the realm of solar values deduced from inversion of helioseismic data, yet case AB stands out in having the systematic decrease of Ω with latitude extending almost to the poles, which appears to be another distinguishing feature of the actual solar Ω profiles. Further, case AB displays little radial variation in Ω at intermediate and high latitudes (from, say, 45° onward) as the angular velocity continues to decrease poleward. Such behavior is most interesting, and it is necessary to understand just which convective properties within case AB allow it to come into reasonable contact with the helioseismic profiles for Ω deduced in the bulk of the solar convection zone.

The Ω profiles in Figure 4 have been formed from temporal averages spanning multiple rotation periods as indicated. It is appropriate to consider if these represent truly "spun-up" solutions in a statistical sense and further whether several distinctive Ω profiles could be achieved for the same control parameters. Both issues may be intertwined since the rate of approach to equilibration can be influenced by the attraction characteristics of that differential rotation state and, of course, by the amplitude of the fluxes available to redistribute angular momentum to achieve that state (see § 4.1). This overall dynamical system of turbulent convection is sufficiently complex that we are uncertain whether there may exist multiple basins of attraction leading to different classes of differential rotation. For instance, is the behavior of case AB with noticeably slow rotation at high latitudes an example of one class of behavior and our other cases that of another family? Could such families overlap in parameter space, or are there just gradual variations in behavior in Ω with changes in the parameters? We have so far sought to address some of these questions by perturbing the evolving solutions to see if they might flip to another state, but they have not done so. We plan to examine such issues of solution uniqueness in our following studies in which we seek to extend the slow-pole characteristics of case AB to other parameter settings involving more complex convection.

As to the relative maturity of the spun-up states shown in Figure 4, these vary from case to case because of the rapidly increasing computational expense in dealing with the finer spatial resolution required by the more complex simulations. Cases AB and C were both started from case B, which had already been run for over 4000 days of elapsed simulation time (or a nominal 143 rotation periods involving about 28 days each). At this point case B appeared to be statistically stationary in terms of the kinetic energy associated with the differential rotation, although it, like most of the other simulations, exhibits small fluctuations in Ω profiles determined from single-rotation averages, especially at the higher latitudes. Case AB was evolved for about 2300 days (82 rotation periods), and we illustrate in Figure 6*a* a succession of Ω profiles with latitude sampling the last 600 days in the simulation. The solid curve there is an average formed over 10 rotations (consistent with the contour plot in Fig. 4), and we see that the individual rotation averages being sampled form a narrow envelope around it. There is evidently some symmetry breaking between the two hemispheres. We believe that the differential rotation for case AB is now an effectively stationary state (as is also confirmed in studying the angular momentum flux balance in Fig. 11). The more turbulent case C was evolved for about 500 days (18 rotations) after being initiated from case B, and a set of its angular velocity profiles are shown sampling the last 300 days in Figure 6*b*. We are less certain of its stationarity, but we could not detect any systematic trends in the evolution of its differential rotation over the last 10 rotations. We saw no evidence of a slow pole developing, but that may well require more extended computations than could be presently arranged. Figure 6 serves to emphasize that the angular velocity even in the Sun may be expected to vary somewhat from one rotation to another, with the samplings here providing a sense of the amplitude of those changes.

3.4. *Meridional Circulation Patterns*

The time-averaged meridional circulations that accompany the vigorous convection in the five cases are shown in Figure 7. The typical amplitudes in these large-scale circulations are about 20 m s^{-1} and are thus comparable to the values deduced from local domain helioseismic probing of the uppermost convection zone based on either time-distance

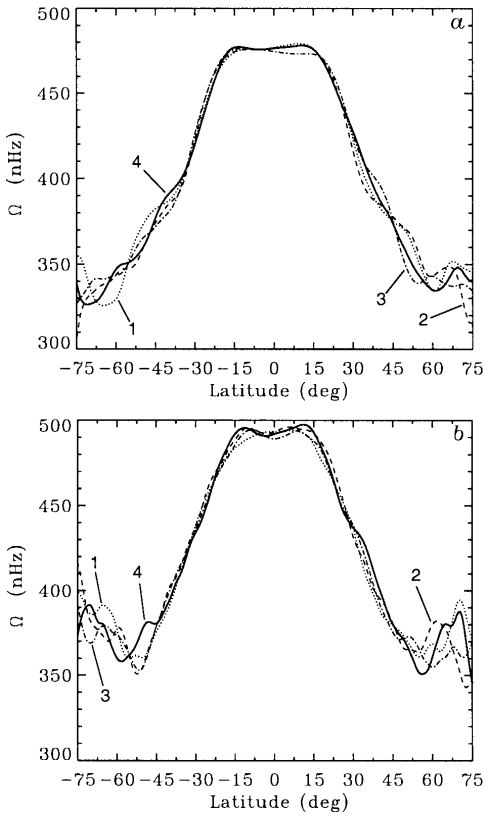

FIG. 6.—Succession of time-averaged Ω profiles with latitude at $r = 0.96\ R_\odot$. (*a*) For case AB, a numbered sequence of single-rotation averages spanning an interval of 600 days in the late evolution of the system with the bold curve 4 denoting an average over the last 275 days in the simulation. (*b*) For case C, dealing with samples in a 300 day interval, and the bold curve 4 representing an average over the final 175 days. The variations are representative of small changes in the differential rotation that accompany changes in the convection once a mature statistical state has been achieved.

methods (e.g., Giles, Duvall, & Scherrer 1998) or ring diagram analyses (Schou & Bogart 1998; Haber et al. 1998). There is little change in meridional circulation amplitudes as we increase the level of turbulence in going from case A to case D. However, multicell structures in these circulations become more intricate with the increased complexity of the convection. At lower latitudes the circulation in both hemispheres is poleward near the top of the domain, with return flows at various depths. All cases display multiple cells with radius and latitude and never only one big meridional cell, as is often used in mean field models dealing with differential rotation (e.g., Rekowski & Rüdiger 1998; Durney 2000) or with Babcock-Leighton dynamos (e.g., Choudhuri, Schüssler, & Dikpati 1995; Dikpati & Charbonneau 1999). The resulting axisymmetric meridional circulation is maintained by Coriolis forces acting on the mean zonal flows that appear as the differential rotation, by buoyancy forces, by Reynolds stresses, and by pressure gradients. Given these competing processes, it is not self-evident what pattern of circulation cells should result nor how many should be present in depth or latitude. Our five simulations have shown that there is some variety in the meridional circulations achieved, all of which involve multicelled structures. Since the meridional circulation kinetic energy (MCKE) is typically about 2 orders of magnitude smaller than the differential rotation kinetic energy (DRKE), as we will detail in § 3.5 and Table 2, small variations in the differential rotation can yield substantial changes in the circulations. This is likewise true of the time-varying Reynolds stresses from the evolving convection, which again has a kinetic energy (CKE) much larger than that of the meridional circulations. This may explain the complex time dependence realized by the meridional flows and the need to use long time averages in defining their mean properties.

Another rendition of the time-averaged meridional circulations achieved in cases AB and C is shown in Figure 8 using a stream function Ψ based on the zonally averaged mass flux (as in eq. [7] of Miesch et al. 2000). In case AB (Fig. 8*a*) there are two circulation cells positioned above each other in radius at low latitudes. The stronger upper one (solid contours representing counterclockwise circulation) involves poleward flow that extends from the equator to about 30° latitude near the top of the domain in the northern hemisphere. The southern hemisphere has likewise poleward flow near the top at low latitudes, with ascending motions again present from the equator to about 20° latitude. At latitudes greater than about 30° the relatively weak flow near the top is mainly equatorward in both hemispheres but exhibits fluctuations. A quantitative measure of this for case AB is provided in Figure 9*a* that displays the mean velocity component $\hat{v}_\theta$ with latitude at two depths near the top of the domain. The poleward flow in both hemispheres peaks at about 20° latitude and then decreases rapidly, changing to weak equatorward flow above 30°, which attains about one-third that peak amplitude. Turning to case C in Figure 8*b*, it exhibits three circulation cells positioned radially at low latitudes, with the outermost again yielding poleward flow at the top of the domain that extends to about 35° in latitude. At higher latitudes the mean meridional flow is again equatorward near the top, attaining a peak amplitude for $\hat{v}_\theta$ (detailed in Fig. 9*b*) that is comparable to the poleward one from the low latitudes, unlike in case AB. Of the three meridional cells at low latitudes in case C, much as for model *TUR* in Miesch et al. (2000, their Fig. 16*a*), the deepest cell involves a strong counterclockwise circulation that extends to high latitudes, yielding a submerged poleward flow there that lies below the equatorward flow at the top of the domain. Such behavior involving a third deep circulation cell that extends to high latitudes is also seen in cases B and D. This strong third cell appears to be of significance in the continuing net poleward transport of angular momentum by the meridional circulations (see § 4.1 and Fig. 11) in all these cases at latitudes above about 30°. This is not realized in case AB and may contribute to its slow pole behavior.

It is encouraging that we have poleward circulations in the upper regions of the simulations, which is in accord with the general sense of the mean flows near the surface being deduced from local helioseismology, although two-cell behavior with latitude has been detected recently only in the northern hemisphere near the peak of solar activity (Haber

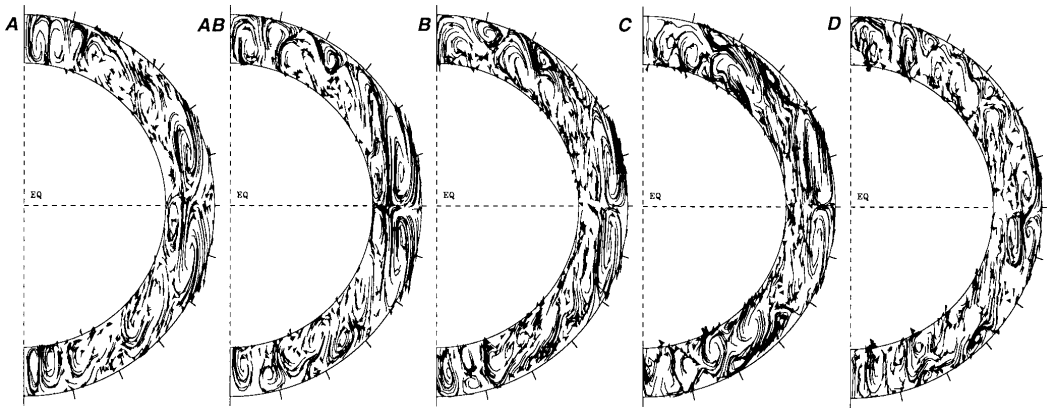

FIG. 7.—Temporal and longitudinal averages of the meridional flows achieved in the cases A, AB, B, C, and D, deduced from sampling in 295, 275, 275, 175, and 35 days, respectively. Shown are random streak lines whose length is proportional to flow speed, with arrowheads indicating flow sense. The typical speeds in these meridional circulations are about 20 m s^{-1}. For all the cases, strong poleward cells are present near the surface at low latitudes as well as return flows at middepth.

et al. 2000). Such symmetry breaking in the two solar hemispheres is an interesting property and one that is also occasionally realized in our simulations as the convection patterns evolve. The helioseismic probing with ring diagram methods and explicit inversions is able to sense the meridional circulations only fairly close to the solar surface, typically extending to depths of about 20 Mm or to a radius of 0.97 $R_\odot$, whereas our simulations have their upper boundary slightly below this level at 0.96 $R_\odot$. Thus, we must be cautious in interpreting similar behavior in the meridional circulations since our models and the ring diagram analysis do not explicitly overlap in radius. Helioseismic assessments based on time-distance methods (Giles 1999; Chou & Dai 2001) and annular rings centered on the poles (Braun & Fan 1998) report detecting effects attributable to meridional circulations with a mainly poleward sense to depths corresponding to 0.90 or even 0.85 $R_\odot$. Such results are most interesting, but considerable further work on inversions would be required to provide detailed profiles of the circulations with depth. As these mappings become available, they may be able to confirm or refute the multicell radial structure of meridional circulation (Fig. 7) typically realized in our simulations.

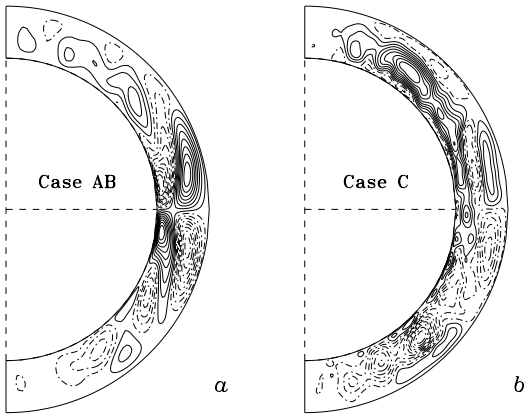

FIG. 8.—Streamlines of the mean axisymmetric meridional circulation achieved in (*a*) case AB averaged over 275 days and in (*b*) case C averaged over 175 days. Solid contours denote counterclockwise circulation (and dashed contours clockwise), equally spaced in value. In case AB, two circulation cells are present with radius at low latitudes and only weak circulations at latitudes above 30°. Case C possesses three cells at low latitudes, with the deepest extending prominently to high latitudes.

3.5. *Energetics of the Convection and the Mean Flows*

The overall energetics within these shells of rotating convection have some interesting properties in addition to the mean zonal and meridional flows that coexist with the complex convective motions. The convection is responsible for transporting outward the solar flux emerging from the deep interior. We should recall, as discussed in detail in Miesch et al. (2000), that the radial flux balance in these convective shells involves four dominant contributors, namely, the enthalpy or convective flux F_c, the radiative flux F_r, the kinetic energy flux F_k, and finally the unresolved eddy flux F_u, which add up to form the total flux F_t. Figure 10*a* shows the flux balance with radius achieved in our most turbulent case D as averaged over horizontal surfaces and converted to luminosities. The radiative flux becomes significant deep in the layer because of the steady increase of radiative conductivity with depth, and indeed by construction it suffices to carry all the imposed flux through the lower boundary of our domain, where the radial velocities and thus the convective flux vanishes. A similar role near the top of the layer is played by the subgrid-scale turbulence that yields F_u, which being proportional to a specified eddy diffusivity function κ and the mean radial gradient of entropy, suffices to carry the total flux through the upper boundary and prevents the

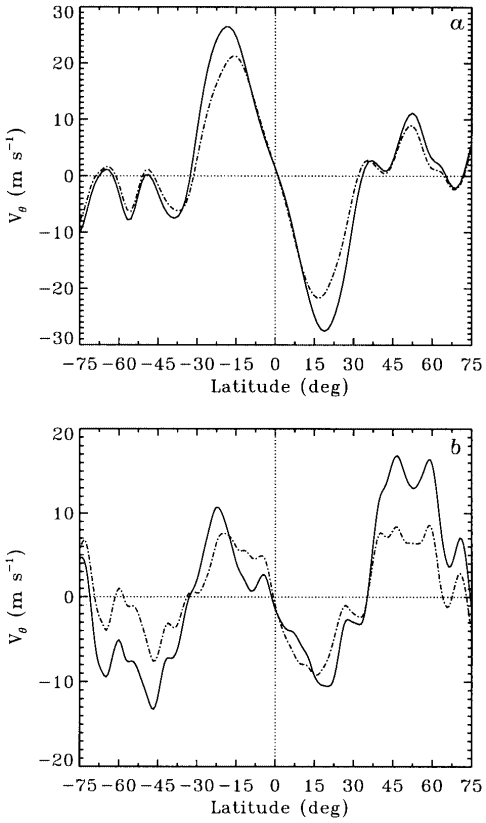

FIG. 9.—Mean velocity component $\tilde{v}_\theta$ with latitude at the two depths $r = 0.96$ (*solid line*) and 0.94 $R_\odot$ (*dash-dotted line*) showing (*a*) case AB and (*b*) case C. Positive values correspond to flow directed from north (positive latitudes) to south (negative latitudes). At low latitudes the flows are poleward in both hemispheres, but whereas case C exhibits fairly strong equatorward flow at latitudes above 35°, case AB possesses much weaker circulations there.

entropy gradient there from becoming too superadiabatic compared to the scales of convection that we are prepared to resolve spatially. Over most of the interior of the shell, the strong correlations between radial velocities and temperature fluctuations yield the enthalpy flux F_e that transports upward almost all of the imposed flux, and this peaks near the middle of the layer. The kinetic energy flux F_k works against the others by being directed downward, a result of the fast downflow sheets and plumes achieved by effects of compressibility (Hurlburt, Toomre, & Massaguer 1986). These general properties are shared by our five cases, all of which have achieved good overall flux balance with radius, as can be assessed by examining F_t.

Figure 10*b* presents the kinetic energy spectra with azimuthal wavenumber m at three depths, and averaged in time, as realized in the case D simulation. The spectra are fairly broad, with a plateau of power extending up to about $m = 30$ corresponding to some of the most vigorously driven scales and then a rapid decrease involving about 5 orders of magnitude to the highest wavenumber of 340. The decrease is more rapid for the spectra formed near the top of the shell. These spectra suggest that the flows are well resolved, with a reasonable scale separation between the dominant energy input range and the wide interval over which dissipation functions. We cannot readily identify a clear inertial subrange, although for reference we include some power laws. We also refer to Hathaway et al. (1996, 2000) for a discussion of recent observational inferences about the solar kinetic energy spectrum that does not seem to indicate any clear scaling law.

Table 2 summarizes various rms velocities that characterize our five simulations as sampled in the middle of the layer where the enthalpy flux also peaks. The rms radial velocity $\tilde{v}_r$ increases monotonically in going through the sequence of cases A, AB, B, C, to D. The associated rms Reynolds number $\tilde{R}_e$ in Table 1 increases also (although part of this is due to changes in the diffusivities), varying by a factor of about 15 from our laminar to most turbulent solutions. The rms longitudinal velocity $\tilde{v}_\phi$ has the greatest amplitude in all the cases. However, a removal of the mean zonal flow compo-

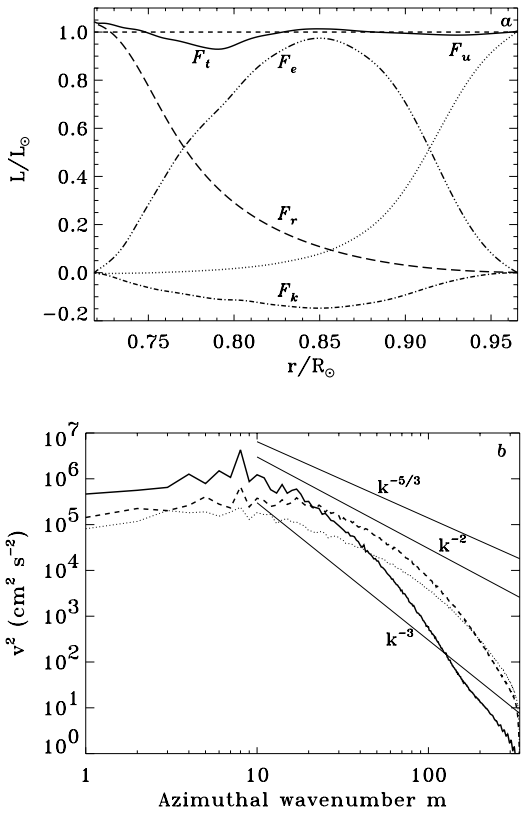

FIG. 10.—(*a*) Radial transport of energy in case D achieved by the fluxes F_r, F_e, F_k, and F_u, and their total F_t, all normalized by the solar luminosity. (*b*) Time-averaged azimuthal wavenumber spectra of the kinetic energy on different radial surfaces (*solid curve*: $r/R_\odot = 0.95$; *dashed curve*: 0.84; *dotted curve*: 0.73) for case D with $l_{max} = 340$. The results have been averaged over 35 days. Superimposed are the power laws $k^{-5/3}$, k^{-2}, and k^{-3}; no clear inertial subrange is identifiable.

nent responsible for the differential rotation yields $\tilde{v}'_\phi$. Comparison of this with the radial and latitudinal rms velocities reveals that all possess very comparable amplitudes, suggesting fairly isotropic convective motions near the midplane. Table 2 also assesses the volume and time-averaged total kinetic energy (KE), that associated with the DRKE, with the MCKE, and with the convection itself (CKE). In all of our solutions the DRKE and CKE are comparable, and the MCKE is much smaller. Table 2 reveals a most interesting contrast in behavior for the two paths. Following path 1 (involving cases A, B, and C, with decreasing P_r), we find that KE in the solutions increases steadily with increasing flow complexity. This would be expected since the buoyancy driving has strengthened relative to the dissipative mechanisms as measured by the increasing Rayleigh number R_a (Table 1). Path 2 (involving cases AB, B, and D, with P_r kept fixed at 0.25) is quite different as R_a increases: here the total kinetic energy KE remains nearly constant. A consequence is that with increasing complexity and increasing CKE along path 2, the DRKE must in turn decrease, and $\Delta\Omega$ becomes smaller. This striking property of achieving a nearly constant KE along path 2 (where both R_e and P_e increase comparably) is a remarkable feature of this intricate rotating system that is currently unexplained.

Our solutions typically exhibit small differences in behavior in the two hemispheres, as can be detected in the time-averaged Ω contours shown in Figure 4 and in the associated latitudinal cuts at fixed radius displayed in Figure 6 for cases AB and C. The meridional circulations likewise show some symmetry breaking in their response between the northern and southern hemispheres in Figure 7, which is further quantified for cases AB and C in showing the meridional streamlines in Figure 8 and in examining the latitudinal variation of the mean velocity component $\hat{v}_\theta$ in Figure 9. A sense of these asymmetries can also be assessed by examining differences in the kinetic energy of differential rotation in the two hemispheres. For case AB, DRKE in the northern hemisphere is 2.12×10^6 and 2.09×10^6 ergs cm^{-3} in the southern hemisphere, or a 1.6% difference. For case C, the corresponding values are 1.82×10^6 and 1.76×10^6 ergs cm^{-3}, or 3.6%. We expect that such symmetry breaking is likely to evolve slowly, with neither hemisphere favored. We plan to study aspects of symmetry breaking further with more extended simulations in the near future. Such efforts are inspired by the evolving meridional circulations and mean zonal flows being detected by helioseismology (Haber et al. 2000, 2002) and the differing solar rotation rates in the two hemispheres deduced from tracking sunspots (Howard, Gilman, & Gilman 1984).

4. INTERPRETING THE DYNAMICS

Our shells of rotating compressible convection are very complicated dynamical systems in terms of the nonlinear feedbacks and couplings that operate. It is difficult from first principles to predict or explain their overall behavior in terms of the differential rotation and meridional circulations that can be achieved and sustained as we sample different sites in parameter space. The five simulations represent numerical experiments that seek to probe some of the families of responses within a highly simplified version of the solar convection zone. Although most of our approximations here seem reasonable and necessary to yield a problem tractable to computational experiments, we do not fully know their impact and thus must draw our interpretations about the operation of the overall dynamics with considerable caution. The numerical solutions have the enormous advantage that we can interrogate them in detail to study various balances and fluxes, and these help to provide insights about the dynamical system.

4.1. *Redistributing the Angular Momentum*

Our choice of stress-free boundaries at the top and bottom of the computational domain has the advantage that no net torque is applied to our convective shells, resulting in the conservation of the angular momentum. We seek here to identify the main physical processes responsible for redistributing the angular momentum within our rotating convective shells, thus yielding the differential rotation seen in our five cases. We may assess the transport of angular momentum within these systems by considering the mean radial ($\mathscr{F}_r$) and latitudinal ($\mathscr{F}_\theta$) angular momentum fluxes. As discussed in Elliott et al. (2000), the ϕ-component of the momentum equation expressed in conservative form and averaged in time and longitude yields

$$\frac{1}{r^2}\frac{\partial(r^2\mathscr{F}_r)}{\partial r} + \frac{1}{r\sin\theta}\frac{\partial(\sin\theta\mathscr{F}_\theta)}{\partial\theta} = 0 \,, \tag{7}$$

involving the mean radial angular momentum flux,

$$\mathscr{F}_r = \hat{\rho} r \sin\theta \left[-\nu r \frac{\partial}{\partial r}\left(\frac{\hat{v}_\phi}{r}\right) + \widehat{v'_r v'_\phi} + \hat{v}_r\left(\hat{v}_\phi + \Omega_0 r \sin\theta\right)\right], \tag{8}$$

and the mean latitudinal angular momentum flux

$$\mathscr{F}_\theta = \hat{\rho} r \sin\theta \left[-\nu \frac{\sin\theta}{r}\frac{\partial}{\partial\theta}\left(\frac{\hat{v}_\phi}{\sin\theta}\right) + \widehat{v'_\theta v'_\phi} + \hat{v}_\theta\left(\hat{v}_\phi + \Omega_0 r \sin\theta\right)\right]. \tag{9}$$

In the above expressions for both fluxes, the first terms in each bracket are related to the angular momentum flux due to viscous transport (which we denote as $\mathscr{F}_{r,V}$ and $\mathscr{F}_{\theta,V}$), the second term to the transport due to Reynolds stresses ($\mathscr{F}_{r,R}$ and $\mathscr{F}_{\theta,R}$), and the third term to the transport by the meridional circulation ($\mathscr{F}_{r,M}$ and $\mathscr{F}_{\theta,M}$). The Reynolds stresses above are associated with correlations of the velocity components such as the $\widehat{v'_r v'_\theta}$ correlation, which arise from organized tilts within the convective structures, especially in the downflow plumes (see, e.g., Brummell et al. 1998; Miesch et al. 2000).

In Figure 11 we show the components of $\mathscr{F}_r$ and $\mathscr{F}_\theta$ for cases A, AB, B, and C, having integrated along colatitude and radius, respectively, to deduce the net fluxes through shells at various radii and through cones at various latitudes, namely, in the manner

$$I_{\mathscr{F}_r}(r) = \int_0^\pi \mathscr{F}_r(r,\theta) r^2 \sin\theta \, d\theta \,,$$
$$I_{\mathscr{F}_\theta}(\theta) = \int_{r_{\rm bot}}^{r_{\rm top}} \mathscr{F}_\theta(r,\theta) r \sin\theta \, dr \,, \tag{10}$$

and then identify in turn the contributions from viscous (V), Reynolds stresses (R), and meridional circulation (M) terms. This representation is helpful in considering the sense and amplitude of the transport of angular momentum within the convective shells by each component of $\mathscr{F}_r$ and $\mathscr{F}_\theta$.

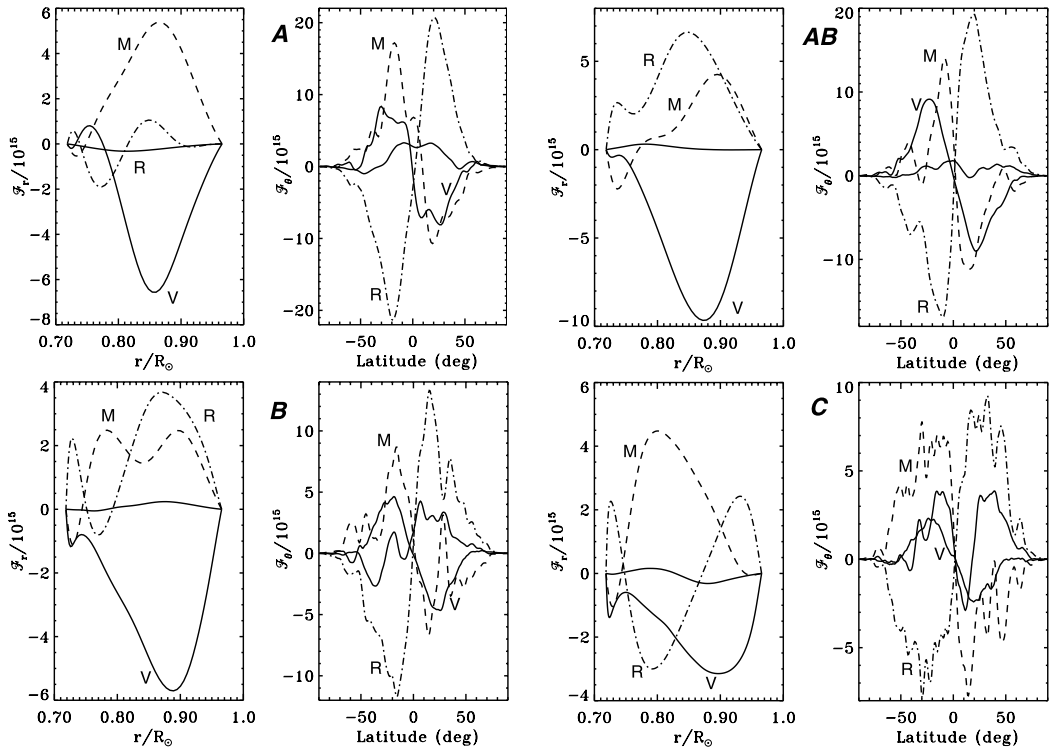

FIG. 11.—Time average of the latitudinal line integral of the angular momentum flux $\mathcal{F}_r$ (*left-hand panels in each pair*) and of the radial line integral of the angular momentum flux $\mathcal{F}_\theta$ (*right-hand panels*) for cases A (*top left*), AB (*top right*), B (*bottom left*), and C (*bottom right*). The fluxes have been decomposed into their viscous (labeled V), Reynolds stress (R), and meridional circulation (M) components. The solid curves represent the total fluxes and serve to indicate the quality of stationarity achieved. The positive values represent a radial flux that is directed outward and a latitudinal flux directed from north to south. The fluxes for cases A, AB, B, and C have been averaged over periods of 295, 275, 275, and 175 days, respectively.

Turning first to the radial fluxes in the leftmost of each pair of panels in Figure 11, we note that the integrated viscous flux $\mathcal{F}_{r,V}$ is negative (where, for simplicity, we drop I), implying a radially inward transport of angular momentum. This property is in agreement with the positive radial gradient in the angular velocity profiles achieved in our four cases, as is seen in Figure 4 in the radial cuts for different latitudes of Ω. Such downward transport of angular momentum is well compensated by the two other terms $\mathcal{F}_{r,\mathrm{R}}$ and $\mathcal{F}_{r,M}$, having reached a statistical equilibrium of nearly no net radial flux, as can be seen by noting that the solid curve $\mathcal{F}_r$ is close to zero. Although all of our solutions possess complicated temporal variations, our sampling in time to obtain the averaged fluxes suggest that we are sensing the equilibrated state reasonably well. As the level of turbulence is increased in going from case A to case C, $\mathcal{F}_{r,V}$ reduces in amplitude and the transport of angular momentum by the Reynolds stresses and by the meridional circulation change accordingly to maintain equilibrium. The meridional circulation as $\mathcal{F}_{r,M}$ involves a strong dominantly outward transport of angular momentum. The Reynolds stresses as $\mathcal{F}_{r,\mathrm{R}}$ vacillate in their sense with depth, although they consistently possess outward transport in the upper portions of the domain. Case AB is distinguished by $\mathcal{F}_{r,\mathrm{R}}$ being directed outward throughout the domain. Detailed examination with radius and latitude of the Reynolds stress contributions to the angular momentum fluxes in equations (7)–(9) reveals that the "flux stream functions" (not shown) possess multicelled structures with radius at latitudes above 45° for all cases except case AB. This striking difference in case AB of having a big positive $\mathcal{F}_{r,\mathrm{R}}$ appears to influence the redistribution of angular momentum at high latitudes. This may be key in the monotonic decrease of Ω with latitude of case AB extending into the polar regions and provides our first clue for how issue 1 is resolved within this case. In a broader sense in considering all of our cases, we deduce that in the radial direction the transport of angular momentum is significantly affected by both the meridional circulation and the Reynolds stresses.

The latitudinal transport of angular momentum $\mathcal{F}_\theta$ in the rightmost of the panels in Figure 11 involves more complicated and sharper variations in latitude. This comes about because of the more intricate latitudinal structure of the different terms contributing to the transport. Here the transport of angular momentum by Reynolds stresses $\mathcal{F}_{\theta,\mathrm{R}}$ appears to be the dominant one, being consistently directed toward the equator (i.e., negative in the southern hemisphere and positive in the northern hemisphere). This is an

important feature since it implies that the equatorial acceleration observed in our simulations is mainly due to the transport of angular momentum by the Reynolds stresses and thus is of dynamical origin. As we try to understand issue 2, concerned with retaining a significant $\Delta\Omega$ as the flow complexity is increased, we find that the variation of angular momentum fluxes by Reynolds stresses with increasing complexity along paths 1 and 2 are fairly similar in character. Along both these paths the Reynolds stress fluxes remain prominent, and this appears to sustain the large $\Delta\Omega$, thereby resolving issue 2 for solutions with the level of turbulence attained in cases C and D (the latter is not shown in Figure 11, but its transport properties are comparable to those of case C). Further, we see that the transport by meridional circulation $\mathscr{F}_{\theta,M}$ is opposite to $\mathscr{F}_{\theta,\mathrm{R}}$, with the meridional circulation seeking to slow down the equator and speed up the poles. A distinguishing feature of case AB is that $\mathscr{F}_{\theta,M}$ becomes small at latitudes above 30°, with the tendency of the meridional circulation to try to spin up the high latitudes sharply diminished compared to the other cases. This appears to result from the strong meridional circulation in case AB being largely confined to the interval from the equator to 30° in latitude (Fig. 8*a*), with only a weak response at higher latitudes. This property of $\mathscr{F}_{\theta,M}$, together with the uniformly positive $\mathscr{F}_{r,\mathrm{R}}$, provides the second clue for how issue 1 appears to be resolved by case AB. As the level of turbulence is increased, we find a reduction in the amplitudes of all the components of $\mathscr{F}_{\theta}$, with $\mathscr{F}_{\theta,V}$ always being the smallest and transporting the angular momentum poleward in the same sense as $\mathscr{F}_{\theta,M}$. For $\mathscr{F}_{\theta,\mathrm{R}}$, this lessening amplitude appears to come about from the increasing complexity of the flows implying smaller correlations in the Reynolds stress terms, but it is likely that strengthening coherent turbulent plumes can serve to rebuild such correlations (Brummell et al. 1998).

Our estimates of the latitudinal transports of angular momentum yield fairly good equilibration for cases A and AB, with little net latitudinal flux, but the more turbulent cases such as C are sufficiently complex that achieving such latitudinal balance is a slow process in the temporal averaging. We conclude that the Reynolds stresses have the dominant role in achieving the prograde equatorial rotation seen in our simulations, with its effectiveness limited by the opposing transport of angular momentum by the meridional circulation. The viscous transports are becoming more negligible as we achieve more turbulent flows by reducing the eddy diffusivities.

4.2. *Baroclinicity and Thermal Winds*

Convection influenced by rotation can lead to latitudinal heat transport in addition to radial transport, thereby producing latitudinal gradients in temperature and entropy even if none were imposed by the boundary conditions. This further implies that surfaces of constant mean density and mean pressure will not coincide, thereby admitting baroclinic terms in the vorticity equations (Pedlosky 1987; Zahn 1992). Baroclinicity has been argued to possibly have a pivotal role in obtaining differential rotation profiles whose angular velocity, like the Sun, are not constant on cylinders (e.g., Kitchatinov & Rüdiger 1995). We shall here analyze our cases AB and C from that perspective, finding that although a small latitudinal entropy gradient is realized, the resulting differential rotation as exhibited in our solutions by the mean longitudinal velocity $\hat{v}_\phi$ cannot be accounted for principally by the baroclinic term. To make such interpretation specific, we should turn as in Elliott et al. (2000) to the mean (averaged in longitude and time) zonal component of the curl of the momentum equation (2), expressed as

$$\epsilon_{\phi ij}\frac{\partial}{\partial x_i}\left[\widehat{v_k(\partial v_j/\partial x_k)}+\hat{\rho}^{-1}\frac{\partial}{\partial x_k}\widehat{\mathscr{D}_{kj}} = 2\Omega_0\frac{\partial \hat{v}_\phi}{\partial z}+\hat{\rho}^{-2}\nabla\hat{\rho}\times\nabla\hat{p}\Big|_\phi\right], \quad (11)$$

where the Einstein summation convention has been adopted, ϵ represents the permutation tensor, and

$$\frac{\partial}{\partial z}\equiv\cos\theta\frac{\partial}{\partial r}-\frac{\sin\theta}{r}\frac{\partial}{\partial\theta}$$

is the derivative parallel to the rotation axis. This vorticity equation is helpful in examining the relative importance of different forces in meridional planes; here terms arising from Reynolds and viscous stresses are on the left and those from Coriolis and baroclinic effects on the right. If one were to simply neglect the Reynolds and viscous stresses, we obtain the simplest version of a "thermal wind balance" in which departures of zonal winds from being constant on cylinders aligned with the rotation axis are accounted for by the baroclinic term involving crossed gradients of density and pressure, namely,

$$2\Omega_0\frac{\partial\hat{v}_\phi}{\partial z}=-\hat{\rho}^{-2}\nabla\hat{\rho}\times\nabla\hat{p}\Big|_\phi. \quad (12)$$

With the superadiabatic gradient expressed as

$$\frac{1}{c_{\mathrm{P}}}\nabla\hat{S}=\frac{1}{\gamma\hat{p}}\nabla\hat{p}-\frac{1}{\hat{\rho}}\nabla\hat{\rho}, \quad (13)$$

where γ is the logarithmic derivative of pressure with respect to density at constant specific entropy, we can rewrite equation (12) as

$$\frac{\partial\hat{v}_\phi}{\partial z}=\frac{1}{2\Omega_0\hat{\rho}c_{\mathrm{P}}}\nabla\hat{S}\times\nabla\hat{p}\Big|_\phi=\frac{g}{2\Omega_0 r c_{\mathrm{P}}}\frac{\partial\hat{S}}{\partial\theta}, \quad (14)$$

having neglected turbulent pressure. Thus, breaking the Taylor-Proudman constraint that requires rotation to be constant on cylinders, with $\partial\hat{v}_\phi/\partial z$ equal to zero, can be achieved by establishing a latitudinal entropy gradient. However, Reynolds and viscous stresses can also serve to break that constraint, and indeed we next show that those terms are at least as important as the baroclinic term.

We turn in Figure 12 to an analysis of case AB in terms of how well a simple thermal wind balance is achieved or violated. Figures 12*a* and 12*b* display the temporal mean zonal velocity $\hat{v}_\phi$ and its gradient $\partial\hat{v}_\phi/\partial z$, with the latter having pronounced variations at midlatitudes near the top of the spherical shell and others at lower latitudes near the bottom of the domain. The baroclinic term (as on right-hand side of eq. [14]) is shown in Figure 12*c*, possessing the largest amplitudes close to the base of the shell at low latitudes, with a tongue connecting to midlatitudes in traversing the shell. The difference between this baroclinic term and the actual $\partial\hat{v}_\phi/\partial z$, as shown in Figure 12*d*, is a measure of the effectiveness of a thermal wind balance in case AB. It is evident that baroclinicity yields a fair semblance of a balance over much of the deeper layer, with the baroclinic term (Fig. 12*c*) typi-

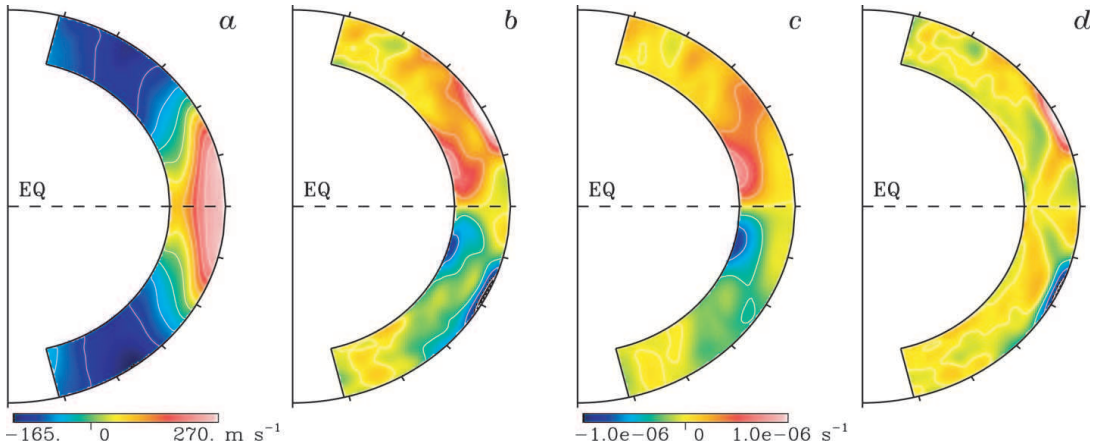

FIG. 12.—Temporal and longitudinal average for case AB of (*a*) the longitudinal velocity $\hat{v}_\phi$, (*b*) its derivative along the *z*-axis, $\partial\hat{v}_\phi/\partial z$, (*c*) the baroclinic term in the meridional force balance (see eq. [14]), and (*d*) the difference between the last two terms [namely, (*b*) minus (*c*)]. The results have been averaged over a period of 275 days. Panel *d* shows that there are major departures from a simple thermal wind balance, especially near the top of the domain. The same color scale is used in (*b*), (*c*), and (*d*).

cally being greater in amplitude than $\partial\hat{v}_\phi/\partial z$ (Fig. 12*b*) there. However, the major regions of departure with opposite signs in the two hemispheres show that in the upper domain, between latitudes of about 15° and 45°, that balance is quite severely violated: there the Reynolds stress terms in equation (11) involving vortex tube stretching and tilting become the main players. This broad site coincides with regions of strong latitudinal gradient in $\hat{v}_\phi$ and is centered in latitude where the relative rotation changes sense from prograde to retrograde. What we have learned from this is that whereas the convection does establish a latitudinal gradient of entropy that is needed for baroclinic terms to achieve aspects of thermal wind balance over the deeper portions of the domain, the Reynolds stresses have an equally crucial role in the meridional force balance over portions of the upper domain. The more turbulent case C is likewise analyzed in Figure 13, and it generally exhibits comparable behavior. The baroclinic term (Fig. 13*c*) captures much of the $\partial\hat{v}_\phi/\partial z$ variation (Fig. 13*b*) at midlatitudes over most of the deep shell, but there are large departures (Fig. 13*d*) in thin domains near the top and bottom of the shell, again between 15° and 45° in latitude. Thus, here too the Reynolds stress terms are significant players in the overall balance.

The latitudinal entropy and temperature gradients established within our simulations should be examined further. We show in Figure 14 the time- and longitude-averaged specific entropy fluctuations $\hat{S}$ and temperature fluctuations $\hat{T}$ for cases AB and C, presenting both color contour renderings across the shell and their variations with latitude at three depths. Our model AB, which exhibits the strongest differential rotation, also possesses the greatest temperature and entropy contrasts with latitude. We see from the latitudinal cuts of temperature that a $\Delta\Omega$ on the order of 30% involves a pole-equator temperature variation of about 4–8 K, the pole being warmer. These temperature contrasts are very small compared to the mean temperature near the top of our domain of about 10^5 K and of 2×10^6 K near its base. There is some evidence of a latitudinal variation in the photospheric temperature of at least a few kelvins with the same sense obtained from observations of the solar limb (see, e.g., Kuhn 1998), although relative variations of such small amplitude are very difficult to measure. We note that our temperature fields show some banding with latitude near the top of the domain, with the equator slightly warm, then attaining relatively cool values with minima at about latitude 35°, followed by rapid ascent to warm values at high latitudes. The behavior is monotonic with latitude at greater depths, as it is consistently so for entropy at all depths. These differences between temperature and entropy are accounted for by effects of the pressure field necessary to drive the meridional circulation.

In summary, although our solutions attain close to a thermal wind balance over large portions of the domain, the departures elsewhere are most significant. These arise from the Reynolds stresses that have a crucial role in establishing the differential rotation profiles realized in our simulations. The baroclinicity in our solutions, resulting from latitudinal heat transport that sets up a pole-to-equator temperature and entropy contrast, contributes to Ω not being constant on cylinders, but it is not the dominant player as envisioned in some discussions of mean-field models of solar differential rotation (e.g., Kitchatinov & Rüdiger 1995; Rekowski & Rüdiger 1998; Durney 1999, 2000).

5. CONCLUSIONS

Our five simulations studying the coupling of turbulent convection and rotation within full spherical shells have revealed that strong differential rotation contrasts can be achieved for a range of parameter values. With these new models, we have focused on two fundamental issues raised in comparing the solar differential rotation deduced from helioseismology with the profiles achieved in the prior three-dimensional simulations of turbulent convection with the ASH code (Miesch et al. 2000; Elliott et al. 2000). As issue 1, the Sun appears to possess remarkably slow poles, with Ω decreasing steadily with latitude even at mid- and high lati-

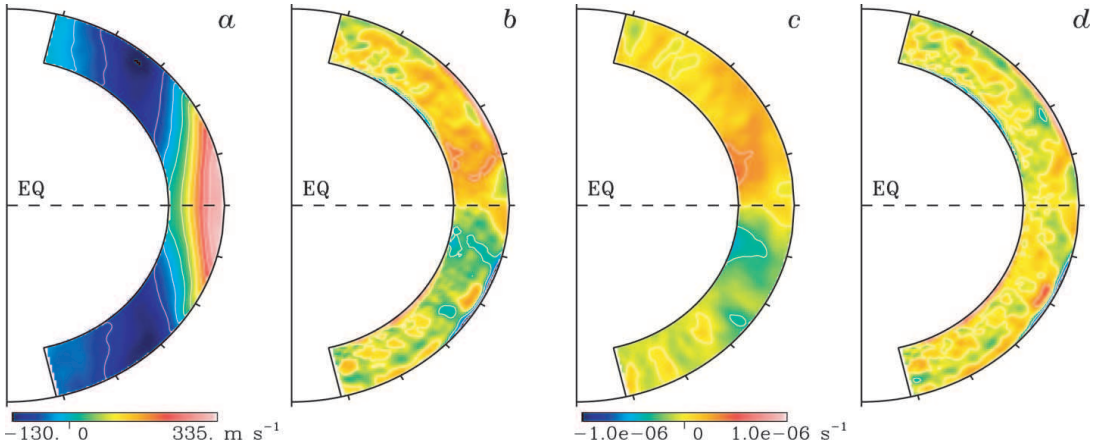

FIG. 13.—As in Fig. 12, but analyzing the role of baroclinicity in the more turbulent case C in maintaining the differential rotation. There are significant departures from a thermal wind balance in thin regions near the top and bottom of the shell.

tudes (Fig. 1). In contrast, the previous models showed little variation in Ω at the higher latitudes, having achieved most of their latitudinal angular velocity contrast $\Delta\Omega$ in going from the equator to about 45°. As issue 2, there was a tendency for $\Delta\Omega$ to diminish or even decrease sharply within the prior simulations as the convection became more turbulent, yielding values of $\Delta\Omega$ that were becoming small compared to the helioseismic deductions. In seeking to resolve these two issues, we have explored two paths in parameter space that yield complex and turbulent states of convection. Path 1 involves decreasing the Prandtl number in the sequence of cases A, B, and C, while keeping the Péclet number nearly constant. Path 2 maintains a constant Prandtl number as both the Reynolds and Péclet number are increased in the sequence of cases AB, B, and D. On both paths the convective Rossby number has been chosen to be less than unity, thereby maintaining a strong rotational influence on the convection even as the flows become more intricate.

In dealing with issue 1, our case AB provides the first indications that it is possible to attain solutions in which the polar regions rotate significantly slower than the midlatitudes (Fig. 4). There is a monotonic decrease from the fast (prograde) equatorial rate in Ω to the slow (retrograde) rate of the polar regions. Further, that case AB has Ω nearly constant on radial lines at the higher latitudes, again in the spirit of the helioseismic inferences. We do not fully understand why in case AB such a strikingly different Ω profile results compared to that in our other solutions (and of the progenitor simulations) in which the contrast $\Delta\Omega$ is mainly achieved in the lower latitudes. Our principal clues come from Figure 11, where we find that only in case AB is the Reynolds stress component of the net radial angular momentum flux $\mathscr{F}_{r,\mathrm{R}}$ (through shells at various radii) uniformly directed outward. From having examined in detail angular momentum flux stream functions (not shown) with radius and latitude consistent with equations (7)–(9), we observed that the Reynolds stress contributions to such transport possessed multicelled structures with radius at high latitudes in all the cases except case AB. The single-cell behavior there for case AB appears to enable more effective extraction of angular momentum by Reynolds stresses from the high to the low latitudes, thereby yielding a distinctive rotational slowing of the high latitudes. Further, case AB possesses strong meridional circulations at low latitudes but only feeble ones at latitudes above 30°, unlike other solutions such as case C (Figs. 8 and 9). This yields a weak meridional component $\mathscr{F}_{\theta,M}$ (seeking to spin up the poles) to the latitudinal angular momentum flux, thereby allowing the equatorward transport by the Reynolds stress component $\mathscr{F}_{\theta,\mathrm{R}}$ to succeed in extracting angular momentum from the higher latitudes. Such polar slowing also leads to case AB possessing the greatest $\Delta\Omega$ attained in our five simulations (Table 2).

We also considered the possibility that the slow pole behavior in case AB may have baroclinic origins. This can result from suitable correlations in velocity and thermal structures yielding a latitudinal heat flux that may produce substantial entropy variations at the higher latitudes, thereby leading to greater baroclinic contributions in equation (11) that define the variation of mean zonal velocity. Examination of Figure 12 at high latitudes does not reveal a prominent baroclinic contribution, and this is consistent with the bland variation of entropy for case AB (Fig. 14) at latitudes above about 40°. We conclude that the origin of the slow rotation rate in polar regions appears to be primarily dynamical, being associated with the Reynolds stress transports and not with baroclinicity that arises from latitudinal heat transport serving to establish a sufficiently warm pole. Although case AB provides a solution that resolves issue 1, it is unique in achieving this among our five simulations. It may be that in parameter space there only exists a small basin of attraction for such behavior, although we think it more likely that several solution states may coexist for the same control parameters, one of which exhibits the gradual rotational slowing at high latitudes and others having most Ω variations confined to low and midlatitudes. We plan to examine whether the slow pole characteristics of case AB can be maintained at nearby sites in parameter space if started from initial conditions corresponding to case AB and plan to report on this in the future.

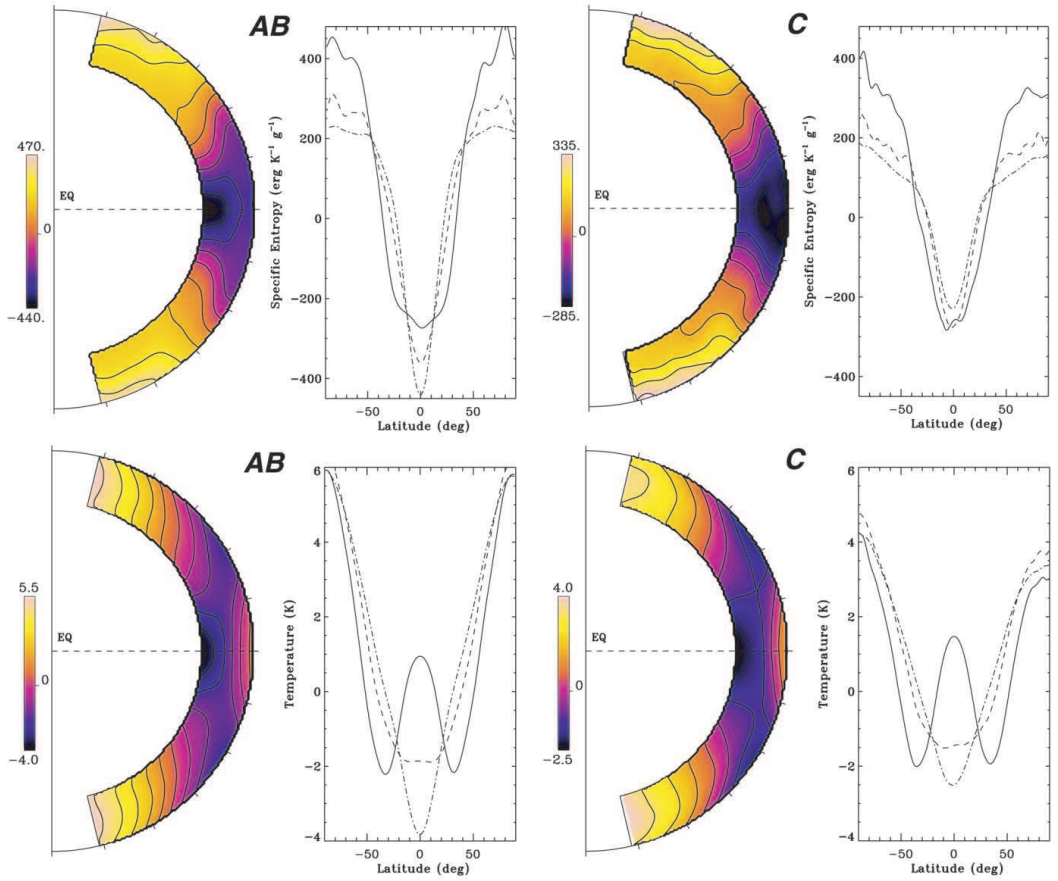

FIG. 14.—Temporal and longitudinal averages for cases AB and C of the specific entropy (*upper panels*) and temperature fluctuations (*lower panels*), accompanied by latitudinal profiles at the base (*dash-dotted line*), at the middle (*dashed line*) and at the top (*solid line*) of the convective domain. The results have been averaged over periods in turn of 275 and 175 days. The presence of a latitudinal variation of entropy is consistent with the baroclinic term (shown in Figs. 12 and 13) and involves an equator to pole temperature contrast of at most 4–8 K near the top where the mean temperature is about 10^5 K.

Issue 2 concerns sustaining a strong differential rotation with latitude as the convection becomes more complex. The two paths that we have explored in parameter space to achieve more complex and turbulent states yield relative angular velocity contrasts $\Delta\Omega/\Omega_0$ in latitude that are comparable to values deduced from helioseismology, with both our models and apparently the Sun possessing a contrast on the order of 30%. Further, this is accomplished while imposing an upper thermal boundary condition that ensures a uniform emerging heat flux with latitude, as suggested in Elliott et al. (2000). As the solutions become turbulent path 1 involving a decreasing Prandtl number is somewhat more effective in attaining large $\Delta\Omega$ than path 2, which has the Prandtl number fixed at 0.25 as both diffusivities are decreased. This holds out hope that even more turbulent solutions will act likewise.

We have shown that the strong $\Delta\Omega$ results from the role of the Reynolds stresses in redistributing the angular momentum. This transport is established by correlations in velocity components arising from convective structures that are tilted toward the rotation axis and depart from the local radial direction and away from the meridional plane. These yield both $v_r v_\phi$ and $v_\theta v_\phi$ correlations necessary for the Reynolds stress contributions to the radial and latitudinal angular momentum fluxes analyzed in Figure 11. The fast downflow plumes have a dominant role in such Reynolds stresses, much as seen in local studies (Brummell et al. 1998). Our simulations have attained a spatial resolution adequate to begin to attain coherent structures amidst the turbulence, which is believed to be a key in sustaining strong Reynolds stresses at higher turbulence levels. This has the consequence that all our spherical shells possess fast prograde equatorial rotation relative to the reference frame. There are some contributions toward maintaining the differential rotation from the latitudinal heat transport inherent in our convection that serves to establish a warm pole (with

a contrast of a few kelvins) relative to the equator, with baroclinicity and a partial thermal wind balance helping to yield equatorial acceleration. The meridional circulations generally work to oppose such tendencies by redistributing angular momentum so as to try to spin up the poles. Our simulations on paths 1 and 2 confirm that strong differential rotation with fast equators has its primary origin in angular momentum transport associated with the Reynolds stresses. Such prominent transports serve to resolve issue 2. Our next challenge is to satisfy issue 1 simultaneously with issue 2 in the more turbulent solutions, which may also lead to Ω being more nearly constant on radial lines at mid- to high latitudes.

Although our results for Ω have made promising contacts with helioseismic deductions about the state of solar differential rotation in the bulk of the convection zone, there are also major issues that we have not yet tackled. We must evaluate more advanced subgrid-scale terms in representing the unresolved turbulence within such simulations, especially in the near-surface regions. Foremost are also questions of how does the presence of a region of penetration below the convection zone influence the angular momentum redistribution in the primary zone above and does the tachocline of shear that is established near the interface with the deeper radiative interior modify properties within the convection zone itself? We are keen to also investigate aspects of the rotational shear evident close to the solar surface. This is just now becoming computationally feasible and involves extending our computational domain upward and beginning to resolve supergranular motions there, as discussed in DeRosa & Toomre (2001) in preliminary studies with thin shells. We are still at early stages with our simulations using ASH to study turbulent convection in spherical shells, yet it is comforting that the mean differential rotation profiles realized in some of the simulations are beginning to capture many of the dominant features for Ω deduced from the helioseismic probing.

We thank Nicholas Brummell, Marc DeRosa, Julian Elliott, Peter Gilman, Mark Miesch, and Jean-Paul Zahn for useful discussions and comments during the writing phase of this paper and the referee for encouraging us to clarify the objectives and thrust of the presentation. This work was partly supported by NASA through SEC Theory Program grant NAG 5-8133 and by NSF through grant ATM 9731676. Various phases of the simulations with ASH were carried out with NSF PACI support of the San Diego Supercomputer Center (SDSC), the National Center for Supercomputing Applications (NCSA), and the Pittsburgh Supercomputing Center (PSC). Much of the analysis of the extensive data sets was carried out in the Laboratory for Computational Dynamics (LCD) within JILA.

REFERENCES

Brandenburg, A., Jennings, R. L., Nordlund, Å., Rieutord, M., Stein, R. F., & Tuominen, I. 1996, J. Fluid Mech., 306, 325
Braun, D. C., & Fan, Y. 1998, ApJ, 508, L105
Brummell, N. H., Cattaneo, F., & Toomre, J. 1995, Science, 269, 1370
Brummell, N. H., Clune, T. L., & Toomre, J. 2002, 570, 825
Brummell, N. H., Hurlburt, N. E., & Toomre, J. 1996, ApJ, 473, 494
———. 1998, ApJ, 493, 955
Brun, A. S., & Toomre, J. 2001, in Helio- and Asteroseismology at the Dawn of the Millenium, ed. A. Wilson (ESA SP-464; Noordwijk: ESA), 619
Brun, A. S., Turck-Chièze, S., & Zahn, J.-P. 1999, ApJ, 525, 1032
Canuto, V. M. 1999, ApJ, 524, 311
Cattaneo, F. 1999, ApJ, 515, L39
Charbonneau, P., Dikpati, M., & Gilman, P. A. 1999, ApJ, 526, 523
Chou, D.-Y., & Dai, D.-C. 2001, ApJ, 559, L175
Choudhuri, A. R., Schüssler, M., & Dikpati, M. 1995, A&A, 303, L29
Clune, T. L., Elliott, J. R., Glatzmaier, G. A., Miesch, M. S., & Toomre, J. 1999, Parallel Comput., 25, 361
DeRosa, M. L., & Toomre, J. 2001, in Helio- and Asteroseismology at the Dawn of the Millenium, ed. A. Wilson (ESA SP-464; Noordwijk: ESA), 595
Dikpati, M., & Charbonneau, P. 1999, ApJ, 518, 508
Durney B. R. 1999, ApJ, 511, 945
———. 2000, ApJ, 528, 486
Elliott, J. R., Miesch, M. S., & Toomre, J. 2000, ApJ, 533, 546
Giles, P. M. 1999, Ph.D. thesis, Stanford University
Giles, P. M., Duvall, T. L., Jr., & Scherrer, P. H. 1998, in Structure and Dynamics of the Interior of the Sun and Sun-like Stars, ed. S. G. Korzennik & A. Wilson (ESA SP-418, Vol. 2; Noordwijk: ESA), 775
Gilman, P. A. 2000, Sol. Phys., 192, 27
Gilman, P. A., & Miller, J. 1986, ApJS, 61, 585
Glatzmaier, G. A. 1985, ApJ, 291, 300
———. 1987, in The Internal Solar Angular Velocity, ed. B. R. Durney & S. Sofia (Dordrecht: D. Reidel), 263
Glatzmaier, G. A., & Gilman, P. 1982, ApJ, 256, 316
Gough, D. O. 1969, J. Atmos. Sci., 26, 448
Gough, D. O., & McIntyre, M. E. 1998, Nature, 394, 755
Gough, D. O., & Toomre, J. 1991, ARA&A, 29, 627
Grote, E., & Busse, F. H. 2000, Fluid Dyn. Res., 28, 349
Haber, D. A., Hindman, B. W., Toomre, J., Bogart, R. S., Larsen, R. M., & Hill, F. 2002, ApJ, 570, 855
Haber, D. A., Hindman, B. W., Toomre, J., Bogart, R. S., Schou, J., & Hill, F. 1998, in Structure and Dynamics of the Sun and Sun-like Stars, ed. S. G. Korzennik & A. Wilson (ESA SP-418, Vol. 2; Noordwijk: ESA), 791
Haber, D. A., Hindman, B. W., Toomre, J., Bogart, R. S., Thompson, M. J., & Hill, F. 2000, Sol. Phys., 192, 335
Harvey, J. W., et al. 1996, Science, 272, 1284
Hathaway, D. H., Beck, J. G., Bogart, R. S., Bachmann, K. T., Khatri, G., Petitto, J. M., Han, S., & Raymond, J. 2000, Sol. Phys., 193, 495
Hathaway, D. H., et al. 1996, Science, 272, 1306
Howard, R., Gilman, P. A., & Gilman, P. I. 1984, ApJ, 283, 373
Howe, R., Christensen-Dalsgaard, J., Hill, F., Komm, R. W., Larsen, R. M., Schou, J., Thompson, M. J., & Toomre, J. 2000a, Science, 287, 2456
———. 2000b, ApJ, 533, L163
Hurlburt, N. E., Toomre, J., & Massaguer, J. M. 1986, ApJ, 311, 563
Kichatinov, L. L., & Rüdiger, G. 1995, A&A, 299, 446
Kuhn, J. R. 1998, in Structure and Dynamics of the Sun and Sun-like Stars, ed. S. G. Korzennik & A. Wilson (ESA SP-418, Vol. 2; Noordwijk: ESA), 871
Lesieur, M. 1997, Turbulence in Fluids (Dordrecht: Kluwer)
Libbrecht, K. G. 1989, ApJ, 336, 1092
Miesch, M. S. 2000, Sol. Phys., 192, 59
Miesch, M. S., Elliott, J. R., Toomre, J., Clune, T. L., Glatzmaier, G. A., & Gilman, P. A. 2000, ApJ, 532, 593
Pedlosky, J. 1987, Geophysical Fluid Dynamics (New York: Springer)
Porter, D. H., & Woodward, P. R. 2000, ApJS, 127, 159
Rieutord, M., & Zahn, J.-P. 1995, A&A, 296, 127
Rekowski, B. V., & Rüdiger, G. 1998, A&A, 335, 679
Robinson, F. J., & Chan, K. L. 2001, MNRAS, 321, 723
Scherrer, P. H., et al. 1995, Sol. Phys., 162, 129
Schou, J., et al. 1998, ApJ, 505, 390
Schou, J., & Bogart, R. S. 1998, ApJ, 504, L131
Schüssler, M. 1987, in The Internal Solar Angular Velocity, ed. B. R. Durney & S. Sofia (Dordrecht: D. Reidel), 303
Spiegel, E. A., & Zahn, J.-P. 1992, A&A, 265, 106
Stein, R. F., & Nordlund, Å. 1998, ApJ, 499, 914
Sun, Z.-P., & Schubert, G. 1995, Phys. Fluids, 7, 2686
Takehiro, S.-I., & Hayashi, Y.-Y. 1999, Geophys. Astrophys. Fluid Dyn., 90, 43
Thompson, M. J., et al. 1996, Science, 272, 1300
Tobias, S. M., Brummell, N. H., Clune, T. L., & Toomre, J. 2001, ApJ, 549, 1183
Toomre, J., Christensen-Dalsgaard, J., Howe, R., Larsen, R. M., Schou, J., & Thompson, M. J. 2000, Sol. Phys., 192, 437
Ward, F. 1966, ApJ, 145, 416
Zahn, J.-P. 1992, A&A, 265, 115
———. 2000, in Ann. NY Acad. Sci., 898, Astrophysical Turbulence and Convection, ed. J. R. Buchler & H. Kandrup, 90

4.7.2 On the interaction between differential rotation and magnetic fields in the Sun

par Brun 2004, Solar Physics, 220, 333

ON THE INTERACTION BETWEEN DIFFERENTIAL ROTATION AND MAGNETIC FIELDS IN THE SUN

ALLAN SACHA BRUN
DSM/DAPNIA/SAp, CEA Saclay, 91191 Gif-sur-Yvette Cedex, France;
e-mail sacha.brun@cea.fr

(Received 1 December 2003; accepted 30 December 2003)

Abstract. We have performed 3-D numerical simulations of compressible convection under the influence of rotation and magnetic fields in spherical shells. They aim at understanding the subtle coupling between convection, rotation and magnetic fields in the solar convection zone. We show that as the magnetic Reynolds number is increased in the simulations, the magnetic energy saturates via nonlinear dynamo action, to a value smaller but comparable to the kinetic energy contained in the shell, leading to increasingly strong Maxwell stresses that tend to weaken the differential rotation driven by the convection. These simulations also indicate that the mean toroidal and poloidal magnetic fields are small compared to their fluctuating counterparts, most of the magnetic energy being contained in the non-axisymmetric fields. The intermittent nature of the magnetic fields generated by such a turbulent convective dynamo confirms that in the Sun the large-scale ordered dynamo responsible for the 22-year cycle of activity can hardly be located in the solar convective envelope.

1. Introduction

Observations of the solar convective surface reveal that it rotates differentially, the equatorial regions being about 30% faster that the polar regions. Thanks to helioseismology, it has been demonstrated that this strong differential rotation imprints the whole convective envelope to then become uniform in the radiative interior (Thompson *et al.*, 2003; Couvidat *et al.*, 2003). This transition occurs at the base of the convection zone ($r \simeq 0.71\ R_\odot$, where $R_\odot$ is the solar radius) in a thin shear layer called the tachocline. The Sun also exhibits both random and cyclic magnetic activity with phenomena as diverse as coronal mass ejections, prominences and sunspots (Stix, 2002). Understanding the physical processes behind such a complex magnetohydrodynamical (MHD) system and how they are interacting to yield ordered properties such as the large-scale mean flows or the 22-year cycle, has turned out to be one of the major challenges of modern astrophysics (Brummel, Cataneo, and Toomre, 1995; Ossendrijver, 2003). Indeed such intricate nonlinear interactions can not be directly predicted from first principles. Therefore alternative techniques have been developed to improve our 'physical intuition' about the working of such complex dynamical processes. For example, mean field theory (Moffat, 1978; Krause and Rädler, 1980) has been succesful at laying down the basic principles behind the solar dynamo, such as the ω and α effects. More

Solar Physics **220:** 333–345, 2004.

recently, fully nonlinear 3-D MHD simulations have started to refine and to improve our understanding. It is currently believed that our star operates a dynamo at two differing ranges of spatial and temporal scales (Cattaneo and Hughes, 2001). The global dynamo yielding the regular 22-year cycle and butterfly diagrams for sunspot emergence is likely to be seated within the tachocline (Parker, 1993). The origin of the rapidly varying and smaller scale magnetism is probably due to local dynamo action.

We would like here to address some aspects of the nonlinear coupling between convection, rotation and magnetic fields in the Sun. We believe that numerical simulations of a rotating conducting convective fluid in full spherical geometry could help understanding of this difficult problem. Unfortunately even today 3-D simulations of the whole solar dynamo problem are intractable considering the 6 orders of spatial and temporal scales realized in the turbulent solar convection zone. As an alternative one can split the dynamo problem into 'blocks' that answer specific questions, such as magnetic field amplification, magnetic field pumping, flux tube rising ... Following the pioneering work of Gilman and Glatzmaier (Gilman, 1983; Glatzmaier, 1987), we have conducted global, high-resolution (up to spherical harmonic degree $\ell_{\max} = 340$), 3-D MHD simulations of the bulk of the solar convection zone. Since both the α and ω effects are thought to play a crucial role in the working of the solar dynamo, we are interested in studying the interplay between differential rotation and magnetic fields and how dynamo generated magnetic fields feedback on the large scale convection via Lorentz forces. In particular we would like to address the following two questions: (a) Are there numerical solutions that both display a dynamo generated magnetic field and retain a strong differential rotation profiles as deduced by helioseismic inversions? (b) What are the respective roles of the Reynolds and Maxwell stresses and of the large-scale magnetic torque in the transport of the angular momentum in our turbulent convective rotating shells?

We briefly present in Section 2 our numerical model and the anelastic spherical harmonics (ASH) code used in this work. In Section 3 we discuss the influence of magnetic fields on the turbulent rotating convective zone, compare our results with past and present observations of the Sun and with earlier 3-D MHD numerical simulations of the solar convection envelope. We then summarize in Section 4 our findings.

2. Formulating the Problem

The ASH code solves the 3-D MHD anelastic equations of motion in a rotating spherical shell geometry using a pseudo spectral semi-implicit method (Clune *et al.*, 1999; Brun, Miesch, and Toomre, 2004). The anelastic approximation captures the effects of density stratification without having to resolve sound waves which would severely limit the time steps. The resulting equations are fully non-

linear in velocity and magnetic field variables; the thermodynamic variables are separated with respect to a spherically symmetric and evolving mean state (denoted with an overbar) and fluctuations about this mean state:

$$\nabla \cdot (\bar{\rho}\mathbf{v}) = 0, \tag{1}$$

$$\bar{\rho}\left(\frac{\partial \mathbf{v}}{\partial t} + (\mathbf{v}\cdot\nabla)\mathbf{v} + 2\Omega_0 \times \mathbf{v}\right) = -\nabla P + \rho\mathbf{g} + \frac{1}{4\pi}(\nabla \times \mathbf{B}) \times \mathbf{B} - \\ -\nabla \cdot \mathcal{D} - [\nabla \bar{P} - \bar{\rho}\mathbf{g}], \tag{2}$$

$$\bar{\rho}\bar{T}\frac{\partial S}{\partial t} + \bar{\rho}\bar{T}\mathbf{v}\cdot\nabla(\bar{S}+S) = \nabla\cdot[\kappa_r\bar{\rho}c_p\nabla(\bar{T}+T) + \kappa\bar{\rho}\bar{T}\nabla(\bar{S}+S)] + \\ + \frac{\eta}{4\pi}(\nabla\times\mathbf{B})^2 + 2\bar{\rho}\nu\left[e_{ij}e_{ij} - 1/3(\nabla\cdot\mathbf{v})^2\right], \tag{3}$$

$$\frac{\partial \mathbf{B}}{\partial t} = \nabla\times(\mathbf{v}\times\mathbf{B}) - \nabla\times(\eta\nabla\times\mathbf{B}), \tag{4}$$

where $\mathbf{v} = (v_r, v_\theta, v_\phi)$ is the local velocity in spherical coordinates in the frame rotating at constant angular velocity $\Omega_0 = \Omega_o \mathbf{e}_z$, $\mathbf{B}$ is the magnetic field, κ_r is the radiative diffusivity, η is the effective magnetic diffusivity, ν and κ are effective eddy diffusivities, $\mathcal{D}$ is the viscous stress tensor and e_{ij} is the strain rate tensor. All the other variables have their usual meaning.

We use a toroidal and poloidal decomposition that enforces the mass flux and the magnetic fields to remain divergence free. The effects of the steep entropy gradient close to the surface has been softened by introducing a subgrid scale (SGS) transport of heat to account for the unresolved motions, and enhanced diffusivities are used in these large eddy simulations (LES). The boundary conditions at the top and bottom of the computational domain are stress-free impenetrable walls for the velocity field, constant entropy gradient for the entropy and match to a potential field for the magnetic field.

The model is a simplified description of the solar convection zone: solar values are taken for the heat flux, rotation rate, mass and radius, and a perfect gas is assumed. The computational domain extends from 0.72 $R_\odot$ to 0.96 $R_\odot$, thereby concentrating on the bulk of the unstable zone and here not dealing with penetration into the radiative interior nor with the partially ionized surface layers. The maximum numerical resolution used in case $M3$ is $N_r = 129$ radial collocation points and $N_\theta = 512$ and $N_\phi = 1024$ latitudinal and longitudinal grid points (corresponding to taking all degrees up to the spherical harmonic degree $\ell_{\max} = 340$). The typical density difference across the shell in radius is about 30.

We start our MHD simulations from an already evolved and equilibrated purely hydrodynamical solution, namely case H, characterized by a Rayleigh number $Ra = 10^5$, a Taylor number $Ta = 1.2 \times 10^6$ and a Prandtl number $P_r = 1/8$. This case possesses a strong, almost solar-like differential rotation (cf. Figure 3

and Brun, Miesch, and Toomre, 2004). A seed axisymmetric dipolar magnetic field is then introduced in the convective spherical shell and the simulations evolved in time.

In the following section we report on the main results obtained with our numerical simulations by comparing two magnetic cases, $M1$ and $M3$, among many others that we have computed. These two cases possess in turn a magnetic Prandtl number $P_m = \nu/\eta$ of 2 and 4, leading in case $M3$ to a rms magnetic Reynolds number ($R_m = \tilde{v}L/\eta$, where L is the shell thickness and $\tilde{v}$ a representative rms velocity), about a factor of two bigger than in case $M1$. Both simulations have been started with a magnetic energy (ME) seven order of magnitude smaller than the total kinetic energy (KE) contained in the non-magnetic convective case H (i.e., $(ME/KE)_0 = 10^{-7}$).

3. Rotating Convective Zone and Associated Mean Flows in the Presence of Magnetic Fields

The interaction between differential rotation and magnetic fields is complex and nonlinear; the differential rotation amplifies the mean toroidal magnetic field via the ω-effect and the Lorentz forces feedback on the flow as soon as the mean or fluctuating magnetic fields reach a threshold amplitude. We have found in the numerical experiments presented here that the magnetic fields do have a strong influence on the resulting mean flows achieved in convective spherical shells but not exactly in the way anticipated by mean field theory.

3.1. KINETIC AND MAGNETIC ENERGY DISTRIBUTIONS

Let us first consider the energy budget in our simulations as we break down the kinetic and magnetic energies into axisymmetric and non-axisymmetric parts. In Figure 1 we display the time trace of the kinetic and magnetic energies of $M1$ and $M3$ over respectively 1200 and 4000 days (corresponding in each case to several ohmic decay times $\tau_\eta = \tilde{v}L/(\pi^2\eta)$). We see that the magnetic energy of case $M1$ (hereafter ME1) is decaying whereas that in case $M3$ (ME3) has grown by more than a factor of 10^5, reaching a value of 7% of the kinetic energy (KE3). This clearly indicates that case $M3$ is running an efficient dynamo. The exponential growth of ME3 at the beginning of the temporal evolution (first 600 days) and its subsequent nonlinear saturation, due to the feedback from the Lorentz forces, are typical of dynamo action and are in good agreement with the expected properties of a stellar dynamo (cf., Cattaneo, Hughes, and Weiss, 1991). The rise of ME3 leads to a decrease of KE3 (by 37%), but does not totally compensate for that reduction. We found that the sum of KE3+ME3 is smaller than the initial kinetic energy KE0 contained in case H, indicating that the energy redistribution in our convective shells is modified by the presence of magnetic fields. To assess the cause of the

large reduction of KE3, we also display in Figure 1 the kinetic energy contained in the differential rotation (DRKE3) and in the convective motions (CKE3) (that in the meridional circulation is only $\sim 0.3\%$ of KE3). It is clear that DRKE3 is more affected by the presence of magnetic energy than CKE3, becoming even smaller than CKE3 after 3800 days. This result suggests that the decrease in kinetic energy is due to a weakening of the energy contained in the differential rotation rather than in a less vigorous convection. In case $M3$, ME is found to be equal or above local equipartition near the top of the domain, for about 2% of the surface area. The radial distribution of ME3 peaks near the bottom of the shell. This is certainly due to magnetic pumping by the strongest downflows or plumes (Tobias *et al.*, 2001).

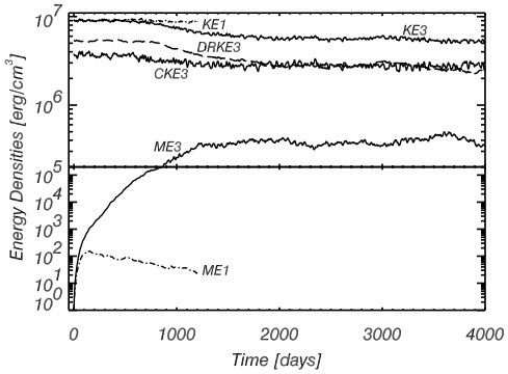

Figure 1. Temporal evolution of the kinetic energy (KE) and magnetic energy (ME) for cases $M1$ and $M3$, involving respectively rms magnetic Reynolds numbers R_m of 250 and 500.

The mean toroidal and poloidal magnetic energies (TME and PME) contribute respectively only 1.5% and 0.5% of ME3. The non-axisymmetric magnetic fields thus contained 98% of the total magnetic energy. In the Sun, the mean toroidal field is about 2 orders of magnitude larger than the mean poloidal field. The fact that in our simulation of global-scale convection this ratio is of order 1, indicates that the Sun must generate the strong large scale mean toroidal field outside its convective zone. The stably stratified tachocline at the base of the solar convection zone seems a natural location to amplify even further the mean toroidal field to the required observational level. Pumping of the magnetic field by turbulent convective plumes could certainly help in continuously supplying the tachocline with fields produced in the solar envelope.

When comparing the energy redistribution achieved in our simulations with that found in the earlier numerical simulations of the solar convective envelope by Gilman (1983), using the Boussinesq approximation, and by Glatzmaier (1987) using the anelastic approximation, we find a good overall agreement. For instance,

we all find that the larger is the magnetic energy contained in the convective shell, the smaller is DRKE, resulting in a damping of the differential rotation (cf., Section 3.3). We also find that increasing the magnetic Prandlt number P_m, leads to a larger amplitude of the magnetic energy. The main differences are found in the relative amplitude of the mean toroidal and poloidal magnetic energies achieved in the simulations. We have seen that TME and PME in case $M3$ are rather small compared to both ME and KE. In the work of Glatzmaier, ME is only about 0.1% of KE, so being relatively much smaller than in case $M3$, but TME represents 85% of that total. This is certainly due to the presence in these simulations of a stable region at the bottom of the convective envelope. In the work of Gilman discussing several cases, there is one case that possesses a ratio ME/KE of about 7% as in case $M3$ (case with $Q = \eta/\kappa = 1.7$), but TME and PME are again found to be a significant fraction of ME ($\sim$ 20%). The case with $Q = 0.5$ possesses a small mean magnetic energy $TME + PME \sim 3.5\%$, closer to that found in case $M3$, but its magnetic energy rose to 45% of KE. At that level of magnetism the kinetic energy contained in the differential rotation (DRKE) drops to only 30% of KE, resulting in an excessively weak differential rotation. Such strong damping of the angular velocity is not observed in case $M3$ (cf. Section 3.3). Certainly the different sets of parameters (Ra, Ta, P_r, and P_m) used in their simulations by the three authors, explain for the most part the differences seen in the energy ratios, making a direct quantitative comparison rather difficult. Another explanation could be the numerical resolution used in the simulations, since in our study it is more than 10 times larger (e.g., $\ell_{\max} = 340$ vs $\ell_{\max} = 24$ or 32 in the earlier studies). We indeed find that the magnetic energy spectrum in case $M3$ (not shown) does not peak at the azimuthal wavenumber $m = 0$ as in the cases published by Gilman (1983), but between $m = 1$ and 10, confirming the non-axisymmetric nature of the magnetic fields.

3.2. MORPHOLOGY OF THE VELOCITY AND MAGNETIC FIELDS

The convection realized in cases H, $M1$ and $M3$ is intricate and time dependent, involving continuous shearing, cleaving and merging of the convective cells. Figure 2 displays for case $M3$ the radial, latitudinal and longitudinal components of both the velocity and magnetic fields near the top of the domain at one instant in time.

We note that the radial velocity (top left panel) is asymmetric, downflows being concentrated in narrow lanes surrounding the broad upflows. Pronounced vortical structures are evident at the interstices of the downflows network. They are cyclonic, i.e., counterclockwise in the northern hemisphere and clockwise in the southern one. The strongest of these vortex tubes or 'plumes' extend through the whole domain depth. These plumes represent coherent structures that are surrounded by more chaotic flows. They tend to align with the rotation axis and to be tilted away from the meridional planes, leading to Reynolds stresses that are crucial ingredi-

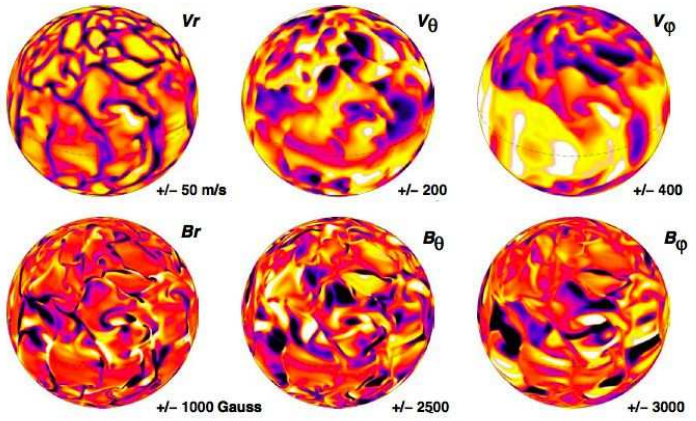

Figure 2. Snapshot of the radial, latitudinal and longitudinal velocities (*upper row*) and magnetic fields (*lower row*) in case *M*3 near the top (0.96 $R_\odot$) of the spherical domain. Downflows and negative polarity appear dark. Representative min/max amplitudes for the velocities (in m s^{-1}) and for the magnetic fields (in gauss) are indicated at the bottom right of each panel. The *dashed curve* delineates the equator.

ents in redistributing the angular momentum within the shell (cf., Section 3.3). The latitudinal velocity v_θ is more patchy and symmetric than v_r. The horizontal velocity v_ϕ possesses the clear banded signature of the differential rotation driven by the convection with a fast/prograde equator and slow/retrograde high latitude regions. The strongest downflow lanes are apparent in the horizontal velocities.

Turning now to the bottom row of Figure 2, we notice that the magnetic fields possess a finer structure than the velocity fields (due to our choice of $P_m > 1$), and that the radial and horizontal components of the magnetic fields possess different morphologies. The radial magnetic field has been swept into the downflow lanes. This is not the case for the horizontal fields, where large patches of a given polarity are found in the middle of the convective cells. Strong magnetic field gradients are present near the downflows network, where the magnetic fields are continously sheared and streched. Substantial magnetic helicity is present, involving complex winding of the toroidal magnetic fields along their length, with both polarities interchanging their position into intricate structures. There are no obvious correlations between the two horizontal vector fields. By contrast the strongest (unsigned) radial magnetic field $|B_r|$ does correlate with the strongest downflow lanes seen in the radial velocity. In all the six fields displayed, a clear north–south asymmetry is present.

3.3. DIFFERENTIAL ROTATION WITH OR WITHOUT MAGNETIC FIELDS

Figure 3 (left panel) shows the sidereal angular velocity $\Omega(r, \theta)$ of case H (converted into nHz, with $\Omega_o/2\pi = 414$ nHz). There is a strong rotational contrast $\Delta\Omega$ between the fast equator and the slow high-latitude regions. The contrast $\Delta\Omega$ from 0° to 60° is 140 nHz equivalent to a $\Delta\Omega/\Omega_o$ of about 34%. There is some constancy along radial lines at mid latitudes (45–75°) and a systematic decrease of Ω with latitude even in the polar regions. The angular velocity profile is in good qualitative agreement with helioseismic inversions of the solar differential rotation (Thompson *et al.*, 2003). The differential rotation profile in case H is due to the equatorward transport of angular momentum by Reynolds stresses, themselves closely related to the tilted plumes realized in turbulent convective flows which are the source of velocity correlations such as $\widetilde{v_r' v_\phi'}$. These Reynolds stresses oppose the poleward transport of angular mometum by viscous stresses and meridional circulation and lead to an equatorial acceleration (Brun and Toomre, 2002).

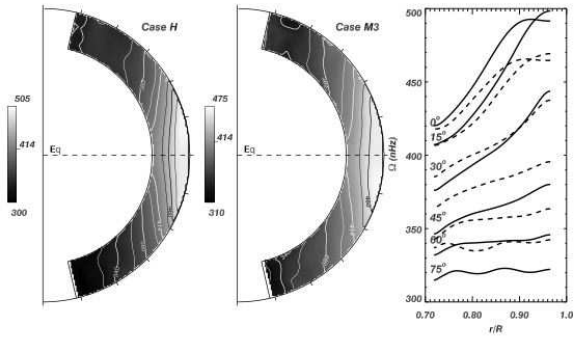

Figure 3. Temporal and longitudinal averages of the angular velocity profiles achieved in case H and $M3$ over an interval of 100 days (shown as contour plots). These cases exhibit a prograde equatorial rotation and a strong contrast $\Delta\Omega$ from equator to pole, as well as possess a high-latitude region of particularly slow rotation. In the *right panel*, displaying radial cuts of Ω at indicated latitudes for both cases, the reduction in $\Delta\Omega$ due to the nonlinear feed back of the Lorentz forces (*solid* vs *dashed lines*) can be assessed.

In Figure 3 (middle panel) we display the Ω profile achieved in case $M3$. Case $M1$ possesses a differential rotation identical to case H and is not shown. With fairly strong magnetic fields sustained within the bulk of the convection zone in case $M3$, it is to be expected that the differential rotation Ω will respond to the feedback from the Lorentz forces. As seen in Section 3.1 the main effect of the Lorentz forces is to extract energy from the kinetic energy stored in the differential rotation. As a consequence $\Delta\Omega/\Omega_o$ drops by $\sim$ 30% in going from 34% in case H down to 24% in case $M3$. This value is thus even closer to the value of 22%

(between 0° and 60° of latitude) inferred from seismic inversion of the solar profile (Thompson *et al.*, 2003). Since the convection is still able to maintain an almost solar-like angular velocity contrast from low-to-high latitudes, the magnetic field does not reduce the differential rotation as much as one might expect. One possible explanation for such a mild reduction of the differential rotation contrast could be the fact that ME is only 7% of KE. In Section 3.1 we have shown that a rather high level of magnetism is needed to damp the differential rotation significantly (around a ratio of ME/KE of about 0.25, see also Gilman, 1983). The fact that in case $M3$ the mean poloidal magnetic field is weak compared to its fluctuating counterpart, indicates that the slowing down of the differential rotation is not due to the torque applied by the large-scale axisymmetric magnetic fields but to a more subtle effect connected to the twisted structure of the magnetic fields.

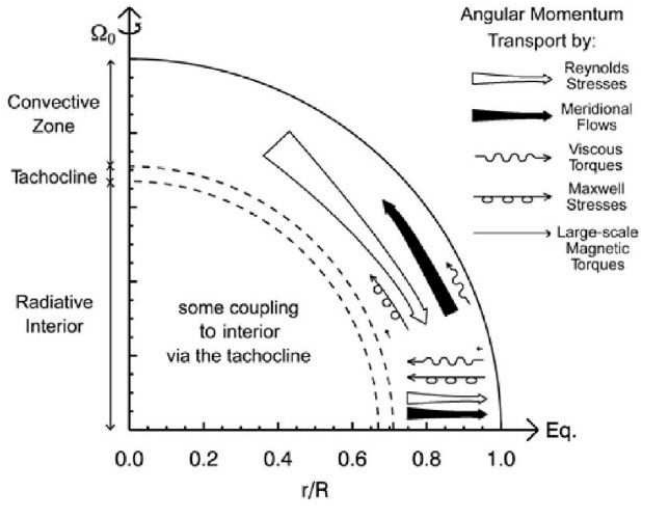

Figure 4. Illustration of the balance of angular momentum in latitude and radius in case $M3$ between the Reynolds stresses, Maxwell stresses, viscous torques, large-scale magnetic torques and the meridional circulation. The arrow length is proportional to the amplitude of the process.

A careful study of the redistribution of the angular momentum in our shell reveals that the source of the reduction of the latitudinal contrast of Ω can be attributed to the poleward transport of angular momentum by the Maxwell stresses (cf. Figure 4, and Brun *et al.*, 2004 for more details). The large-scale magnetic torques are found to be 2 orders of magnitude smaller, confirming the small dynamical role played by the mean fields in our simulations. The Reynolds stresses now need to balance the angular momentum transport by the meridional circulation, the viscous

diffusion and the Maxwell stresses. This results in a less efficient speeding up of the equatorial regions. However, the Maxwell stresses are not yet the main players in redistributing the angular momentum and case $M3$ is able to sustain a strong differential rotation as observed in the present Sun. There is good agreement between this work and the earlier studies of Gilman (1983) and Glatzmaier (1987) on the role of the Maxwell and Reynolds stresses in redistributing the angular momentum in the shell. We all find that the magnetic fields tend to make the rotation profile more uniform. Our results differ on the actual strength of such reduction and on the profile of angular velocity achieved.

Based on observations of the Sun by J. Hevelius in 1642–1644, Eddy, Gilman, and Trotter (1976) showed that during this period, the few observed solar sunspots in the equatorial regions were rotating about 4% faster than today. We believe that the fact that case $M1$ (or equivalently case H) is rotating faster than case $M3$ (because of the absence of substantial magnetic stresses acting to slow down the equatorial regions and speed up the poles), has some bearing on Eddy, Gilman, and Trotter's results. Certainly a reduced level of magnetism in a convective zone could lead to faster equatorial region and slower polar regions, i.e., to a larger differential rotation contrast. It is not clear if during the Maunder minimum only the large-scale dynamo action seated in the tachocline was reduced in amplitude (explaining the fewer number of observed sunspots), or if the small scale dynamo action generated by the turbulent convective motions was weaker as well. Let's assume here that both dynamos were weaker in the Sun during the Maunder minimum, and that reduced/weaker Maxwell stresses (and/or large-scale magnetic torques) resulted in a faster equatorial region, in a way similar to what is realized in cases H or $M1$. We can then use our simulated Ω profile to deduce the latitudinal distribution of the change in Ω with or without the feedback of strong magnetic fields. We found that such a function of θ (the colatitude) varies from about -6% ($\theta = 0$) to about $+6\%$ ($\theta = 90°$) in comparing cases H and $M3$. If we now apply this scaling function to the present surface differential rotation, here approximated as $\Omega_\odot(\theta) = 456 - 72 \times \cos^2(\theta) - 42 \times \cos^4(\theta)$, we can extrapolate the solar differential rotation profile to a period of 'grand activity minimum'.

Figure 5 displays the current, mid-1600s and extrapolated Ω profiles (the old profile being limited to the $\pm 20°$ band, cf. Figures 3 and 4 of Eddy, Gilman, and Trotter, 1976). The agreement between the extrapolated curve and the old data points is reasonable, and corresponds to a faster rotation by about 4 to 5% at the equator. In Eddy, Gilman, and Trotter the old and present rotational curves meet at a latitude of about $\pm 20°$, whereas in the extrapolated rotation curve it occurs at 30°. Beyond this latitude of 30°, the extrapolated rotational curve predicts that these regions were likely rotating slower than today.

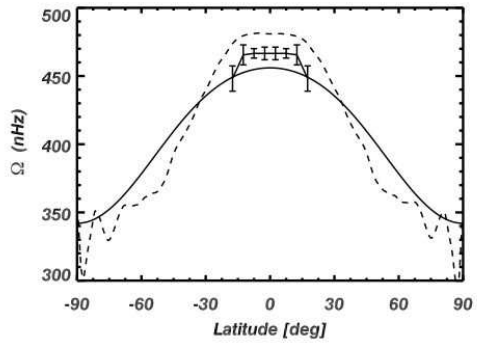

Figure 5. Possible surface differential rotation profile of the Sun during the quiet magnetic phase of the Maunder minimum. The current solar profile is shown in plain solid and the modified profile (*dashed line*) is deduced after multiplying the solid line by the scaling law $(\Omega_{surf-H}(\theta) - \Omega_{surf-M3}(\theta))/\Omega_{surf-H}(\theta)$. The *solid line* superimposed with 1-σ error bars, reproduces the results of Eddy *et al.* (1976) during the 1642-1644 period. In the $\pm 20°$ latitudinal band the agreement between the extrapolated curve and Eddy *et al.* study is reasonable.

4. Conclusions

Our 3-D MHD simulations of convection in deep spherical shells, achieved through the use of massively parallel supercomputers, are showing how the strong differential rotation present in the Sun may be maintained through fairly complex redistribution of angular momentum by the turbulent compressible flows in a conducting media. We have studied the interaction of convection and rotation with seed magnetic fields in such shells, and found solutions in which sustained magnetic dynamo action can be realized without unduly reducing the angular velocity contrasts maintained by the convection, thus answering positively question (a) raised in the Introduction. In seeking to answer question (b), we have found that the Maxwell stresses oppose the Reynolds stresses and seek to speed up the poles and that the large-scale magnetic torques play almost no role. The reduction in differential rotation is thus not due to the torque applied by the large-scale axisymmetric (i.e., $m = 0$) magnetic fields but to a more subtle braking effect exerted by the non-axisymmetric magnetic fields. In our models, the stronger are the dynamo generated fields, the weaker is the differential rotation, confirming the earlier results of Gilman (1983) and Glatzmaier (1987). We find that above a ratio of magnetic to kinetic energy of about 0.25, the differential rotation becomes excessively damped. It seems that a ratio of ME/KE of about 0.05–0.07 leads to a reduction of the differential rotation compatible with that seen in the Sun when comparing past and present observations (cf., Section 3.3). In the context of a mean field solar dynamo, our results imply that the ω-effect is likely 'quenched' more strongly than the 'α'-

effect by the presence of magnetic fields. But the fibril and intermittent nature of the dynamo generated magnetic fields seen in our simulations casts some doubts on the ability of mean field dynamo concepts to truly capture the intricate interplay between convection, rotation and magnetic fields. Our simulations of large-scale convection in spherical geometry strengthen the current paradigm that the strong mean toroidal magnetic field at the origin of the surface sunspots is likely stored and amplified in the tachocline at the base of the solar convective zone. The role of the convective envelope being to continuously produce, pump down and supply the disorganized magnetic fields to the tachocline. We are aware that the numerical experiments discussed in this work represent at best a crude description of the solar dynamics and that great care has to be taken in extending their results to the Sun. In reality the Sun is much more complex with the presence of strong shear layers both at the bottom and at the top of its convective zone and the possibility to globally reorganize its magnetic field and helicity via intense coronal mass ejections. We intend to address some of these issues in forthcoming papers.

Acknowledgements

The author is grateful to J. J. Aly, M. S. Miesch, J. Toomre, S. Turck-Chièze and J.-P. Zahn for enlightening discussions and to the anonymous referee for his constructive comments. The simulations with ASH were carried out with NSF NPACI support to various American supercomputer centers and within CCRT at CEA.

References

Brummell, N. H., Cattaneo, F., and Toomre, J.: 1995, *Science* **269**, 1370.
Brun, A. S. and Toomre, J.: 2002, *Astrophys. J.* **570**, 865.
Brun, A. S., Miesch, M., and Toomre, J.: 2004, *Astrophys. J.*, submitted.
Cattaneo, F. and Hughes, D. W.: 2001, *Astron. Geophys.* **42**, 18.
Cattaneo, F., Hughes, D. W., and Weiss, N. O.: 1991, *Monthly Notices Royal Astron. Soc.* **253**, 479.
Clune, T. L., Elliott, J. R., Glatzmaier, G. A., Miesch, M. S., and Toomre, J.: 1999, *Parallel Comput.* **25**, 361.
Couvidat, S., Garcia, R. A., Turck-Chièze, S., Corbard, T., Henney, C. J. and Jimenez-Reyes, S.: 2003, *Astrophys. J.* **597**, L77.
Eddy, J. A., Gilman, P. A., and Trotter, D. E.: 1976, *Solar Phys.* **46**, 3.
Gilman, P. A.: 1983, *Astrophys. J.* **53**, 243.
Glatzmaier, G. A.: 1987, in *The Internal Solar Angular Velocity*, B. R. Durney and S. Sofia (eds.), D. Reidel, Dordrecht, p. 263.
Krause, F. and Rädler, K. H.: 1980, *Mean Field Magnetohydrodynamics and Dynamo Theory*, Pergamon, Oxford.
Moffat, H. K.: 1978, *Magnetic Field Generation in Electrically Conducting Fluids*, Cambridge University, Cambridge.
Ossendrijver, M.: 2003, *Astron. Astrophys. Rev.* **11**, 287.
Parker, E. N.: 1993, *Astrophys. J.* **408**, 707.

Stix, M.: 2002, *The Sun, an Introduction*, 2nd edition, Springer, Berlin.
Thompson, M. J., Christensen-Dalsgaard, J., Miesch, M. S., and Toomre, J.: 2003, *Ann. Rev. Astron. Astrophys.* **41**, 599.
Tobias, S. M., Brummell, N. H., Clune, T. L., and Toomre, J.: 2001, *Astrophys. J.* **549**, 1183.

4.7.3 Global-scale turbulent convection and magnetic dynamo action in the solar envelope

par Brun, Miesch & Toomre 2004, ApJ, 614, 1073

The Astrophysical Journal, 614:1073–1098, 2004 October 20

GLOBAL-SCALE TURBULENT CONVECTION AND MAGNETIC DYNAMO ACTION IN THE SOLAR ENVELOPE

Allan Sacha Brun
DSM/DAPNIA/SAp, CEA Saclay, 91191 Gif-sur-Yvette Cedex, France

Mark S. Miesch
High Altitude Observatory, National Center for Atmospheric Research, Boulder, CO 80307-3000

and

Juri Toomre
JILA, University of Colorado, 440 UCB, Boulder, CO 80309-0440
Received 2004 March 22; accepted 2004 June 23

ABSTRACT

The operation of the solar global dynamo appears to involve many dynamical elements, including the generation of fields by the intense turbulence of the deep convection zone, the transport of these fields into the tachocline region near the base of the convection zone, the storage and amplification of toroidal fields in the tachocline by differential rotation, and the destabilization and emergence of such fields due to magnetic buoyancy. Self-consistent magnetohydrodynamic (MHD) simulations that realistically incorporate all of these processes are not yet computationally feasible, although some elements can now be studied with reasonable fidelity. Here we consider the manner in which turbulent compressible convection within the bulk of the solar convection zone can generate large-scale magnetic fields through dynamo action. We accomplish this through a series of three-dimensional numerical simulations of MHD convection within rotating spherical shells using our anelastic spherical harmonic (ASH) code on massively parallel supercomputers. Since differential rotation is a key ingredient in all dynamo models, we also examine here the nature of the rotation profiles that can be sustained within the deep convection zone as strong magnetic fields are built and maintained. We find that the convection is able to maintain a solar-like angular velocity profile despite the influence of Maxwell stresses, which tend to oppose Reynolds stresses and thus reduce the latitudinal angular velocity contrast throughout the convection zone. The dynamo-generated magnetic fields exhibit a complex structure and evolution, with radial fields concentrated in downflow lanes and toroidal fields organized into twisted ribbons that are extended in longitude and achieve field strengths of up to 5000 G. The flows and fields exhibit substantial kinetic and magnetic helicity although systematic hemispherical patterns are only apparent in the former. Fluctuating fields dominate the magnetic energy and account for most of the back-reaction on the flow via Lorentz forces. Mean fields are relatively weak and do not exhibit systematic latitudinal propagation or periodic polarity reversals as in the Sun. This may be attributed to the absence of a tachocline, i.e., a penetrative boundary layer between the convection zone and the deeper radiative interior possessing strong rotational shear. The influence of such a layer will await subsequent studies.

Subject headings: convection — MHD — Sun: magnetic fields — turbulence

1. TURBULENT MAGNETIC SUN

The Sun is a magnetic star whose variable activity has profound effects on our technological society on Earth. The high-speed solar wind and its energetic particles, coronal mass ejections, and explosive flares are all linked to the changing magnetic fields within the extended solar atmosphere. Such events can serve to damage satellites in space and power grids on the ground and interrupt communications. Thus, there is keen interest in being able to forecast the behavior of the magnetic structures. Yet this has proved to be difficult, since the eruption of new magnetic flux through the solar surface appears to have a dominant role in the evolution of field configurations in the solar atmosphere, as does the shuffling of field footpoints by the subsurface turbulence.

The origin of the solar magnetic fields must rest with dynamo processes occurring deep within the star in the spherical shell of intensely turbulent convection that occupies the outer 29% in radius below the solar surface. Within this convection zone, complex interactions between compressible turbulence and rotation of the star serve to redistribute angular momentum so that a strong differential rotation is achieved. Further, since the fluid is electrically conducting, currents will flow and magnetic fields must be built. However, there are many fundamental puzzles about the dynamo action that yields the observed fields.

The magnetic fields, like the underlying turbulence, can be both orderly on some scales and chaotic on others. Most striking is that the Sun exhibits 22 yr cycles of global magnetic activity, involving sunspot eruptions with very well defined rules for field parity and emergence latitudes as the cycle evolves. Coexisting with these large-scale ordered magnetic structures are small-scale but intense magnetic fluctuations that emerge over much of the solar surface, with little regard for the solar cycle. This diverse range of activity is most likely generated by two conceptually distinct magnetic dynamos (e.g., Weiss 1994; Childress & Gilbert 1995; Cattaneo 1999; Cattaneo & Hughes 2001; Ossendrijver 2003). These involve a *small-scale dynamo*, functioning within the intense turbulence of the upper convection zone, that builds the chaotic magnetic

fluctuations and a *global dynamo*, operating within both the deeper convection zone and the strong rotational shear of the tachocline at its base, that builds the more ordered fields.

1.1. *Building Magnetic Fields in the Sun*

The pairing of opposite-polarity sunspots in the east-west direction within active regions is most readily interpreted as the surface emergence of large-scale toroidal field structures. These structures are created somewhere below the photosphere and rise upward, bending to pierce the photosphere in the form of curved tubes. The current paradigm for large-scale dynamo action (e.g., Parker 1993) involves two major components. First, strong toroidal field structures must be generated. This is believed to occur as a result of the stretching that any differential rotation in latitude or radius will impose on any weak existing poloidal field. This first process is often referred to as the ω-effect after its parameterization within the framework of mean field electrodynamics (e.g., Moffatt 1978; Krause & Rädler 1980; Parker 1989). Helioseismology has shown that gradients in angular velocity are particularly strong in the tachocline, pointing to this interface region between the convection zone and the deeper radiative interior as the likely site for the generation of strong toroidal fields. Second, an inverse process is required to complete the cycle, regenerating the poloidal field from the toroidal field. Different theories exist for the operation of this process (known as the α-effect). Some have the poloidal field regenerated at the surface through the breakup and reconnection of the large-scale field that emerges as active regions, where this field has gained a poloidal component owing to Coriolis forces during its rise, with meridional flows having a key role in transporting such flux both poleward and down toward the tachocline (e.g., Babcock 1961; Leighton 1969; Wang & Sheeley 1991; Durney 1997; Dikpati & Charbonneau 1999). Others believe that the poloidal field is regenerated by the cumulative action of many small-scale cyclonic turbulent motions on the field throughout the convection zone, rather than just close to the surface (e.g., Parker 1993). In either scenario, there is separation in the sites of generation of toroidal field (in the strong shear of the tachocline) and regeneration of poloidal field (either near the surface or in the bulk of the convection zone), yielding what is now broadly called an *interface dynamo* (Parker 1993). Recent mean field dynamo approaches (e.g., Rüdiger & Brandenburg 1995; Tobias 1996; Charbonneau & MacGregor 1997; Beer et al. 1998) suggest that such an interface model can circumvent the problem of strong α-quenching by mean magnetic fields (Cattaneo & Hughes 1996), thereby being capable of yielding field strengths comparable to those inferred from observations.

The interface dynamo paradigm is thus based on the following underlying processes or building blocks:

1. The α-effect: the generation of the background weak poloidal field, either by cyclonic turbulence within the convection zone or by breakup of active regions.
2. The β-effect or turbulent transport: the transport of the weak poloidal field from its generating region to the region of strong shear, the tachocline.
3. The ω-effect: the organization and amplification of the magnetic field by differential rotation, particularly by large-scale rotational shear in the tachocline, into strong, isolated magnetic structures that are toroidal in character.
4. Magnetic buoyancy: the rise and transport of the large-scale toroidal field by magnetic buoyancy into and through the convection zone either to be shredded and recycled or to emerge as active regions.

Since all models presume close linkages between the differential rotation of the Sun and the operation of its global dynamo, let us briefly review what is known about the angular velocity Ω profile with radius and latitude. Helioseismology, which involves the study of the acoustic *p*-mode oscillations of the solar interior (e.g., Gough & Toomre 1991), has provided a new window for studying dynamical processes deep within the Sun. This has been enabled by the nearly continuous and complementary helioseismic observations provided from the vantage point of both the *SOHO* spacecraft with the high-resolution Michelson Doppler Imager (SOI MDI; Scherrer et al. 1995) and the ground-based Global Oscillation Network Group (GONG) set of six related instruments distributed at different longitudes across the Earth (Harvey et al. 1996). Helioseismology has revealed that the rotation profiles obtained by inversion of frequency splittings of the *p*-modes (e.g., Thompson et al. 1996, 2003; Schou et al. 1998; Howe et al. 2000) have a striking behavior that is unlike any anticipated by convection theory prior to such probing of the interior of a star. The strong latitudinal variation of angular velocity Ω observed near the surface, where the rotation is considerably faster at the equator than near the poles, extends through much of the convection zone depth (about 200 Mm) with relatively little radial dependence. Another striking feature is the tachocline (e.g., Spiegel & Zahn 1992), a region of strong shear at the base of the convection zone where Ω adjusts to apparent solid-body rotation in the deeper radiative interior. A thin *near-surface shear layer* is also present in which Ω increases with depth at intermediate and low latitudes. This subsurface region is now being intensively probed using local domain helioseismic methods, revealing the presence of remarkable large-scale meandering flow fields much like jet streams, banded zonal flows, and evolving meridional circulations, all of which contribute to what is called solar subsurface weather (SSW; Haber et al. 2000, 2002; Toomre 2002).

1.2. *Studying Elements of the Global Dynamo*

Computational resources are currently insufficient to enable modeling a complete dynamical system incorporating all the diverse aspects of the large-scale solar dynamo. Our goal is therefore to study individually some of the essential processes, with a view to eventually combine such findings into a more complete nonlinear interface-type solar dynamo model as resources become available. In this spirit, there has been substantial theoretical progress recently in trying to understand how the differential rotation profiles deduced from helioseismology may be established in the bulk of the convection zone. Building on the early three-dimensional numerical simulations of rotating convection in spherical shells (e.g., Gilman & Miller 1981; Glatzmaier & Gilman 1982; Glatzmaier 1985a, 1985b, 1987; Sun & Schubert 1995), recent modeling using the anelastic spherical harmonic (ASH) code on massively parallel supercomputers (e.g., Miesch et al. 2000; Elliott et al. 2000; Brun & Toomre 2002) has permitted attaining fairly turbulent states of convection in which the resulting Ω profiles now begin to capture many elements of the deduced interior profiles. These simulations possess fast equatorial rotation, substantial contrasts in Ω with latitude, and reduced tendencies for Ω to be constant on cylinders. The role of the Reynolds stresses and of meridional circulations within such convection in redistributing the angular momentum to achieve such

differential rotation over much of the convection zone is becoming evident. However, the simulations with ASH have only just begun to examine how the near-surface rotational shear layer may be established (DeRosa et al. 2002), whereas the formation and maintenance of a tachocline near the base of the convection zone have only been tentatively considered within three-dimensional simulations that admit downward penetration (Miesch et al. 2000).

Dynamics within the solar tachocline and overshoot region are thought to be extremely complex (e.g., Gilman 2000; Ossendrijver 2003). The upper portion of the tachocline may extend into the convective envelope, whereas the lower portion consists of a stably stratified, magnetized shear flow. Turbulent penetrative convection transfers mass, momentum, energy, and magnetic fields between the convection zone and radiative interior both directly and through the generation of internal waves, particularly gravity waves, which can drive oscillatory zonal flows and large-scale circulations. Instabilities driven by shear and magnetic buoyancy further influence the structure and evolution of the tachocline and likely play an important role in the solar activity cycle. Understanding these various processes will require much future work beyond the scope of this paper.

Our objective here is to expand on the purely hydrodynamical simulations with ASH to begin to study the magnetic dynamo action that can be achieved by global-scale turbulent flows within the bulk of the solar convection zone. These studies build on the pioneering modeling that was able to resolve fairly laminar but intricate magnetohydrodynamic (MHD) convection and its dynamo action within rotating spherical shells (e.g., Gilman & Miller 1981; Gilman 1983; Glatzmaier 1987). Other related dynamo simulations have also considered deeper shells (e.g., Kageyama et al. 1993; Kageyama & Sato 1997). We turn now to more complex states associated with the turbulent flows that can be resolved using the ASH code. Much as in Brun & Toomre (2002) and its immediate progenitors, we deal primarily with the bulk of the convection zone by imposing stress-free and impenetrable upper and lower boundaries to the shell, thereby ignoring the region of penetration of flows into the deeper radiative interior. Thus, issues concerning the tachocline are not dealt with, including the downward transport of magnetic fields (β-effect) into this region where strong toroidal fields may be stretched into existence. Likewise the stability of these fields and the buoyant rise and emergence of flux tubes are not studied in detail, although magnetic buoyancy is allowed in our ASH simulations via the anelastic approximation. Rather, the simulations reported here examine the α- and ω-effects within much of the convective interior, inspired particularly by the Gilman & Miller (1981) studies, but now having the ability to resolve turbulent convection and the fairly realistic differential rotation that it is able to sustain.

The convection in many previous studies of dynamo action in rotating spherical shells is dominated by so-called banana cells: columnar rolls aligned with the rotation axis. These cells possess substantial helicity and generally drive a large differential rotation, thus providing all the necessary ingredients for an α-ω dynamo. Sustained dynamo action is indeed observed for a variety of parameter regimes, but the results are generally not solar-like. The first studies by Gilman & Miller (1981) revealed no solutions with periodic field reversals. Cyclic, dipolar dynamos were found by Gilman (1983) and Glatzmaier (1984, 1985a, 1985b) for somewhat higher Rayleigh numbers, but the periods were significantly shorter than the solar activity cycle ($\sim$1–10 yr) and toroidal fields were found to propagate poleward during the course of a cycle rather than equatorward as in the Sun. Furthermore, these relatively low resolution simulations could not capture the intricate structure of the fluctuating field components known to exist in the solar atmosphere.

More recent simulations of MHD convection in rotating spherical shells have generally focused on parameter regimes more characteristic of the geodynamo and other planetary interiors (e.g., Kageyama & Sato 1997; Christensen et al. 1999; Roberts & Glatzmaier 2000; Busse 2000a, 2000b; Ishihara & Kida 2002). Relative to the Sun, convective motions in the planetary interiors are much more influenced by rotation (lower Rossby numbers) and diffusion (lower Reynolds and magnetic Reynolds numbers) and much less influenced by compressibility (mild density stratification). Although such simulations have achieved higher resolution relative to Gilman and Glatzmaier's earlier work, they are still generally dominated by banana cells owing to the strong rotational influence. They often tend to produce mean fields of a dipolar nature, although quadrupolar configurations are preferred in some parameter regimes, generally characterized by high Rayleigh numbers and low magnetic Prandtl numbers (Grote et al. 1999, 2000; Busse 2000b). Cyclic solutions have been found, but field reversals are more often aperiodic, particularly for high Rayleigh numbers.

In this paper we report simulations of hydromagnetic dynamo action in the solar convection zone at unprecedented spatial resolution. Our primary objective is to gain a better understanding of magnetic field amplification and transport by turbulent convection in the solar envelope and the essential role that such processes play in the operation of the solar dynamo. In § 2 we describe our numerical model and our simulation strategy in which we introduce a small seed magnetic field into an existing hydrodynamic simulation. In § 3 we discuss some properties of this hydrodynamic progenitor simulation and the exponential growth and nonlinear saturation of the seed field. We then investigate the intricate structure and evolution of the dynamo-generated fields in § 4 and their back-reaction on mean flows in § 5. Here we focus on the turbulent or fluctuating (nonaxisymmetric) field components that are found to dominate the magnetic energy. We consider the mean (axisymmetric) field components separately in § 6. In § 7 we discuss the magnetic and kinetic helicity found in our dynamo simulations and present spectra and probability density functions (pdf's) for various fields. We summarize our primary results and conclusions in § 8.

2. MODELING APPROACH

2.1. *Anelastic MHD Equations*

In this paper we report three-dimensional numerical experiments designed to investigate the complex MHD of the solar convection zone in spherical geometries. We have extended our already well-tested hydrodynamic ASH code (see Clune et al. 1999; Miesch et al. 2000; Brun & Toomre 2002) to include the magnetic induction equation and the feedback of the field on the flow via Lorentz forces and ohmic heating. Thus, the ASH code is now able to solve the full set of three-dimensional MHD anelastic equations of motion in a rotating, convective spherical shell (Glatzmaier 1984) with high resolution on massively parallel computing architectures. These equations are fully nonlinear in velocity and magnetic field variables, but under the anelastic approximation the thermodynamic variables are linearized with respect to a

spherically symmetric and evolving mean state having a density $\bar{\rho}$, pressure $\bar{P}$, temperature $\bar{T}$, and specific entropy $\bar{S}$. Fluctuations about this mean state are denoted by ρ, P, T, and S. The resulting equations are

$$\nabla\cdot(\bar{\rho}\boldsymbol{v}) = 0, \tag{1}$$

$$\nabla\cdot\boldsymbol{B} = 0, \tag{2}$$

$$\bar{\rho}\left[\frac{\partial \boldsymbol{v}}{\partial t} + (\boldsymbol{v}\cdot\nabla)\boldsymbol{v} + 2\Omega_0\times\boldsymbol{v}\right] = -\nabla P + \rho\boldsymbol{g} + \frac{1}{4\pi}(\nabla\times\boldsymbol{B})\times\boldsymbol{B} - \nabla\cdot\boldsymbol{\mathcal{D}} - \left(\nabla\bar{P} - \bar{\rho}\boldsymbol{g}\right), \tag{3}$$

$$\bar{\rho}\bar{T}\frac{\partial S}{\partial t} + \bar{\rho}\bar{T}\boldsymbol{v}\cdot\nabla\left(\bar{S}+S\right) = \nabla\cdot[\kappa_r\bar{\rho}c_p\nabla\left(\bar{T}+T\right) + \kappa\bar{\rho}\bar{T}\nabla\left(\bar{S}+S\right)] + \frac{4\pi\eta}{c^2}\boldsymbol{j}^2 + 2\bar{\rho}\nu\left[e_{ij}e_{ij} - \frac{1}{3}(\nabla\cdot\boldsymbol{v})^2\right] + \bar{\rho}\epsilon, \tag{4}$$

$$\frac{\partial \boldsymbol{B}}{\partial t} = \nabla\times(\boldsymbol{v}\times\boldsymbol{B}) - \nabla\times(\eta\nabla\times\boldsymbol{B}), \tag{5}$$

where $\boldsymbol{v} = (v_r,\ v_\theta,\ v_\phi)$ is the local velocity in spherical coordinates in the frame rotating at constant angular velocity Ω_0, $\boldsymbol{g}$ is the gravitational acceleration, $\boldsymbol{B} = (B_r,\ B_\theta,\ B_\phi)$ is the magnetic field, $\boldsymbol{j} = (c/4\pi)(\nabla\times\boldsymbol{B})$ is the current density, c_p is the specific heat at constant pressure, κ_r is the radiative diffusivity, η is the effective magnetic diffusivity, and $\mathcal{D}$ is the viscous stress tensor, involving the components

$$\mathcal{D}_{ij} = -2\bar{\rho}\nu\left[e_{ij} - \tfrac{1}{3}(\nabla\cdot\boldsymbol{v})\delta_{ij}\right], \tag{6}$$

where e_{ij} is the strain rate tensor and ν and κ are effective eddy diffusivities. A volume heating term $\bar{\rho}\epsilon$ is also included in these equations for completeness, but it is insignificant in the solar envelope. When our model is applied to other stars, such as A-type stars (Browning et al. 2004), this term represents energy generation by nuclear burning. To complete the set of equations, we use the linearized equation of state

$$\frac{\rho}{\bar{\rho}} = \frac{P}{\bar{P}} - \frac{T}{\bar{T}} = \frac{P}{\gamma\bar{P}} - \frac{S}{c_p}, \tag{7}$$

where γ is the adiabatic exponent, and assume the ideal gas law

$$\bar{P} = \mathcal{R}\bar{\rho}\bar{T}, \tag{8}$$

where $\mathcal{R}$ is the gas constant. The reference or mean state (indicated by overbars) is derived from a one-dimensional solar structure model (Brun et al. 2002) and is continuously updated with the spherically symmetric components of the thermodynamic fluctuations as the simulation proceeds. It begins in hydrostatic balance so the bracketed term on the right-hand side of equation (3) initially vanishes. However, as the simulation evolves, turbulent and magnetic pressure drives the reference state slightly away from hydrostatic balance.

Because of limitations in computing resources, no simulation achievable now or in the near future can hope to directly capture all scales of solar convection from global to molecular dissipation scales. The simulations reported here resolve nonlinear interactions among a larger range of scales than any previous MHD model of global-scale solar convection, but motions still must exist in the Sun on scales smaller than our grid resolution. In this sense, our models should be regarded as large-eddy simulations (LESs) with parameterizations to account for subgrid-scale (SGS) motions. Thus, the effective eddy diffusivities ν, κ, and η represent momentum, heat, and magnetic field transport by motions that are not resolved by the simulation. They are allowed to vary with radius but are independent of latitude, longitude, and time for a given simulation. Their amplitudes and radial profiles are varied depending on the resolution and objectives of each simulation. In the simulations reported here, ν, κ, and η are assumed to be proportional to $\bar{\rho}^{-1/2}$.

The velocity, magnetic, and thermodynamic variables are expanded in spherical harmonics $Y_{\ell m}(\theta,\ \phi)$ for their horizontal structure and in Chebyshev polynomials $T_n(r)$ for their radial structure (see the Appendix). This approach has the advantage that the spatial resolution is uniform everywhere on a sphere when a complete set of spherical harmonics is used up to some maximum in degree ℓ (retaining all azimuthal orders $m \le \ell$ in what is known as triangular truncation).

The anelastic approximation captures the effects of density stratification without having to resolve sound waves, which would severely limit the time step. In the MHD context, the anelastic approximation filters out fast magnetoacoustic waves but retains the Alfvén and slow magnetoacoustic modes. In order to ensure that the mass flux and the magnetic field remain divergenceless to machine precision throughout the simulation, we use a toroidal-poloidal decomposition as

$$\bar{\rho}\boldsymbol{v} = \nabla\times\nabla\times(W\hat{\boldsymbol{e}}_r) + \nabla\times(Z\hat{\boldsymbol{e}}_r), \tag{9}$$

$$\boldsymbol{B} = \nabla\times\nabla\times(C\hat{\boldsymbol{e}}_r) + \nabla\times(A\hat{\boldsymbol{e}}_r). \tag{10}$$

The Appendix lists the full set of anelastic MHD equations as solved by the numerical algorithm, involving the spherical harmonic coefficients of the stream functions W and Z and the magnetic potentials C and A. This system of equations requires 12 boundary conditions in order to be well posed. Since assessing the angular momentum redistribution in our simulations is one of the main goals of this work, we have opted for torque-free velocity and magnetic boundary conditions:

1. Impenetrable top and bottom: $v_r = 0|_{r=r_{\rm bot},r_{\rm top}}$.
2. Stress-free top and bottom: $(\partial/\partial r)(v_\theta/r) = (\partial/\partial r)(v_\phi/r) = 0|_{r=r_{\rm bot},r_{\rm top}}$.
3. Constant entropy gradient at top and bottom: $\partial\bar{S}/\partial r = \text{const}|_{r=r_{\rm bot},r_{\rm top}}$.
4. Match to an external potential magnetic field at top and bottom: $\boldsymbol{B} = \nabla\Phi \Rightarrow \Delta\Phi = 0|_{r=r_{\rm bot},r_{\rm top}}$, or impose a purely radial magnetic field at top and bottom (match to highly permeable external media; Jackson 1999), i.e., $B_\theta = B_\phi = 0|_{r=r_{\rm bot},r_{\rm top}}$.

The main difference between having a potential or a purely radial magnetic field is that with the latter the Poynting flux is zero at the shell surface, and thus there is no leakage of magnetic energy through the boundaries (see § 3.2).

2.2. *Numerical Experiments*

Our numerical model is a simplified portrayal of the solar convection zone: solar values are taken for the heat flux, rotation rate, mass, and radius, and a perfect gas is assumed. The computational domain extends from $0.72R_*$ to $0.97R_*$ (with R_* the solar radius), thereby focusing on the bulk of the unstable zone without yet considering penetration into the radiative interior or smaller scale convective motions near the photosphere. The depth of the convection zone is therefore

TABLE 1
PARAMETERS FOR THE FOUR SIMULATIONS

Parameter	H	M1	M2	M3
N_r, N_θ, N_ϕ	64, 256, 512	64, 256, 512	64, 256, 512	128, 512, 1024
Ra	8.1×10^4	8.1×10^4	8.1×10^4	8.1×10^4
Pr_m	...	2	2.5	4
Ro_c	0.73	0.73	0.73	0.73
η (cm^2 s^{-1})	...	7×10^{11}	5.6×10^{11}	3.5×10^{11}
τ_η (days)	...	495	620	990
Re	136	136	133	121
Re_m	...	272	334	486
Λ	...	1.5×10^{-3}	4.5×10^{-2}	20
Pe	20	17	16	15
Ro	0.15	0.12	0.12	0.11

NOTES.—N_r, N_θ, and N_ϕ are the number of radial, latitudinal, and longitudinal mesh points, respectively. All simulations have an inner radius $r_{\mathrm{bot}} = 5.0 \times 10^{10}$ cm and an outer radius $r_{\mathrm{top}} = 6.72 \times 10^{10}$ cm, and all quantities listed here are evaluated at midlayer depth. In all cases, $\nu = 1.4 \times 10^{12}$ and $\kappa = 1.1 \times 10^{13}$ at midlayer depth and the Prandtl number $\mathrm{Pr} = \nu/\kappa = 0.125$. Furthermore, the rotation rate of the coordinate system $\Omega_0 = 2.6 \times 10^{-6}$ s^{-1} in all cases, yielding a Taylor number of $\mathrm{Ta} = 4\Omega_0^2 L^4/\nu^2 = 1.2 \times 10^6$, where $L = r_{\mathrm{top}} - r_{\mathrm{bot}}$. Also listed are the Rayleigh number $\mathrm{Ra} = (-\partial\bar{\rho}/\partial S)\Delta S g L^3/\rho\nu\kappa$, the magnetic Prandtl number $\mathrm{Pr}_m = \nu/\eta$, the convective Rossby number $\mathrm{Ro}_c = (\mathrm{Ra}/\mathrm{Ta}\,\mathrm{Pr})^{1/2}$, the Reynolds number $\mathrm{Re} = \tilde{v}'L/\nu$, the magnetic Reynolds number $\mathrm{Re}_m = \tilde{v}'L/\eta$, the Elssasser number $\Lambda = \tilde{B}^2/4\pi\bar{\rho}\eta\Omega_0$, the Péclet number $\mathrm{Pe} = \mathrm{Re}\,\mathrm{Pr} = \tilde{v}'L/\kappa$, the Rossby number $\mathrm{Ro} = \tilde{v}'/2\Omega_0 L$, and the ohmic diffusion time $\tau_\eta = L^2/(\pi^2\eta)$, where $\tilde{v}'$ is the rms convective velocity and $\tilde{B}$ is the rms magnetic field. A Reynolds number based on the peak velocity at midlayer depth would be about a factor of 5 larger.

$L = 1.72 \times 10^{10}$ cm, and the background density varies across the shell by about a factor of 30. Outward heat transport by unresolved convective motions near the surface is modeled by locally increasing the component of the SGS eddy diffusivity κ, which operates on the mean (horizontally averaged) entropy gradient, thus allowing the simulation to achieve flux equilibrium (see § 3.2). Meanwhile, the influence of unresolved motions on the flow itself is taken into account through the SGS eddy diffusivities ν, κ, and η.

The magnetic simulations discussed here were all initiated from the same nonmagnetic progenitor simulation, which we refer to as case H. Case H is well evolved, with a complex convective structure and a solar-like differential rotation profile (§ 3.1).

A small seed magnetic field is then introduced and its evolution is followed via the induction equation. The seed field is dipole in nature but soon develops a more complicated structure as it is amplified by the convective motions. If the magnetic diffusivity is sufficiently small, the field will continue to amplify until it reaches a nonlinear saturation level where production balances dissipation. In order to determine whether sustained dynamo action is achieved, the simulation must be evolved for at least several ohmic diffusion times $\tau_\eta = L^2/(\pi^2\eta)$ (see Moffatt 1978; Jacobs 1987). We have conducted three MHD simulations, cases M1, M2, and M3, each with progressively lower values of the magnetic diffusivity (see Table 1).

It is currently impractical to perform dynamo calculations with a spatial resolution comparable to our most turbulent hydrodynamic cases ($N_\theta = 1024$, $N_\phi = 2048$, $N_r = 256$), which achieve a rms Reynolds number Re of over 700. The increased workload required to solve the magnetic induction equation and the long time integrations necessary to reliably assess dynamo action cannot be easily achieved with currently available computational resources. In order to achieve dynamo action in more moderately turbulent simulations such as those considered here ($\mathrm{Re} \sim 150$), the magnetic Prandtl number $\mathrm{Pr}_m = \nu/\eta$ must be greater than unity, whereas in the Sun it is significantly less than unity (based on microscopic values for ν and η). This is a well-known difficulty in dynamo simulations within astrophysical or geophysical contexts (see, e.g., Christensen et al. 1999). However, the diffusivities in our simulations arise from unresolved convective motions, not microscopic processes, and the effective transport properties of such motions are thought to yield Prandtl and magnetic Prandtl numbers of order unity.

3. CONVECTION, ROTATION, AND THE GENERATION OF FIELDS

3.1. *Progenitor Nonmagnetic Convection*

Figure 1 illustrates the convective structure and differential rotation for the hydrodynamical progenitor case H immediately prior to introducing a seed magnetic field. The radial velocity near the top of the domain is shown using a Mollweide projection, which displays the entire horizontal layer with minimal distortion. The circular arcs ($\pm 90^\circ$) encompass a hemisphere, and the rest of the globe is contained in the lunes on either side. The convection patterns are complex, time dependent, and asymmetric owing to the density stratification, consisting of relatively weak, broad upflows with narrow, fast downflows around their periphery. This asymmetry translates into a net downward transport of kinetic energy. The strong correlations between warm upward motions and cool downward motions are essential in transporting heat outward.

There is a clear difference in the size and structure of the convective patterns at low and high latitudes. Near the equator the downflow lanes tend to align with the rotation axis in the north/south direction, whereas at higher latitudes ($\gtrsim 25^\circ$) they tend to be more isotropic and of smaller spatial extent. Part of this behavior can be understood by considering the cylinder that is aligned with the rotation axis and tangent to the inner boundary. This tangent cylinder intersects the outer boundary at latitudes of about 42°. It is well known that in a rotating convective shell the flow dynamics is different inside and outside of the inner tangent cylinder (Busse 1970; Busse & Cuong 1977). The connectivity of the flow, the influence

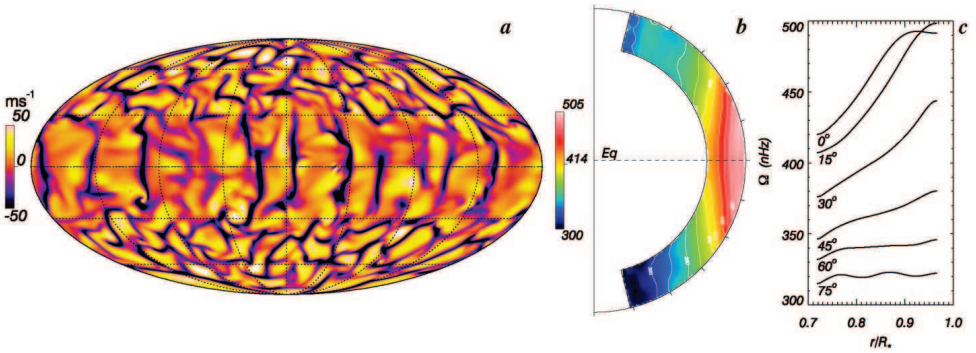

FIG. 1.—(*a*) Radial velocity near the top of the shell for case H shown using a Mollweide projection. Dashed lines indicate the equator, as well as meridians and parallels every 45° and 30°, respectively. Downflows appear dark and upflows bright. (*b*) Angular velocity Ω in case H averaged over longitude and time, with brighter tones indicating more rapid rotation (see color tables). (*c*) Mean angular velocity shown as a function of radius for the indicated latitudes, averaged over both hemispheres.

of Coriolis forces, and the distance to the rotation axis are different in the polar regions relative to the equatorial regions, leading to different convective patterns in mildly turbulent simulations such as case H. At low Reynolds numbers the transition between equatorial modes and polar modes occurs near the tangent cylinder. As the Reynolds number is increased, this transition moves to lower latitudes and becomes less apparent. For example, Brun & Toomre (2002) have demonstrated that increasing the level of turbulence in the simulations makes the convective patterns in the equatorial region more isotropic and extended downflow lanes become difficult to isolate within the convective network.

Vortical plumes are evident at the interstices of the downflow network, representing coherent structures that are surrounded by more chaotic flows. The sense of the vorticity is generally cyclonic: counterclockwise in the northern hemisphere and clockwise in the southern hemisphere. The strongest downflow plumes extend through the entire depth of the domain. They tend to align with the rotation axis and to tilt away from the meridional plane, leading to Reynolds stresses that are crucial ingredients in redistributing the angular momentum within the shell (see § 5; see also Miesch et al. 2000; Brun & Toomre 2002). Downflow lanes and plumes are continually advected, sheared, and distorted by differential rotation and nonlinear interactions with other flow structures.

The differential rotation in case H is shown in Figures 1*b* and 1*c*, expressed in terms of the sidereal angular velocity Ω. The angular velocity of the rotating reference frame is 414 nHz, which corresponds to a rotation period of 28 days. In the contour plot, the polar regions have been omitted owing to the difficulty of forming stable averages there as a result of the small moment arm and small averaging domain.

Case H exhibits a differential rotation profile that is in good agreement with the solar internal rotation profile inferred from helioseismology in the bulk of the convection zone (Thompson et al. 2003). Angular velocity contours at midlatitudes are nearly radial, and the rotation rate decreases monotonically with increasing latitude as in the Sun. The latter property, in particular, represents an important improvement over most previous spherical convection simulations in which the latitudinal angular velocity contrast $\Delta\Omega$ was confined mainly to mid- and low latitudes, namely, outside of the inner tangent cylinder. The angular velocity profile in such simulations is generally sensitive to the parameters of the problem, and more solar-like profiles such as case H can be achieved by varying the Reynolds and Prandtl numbers in particular (Elliott et al. 2000; Brun & Toomre 2002). The differential rotation contrast between the equator and latitudes of 60° in case H is 140 nHz (or 34% relative to the frame of reference), somewhat larger than the 92 nHz (or 22%) variation implied by helioseismology. The rotation profile of case H exhibits some asymmetry with respect to the equator, particularly at high latitudes (Fig. 1*b*), although such asymmetries are expected to diminish over a longer temporal average. Since the convection itself is generally asymmetric, it is not surprising that the mean flows driven by the convection are as well.

Mean field models of the solar differential rotation have advocated that a thermal wind balance (involving latitudinal temperature gradients) may be the cause of the noncylindrical angular velocity profile (Kichatinov & Rüdiger 1995; Durney 1999). This may come about if baroclinic convective motions produce latitudinal heat flux, leading to a breakdown of the Taylor-Proudman theorem (Pedlosky 1987). A pole-equator temperature contrast of a few degrees kelvin is compatible with a $\Delta\Omega/\Omega_0$ of ~30%. Although it is indeed true that case H exhibits latitudinal entropy and temperature gradients, these are not the dominant players in driving the differential rotation throughout the shell. Rather, we find that the Reynolds stresses are the main agents responsible for maintaining the rotation profiles in our simulations (see § 5).

3.2. *Achieving Sustained Dynamo Action*

We now consider the dynamo possibilities that such intricate convective patterns and large differential rotation can lead to. As stated earlier, we have introduced a seed magnetic poloidal field into our hydrodynamical case H for three different values of the magnetic diffusivity η, corresponding to cases M1, M2, and M3 (Table 1). Figure 2 shows the magnetic and kinetic energy evolution for these three cases. We note that over more than 4000 days (corresponding to several ohmic decay times; see Table 1) the two least diffusive cases M2 and M3 achieve a sustained magnetic energy (ME), the amplitude of which

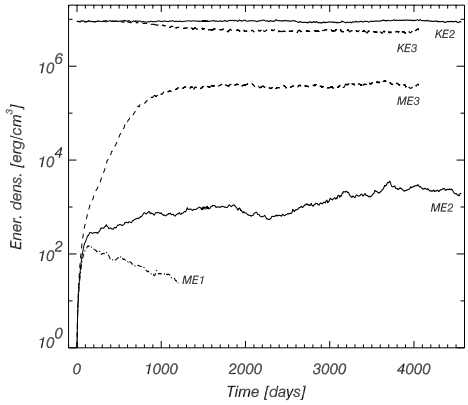

FIG. 2.—Temporal evolution of the volume-integrated kinetic energy density (KE) and magnetic energy density (ME) shown for cases M1 ($\mathrm{Re}_m = 272$), M2 ($\mathrm{Re}_m = 334$), and M3 ($\mathrm{Re}_m = 486$), represented by dot-dashed, solid, and dashed lines, respectively.

depends on η. The initial exponential growth of ME in case M3 lasts for about 600 days, after which the nonlinear feedback of the Lorentz forces on the flow begins to saturate the dynamo. For case M2, which has a slower growth rate, another linear phase seems to last for at least 4000 days, and it is unclear whether it has truly saturated. By contrast, case M1 is clearly decaying, since the rate of generation of magnetic fields in the entire shell volume $[\int_V \boldsymbol{v}\cdot(\boldsymbol{B}\times\boldsymbol{j})\,dV]$ cannot compensate for the rate of destruction by ohmic diffusion $(\int_V 4\pi\eta/c\boldsymbol{j}^2\,dV)$. Interpolating between cases M1 and M2 to find the zero growth rate yields a critical magnetic diffusivity at midlayer depth $\eta \sim 5.9\times10^{11}$ cm s^{-2}. In terms of the magnetic Reynolds number (see Table 1), we find that Re_m must be at least 300 for sustained dynamo action to occur. This value of Re_m is about 25% larger than in the incompressible simulations of Gilman (1983), which consider a simpler configuration.

Upon saturation, the kinetic energy (KE) in model M3 has been reduced by about 40% compared to its initial value, say, KE_0, given by case H (see Table 2). This change is mostly due to a reduction of the energy contained in the differential rotation (DRKE), which drops by over 50%. By contrast, the energy contained in the convective motions (CKE) only decreases by about 27%, which implies an increased contribution of the nonaxisymmetric motions to the total kinetic energy balance.

TABLE 2
REPRESENTATIVE VELOCITIES, MAGNETIC FIELDS, ENERGIES, AND DIFFERENTIAL ROTATION

Parameter	H	M1	M2	M3
Middle of Convective Zone				
$\tilde{v}_r$	61	60	59	58
$\tilde{v}_\theta$	63	62	61	54
$\tilde{v}_\phi$	137	137	136	104
$\tilde{v}'_\phi$	68	68	67	59
$\tilde{v}$	163	162	161	131
$\tilde{v}'$	111	111	109	99
$\tilde{B}_r$	...	21	100	1752
$\tilde{B}_\theta$	...	23	110	1855
$\tilde{B}_\phi$	...	29	144	2277
$\tilde{B}'_\phi$	...	28	141	2239
$\tilde{B}$	...	42	207	3420
$\tilde{B}'$	...	41	205	3386
Volume Average				
KE	9.01×10^6	8.74×10^6	8.96×10^6	5.26×10^6
DRKE/KE (%)	59.3	57.4	57.8	49.5
MCKE/KE (%)	0.3	0.4	0.4	0.5
CKE/KE (%)	40.4	42.2	41.8	50.0
ME	...	$<10^2$	1223	3.47×10^5
ME/KE (%)	...	$<10^{-3}$	0.014	6.6
MTE/ME (%)	...	...	1.4	1.5
MPE/ME (%)	...	...	0.6	0.5
FME/ME (%)	...	...	98	98
$\Delta\Omega/\Omega_0$ (%)	34	34	34	24

NOTES.—Listed for each simulation are the rms amplitude of the velocity $\tilde{v}$ and each of its components, $\tilde{v}_r$, $\tilde{v}_\theta$, and $\tilde{v}_\phi$, averaged over time at a layer in the middle of the convection zone. Also listed are the rms amplitudes of the fluctuating total and zonal velocity, $\tilde{v}'$ and $\tilde{v}'_\phi$, obtained after subtracting out the temporal and azimuthal mean. For the magnetic simulations, we include the corresponding rms amplitudes of the magnetic field and its components, $\tilde{B}$, $\tilde{B}_r$, $\tilde{B}_\theta$, $\tilde{B}_\phi$, $\tilde{B}'$, and $\tilde{B}'_\phi$. Velocities are expressed in m s^{-1} and magnetic fields in G. The kinetic energy density KE $(\frac{1}{2}\bar{\rho}\tilde{v}^2)$, averaged over volume and time, is also listed along with the relative contributions from nonaxisymmetric convection (CKE), as well as the axisymmetric differential rotation (DRKE) and meridional circulation (MCKE). We also list, where appropriate, the average magnetic energy density ME $(\tilde{B}^2/8\pi)$ and the relative contribution from each of its components, including the fluctuating (nonaxisymmetric) field FME and the mean (axisymmetric) toroidal and poloidal fields MTE and MPE. The relative latitudinal contrast of angular velocity $\Delta\Omega/\Omega_0$ between latitudes of 0° and 60° near the top of the domain is also stated for each case (averaged over both hemispheres).

For case M3, the decrease in KE first becomes apparent after about 600 days of evolution, when the ME reaches roughly 0.5% of KE_0. After 1200 days, the ME reaches a value of about 8% of the KE and retains that level for more than 3 ohmic decay times τ_η. The ME in case M2 is still too small ($\leq$0.1%) even after 4000 days for Lorentz forces to have a significant influence on the convective motions, as demonstrated by comparing the kinetic energy evolution in cases M2 and M3.

It is instructive to briefly consider the exchange of energy among different reservoirs in our simulations. We refer to Starr & Gilman (1966) for a more detailed discussion of energy exchange in an MHD system. We first note that both the total kinetic and magnetic energies remain small compared to the total potential, internal, and rotational energies contained in the shell. Further, the magnetic energy must arise from the conversion of kinetic energy, but this does not necessarily lead to a decrease in the total kinetic energy because the motions may draw on other reservoirs. Yet, in all of our magnetic simulations, energy is redistributed such that the sum of the kinetic and magnetic energy is less than the total kinetic energy contained in case H. The net energy deficit can be attributed primarily to the reduction in strength of the differential rotation by Maxwell stresses. This means that in a convection zone the way the energy is redistributed among and within the different reservoirs is modified by the presence of magnetic field, but these modifications remain small in the cases presented here. We refer to Cattaneo et al. (2003) for a detailed study of the influence of an imposed magnetic field on Boussinesq convection.

To further investigate the role played by the different agents in transporting energy, we illustrate in Figure 3 the contribution of various physical processes to the total radial energy flux through the shell, converted to luminosity and normalized to the solar luminosity. The net luminosity, $L(r)$, and its components are defined as

$$F_e + F_k + F_r + F_u + F_v + F_m = \frac{L(r)}{4\pi r^2}, \tag{11}$$

with

$$F_e = \bar{\rho} c_p \overline{v_r T'}, \tag{12}$$

$$F_k = \frac{1}{2}\bar{\rho}\overline{v^2 v_r}, \tag{13}$$

$$F_r = -\kappa_r \bar{\rho} c_p \frac{d\bar{T}}{dr}, \tag{14}$$

$$F_u = -\kappa \bar{\rho} \bar{T} \frac{d\bar{S}}{dr}, \tag{15}$$

$$F_v = -\overline{\boldsymbol{v}\cdot\boldsymbol{\mathcal{D}}}, \tag{16}$$

$$F_m = \frac{c}{4\pi}\overline{E_\theta B_\phi - E_\phi B_\theta}, \tag{17}$$

where $\boldsymbol{E} = 4\pi\eta \boldsymbol{j} c^{-2} - (\boldsymbol{v}\times\boldsymbol{B})c^{-1}$ is the electric current, F_e is the enthalpy flux, F_k is the kinetic energy flux, F_r is the radiative flux, F_u is the unresolved eddy flux, F_v is the viscous flux, and F_m is the Poynting flux. The unresolved eddy flux F_u is the heat flux due to SGS motions, which, in our LES-SGS approach, takes the form of a thermal diffusion operating on the mean entropy gradient. Its main purpose is to transport energy outward through the impenetrable upper boundary where the convective fluxes F_e and F_k vanish and the remaining fluxes are small. It should not be mistaken with F_r, which is the flux due to radiative diffusion and which operates on the mean temperature gradient. The radiative diffusivity, κ_r, is derived from a one-dimensional solar structure model (Brun et al. 2002), whereas the eddy diffusivity κ is chosen to model the effects of small-scale motions and to ensure that the flow is well resolved. There is an additional energy flux, F_v, which arises from the SGS eddy viscosity, ν.

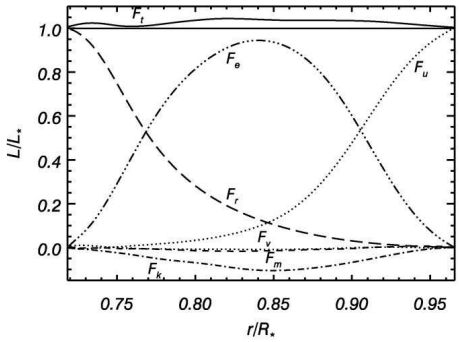

FIG. 3.—Energy flux balance with radius, averaged over horizontal surfaces and in time. The net radial energy flux in case M3 (*solid line*) is expressed as an integrated luminosity through horizontal shells and normalized with respect to the solar luminosity, L_*. In the other curves, this net flux is separated into components as defined in eqs. (11)–(17), including the enthalpy flux F_e, the radiative flux F_r, the unresolved eddy flux F_u, the kinetic energy flux F_k, the Poynting flux F_m, and the viscous flux F_v.

If the simulation were in a thermally relaxed state, the total flux through each horizontal surface would be constant and equal to the solar luminosity that is applied at the upper and lower boundaries: $L(r) = L_*$. Figure 3 indicates that the normalized net flux L/L_* (*solid line*) is indeed close to unity, implying that the simulation is close to thermal equilibrium.

The enthalpy flux here carries up to 90% of the solar luminosity in the bulk of the convective zone, and F_r and F_u carry the energy at, respectively, the bottom and top of the domain where F_e vanishes. The remaining fluxes F_k, F_v, and F_m are relatively small and negative in most of the domain. The downward direction of the kinetic energy flux is due to the asymmetry between the fast downflow lanes and the slower broad upflows. This downward flux carries about 10% of the solar luminosity and possesses a bigger amplitude than either F_v or F_m. The low amplitude of F_v confirms that in our simulations inertia dominates over viscous effects, i.e., the Reynolds number in all cases is much greater than unity. Similarly, the low amplitude of the Poynting flux confirms that magnetic processes in case M3 do play a role in the overall energy transport but not to the point of significantly modifying the flux balance established in the nonmagnetic progenitor case H. The volume-integrated ME is about 10% of KE; it would likely require a much higher level of magnetism in order for the Poynting flux to have a substantial influence on the net energy transport.

The Poynting flux F_m is also influenced by our choice of magnetic boundary conditions. In all the magnetic cases presented here we match the computed field to an internal and external potential field at every time step. This leads to a nonzero electromagnetic flux through the boundaries. We have investigated the impact of such magnetic energy "leakage" on the dynamo action by computing one case in which the magnetic field was required to be purely radial at the boundaries, yielding

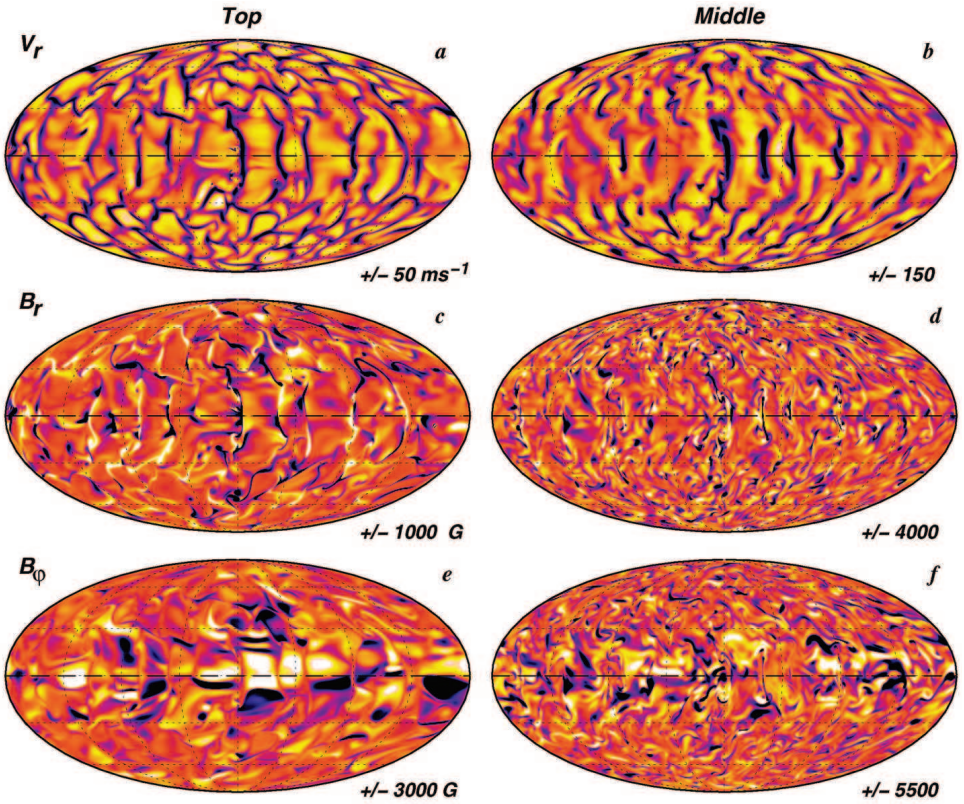

FIG. 4.—Global views at one instant in time of the radial velocity component (*top panels*) and the radial and longitudinal magnetic field components (*middle and bottom panels*) in case M3 near the top (*left panels*) and middle (*right panels*) of the computational domain. Dark tones in turn represent downflow, inward, and westward fields, with the ranges for each color table indicated. The color table is as in Fig. 1.

no net Poynting flux through the shell ($F_m = 0$ at the top and bottom boundaries). The effect of closed as opposed to open boundary conditions seems to be that in the former the magnetic energy amplification is more efficient, with potentially a lower dynamo threshold. But since in the solar case such magnetic energy ''leakage'' exists both at the bottom via, for example, turbulent pumping (Tobias et al. 2001) and at the photosphere via, for example, magnetic eruptions, we consider that our choice of boundary conditions is reasonable for the solar dynamo problem. We further believe that open magnetic boundary conditions play a central role in regulating the magnetic dynamo action in the convection zone, by providing an outlet for the magnetic energy and also most likely for the magnetic helicity.

4. CONVECTIVE AND MAGNETIC STRUCTURES

4.1. *Flow Patterns and Their Evolution*

The structure of the convection in simulation M3 is illustrated in Figure 4. The convective patterns are qualitatively similar to the hydrodynamic case H, which can be seen by comparing the radial velocity field in the top left panel of Figure 4 to that shown in Figure 1. Cases M1 and M2 also exhibit similar patterns because the magnetic fields in these simulations never grow strong enough to exert a substantial influence on the global flow structure. However, Lorentz forces in localized regions of case M3 do have a noticeable dynamical effect, particularly with regard to the evolution of strong downflow lanes where magnetic tension forces can inhibit vorticity generation.

The horizontal structure of the radial and longitudinal magnetic field is also shown in Figure 4. Many of the main features are qualitatively similar to simulations of turbulent, compressible magnetoconvection in Cartesian geometries (Cattaneo 1999; Stein & Nordlund 2000; Tobias et al. 2001). The magnetic field generally has a finer and more intricate structure than the velocity field because of the smaller diffusion ($\mathrm{Pr}_m = \nu/\eta = 4$ in this simulation) and also the nature of the advection terms in the induction equation, which are similar in

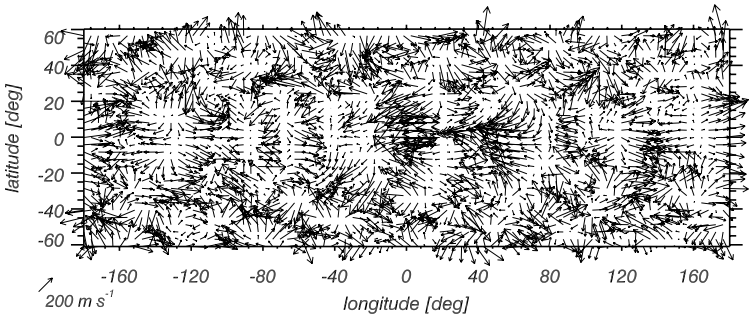

FIG. 5.—Horizontal velocity vectors near the top of the domain in case M3 shown for the latitude range $\pm 60^\circ$ at the same level and time as in the left panels of Fig. 4. The axisymmetric velocity component has been subtracted out and the display grid is undersampled relative to the horizontal resolution of the simulation in order to improve clarity. This sampling does not capture more localized features such as vertically aligned vortex tubes, which can be seen on higher resolution images but occur on scales smaller than the sampling grid.

form to those in the vorticity equation (e.g., Biskamp 1993). Near the top of the shell, the radial magnetic field B_r is mainly concentrated in the downflow lanes, where both polarities coexist in close proximity. By contrast, the toroidal field B_ϕ near the surface appears more distributed and more patchy, characterized by relatively broad regions of uniform polarity, particularly near the equator. The magnetic field topology generally does not exhibit any clear symmetries about the equator, although some of the B_ϕ patches at low latitudes do have an antisymmetric counterpart.

In the middle of the shell the magnetic fluctuations appear of smaller scale and more distributed, but they are still very intermittent. Strong vertical fields of mixed polarity still correlate well with downflow lanes and plumes. The longitudinal field is more filamentary and is organized in longitudinally elongated structures, having been stretched by the gradients in angular velocity (see also § 4.2).

Throughout the shell, the magnetic field patterns evolve rapidly, as fields are continuously transported, distorted, and amplified by convective motions. Of particular importance near the top of the shell are the horizontal flows, shown in Figure 5 for case M3. Regions of convergence and divergence are apparent, as are swirling vortices, which occur most frequently at mid- and high latitudes and generally have a cyclonic sense (counterclockwise in the northern hemisphere and clockwise in the southern). Such flows stretch the horizontal field and sweep the vertical field into vortical downflow lanes where it is twisted, thus generating magnetic helicity. Horizontally converging flows also squeeze together fields of mixed polarity, driving magnetic reconnection.

The convective patterns visible in the vertical velocity field of Figure 4 are also evident in the horizontal velocity patterns of Figure 5, particularly the dichotomy between low latitudes, which are dominated by extended downflow lanes oriented north-south (visible here as lines of horizontal convergence), and higher latitudes, which possess a smaller scale, more isotropic downflow network. If they exist in the Sun, such large-scale convective patterns may ultimately be detectable in similar horizontal flow maps inferred from local-domain helioseismic analyses using time-distance and ring-diagram procedures (e.g., Haber et al. 2002; Hindman et al. 2004). However, currently such helioseismic flow maps are limited to the upper few percent of the solar envelope, monitoring SSW (Toomre 2002). This lies outside the computational domain considered here.

The dynamical richness and rapid time evolution of the flow and magnetic field patterns are highlighted in Figure 6. The radial magnetic field, the radial velocity field, and the horizontal flow all exhibit an intricate structure that evolves substantially on timescales of weeks and even days. Low-latitude features tend to drift eastward relative to higher latitude features as a result of advection by the differential rotation and also inherent pattern propagation relative to the local rotation rate. At the tracking rate used in Figure 6, this leads generally to a rightward movement of patterns near the equator and a leftward movement of patterns near the southern edge of the region shown (latitude -60°). In between, particularly at a latitude of about -25°, the distinctive patterns at low and high latitudes meet, giving rise to a particularly complex dynamical evolution. The north-south aligned downflow lanes at low latitudes temporarily link to the high-latitude network as they drift by, and features caught in this interaction region are rapidly sheared and distorted, forming filaments and vortices that then mix and merge with other structures.

Figure 6 highlights the evolution of several features in particular, indicated by letters. The first of these, A, is a multipolar region that appears to represent several flux tubes passing through the horizontal plane being visualized. After they form, these localized features are rapidly sheared by convective motions, distorting and separating into flux sheets that then merge with other features and lose their identity over the course of about 2 weeks. Feature B begins as a flux sheet confined to a north-south oriented downflow lane where the polarity of the field is radially inward. By the second frame, flux of the opposite polarity (radially outward; indicated by white) is advected into the downflow lane where it is then wrapped up by the cyclonic vorticity and rapidly dissipated as it reconnects with the existing field. Similar dynamics are also occurring in feature C, which illustrates the merging of two flux sheets of opposite polarity in a downflow lane (particularly evident in the rightmost frame). The lower portion of the outward-polarity sheet (*white*) extends into the interface region at latitude -25°, where extended low-latitude downflow lanes merge with the high-latitude network. The intense vorticity and shear in this region twist and stretch the field, dramatically changing its appearance on a timescale of several days.

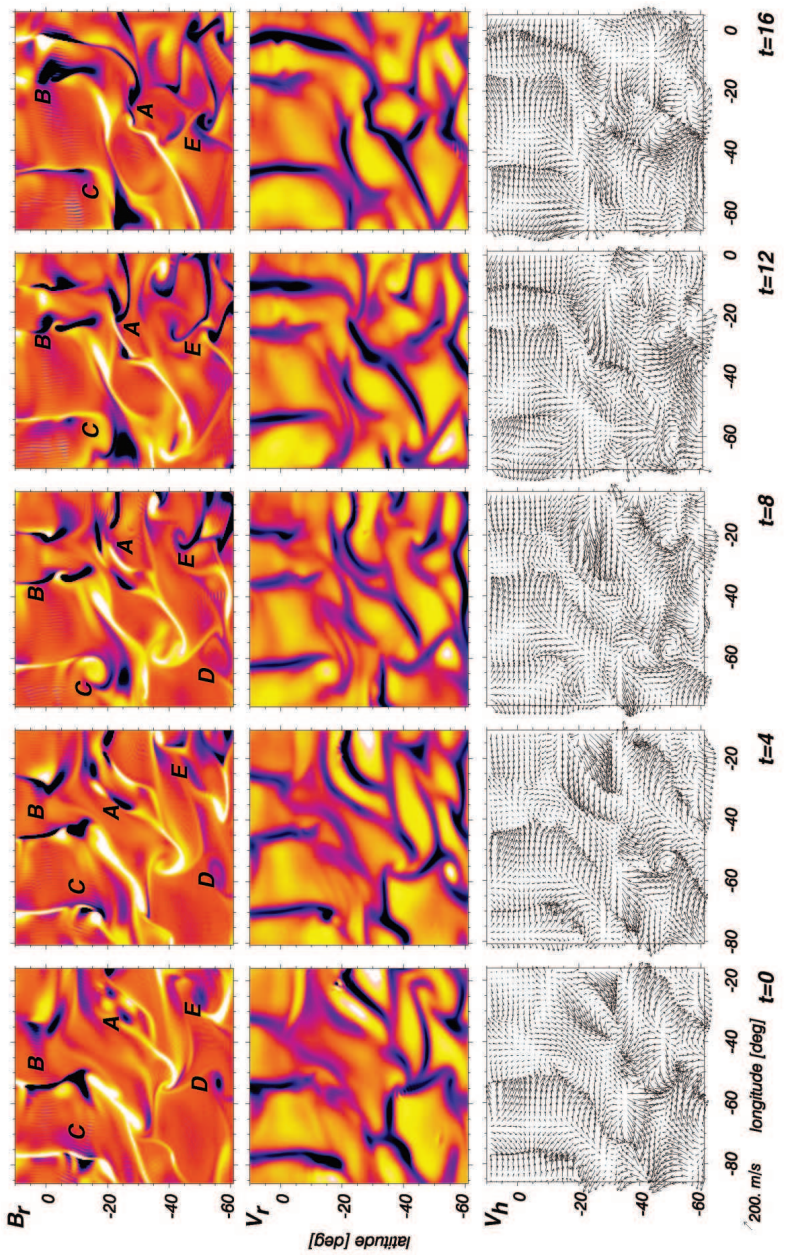

FIG. 6.—Radial magnetic field (B_r; *top panels*), radial velocity (v_r; *middle panels*), and horizontal flow vectors ($\mathbf{v}_h$; *bottom panels*) shown for a selected horizontal domain near the top of the shell in case M3. A sequence of five snapshots is shown, each separated by an interval of 4 days, with time increasing from left to right. This region spans 70° in both latitude and longitude; the longitude range shifts eastward by 5° with each successive snapshot in order to track some of the flow features. Particular features are indicated with labels. The horizontal level and the time of the first snapshot correspond to the global views shown in the left panels of Fig. 4 and in Fig. 5. The color table is the same as in Fig. 1.

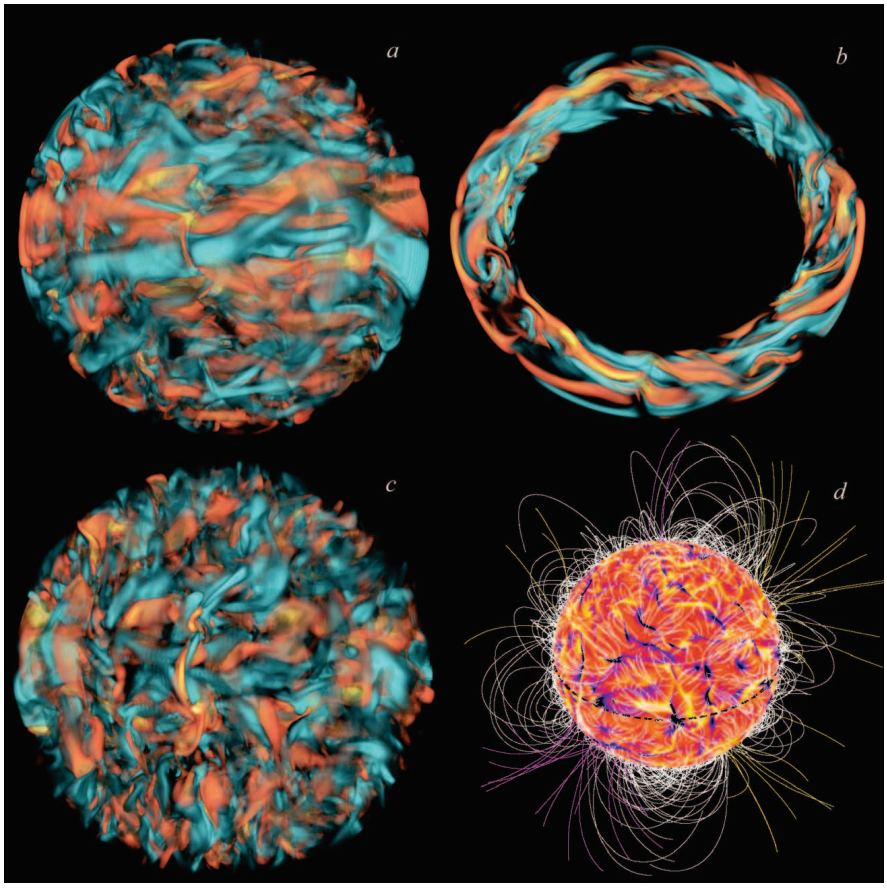

FIG. 7.—(*a*, *c*) Volume renderings of the toroidal (B_ϕ) and radial (B_r) magnetic fields in case M3 at one instant in time (the same as in Fig. 4). Red tones indicate outward and eastward (prograde) fields, and blue tones denote inward and westward (retrograde) fields. (*b*) Selected subvolume of B_ϕ including the full span of longitude and radius but only a narrow band in latitude centered around the equator. The equatorial plane is tilted nearly perpendicular to the viewing in order to highlight the radial and longitudinal structure. Typical field strengths are about 1000 G for B_r and 3000 G for B_ϕ. (*d*) Potential field extrapolation of the radial magnetic field at the top of the computational domain. The radial field at the surface is shown in an orthographic projection, and the visualization traces individual field lines indicated in white if they form closed loops and in yellow or magenta if they represent an open field of positive (outward) or negative (inward) polarity, respectively.

The most intense downflow plumes often possess enough vorticity to evacuate the core of the plume owing to centrifugal forces, and buoyancy forces acting on the resulting decrease in density lead to a flow reversal, creating a new upflow region that then diverges horizontally as a result of the density stratification (Brandenburg et al. 1996; Brummell et al. 1998; Miesch et al. 2000). Such dynamics is occurring in feature D of Figure 6, now in the presence of a magnetic field. By the second frame, a new upflow is created in this manner (*middle panels*) that rapidly expands horizontally and interacts with the surrounding flow. There is a vertical flux tube present in the original downflow, but it is rapidly dispersed as the flow reverses, losing all coherence by the fourth frame. Feature E is another example of how the field can be wrapped up by the vorticity in downflow lanes, particularly at mid- and high latitudes where the rotation vector has a large vertical component.

4.2. *Morphology of Magnetic Fields*

Horizontal cross sections as in Figures 4–6 are informative, but they provide limited insight into the three-dimensional structure of the flow and of the magnetic field in particular. Further insight requires volume visualizations as shown in Figure 7.

The toroidal and radial magnetic fields in Figures 7*a* and 7*c* have a very different appearance, consistent with the contrast noted previously in Figure 4. Whereas B_r is concentrated into

vertically oriented sheets and filaments, B_ϕ is organized into relatively broad ribbons and tubes that extend mainly in longitude. Figure 7*b* further demonstrates the ribbon-like topology of the toroidal field, showing in particular that the low-latitude horizontal patches near the surface have a relatively small vertical extent, although some meander in radius. Substantial magnetic helicity is present throughout, involving complex winding of the toroidal field structures along their length. Some features resemble magnetic flux tubes, but they generally do not remain coherent long enough for magnetic buoyancy forces to induce them to rise.

Whereas some toroidal field structures maintain coherence over global scales, the radial field is generally dominated by smaller scale fluctuations. In particular, radial field structures near the top of the domain rarely penetrate deep into the convection zone, although individual field lines maintain some connectivity throughout the shell. This connectivity also extends outside of the computational domain because of the boundary conditions that match the interior field to an external potential field. The structure of this potential field above the outer surface is illustrated in Figure 7*d*. The extrapolation shown in the figure treats the radial field near the top of the domain as a source surface and requires that the field be radial at $2.5R_*$, although field lines are only shown out to a radius of $1.5R_*$.

As in the Sun, the surface magnetic field is complex, featuring bipolar regions, nested loops, and an intricate web of connectivity between both local and widely separated regions on the surface. Although some large loops span both hemispheres, dipolar or quadrupolar components are not evident and open field is not confined to or even preferred in the polar regions. Axisymmetric field components are indeed present (see § 6), but the field morphology near the surface and throughout the shell is dominated by smaller scale turbulent structures.

The magnetic energy in the potential field extrapolation decreases rapidly with increasing radius, as spherical harmonic components decay in proportion to $r^{-(l+1)}$. A less dramatic outward gradient of magnetic energy also occurs within the computational domain as demonstrated in Figure 8. Here we display the radial profile of the total magnetic energy density integrated over the horizontal dimensions after having broken it down into mean (axisymmetric) and fluctuating (nonaxisymmetric) poloidal and toroidal components in the following manner:

$$\mathrm{MTE} = \frac{1}{8\pi}\langle B_\phi\rangle^2, \tag{18}$$

$$\mathrm{MPE} = \frac{1}{8\pi}\left(\langle B_r\rangle^2+\langle B_\theta\rangle^2\right), \tag{19}$$

$$\mathrm{FTE} = \frac{1}{8\pi}\left[\left(B_\phi - \langle B_\phi\rangle\right)^2\right], \tag{20}$$

$$\mathrm{FPE} = \frac{1}{8\pi}\left[(B_r - \langle B_r\rangle)^2+(B_\theta - \langle B_\theta\rangle)^2\right], \tag{21}$$

$$\mathrm{FME} = \frac{1}{8\pi}\left[(B_r - \langle B_r\rangle)^2+(B_\theta - \langle B_\theta\rangle)^2+\left(B_\phi - \langle B_\phi\rangle\right)^2\right], \tag{22}$$

where the angle brackets denote a longitudinal average.

The magnetic energy generally peaks toward the bottom of the shell for both the mean and fluctuating field components. This is due in part to the spherical divergence and the density stratification. Downward pumping of magnetic fields by convective motions also plays a role, but the pumping is not as effective as in penetrative convection simulations where the underlying stable region provides a reservoir where the field can be accumulated and stored (see Tobias et al. 2001).

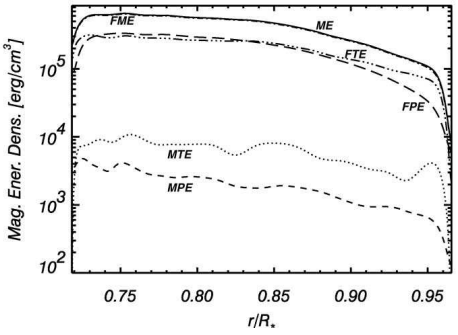

FIG. 8.—Radial profiles of the magnetic energy in case M3. Shown are integrals over horizontal surfaces and averages in time of the total magnetic energy (ME), the energy in the mean (axisymmetric) toroidal field (MTE) and the mean poloidal field (MPE), and the energy in the fluctuating (nonaxisymmetric) fields, including the toroidal component (FTE), the poloidal component (FPE), and their sum (FME).

Figure 8 also shows that the magnetic energy contained in the mean field components is more than an order of magnitude smaller than that contained in the nonaxisymmetric fluctuations. Most of the mean field energy is in the toroidal field, which exceeds the energy in the poloidal field by about a factor of 3 owing to the stretching and amplification of toroidal field by differential rotation (the ω-effect). This ratio is smaller than in the Sun, where the mean toroidal field is estimated to be about 2 orders of magnitude more energetic than the mean poloidal field. This discrepancy can again be attributed to the absence of an overshoot region and a tachocline, where the toroidal field can be stored for extended periods while it is amplified by relatively large angular velocity gradients (see § 6). For the nonaxisymmetric fluctuations, the magnetic energy is approximately equally distributed among the toroidal and poloidal fields, indicating that the turbulent convection can efficiently generate both components in roughly equal measure, implying that the ω-effect plays a lesser role.

5. DIFFERENTIAL ROTATION AND MERIDIONAL CIRCULATION

Surface measurements and helioseismic inferences of large-scale, axisymmetric, time-averaged flows in the Sun currently provide the most important observational constraints on global-scale models of solar convection. The structure, evolution, and maintenance of mean flows (averaged over longitude and time) have therefore been a primary focus of previous global convection simulations (Glatzmaier 1987; Miesch et al. 2000; Elliott et al. 2000; Brun & Toomre 2002). Of particular importance is the mean longitudinal flow, i.e., the differential rotation, which is now reasonably well established from helioseismic inversions, although investigations continue to scrutinize its detailed spatial structure and temporal evolution (Thompson et al. 2003). The mean circulation in the meridional plane has only been probed reliably in the surface layers of the Sun through Doppler measurements (Hathaway et al. 1996) and

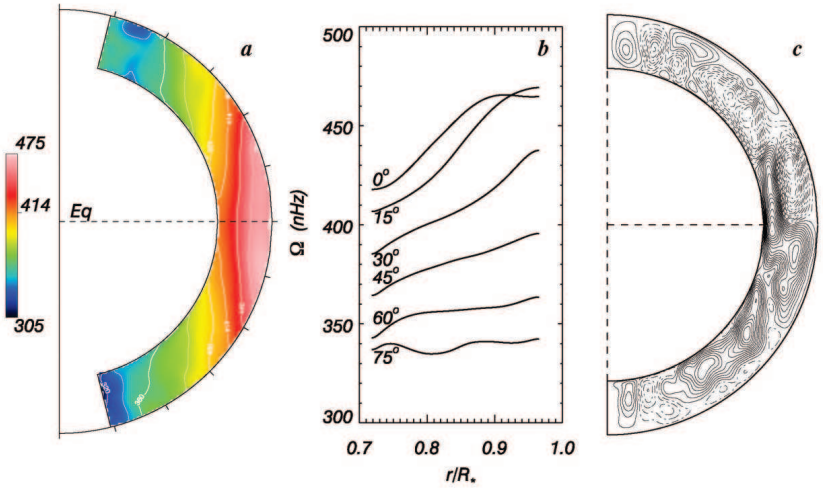

FIG. 9.—(*a*, *b*) Angular velocity profile in case M3 averaged over longitude and time (spanning an interval of 150 days late in the simulation). White/red and blue/green tones in (*a*) denote faster and slower rotation, respectively. Radial profiles are plotted in (*b*) for selected latitudes. (*c*) Meridional circulation in case M3 averaged over longitude and time, represented as streamlines of the mass flux. Solid contours denote clockwise circulation and dashed contours counterclockwise circulation.

local-area helioseismology (e.g., Haber et al. 2002). Here we discuss the mean flows achieved in our simulations and compare them with solar observations and previous numerical models.

5.1. *Attributes of Mean Flows*

With fairly strong magnetic fields sustained within the bulk of the convection zone in case M3, it is to be expected that the differential rotation Ω will respond to the feedback from the Lorentz forces. Figure 9*a* shows the time-averaged angular velocity achieved in case M3, which exhibits a prograde equatorial rotation with a monotonic decrease in angular velocity toward higher latitudes as in the Sun. The main effect of the Lorentz forces is to extract energy from the differential rotation. The kinetic energy contained in the differential rotation drops by a factor of 2 after the addition of magnetic fields, and this decrease accounts for over 70% of the total kinetic energy difference (see § 3.2). This is reflected by a 30% decrease in the angular velocity contrast $\Delta\Omega$ between the equator and latitudes of 60°, going from 140 nHz (or 34% compared to the reference frame Ω_0) in the hydrodynamic case H to 100 nHz (or 24%) in case M3. This value is close to the contrast of 22% inferred from helioseismic inversion of the solar profile (Thompson et al. 2003). Thus, the convection is still able to maintain an almost solar-like angular velocity contrast despite the inhibiting influence of Lorentz forces.

Eddy et al. (1976) have deduced from a careful study of solar activity records during the Maunder minima that the Sun was rotating about 3%–4% faster in the equatorial region during that period than it does at present and that the angular velocity contrast between the equator and latitudes of 20° may have been as much as a factor of 3 larger. The somewhat faster rotation rate and larger $\Delta\Omega$ in case H (and M2) relative to case M3 further suggest that a reduced level of the Sun's magnetism may lead to greater differential rotation (Brun 2004).

In Figure 9*c* we display the meridional circulation realized in case M3. This meridional circulation is maintained by buoyancy forces, Reynolds stresses, pressure gradients, Maxwell stresses, and Coriolis forces acting on the differential rotation. Since these relatively large forces nearly cancel one another, the circulation can be thought of as a small departure from (magneto)geostrophic balance, and the presence of a magnetic field can clearly influence its subtle maintenance. In case M3, the meridional circulation exhibits a multicell structure in both latitude and radius and possesses some asymmetry with respect to the equator. In particular, two vertical cells are present at low latitudes in the northern hemisphere, whereas only one is present in the southern hemisphere. Since the convection possesses some asymmetry (cf. Fig. 4), it is not surprising that the meridional circulation does the same.

Given the competing processes for its origin, this weak flow is not straightforward to predict. Typical amplitudes for the velocity are of order 25 m s^{-1}, comparable to local helioseismic deductions (Haber et al. 2002). The flow near the outer boundary is directed poleward at low latitudes, with return flow deeper down. The temporal fluctuations in the meridional circulation are large and thus stable time averages are only attained by frequent sampling over many rotation periods. The kinetic energy contained in the meridional circulation (MCKE) is about 2 orders of magnitude smaller than that contained in the differential rotation and convective motions and is more than an order of magnitude less than the total magnetic energy (ME; see Table 2). As a result, small fluctuations in the convective motions, differential rotation, and Lorentz forces can lead to major variations in the circulation. Some of the helioseismic inferences suggest the presence of single-cell circulations, which are at odds with our multicell patterns. However, these inferences vary from year to year and there is recent evidence that multicell structure and equatorial asymmetries are

developing in the meridional circulation patterns just below the photosphere as the current solar cycle advances (Haber et al. 2002).

5.2. *Redistribution of Angular Momentum*

We can better understand how the differential rotation profile in case M3 is achieved by identifying the main physical processes responsible for redistributing angular momentum within our rotating convective shells. Our choice of stress-free and potential-field boundary conditions at the top and bottom of the computational domain has the advantage that no net external torque is applied, and thus angular momentum is conserved. We may assess the transport of angular momentum within these systems by considering the mean radial ($\mathcal{F}_r$) and latitudinal ($\mathcal{F}_\theta$) angular momentum fluxes, extending the procedure used in Brun & Toomre (2002) to the magnetic context (see also Elliott et al. 2000). Let us consider the ϕ-component of the momentum equation expressed in conservative form and averaged in time and longitude (denoted by hat):

$$\frac{1}{r^2}\frac{\partial(r^2\mathcal{F}_r)}{\partial r}+\frac{1}{r\sin\theta}\frac{\partial(\sin\theta\mathcal{F}_\theta)}{\partial\theta}=0, \tag{23}$$

involving the mean radial angular momentum flux

$$\mathcal{F}_r=\bar{\rho}r\sin\theta\left[-\nu r\frac{\partial}{\partial r}\left(\frac{\hat{v}_\phi}{r}\right)+\widehat{v_r'v_\phi'}+\hat{v}_r\left(\hat{v}_\phi+\Omega r\sin\theta\right)-\frac{1}{4\pi\bar{\rho}}\widehat{B_r'B_\phi'}-\frac{1}{4\pi\bar{\rho}}\hat{B}_r\hat{B}_\phi\right] \tag{24}$$

and the mean latitudinal angular momentum flux

$$\mathcal{F}_\theta=\bar{\rho}r\sin\theta\left[-\nu\frac{\sin\theta}{r}\frac{\partial}{\partial\theta}\left(\frac{\hat{v}_\phi}{\sin\theta}\right)+\widehat{v_\theta'v_\phi'}+\hat{v}_\theta\left(\hat{v}_\phi+\Omega r\sin\theta\right)-\frac{1}{4\pi\bar{\rho}}\widehat{B_\theta'B_\phi'}-\frac{1}{4\pi\bar{\rho}}\hat{B}_\theta\hat{B}_\phi\right]. \tag{25}$$

In the above expressions for both fluxes, the terms on the right-hand side denote contributions, respectively, from viscous diffusion (which we denote as $\mathcal{F}_r^{\rm VD}$ and $\mathcal{F}_\theta^{\rm VD}$), Reynolds stresses ($\mathcal{F}_r^{\rm RS}$ and $\mathcal{F}_\theta^{\rm RS}$), meridional circulation ($\mathcal{F}_r^{\rm MC}$ and $\mathcal{F}_\theta^{\rm MC}$), Maxwell stresses ($\mathcal{F}_r^{\rm MS}$ and $\mathcal{F}_\theta^{\rm MS}$), and large-scale magnetic torques ($\mathcal{F}_r^{\rm MT}$ and $\mathcal{F}_\theta^{\rm MT}$). The Reynolds stresses are associated with correlations of the fluctuating velocity components that arise from organized tilts within the convective structures, especially in the downflow plumes (e.g., Brummell et al. 1998; Miesch et al. 2000). In the same spirit the Maxwell stresses are associated with correlations of the fluctuating magnetic field components that arise from tilt and twist within the magnetic structures.

In Figure 10 we show the components of $\mathcal{F}_r$ and $\mathcal{F}_\theta$ for case M3, having integrated over colatitude and radius as follows:

$$I_r(r)=\int_0^\pi \mathcal{F}_r(r,\ \theta)r^2\sin\theta\,d\theta,$$
$$I_\theta(\theta)=\int_{r_{bot}}^{r_{top}}\mathcal{F}_\theta(r,\ \theta)r\sin\theta\,dr. \tag{26}$$

Thus, I_r represents the net angular momentum flux through horizontal shells at different radii and I_θ represents the net flux through cones at different latitudes. We then identify in turn the contributions from viscous diffusion (VD), Reynolds stresses (RS), meridional circulation (MC), Maxwell stresses (MS), and large-scale magnetic torques (MT). This representation is helpful in assessing the sense and amplitude of angular momentum transport within the convective shells by each component of $\mathcal{F}_r$ and $\mathcal{F}_\theta$.

Turning first to Figure 10*a*, we see that the radial differential rotation is being maintained by Reynolds stresses and meridional circulation, $I_r^{\rm RS}$ and $I_r^{\rm MC}$, which both transport angular momentum radially outward. This outward transport is opposed by the viscous flux $I_r^{\rm VD}$, which is radially inward as implied by the positive radial angular velocity gradient seen in Figure 9*b*. The Maxwell stresses $I_r^{\rm MS}$ also act to oppose the generation of differential rotation by the convection, possessing the same sign and amplitude as the viscous torque. The large-scale magnetic torques are very small but negative as well, helping to decelerate the surface and speed up the bottom of the shell. The net radial flux I_r, represented by the solid line, is nearly zero, indicating that the flow has achieved an approximate statistical equilibrium and that our sampling in time captures this equilibrated state reasonably well, despite the large temporal variations typically present in our simulations.

The latitudinal angular momentum flux I_θ exhibits a more complicated interplay among its various components than I_r, as demonstrated in Figure 10*b*. Here the angular momentum transport is dominated by Reynolds stresses $I_\theta^{\rm RS}$ that are consistently directed toward the equator (i.e., negative in the southern hemisphere and positive in the northern hemisphere). This feature implies that the equatorial acceleration observed in our simulations is mainly due to the transport of angular momentum by the Reynolds stresses. Further, unlike the radial angular momentum balance, we see that the transport by meridional circulation $I_\theta^{\rm MC}$ is opposite to $F_\theta^{\rm RS}$, with the meridional circulation seeking to slow down the equator and speed up the poles. The viscous torque $I_\theta^{\rm VD}$ is in the same direction but is a factor of 4 smaller in amplitude. These results are identical to that deduced from case H (much as in Brun & Toomre 2002). The main difference in case M3 comes from the Maxwell stress component $I_\theta^{\rm MS}$, which opposes the Reynolds stresses as in the radial angular momentum balance. The large-scale magnetic torque $I_\theta^{\rm MT}$ is again found to be negligible. The total flux I_θ vacillates around zero, indicating no net latitudinal angular momentum transport and an acceptable equilibrated solution.

The reduction in the latitudinal contrast of Ω between cases H and M3 can be partially attributed to a global decrease in the kinetic energy of the convection (see Table 2). The rms Reynolds number of case M3 is about 12% less than in case H, reflecting the stabilizing influence of magnetic fields. However, the convection kinetic energy is only reduced by about 27%, whereas the differential rotation kinetic energy is reduced by over 50%. Figure 10 indicates that this large decrease in DRKE is due to the poleward transport of angular momentum by Maxwell stresses. In case M3 the Reynolds stresses must balance the angular momentum transport by the meridional circulation, the viscous diffusion, and the Maxwell stresses, which leads to a less efficient acceleration of the equatorial regions. Since the magnetic energy is only about 7% of the kinetic energy in case M3 (see Table 2), the Maxwell stresses are not the main players in redistributing the angular momentum, but they do contribute more than the viscous torque $I_\theta^{\rm VD}$ in the latitudinal balance. If the magnetic energy were to exceed about 20% of the total kinetic energy, Maxwell stresses and

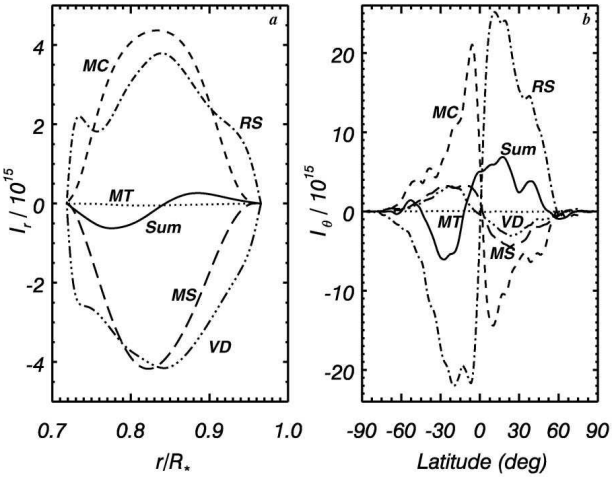

FIG. 10.—Temporal average of (*a*) the integrated vertical angular momentum flux I_r and (*b*) the integrated latitudinal angular momentum flux I_θ for case M3. The fluxes have been decomposed into their viscous diffusion (labeled VD), Reynolds stress (RS), meridional circulation (MC), Maxwell stress (MS), and large-scale magnetic torque (MT) components. The solid lines represent the sum of these components and serve to indicate the quality of stationarity achieved. Positive values represent a radial flux that is directed outward and a latitudinal flux directed from north to south. The interval chosen for the time averages spans 150 days late in the simulation (as in Fig. 9). The radial integrated flux I_r has been normalized by $r_{\rm top}^2$.

magnetic torques may become strong enough to suppress the differential rotation almost entirely (Gilman 1983; Brun 2004). The Sun may have ways of avoiding this by expelling some of its magnetic flux.

We emphasize that the suppression of vertical and latitudinal differential rotation by Lorentz forces in our simulations is dominated by the fluctuating magnetic field components $I^{\rm MS}$, not the mean field components $I^{\rm MT}$. Magnetic tension forces associated with the mean poloidal field do tend to inhibit rotational shear as in axisymmetric models (MacGregor & Charbonneau 1999), but this intuitive "rubber band" effect is far less efficient than the more subtle Maxwell stresses induced by correlations among the turbulent magnetic field components.

Brun & Toomre (2002) have found that as the level of turbulence is increased, $I^{\rm VD}$ reduces in amplitude and the transport of angular momentum by the Reynolds stresses $I^{\rm RS}$ and by the meridional circulation $I^{\rm MC}$ changes accordingly to maintain equilibrium. Here the presence of a fourth agent, namely, the Maxwell stresses, can modify this force balance and thus alter the equilibrium rotation profile.

An important feature of the rotation profile in case H and also in case AB of Brun & Toomre (2002) is a monotonic decrease in angular velocity with increasing latitude that persists all the way to the polar regions. This relatively slow polar rotation is supported by helioseismic inversions but is generally difficult to achieve in numerical simulations of convection because regions close to the rotation axis undergo a prograde acceleration if fluid parcels tend to conserve their angular momentum. Thus, it is promising to see that case M3 has retained relatively slow rotation at high latitudes even in the presence of magnetic fields.

Figure 10*b* indicates that the prograde equatorial rotation seen in case M3 is due to equatorward angular momentum transport by Reynolds stresses and that the meridional circulation tends to oppose this transport. In many previous simulations, the poleward angular momentum transport by the meridional circulation extends to higher latitudes, tending to spin up the poles. Thus, the slow polar rotation in case M3 and its hydrodynamic predecessors, cases H and AB, seems to come about from a relatively weak meridional circulation at high latitudes (see also Brun & Toomre 2002). The absence of strong high-latitude circulation cells permits a more efficient extraction of angular momentum by the Reynolds stresses from the polar regions toward the equator, yielding the interesting differential rotation profile that is achieved. Since the Maxwell stresses also transport angular momentum toward the poles, the polar regions in case M3 are found to rotate slightly faster than in case H. However, the angular momentum transport by Maxwell stresses is distributed such that the global rotation retains the attribute of a monotonic decrease of Ω with latitude.

6. EVOLUTION OF MEAN MAGNETIC FIELDS

It is clear from the results presented (see, e.g., Figs. 4, 7, 8, and 10) that the magnetic field is dominated by the fluctuating or turbulent (nonaxisymmetric) component. However, the mean (axisymmetric) field components have particular significance with regard to solar dynamo theory; thus, it is instructive to explore their structure and evolution in detail. In particular, we wish to understand our simulation results in the context of solar observations although we are aware that we are still missing important "dynamo building blocks" (see § 1.1) such as magnetic pumping into a tachocline-like shear layer. Our results provide fundamental insight into the generation of mean magnetic fields by turbulent convection and as such can be used to evaluate and improve mean field dynamo models that do not explicitly consider the turbulent field and flow

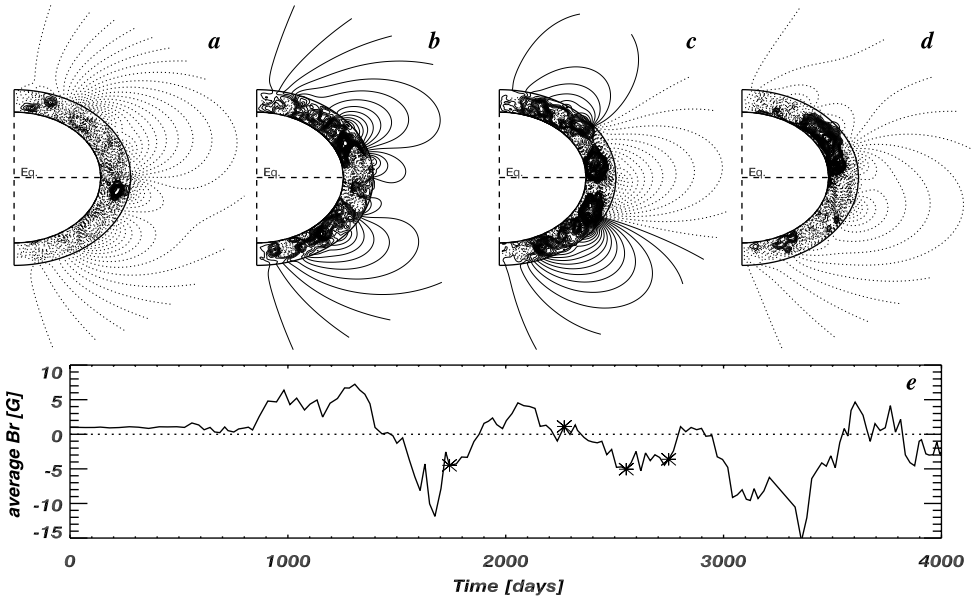

FIG. 11.—Temporal evolution of the mean poloidal field for case M3. (*a–d*) Structure of the field at four selected times after the magnetic energy has reached a statistically steady state. Solid contours denote positive polarity (clockwise orientation), and dotted contours denote negative polarity. (*e*) Mean radial field at the outer boundary averaged over the northern hemisphere, shown over the course of the entire simulation. The average polarity reverses after about 1750 days and several more times afterward on a timescale of about 500 days. However, the field generally exhibits a complex topology with both symmetric and antisymmetric components. The instants in time corresponding to the top panels are indicated in (*e*) with asterisks.

components (e.g., Krause & Rädler 1980; Ossendrijver 2003). In what follows, we define the mean poloidal field in terms of the longitudinally averaged radial and latitudinal components, $\langle B_p \rangle = \langle B_r \rangle \hat{\boldsymbol{e}}_r + \langle B_\theta \rangle \hat{\boldsymbol{e}}_\theta$, and the mean toroidal field in terms of the longitudinally averaged longitudinal component, $\langle B_t \rangle = \langle B_\phi \rangle \hat{\boldsymbol{e}}_\phi$.

The generation of the mean toroidal field in our simulations is due to the shearing, stretching, and twisting of mean and fluctuating poloidal fields by differential rotation (the ω-effect) and helical convective motions (the α-effect). Likewise, mean poloidal fields are generated from fluctuating toroidal fields via the α-effect. The α-effect arises from correlations between turbulent flows and fields as expressed in the mean (longitudinally averaged) induction equation by the term $\Psi = \langle \nabla \times (\boldsymbol{v}' \times \boldsymbol{B}') \rangle$, where primes indicate that the axisymmetric component has been subtracted off and angular brackets indicate a longitudinal average (Moffatt 1978; Stix 2002; Brandenburg & Subramanian 2004). We find that the fluctuating fields in our simulations are much stronger than the mean fields, accounting for up to 98% of the total magnetic energy, and the scale and amplitude of their correlations are not small in any sense and therefore cannot be reliably parameterized in terms of the mean field. It appears that the generation of mean fields in our simulations is not due to the α-effect in the traditional sense, but rather to a more complex interplay between turbulent magnetic field and flow components. The chaotic nature of these turbulent components gives rise to intricate structure and aperiodic evolution in the mean fields.

6.1. *Poloidal Fields*

Figure 11 illustrates the structure and evolution of the mean poloidal field in case M3. Figures 11*a*–11*d* show four snapshots of the magnetic lines of force of $\langle B_p \rangle$ within the convective domain along with a potential extrapolation of the external field up to $2R_*$. The initial seed field was dipolar (i.e., antisymmetric with respect to the equator), but symmetric fields (i.e., quadrupolar configurations) are also realized in our simulations, as in Figure 11*c*. The evolution of the poloidal magnetic field from an antisymmetric to a symmetric profile with respect to the equator is made possible because of the nonlinear and asymmetric nature of the convection that amplifies the field through dynamo action. The continuous exchange between dipolar and quadrupolar topologies, as well as higher order multipoles, results in magnetic fields with intricate configurations and with no clear equatorial symmetry preferences. Within the convective shell the presence of strong magnetic field gradients and magnetic diffusion leads to continuous reconnection of the magnetic field lines.

The perpetual regeneration of magnetic flux by the convection can lead to a global reversal of the magnetic field polarity. Figure 11*e* shows the temporal evolution of the average polarity of the poloidal field in case M3, defined in terms of the radial magnetic field B_r averaged over the northern hemisphere of the outer boundary. This is a measure of the total magnetic flux that passes through the northern hemisphere at the outer surface of the shell, and since $\nabla \cdot \boldsymbol{B} = 0$ outside as well as

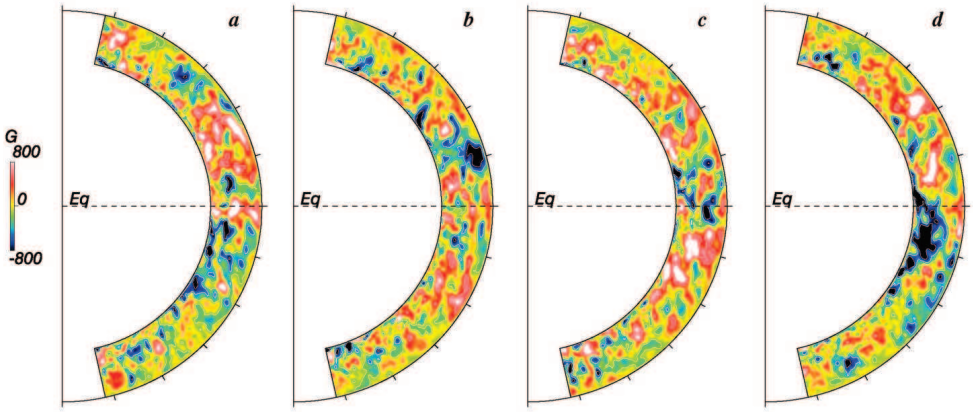

FIG. 12.—Evolution of the mean toroidal field for case M3, as a companion to Fig. 11. Red and blue tones denote eastward (prograde) and westward (retrograde) field, respectively, as indicated by the color table.

inside the domain, the same flux of opposite polarity must also pass through the southern hemisphere. A positive value indicates that the field is outward on average in the northern hemisphere, as in the dipolar initial conditions. By contrast, a negative value indicates that the average polarity is opposite to that imposed in the initial conditions.

The flat evolution over the first 800 days corresponds to the linear growth phase of the magnetic energy, where the field evolves slowly away from its imposed initial dipolar topology and north-south orientation. As the fields with negative polarity gain in strength, a complex competition between the two polarities, directly related to the turbulent nature of the dynamo, leads to a chaotic and irregular variation of the average polarity. Several field reversals do occur on a timescale of about 500 days, but there is little evidence for systematic cyclic behavior. This timescale is comparable to the 1.5 yr periods found by Gilman (1983) in some of his Boussinesq dynamo simulations. Glatzmaier (1985a, 1987) inferred longer reversal timescales ($\sim$10 yr) in his simulations that incorporated compressibility via the anelastic approximation as here and included convective penetration into an underlying stable region. Like Glatzmaier's, our simulations only cover about 10 yr so they would not capture longer term cyclic behavior if it were present. However, the chaotic short-term evolution suggests that longer term periodic behavior is unlikely for the configuration that we have adopted here.

Our high-resolution simulations confirm that the timescale for field reversal within the convective envelope itself is too short and that without a stable layer such as the solar tachocline such simulations are unlikely to reproduce the global-scale dynamo and 22 yr activity cycle observed in the Sun. There is no systematic latitudinal propagation of $\langle B_p \rangle$ over the 4000 days that we have been able to compute. Rather, the temporal evolution of $\langle B_p \rangle$ is quite complex and highly unpredictable, governed by advection and amplification by turbulent convective motions. Both Gilman and Glatzmaier found poleward propagation of $\langle B_p \rangle$. The main difference between their convective dynamo simulations and ours comes from the level of turbulence and nonaxisymmetry. In case M3, the axisymmetric fields are weak and do not control the dynamical evolution of the flow and magnetic fields but seem, on the contrary, passive, which could in part explain their erratic evolution. The mean poloidal field is generated mainly by the coupling between fluctuating field and flow components, and the generation rate is not in general proportional to the strength of the mean field as is assumed in the classical α-effect.

6.2. *Toroidal Fields*

Figure 12 shows the mean toroidal magnetic field $\langle B_t \rangle$ for the same time snapshots as displayed in Figure 11. We can readily see that it possesses small-scale structure that varies substantially with time. Mixed polarities and intricate topologies are present throughout the simulation domain, with no evident symmetries with respect to the equator. Instantaneous snapshots or time averages reveal weak responses with varying symmetries, but these do not persist for any extended interval. Structures resembling thin tubes with circular cross sections are present, but they generally do not remain coherent long enough to rise and emerge through the surface as a result of magnetic buoyancy. No systematic latitudinal propagation of $\langle B_t \rangle$ is evident in this time sequence or in any that we have studied. This is in contrast with solar observations that reveal regular trends in the emergence of sunspots and related magnetic flux over the 22 yr activity cycle.

The mean toroidal field contains about 1.5% of the total magnetic energy, about a factor of 3 larger than the energy in the mean poloidal field. The production terms in the mean induction equation due to differential rotation (the ω-effect) and convective motions (the α-effect) are of the same order so our simulations may be loosely classified as α^2-ω dynamos.

In the Sun the ratio of mean toroidal to poloidal magnetic energy is at least 100, suggesting that the Sun may not be generating its mean toroidal field solely in the convective zone. Glatzmaier (1984, 1985a, 1985b, 1987) incorporated convective penetration into an underlying stable layer in his dynamo simulations and found that $\langle B_t \rangle$ was a significant fraction ($\sim$85%) of the total magnetic energy. This result suggests that strong axisymmetric toroidal fields are generated

mainly in the stable layer via the ω-effect and strengthens the current paradigm that convection in the solar envelope cannot amplify the mean toroidal field to observed levels without the presence of convective penetration into a stably stratified shear layer such as the solar tachocline. The convection zone continuously supplies disorganized magnetic fields over a wide range of spatial scales to the tachocline, where they are then amplified and organized into extended toroidal structures.

7. FURTHER ASPECTS OF FIELD GENERATION

7.1. *Helicity in Flows and Fields*

It has long been realized that helicity can play an essential role in hydromagnetic dynamo action, particularly in the solar context. Parker's (1955) classical paradigm for the solar dynamo relies on twisting motions in order to generate poloidal field from toroidal field and thus drive the solar activity cycle. Mean field analyses of homogeneous MHD turbulence based on the assumption of scale separation yield an explicit expression for the regeneration rate of the magnetic field (the α-effect) that is directly proportional to the kinetic helicity of the flow, defined as the dot product of velocity and vorticity: $H_k = \boldsymbol{\omega} \cdot \boldsymbol{v}$ (e.g., Moffatt 1978; Krause & Rädler 1980).

The kinetic helicity provides a measure of how much twist is present in the velocity field. Magnetic twist (and writhe; see Moffatt & Ricca 1992) is often measured by the magnetic helicity, defined as the dot product of the magnetic field and the vector potential: $H_m = \boldsymbol{A} \cdot \boldsymbol{B}$. This quantity has particular theoretical significance because it is conserved in ideal (dissipationless) MHD (Biskamp 1993). However, magnetic helicity is very difficult to measure reliably on the Sun. From an observational standpoint, a more practical measure of magnetic twist is the current helicity, defined as the scalar product of the magnetic field and current density: $H_c = \boldsymbol{J} \cdot \boldsymbol{B}$.

Measurements of the radial component of the current helicity in the solar photosphere have revealed a weak latitudinal dependence, tending toward negative values in the northern hemisphere and positive values in the southern hemisphere (Pevtsov et al. 1994, 1995). Helicity indicators in the chromosphere and corona reveal similar hemisphere rules for a variety of structures; the pattern is particularly strong for relatively large scale features such as X-ray sigmoids (Zirker et al. 1997; Pevtsov 2002; Pevtsov et al. 2003). It has been suggested that the expulsion of this magnetic helicity by coronal mass ejections may play a crucial role in altering the global topology of the coronal field during polarity reversals (Low 2001; Low & Zhang 2004).

Figure 13 illustrates the kinetic and current helicity in simulation M3. The kinetic helicity shows a clear variation with latitude. Its amplitude peaks in the upper convection zone where it is negative in the northern hemisphere and positive in the southern hemisphere, reflecting the influence of rotation and density stratification; expanding upflows spin down and contracting downflows spin up, tending to conserve their angular momentum (e.g., Miesch et al. 2000). In the lower convection zone the helicity reverses as downflows encounter the lower boundary and diverge, inducing anticyclonic vorticity. The horizontal view in Figure 13 indicates that much of the kinetic helicity is confined to downflow lanes, reflecting their vortical nature.

The current helicity also tends to peak in downflow lanes, but its latitudinal variation is much less systematic than the kinetic helicity. Current helicity of both signs appears in each hemisphere, often juxtaposed in the same downflow lane. The amplitude of the magnetic helicity peaks in the lower convection zone where there is a weak pattern of positive and negative values in the northern and southern hemisphere, respectively.

These simulation results suggest that the helicity patterns observed in the solar atmosphere may not be produced by turbulent convection in the envelope. Rather, they may originate in the tachocline where flux tubes are formed and subsequently rise to the surface owing to magnetic buoyancy to form active regions. Alternatively, the patterns may arise from the action of Coriolis forces as flux tubes rise through the convection zone or from footpoint motions after they have emerged (e.g., Pevtsov 2002; Fan 2004).

7.2. *Spectral Distributions*

The convection patterns shown in Figure 4 suggest that the magnetic field possesses relatively more small-scale structure than the velocity field. This is verified by the energy spectra shown in Figure 14. The slope of the magnetic energy spectrum is much shallower than the kinetic energy spectrum and generally peaks at higher wavenumbers. Thus, the magnetic energy equals or exceeds the kinetic energy at small scales, even though the ratio of total magnetic to kinetic energy remains small. Throughout most of the convection zone, the magnetic energy spectrum peaks near $\ell \sim 30$, compared with $\ell \sim 12$–15 for the kinetic energy. Near the top of the domain the kinetic energy spectrum peaks at somewhat larger scales $\ell \sim 10$, whereas the magnetic energy spectrum remains relatively flat in the range $\ell = 1$–20.

At degrees $\ell \gtrsim 30$, the spectra suggest some power-law behavior, but it extends for less than a decade in degree so these simulations do not possess an extended inertial range. The slope of the kinetic energy spectrum is substantially steeper than that expected for homogeneous, isotropic, incompressible turbulence, with ($\ell^{-3/2}$) or without ($\ell^{-5/3}$) magnetic fields (e.g., Biskamp 1993). Estimates based on curve fits to the kinetic energy spectrum yield slopes steeper than ℓ^{-3}. The magnetic energy spectra are shallower but still fall off faster than predicted for homogeneous, isotropic, incompressible MHD turbulence ($\ell^{-3/2}$).

7.3. *Probability Density Functions*

The pdf's can generally provide more information about the structure and dynamics of a flow than spectral analyses alone. Indeed, in a homogeneous flow, the energy spectra are simply related to the first moment of the corresponding two-point pdf. We here consider the one-point pdf of the velocity and magnetic field variables as given by the histogram of values at all grid points, corrected for the grid convergence at the poles. Results are shown in Figure 15.

Idealized isotropic, homogeneous turbulence has Gaussian velocity pdf's, but departures from Gaussian statistics are known to be present in real-world turbulent flows. Velocity differences and derivatives in particular generally have non-Gaussian pdf's that are often characterized by stretched exponentials $\exp(-\beta)$ with $0.5 \leq \beta \leq 2$ (e.g., She et al. 1988; Castaing et al. 1990; Vincent & Meneguzzi 1991; Kailasnath et al. 1992; Pumir 1996). The tails of the distributions are often nearly exponential ($\beta \approx 1$) but can be even flatter, particularly in the viscous dissipation range. A flat slope ($\beta < 2$) indicates an excess of extreme (high amplitude) events relative to a Gaussian distribution, thus reflecting spatial intermittency in the flow that may be associated with coherent

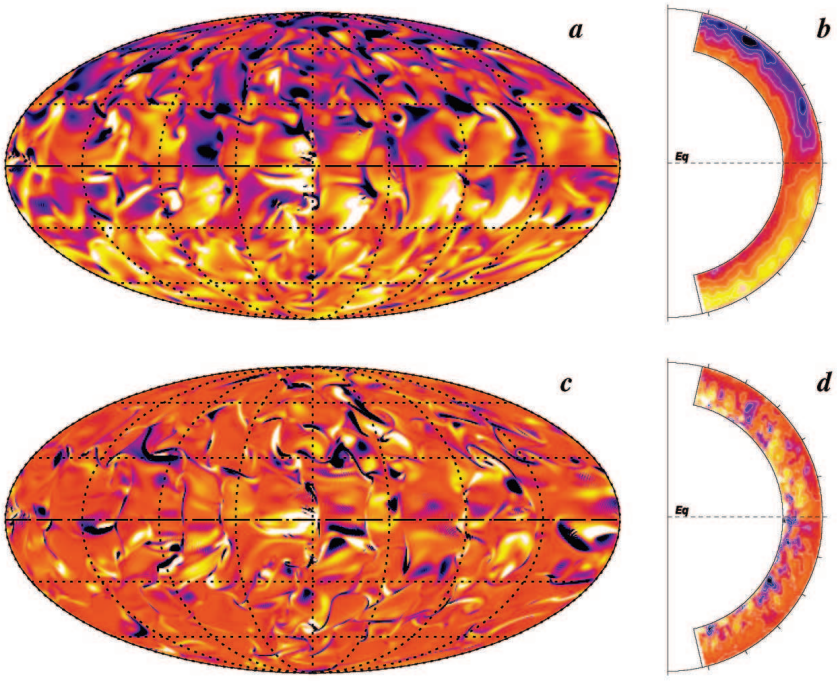

FIG. 13.—(*a*, *b*) Kinetic helicity H_k and (*c*, *d*) current helicity H_c in case M3. Panels (*a*) and (*c*) show global views at the same time and horizontal level (near the top of the layer) as in Fig. 4, and panels (*b*) and (*d*) display meridional profiles averaged over longitude and time. Bright tones denote positive values and dark tones negative values (the color table is as in Fig. 1).

structures (e.g., Vincent & Meneguzzi 1991; Lamballais et al. 1997).

Another way to quantify the asymmetry and intermittency of selected flow and field variables is through moments of the pdf, in particular the skewness $\mathcal{S}$ and kurtosis $\mathcal{K}$, defined as

$$\mathcal{S} = \frac{\int (x-\mu)^3 f(x)\,dx}{\sigma^3 \int f(x)\,dx}, \quad \mathcal{K} = \frac{\int (x-\mu)^4 f(x)\,dx}{\sigma^4 \int f(x)\,dx}, \quad (27)$$

where $f(x)$ is the pdf, x is the abscissa, μ is the mode of the distribution, and σ is the standard deviation:

$$\sigma = \left[\frac{\int (x-\mu)^2 f(x)\,dx}{\int f(x)\,dx}\right]^{1/2}. \quad (28)$$

Gaussian pdf's are characterized by $\mathcal{S} = 0$ and $\mathcal{K} = 3$ and exponential pdf's ($\beta = 1$) by $\mathcal{S} = 0$ and $\mathcal{K} = 6$. A large value for $\mathcal{S}$ indicates asymmetry in the pdf, whereas a large value of $\mathcal{K}$ indicates a high degree of spatial intermittency.

The pdf's for turbulent, compressible, MHD convection in Cartesian geometries have been reported by Brandenburg et al. (1996). They found that the velocity pdf's were generally asymmetric and intermittent, with $\mathcal{K} \simeq 4$–5 for the horizontal components and $\mathcal{K} \simeq 8$ for the vertical component. The vorticity, magnetic field, and current density were more symmetric but also much more intermittent, possessing kurtosis values of $\mathcal{K} \simeq 20$ for $\boldsymbol{B}$ and ω and $\mathcal{K} \simeq 30$ for $\boldsymbol{J}$.

The pdf's in case M3 (Fig. 15) are qualitatively similar to those found by Brandenburg et al. (1996). The radial velocity has nearly exponential tails ($\mathcal{K} = 4.6$) and a negative skewness ($\mathcal{S} = -0.98$); the fastest downflows are more than 150 m s^{-1} compared to about 120 m s^{-1} for upflows. The zonal velocity, v_ϕ, is more Gaussian ($\mathcal{K} = 2.4$) but still asymmetric ($\mathcal{S} = 0.45$), reflecting the influence of the differential rotation. The enstrophy also appears nearly exponential but with two distinct slopes, flattening out for the highest amplitude events. This implies a very high degree of intermittency ($\mathcal{K} = 270$). The radial and toroidal magnetic fields are more intermittent than the velocity field ($\mathcal{K} = 79$, 11) and appear to be more symmetric, although several outlier points in the extreme tails of the B_r pdf give rise to a relatively large skewness, $\mathcal{S} = -1.3$ ($\mathcal{S} = 0.18$ for the B_ϕ pdf). Maximum field strengths reach about 5000 G for the toroidal field and somewhat less (2000 G) for the radial field. The relatively intermittent spatial structure of the magnetic field is also apparent in the pdf of J^2, which possesses an even higher kurtosis ($\mathcal{K} = 440$) than the enstrophy. Note that the kurtosis values quoted here for the enstrophy and current density pdf's are much higher than those reported by Brandenburg et al. (1996) primarily because they considered

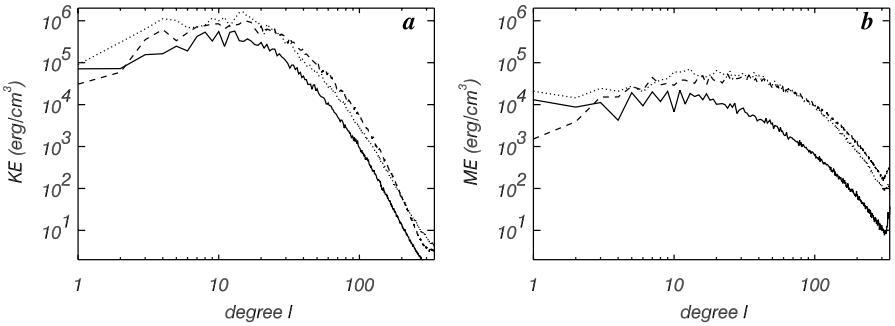

FIG. 14.—Time-averaged (*a*) kinetic and (*b*) magnetic energy spectra shown vs. spherical harmonic degree ℓ (including all azimuthal wavenumbers m but $m = 0$), for case M3 near the top, middle, and bottom of the convection zone (*solid, dashed, and dotted lines, respectively*).

the linear vector fields ω and $\boldsymbol{J}$ whereas we have considered the nonlinear scalar products ω^2 and J^2.

8. SUMMARY

In this paper we report the highest resolution three-dimensional simulations achieved to date of hydromagnetic dynamo action by global-scale turbulent convection and differential rotation in the solar envelope. Building on our own previous hydrodynamic simulations and the pioneering dynamo models of Gilman (1983) and Glatzmaier (1984), we have investigated the generation and maintenance of mean and fluctuating magnetic fields in the solar convection zone, focusing on their structure, evolution, and dynamical influence on the flow field through Lorentz forces. Our simulations are not intended to provide a comprehensive model of the solar dynamo; they do not address important ingredients such as toroidal field generation and storage in the tachocline or flux emergence through the photosphere. Still, they provide essential insight into a crucial element of the global dynamo process, namely, the generation of and coupling between poloidal and toroidal magnetic fields in the convection zone, which is often described in terms of an α-effect and ω-effect.

The numerical experiments we have performed involve the addition of a small seed magnetic field to an existing hydrodynamic simulation. For the parameter regimes considered here, we find that sustained dynamo action occurs when the magnetic Reynolds number Re_m exceeds about 300. If this is the case, then the seed magnetic field grows exponentially and subsequently saturates, reaching a statistically steady state as Lorentz forces begin to feed back on the flow field. Throughout most of this paper we focus on our simulation with the lowest magnetic diffusivity, case M3 ($\mathrm{Re}_m = 486$), in which the steady state magnetic energy is about 7% of the total kinetic energy contained in the convection and differential rotation. At this level of magnetism, Lorentz forces are not strong enough to dramatically change the appearance of the flow; convective patterns in case M3 are similar to those in the nonmagnetic progenitor simulation, case H. Furthermore, the radial energy flux balance through the shell is essentially unaffected; the Poynting flux is negligible and the net convective and diffusive energy fluxes are nearly the same as in case H.

Although Lorentz forces have little effect on the appearance of the convection in case M3 relative to case H, they do have a substantial influence on the structure and evolution of mean flows. Fluctuating magnetic fields transport angular momentum poleward via Maxwell stresses, decreasing the magnitude of the differential rotation. This leads to a decrease in the angular velocity contrast between the equator and latitudes of 60° from 34% in case H to 24% in case M3. Magnetic tension forces associated with the mean (axisymmetric) poloidal field also tend to suppress rotational shear, but this process is much less efficient than Maxwell stresses and plays a negligible role in the maintenance of the global rotation profile. Despite the inhibiting effects of Lorentz forces, case M3 is able to sustain a strong differential rotation comparable in amplitude and structure to the solar internal rotation inferred from helioseismology.

The meridional circulation in the simulations reported here is generally characterized by multiple cells in latitude and radius and large temporal variations over timescales of weeks and months. This spatial and temporal variation is not surprising, since the circulation arises from small differences in large forces that fluctuate substantially in space and time, including Reynolds stresses, Maxwell stresses, thermal (baroclinic) driving, and Coriolis forces operating on the differential rotation. Still, it is in sharp contrast to many solar dynamo models that assume that the meridional circulation is relatively smooth and steady, dominated by one or two large cells in each hemisphere (e.g., Wang & Sheeley 1991; Durney 1997; Dikpati & Charbonneau 1999). Doppler measurements of photospheric flows and local-domain helioseismic inversions typically reveal systematic circulation patterns in the surface layers of the Sun, with poleward flow of about 20 m s^{-1} at low latitudes and some time variation (e.g., Hathaway et al. 1996; Haber et al. 2000). Although these analyses lie outside our computational domain, the results are roughly consistent with our simulations: the meridional flows at low latitudes near the top of the shell are consistently poleward when averaged over several months, although these cells only extend up to about 30° in latitude (see Fig. 9). Somewhat deeper helioseismic probing (down to $\sim 0.98 R_*$), still in local domains, provides some evidence for large temporal fluctuations and multiple cells in radius (Haber et al. 2002), but little is currently known about circulation patterns below about $0.97 R_*$. Characterizing the nature of the meridional flow in the deep convection zone is thus an important future challenge for helioseismology.

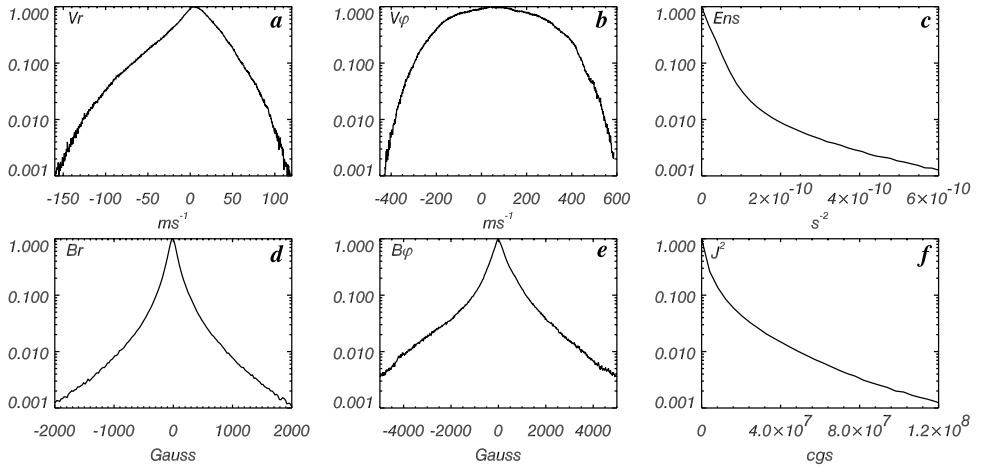

FIG. 15.—The pdf's of (*a*) the radial velocity v_r, (*b*) the zonal velocity v_ϕ, (*c*) the enstrophy ω^2, (*d*) the radial magnetic field B_r, (*e*) the toroidal magnetic field B_ϕ, and (*f*) the square of the current density J^2 in case M3. All pdf's are averaged over time and correspond to a horizontal level near the top of the shell.

About 98% of the magnetic energy in our simulations is contained in the fluctuating (nonaxisymmetric) field components that dominate the Lorentz forces and the induction equation. These components exhibit a complex spatial structure and rapid time evolution as they are amplified, advected, and distorted by convective motions. The distortion is particularly pronounced at midlatitudes, around 25°, where there is a change in the nature of the convective patterns from the north-south aligned downflow structures that dominate the equatorial regions to the more isotropic high-latitude network. The magnetic field possesses more small-scale structure and is significantly more intermittent than the velocity field, a result that is best demonstrated by considering the spectra and pdf's presented in § 7. The pdf's are in general non-Gaussian and asymmetric, in contrast to homogeneous, isotropic turbulence.

There is a noticeable difference in the topology of the radial and toroidal magnetic field components. Particularly near the top of the convection zone, the radial field B_r concentrates in downflow lanes where fields of opposite polarity are brought together by converging horizontal flows, thus promoting magnetic reconnection, and where magnetic structures are twisted and distorted by vorticity and shear. Both the kinetic helicity $\boldsymbol{\omega}\cdot\boldsymbol{v}$ and the current helicity $\boldsymbol{J}\cdot\boldsymbol{B}$ peak in these vortical downflow lanes. However, unlike the kinetic helicity, the current helicity does not exhibit a strong sign reversal in the northern and southern hemispheres; both signs are distributed across all latitudes, often in close proximity. A potential extrapolation of the radial field beyond the outer boundary of our domain reveals a complex web of magnetic loops, exhibiting both local and long-range connectivity across the surface.

Relative to the radial field, the toroidal field B_ϕ is organized into larger scale ribbons and sheets that are stretched out in longitude by the differential rotation and that are not in general confined to downflow lanes. Near the top of the convection zone, broad patches of like-signed toroidal field exist between the north-south aligned downflow lanes at low latitudes. These patches are typically confined to the surface layers, with a relatively small radial extent. Although some structures resemble toroidal flux tubes, they are rapidly advected and distorted by convective motions and generally lose their identity before magnetic buoyancy forces would otherwise cause them to rise and emerge from the surface. Peak field strengths reach about 4000–5000 G for the toroidal field and about 2000 G for the radial field.

The mean poloidal and toroidal fields have much smaller amplitudes than the fluctuating fields in our simulations, but nevertheless they have particular significance for solar dynamo theory. Our simulations do not exhibit the organized structure, systematic propagation patterns, and periodic polarity reversals that are known to exist in the Sun. Rather, they possess a relatively complex spatial and temporal dependence that can be attributed to the highly nonlinear nature of the fluctuating velocity and magnetic field correlations through which they are principally maintained.

The energy in the mean toroidal field in case M3 is about a factor of 3 larger than that in the mean poloidal field. This asymmetry suggests that the differential rotation plays an important role in the generation of mean fields via the ω-effect, in addition to the contribution from convective motions that can be loosely regarded as a (nontraditional) α-effect. By contrast, the fluctuating poloidal and toroidal fields are comparable in amplitude, suggesting that the ω-effect plays a smaller role. However, the influence of differential rotation is still evident in the morphology of the fluctuating toroidal field (see Fig. 7*b*). The magnitude of the mean poloidal field near the surface in our simulations (∼5–10 G; see Fig. 11) is comparable to the large-scale poloidal field at the surface of the Sun estimated from photospheric and coronal observations (e.g., Gibson et al. 1999). However, the peak strength of the mean toroidal field in our simulations (∼800 G) is less than the field strength thought to exist in concentrated flux tubes in the solar interior where the estimated field strength ranges from 10^4–10^5 G near the base of the convection zone to $\sim 10^3$ G near the surface (e.g., Fisher et al. 2000). The relatively weak toroidal fields in our simulations

can likely be attributed to the absence of a tachocline where toroidal flux can be efficiently stored and amplified by strong rotational shear.

The tachocline is an essential ingredient of the solar dynamo that is missing from the models reported here. It likely plays a central role in many aspects of the solar activity cycle, including the structure, strength, and emergence latitudes of sunspots and active regions as reflected, for example, by the well-known "butterfly diagram." The large differential rotation and stable stratification in the lower portion of the tachocline promote the generation and storage of strong toroidal fields, which are thought to account for much of the magnetic activity observed in the solar atmosphere. Coupling between the convection zone and the radiative interior may also help to regularize the structure and evolution of the mean poloidal field, producing dipole configurations and cyclic reversals. We are now working to improve our dynamo simulations by incorporating convective penetration into an underlying stable region and a layer of rotational shear similar in nature to the solar tachocline. Results from these models will be published in forthcoming papers.

We thank Nicholas Brummell, Marc DeRosa, Emmanuel Dormy, Peter Gilman, Annick Pouquet, and Jean-Paul Zahn for helpful discussions. This work was partly supported by NASA through SEC Theory Program grants NAG5-8133, NAG5-12815 and work orders W-10, 175 and W-10, 177, and by NSF through grant ATM-9731676. Various phases of the simulations with ASH were carried out with NSF PACI support of the San Diego Supercomputer Center (SDSC), the National Center for Supercomputing Applications (NCSA), and the Pittsburgh Supercomputing Center (PSC), as well as with the Centre de Calcul pour la Recherche et la Technologie (CCRT) of CEA at Bruyère-le-Chatel. Much of the analysis of the extensive data sets was carried out in the Laboratory for Computational Dynamics (LCD) within JILA.

APPENDIX

MODEL EQUATIONS

The anelastic equations (1)–(7) (§ 2.1) define our physical model. Here we express these equations as they are solved by our numerical algorithm, making use of the velocity and magnetic field decomposition in equations (8) and (9). Diagnostic equations for the stream functions and potentials W, Z, A, and C are obtained by considering the vertical component of the momentum and induction equations and the vertical component of their curl. A Poisson equation for pressure can then be derived by taking the divergence of the momentum equation. However, the additional radial derivative this would require can compromise the accuracy of the solution, particularly when applied to the nonlinear advection terms. Since horizontal derivatives are more accurate than vertical derivatives, we choose to only take the horizontal divergence of the momentum equations rather than the full divergence. This results in a diagnostic equation for the horizontal divergence of the velocity field, which involves $\partial W/\partial r$ and the horizontal Laplacian of the pressure perturbation P. The system also includes the energy equation expressed in terms of the specific entropy perturbation S. A spherical harmonic transformation is applied to the governing equations before they are discretized in time so the time stepping occurs in spectral space: (ℓ, m, r). After some manipulation, the governing equations for the spherical harmonic coefficients of the state variables can be expressed as follows:

$$\frac{\ell(\ell+1)}{r^2}\frac{\partial W_{\ell m}}{\partial t} = \mathcal{L}^W + \mathcal{N}^W, \tag{A1}$$

$$-\frac{\ell(\ell+1)}{r^2}\frac{\partial}{\partial t}\left(\frac{\partial W_{\ell m}}{\partial r}\right) = \mathcal{L}^P + \mathcal{N}^P, \tag{A2}$$

$$\frac{\ell(\ell+1)}{r^2}\frac{\partial Z_{\ell m}}{\partial t} = \mathcal{L}^Z + \mathcal{N}^Z, \tag{A3}$$

$$\frac{\partial S_{\ell m}}{\partial t} = \mathcal{L}^S + \mathcal{N}^S, \tag{A4}$$

$$\frac{\ell(\ell+1)}{r^2}\frac{\partial A_{\ell m}}{\partial t} = \mathcal{L}^A + \mathcal{N}^A, \tag{A5}$$

$$\frac{\ell(\ell+1)}{r^2}\frac{\partial C_{\ell m}}{\partial t} = \mathcal{L}^C + \mathcal{N}^C. \tag{A6}$$

In these expressions, the $\mathcal{L}$ denote the linear diffusion, pressure gradient, buoyancy, and volume heating terms that are implemented using a semi-implicit, Crank-Nicholson time-stepping method:

$$\mathcal{L}^W = -\frac{\partial P_{\ell m}}{\partial r} - g\rho_{\ell m} + \nu\left[\frac{\ell(\ell+1)}{r^2}\right]\left\{\frac{\partial^2 W_{\ell m}}{\partial r^2} + \left(2\frac{d\ln\nu}{dr} - \frac{1}{3}\frac{d\ln\bar{\rho}}{dr}\right)\frac{\partial W_{\ell m}}{\partial r}\right.$$
$$\left. - \left[\frac{4}{3}\left(\frac{d\ln\nu}{dr}\frac{d\ln\bar{\rho}}{dr} + \frac{d^2\ln\bar{\rho}}{dr^2} + \frac{1}{r}\frac{d\ln\bar{\rho}}{dr} + \frac{3}{r}\frac{d\ln\nu}{dr}\right) + \frac{\ell(\ell+1)}{r^2}\right]W_{\ell m}\right\},$$

$$\mathcal{L}^P = \left[\frac{\ell(\ell+1)}{r^2}\right] P_{lm} - \nu\left[\frac{\ell(\ell+1)}{r^2}\right]\left\{\frac{\partial^3 W_{\ell m}}{\partial r^3} + \left(\frac{d\ln\nu}{dr} - \frac{d\ln\bar{\rho}}{dr}\right)\frac{\partial^2 W_{\ell m}}{\partial r^2}\right.$$
$$\left. - \left[\frac{2}{r}\frac{d\ln\bar{\rho}}{dr} + \frac{d^2\ln\bar{\rho}}{dr^2} + \frac{2}{r}\frac{d\ln\nu}{dr} + \frac{d\ln\nu}{dr}\frac{d\ln\bar{\rho}}{dr} + \frac{\ell(\ell+1)}{r^2}\right]\frac{\partial W_{\ell m}}{\partial r} - \left(\frac{d\ln\nu}{dr} + \frac{2}{r} + \frac{2}{3}\frac{d\ln\bar{\rho}}{dr}\right)\frac{\ell(\ell+1)}{r^2} W_{\ell m}\right\},$$

$$\mathcal{L}^Z = \nu\left[\frac{\ell(\ell+1)}{r^2}\right]\left\{\frac{\partial^2 Z_{\ell m}}{\partial r^2} + \left(\frac{d\ln\nu}{dr} - \frac{d\ln\bar{\rho}}{dr}\right)\frac{\partial Z_{\ell m}}{\partial r} - \left[\frac{2}{r}\frac{d\ln\nu}{dr} + \frac{d\ln\bar{\rho}}{dr}\frac{d\ln\nu}{dr} + \frac{d^2\ln\bar{\rho}}{dr^2} + \frac{2}{r}\frac{d\ln\bar{\rho}}{dr} - \frac{\ell(\ell+1)}{r^2}\right] Z_{\ell m}\right\},$$

$$\mathcal{L}^S = -\frac{\ell(\ell+1)}{r^2}\frac{d\bar{S}}{dr} W_{\ell m} + \frac{\kappa_r C_P}{\bar{T}}\left\{\frac{\partial^2}{\partial r^2} + \left[\frac{d}{dr}\ln\left(r^2\kappa_r\bar{\rho}\right)\right]\frac{\partial}{\partial r}\right\}\left(T_{\ell m} + \bar{T}\right) - \frac{\kappa_r C_P}{\bar{T}}\frac{\ell(\ell+1)}{r^2} T_{\ell m}$$
$$+ \kappa\left\{\frac{\partial^2}{\partial r^2} + \left[\frac{d}{dr}\ln\left(r^2\kappa\bar{\rho}\bar{T}\right)\right]\frac{\partial}{\partial r}\right\}\left(S_{\ell m} + \bar{S}\right) - \kappa\frac{\ell(\ell+1)}{r^2} S_{\ell m},$$

$$\mathcal{L}^A = \eta\left[\frac{\ell(\ell+1)}{r^2}\right]\left[\frac{\partial^2 A_{\ell m}}{\partial r^2} + \frac{d\ln\eta}{dr}\frac{\partial A_{\ell m}}{\partial r} - \frac{\ell(\ell+1)}{r^2} A_{\ell m}\right],$$

and

$$\mathcal{L}^C = \eta\left[\frac{\ell(\ell+1)}{r^2}\right]\left[\frac{\partial^2 C_{\ell m}}{\partial r^2} - \frac{\ell(\ell+1)}{r^2} C_{\ell m}\right].$$

The perfect gas equation of state implies

$$\rho_{\ell m} = \bar{\rho}\left(\frac{1}{\gamma}\frac{P_{\ell m}}{\bar{P}} - \frac{S_{\ell m}}{c_p}\right) \tag{A7}$$

and

$$T_{\ell m} = \bar{T}\left(\frac{\gamma - 1}{\gamma}\frac{P_{\ell m}}{\bar{P}} + \frac{S_{\ell m}}{c_p}\right). \tag{A8}$$

The $\mathcal{N}$ terms in equations (A1)–(A6) include nonlinear advection terms that are implemented using an explicit, two-level Adams-Bashforth time-stepping method. Although the Coriolis terms are formally linear, they are also included in the $\mathcal{N}$ terms because, unlike the other linear terms, the resulting coefficients depend on azimuthal wavenumber m, and they couple the vertical vorticity equation to the vertical momentum and horizontal divergence equations. This would greatly complicate the matrix solution involved in the Crank-Nicholson method. Thus, the $\mathcal{N}$ terms in the momentum equations include Coriolis terms, which can be written in spherical harmonic space as

$$\mathcal{N}^W = \mathcal{A}^W_{\ell m} + \tau + \frac{2\Omega_0}{r}\left[\imath m\frac{\partial W_{\ell m}}{\partial r} - (\ell-1)c^m_\ell Z^m_{\ell-1} + (\ell+2)c^m_{\ell+1} Z^m_{\ell+1}\right],$$

$$\mathcal{N}^P = \mathcal{A}^P_{\ell m} + \frac{2\Omega_0}{r^2}\left\{-\imath m\left[\frac{\partial W_{\ell m}}{\partial r} + \frac{\ell(\ell+1)}{r} W_{\ell m}\right] + \left(\ell^2 - 1\right)c^m_\ell Z^m_{\ell-1} + \ell(\ell+2)c^m_{\ell+1} Z^m_{\ell+1}\right\},$$

and

$$\mathcal{N}^Z = \mathcal{A}^Z_{\ell m} + \frac{2\Omega_0}{r^2}\left[-\frac{\ell(\ell^2-1)}{r}c^m_\ell W^m_{\ell-1} + \frac{\ell(\ell+1)(\ell+2)}{r}c^m_{\ell+1} W^m_{\ell+1} + \left(\ell^2-1\right)c^m_\ell\frac{\partial W^m_{\ell-1}}{\partial r} + \ell(\ell+2)c^m_{\ell+1}\frac{\partial W^m_{\ell+1}}{\partial r} + \imath m Z_{\ell m}\right].$$

The τ appearing in $\mathcal{N}^W$ is the departure of the reference state from hydrostatic equilibrium (Clune et al. 1999). The $\mathcal{A}^i_{\ell m}$ in these equations represent the spherical harmonic coefficients of the nonlinear velocity advection terms and Lorentz forces. If we define their corresponding configuration space representation as

$$\mathcal{A}^i(r,\ \theta,\ \phi,\ t) = \sum_{\ell,m}\mathcal{A}^i_{\ell m}(r,\ t) Y_{\ell m}(\theta,\ \phi) \qquad (i = W,\ P,\ Z), \tag{A9}$$

then

$$\mathcal{A}^W = -\bar{\rho}\left(v_r\frac{\partial v_r}{\partial r} + \frac{v_\theta}{r}\frac{\partial v_r}{\partial \theta} + \frac{v_\phi}{r\sin\theta}\frac{\partial v_r}{\partial \phi} - \frac{v_\theta^2 + v_\phi^2}{r}\right) + J_\theta B_\phi - J_\phi B_\theta, \tag{A10}$$

$$\mathcal{A}^P = \frac{1}{r\sin\theta}\left[\frac{\partial}{\partial\theta}(\sin\theta\mathcal{A}_\theta) + \frac{\partial \mathcal{A}_\phi}{\partial\phi}\right], \tag{A11}$$

and

$$A^Z = \frac{1}{r\sin\theta}\left[\frac{\partial}{\partial\theta}(\sin\theta\mathcal{A}_\phi) - \frac{\partial \mathcal{A}_\theta}{\partial\phi}\right], \tag{A12}$$

where

$$\mathcal{A}_\theta = -\bar{\rho}\left(v_r\frac{\partial v_\theta}{\partial r} + \frac{v_\theta}{r}\frac{\partial v_\theta}{\partial\theta} + \frac{v_\phi}{r\sin\theta}\frac{\partial v_\theta}{\partial\phi} + \frac{v_r v_\theta}{r} - \frac{\cos\theta}{r\sin\theta}v_\phi^2\right) + J_\phi B_r - J_r B_\phi, \tag{A13}$$

$$\mathcal{A}_\phi = -\bar{\rho}\left(v_r\frac{\partial v_\phi}{\partial r} + \frac{v_\theta}{r}\frac{\partial v_\phi}{\partial\theta} + \frac{v_\phi}{r\sin\theta}\frac{\partial v_\phi}{\partial\phi} + \frac{v_r v_\phi}{r} + \frac{\cos\theta}{r\sin\theta}v_\theta v_\phi\right) + J_r B_\theta - J_\theta B_r, \tag{A14}$$

and $\boldsymbol{J} = \nabla\times\boldsymbol{B}/(4\pi)$. The dimensional current density is given by $\boldsymbol{j} = c\boldsymbol{J}$.

Likewise, the remaining $\mathcal{N}$ terms represent the spherical harmonic coefficients corresponding to the nonlinear terms in the energy and induction equations:

$$\mathcal{A}^i(r,\ \theta,\ \phi,\ t) = \sum_{\ell,m}\mathcal{N}^i(\ell,\ m,\ r,\ t)Y_{\ell m}(\theta,\ \phi) \qquad (i = S,\ A,\ C), \tag{A15}$$

where

$$\mathcal{A}^S = v_r\frac{\partial s}{\partial r} + \frac{v_\theta}{r}\frac{\partial s}{\partial\theta} + \frac{v_\phi}{r\sin\theta}\frac{\partial S}{\partial\phi} + \frac{2\nu}{\bar{T}}\left[e_{ij}e_{ij} - \frac{1}{3}\left(v_r\frac{d\ln\bar{\rho}}{dr}\right)^2\right] + \frac{4\pi\eta}{c^2\bar{\rho}\bar{T}}j^2 + \frac{\epsilon}{\bar{T}}, \tag{A16}$$

$$\mathcal{A}^A = -\frac{1}{r^2\sin\theta}\frac{\partial}{\partial\theta}\left(\sin\theta\frac{\partial\mathcal{E}_r}{\partial\theta}\right) - \frac{1}{r^2\sin^2\theta}\frac{\partial^2\mathcal{E}_r}{\partial\phi^2} + \frac{1}{r^2}\frac{\partial}{\partial r}\left\{\frac{r}{\sin\theta}\left[\frac{\partial}{\partial\theta}(\sin\theta\mathcal{E}_\theta) + \frac{\partial\mathcal{E}_\phi}{\partial\phi}\right]\right\}, \tag{A17}$$

$$\mathcal{A}^C = \frac{1}{r\sin\theta}\left[\frac{\partial}{\partial\theta}(\sin\theta\mathcal{E}_\phi) - \frac{\partial\mathcal{E}_\theta}{\partial\phi}\right], \tag{A18}$$

and $\mathcal{E} = \boldsymbol{v}\times\boldsymbol{B}$.

The boundary conditions discussed in § 2.1, expressed here in spectral space, require that the boundaries be impenetrable,

$$W_{\ell m}(r_{\rm bot},\ t) = W_{\ell m}(r_{\rm top},\ t) = 0, \tag{A19}$$

and stress-free,

$$\frac{\partial^2 W_{\ell m}}{\partial r^2}(r,\ t) - \left(\frac{2}{r} + \frac{d\ln\bar{\rho}}{dr}\right)\frac{\partial W_{\ell m}}{\partial r}(r,\ t) = 0 \qquad (r = r_{\rm bot},\ r_{\rm top}), \tag{A20}$$

$$\frac{\partial Z_{\ell m}}{\partial r}(r,\ t) - \left(\frac{2}{r} + \frac{d\ln\bar{\rho}}{dr}\right)Z_{\ell m}(r,\ t) = 0 \qquad (r = r_{\rm bot},\ r_{\rm top}). \tag{A21}$$

We also fix the entropy gradient at the top and bottom boundaries at the value defined by the initial reference state by requiring the perturbation entropy gradient to vanish:

$$\frac{\partial S_{\ell m}}{\partial r}(r_{\rm bot},\ t) = \frac{\partial S_{\ell m}}{\partial r}(r_{\rm top},\ t) = 0. \tag{A22}$$

The magnetic boundary conditions are chosen such that the interior field is continuous with an external potential field above and below the computational domain:

$$A_{\ell m}(r_{\rm bot},\ t) = A_{\ell m}\big(r_{\rm top},\ t\big) = 0, \tag{A23}$$

$$\frac{\partial C_{\ell m}}{\partial r}\big(r_{\rm top},\ t\big) + \frac{\ell}{r_{top}} C_{\ell m}\big(r_{\rm top},\ t\big) = 0, \qquad \frac{\partial C_{\ell m}}{\partial r}(r_{\rm bot},\ t) - \frac{\ell+1}{r_{bot}} C_{\ell m}(r_{\rm bot},\ t) = 0. \tag{A24}$$

For comparison purposes, we also did several simulations in which the magnetic field was required to be radial at the boundaries, corresponding to a highly permeable external medium (Jackson 1999):

$$\frac{\partial C_{\ell m}}{\partial r}(r,\ t) = 0, \qquad A_{\ell m}(r,\ t) = 0 \qquad \big(r = r_{\rm bot},\ r_{\rm top}\big). \tag{A25}$$

Further details on the numerical algorithm are discussed in Clune et al. (1999).

REFERENCES

Babcock, H. W. 1961, ApJ, 133, 572
Beer, J., Tobias, S. M., & Weiss, N. O. 1998, Sol. Phys., 181, 237
Biskamp, D. 1993, Nonlinear Magnetohydrodynamics (Cambridge: Cambridge Univ. Press)
Brandenburg, A., Jennings, R. L., Nordlund, Å., Rieutord, M., Stein, R. F., & Tuominen, I. 1996, J. Fluid Mech., 306, 325
Brandenburg, A., & Subramanian, K. 2004, preprint (astro-ph/0405052)
Browning, M. K., Brun, A. S., & Toomre, J. 2004, ApJ, 601, 512
Brummell, N. H., Hurlburt, N. E., & Toomre, J. 1998, ApJ, 493, 955
Brun, A. S. 2004, Sol. Phys., 220, 333
Brun, A. S., Antia, H. M., Chitre, S. M., & Zahn, J.-P. 2002, A&A, 391, 725
Brun, A. S., & Toomre, J. 2002, ApJ, 570, 865
Busse, F. H. 1970, Phys. J. Fluid Mech., 44, 441
———. 2000a, Annu. Rev. Fluid Mech., 32, 383
———. 2000b, Phys. Fluids, 14, 1301
Busse, F. H., & Cuong, P. G. 1977, Geophys. Astrophys. Fluid Dyn., 8, 17
Castaing, B., Gagne, Y., & Hopfinger, E. J. 1990, Physica D, 46, 177
Cattaneo, F. 1999, ApJ, 515, L39
Cattaneo, F., Emonet, T., & Weiss, N. O. 2003, ApJ, 588, 1183
Cattaneo, F., & Hughes, D. W. 1996, Phys. Rev. E, 54, 4532
———. 2001, Astron. Geophys., 42 (3), 18
Charbonneau, P., & MacGregor, K. B. 1997, ApJ, 486, 502
Childress, S., & Gilbert A. D. 1995, Stretch, Twist, Fold: The Fast Dynamo (Berlin: Springer)
Christensen, U., Olson, P., & Glatzmaier, G. A. 1999, Geophys. J. Int., 138, 393
Clune, T. L., Elliott, J. R., Glatzmaier, G. A., Miesch, M. S., & Toomre, J. 1999, Parallel Comput., 25, 361
DeRosa, M. L., Gilman, P. A., & Toomre, J. 2002, ApJ, 581, 1356
Dikpati, M., & Charbonneau, P. 1999, ApJ, 518, 508
Durney, B. R. 1997, ApJ, 486, 1065
———. 1999, ApJ, 511, 945
Eddy, J. A., Gilman, P. A., & Trotter, D. E. 1976, Sol. Phys., 46, 3
Elliott, J. R., Miesch, M. S., & Toomre, J. 2000, ApJ, 533, 546
Fan, Y. 2004, Living Reviews in Solar Physics, http://solarphysics.livingreviews.org
Fisher, G. H., Fan Y., Longcope, D. W., Linton, M. G., & Pevtsov, A. A. 2000, Sol. Phys., 192, 119
Gibson, S. E., et al. 1999, ApJ, 520, 871
Gilman, P. A. 1983, ApJS, 53, 243
———. 2000, Sol. Phys., 192, 27
Gilman, P. A., & Miller, J. 1981, ApJS, 46, 211
Glatzmaier, G. A. 1984, J. Comput. Phys., 55, 461
———. 1985a, ApJ, 291, 300
———. 1985b, Geophys. Astrophys. Fluid Dyn., 31, 137
———. 1987, in The Internal Solar Angular Velocity, ed. B. R. Durney & S. Sofia (Dordrecht: Reidel), 263
Glatzmaier, G. A., & Gilman, P. 1982, ApJ, 256, 316
Gough, D. O., & Toomre, J. 1991, ARA&A, 29, 627
Grote, E., Busse, F. H., & Tilgner, A. 1999, Phys. Rev. E, 60, 5025
———. 2000, Phys. Earth Planet. Inter., 117, 259
Haber, D. A., Hindman, B. W., Toomre, J., Bogart, R. S., Larsen, R. M., & Hill, F. 2002, ApJ, 570, 855
Haber, D. A., Hindman, B. W., Toomre, J., Bogart, R. S., Thompson, M. J., & Hill, F. 2000, Sol. Phys., 192, 335
Harvey, J. W., et al. 1996, Science, 272, 1284
Hathaway, D. H., et al. 1996, Science, 272, 1306
Hindman, B. W., Gizon, L., Duvall, T. L., Jr., Haber, D. A. & Toomre, J. 2004, ApJ, 613, 1266
Howe, R., Christensen-Dalsgaard, J., Hill, F., Komm, R. W., Larsen, R. M., Schou, J., Thompson, M. J., & Toomre, J. 2000, ApJ, 533, L163
Ishihara, N., & Kida, S. 2002, J. Fluid Mech., 465, 1
Jackson, J. D. 1999, Classical Electrodynamics (3rd ed.; New York: Wiley)
Jacobs, J. A. 1987, Geomagnetism (London: Academic)
Kageyama, A., & Sato, T. 1997, Phys. Rev. E, 55, 4617
Kageyama, A., Watanabe, K., & Sato, T. 1993, Phys. Fluids B, 5, 2793
Kailasnath, P., Sreenivasan K. R., & Stolovitzky, G. 1992, Phys. Rev. Lett., 68, 2766
Kichatinov, L. L., & Rüdiger, G. 1995, A&A, 299, 446
Krause, F., & Rädler, K.-H. 1980, Mean-Field Magnetohydrodynamics and Dynamo Theory (1st ed.; Oxford: Pergamon)
Lamballais, E., Lesieur, M., & Métais, O. 1997, Phys. Rev. E, 56, 6761
Leighton, R. B. 1969, ApJ, 156, 1
Low, B. C. 2001, J. Geophys. Res., 106, 25141
Low, B. C., & Zhang, M. 2004, in Solar Variability and Its Effect on Climate (Geophys. Monogr. 141; Washington: AGU), 51
MacGregor, K. B., & Charbonneau, P. 1999, ApJ, 519, 911
Miesch, M. S., Elliott, J. R., Toomre, J., Clune, T. L., Glatzmaier, G. A., & Gilman, P. A. 2000, ApJ, 532, 593
Moffatt, H. K. 1978, Magnetic Field Generation in Electrically Conducting Fluids (Cambridge: Cambridge Univ. Press)
Moffatt, H. K., & Ricca, R. L. 1992, Proc. R. Soc. London A, 439, 411
Ossendrijver, M. 2003, A&A Rev., 11, 287
Parker, E. N. 1955, ApJ, 122, 293
———. 1989, Cosmical Magnetic Fields: Their Origin and Their Activity (Oxford: Clarendon)
———. 1993, ApJ, 408, 707
Pedlosky, J. 1987, Geophysical Fluid Dynamics (New York: Springer)
Pevtsov, A. A. 2002, in Multiwavelength Observations of Coronal Structures and Dynamics, ed. P. Martens & D. Cauffman (COSPAR Colloq. Ser. 13; Dordrecht: Pergamon), 125
Pevtsov, A. A., Balasubramaniam, K. S., & Rogers, J. W. 2003, ApJ, 595, 500
Pevtsov, A. A., Canfield, R. C., & Metcalf, T. R. 1994, ApJ, 425, L117
———. 1995, ApJ, 440, L109
Pumir, A. 1996, Phys. Fluids, 8, 3112
Roberts, P. H., & Glatzmaier, G. A. 2000, Rev. Mod. Phys., 72, 1081
Rüdiger, G., & Brandenburg, A. 1995, A&A, 296, 557
Scherrer, P. H., et al. 1995, Sol. Phys., 162, 129
Schou, J., et al. 1998, ApJ, 505, 390
She, Z.-S., Jackson, E., & Orszag, S. A. 1988, J. Sci. Comput., 3, 407
Spiegel, E. A., & Zahn, J.-P. 1992, A&A, 265, 106
Starr, V. P., & Gilman, P. A. 1966, Pure Appl. Geophys., 64, 145
Stein, R. F., & Nordlund, Å. 2000, Sol. Phys., 192, 91
Stix, M. 2002, The Sun: An Introduction (2nd ed.; Berlin: Springer)
Sun, Z.-P., & Schubert, G. 1995, Phys. Fluids, 7, 2686
Thompson, M. J., Christensen-Dalsgaard, J., Miesch, M. S., & Toomre, J. 2003, ARA&A, 41, 599
Thompson, M. J., et al. 1996, Science, 272, 1300
Tobias, S. M. 1996, A&A, 307, L21
Tobias, S. M., Brummell, N. H., Clune, T. L., & Toomre, J. 2001, ApJ, 549, 1183
Toomre, J. 2002, Science, 296, 64
Vincent, A., & Meneguzzi, M. 1991, J. Fluid Mech., 225, 1
Wang, Y. M., & Sheeley, N. R. 1991, ApJ, 375, 761
Weiss, N. O. 1994, in Lectures on Solar and Planetary Dynamos, ed. M. R. E. Proctor & A. D. Gilbert (Cambridge: Cambridge Univ. Press), 59
Zirker, J. B., Martin, S. F., Harvey, K., & Gaizauskas, V. 1997, Sol. Phys., 175, 27

Chapitre 5

Zone Radiative et Tachocline Solaire

5.1 Contexte Général

Dans le chapitre précédent nous avons étudié la dynamique hautement turbulente des couches externes du Soleil, où la convection, la turbulence, la présence d'un écoulement cisaillé à grande échelle (la rotation différentielle) et d'une circulation méridienne et la génération de champs magnétiques intenses par effet dynamo prennent place et interagissent non linéairement. En comparaison les couches plus profondes du Soleil, formant la zone radiative s'étendant de $r = 0$ à $0.713\ R_\odot$, stablement stratifiée (sans mouvements convectifs), c'est à dire avec un gradient de température subadiabatique, pourraient sembler bien calmes et immobiles! Rien n'est moins vrai!!! En effet la zone radiative du Soleil est également sugette à des écoulements grandes échelles, à la présence d'ondes internes (gravités, inertielles, voire Alfveno-gravito-inertielles) transportant non localement du moment cinétique, ou à de la turbulence liée à des instabilités trouvant leur source principalement dans la rotation (instabilités baroclines par exemple) et/ou dans la présence de champs magnétiques. L'étude de la stabilité et des propriétés dynamiques des zones radiatives sous l'influence couplée de la rotation et du magnétisme et le mélange de la composition chimique qui peut en résulter, fascinent les astrophysiciens depuis longtemps et nombres d'articles ont été écrits sur ce sujet (voir Tayler 1973, 1980, Mestel & Moss 1977, Mestel & Weiss 1987, Mestel 1999, Zahn 1983, 1992, 2004, Spruit et al. 1983, Spruit 1999, 2002 et les nombreuses références cités dans ces articles). Avec l'avénement de l'héliosismologie et l'inversion du profil de rotation du Soleil en rayon et latitude de la surface jusqu'à une profondeur $r = 0.2-0.4R_\odot$ (voir chapitre 2), résultant en la mise en évidence d'un profil de rotation quasi-rigide de la zone radiative (contrairement au profil cisaillé de la zone convective)

et de l'existence d'une tachocline (voir plus bas), expliquer le profil de rotation interne du Soleil est devenu une des grandes priorités de la communauté scientifique. En effet, d'après le célèbre paradoxe de Von-Zeipel, il n'est pas possible d'avoir une équilibre hydrostatique stable pour une zone radiative en rotation. La divergence non-nulle du flux radiatif le long des équipotenitelles d'une étoile en rotation déclenche une circulation méridienne lente (dans le cas solaire), dite d'Eddington-Sweet (voir Sweet 1950, Talon 1997, Zahn 2004) qui si l'étoile tourne de façon uniforme, tendra à établir une rotation différentielle en équilibre avec le gradient de température en latitude (i.e la balance du vent thermique, voir Appendice 4.2, Busse 1981, Zahn 2005). Si la dissipation visqueuse est prise en compte alors le profil de rotation différentiel sera maintenu par advection de moment cinétique associé à la circulaton méridienne, dans le cas inverse la circulation méridienne une fois le vent thermique établi s'arrète. Nous voyons donc que nous pourrions naturellement nous attendre à ce que la zone radiative du Soleil subisse des épisodes de mélange à grande échelle (important pour l'évolution chimique du Soleil), et que son profil de rotation soit différentiel. Vu que cela ne semble pas etre le cas pour ce dernier, il faut invoquer des processus de redistribution du moment cinétique qui agissent sur des temps plus courts qu'un temps d'Edington-Sweet ($\sim 10^7$ ans dans le Soleil). Aujourd'hui plusieurs scénari sont avancés pour expliquer le profil rigide de la zone radiative: celui ci est dû soit à l'action d'ondes internes (Zahn et al. 1997, Talon et al. 2002, Charbonnel et Talon 2005, Rogers & Glatzmaier 2005), soit à l'action d'un champ magnétique fossile (Spruit 1999, 2002, Gough & Mc Intyre 1998). Nous renvoyons le lecteur à la section 5.4 pour une discussion préliminaire d'un instabilité MHD non axisymmétrique apparue dans nos calculs de la zone radiative solaire et nous référons aux articles cités plus haut pour compléter notre discussion des problématiques liées à la zone radiative solaire.

Etroitement connecté a l'établissement ou le maintient d'un profil rigide de la zone radiative, sont les problématiques liées à l'existence, la finesse et les propriètés dynamiques de la tachocline. La tachocline est la zone de transition dans le Soleil entre sa rotation différentielle de la zone convective et celle solide de sa zone radiative interne. Elle est située environ à 0.7 $R_\odot$ et s'étend sur 2-4% du rayon solaire (Figure 5.1 et Charbonneau et al. 1998, Corbard et al. 1999, Couvidat et al. 2003, Thompson et al. 2003). Son existence n'a été mise en évidence par l'héliosismologie que depuis la fin des années 80 et le premier modèle a été développé au en 1992 par E.A. Spiegel et J.-P. Zahn, également à l'origine du nom (tacho=vitesse, cline=pente). Cette zone de fort cisaillement en vitesse joue vraisemblablement un rôle crucial dans la dynamo solaire puisqu'elle serait à la fois à l'origine de la forte amplification du champ magnétique toroidal (sous forme de structures allongées par effet ω) et de son stockage (sur plusieurs

années dans sa partie inférieure et stablement stratifiée) voir chapitre 4. Cependant plusieurs problèmes sur la structure même de cette couche limite reste à résoudre : pourquoi est-elle si fine (seulement 25000 km), quel rôle le champ magnétique joue dans sa dynamique propre, comment le champ magnétique interne (fossile? Gough & McIntyre 1998) interagit avec le champ dynamo, quels types de circulations (lentes ou rapides) et de turbulence (isotrope ou anisotrope) possède-t-elle ?

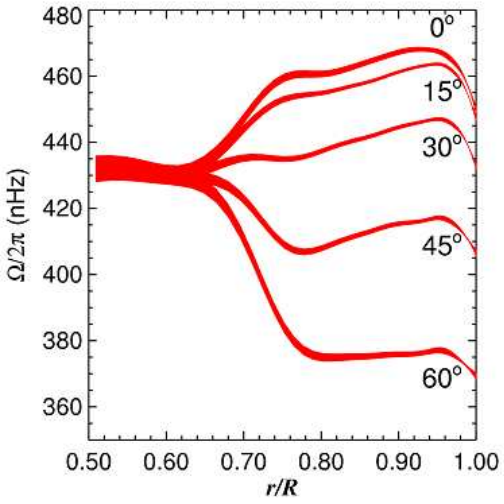

FIG. 5.1 – *Profil de rotation solaire centré sur la tachocline (données GONG). On remarque le fort gradient radial à la base de la zone convective ($r \sim 0.7$ R), permettant la transition entre la rotation différentielle de surface et celle solide de l'intérieur radiatif.*

En suivant Spiegel et Zahn (1992) on peut montrer que le profil de rotation va pénétrer par hyperdiffusion thermique et diffusion visqueuse dans l'intérieur radiatif, si rien ne s'oppose à sa progression. L'équation 4.10 de leur papier donne:

$$\frac{\partial \tilde{\Omega}_i}{\partial t} + \kappa \left(\frac{2\Omega_0}{N}\right)^2 \left(\frac{r^2}{\lambda_i}\right)^2 \frac{\partial^4 \tilde{\Omega}_i}{\partial r^4} - \nu_V \frac{\partial^2 \tilde{\Omega}_i}{\partial r^2} = 0 \tag{5.1}$$

où $\tilde{\Omega}$ est la rotation différentielle, N la fréquence de Brunt-Väissala, λ une valeur propre associée à la dépendance en latitude de la solution et ν_V la viscosité turbulente verticale. Sur la Figure 5.2a, nous traçons pour différentes valeurs du nombre de Prandtl, l'augmentation de l'épaisseur de la tachocline (donc la pénétration de la rotation différentielle $\tilde{\Omega}$) dans la zone radiative en fonction du temps, déduite de l'équation 5.1. Nous déduisons de cette figure qu'il est nécessaire d'avoir un nombre Pr inférieur

à 0.01 pour que l'hyperdiffusion thermique domine la diffusion visqueuse. Figure 5.2b nous représentons les nombres de Prandtl, Prandtl magnétique et de Roberts dans le Soleil en fonction du rayon (déduit d'un modèle solaire 1-D évolué jusqu'à 4.6 Gans, voir Brun et al. (2002)). Nous voyons que Pr est toujours inférieur à 10^{-5} dans le Soleil, ce qui confirme que la propagation de la tachocline est dû à des effets thermiques plutôt que visqueux.

Afin d'expliquer la finesse de la tachocline solaire, Spiegel & Zahn (1992) ont proposé un solution purement hydrodynamique basée sur l'anisotropie de la turbulence dans la zone d'overshooting située à la base de la zone convective solaire. En transportant plus efficacement le moment cinétique horizontalement que verticalement (à cause de la stratification), la turbulence efface le gradient latitudinal de rotation ce qui permet de stopper la progression du cisaillement vers l'intérieur. Elliott (1997) a vérifié numériquement à 2-D que ce processus de turbulence anisotrope donnait bien ce résultat. Plus récemment, Miesch (2003) a validé le concept de l'existence d'un transport anisotrope dans une zone stablement stratifiée turbulente. Cependant beaucoup d'auteurs ont préféré considérer l'aspect MHD de la tachocline, vu qu'il est vrai que la présence d'un champ magnétique est très probable à la base de la zone convective solaire. Deux types de modèles MHD de la tachocline sont alors apparus, lents et rapides (Gilman 2000, Brun 2000). Dans les modèles lents (Rudiger & Kitchatinov 1997, Gough & McIntyre 1998, MacGregor & Charbonneau 1999, Garaud 2002, McIntyre 2003), c'est un champ fossile interne au Soleil qui, par diffusion ohmique, s'oppose à la propagation thermique de la tachocline. Les circulations dans la tachocline sont lentes ($< \mu m/s$) et le processus évolue sur des temps longs ($> 10^6$ ans). Dans les modèles dits rapides, c'est le champ dynamo, principalement toroidal, qui joue un rôle dominant en régulant la dynamique de la tachocline et déclenchant potentiellement des instabilités MHD (Gilman 2000, Dikpati, Cally & Gilman 2004, Forgacs-Dajka 2004). Comme la quasi-totalité de ces modèles sont 2-D (ou 3-D MHD shallow water dans le cas de Dikpati et al. 2004), il parait naturel de s'attaquer au problème que représente la dynamique de la tachocline de façon complètement tridimensionnelle en prenant en compte l'évolution du champ poloidal, la présence d'une circulation méridienne et l'aspect non axisymétrique de la tachocline.

5.2 Le Modèle Numérique

Nous avons donc entrepris, de modéliser dans un premier temps et dans le cas 3-D MHD général, la zone radiative du Soleil entre r=0.3 et 0.7 R en utilisant le code ASH. Notre première intention est de tester l'hypothèse de la tachocline MHD lente

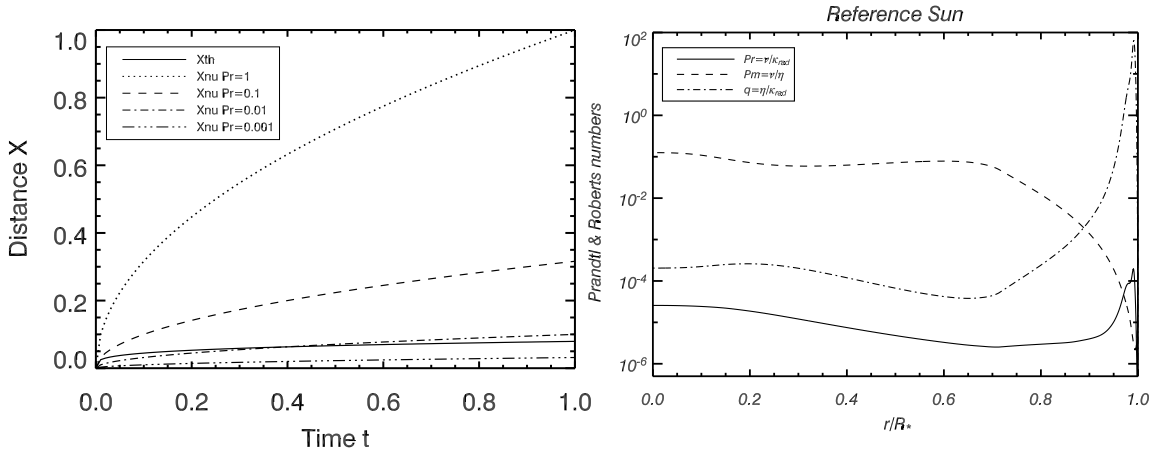

FIG. 5.2 – *a) Propagation en fonction du temps (normalisé par le temps thermique), soit via diffusion visqueuse, soit par hyperdiffusion thermique du cisaillement imposée par la zone convective. On constate qu'il faut que Pr soit inférieur à* 10^{-2} *pour que les processus thermiques dominent comme agent responsable de la progression du cisaillement. b) Nombres de Prandtl, Prandtl magnétique et Roberts en fonction du rayon dans le Soleil (valeurs correctes à un facteur 5 près). On remarque que dans la zone radiative, ces nombres varient peu et sont ordonnés tels que:* $Pr < Q < Pm$.

(proposée par Gough & McIntyre 1998), mais aussi potentiellement rapide, si des instabilités apparaissent. Pour cela nous intégrons dans le temps les équations MHD anélastiques (cf. Appendice 1), pour suivre l'évolution et l'interaction dans une zone radiative d'un champ magnétique avec un champ de vitesse (y compris leur composante poloidale), dans une configuration proche de celle décrite par Gough & McIntyre (1998). Contrairement aux modèles discutés au chapitre précédent, nous démarrons nos modèles de la tachocline solaire, à partir d'un gradient d'entropie stable (i.e positif) ne permettant pas le développement de la convection dans le domaine modélisé. Afin de simuler l'action de la rotation différentielle de la zone convective sur l'intérieur radiatif, nous imposons en permanence un cisaillement en latitude au haut du domaine. Pour le profil en colatitude du cisaillement, nous utilisons la formule suivante qui représente une bonne approximation du profil solaire:

$$\Omega_{bcz}(\theta)/2\pi = A + B\cos^2\theta + C\cos^4\theta\,, \tag{5.2}$$

avec $A = 456$, $B = -42$ et $C = -72$ nHz (Thompson et al. 2003). Les autres conditions aux limites sont:

– murs impénétrables pour la vitesse en haut et en bas

– conditions sans couple pour la vitesse en bas
– luminosité imposée égale luminosité transférée
– raccord à un champ magnétique potentiel en haut et en bas

ce qui se traduit par:

$$\begin{aligned} v_r &= 0|_{r=r_{bot},r_{top}}\ , \\ \frac{\partial}{\partial r}\left(\frac{v_\theta}{r}\right) &= \frac{\partial}{\partial r}\left(\frac{v_\phi}{r}\right) = 0|_{r=r_{bot}}\ , \\ \frac{\partial \bar{S}}{\partial r} &= cst|_{r=r_{bot},r_{top}}\ , \\ \mathbf{B} = \boldsymbol{\nabla}\Phi &=> \Delta\Phi = 0|_{r=r_{bot},r_{top}} \text{ dans le demi domaine} \end{aligned}$$

Afin de déterminer la vitesse de rotation de la zone radiative Ω_0 (du repère), nous évaluons (comme dans Gilman et al. (1989)), la vitesse de rotation nécessaire pour obtenir une balance des couples (ici supposés reliés à une diffusivité turbulente) à l'interface entre la zone de convection et la zone radiative. Le résultat de cette intégrale donne, comme vitesse angulaire:

$$\Omega_0/2\pi = A + B/5 + 3/35C = 441 \text{ nHz} \tag{5.3}$$

Il est intéressant de remarquer que les inversions héliosismiques du profil de rotation de la zone radiative solaire (aussi profondes que $0.2 - 0.3R$, Couvidat et al. 2003, Thompson et al. 2003) prédisent un profil presque plat (en rotation solide), tournant à une vitesse proche de Ω_0 déduit de l'équation 5.3.

Nous démarrons nos simulations avec un champ magnétique initial de type dipolaire et laissons évoluer le modèle sur une échelle de temps correspondant à l'âge actuel du Soleil (sachant qu'un jour dans la simulation correspond à $\sim 10^5$ ans en réalité). Nous ne prenons pas en compte pour l'instant le ralentissement de Ω_0 (par frein magnétique, Skumanich (1972)) et la variation de $\Delta\Omega$ associée. Dans la plupart des modèles calculés la résolution horizontale est $N_\theta \times N_\phi = 128 \times 256$ et N_r vaut 65, 129 ou 193 selon la valeur décroissante du nombre de Prandtl.

5.3 Premiers Résultats

Nous avons calculé plusieurs modèles de tachocline, en variant les nombres Pr, Pm et Q, pour déterminer l'espace de paramètres pour lequel un champ fossile empêche la progression de la tachocline.

Sur la Figure 5.3a, nous représentons la vitesse angulaire $\Omega(r,\theta)$ (ou $\tilde{\Omega}$ dans la notation de Spiegel & Zahn), obtenue dans une zone radiative, quand on impose au

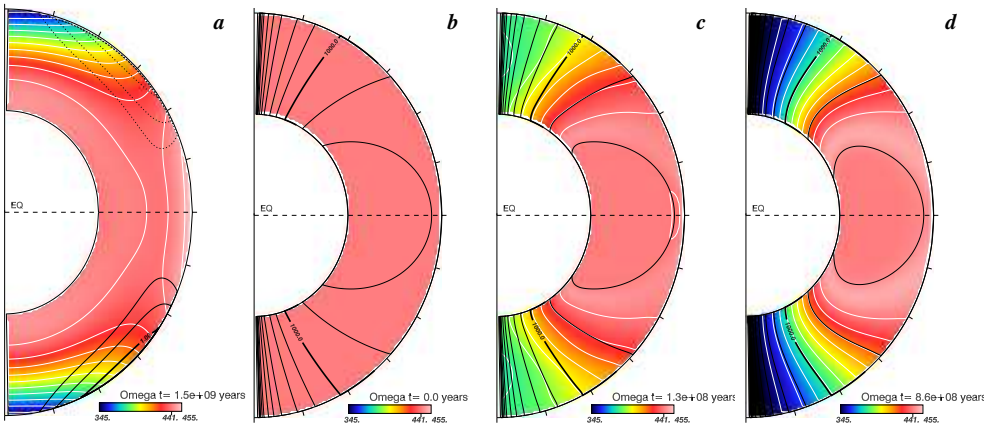

FIG. 5.3 – *a) Profil de rotation réalisé dans la zone radiative après 1.5 Gans si aucun champ magnétique n'est présent (cas Pr=10^{-3}) (pour ce panneau uniquement, les lignes noires pleines (sens anti-horaire) et en pointillés représentent la circulation méridienne). b-d)Evolution du profil de rotation (contours en couleur) + champ poloidal (lignes noires) respectivement au début, puis à 400 et 800 Mans. Dans ce cas où le champ B initial est non confiné, le système évolue très vite vers l'état d'isorotation de la rotation différentielle avec les lignes du champ poloidal, ou loi de Ferraro (Chouduri 1998), (cas Pr=10^{-3}, Q=10^{-2} et Pm=10^{-1})*

haut du domaine une condition aux limites en vitesse cisaillée (suivant léquation 5.2). Nous voyons qu'un tel cisaillement s'est propagé bien plus profondément ($d > 0.05R_\odot$) que les inversions héliosismiques ne le suggèrent, confirmant dans un calcul à trois dimensions, les résultats de Spiegel & Zahn (1992) et Elliott (1997). Cette propagation thermique du cisaillement (voir aussi figure 5.2a) est dûe à la différence en température associée ($\sim \partial T/\partial\theta$, via la balance du vent thermique, voir appendice 4.2) qui diffuse vers l'intérieur et se faisant génère une circulation méridienne qui transporte le moment cinétique tel que la balance du vent thermique soit réalisée au travers de la tachocline. Cette circulation méridienne réalisée dans la tachocline est lente, avec un temps de ventilation de l'ordre du 10^6 ans. Comme nous voulons ici discuter l'effet d'un champ magnétique sur la propagation de la tachocline, nous avons considéré plusieurs configurations initiales de champ magnétique (non confiné, confiné ou enfoui) et plusieurs intensités. Si le champ initial n'est pas assez intense, alors la solution évolue comme dans le cas purement hydro, vers une tachocline trop épaisse. Par contre au delà d'un certain seuil, le champ magnétique est suffisamment intense pour altérer l'évolution purement diffusive du cisaillement, mais il semble que la topologie du champ et pas seulement son amplitude joue aussi un rôle.

Dans les Figures 5.3b-d, nous représentons l'évolution d'un cas possédant un champ

magnétique initial non confiné, c'est à dire que les lignes de champ traversent le haut du domaine. On y voit de nouveau la vitesse angulaire (contours couleurs) mais aussi les lignes du champ magnétique poloidal (en noir). Vers l'équateur le champ magnétique s'oppose bien à la propagation de la tachocline, mais vers les pôles il en facilite la pénétration, car la vitesse angulaire tend à être constante le long des lignes de force du champ poloidal (loi de Ferraro), lesquelles sont ancrées dans la zone convective en rotation différentielle. La situation est donc plus complexe qu'anticipée. Le cas où le champ magnétique est confiné proche du haut du domaine, résulte également en une situation mitigée, avec des pôles suivant la loi de Ferraro et une zone équatoriale restreinte en rotation solide, ce qui n'était pas le cas dans l'étude de McGregor & Charbonneau (1999), qui semblait favoriser cette solution. Nous pensons que le fait de prendre en compte l'évolution du champ magnétique poloidal est très important. En effet dans le cas peu confiné, les lignes s'ancrent très vite, par diffusion ohmique, dans le haut du domaine et la solution évolue vers le cas non confiné. En figeant l'évolution du champ poloidal, beaucoup d'auteurs en sous estiment l'importance, y compris dans le déclenchement d'instabilités (voir section suivante). À la vue de ces résultats on peu douter de l'efficacité d'un champ à confiner la tachocline et donc préférer une autre solution du type tachocline rapide ou hydrodynamique comme Spiegel & Zahn (1992). Cependant afin de donner toutes ses chances au modèle proposé par Gough & McIntyre, reposant sur l'existence d'une couche magnétique impéchant au champ poloidal de s'ancrer dans la rotation différentielle de la zone convective, nous avons considéré un troisième cas. Dans ce cas nous avons enfoui profondément le champ ($r < 0.5R$). Sur la Figure 5.4, nous représentons pour cet autre cas, l'évolution de la rotation différentielle (contours couleur) et du champ poloidal (lignes noires). Nous voyons que dans ce cas, après plus de 3.8 Gans d'évolution, la zone d'isorotation du champ de vitesse avec le champ magnétique est plus réduite en étant localisée plus proche des pôles que dans les cas précédents. Or l'héliosismologie ne peut contraindre efficacement le profil de rotation solaire au delà de 70 degrés de latitude. À plus basse latitude le profil de rotation du modèle est plutôt uniforme. En laissant la tachocline pénétrer légèrement dans l'intérieur grâce à un confinement plus profond du champ, nous avons permis aux deux processus de se rencontrer et d'interagir plus librement. Cette interaction donne naissance à une couche limite magnétique proche de celle de Gough & McIntyre (1998), zone dans laquelle de forts champs toroidaux sont créés (voir figure 5.4 droite). Il semble donc qu'il y existe un domaine réduit où un champ fossile pourrait s'opposer à la propagation de la tachocline. Il faut cependant pouvoir justifier la présence dans le Soleil d'un champ magnétique aussi confiné.

Il se peut aussi que l'ancrage des lignes de force dans la zone convective soit moins

efficace en présence de turbulence, et que des valeurs plus réalistes des diffusivités (visqueuses, thermiques et magnétiques) pourraient modifier les résultats (même si nous avons volontairement conservé leur hiérarchie). Nous espérons pouvoir résoudre cela dans un futur proche, en traitant simultanément et de façon auto consistante avec le code ASH les zones radiatives et convectives.

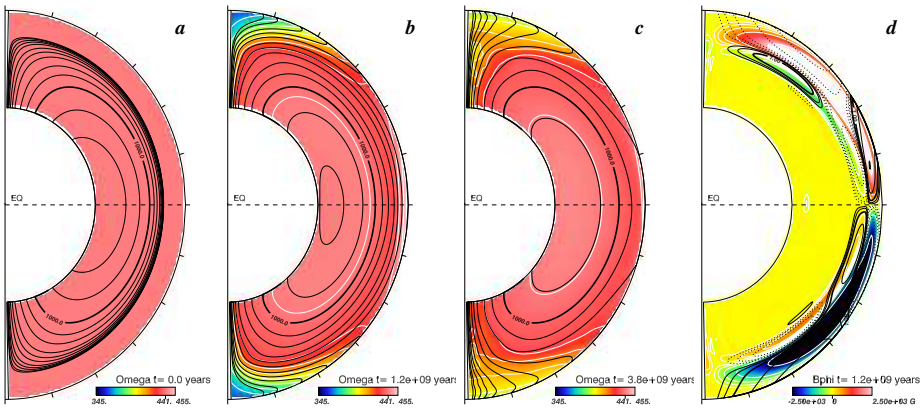

FIG. 5.4 – *a,b,c) Évolution du profil de rotation + champ poloidal respectivement au début, à 1.2 Gans et 3.8 Gans, d) champ toroidal et circulation méridienne à 1.2 Gans*

5.4 Instabilités Magnétiques en Zone Radiative

Un problème souvent soulevé avec le confinement magnétique de la tachocline par un champ fossile, est la forme purement dipolaire considérée dans ces modèles (Kitchatinov et Rudiger 1997, Gough & McIntyre 1998, ...). En effet il est bien établi depuis le travail pionnier de Tayler et collaborateurs (Tayler 1973, 1980; Markey & Tayler 1973, 1974) que dans une zone purement radiative (sans effet rotationnel) un champ magnétique purement poloidal (par exemple dipolaire) ou toroidal (par exemple sous la forme d'un tore) est instable (voir aussi Wright 1973). Tayler en déduit que dans une zone radiative vraisemblablement le champ doit posséder une configuration mixte poloidale et toroidale. Récemment, Spruit (2002) et Brainwaith & Spruit (2004), ont considéré ce problème à nouveau et ont pu démontrer numériquement qu'effectivement en général un champ magnétique aléatoire évolue vers une structure mixte, couplée toroidale-poloidale. Ces travaux ne prenaient pas en compte l'effet de la rotation ou d'un cisaillement comme ils existent avec la tachocline. Dans le cas de la rotation rapide, Pitts & Tayler (1985) ont démontré en suivant la même approche linéaire, que la rotation pouvait retarder l'instabilité (taux de croissance σ^2/Ω_0 plutôt que σ), mais

pas la faire disparaître. Nous avons donc voulu regarder systématiquement l'effet de la rotation et du cisaillement tachocline sur cette instabilité.

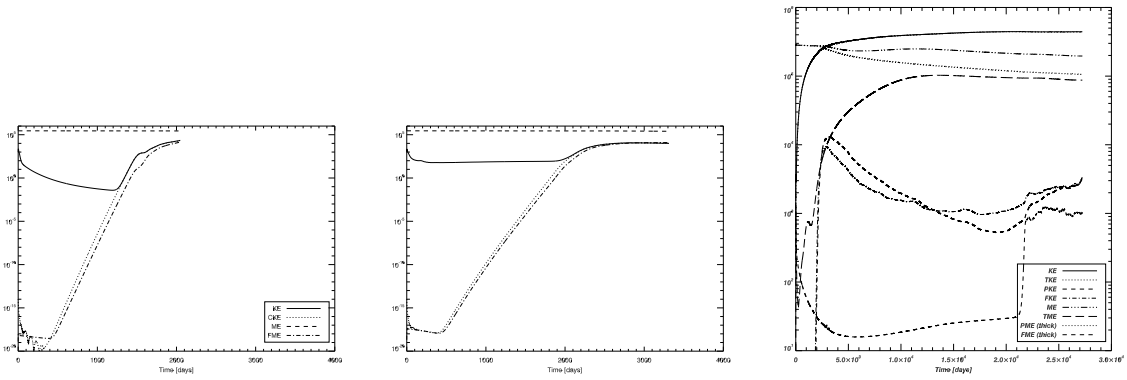

FIG. 5.5 – *Évolution temporelle des énergies magnétiques et cinétiques dans l'intérieur radiatif a) cas dipole sans rotation, b) cas dipole avec rotation c) cas tachocline*

Sur la Figure 5.5, nous montrons l'évolution temporelle des énergies cinétiques et magnétiques dans trois cas:

- champ dipolaire sans rotation ni cisaillement
- champ dipolaire avec rotation sans cisaillement
- champ dipolaire avec rotation et cisaillement (simu tachocline)

Nous voyons clairement que dans les 3 cas les énergies magnétiques et cinétiques non axisymétriques (FKE & FME) croissent fortement, puis saturent. La rotation modifie clairement le taux de croissance, comme cela est visible en comparant les pentes des courbes de FKE & FME (dans leur phase exponentielle) entre les panneaux a et b. Pour le 3eme cas, la présence du cisaillement tachocline rend l'évolution plus complexe avec la création d'un fort champ toroidal, mais elle ne semble pas modifier la croissance initiale de l'instabilité du champ magnétique par rapport au cas 2 incluant seulement les effets de la rotation.

Sur la figure 5.6, nous représentons pour le cas tachocline, un instantané de la vitesse et du champ longitudinal en fonction de la profondeur après que l'instabilité se soit déclenchée. On y voit clairement l'existence dans la région où le champ magnétique est présent, de structures non-axisymétriques de petites échelles (en accord avec les résultats de Brainwaith & Spruit 2004). La présence à grand degré ℓ et azymuthal m, d'une instabilité dans nos simulations tachocline, justifie a posteriori l'approche tridimensionnelle et originale de cette étude. Nous pensons que ces simulations encouragent le développement d'un modèle 3D complet du Soleil, tant les interactions entre zones

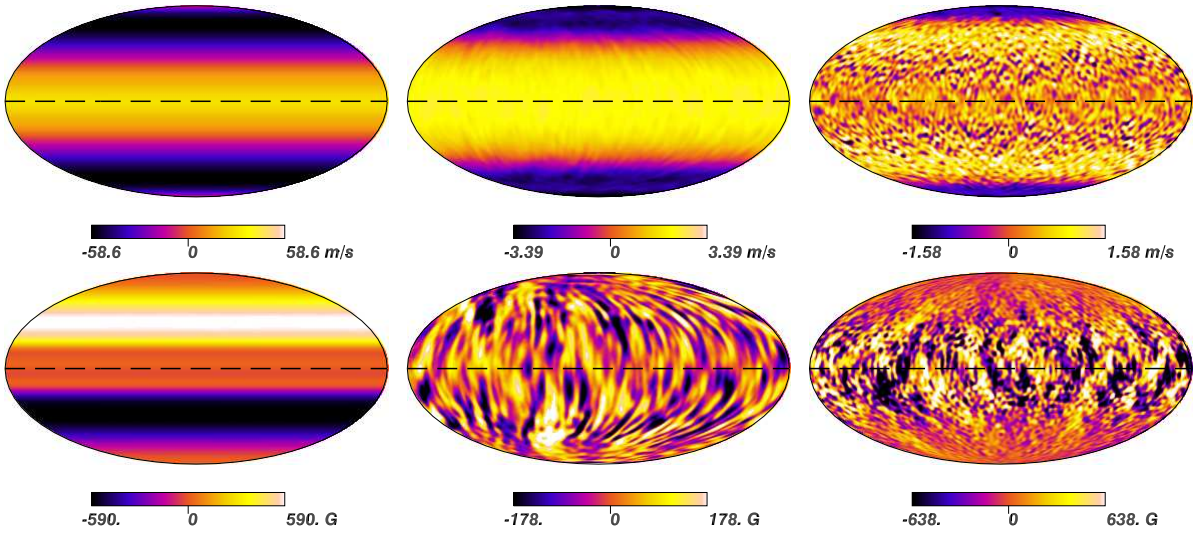

FIG. 5.6 – *Projection horizontale (de Mollweide) de la vitesse et champ magnétique longitudinal dans l'intérieur radiatif en fonction de la profondeur (respectivement de gauche à droite, r=0.7, 0.5 et 0.35 R).*

radiatives et convectives semblent cruciales pour comprendre notre étoile. Ces travaux récents sur la dynamique de l'interieur radiatif du Soleil sont toujours en cours de développement. Le travail concernant le confinement magnétique de la tachocline a été soumis en juillet 2005 à A&A.

5.5 Article publiés

5.5.1 The Solar Tachocline: Where do we stand?

par Brun 2000, SoHO10-GONG2000, ESA SP-464, 273

THE SOLAR TACHOCLINE: WHERE DO WE STAND?

Allan Sacha Brun
JILA, University of Colorado, Boulder, CO 80309-0440, USA

ABSTRACT

This paper reviews some of the basic features of the tachocline of shear present at the base of the solar convective zone. We discuss some aspects of its dynamics and evaluate processes capable of stopping the spread of the shear deeper into the radiative interior. By taking into account the macroscopic mixing occuring within this thin layer, we can improve substantially the agreement between recent 1–D solar models and quantities inferred from observing the Sun, such as the radial sound speed profile or the photospheric abundances of light elements.

1. INTRODUCTION

The rotation profile exhibited by the Sun throughout its interior (Schou et al. 1998) is still puzzling theoretician even after many years of sustained effort. There are several unanswered questions: Why does the solar core rotate so slowly (approximately at the rate of the mid-latitude external layers)? Why does the differential rotation of the convective zone not exhibit cylinder-like rotation? Why is the transition so thin between the differentially-rotating convective zone and the almost uniformly-rotating radiative interior? It is not our intention to address all these difficult questions (see Brun & Toomre 2000 for a discussion of the solar differential rotation problem), but rather to discuss some aspects of the properties of the tachocline and how they are related to the global dynamics and evolution of the Sun. The main reason for our interest in the tachocline is that in this thin region several important processes for the global dynamics and activity cycles of the Sun take place and interact:

- the global solar dynamo is supposely at work within this layer, with the creation and storage of toroidal magnetic field depending on its thickness and radial shear profile
- the turbulent pummeling of the convective downflows (plumes) on the stable layer establish an overshoot region and produce gravity waves
- it is mainly located where the change in the transport of energy occurs from convection to radiation
- its proximity to the thermonuclear burning zone of lithium ^{7}Li and beryllium ^{9}Be influences their photospheric composition due to the extra macroscopic mixing it produces

Therefore understanding the role played by the tachocline on the solar structure and dynamics is really important. The characteristic of the tachocline are now reasonably well established by helioseismic inversions (Corbard et al. 1999), and likewise are the thermodynamic properties of this layer using up to date standard solar models (see Table 1).

Table 1. Solar Tachocline Parameters

location	$0.691 \pm 0.004\ R_\odot$
width	$< 0.05 R_\odot$
ρ range	~0.16-0.32 g/cm^3
T range	~2.0-2.8 10^6 K

Let us now review the basic physical principles governing this transition layer. The presence of latitudinal differential rotation at the base of the convection zone induces a latitudinal temperature gradient, or thus $\Omega(\theta) \rightarrow \nabla T(\theta)$. Without any limiting process this temperature gradient will diffuse inwards on a thermal diffusion time scale, enforcing differential rotation deep into the radiative interior of the Sun. Yet helioseismic observations indicate a uniform rotation profile in the radiation zone.

We thus have to invoke a process to hinder the spread of the tachocline deeper down into the radiative interior. There are several possibilities: the stable stratification of radiative zone, the presence of a μ gradient created by microscopic diffusion, and properties of anisotropic turbulence and magnetic fields. The first effect, the stable stratification of the radiative zone, would indeed slow down the spread of the tachocline, changing the thermal diffusion (2^{nd} order spatial derivative) to a hyper-diffusion (4^{th} order), but in spite of that the layer would still extend to one-third of the radius in the present Sun as estimated by Spiegel & Zahn (1992, or SZ92), which is

Proc. SOHO 10/GONG 2000 Workshop, 'Helio- and Asteroseismology at the Dawn of the Millennium', Santa Cruz de Tenerife, Tenerife, Spain, 2-6 October 2000 (ESA SP-464, January 2001)

far too deep. We are thus left with three processes. The presence of a gradient of composition is often used to damp instabilities in the radiative interior of the Sun (Vauclair 1999). Unfortunately SZ92 have shown that instead of stopping the spread, the presence of a μ-gradient, as built up at the base of the convection by the Sun during its evolution due to gravitational settling of chemical elements, will increase the spreading rate leading to an even thicker tachocline. So we are left with just two processes to yield a narrow tachocline: namely magnetic fields or anisotropic turbulence.

Presently several hydrodynamical or MHD models of this shear layer and its extent have been proposed using either of the last two processes. We can classify them according to whether there are slow or fast motions in the tachocline: In the first category of a slow tachocline, there are mainly two models which have been worked out in some details to explain the thiness of the tachocline: SZ92 using anisotropic turbulence and Gough & McIntyre (1998) using a weak secular magnetic field.

We know that the model of tachocline developed by SZ92 is giving satisfying results for the extent of this layer, thus confirming that an anisotropic turbulence could stop the diffusion of the tachocline downward. There have been comments on the validity of their assumptions regarding the instability of the solar latitudinal differential rotation and on the resulting angular momentum transport properties of such an instability. Arguments were given in favor of a linearly stable solar differential rotation if no magnetic fields were present to destabilize the layer (Watson 1981, Charbonneau, Dikpati & Gilman 1999), or as in Gough & McIntyre (1998) that the angular momentum transport via anisotropic turbulence would lead to an increase rather than to a decrease of the differential rotation within the tachocline. However, a more recent study by Dipkati & Gilman (2000), using a shallow water model to include the radial dependence of the tachocline (Pedlosky 1990), has shown that the solar differential rotation profile could be unstable to linear shear instabilities even without magnetic fields, thus confirming the possibility of invoking anisotropic horizontal turbulence (due to the radial stiffness of the radiative zone) to hinder the spread of the tachocline. Yet most of the work done on the stability of the solar differential rotation profile have only used linear perturbation analysis. But as already shown by Richard & Zahn (1999), using results from a Couette-Taylor experiment, the intense level of turbulence present in the Sun is likely to make the latitudinal rotation profile unstable to nonlinear shear perturbations. Thus it is even more likely to generate an anisotropic horizontal turbulence which will act to reduce the latitudinal differential rotation and to stop the spread of the tachocline deeper down. Given these new studies we could consider SZ92 as a valid first-order model of the tachocline. Possibly of a greater concern is that SZ92 did not take into account the action of magnetic fields, assuming that the hydrodynamical anisotropic turbulence will dominate the dynamical influence of such fields. This issue may need to be revisited. The resulting meridional circulation in SZ92 due to the anisotropic turbulence present in the tachocline has an overturning time of the order of a million years. For this reason we call it a slow tachocline (see also Gilman 2000), and we will see in §3 what is the influence of such macroscopic mixing on the solar photospheric abundances.

Gough & McIntyre (1998) propose that the tachocline is confined close to the base of the convective zone due to the outward diffusion of a secular magnetic field balancing the inward diffusion of the differential rotation. But no magnetic field is present within the tachocline itself. This results in a slow two-cell meridional circulation within the tachocline, with again an overturning time of about a million years. An important attribute of this model is that it also proposes a solution for the uniform rotation of the central part of the Sun, using Ferraro's law of isorotation of the magnetic field (Cowling 1976). Yet their model is unclear on how they could avoid the secular magnetic field being carried through the tachocline at mid latitude by the two-cell structure of their meridional circulation where there is no opposing inward diffusion of differential rotation. Furthermore, by excluding the presence of magnetic fields within the tachocline, they ignore the action of any dynamo generated fields and the possible interaction of these fields with the magnetic field in the deeper interior.

We now turn to the second class of tachocline models, namely the fast tachocline ones. We will briefly discuss the model developed by Gilman & Fox (1997) and expanded subsequently in a series of papers. In their approach the tachocline is considered to be magnetized with the source of the anisotropic turbulence being a magnetic instability. The resulting meridional circulation has an overturning time of the order of months or years. However in this model only the latitudinal and longitudinal variations have been taking into account to describe the dynamics of the tachocline, while ignoring its radial variation. This drastic simplification is beginning to be addressed by the shallow water model of Dipkati & Gilman (2000), in which the influence of the radial dimension has been introduced; they find new classes of instabilities even in the non-magnetized case. They intend to soon develop a magnetic shallow water model of the tachocline.

Although the dynamical properties of the tachocline have received considerable recent attention it may still be too early to decide whether or not this region is turbulent, or if the magnetic field is frozen in it or acts only to oppose the inward diffusion. However some properties of the solar tachocline will help to discriminate between these theories, such as the latitude where the differential rotation match the almost uniform rotation of the solar core, its prolateness, the temporal variation of its thickness h as a function of the solar cycle or on a longer evolutive time scale as the Sun spun down during its evolution on the main sequence.

2. IMPLEMENTING TACHOCLINE MIXING IN SOLAR MODELS

We will now discuss recent 1–D solar models, using the description of Spiegel & Zahn to characterize the motions present in the tachocline and their mixing properties. We first recall how we build solar models including a macroscopic diffusivity D_T. Then we compare our results to the most recent helioseismic data and surface abundance observations for ^{7}Li and ^{9}Be.

Macroscopic mixing may be treated in solar models by adding an effective diffusivity D_T in the equation for the time evolution of the concentration of chemical species. To establish this coefficient for the tachocline, we use SZ92 where anisotropic turbulence serves to stop the spread of the layer. This anisotropic diffusion will also modify the advective transport of chemicals. Chaboyer & Zahn (1992) have shown that the result may be expressed as a diffusive transport in the vertical direction. Using these results, Brun, Turck-Chièze & Zahn (1999) have derived an expression for the macroscopic diffusivity D_T, taking into account the differential rotation profile and the tachocline thickness h:

$$D_T \propto \nu_H (h/r_{bcz})^2 (\hat{\Omega}/\Omega)^2,$$

where ν_H is the horizontal effective viscosity, r_{bcz} is the radius at the base of the convective zone, and $\hat{\Omega}$ characterize the solar differential rotation of the convective zone. In our solar models, we treat h as an adjustable parameter, chosen to agree with the helioseismic determination of the tachocline thickness, namely $h \leq 0.05 R_\odot$ (Corbard et al. 1999).

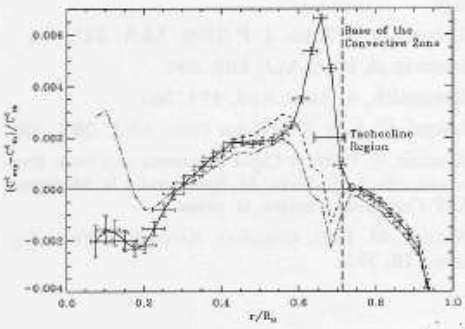

Figure 1. Squared sound speed difference between GOLF+MDI data (error bars) and the reference model (solid curve), model B_{tz} that incorporates time dependent macroscopic mixing in the tachocline region (dashed curve) and model B_{tpp} where the (pp) reaction rate S_{11} has been artificially increased by 5% (dash-three-dots curve). Also shown are the tachocline extent and the base of the convective zone (vertical long dashed line).

3. RESULTING SOUND SPEED PROFILE AND LIGHT ELEMENTS SURFACE ABUNDANCE

Starting from the reference model of Brun, Turck-Chièze & Zahn (1999, or BTZ99) built with the CESAM code (Morel 1997), we introduce our coefficient D_T in the diffusion equation of chemical species, and follow the time evolution of the solar model from the pre-main sequence (PMS) to an age of 4.6 Gyr. In Figures 1 and 2 (see BTZ99 for a more detailed discussion), we compare the results of our reference model (which has only microscopic diffusion) with two models (namely B_{tz} and B_{tpp}) which includes the macroscopic mixing in the tachocline as explained above, taking into account its variation in time as the Sun is spun down by the magnetic braking of its wind Skumanich (1972).

As expected, with macroscopic mixing the composition profile below the convective zone is smoother and flatter over the depth of the tachocline. Since there is less settling of helium, its photospheric abundance $^4\mathrm{He}_s = 0.251$ is slightly higher, in better agreement with the helioseismically determined value. This indicates that the purely microscopic diffusive model is overestimating by 25% the effect of gravitational settling on chemical species during the Sun's evolution.

The effect on the sound speed is displayed in Figure 1. When the macroscopic transport is neglected (*solid curve* with error bars), the squared sound speed difference reveals a peak just below the convective zone, coinciding with the tachocline. Macroscopic diffusion acts to reduce this peak, but when one recalibrates the model to yield the present abundance of heavy elements ($Z/X = 0.0245 \pm 0.002$), the effect is rather minor (if one does not change the opacities or the nuclear reaction rates). On the other hand, if the heavy elements are left free to adjust within the observational uncertainties, the peak is completely removed, leaving only a broad bump positioned at 0.6 $R_\odot$ (*dashed curve*), which presumably is due to another cause. As well, if one increases the proton-proton (pp) nuclear reaction by less than 5% and allows for macroscopic mixing within the tachocline, the resulting sound speed profile (model B_{tpp}, *dash-three-dots curve*) is also in relatively good agreement with the helioseismic inversion data at the base of the convective zone. Namely, the peak has disappeared, but the effect in the core indicates that an increase of 5% of S_{11} is exaggerated confirming *a posteriori* the theoretical upper limit of 2% (Adelberger et al. 1998). Therefore it is encouraging to see that by introducing macroscopic mixing in the tachocline and by varying the main microscopic processes within their theoretical and/or observational errors bars, we could improve substantially the agreement between the Sun and our models.

Another constraint comes from the surface abundances of chemical species. The two light elements ^{7}Li and ^{9}Be are extremely sensitive to mixing processes occurring in stars because their nuclear burn-

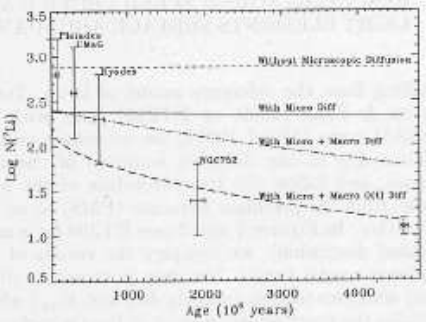

Figure 2. Depletion of ^7Li versus evolution time for several solar models: no microscopic diffusion (dash), with microscopic diffusion (solid curve) and with mixing within the tachocline: no time dependence (dash-three-dots), and with a time dependence (i.e model B_{tz}, with initial heavy element abundance $Z_0 = Z_0^{ref} = 0.01959$) (long dash). We superimpose on the theoretical curves the open cluster observations (see BTZ99 and references therein).

ing temperatures are rather low (respectively 2.5 10^6 and 3.2 10^6 K). The new observational constraints can only be satisfied if those chemical species are mixed in a rather thin layer below the convective zone in order to preserve ^{9}Be, which is very little depleted according to Balachandran & Bell (1998). This is the case with our tachocline model, which extends only 5% below the base of the convective zone.

In Figure 2 we show the resulting lithium depletion occurring during the Sun's evolution with different models, including one without any diffusive processes. Clearly only the diffusive models including macroscopic mixing in the tachocline yield a substantial depletion during main sequence evolution, in agreement with the observations (superimposed with their inherent error on the theoretical curves). But it is important to note that in this model of the solar tachocline its thickness and the strength of mixing present in the layer have been larger in the past when the Sun was rotating faster (see BTZ99). When this time dependence is included in the models (as in model B_{tz}), the lithium is burned more effectively and the models present a reasonable value of the solar ^{7}Li depletion ($\sim$ 100). However, the lithium depletion during PMS is probably overestimated due to the crude spin-down law we have adopted (see Piau & Turck-Chièze these proceedings for a detailed discussion on the PMS phases). We have also neglected the influence of the possibly strong magnetic field present in the early phases of the Sun.

In conclusion, our results show that it is important to assess the evolution of the photospheric abundance of the three elements ^{4}He, ^{7}Li, ^{9}Be, and to examine their sensitivity to macroscopic as well as microscopic processes. This study encourages the introduction of macroscopic processes in stellar evolution models, and demonstrates the crucial role of the thin tachocline layer below the convective zone.

I thank J.-P. Zahn, J. Toomre, N. Brummell and S. Turck-Chièze for useful discussions and the organizers for their financial support. This work was partly supported by NASA through grants NAG5-2256 and NAG5-8133.

REFERENCES

Adelberger, E. et al. 1998, Rev. Mod. Phys., **70** (4), 1265.

Balachandran, S. & Bell, R.A. 1998, Nature, **392**, 791.

Brun, A.S., Turck-Chièze, S. & Zahn, J.-P. 1999, ApJ, **525**, 1032.

Brun, A. S. & Toomre, J. 2000, these proceedings.

Chaboyer, B. & Zahn, J.-P. 1992, A&A, **253**, 173.

Charbonneau, P., Dikpati, M. & Gilman, P. A. 1999, ApJ, **526**, 513.

Corbard, T. et al. 1999, A&A, **344**, 696.

Cowling, T. G. 1976, Magnetohydrodynamics, Bristol, England.

Gilman, P. A. & Fox, P. A. 1997, ApJ, **484**, 439.

Gilman, P. A. 2000, Solar Phys., **192**, 27.

Dipkati, M. & Gilman, P. 2000, ApJ, in press.

Gough, D. O. & McIntyre, M. E. 1998, Nature, **394**, 755.

Morel, P. 1997, A&AS, **124**, 597.

Pedlosky, J. 1990, Geophysical Fluid Dynamics, Springer-Verlag, Berlin.

Piau, L. & Turck-Chièze, S. 2000, these proceedings.

Richard, D. & Zahn, J.-P. 1999, A&A, **347**, 734

Schou et al. 1998, ApJ, **505**, 390.

Skumanich, A. 1972, ApJ, **171**, 565.

Spiegel, E. A. & J.-P. Zahn 1992, A&A, **265**, 106.

Vauclair, S. 1999, in Light Elements and their Evolution, eds. L. da Silva, M. Spite and J.R. Medeiros, ASP Conference Series, in press

Watson, M. 1981, Geophys. Astrophys. Fluid Dynam., **16**, 285.

5.5.2 Magnetic confinement of the solar tachocline

par Brun, A.S. & Zahn, J.-P., A&A accepté

Astronomy & Astrophysics manuscript no.
(will be inserted by hand later)

Magnetic confinement of the solar tachocline

A. S. Brun[1,2] and J.-P. Zahn[2]

[1] DSM/DAPNIA/Service d'Astrophysique, CEA Saclay, F-91191 Gif-sur-Yvette, France; AIM, UMR n° 7158, CEA - CNRS - Université Paris 7
e-mail: sacha.brun@cea.fr

[2] LUTH, Observatoire de Paris, F-92195 Meudon, France
e-mail: jean-paul.zahn@obspm.fr

Received ; accepted

Abstract. We have performed 3-D MHD simulations of the solar radiative interior to study the magnetic confinement of the tachocline. Starting with a purely poloidal magnetic field and a latitudinal shear meant to be imposed by the convection zone at the top of the numerical domain, we have investigated the subtle interactions between magnetic fields, rotation and shear, and the conditions required to prevent the radiative spread of the tachocline. In all cases we have explored, the dipole field ends up connecting with the convection zone, whose differential rotation is then imprinted at high latitude (above 45°) throughout the radiative interior, according to Ferraro's law of isorotation. Rotation remains uniform in the lower latitude region which is contained within closed field lines, i.e. lines which have not yet opened. We find that the formation of a magnetopause is not sufficient to stop the inward progression of the differential rotation: the meridional flow is too slow to bend the magnetic field lines. Thus the observed thinness of the tachocline cannot be invoked as a proof for an internal magnetic field, as was suggested by Gough and McIntyre (1998). The interaction of the mean poloidal field with the spreading shear generates a mean toroidal field about as strong as the mean poloidal field. Further, we observe the development of a non-axisymmetric magnetohydrodynamic instability triggered by the initial purely poloidal configuration of our fossil field (as discussed by Tayler in the 70-80's); the resulting mixed poloidal/toroidal state then slowly decays through ohmic diffusion. We do not find dynamo action as such in the radiative interior, since the mean poloidal field is not regenerated. But the instability persists during the whole evolution, while slowly decaying with the mean poloidal field; it is probably maintained by small departures from isorotation.

Key words. MHD – turbulence – Sun: rotation – stars: evolution – stars: rotation

1. Introduction - Motivation

One of the great achievements of helioseismology was to map out the internal rotation of the Sun (Brown et al. 1989). It revealed that the convection zone was rotating differentially, with the angular velocity varying little in depth, and that the radiative interior was in quasi-uniform rotation. The transition between these two regimes occurs in a thin layer, the tachocline, which seems to straddle the boundary between the convection zone and the radiation zone. It is still a matter of debate whether the whole tachocline is turbulent, due to thermal convection, or only part of it.

Here we shall assume that at least some differential rotation is applied on the top of the radiation zone proper, excluding the subadiabatic overshoot region. Then, in the absence of other physical processes, this differential rotation should spread into the radiation zone, as was shown by Spiegel & Zahn (1992). That spread is due to the thermal diffusion of the temperature fluctuation which is generated in latitude, along isobars, by the differential rotation. These are tightly linked by the baroclinic relation; therefore, as the temperature fluctuation expands downwards, so does also the differential rotation. The process is not just a diffusion in this stably stratified medium, since it involves also meridional currents: the temporal variation of all fluctuations is proportional to the square of the laplacian, and some refer to it as a hyper-diffusion. Viscosity too contributes to the spread, but only slightly. The whole process is very slow, but in the present Sun the tachocline should reach down to 0.3 in radius, in the absence of any other physical process.

Since this is not observed (Charbonneau et al. 1998, Corbard et al. 1999), one has to invoke a mechanism which tends to suppress the differential rotation in latitude, which is the cause of the spread. In Spiegel & Zahn's model, this is achieved by a turbulent anisotropic viscosity, with much stronger transport in the horizontal than in the vertical direction, which halts the spread of the tachocline. Established originally in the thin layer limit, this property was confirmed by 2-dimensional simulations performed by Elliott (1997). The fact that such turbulence acts to reduce the angular velocity gradient has been questioned by Gough & McIntyre (1998), who cite geophysical examples where horizontal turbulence drives the system away from uniform rotation. On the other hand, in Couette-Taylor experiments turbulence reduces the angular velocity gradient, when angular momentum increases outward and the flow is linearly stable; in other words it acts to suppress the shear which is responsible for the instability (Richard & Zahn 1999). This trend appears also in numerical 3-dimensional simulations of the turbulent overshoot region which have been carried out by Miesch (2003).

Send offprint requests to: A. S. Brun

Another way to oppose the spread of the tachocline is by magnetic stresses. The first to address the problem were Rüdiger & Kitchatinov (1997). In their model, a steady magnetic field confined in the radiation zone opposes the viscous spread of the differential rotation applied on the top; the tachocline reduces then to a very thin Ekman-Hartmann layer. MacGregor & Charbonneau (1999) confirmed that result, but they considered also another case, where the poloidal field was allowed to thread into the differentially rotating convection zone. A rather weak field suffices then to imprint the differential rotation throughout the radiation zone, thus enforcing Ferraro's law (Ferraro 1937):

$$\mathbf{B} \cdot \boldsymbol{\nabla} \Omega = 0,$$

where $\mathbf{B}$ is the magnetic field and Ω the angular velocity. These models, however, were rather crude, since they did not allow for the ohmic diffusion of the poloidal field; moreover, they ignored thermal diffusion and the associated meridional circulation.

The model outlined by Gough & McIntyre (1998) includes most physical processes that are likely to operate in the upper radiation zone: the tachocline circulation is driven by thermal diffusion, and its spread is halted by the fossil field which resides beneath. The field does not penetrate into the tachocline, except perhaps in a narrow region of up-welling flow, and therefore it does not transmit the differential rotation of the convection zone to the deep interior. Actual calculations of this model have been carried out by Garaud (2000, 2002), seeking directly the stationary solution sketched by Gough & McIntyre, although in her case the tachocline circulation is driven through Ekman pumping; some of her solutions show indeed a tendency for magnetic confinement, but a substantial differential rotation persists throughout the radiation zone, particularly at high latitude.

The models discussed above favor a slow version of the tachocline with typical ventilation time of order 10^6 yr. Gilman and collaborators (Gilman & Fox 1997; Dikpati, Cally & Gilman 2004 and references therein) developed a series of models that showed that the tachocline could become unstable through magnetic instability of toroidal structures embedded in it, resulting in a fast latitudinal angular momentum transport that suppresses the shear and limits its inward diffusion. Forgacs-Dájka and Petrovay (2002) considered the effect of an oscillating dynamo field of 22 yr period and found that it could too suppress the spread of the solar tachocline. Both models favor a rather fast tachocline with ventilation times of order a rotation period or the duration of the solar cycle (Gilman 2000).

In the present paper we examine a model of the solar radiative zone and tachocline similar to that of Gough & McIntyre. But we consider the time-dependent problem, starting from various initial conditions, and this for two reasons: i) both the tachocline spread and the diffusion of the magnetic field proceed very slowly, and thus it is not clear that a stationary solution can be reached by the age of the Sun; ii) such a stationary

solution may not be unique, but it may actually depend on the initial conditions. A similar approach has be taken recently by Sule et al. (2004); we differ from their work in that we let the poloidal field diffuse, and in our case the tachocline circulation is driven mainly by thermal diffusion, as in the Sun.

Moreover, we use for our simulations the 3-dimensional code ASH (see further down) and resolve the Alfvén crossing time; this enables us to describe non-axisymmetric hydrodynamical instabilities which may lead to drastic reconfigurations of the magnetic field, as was recently demonstrated numerically by Braithwaite and Spruit (2004; see also Braithwaite & Nordlund 2005), following the pioneering work of Tayler (Tayler 1973, Pitts & Tayler 1985).

2. The model

We make use of the well-tested hydrodynamic ASH code (anelastic spherical harmonic; see Clune et al. 1999, Miesch et al. 2000, Brun & Toomre 2002) which has been extended to include the magnetic induction equation and the feedback of the field on the flow via Lorentz forces and ohmic heating (see Brun, Miesch & Toomre 2004 for more details). We examine here the nonlinear interaction between a shearing flow, i.e. the differential rotation imposed by the convection zone on the top of the radiative interior, and a fossil magnetic field, in order to assess whether such a field can hinder the spread of the tachocline deep in the radiative zone and thus keep it thin as was revealed by helioseismic inversions (Charbonneau et al. 1998, Corbard et al. 1999).

Our numerical model is a simplified portrayal of the solar radiation zone: solar values are taken for the heat flux, rotation rate, mass and radius, and a perfect gas is assumed. The computational domain extends from $r_{\rm bot} = 0.35\,R_\odot$ to $r_{\rm top} = R = 0.72\,R_\odot$ ($R_\odot$ is the solar radius), thereby focusing on the bulk of the stable zone without yet considering interaction with the convective envelope, nor including the nuclear central region. The vertical extent of the computational domain is therefore $D = 2.5 \times 10^{10}$ cm and the background density varies across the shell by about a factor of 17.

2.1. Governing equations

The ASH code solves the full set of 3–D MHD anelastic equations of motion (Glatzmaier 1984) in a rotating spherical shell on massively-parallel computing architectures (Brun, Miesch & Toomre 2004). Depending on the sign of the initial mean entropy gradient considered in the model, either negative or positive, convection or radiation zones can be simulated. The anelastic approximation is used to retain the important effects of density stratification without having to track the sound waves (i.e. $\partial\rho/\partial t = 0$). The MHD anelastic equations are fully nonlinear in velocity and magnetic field variables, but under the anelastic approximation the thermodynamic variables are linearized with

respect to a spherically symmetric and evolving mean state, with density $\bar{\rho}(r,t)$, pressure $\bar{P}(r,t)$, temperature $\bar{T}(r,t)$ and specific entropy $\bar{S}(r,t)$. Fluctuations about this mean state are denoted by ρ, P, T, and S. The resulting equations are:

$$\boldsymbol{\nabla}\cdot(\bar{\rho}\mathbf{v}) = 0, \tag{1}$$

$$\boldsymbol{\nabla}\cdot\mathbf{B} = 0, \tag{2}$$

$$\begin{aligned}\bar{\rho}\left(\frac{\partial\mathbf{v}}{\partial t}+(\mathbf{v}\cdot\boldsymbol{\nabla})\mathbf{v}+2\boldsymbol{\Omega_0}\times\mathbf{v}\right) &= -\boldsymbol{\nabla}P+\rho\mathbf{g}+\frac{1}{4\pi}(\boldsymbol{\nabla}\times\mathbf{B})\times\mathbf{B}\\ &- \boldsymbol{\nabla}\cdot\boldsymbol{\mathcal{D}}-[\boldsymbol{\nabla}\bar{P}-\bar{\rho}\mathbf{g}],\end{aligned} \tag{3}$$

$$\begin{aligned}\bar{\rho}\bar{T}\frac{\partial S}{\partial t}+\bar{\rho}\bar{T}\mathbf{v}\cdot\boldsymbol{\nabla}(\bar{S}+S) &= \boldsymbol{\nabla}\cdot[\kappa_r\bar{\rho}c_p\boldsymbol{\nabla}(\bar{T}+T)+\kappa\bar{\rho}\bar{T}\boldsymbol{\nabla}(\bar{S}+S)]\\ &+ \frac{4\pi\eta}{c^2}\mathbf{j}^2+2\bar{\rho}\nu\left[e_{ij}e_{ij}-1/3(\boldsymbol{\nabla}\cdot\mathbf{v})^2\right]+\bar{\rho}\epsilon,\end{aligned} \tag{4}$$

$$\frac{\partial\mathbf{B}}{\partial t} = \boldsymbol{\nabla}\times(\mathbf{v}\times\mathbf{B})-\boldsymbol{\nabla}\times(\eta\boldsymbol{\nabla}\times\mathbf{B}), \tag{5}$$

where $\mathbf{v}=(v_r,v_\theta,v_\phi)$ is the local velocity in spherical coordinates in the frame rotating at constant angular velocity $\boldsymbol{\Omega_0}$, $\mathbf{g}$ is the gravitational acceleration, $\mathbf{B}=(B_r,B_\theta,B_\phi)$ is the magnetic field, $\mathbf{j}=c/4\pi\,(\boldsymbol{\nabla}\times\mathbf{B})$ is the current density, c_p is the specific heat at constant pressure, κ_r is the radiative diffusivity, η is the effective magnetic diffusivity, and $\boldsymbol{\mathcal{D}}$ is the viscous stress tensor, involving the components

$$\mathcal{D}_{ij} = -2\bar{\rho}\nu[e_{ij}-1/3(\boldsymbol{\nabla}\cdot\mathbf{v})\delta_{ij}], \tag{6}$$

where e_{ij} is the strain rate tensor, and ν and κ are effective eddy diffusivities. A volume heating term $\bar{\rho}\epsilon$ is also included in these equations for completeness (see Brun, Browning, Toomre 2005). We ignore the nuclear energy generation. To complete the set of equations, we use the linearized equation of state

$$\frac{\rho}{\bar{\rho}}=\frac{P}{\bar{P}}-\frac{T}{\bar{T}}=\frac{P}{\gamma\bar{P}}-\frac{S}{c_p}, \tag{7}$$

where γ is the adiabatic exponent, and assume the ideal gas law

$$\bar{P}=\mathcal{R}\bar{\rho}\bar{T} \tag{8}$$

where $\mathcal{R}$ is the gas constant. We neglect the composition gradient due to element settling. The reference or mean state (indicated by overbars) is derived from a one-dimensional solar structure model (Brun et al. 2002) and can be updated with the spherically-symmetric components of the thermodynamic fluctuations as the simulation proceeds. The model begins in hydrostatic balance so the bracketed term on the right-hand-side of equation (3) initially vanishes. Departure from this hydrostatic balance are found to be small.

Due to limitations in computing resources, no simulation achievable now or in the near future can hope to directly use microscopic values for the diffusivities. The simulations reported here resolve nonlinear interactions among a larger range of scales than any previous MHD model of the solar radiative interior, but motions still exist in the Sun on scales much smaller than our grid resolution. In this sense, our models should be regarded as

large-eddy simulations (LES) with parameterizations to account for subgrid-scale (SGS) motions. Thus the effective eddy diffusivities ν, κ, and η represent momentum, heat, and magnetic field transport by motions which are not resolved by the simulation. They are allowed to vary with radius but are independent of latitude, longitude, and time for a given simulation. Their amplitudes and radial profiles are varied depending on the resolution and objectives of each simulation. In the simulations reported here, ν, κ, and η are assumed to be proportional to $\bar{\rho}^{-1/2}$.

2.2. Integration domain, boundary conditions

The system of equations to be solved with ASH requires 12 boundary conditions. At the top of the numerical domain we impose a differential rotation meant to be enforced by the turbulent convection zone. Following helioseismic inversions (Thompson et al. 2003), we apply the following law:

$$\Omega(r_{\rm top},\theta) = A + B\cos^2\theta + C\cos^4\theta, \tag{9}$$

The uniform rotation which has the same specific angular momentum (Gilman et al. 1989) is

$$\Omega_0 = A + \frac{1}{5}B + \frac{3}{35}C; \tag{10}$$

we shall apply this uniform rotation initially to the whole radiation zone, and therefore there will be no net viscous flux across the boundary.

For the remaining top and bottom boundary conditions, we impose:

1. impenetrable walls at top and bottom:

$$v_r = 0|_{r=r_{\rm bot},r_{\rm top}},$$

2. stress free at bottom:

$$\frac{\partial}{\partial r}\left(\frac{v_\theta}{r}\right) = \frac{\partial}{\partial r}\left(\frac{v_\phi}{r}\right) = 0|_{r=r_{\rm bot}},$$

3. constant entropy gradient at top and bottom:

$$\frac{\partial \bar{S}}{\partial r} = cst|_{r=r_{\rm bot},r_{\rm top}},$$

4. and we match the magnetic field to an external potential field at top and bottom:

$$\mathbf{B} = \boldsymbol{\nabla}\Phi \rightarrow \Delta\Phi = 0|_{r=r_{\rm bot},r_{\rm top}}.$$

Our choice of magnetic boundary conditions ensures that no magnetic torques are applied to the numerical domain.

2.3. Choosing the physical parameters

In Gough & McIntyre's model, a magnetic boundary layer, or magnetopause, separates the magnetic interior from the tachocline void of magnetic field; its thickness δ is determined by the relative strength of the two diffusion processes and that of the magnetic field:

$$\left(\frac{\delta}{R}\right)^6 = \frac{2}{L^4}\frac{(t_{\rm A})^2}{t_{\rm ES}\,t_{\rm B}}, \tag{11}$$

where $R = r_{\rm top}$, and $L \approx 4.5$ is related to the latitudinal structure of the tachocline. Here we have introduced the Alfvén crossing time $t_{\rm A} = R/V_{\rm A} = R\sqrt{4\pi\bar{\rho}}/B$; $t_{\rm B} = R^2/\eta$ is the magnetic diffusion time, and $t_{\rm ES} = (N/\Omega_0)^2(R^2/\kappa)$ the local Eddington-Sweet time. B is the magnetic field strength and N the buoyancy frequency.

Expressing that the diffusion of the magnetic field is halted by the downflow of the tachocline circulation, one gets the following relation between the thickness δ of the magnetopause and Δ, that of the tachocline :

$$\left(\frac{\Delta}{R}\right)^3 = \frac{1}{L}\left(\frac{\delta}{R}\right)\frac{t_{\rm B}}{t_{\rm ES}}\left(\frac{\widehat{\Omega}}{\Omega_0}\right), \tag{12}$$

where $\widehat{\Omega}/\Omega_0 \approx 1/5$ is a measure of the differential rotation.

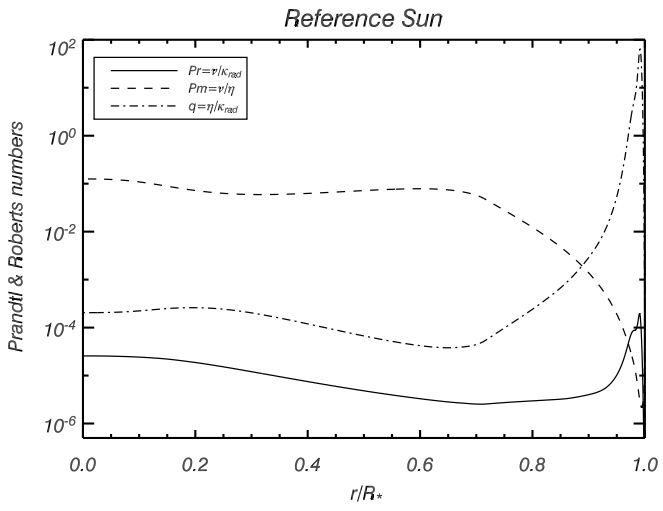

Fig. 1. Radial dependence of the Prandtl P_r, magnetic Prandtl P_m and Roberts Q numbers in the Sun based on the microscopic values of the diffusivities for a ionized hydrogen gas (Zeldovich et al. 1983).

Figure 1 shows the variation with depth of the non-dimensional numbers that characterize the microscopic diffusivities in the Sun. Typical values for the relevant parameters in the upper radiation zone are given in Table 1. In our model we had to increase all

Parameter	Symbol	Sun	Simulation
thermal diffusivity	κ	10^7	$8\,10^{12}$
magnetic diffusivity	η	10^3	$8\,10^{10}$
viscosity	ν	30	$8\,10^9$
Prandtl number	ν/κ	$3\,10^{-6}$	10^{-3}
Roberts number	η/κ	10^{-4}	10^{-2}
Magnetic Prandtl nb	ν/η	$3\,10^{-2}$	10^{-1}
Froude number	$(\Omega_0/N)^2$	$2\,10^{-6}$	10^{-4}
Ekman number	$\nu/2\Omega_0 R^2$	$2\,10^{-15}$	$6\,10^{-7}$
Alfvén time (for 1 G)	t_A	$5\,10^{10}$	$5\,10^{10}$
Ohmic diffusion time	t_B	$2.5\,10^{18}$	$3.125\,10^{10}$
viscous diffusion time	t_ν	$8.333\,10^{19}$	$3.125\,10^{11}$
Eddington-Sweet time	t_{ES}	$1.25\,10^{20}$	$3.125\,10^{12}$

Table 1. Typical values of the relevant parameters in the upper radiation zone of the Sun, and values adopted for the model (in cgs units, when applies).

diffusivities, but we took care to respect their hierarchy. We chose the viscosity ν as small as allowed by our numerical resolution, in order to ensure that the tachocline be driven by thermal diffusion, as in the Sun, rather than through Ekman pumping. Another way to look at the problem is to make sure that the spread due to thermal hyper-diffusion, which scales as $\Delta/R \approx (t/t_{\rm ES})^{1/4}$, still exceeds the viscous spread $\Delta/R \approx (t/t_\nu)^{1/2}$ at the age of the Sun (with $t_\nu = R^2/\nu$), which measured in Eddington-Sweet time is $t_\odot/t_{\rm ES} = 1.2\,10^{-3}$; this is guaranteed if the Prandtl number is less than $\nu/\kappa = 3\,10^{-3}$, hence our choice of $\nu/\kappa = 10^{-3}$.

The Froude number Ω_0/N was also increased to meet the numerical requirements; since this enhances the ventilation speed, it may also account for the fact that the Sun was rotating faster in the past. With these parameters, taking a field of 1kG yields a tractable thickness for the magnetic boundary layer: $\delta/R = 2.2\,10^{-2}$ according to (11). From (12) the corresponding tachocline thickness is then $\Delta/R = 2.1\,10^{-2}$, and the magnetic Reynolds number based on the Alfvén speed $R_m = t_B/t_A$ will range between 0 and a few 10^3 in the computational domain.

2.4. Numerical resolution

The global code ASH solves in a 3-D rotating spherical shell the set of equations (1-5) in the anelastic approximation. This has the great advantage that the Courant stability criterion is based on the slow motions present in the radiative zone rather than on the sound speed, thus allowing for larger time steps. In the MHD context, the anelastic

approximation filters out fast magneto-acoustic waves but retains the Alfvén and slow magneto-acoustic modes.

The ASH code is based on the so-called pseudo-spectral numerical method to solve the system of partial differential equation introduced above (Glatzmaier 1984, Canuto et al. 1988, Boyd 1989, Clune et al. 1999). In this numerical method, the main variables are projected onto orthogonal functions/polynomials rather than discretized on a mesh grid as with finite differences. One big advantage of this method is that in spectral space, derivatives are straightforward multiplications, rather than variations as in finite difference scheme, which are numerically less precise. Since we want to solve the MHD equations in spherical geometry, it is natural to use the spherical system of coordinates (r, θ, ϕ) and to use a decomposition of the main variables on spherical harmonics $Y_{\ell m}(\theta, \phi)$ for the horizontal dimensions. This approach has the advantage that the spatial resolution is uniform everywhere on a sphere when a complete set of spherical harmonics is used up to some maximum in degree ℓ (retaining all azimuthal orders $m \leq \ell$ in what is known as triangular truncation). Gaussian quadrature impose that we use the relation $\ell_{max} = (2N_\theta - 1)/3$, and $N_\phi = 2N_\theta$ for the horizontal resolution (Boyd 1989). For the radial direction we choose to project our functions onto Chebyshev polynomials $T_n(r)$, using N_r Gauss-Lobatto collocation points (Canuto et al. 1995). Typical grid resolution for our models is $N_r = 193$, $N_\theta = 128$ and $N_\phi = 256$.

In order to ensure that the mass flux and the magnetic field remain divergence-less to machine precision throughout the simulation, we use a toroidal–poloidal decomposition as:

$$\bar{\rho}\mathbf{v} = \boldsymbol{\nabla} \times \boldsymbol{\nabla} \times (W\hat{\mathbf{e}}_r) + \boldsymbol{\nabla} \times (Z\hat{\mathbf{e}}_r), \tag{13}$$

$$\mathbf{B} = \boldsymbol{\nabla} \times \boldsymbol{\nabla} \times (C\hat{\mathbf{e}}_r) + \boldsymbol{\nabla} \times (A\hat{\mathbf{e}}_r) \quad . \tag{14}$$

More details on the numerical method can be found in Clune et al. (1999) and Brun, Miesch & Toomre (2004).

2.5. Initial conditions

At $t = 0$ the computational domain is motionless, except for a uniform rotation $\Omega = \Omega_0$ defined in (10), and for the differential rotation (9) imposed at the top boundary $r = r_{\rm top}$, where the following values have been chosen for A, B and C in expression (9) (modulo a factor of 2π): $A = 456$, $B = -42$ and $C = -72$.

Initially we apply a purely axisymmetric meridional field $\boldsymbol{B}_p = B_r \boldsymbol{e}_r + B_\theta \boldsymbol{e}_\theta$, with

$$B_r = \frac{B_0}{r^2 \sin\theta} \frac{\partial \Psi}{\partial \theta}, \qquad B_\theta = -\frac{B_0}{r \sin\theta} \frac{\partial \Psi}{\partial r}; \tag{15}$$

$\Psi(r, \theta)$ is constant on field lines, and is related to the azimuthal component of the vector potential: $\Psi = r \sin\theta A_\phi$. For a dipolar field $\Psi \propto \sin^2\theta R^3/r$; here we take instead

$$\Psi = (r/R)^2 (R_B - r)^2 \sin^2\theta \qquad \text{for } r \leq R_B$$

$$\Psi = 0 \qquad \text{for } r \geq R_B, \tag{16}$$

which confines the field in the sphere of radius R_B.[1]

This parameter R_B thus determines the degree of confinement of the initial field; we shall consider the 3 cases:

- I. $R_B >> r_{\rm top}$ - the field threads into the convection zone,
- II. $R_B = r_{\rm top} = 0.72 R_\odot$ - the field is just barely confined in the radiation zone,
- III. $R_B = 0.64 R_\odot$ - the initial field is buried deep in the radiation zone.

3. Results

The interaction of rotation and magnetic field in the solar radiative zone is found to be very sensitive to the initial magnetic field configuration; we shall examine in turn cases I, II and III.

3.1. Case I: Initial field threading into the convection zone

In this first case, at $t = 0$ the magnetic field lines are already threading into the convection zone where the differential rotation is applied, as can be seen on Fig. 2a. The torque applied by the shear at the top of the domain is quickly transmitted throughout the radiation zone, first at high latitudes where the direction of the field lines is almost radial (Fig. 2b) and then more slowly at lower latitudes (Fig. 2c). Such a strong differential rotation in latitude in the solar radiative interior is not observed in helioseismic inversions (Thompson et al. 2003, Couvidat et al. 2003). Clearly, in this case the magnetic stresses do not oppose the inward propagation of the shear but they favor it. (Similar results have been found in 2-D by MacGregor & Charbonneau 1999). The transport of angular momentum by Maxwell stresses is too fast, and prevents the magnetopause to form. Meridonal flows do exist but they are not found to play a significant role: they are unable to oppose the spread of the latitudinal shear. Their amplitude in the simulation is about 1 m/s, which corresponds (after rescaling) to a real solar ventilation speed of 10^{-7} m/s, much less than in the non-magnetic case ($\approx 10^{-5}$ m/s).

The interaction between the poloidal field and the shear leads initially to a fast increase of the axisymmetric toroidal field, which then saturates as the isocontours of Ω become more and more aligned with the axisymmetric poloidal field, tending to Ferraro's law of isorotation. Its strength, over a short interval of time, is larger than that of the axisymmetric poloidal field, before equilibrating at the same amplitude. These mean toroidal fields are not found to become unstable. As a consequence there are no processes that could regenerate the mean poloidal field, and its intensity slowly decays away,

[1] Charbonneau and MacGregor (1993) took a similar form for Ψ; we differ from them by enforcing the continuity of B_θ at R_B, thus suppressing there the current sheet.

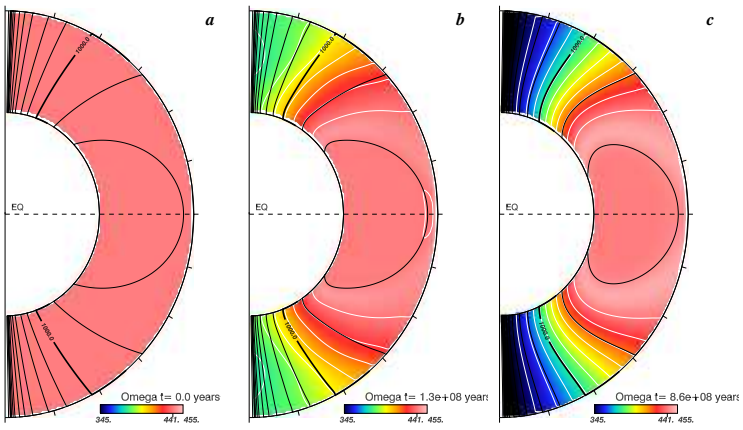

Fig. 2. Case I. Temporal evolution, over 860 Myr, of the angular velocity Ω (color contours) and the mean axisymmetric poloidal field (superimposed black lines).

followed by the other components of the field. However, in the early phase of evolution we find that the non-axisymmetric fluctuating fields undergo a fast growth linked to the development of a MHD instability of the initial poloidal magnetic field configuration. This instability has been discussed in detail by Tayler and collaborators; we shall describe it in more detail in §3.4. It is however worth noting that this instability develops later than in cases II and III, taking roughly twice as long to start. This delay is certainly due to the anchoring of the field lines in the convection zone, that quickly leads to the generation of a stabilizing mean toroidal component.

3.2. Case II: Initial field barely confined in the radiation zone

In the second case, the magnetic field lines do not penetrate into the convection zone but come very close to it, as can be seen on Fig. 3a. At the beginning of the simulation, the viscous torque associated to the imposed shear at the top of the domain do not drag the magnetic field lines, and as a consequence no physical processes are available for quickly transmitting the latitudinal shear. This particular configuration of the magnetic field has been chosen in the 2-D calculation of Rudiger & Kitchatinov (1997) and MacGregor & Charbonneau (1999) to demonstrate the confinement of the tachocline. If the initial poloidal magnetic field is kept fixed in time, as in these 2-D calculations, the curved/horizontal profile of the magnetic field is quite efficient at stopping the inward diffusion of the latitudinal shear. However, in our 3-D simulations we find that the magnetic field quickly diffuses outward (given the closeness of the top boundary), where it connects with the imposed rotation (Fig. 3b). As the more intense field lines reach the top boundary, and slowly drift toward the polar regions while becoming more radial, Ferraro's law of isorotation is reached once more, first at high latitude and then at lower

latitude (Fig. 3c). It takes about 8 times longer for Ferraro's law to be achieved in case II than in case I. However this is still a very fast process, accomplished at an age of 0.2 Gyr in equivalent solar units. Here again the internal magnetic field fails to prevent the inward spread of the shear because the magnetopause does not have the time to form, and as a consequence there is no meridional circulation to oppose the spread of the latitudinal shear by bending horizontally the magnetic field lines. Meridional flows do exist but here again they do not play a significant role.

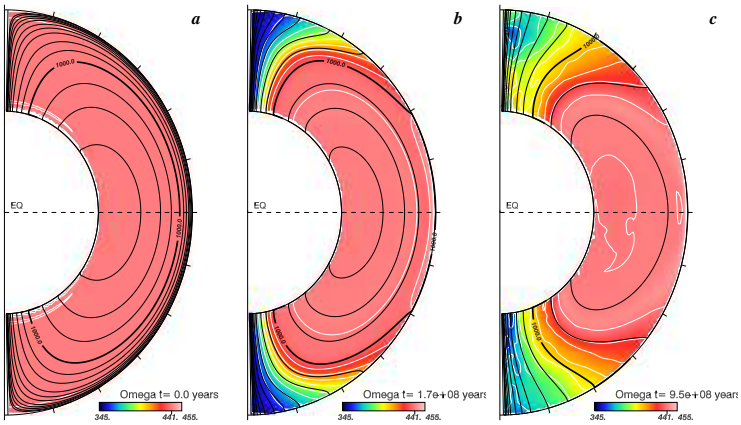

Fig. 3. Case II. Temporal evolution, over 950 Myr, of the angular velocity Ω (color contours) and the mean axisymmetric poloidal field (superimposed black lines).

As soon as the field lines succeed at making contact with the shear, the situation we have observed in the first case is again realized. The interaction between the poloidal field and the shear leads initially to an increase of the axisymmetric toroidal field, but it takes about 8 times longer to reach the same level than that reached in case I. The energy in the mean toroidal field (TME) saturates as the isocontours of Ω become more and more aligned with the axisymmetric poloidal field. Its strength is close to that of the axisymmetric poloidal field (PME) and reach about 2-3 kG, but contrary to case I, where TME for a short period of time was greater than PME (early phases), here TME is always smaller. No instabilities of the mean toroidal field is found, but as with case I, a quick non-axisymmetric MHD instability of the mean poloidal field develops in the early phase (see §3.4). We can thus conclude that case II leads to the same state of differentially rotating radiative interior as case I, except that this occurs later. We thus do not confirm the results of Rudiger & Kitchatinov (1997) and MacGregor & Charbonneau (1999), that a barely confined field is more efficient at preventing the spread of the tachocline. The temporal evolution of the mean poloidal field plays here a crucial role by allowing the field to connect to the imposed upper shear.

3.3. Case III. Initial field buried deeply in the radiation zone

In this last case, the magnetic field lines are confined below $r = R_B < r_{\rm top}$, to let the tachocline penetrate into the interior before encountering the fossil field (Fig. 4a). When the field lines make contact with the shear (see Fig. 4b), we notice a fast increase of the mean toroidal energy in a thin latitudinal band, which corresponds to the magnetopause anticipated by Gough & McIntyre (see Fig. 5a). In case III, TME reach a level equivalent to that found in cases I and II at even longer time, respectively 20 or 2.5 times later. This is expected since at the beginning the mean poloidal field do not interact with the shear.

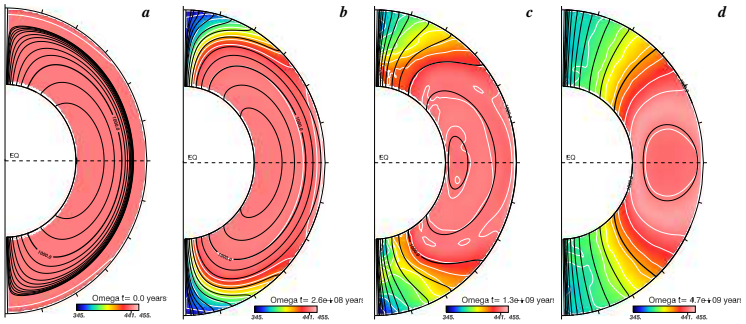

Fig. 4. Case III. Temporal evolution of the angular velocity Ω (color contours) and the mean axisymmetric poloidal field (superimposed black lines). **a-d)** sequence spanning 4.7 Gyr of the dipolar magnetic field in the presence of rotation and shear. We note the connection of the field lines with the imposed top shear and the resulting Ferraro law of isorotation at latitude greater than 40-45°.

At 280 Myr, the meridional circulation in the tachocline consists of three superposed counter-rotating cells, of which the largest spans the whole hemisphere, much like a dipole. The octopolar shape observed in the non-magnetic tachocline is recovered very close to the top boundary, with an up-welling located around the latitude of 35°. This meridional circulation is unable to prevent the outward diffusion of the magnetic field lines (Figs. 4b-d): its speed is insufficient to bend the field lines, or to drag and gather them. The direct consequence of this inefficiency is that the field lines eventually connect to the shear imposed at the top of the domain by diffusing through the magnetopause. This results in an upward shift of the magnetopause, which is the seat of a strong generation of toroidal field (via Ω-effect) - notice the migration of B_ϕ between Figs. 5a and b. Then as the field lines gradually connect to the shear imposed at higher latitudes, becoming more radially oriented they communicate via Maxwell stresses the differential rotation of the convection zone to the bottom of the domain, as in the two previous cases. At 4.7 Gyr, the meridional circulation has shrunk into a two thin dipolar cells.

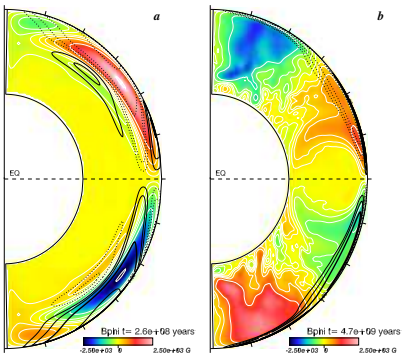

Fig. 5. a-b) Case III. Temporal evolution of the associated toroidal field (color contours) and of the meridional circulation (superimposed black lines) at t=280 Myr and 4.7 Gyr. We clearly see the early formation of a magnetopause with intense mean (axisymmetric) toroidal field, and then the development at high latitudes of toroidal field associated with the progression of the latitudinal shear in the computational domain. The presence of a large scale shear helps the magnetic field to reach a more stable mixed poloidal/toroidal configuration.

We have run Case III with different values of the confinement depth R_B and of the Prandtl number ν/κ, which allows us to conclude that the appearance of differential rotation in the radiative interior depends mainly on the time it takes for the poloidal field lines to connect with the convection zone: the deeper the field is buried initially and the longer it can maintain uniform rotation within its closed field lines. Thus Ferraro's law of isorotation, with a radiative interior rotating differentially, is the most likely outcome of the interaction of poloidal field with a latitudinal shear. The initial state of solid rotation only lasts as long as the fields lines have not diffused outward and connected with the convection zone.

3.4. Instabilities

Our three-dimensional MHD simulations of the solar radiative interior reveal another interesting and fundamental aspect: the occurrence of a non-axisymmetric instability of the initial purely poloidal field. In Fig. 6, we display the temporal evolution, in case III, of various components of the kinetic (KE) and magnetic (ME) energies; cases I and II have similar behavior. PKE & PME designate respectively the mean (axisymmetric) poloidal components of KE and ME, TKE & TME their toroidal components, and FKE & FME their non-axisymmetric components (see Brun et al. 2004 for their analytic expressions). Right from the onset, starting from an extremely weak non-axisymmetric velocity field, FKE & FME rise exponentially by many orders of magnitude on a very short time, and then saturate at a level close to TME. Thereafter all energies but one slowly decline, on a time scale of order 1.2 Gyr which is that of the ohmic dissipation of the mean poloidal

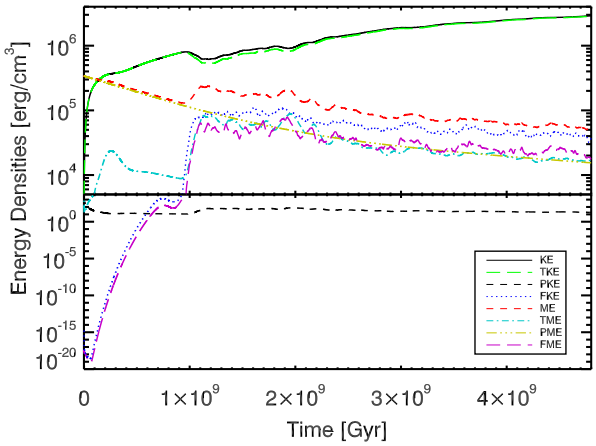

Fig. 6. Temporal evolution of kinetic and magnetic energies in the presence of rotation and shear. We clearly see the development of a non-axisymmetric instability (characterized by the fast increase of FKE and FME) which is associated with the unstable configuration of the purely dipolar intial field introduced in our simulation.

field PME; the exception is the mean azimuthal energy TKE, which steadily increases as the shear spreads deeper and to lower latitudes. The kinetic energy of the meridional flow (PKE) is the smallest of all energies; it is mostly concentrated toward the top of the domain.

This nonlinear calculation is in qualitative agreement with the linear analysis performed by Tayler and collaborators (Markey & Tayler 1973, 1974; Tayler 1980; Pitts & Tayler 1985). In their study, Tayler and collaborators considered the adiabatic stability of purely poloidal or toroidal magnetic field configurations in a stably stratified stellar interior. They found that magnetic field configurations were more stable in a mixed poloidal/toroidal field configuration, with TME roughly equal to PME. In their paper Pitts & Tayler included the effect of fast rotation in the stability analysis. They found that rotation was mainly delaying the triggering of the instability but not suppressing it. Here we find that the energy in the axisymmetric components TME and PME are of about the same amplitude, but that the fluctuating toroidal energy (FTE) is 3 times larger than the fluctuating poloidal energy (FPE). We note that FKE saturates at a value close to FME, which indicates that we are observing Alfvén waves.

More recently Braithwaite & Spruit (2004) studied Tayler's instability in a non-rotating polytropic star, by means of 3-D numerical simulations. They found that a random initial magnetic field relaxes in a few Alfvén crossing times into a mixed poloidal/toroidal topology, by exciting a non-axisymmetric small scale instability. This field then slowly decays and migrates toward the surface. Our simulations show similar behavior, as can be seen in Fig. 7, where we display shell views at various depth

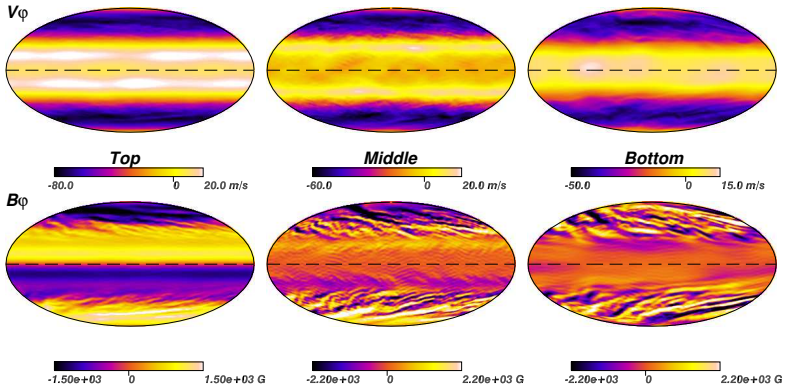

Fig. 7. Case III. Horizontal (Mollweide) projection of the azimuthal velocity and magnetic field, as a function of depth (respectively from left to right: $r = 0.7$, 0.55 and $0.37 R_\odot$) at 4.7 Gyr.

of the longitudinal components of velocity and magnetic field, using Molleweide projections. The instability first starts at the bottom of the domain (we recall that the field in this case was deeply buried) and then propagates upward as the magnetic field diffuses. However we differ here from Braithwaite & Spruit in that we consider the rotating case, impose initially a large scale poloidal field, whose ohmic decay time is of the order of the age of the Sun, and that we keep applying a differential rotation at the top the domain. The persistent small departures from Ferraro's law induce a toroidal field, which first is concentrated in the magnetopause, and later at high latitude (Fig. 5 a-b). This field, structured in isolated bands, is of the kind considered by Tayler (1973), whose work was generalized to 3-D by Zhang, Lao & Schubert (2003): it is known to give rise to non-axisymmetric instabilities. We observe them here in a fully developed regime, over a broad spectrum of scales. One may debate whether the process deserves to be called a dynamo, as suggested by Spruit (2002), since it does not regenerate the mean poloidal field. But it could lead to some localized mixing in the radiation zone, and therefore it may play a role in the chemical evolution of the model star - not in that of the Sun, however, since such a field configuration does not allow for a thin tachocline.

4. Discussion and conclusions

We undertook these 3-D simulations to check whether a fossil magnetic field can prevent the radiative spread of the solar tachocline, as was suggested by Gough and McIntyre (1998). In all cases we have explored, the outcome is always that the initial dipole field connects with the convection zone, and that it then imprints the differential rotation of that zone throughout the radiative interior, according to Ferraro's law, at latitudes higher than 40-45° (see Figs. 4c-d). When the initial poloidal field threads already into the convection zone, the process takes only a few Alfvén crossing times, as expected. When

it is confined in the radiation zone, the time required for this depends on how deep it is confined. Nearly uniform rotation can only persist inside the outermost closed field line, hence at low latitude. Of course, a deeply buried field will not reach the convection zone by the age of the Sun, but then the tachocline will also have penetrated very far.

The crucial role of the magnetic field configuration in enforcing a given rotation profile was already elucidated by MacGregor and Charbonneau (1999), but they did not let the field diffuse into the convection zone. The stationary solutions built by Garaud (2000, 2002) resemble ours, the main difference being probably that in her case the meridional circulation is driven by Ekman pumping.

We believe that our simulations have captured the essence of the real problem, since they respect the similarity of time-scales characterizing the two competing processes, namely the Ohmic diffusion time of the mean poloidal field and the Eddington-Sweet time which rules the spread of the tachocline. In order to be able to resolve the boundary layers, namely the tachocline, which is the region of strong differential rotation, and the magnetopause, where the magnetic field confronts the tachocline circulation, we had to increase the initial magnetic field by 3 orders of magnitude with respect to the estimate of Gough & McIntyre. This may still be insufficient, since the two boundary layers have similar depth, whereas in their model the magnetopause is much thinner than the tachocline.

A more delicate point is whether the poloidal field lines actually penetrate into the convection zone, as assumed in most models including ours, or whether they are deflected by the turbulent motions, which are probably structured in plumes. We have to wait for realistic simulations of penetrative convection to see how a magnetic field, anchored in the deep interior, will behave there. We intend to tackle this problem in the near future.

Since we used a three-dimensional code, we were able to observe the non-axisymmetric instabilities associated with the field configurations. They are particularly strong in the early phase, because the initial field is purely poloidal, but they persist along the whole simulation, probably fueled by the toroidal field which results from small departures from Ferraro's law of isorotation, which is never completely achieved because of the differential rotation imposed at the top of the domain.

Based on their model, and on the observed thinness of the tachocline, Gough and McIntyre (1998) concluded on the inevitability of a magnetic field in the Sun's radiative zone. We find here - but note the caveats above - that such a field seems unable to prevent the spread of that shear layer, and therefore that the thinness of the tachocline cannot prove nor disprove the existence of a fossil field. Therefore other processes must be invoked to account for the thinness of the tachocline. Or one has to explain why there is no need for such a layer at the top of the radiation zone, and thus how uniform rotation is accomplished already at the base of the convection zone. A first step in that direction has been taken by Forgács-Dajka and Petrovay (2000, 2002): they introduce

the oscillating dynamo field in the region of convective penetration, and they succeed in smoothing out the differential rotation. Then a fossil field could well thread into that turbulent tachocline, and impose uniform rotation below.

But other possibilities are actively explored. Talon and Charbonnel (2005; see also Charbonnel & Talon 2005) have just shown that such uniform rotation can be achieved with internal gravity waves emitted at the base of the convection zone, combined with meridional circulation and shear induced turbulence in the bulk of the radiation zone. Whether it exists or not - will we ever know? - the tachocline has already led to exciting and far reaching work!

It is clear that in order to disentangle between all the theoretical models of the solar tachocline and the radiative interior currently available, a new class of helioseismic instruments has to be developed, in particular to study the deep solar interior. Such efforts have started in Europe (e.g. the DYNAMICS project, Turck-Chièze et al. 2005).

Acknowledgements. We are thankful to N. Brummell and P. Charbonneau with whom we originally discussed aspects of this work. We also acknowledge fruitful discussions with D. Gough, P. Garaud, H. Spruit and J. Toomre. We thank the organizers of the MSI program at the Newton Institute, N.O. Weiss, R. Rossner and D. Hughes for their invitation during fall 2004, where part of this work was completed. Finally we thank the french supercomputer centers CEA-CCRT and CNRS-IDRIS for allocating time to compute our 3-D MHD models of the solar tachocline.

References

Boyd, J. P. 1989, Chebyshev and Fourier Spectral Methods (Berlin: Springer Verlag)

Braithwaite, J. & Nordlund, A. 2005, A&A (preprint)

Braithwaite, J., & Spruit, H. C. 2004, Nature, 431, 819

Brown, T.M., Christensen-Dalsgaard, J., Dziembowski, W.A., Goode, P., Gough, D.O., & Morrow, C.A. (1989). ApJ, 343, 526

Brun, A. S., Antia, H. M., Chitre, S. M. & Zahn, J.-P. 2002, A&A, 391, 725

Brun, A. S., Browning, M. & Toomre 2005, ApJ, 629, 461

Brun, A. S., Miesch, M. S. & Toomre, J. 2004, ApJ, 614, 1073

Brun, A. S., & Toomre, J. 2002, ApJ, 570, 865

Canuto, C., Hussaini, M. Y., Quarteroni, A. & Zang, T. A. 1995, Spectral Methods in Fluid Dynamics (New York: Springer Verlag)

Charbonneau, P., & MacGregor, K. B., 1993, ApJ, 417, 762

Charbonneau, P., Tomczyk, S., Schou, J., & Thompson, M. J. 1998, ApJ, 496, 1015

Charbonnel, C., & Talon, S. 2005, Science (to appear)

Clune, T. L., Elliott, J. R., Glatzmaier, G. A., Miesch, M. S., & Toomre, J. 1999, Parallel Comput., 25, 361

Corbard, T., Blanc-Féraud, L., Berthomieu, G. & Provost, J. 1999, A&A, 344, 696

Couvidat, S., Garcia, R. A., Turck-Chièze, S., Corbard, T., Heney, C. J. & Jiménez-Reyes, S. 2003, 597, L77

Dikpati, M., Cally, P. S. & Gilman, P. A., 2004, ApJ, 610, 597

Elliott, J. R. 1997, A&A, 327, 1222

Ferraro, V. C. A. 1937, MNRAS, 97, 458

Forgacs-Dájka, E. & Petrovay, K. 2000, Sol. Phys., 203, 195

Forgacs-Dájka, E. & Petrovay, K. 2002, A&A, 389, 629

Garaud, P. 2000, PhD thesis, Univ. of Cambridge

Garaud, P. 2002, MNRAS, 329, 1

Gilman, P. A. 2000, Solar Phys., 192, 27

Gilman, P. A., & Fox, P. A. 1997, ApJ, 484, 439

Gilman, P. A., Morrow, C. A. & DeLuca, E. E. 1989, ApJ, 338, 528

Glatzmaier, G. A. 1984, J. Comp. Phys., 55, 461

Gough, D. O., & McIntyre, M. E. 1998, Nature, 394, 755

MacGregor, K. B., & Charbonneau, P. 1999, ApJ, 519, 911

Markey, P. & Tayler, R. J. 1973, MNRAS, 163, 77

Markey, P. & Tayler, R. J. 1974, MNRAS, 168, 505

Miesch, M. S., Elliott, J. R., Toomre, J., Clune, T. L., Glatzmaier, G. A., & Gilman, P. A. 2000, ApJ, 532, 593

Miesch, M. S. 2003, ApJ, 586, 663

Mestel, L. 1953, MNRAS, 113, 716

Pitts, E. & Tayler, R. J. 1985, MNRAS, 216, 139

Richard, D., & Zahn, J.-P. 1999, A&A, 347, 734

Rüdiger, G., & Kitchatinov., L. L. 1997, Astron. Nachr. , 318, 273

Spiegel, E. A., & Zahn, J.-P. 1992, A&A, 265, 106

Spruit, H. C. 2002, A&A, 381, 923

Sule, A., Arlt, R., & Rüdiger, G. 2005, A&A (to appear) astro-ph/0409721

Talon, S., & Charbonnel, C. 2005, A&A (to appear) astro-ph/0505229

Tayler, R. J. 1973, MNRAS, 161, 365

Tayler, R. J. 1980, MNRAS, 191, 151

Thompson, M. J., Christensen-Dalsgaard, J., Miesch, M. S. & Toomre, J. 2003, Ann. Rev. Astron. Astrophys., 41, 599

Turck-Chièze et al. 2005, in ESLAB 2005 Symposium, "Trends in Space Science and Cosmic Vision 2020", ESA-SP in press

Zahn, J.-P. 1992, A&A, 265, 115

Zeldovich, Y. B., Ruzmaikin, A.A. & Sokoloff, D.D. 1983, Magnetic Fields in Astrophysics, (New York: Gordon & Breach)

Zhang, K., Lao, X., Schubert, G. 2003, ApJ, 585, 1124

Chapitre 6

Convection, Rotation et Effet Dynamo dans les Étoiles A

Dans ce chapitre, nous présentons brièvement de récents résultats obtenus avec le code ASH sur la convection turbulente et l'effet dynamo dans les cœurs d'étoiles massives. Nous avons choisi les étoiles A car elles sont l'archétype des étoiles de la séquence principale possédant une convection et un magnétisme (s'il existe, cf. chapitre 2) radicalement différent des étoiles de faible masse plus tardives comme le Soleil. Ces étoiles possèdent en effet un cœur et non pas une enveloppe convective (exception faite d'une très fine enveloppe pour les moins massives des étoiles A, voir chapitre 2) et un magnétisme rare. En effet seules 10 à 15% des étoiles A (dénommées étoiles Ap) possèdent une activité. Ce faible pourcentage est à mettre en perspective avec les étoiles de type solaire qui possèdent toutes une forte activité. En modélisant ces étoiles, nous désirons ainsi élargir notre compréhension de la dynamique et du magnétisme stellaire afin de développer une vue plus globalisante de ce vaste sujet et ne pas reposer notre étude uniquement sur nos simulations du Soleil.

6.1 Contexte Général

La convection centrale présente dans le cœur des étoiles massives a un impact fort sur la structure et l'évolution de celles-ci, cependant peu de choses sont connues sur les propriétés dynamiques d'une telle convection. L'existence de ces cœurs convectifs est dûe à la forte génération d'énergie par réactions nucléaires via le cycle CNO, dont la dépendance en fonction de la température est très raide $\epsilon \propto T^{17}$ (Clayton 1968), ce qui ne permet pas aux seuls photons d'évacuer l'énorme quantité d'énergie ainsi produite. Comme nous l'avons décrit au chapitre 2, le transport convectif de l'énergie dans les modèles d'évolution stellaire, qu'il soit central ou de surface, est déduit de l'approche

de la longueur de mélange et repose sur la résolution d'une équation cubique d'une variable représentant l'efficacité de la convection (Cox & Guili 1968). Cette approche, qui ne prend en compte qu'une seule échelle caractéristique pour la convection, celle-ci variant en fonction de l'échelle de pression du milieu, a certes des vertus de simplicité et d'efficacité. Cependant elle nous renseigne peu sur l'amplitude précise du flux convectif, sa variation temporelle et spatiale (en latitude et longitude), l'établissement de courants moyens tels que la rotation différentielle et la circulation méridienne et leur conséquence sur la redistribution du moment cinétique à l'intérieur de l'étoile. De plus il a rapidement été réalisé, qu'un panache convectif ne s'arrêterait pas net à la frontière entre convection et rayonnement (définie par le changement de signe du gradient d'entropie) mais au contraire pénétrerait dans la zone radiative avoisinante (Roxburgh 1965). Ce phénomène est appelé pénétration convective ou overshooting (Zahn 1991), selon la capacité de ses structures convectives à établir ou non une zone de mélange adiabatique supplémentaire (ce qui peut aussi être caractérisé par le nombre de Péclet, voir définition dans l'Appendice). La MLT dans sa version standard ne dit rien sur la quantité et la variation de cette pénétration. Or nous savons que cela joue un grand rôle dans l'évolution chimique des étoiles, et plus particulièrement des étoiles massives, car cela peut potentiellement apporter de l'hydrogène frais dans le cœur convectif nucléaire et donc modifier le comportement et l'évolution de celui-ci et par répercussion celui de l'étoile. Un autre aspect passionnant de ces étoiles consiste à en expliquer le magnétisme plutôt rare (cf. chapitre 2 et la discussion de la quasi non détection en X des étoiles A). Savoir si de tels cœurs convectifs développent ou non un effet dynamo et dans l'affirmative, si ce magnétisme émerge à la surface ou reste enfoui à l'intérieur de l'étoile, constitue un difficile problème, que seule une approche non linéaire et dynamique peut adresser. En conséquence de quoi, il semble naturel d'étudier tridimensionnellement les propriétés (magnétohydro)dynamiques des cœurs convectifs d'étoiles massives afin de mieux les comprendre, et de les caractériser et ainsi d'enrichir les descriptions plus simples utilisées en évolution stellaire 1-D et éclaircir l'absence de magnétisme dans ces étoiles.

Plusieurs scénari ont été proposés pour expliquer le magnétisme des étoiles A. La théorie du champ fossile suggère que le champ magnétique tient son origine du champ qui traversait le gaz interstellaire dans lequel l'étoile s'est formée. Comme le temps de diffusion ohmique τ_η est très long dans les enveloppes radiatives des étoiles A, le champ primordial peut survivre sur toute la durée de sa séquence principale (Moss 2001). La présence ou non de champ dépend de l'histoire de la formation de l'étoile. Une autre approche considère que l'activité de surface vient d'une dynamo opérant dans le cœur convectif de l'étoile (Charbonneau & McGregor 2001, McGregor & Cassinelli 2003). Le

champ magnétique ainsi créé se trouve expulsé dans la zone d'overshooting et après avoir atteint un certain degré d'amplification via effet ω, il monte à la surface sous l'effet de sa flottaison. Vue la stratification stable de l'enveloppe radiative des étoiles A, tous les tubes ne réussissent pas à émerger à la surface, ce qui pourrait en partie expliquer l'absence de magnétisme (un peu comme en période de Minimum de Maunder où aucune tache solaire n'était visible mais la dynamo opérait toujours (Beer et al. 1998)). Un troisième scénario, plus récent, invoque aussi la présence d'une dynamo, mais cette fois dans l'enveloppe radiative (Spruit 2002, McDonald & Mullan 2004). Ces auteurs s'appuient sur l'instabilité de Tayler (1973) des configurations magnétiques (discutée chapitre 5), pour régénérer la composante poloidale du champ et sur la présence d'un effet ω dans les zones radiatives. Chaque modèle a ces avantages et ces inconvénients (voir Brun et al. 2005 pour plus de détails). Cependant nous pensons que la présence d'une convection turbulente dans le cœur de ces étoiles A peut résulter en ce que ces étoiles développent une dynamo centrale. De plus la configuration renversée par rapport au Soleil (Cœur Convectif - Zone Radiative plutôt que Cœur Radiatif -Zone Convective) suggère la présence d'un *tachocline inverse* et donc potentiellement d'une zone de fort cisaillement capable de générer un champ magnétique toroidal concentré et intense. Afin de confirmer par un calcul non linéaire et turbulent ces considérations, nous avons construit avec le code ASH un modèle 3-D de ces étoiles. Ces résultats ont été publiés dans Browning, Brun et Toomre 2004 et Brun, Browning et Toomre 2005. Une première tentative pour comparer nos résultats de dynamo solaire avec celle des étoiles A, a étée publié dans le compte rendu de la SF2A 2004 (joint au manuscrit).

6.2 Le Modèle

Nous avons donc ajouté au jeu d'équations MHD que le code ASH résout (voir Appendice 1), une source de chaleur interne permettant de simuler la production d'énergie nucléaire par le cycle CNO présent dans les étoiles plus massives que le Soleil. Ici nous considérons le cas d'étoiles A de 2 masses solaires, sur la séquence principale (structure 1-D déduite d'un modèle à $\sim$ 500 Mans), tournant jusqu'à 8 fois plus vite que le Soleil. La présence de la singularité $r = 0$, nous force à omettre les 2% les plus centraux de l'étoile, il ne semble pas cependant que cela ait un effet important sur nos résultats. Notre domaine de calcul inclut le cœur convectif et un tiers de la zone radiative (cf. Figure 6.1), permettant ainsi une étude couplée des deux zones. Afin d'augmenter la résolution dans la transition entre ces deux zones, nous faisons usage de deux domaines de Chebyshev. La résolution est $\ell_{max} = 170$ et Nr=49+33=82, donc moins gourmande que pour le cas solaire discuté chapitre 4.

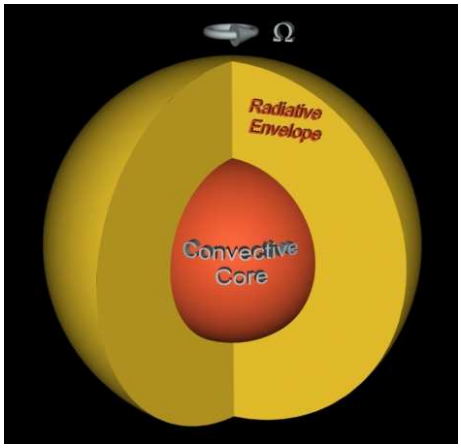

FIG. 6.1 – *Représentation 3D du domaine simulé dans le cas des modèles d'étoiles A, on distingue clairement le cœur convectif et l'enveloppe radiative.*

6.3 Influence de la Rotation sur la Convection Centrale

Sur la Figure 6.2, nous représentons la vitesse radiale réalisée à un instant donné au milieu du cœur convectif et dans la zone d'overshooting ainsi qu'une coupe dans le plan méridien du profil axisymétrique ($m = 0$) de la rotation différentielle. Les motifs convectifs obtenus dans ces cœurs sont très étendus et ne présentent pas de fortes dissymétries entre flots montants et descendants comme dans le cas solaire. Cela est dû à la faible stratification dans le cœur où le contraste de densité n'est que de 2-3. Dans la zone stable, la pénétration de structures convectives génère des ondes de gravité (progressives) qui se propagent par petits paquets principalement horizontalement. Certains modes globaux ont même pu être excité, ce qui peut être dû à notre choix de conditions aux limites pour la vitesse impénétrables qui crée une cavité résonnante artificielle (voir Browning, Brun et Toomre 2004).

Le profil de rotation différentielle réalisé dans les simulations, possède une colonne de rotation rétrograde assez fortement alignée avec l'axe de rotation $\hat{e}_z$. Nous avons fait une étude en fonction du nombre de Rossby convectif (*Roc* cf. Appendice) pour savoir si tous les modèles prédisaient le même profil. Nous avons montré que pour le cas où $\Omega_0 = \Omega_\odot/10$, la colonne est moins présente mais surtout elle est de sens contraire. La transition entre colonne prograde et rétrograde étant aux alentours de $Roc \sim 1$ ($Roc < 1$ indique que les mouvements convectifs ressentent l'influence de la rotation). L'accélération équatoriale est le résultat d'un transport de moment cinétique depuis les pôles vers l'équateur par la turbulence via les tenseurs de Reynolds. Ils doivent s'opposer

à la diffusion visqueuse et à la circulation méridienne qui tendent à accélérer les pôles. Cette dernière possède une structure complexe, composée de plusieurs cellules tant en rayon qu'en latitude. Elle s'étend légèrement dans la zone d'overshooting, permettant ainsi un brassage de la composition chimique entre l'enveloppe radiative et le cœur convectif nucléaire.

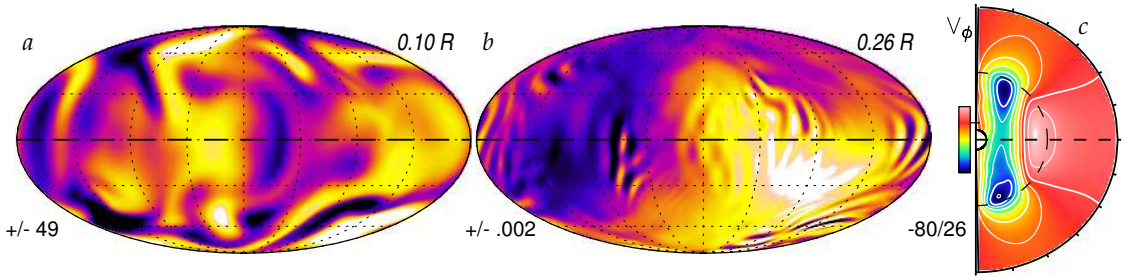

FIG. 6.2 – *Motifs convectifs et rotation différentielle typique d'un modèle d'étoile A obtenu avec le code ASH. On remarque dans la figure du milieu la présence d'onde de gravité excitée par les mouvements convectifs dans la zone d'overshooting. Le profil de rotation dans le domaine est caractérisé par une forte colonne de rotation rétrograde dans le cœur convectif.*

La zone de mélange convectifs forts possède une forme allongée le long de l'axe de rotation et plus importante aux pôles. L'amplitude de la pénétration des mouvements convectifs au delà de cette zone mélangée est plus faible qu'anticipée ($d_{ov} < 0.2H_p$). Celle-ci varie fortement avec la latitude, étant moins importante aux pôles, là où la rotation se fait moins ressentir, ce qui compense l'aspect déformé du cœur. Nous représentons Figure 6.3a, cette structure particulière du voisinage du cœur convectif. On remarque bien cette forme prolate à l'intérieur d'une zone à la forme plus sphérique où nous observons encore la présence de faible mélange (voir Browning, Brun et Toomre 2004, pour plus de détails).

6.4 Effet Dynamo dans les Coeurs Convectifs

À partir des simulations purement hydrodynamiques que nous avons brièvement discutées plus haut, nous avons entrepris d'étudier l'interaction complexe de ces cœurs convectifs avec un champ magnétique et de vérifier l'existence d'un effet dynamo. Nous avons donc introduit un champ dipolaire de faible amplitude dans le domaine simulé (donc dans le cœur convectif mais aussi dans l'enveloppe radiative l'entourant)

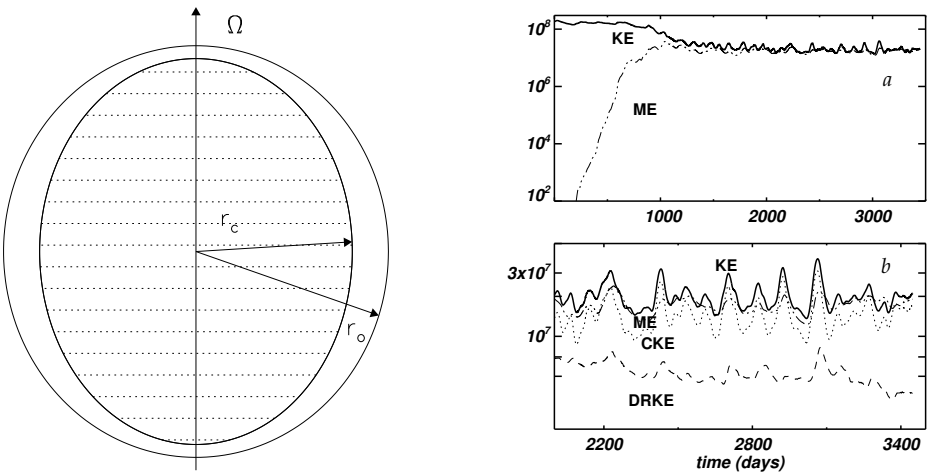

FIG. 6.3 – *a) Schéma mettant en évidence la géométrie prolate du cœur convectif de rayon $r_c(\theta)$ et de la zone d'overshooting de rayon r_o indépendant de la colatitude θ dans nos modèles d'étoiles A, b) Évolution temporelle des énergies cinétiques et magnétiques.*

et laissé évoluer la simulation sur plusieurs temps ohmiques. Sur la Figure 6.3b, nous représentons l'évolution temporelle des énergies cinétiques et magnétiques. Nous remarquons que ME croît par plusieurs ordres de grandeur jusqu'à atteindre une valeur proche de l'équipartition de l'ordre de 40% de KE. Cette valeur est plus importante que dans le cas solaire 4 présenté au chapitre 4. Il semble effectivement que ces cœurs convectifs soient très efficaces pour amplifier le champ magnétique. Cela est peut être dû à la topologie plus connectée des cœurs par rapport aux coquilles sphériques. Les champs magnétiques générés dans ces cœurs sont principalement non axisymétriques, les champs axisymétriques ne comptant que pour 5-8% de l'énergie totale ME. Comme pour les cas 3 et 4 du chapitre 4, le champ induit dans le cœur convectif est principalement fluctuant et intermittent. Il semble que la non axisymétrie des champs soit une propriété assez robuste des dynamos se développant dans les zones convectives turbulentes.

La présence d'une zone de cisaillement intense à la frontière du cœur convectif (une sorte de tachocline inverse) permet l'amplification d'un champ magnétique toroïdal généré par effet ω qui devient la composante dominante dans cette zone et l'enveloppe radiative. Cet aspect très allongé du champ toroidal peut être plus facilement appréhendé si on visualise le champ à trois dimensions. Sur la Figure 6.4 nous représentons une vue 3-D de la vitesse radiale, et des composantes radiales et longitudinales du champ magnétique obtenues dans la simulation correspondant à la Figure 6.3b.

L'amplitude des vitesses et l'intensité du champ magnétique sont trop faibles pour que ceux-ci soient visibles dans la zone radiative. Dans cette représentation, nous voyons clairement comment le champ toroidal est enroulé avec les deux polarités complètement entremêlées. Cette situation est vérifiée dans tout le volume de la simulation mais elle est plus explicite dans la couche de transition entre les deux zones. Nous n'observons cependant pas d'émergence de structures toroidales dans la zone radiative, juste la lente diffusion ohmique du champ. Le champ magnétique radial lui est de plus petite échelle, plus filamenteux et moins connecté sur l'ensemble du domaine que le champ longitudinal. Pour la vitesse radiale, la présence d'un champ magnétique intense ne semble pas modifier grandement son profil, qui reste très symétrique entre flots montants et descendants et alignée le long de l'axe de rotation.

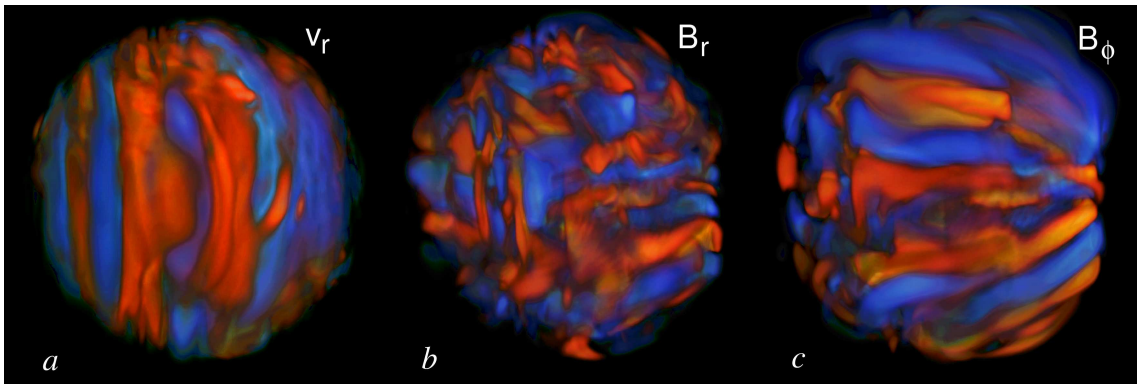

FIG. 6.4 – *Représentation 3D du champ de vitesse radial et des composantes radiales et longitudinales du champ magnétique.*

Cependant, grâce à nos divers calculs de dynamos stellaires, nous semblons avoir mis en évidence que la rotation différentielle, plus que la convection, est fortement affectée par la croissance de l'énergie magnétique et se trouve significativement réduite si $ME/KE > 0.4$. En effet, comme pour le cas solaire (en comparant chapitre 4, les cas 2 & 4) nous voyons que l'effet principal de la croissance du champ magnétique est de rigidifier le cœur convectif et de réduire fortement le contraste de rotation différentielle. Nous avons même obtenu quand le rapport ME/KE est proche de 0.4 des phases oscillantes, où la rétroaction du champ magnétique sur les mouvements réduit trop fortement la convection et la rotation différentielle associée, donc les sources d'amplification du champ, ce qui par répercussion l'affaiblit et donc permet la régénération d'une plus forte convection, puis l'établissement de nouveau d'une rotation différentielle qui renforce le champ, qui peut maintenant rétroagir et ainsi de suite (voir Brun, Browning et Toomre 2005). Nous voyons donc que dans nos simulations il y a une interaction forte et non linéaire entre cisaillement, convection et champ magnétique.

Pour résumer nos résultats sur le cœur convectif des étoiles A (et par extension à celui des étoiles plus massives), il semble clair que la turbulence présente dans ces cœurs génère une forte rotation différentielle et amplifie de façon très efficace le champ magnétique par effet dynamo. Nous trouvons que dans la zone de transition entre la convection et la zone radiative, un champ toroidal fort est maintenu et que les mouvements pénètrent vigoureusement bien que peu profondément. Tous ces ingrédients laissent à penser que ses étoiles entretiennent un champ magnétique durant leur vie sur la SP. Nous ne pouvons pas encore conclure si ce champ magnétique émerge de façon efficace à la surface de l'étoile mais cela parait probable vu la présence de cette *tachocline inverse* qui peut concentrer et amplifier le champ, celui-ci devenant flottant. Létude de l'interaction du champ dynamo avec le champ de l'enveloppe radiative des étoiles massives afin d'en expliquer leur magnétisme est la suite logique de ce travail, et des efforts dans ce sens ont commencés.

6.5 Article publiés

6.5.1 Simulations of core convection in rotating A-type stars: differential rotation and overshooting

par Browning, Brun & Toomre 2004, ApJ, 601, 512

The Astrophysical Journal, 601:512–529, 2004 January 20

SIMULATIONS OF CORE CONVECTION IN ROTATING A-TYPE STARS: DIFFERENTIAL ROTATION AND OVERSHOOTING

Matthew K. Browning, Allan Sacha Brun,[1] and Juri Toomre
JILA and Department of Astrophysical and Planetary Sciences, Campus Box 440, University of Colorado, Boulder, CO 80309-0440
Received 2003 August 13; accepted 2003 September 25

ABSTRACT

We present the results of three-dimensional simulations of core convection within A-type stars of 2 $M_\odot$, at a range of rotation rates. We consider the inner 30% by radius of such stars, thereby encompassing the convective core and some of the surrounding radiative envelope. We utilize our anelastic spherical harmonic code, which solves the compressible Navier-Stokes equations in the anelastic approximation, to examine highly nonlinear flows that can span multiple scale heights. The cores of these stars are found to rotate differentially, with central cylindrical regions of strikingly slow rotation achieved in our simulations of stars whose convective Rossby number (R_{oc}) is less than unity. Such differential rotation results from the redistribution of angular momentum by the nonlinear convection that strongly senses the overall rotation of the star. Penetrative convective motions extend into the overlying radiative zone, yielding a prolate shape (aligned with the rotation axis) to the central region in which nearly adiabatic stratification is achieved. This is further surrounded by a region of overshooting motions, the extent of which is greater at the equator than at the poles, yielding an overall spherical shape to the domain experiencing at least some convective mixing. We assess the overshooting achieved as the stability of the radiative exterior is varied and the weak circulations that result in that exterior. The convective plumes serve to excite gravity waves in the radiative envelope, ranging from localized ripples of many scales to some remarkable global resonances.

Subject headings: convection — stars: interiors — stars: rotation

1. INTRODUCTION AND MOTIVATION

Convection within the cores of massive stars has major impact on their structure and evolution, yet little is known about the detailed properties of such convection. These convective motions, driven by the steep temperature gradient arising from the vigorous burning of the CNO cycle, carry outward a large fraction of the stars' luminosities. In standard one-dimensional stellar models (e.g., Maeder & Meynet 2000), the effects of such convection are usually calculated using simple mixing-length prescriptions, but such approaches involve considerable uncertainties. Mixing-length theory can provide only rough estimates of the energy flux carried by the convection and no effective estimates of the differential rotation or meridional circulation generated by the convective flows, which may have important consequences for mixing and for redistribution of angular momentum within massive stars.

Overshooting from convection zones raises other problems. It has long been realized that convective motions are unlikely to come to a halt at the boundary between the convective core and the stable radiative zone above it. Indeed, upward moving fluid parcels will penetrate into the stable zone, decelerating and mixing with their surroundings (e.g., Roxburgh 1965). Such overshooting motions might bring fresh fuel into the core, thereby prolonging a star's lifetime on the main sequence, and have noticeable effects on its evolution (e.g., Woo & Demarque 2001). Yet estimating the extent of this overshooting is challenging.

Likewise uncertain is the differential rotation achieved within convective cores. In the solar convection zone, Reynolds stresses, meridional circulations, and viscous forces give rise to a prominent differential rotation, now being probed extensively by helioseismology (Gough & Toomre 1991; Schou et al. 1998). Explaining that differential rotation within the Sun has been a major challenge for theory and simulation in recent years, with three-dimensional spherical shell simulations of turbulent convection now beginning to make contact with the helioseismic results (e.g., Miesch et al. 2000; Elliott, Miesch, & Toomre 2000; Brun & Toomre 2002). The presence of such nonuniform rotation deep within more massive stars would have major consequences for the properties of such stars: differential rotation can give rise to shear instabilities that stir and mix material, and may serve to build strong magnetic fields through sustained dynamo action.

Indeed, the generation of magnetic fields within stars by dynamo action must result from large-scale convection in the stellar plasma interacting with rotation. In some stars with convective envelopes, such as the Sun, the building of orderly magnetic fields and cyclic activity is thought to depend sensitively on highly turbulent convection yielding strong differential rotation, including a tachocline of shear at the interface between the bottom of the convection zone and the radiative interior (e.g., Thompson et al. 2003). More generally, correlations between magnetic fields and rotation have been inferred in main-sequence stars ranging from F5 to M9 (Noyes et al. 1984; Mohanty et al. 2002), with these fields also thought to be a result of dynamo action driven by convection, whether occupying an envelope or the full interior. Yet a comprehensive understanding of how this occurs remains elusive. More massive stars with convective cores are similarly likely to admit magnetic dynamo action, for they too possess the necessary ingredients: intensely turbulent convection, a highly conductive medium, and global effects of rotation, all thought to be

[1] New permanent address: DSM/DAPNIA/Service d'Astrophysique, CEA Saclay, 91191 Gif-sur-Yvette, France.

crucial for the building of magnetic fields (Charbonneau & MacGregor 2001). Whether the resulting fields are chaotic or global and orderly may be a sensitive matter.

1.1. *Estimates of Overshooting from Convective Cores*

Some theoretical work has provided constraints on the size of the convective core and the extent of overshooting. Roxburgh (1978, 1989, 1998; see also Zahn 1991) showed that an upper limit to the total size of the convective region can be deduced by considering the integral

$$\int_0^{r_c} (L_{\rm rad} - L)\frac{1}{T^2}\frac{dT}{dr}\,dr = \int_V \frac{\Phi}{T}\,dV > 0, \qquad (1)$$

with L the total nuclear luminosity, $L_{\rm rad}$ the radiative luminosity, Φ the viscous dissipation per unit volume, and r_c the radius of the convective core including overshooting. Since within the convective core some of the nuclear energy must be carried by convection, $L_{\rm rad} < L$ there. Thus, if viscous dissipation is neglected, there must be an overshooting region where $L_{\rm rad} > L$, whose extent can be estimated from this equation. For small convective cores, these considerations yield an overshoot region of size $d \approx 0.18 r_o$, where r_o is the radius of the convectively unstable region (Roxburgh 1992). Rosvick & VandenBerg (1998) found that observations of the stellar cluster NGC 6819 were best fitted by overshooting that is about half the upper limit provided by Roxburgh's constraint.

Various attempts have been made to estimate the extent of overshooting from observations, typically expressed in terms of pressure scale heights. Meynet, Mermilliod, & Maeder (1993), for example, found that best-fit isochrones for a large number of clusters required overshooting that extends for about 0.2–0.3 times the pressure scale height. Perryman et al. (1998) found evidence for a similar degree of overshooting in Hyades stars. In the open cluster M67, whose main-sequence turnoff stars are thought to be near the low-mass end of stars possessing convective cores, some authors have suggested overshooting that is of order 0.1 pressure scale heights (e.g., Maeder & Meynet 1991; Carraro et al. 1994).

1.2. *Challenges Raised by A-Type Stars*

Convective cores are realized for main-sequence stars more massive than about 1.2 $M_\odot$, thereby providing many stars in which the effects of overshooting could be assessed. However, A-type stars exhibit a variety of peculiarities that have made them the subject of particularly detailed study (see Wolff 1983, hereafter W83, for a broad review). We recall that A-type stars possess both a convective core as well as multiple shallow convection zones near the surface. Some of these stars display strong abundance anomalies, with greatly enhanced rare earth element abundances relative to normal stars (e.g., Kurtz 1990). Surface abundance anomalies have also been observed in a variety of other stars (Preston 1974; Gehren 1988; Pinsonneault 1997; Abt 2000). Radiative diffusive separation, wherein radiation pressure drives outward some elements while others sink, is a favored explanation for these abundance features but requires a very stable radiative zone in which this may be occurring. Latour, Toomre, & Zahn (1981) showed that the H and He envelope convection zones in A-type stars are likely linked by penetrative motions that would upset the delicate quiescence needed for radiative diffusion to work effectively. This problem can be avoided if helium gravitationally settles out to greater depths, in which case the deeper convection zone driven primarily by that element's second ionization would not exist (e.g., Vauclair, Vauclair, & Pamjatnikh 1974). Such settling is impeded by meridional circulations within the radiative zone (Michaud et al. 1983), which are thought to increase in amplitude with increasing stellar rotational velocity. It has recently been shown (e.g., Richard, Michaud, & Richer 2001) that in some stars a further iron convection zone is established below the other two surface convective regions, which may lead to deeper mixing within such stars (e.g., Vauclair 2003; Richer, Michaud, & Turcotte 2000). While this basic picture explains many of the observed abundance features, many of the details are not precisely known.

A subset of the A-type stars also possesses strong surface magnetic features that appear to persist for many rotation periods (W83). Such fields may well be oblique rotators of primordial origin (e.g., Mestel 1999). However, if dynamo-generated fields within the convective core were able to rise through the radiative zone, possibly by means of magnetic buoyancy instabilities, they might also influence the surface fields. Recent numerical studies (MacGregor & Cassinelli 2003) have provided tantalizing indications that it may indeed be possible for strong magnetic fields generated in the core to rise to the surface.

The A-type stars also hold interest because of the rich set of observational constraints beginning to be provided by asteroseismological probing of such stars. The pulsating Ap stars exhibit high-order nonradial p-modes, which allow some deductions about stellar radii, temperature, and magnetic fields (e.g., Matthews 1991; Cunha 2002).

1.3. *Modeling Convection in Full Spherical Domains*

The extensive observations of A-type stars and the challenges raised have encouraged us to consider the core convection influenced by rotation that is occurring deep within their interiors. The surface pathologies of A stars clearly raise many questions about their interior dynamics, thereby lending vibrancy to their study. We hope that our modeling will further serve to reveal general dynamical properties of the core convection that is also occurring in other massive stars.

The major uncertainties associated with core convection—the extent of its overshooting into the surrounding radiative envelope and the differential rotation and circulations it establishes—now lead us to undertake simulations of such convection in full spherical geometries that permit global connectivity. We aim to capture much of the essential physics, admitting highly nonlinear flows that can extend over multiple scale heights as they mold the dynamical structure of the convective core. We realize that there may be few observable consequences at the surfaces of these stars of what may be proceeding dynamically at their centers. However, the circulations and gravity waves that may be induced by the core convection may well have implications at the surface, as might magnetic fields being produced by dynamo action deep within these stars. All may depend somewhat sensitively on the rotation rates of the stars.

Advances in supercomputing are now beginning to allow us to examine the properties of core convection in some detail. We begin here by considering three-dimensional hydrodynamic simulations of the inner regions of a 2 $M_\odot$ A-type star. In subsequent papers, we plan to explore the magnetic dynamo action that may be realized in such convective cores and to examine possible instabilities that might allow the resulting magnetic fields to rise to the surface.

In § 2 we describe our formulation of the problem and briefly summarize the computational tools being used. Section 3 discusses the general properties of the nonlinear convective flows realized in the core, including the transport of energy achieved. The redistribution of angular momentum by the convection yields prominent differential rotation profiles that are presented in § 4. Section 5 considers the temporal evolution of convective patterns within the core and examines the gravity waves that are excited within the radiative envelope. Analysis of the penetration and overshooting by the convection is discussed in § 6. The meridional circulations induced by the convection, within both the core and the radiative envelope, are considered in § 7. Section 8 evaluates the manner in which the convection yields strong differential rotation. A summary of our principal findings and their implications is presented in § 9.

2. POSING THE PROBLEM

2.1. *Anelastic Equations*

The simulations described here were performed using our anelastic spherical harmonic (ASH) code. ASH solves the three-dimensional anelastic equations of motion in a rotating spherical geometry using a pseudospectral semi-implicit approach (Clune et al. 1999; Miesch et al. 2000). These equations are fully nonlinear in velocity variables and linearized in thermodynamic variables with respect to a spherically symmetric mean state. This mean state is taken to have density $\bar{\rho}$, pressure $\bar{P}$, temperature $\bar{T}$, and specific entropy $\bar{S}$; perturbations about this mean state are written as ρ, P, T, and S, respectively. The conservation equations of mass, momentum, and energy in this rotating reference frame are therefore written as

$$\nabla\cdot(\bar{\rho}\boldsymbol{v}) = 0, \tag{2}$$

$$\bar{\rho}\left[\frac{\partial \boldsymbol{v}}{\partial t} + (\boldsymbol{v}\cdot\nabla)\boldsymbol{v} + 2\Omega_0 \times \boldsymbol{v}\right] = -\nabla P + \rho\boldsymbol{g} - \nabla\cdot\mathbf{D} - (\nabla\bar{P} - \bar{\rho}\boldsymbol{g}), \tag{3}$$

$$\bar{\rho}\bar{T}\frac{\partial S}{\partial t} = \nabla\cdot[\kappa_r\bar{\rho}c_p\nabla(\bar{T}+T) + \kappa\bar{\rho}\bar{T}\nabla(\bar{S}+S)] - \bar{\rho}\bar{T}\boldsymbol{v}\cdot\nabla(\bar{S}+S) + 2\bar{\rho}\nu\left[\mathbf{e}_{ij}\mathbf{e}_{ij} - \frac{1}{3}(\nabla\cdot\boldsymbol{v})^2\right] + \bar{\rho}\epsilon, \tag{4}$$

where c_p is the specific heat at constant pressure, $\boldsymbol{v} = (v_r, v_\theta, v_\phi)$ is the local velocity in spherical geometry in the rotating frame of constant angular velocity $\boldsymbol{\Omega}_0$, $\boldsymbol{g}$ is the gravitational acceleration, κ_r is the radiative diffusivity, ϵ is the heating rate per unit mass due to nuclear energy generation, and $\mathbf{D}$ is the viscous stress tensor, with components

$$\mathbf{D}_{ij} = -2\bar{\rho}\nu\left[\mathbf{e}_{ij} - \frac{1}{3}(\nabla\cdot\boldsymbol{v})\delta_{ij}\right], \tag{5}$$

where $\mathbf{e}_{ij}$ is the strain rate tensor. Here ν and κ are effective eddy diffusivities for vorticity and entropy. To close the set of equations, linearized relations for the thermodynamic fluctuations are taken as

$$\frac{\rho}{\bar{\rho}} = \frac{P}{\bar{P}} - \frac{T}{\bar{T}} = \frac{P}{\gamma\bar{P}} - \frac{S}{c_p}, \tag{6}$$

assuming the ideal gas law

$$\bar{P} = \mathcal{R}\bar{\rho}\bar{T}, \tag{7}$$

where $\mathcal{R}$ is the gas constant. The effects of compressibility on the convection are taken into account by means of the anelastic approximation, which filters out sound waves that would otherwise severely limit the time steps allowed by the simulation.

Convection in stellar environments occurs over a large range of scales. Numerical simulations cannot, with present computing technology, consider all these scales simultaneously. We therefore seek to resolve the largest scales of the nonlinear flow, which we think are likely to be the dominant players in establishing differential rotation and other mean properties of the core convection zone. We do so within a large-eddy simulation formulation, which explicitly follows larger scale flows while employing subgrid-scale descriptions for the effects of the unresolved motions. Here those unresolved motions are treated as enhancements to the viscosity and thermal diffusivity (ν and κ), which are thus effective eddy viscosities and diffusivities. For simplicity, we have taken these to be functions of radius alone and to scale as the inverse of the square root of the mean density. We emphasize that currently tractable simulations are still many orders of magnitude away in parameter space from the highly turbulent conditions likely to be found in real stellar convection zones. These large-eddy simulations should therefore be viewed only as indicators of the properties of the real flows. We are encouraged, however, by the success that similar simulations (e.g., Miesch et al. 2000; Elliott et al. 2000; Brun & Toomre 2002) have enjoyed in matching the detailed observational constraints for the differential rotation within the solar convection zone provided by helioseismology.

2.2. *Computational Approach*

Thermodynamic variables within ASH are expanded in spherical harmonics $Y_\ell^m(\theta,\phi)$ in the horizontal directions and in Chebyshev polynomials $T_n(r)$ in the radial. Spatial resolution is thus uniform everywhere on a sphere when a complete set of spherical harmonics of degree ℓ is used, retaining all azimuthal orders m. We truncate our expansion at degree $\ell = \ell_{\max}$, which is related to the number of latitudinal mesh points N_θ [here $\ell_{\max} = (2N_\theta - 1)/3$], take $N_\phi = 2N_\theta$ latitudinal mesh points, and utilize N_r collocation points for the projection onto the Chebyshev polynomials. We employ a stacked Chebyshev representation, wherein the computational domain is split into two regions and separate Chebyshev expansions performed for each. The interface between these two regions, here taken to be the approximate boundary between the convective and radiative zones, is thus treated with greater resolution in order to capture elements of the penetrative convection occurring there. We have taken $N_r = 49 + 33 = 82$ and $\ell_{\max} = 85$ in this study for the cases considered here and have used $\ell_{\max} = 170$ for some companion simulations to verify that the spectral resolution was adequate. An implicit second-order Crank-Nicholson scheme is used in determining the time evolution of the linear terms, whereas an explicit second-order Adams-Bashforth scheme is employed for the advective and Coriolis terms. The ASH code has been optimized to run efficiently on massively parallel supercomputers such as the IBM SP-3 and the Compaq TCS-1 and has demonstrated excellent scalability on such machines.

2.3. *Formulation of the Model*

The model considered here is intended to be a simplified description of the inner 30% by radius of a main-sequence A-type star of 2 $M_\odot$, consisting of the convective core (approximately the inner 15% of the star) and a portion of the overlying radiative zone. Contact is made with a one-dimensional stellar model (at an age of 500 Myr) for the initial conditions, adopting realistic values for the radiative opacity, density, and temperature. This one-dimensional model was obtained using the CESAM stellar evolution code (Morel 1997; Brun et al. 2002), which employs the OPAL equation of state and opacities (Iglesias & Rogers 1996; Rogers, Swenson, & Iglesias 1996) and the nuclear cross sections of Adelberger et al. (1998) in describing the microscopic properties of the stellar plasma. Convection is computed within CESAM using a classical mixing-length treatment calibrated on solar models, with some convective overshooting (typically $r = 0.25H_p$) taken into account. Our simulations were initialized using the radial profiles of gravity g, radiative diffusivity $\kappa_{\rm rad}$, mean density $\bar{\rho}$, and mean entropy gradient $d\bar{S}/dr$ as the starting points for an iterative Newton-Raphson solution for the hydrostatic balance and for the gradients of the thermodynamic variables. The mean temperature $\bar{T}$ is then deduced from equation (7). This technique yields mean profiles in reasonable agreement with the one-dimensional stellar model (Fig. 1). The nuclear source of energy ϵ in our simulations is also deduced from the stellar model. For computational convenience, we take $\epsilon = \epsilon_0 \bar{T}^8$, determining the constant ϵ_0 by requiring that the integrated luminosity match the one-dimensional model's surface luminosity.

We have softened the steep entropy gradient contrast encountered in going from the convective core to the surrounding radiative zone, which would otherwise favor the driving of small-scale, high-frequency internal gravity waves that are presently unresolvable given reasonable computational resources. This lessening of the "stiffness" of the system has impact on the extent to which convective motions may overshoot into the radiative region. We have excluded the inner 2% of the star from our computational domain for numerical reasons, namely, that the coordinate systems employed in ASH possess both coordinate singularities at $r = 0$ and decreasing mesh size (and hence highly limited time steps) with decreasing radius. It is difficult to gauge with certainty the effects of excluding this central region, which might in principle both project a Taylor column aligned with the rotation axis (e.g., Pedlosky 1987) into the surrounding fluid, as well as give rise to boundary layers. However, we have seen no evidence that spurious physical responses have been generated by its omission. In trial simulations with both smaller and larger excluded central regions (ranging from 0.3% to 4% of the stellar radius), the properties of the developed mean flows were very similar to those described here.

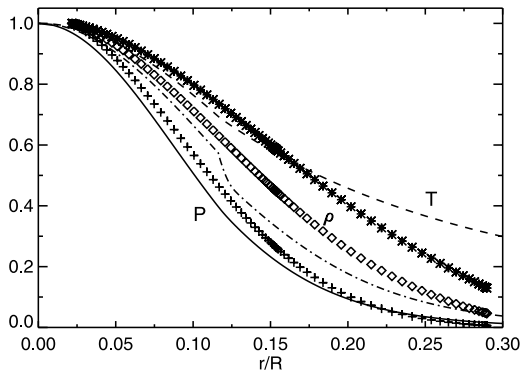

FIG. 1.—Mean radial stratification in the central regions of a 2 $M_\odot$ A-type star, within both a one-dimensional stellar structure model and case C. The mean pressure $\bar{P}$, temperature $\bar{T}$, and density $\bar{\rho}$ are plotted with symbols at their radial mesh locations for case C and as continuous curves for the one-dimensional model. All variables are normalized to their maximum values, which for case C at the inner boundary of the computational domain ($r = 0.022R$) are $\bar{\rho}_0 = 48$ g cm^{-3}, $\bar{T}_0 = 2.0 \times 10^7$ K, and $\bar{P}_0 = 1.4 \times 10^{17}$ dynes cm^{-2}.

As boundary conditions on the spherical domain, we utilize impenetrable and stress-free conditions for the velocity field and constant entropy gradient (i.e., constant emergent flux) at both the inner and outer boundaries. As initial conditions, some simulations have been started from quiescent conditions of uniform rotation whose radial stratification is given by the one-dimensional stellar model; others used evolved states from prior solutions to initiate simulations with reduced diffusivities.

The main parameters of our simulations are summarized in Table 1. In brief, we have modeled the inner regions of 2 $M_\odot$ A-type stars at a range of rotation rates, with nonlinear flows of varying complexity achieved by modifying the effective eddy viscosities and diffusivities ν and κ. Several values of ν and κ are utilized to achieve both laminar and more complex convective flows in some companion cases, all at a Prandtl number $P_r = \nu/\kappa = 0.25$. We consider rotation rates from 1/10 to 4 times the solar rate of $\Omega_0 = 2.6 \times 10^{-6}$ s^{-1} (or 414 nHz), though concentrating primarily on models at the solar rotation rate. Three different values of the maximum entropy gradient $d\bar{S}/dr$ in the radiative region were taken, thus effectively varying the stiffness of the boundary between that region and the convective core, primarily as a way to study the effects on overshooting motions induced by softening that boundary. We have chosen only representative simulations for summary in this paper (and in Table 1) out of a larger total set of computations.

Figure 1 shows the mean radial profiles for temperature, density, and pressure attained in a representative simulation (case C), together with profiles of the same variables in a typical one-dimensional stellar structure model. The evolved simulation possesses somewhat less steep gradients for these variables than does the one-dimensional stellar model, but the functional form of these quantities is largely unchanged by our detailed treatment of the convection.

3. NATURE OF CORE CONVECTION

The flows in all the cases studied are highly time dependent, with complex and intermittent features emerging as the simulations evolve. The convection is characterized by large-scale flows that sweep through much of the unstable core, coupling widely separated sites. Thus, influences of the convective motions are decidedly nonlocal. Such global motions can result because of the topologically connected nature of full spheres. The addition of rotation to these spherical domains admits Coriolis forces and resulting velocity correlations (Reynolds stresses) that yield some surprising effects. In particular, we find that the cores exhibit prominent differential rotation in both radius and latitude, involving in most of our simulations a central column of slow rotation aligned with the rotation axis.

TABLE 1
SUMMARY OF SIMULATION PARAMETERS

Parameter	A	B	C	D	E	C4	F
$\Omega_0/\Omega_\odot$	1	1	1	1	1	4	0.1
$\max d\bar{S}/dr$	1.5×10^{-6}	1.5×10^{-5}	1.5×10^{-5}	1.5×10^{-4}	1.5×10^{-4}	1.5×10^{-5}	1.5×10^{-4}
ν	4.35×10^{11}	2.49×10^{12}	4.35×10^{11}	2.49×10^{12}	4.35×10^{11}	2.49×10^{11}	4.35×10^{11}
κ	1.74×10^{12}	9.96×10^{12}	1.74×10^{12}	9.96×10^{12}	1.74×10^{12}	9.96×10^{11}	1.74×10^{12}
R_a	1.7×10^5	2.0×10^4	1.9×10^5	1.0×10^4	3.3×10^5	2.2×10^6	3.3×10^5
T_a	1.2×10^7	3.6×10^5	1.2×10^7	3.6×10^5	1.2×10^7	5.9×10^8	1.2×10^5
R_o	0.24	0.47	0.25	0.33	0.33	0.12	3.3
R_e	1.7×10^2	1.2×10^1	1.3×10^2	1.1×10^1	1.4×10^2	2.0×10^2	1.7×10^2

NOTES.—All simulations have an inner radius of 3.0×10^9 cm and an outer radius of 4.0×10^{10} cm, with $L = 1.7 \times 10^{10}$ cm the approximate radial extent of the convective core. The Prandtl number $P_r = \nu/\kappa = 0.25$ in all cases. Here evaluated at midlayer depth are the Rayleigh number $R_a = (-\partial\bar{\rho}/\partial\bar{S})\Delta S g L^3/\rho\nu\kappa$ (with ΔS the entropy contrast across the core), the Taylor number $T_a = 4\Omega^2 L^4/\nu^2$, the convective Rossby number $R_{ac} = (R_a/T_a P_r)^{1/2}$, and the rms Reynolds number $\tilde{R}_e = \tilde{v}L/\nu$, where $\tilde{v}$ is a representative rms convective velocity. A Reynolds number based on the peak velocity at middepth would be about 4 times larger. The eddy viscosity ν and eddy conductivity κ at the middle of the core are quoted in $\mathrm{cm}^2\ \mathrm{s}^{-1}$.

Further, the extent of penetration of the convection into the surrounding stable radiative envelope varies from equator to pole, yielding a prolate shape to the central region of nearly adiabatic stratification.

The rich time dependence typical of core convection implies that extended simulation runs must be conducted in order to sample the dynamics. Attaining a statistically equilibrated state in the dynamics typically requires evolving the flows for about 1500 days of physical time, or roughly 60 rotational periods at the nominal solar rate. Deductions about the mean flows accompanying the convection, such as differential rotation and meridional circulation, or of the mean heat transport achieved by the convection require averaging the flows over lengthy periods of time, typically greater than 100 days in the late stages of a simulation. We begin by describing some of the general attributes of the convection realized in our simulations.

3.1. *Topology and Scales of Convective Flows*

Core convection clearly involves global-scale overturning motions that extend over much of the unstable domain. This is illustrated in Figure 2, which presents both a three-dimensional rendering of the instantaneous radial velocity near the outer surface of the convective core studied in case E and an equatorial cut at the same instant through that core domain. Specific regions of upflow and downflow occupy large fractions of the irregular surface (Fig. 2*a*) and extend in radius over much of that unstable volume (Fig. 2*b*). Evidently, there is global connectivity in the flows over well-separated locations, spanning wide ranges in longitude and latitude in both hemispheres. The equatorial cut reveals that the flow patterns involve a prominent azimuthal wavenumber $m = 2$ component, although many other wavenumbers are certainly also involved in describing these overturning motions. Little asymmetry is apparent between upflows and downflows: radially inward and outward motions occur on roughly the same spatial scales and possess comparable flow amplitudes (see also Table 2). This appears to be a consequence of the relatively modest radial density contrast (about 2.5) present across the unstable core. We do not here obtain the fast narrow downflows and much broader upflows realized in far more compressible configurations representative

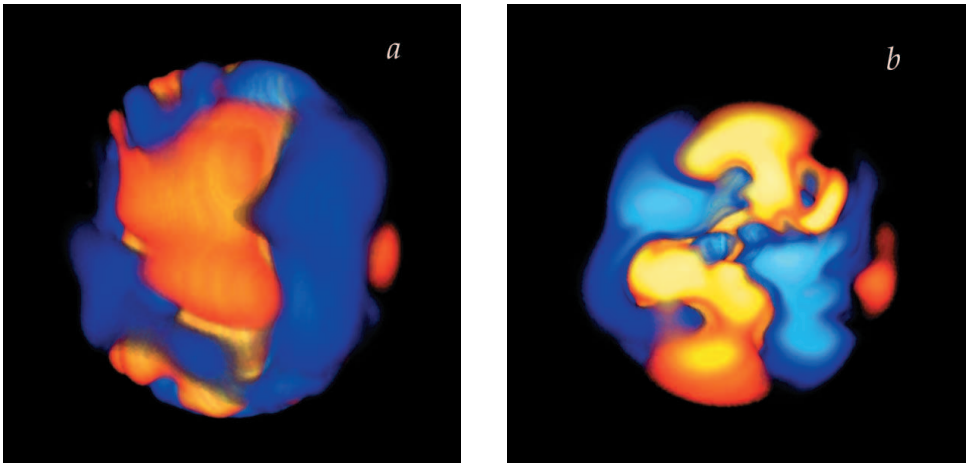

FIG. 2.—Radial velocity at one instant in time for case E, using volume rendering of flow structure (*a*) near the outer boundary of the prolate convective core, with the rotation axis oriented vertically, and (*b*) near the equatorial plane viewed from above. Upflows (radially outward) are rendered as yellow/red tones; downflows are bluish.

TABLE 2
VELOCITIES, ENERGIES, DIFFERENTIAL ROTATION, AND OVERSHOOTING

Parameter	A	B	C	D	E	C4
$\tilde{v}_r$	36	15	28	14	30	26
$\tilde{v}_\theta$	27	24	26	22	26	21
KE	1.0×10^8	3.3×10^7	7.6×10^7	2.2×10^7	7.4×10^7	1.2×10^8
DRKE	5.6×10^7	3.5×10^6	4.6×10^7	5.6×10^6	4.3×10^7	1.0×10^8
CKE	4.2×10^7	2.9×10^7	2.9×10^7	1.6×10^7	3.0×10^7	1.3×10^7
MCKE	2.5×10^6	5.4×10^4	8.6×10^5	2.4×10^4	1.1×10^6	3.7×10^5
$\Delta\Omega/\Omega_0$	65%	26%	56%	28%	62%	36%
$\bar{d}_0$	3.41×10^9	3.35×10^9	2.20×10^9	3.25×10^9	1.75×10^9	2.57×10^9
r_c^e	1.93×10^{10}	1.82×10^{10}	1.80×10^{10}	1.89×10^{10}	1.76×10^{10}	1.89×10^{10}
r_c^p	2.16×10^{10}	1.97×10^{10}	2.05×10^{10}	2.03×10^{10}	2.00×10^{10}	2.05×10^{10}
$\bar{r}_o$	2.34×10^{10}	2.24×10^{10}	2.19×10^{10}	2.10×10^{10}	2.07×10^{10}	2.28×10^{10}

NOTES.—Components of rms velocity components $\tilde{v}_r$ and $\tilde{v}_\theta$ at midcore depth ($r = 0.10R$) are expressed in meters per second. The temporal averages over the full domain of the kinetic energy density (KE), and the energies associated with the differential rotation (DRKE), convection (CKE), and meridional circulation (MCKE), are all expressed in ergs cm^{-3}. The relative angular velocity contrasts $\Delta\Omega/\Omega_0$ between 0° and 60° latitude are stated. The geometry of the prolate convective core and of the surrounding region of overshooting is measured by the radius of the convectively unstable region at the equator (r_c^e) and at the poles (r_c^p), the outer boundary of the region of overshooting ($\bar{r}_o$), and the spherical average of the spatial extent of the overshoot ($\bar{d}_o$), all in centimeters.

of the solar convection zone (Brummell, Hurlburt, & Toomre 1998; Brun & Toomre 2002).

The convectively unstable region that results is mildly prolate in shape (Fig. 2*a*), having greater spatial extent near the poles than near the equator. This nonspheroidal shape (see § 6.1) for the extent of the vigorous convection is a striking feature shared by all our simulations. The rumpled appearance of v_r in this three-dimensional volume rendering comes from emphasizing the large-scale penetrative structure of such velocity fields. In studying time sequences of such renderings, the interface between the well-mixed interior and the radiative exterior looks much like a throbbing heart, as penetrative motions wax and wane and propagate laterally, launching gravity waves in the process (see § 5.2). Analysis of the time evolution of equatorial cuts (Fig. 2*b*) reveals that some flows dive through the central regions of the core to emerge on the other side, with such patterns exhibiting distinctive retrograde motion.

3.2. *Velocity and Thermal Patterns*

We present in Figure 3 global mappings for cases B and C of both the radial velocities v_r and temperature fluctuations T (relative to the average of temperature on a spherical surface at a given radius). These Mollweide projections for the fields are shown both well within the convective interior (at $r = 0.10R$; Fig. 3, *lower panels*) and at the transition into the stable exterior ($r = 0.16R$; Fig. 3, *upper panels*). These mappings reveal that the radial velocity patterns in any given snapshot have a noticeable alignment with the rotation axis. (Such projections exhibit meridian lines as increasingly curved arcs away from the central meridian, which appears as a vertical line; here the lines of constant latitude are indeed parallel.) The more laminar case B (Figs. 3*a*–3*d*, *left*) possesses structures that are largely symmetric about the equator, whereas the lower diffusivities (ν and κ) in case C (Figs. 3*e*–3*h*, *right*) lead to flows with broken symmetries in the two hemispheres as more intricate flows are realized. In both cases the flow structures at high latitudes are more isotropic and of smaller scale, and somewhat faster flows are realized for case C (see also Table 2).

Radial motions in these simulations are intimately linked to fluctuations in temperature. These buoyantly driven flows should typically involve positive T in regions of ascending motion within the unstable core and negative T in descending flows there. Such a positive correlation between v_r and T is largely realized in the lower panels in Figure 3 for both cases showing the $r = 0.10R$ depth where the convection is vigorous. The less complex flows in case B exhibit such correlation readily, whereas in case C there are also sites where the sense of the correlation is reversed. The nature of the correlations changes as motions penetrate into the radiative surroundings. The buoyancy braking that is expected within this region of stable stratification, as at the $r = 0.16R$ depth (Fig. 3, *upper panels*), arises from the radial velocities and temperature fluctuations becoming anticorrelated. The sense of T in both regions is partly controlled by the source term in equation (4) that involves the product of v_r with the radial mean entropy gradient. When the latter gradient changes sign in going from an unstable stratification (superadiabatic in the convective core) to stable (subadiabatic) stratification as flows extend upward into the radiative envelope, so does the sense of T. This correspondence between radial velocities and temperature fluctuations is true only in a general sense: on fine scales, secondary instabilities can drive motions that locally violate these principles. Similarly, the nonlinear advection of temperature fluctuations by motions that twist and turn can lead to unusual combinations of v_r and T at some sites. The anticorrelation of v_r and T in the region of penetration is clearest in case *B* involving the simpler flow fields. Because the thermal diffusivity is larger than the viscosity in these simulations (i.e., the Prandtl number P_r is less than unity, namely, 0.25), thermal structures have a somewhat larger physical scale than do associated features in the radial velocity.

The temperature fluctuations at both depths in Figure 3 have amplitudes of only a few kelvins (compared with the mean temperatures of millions of kelvins found at such depths), which, combined with radial velocities of order 50 m s^{-1} in the bulk of the convective interior and the high heat capacity of the gas, are sufficient to carry outward a good fraction of the emerging flux (see § 3.3). The radial velocities have plummeted to much smaller values just beyond the edge of the convection zone where the motions are beginning to penetrate upward into the radiative zone.

The convective fields in these simulations can be assessed using probability distribution functions (PDFs). Figure 4 shows PDFs for the radial velocity and temperature fluctuations on a

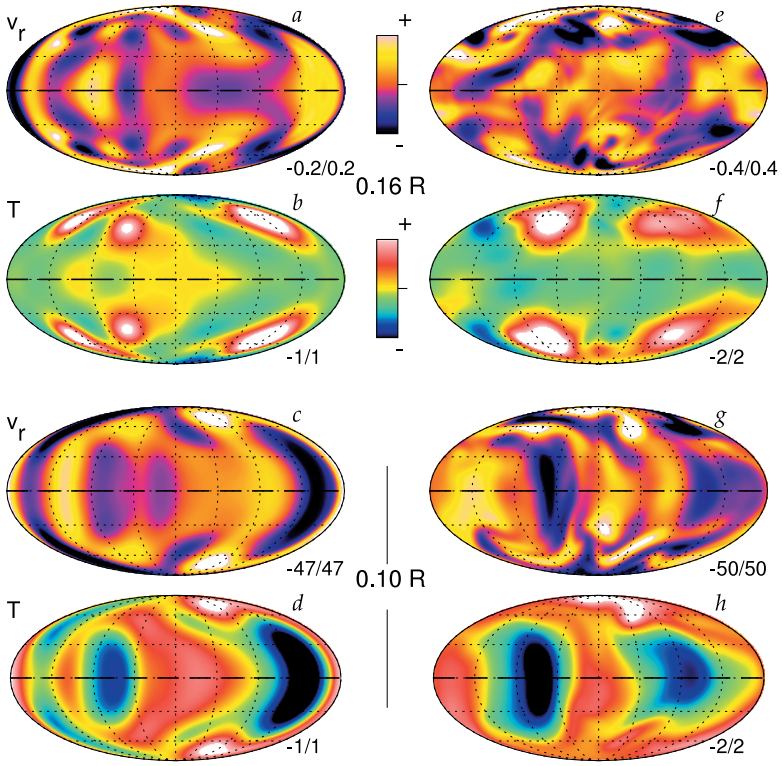

FIG. 3.—Global mappings of radial velocities (v_r) and associated temperature fluctuations (T) at one instant in time for the laminar case B (*left*) and the more complex case C (*right*), shown in Mollweide projection with the dashed horizontal line designating the equator. Two depths are sampled, with the lower panels exhibiting v_r and T within the convective core (at $r = 0.10R$) and the upper panels within the region of overshooting (at $r = 0.16R$). One color rendering is used for v_r and another for T, with the maximum and minimum amplitudes for each field (in meters per second and kelvins) indicated next to each panel.

spherical surface within the convective core ($r = 0.10R$) and the region of overshooting ($r = 0.16R$) of case C, exhibiting both instantaneous PDFs and time-averaged ones. The distributions of radial velocities are largely symmetric Gaussian functions at both depths. The detailed features in the instantaneous PDFs change as the flows evolve. The instantaneous temperature field distributions (Figs. 4*d* and 4*h*) possess spikes, indicating the presence of large-scale coherent temperature structure; at other instants, the spikes may be replaced by broader plateaus. The time-averaged PDFs for T are nonsymmetric, with broad tails extending to positive values in the region of overshooting and to negative ones in the core. These tails serve to compensate for the off-center most probable values that are positive in the core and negative in the overshooting region. Such complexities in the PDFs are realized in all of our simulations and thus are at some variance with simpler relations assumed in mixing-length treatments of convection.

3.3. *Energy Transport*

The release of energy by CNO cycle nuclear burning in the core leads to a progressively increasing local luminosity with radius within the inner parts of our domain. The energy produced in such a distributed fashion gets carried outward primarily by radiative diffusion and mechanical transport of heat (or enthalpy) by the convection. To assess the role convection plays in the overall energy balance, we recall that the rate at which convection transports energy in the radial direction is given by the enthalpy flux

$$F_e(r) = \bar{\rho} c_p \overline{v_r T}, \tag{8}$$

involving a product of the radial velocity with fluctuations in the heat content of the fluid, proportional to T, and averaged over a spherical surface and in time (indicated by the overbar). We may compare F_e with the flux of energy carried by radiation,

$$F_r(r) = -\kappa_r \bar{\rho} c_p \left(\frac{d\bar{T}}{dr} + \overline{\frac{dT}{dr}} \right), \tag{9}$$

with the latter term arising from the mean of radial gradients of temperature fluctuations, which are here negligible. The enthalpy and radiative fluxes largely suffice to carry outward the energy produced by nuclear reactions within the core, yielding a total flux

$$F_t = \frac{L(r)}{4\pi r^2}, \tag{10}$$

where L is the luminosity of the star, which increases with radius until the surface luminosity L_* is attained. (The kinetic

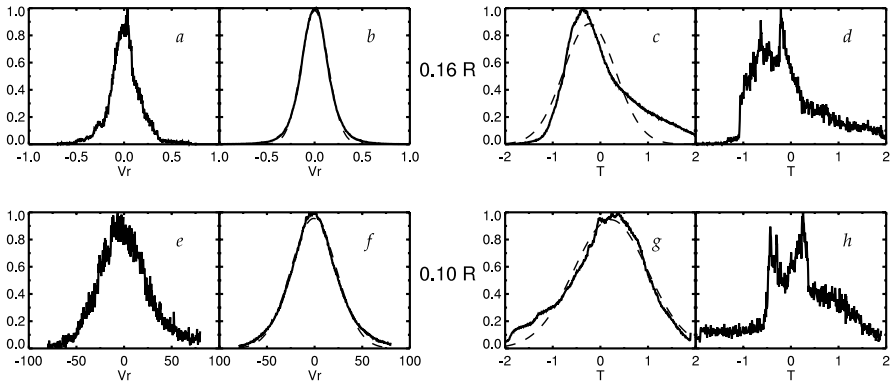

FIG. 4.—Probability distribution functions in case C for radial velocities (*left*) and temperature fluctuations (*right*) within the convective core (e–h; at $r = 0.10R$) and the region of overshooting (a–d; at $r = 0.16R$). (a, d, e, h) Instantaneous PDFs for the two fields; (b, c, f, g) temporal averages over about 180 days together with the best-fit Gaussian of zero mean (*dashed curves*). The distribution of radial velocities very closely approximates a Gaussian, whereas the fluctuations of temperature are slightly asymmetric about their most probable value.

energy flux, the viscous flux, and the flux carried by unresolved subgrid motions are all small compared with F_e and F_r.)

Figure 5 displays the variation with radius of F_r and F_e, expressed as luminosities, for case C. The enthalpy flux is maximized near the middle of the convective core (at $r = 0.08R$), serving to carry about 57% of the local stellar luminosity L there, with the remainder transported by radiation. Since the core convection establishes a nearly adiabatic stratification (with $\nabla - \nabla_{\rm ad} \sim 10^{-7}$), the associated temperature gradient that arises serves to specify a radiative flux F_r that increases steadily with radius. Such a growing F_r forces F_e to decrease in the upper half of the unstable core. Beyond the convectively unstable region, at $\bar{r}_c \sim 0.14R$ (see § 6.2), the enthalpy flux becomes negative, resulting from the anticorrelation of radial velocity and temperature fluctuations as the motions are braked. The radiative flux there must compensate for that inward directed enthalpy flux. Our simulations have not been evolved for a sufficient amount of time to allow this compensation to occur fully, since the relevant thermal relaxation time is long compared with other timescales in the problem. Thus, the total luminosity in Figure 5 displays a small dip at the interface between the convective and radiative zones, which in real stars (or a fully evolved simulation) would be absent.

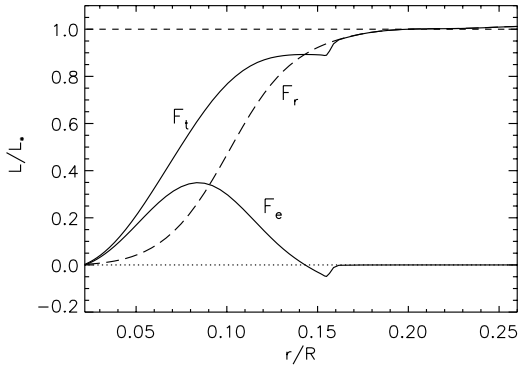

FIG. 5.—Time-averaged radial transport of energy within case C as a function of proportional radius, formed over an interval of about 180 days. Shown are the enthalpy flux F_e and the radiative flux F_r, together with their sum, the total flux F_t; all quantities have been expressed as luminosities. The convective core extends here to about $r = 0.14R$, with the positive F_e there serving to carry as much as 57% of the total flux. The farther region of overshooting involves a small negative (inward directed) enthalpy flux.

The correlations of radial velocity and fluctuating temperature that yield an outward-directed enthalpy flux are achieved in a complicated manner within the bulk of the convective interior. In mapping these variables at one instant in time, it is evident that a number of sites yield an unfavorable correlation, whereas in the main the requisite positive correlation is realized.

The nearly adiabatic stratification achieved by the convection in the bulk of the core is much as in one-dimensional stellar models employing standard mixing-length treatments. However, our self-consistent three-dimensional analysis of convective dynamics and its transports also provides estimates of the stratification in the region of overshooting, which are far more difficult to assess using mixing-length approaches.

4. RESULTING DIFFERENTIAL ROTATION

Convection occurring within deep spherical domains should be strongly influenced by the rotation of the star when the convective overturning time is of the order of or greater than the rotation period. This implies a convective Rossby number R_{oc} (see Table 1) that is of order unity or smaller. The global-scale convection in our models has an overturning period of about 1 month, comparable to the rotation period of a star rotating at the solar rate. Thus, we expect the convection influenced by Coriolis forces to possess correlations between the components of its velocity field. The resulting Reynolds stresses can serve to continuously redistribute angular momentum, leading to angular velocities within the core that are far from uniform rotation. Further, the connected topology of the convective core appears to play an important role in the prominent differential rotation profiles that are realized in our simulations.

4.1. *Central Column of Slow or Rapid Rotation*

We find that strong angular velocity contrasts are established within the convective cores in all our simulations. For model

stars that rotate at least as rapidly as the Sun, these involve roughly cylindrical central columns of decidedly slow rotation (retrograde relative to the reference frame), accompanied by equatorial regions of somewhat enhanced rotational velocity (prograde). As shown in Figure 6 (*left*) for the three cases B, C, and C4, the time-averaged mean longitudinal velocity $\hat{v}_\phi$ exhibits some variations along that central column, with those fluctuations becoming more pronounced as the complexity of the convection increases in going from case B to C (see Fig. 3). There is likewise greater asymmetry in $\hat{v}_\phi$ between the two hemispheres (delineated by the equator) in these cases. Such symmetry breaking may be anticipated as the convection becomes increasingly nonlinear. The convection itself is not symmetric about the equator, and thus mean flows associated with it, including the differential rotation, are likely to exhibit differences in the two hemispheres. The columns of slow rotation extend slightly into the radiative envelopes at high latitudes, in keeping with the prolate shape of the convective core. The presence of the central slow cylinder of rotation does not appear to result from the small inner sphere omitted from our computational domain, for we have found similar columns of slowness for several different sizes of central spheres. Figure 6 (*right*) shows the variation of angular velocity $\hat{\Omega}$ with radius in three latitudinal cuts, providing another assessment of the slowness of the central column and of the speeding up of the equatorial region.

These central columns of slow rotation are largely unexpected and constitute a striking finding of these simulations. A general result from previous studies of convection in deep shells under strong rotational constraints (with R_{oc} small) is that equatorial regions of fast rotation are obtained (e.g., Gilman 1979; Miesch et al. 2000; Brun & Toomre 2002). The conservation of angular momentum requires that other regions be slowed down, and this often appears as higher latitude regions of slowness. The analog in our spherical domain may be the central column of particularly retrograde $\hat{v}_\phi$, for this could compensate for the equatorial speeding up (prograde $\hat{v}_\phi$) of regions with a large moment arm. The continuous redistribution of angular momentum by the convection, involving various effects of Reynolds stresses, meridional circulations, and viscous stresses, is examined in § 8 as we seek to understand the balances needed to account for such central columns of slowness.

We have also considered a more slowly rotating case F, with a rotation rate of $\Omega_0/10$, to examine whether the central column of slowness is still achieved under a weaker rotational influence (with R_{oc} large). The prior studies of convection in shells (Gilman 1978) indicated that under such conditions the equatorial regions may exhibit relatively slow rotation due to the modified transport of angular momentum. If this property of shell convection were to carry over to full spherical domains, then it might follow that the overall conservation of angular momentum could yield central regions of fast rotation to compensate for the equatorial slowness. Figure 7 shows that for case F this is indeed realized. The central region of relatively fast rotation is decidedly less columnar than those of slow rotation in Figure 6, probably because the Taylor-Proudman constraint is weakened. We thus suspect that central columns of slowness may be ubiquitous for stars that rotate sufficiently rapidly that R_{oc} is less than unity. In the remainder of this paper, we concentrate on our simulations that satisfy this criterion (all but case F), since real A-type stars are generally quite rapidly rotating.

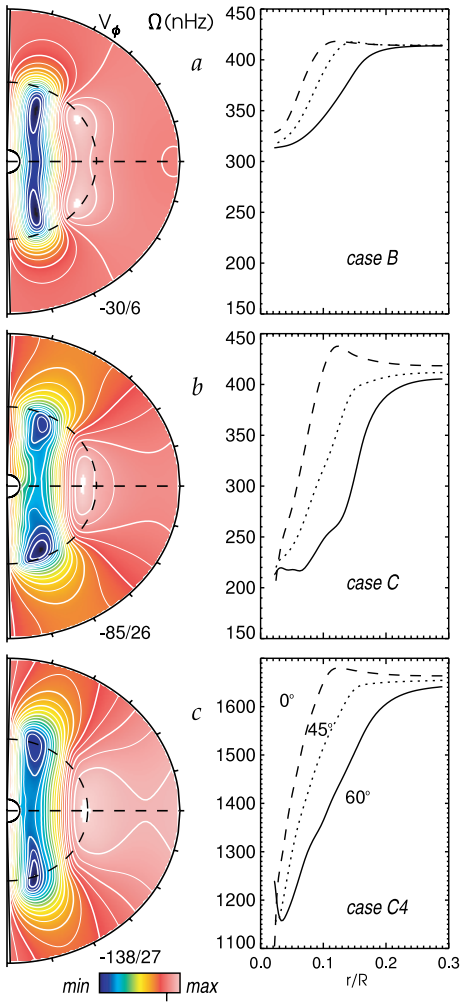

FIG. 6.—Strong differential rotation established by the convection in the three cases B, C, and C4. Shown are the azimuthal velocity $\hat{v}_\phi$ as contour plots in radius and latitude (*left*; with dashed line denoting equator) and the angular velocity $\hat{\Omega}$ with proportional radius for three latitudinal cuts (*right*); both $\hat{v}_\phi$ and $\hat{\Omega}$ are averaged in time (all over intervals of roughly 110 days) and longitude. Maxima and minima of $\hat{v}_\phi$ (in meters per second) are indicated. Cases B (*top*) and C (*middle*) are rotating at the solar rate (414 nHz), and case C4 (*bottom*) rotates 4 times faster. Greater angular velocity contrasts are achieved in the more complex flows of case C (*b*) and case C4 (*c*) than in the laminar case B (*a*), in all cases involving a central column of slowness.

4.2. *Contrasts in Angular Velocity*

We now turn to the time-averaged angular velocity $\hat{\Omega}$ profiles associated with the differential rotation in our convective cores with R_{oc} small, some examples of which are shown as radial cuts at constant latitudes in the right-hand panels of Figure 6 that accompany the views of $\hat{v}_\phi$. The $\hat{\Omega}$ profiles in Figure 6 emphasize that most of the radiative envelope rotates at the

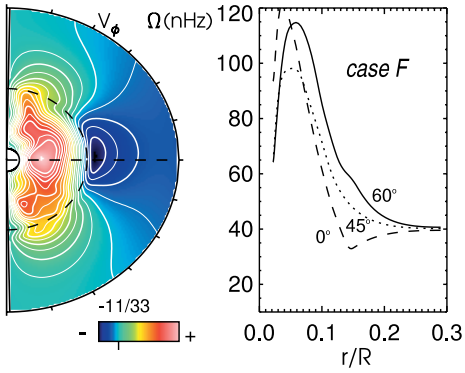

FIG. 7.—Fast column of central rotation realized in case F rotating at 1/10 the solar rate. Shown is the azimuthal velocity $\hat{v}_\phi$ as a contour plot in radius and latitude (*left*; with dashed line denoting equator) and the angular velocity $\hat{\Omega}$ with proportional radius for three latitudinal cuts (*right*); both $\hat{v}_\phi$ and $\hat{\Omega}$ are averaged in time (over 180 days) and longitude. Maxima and minima of $\hat{v}_\phi$, in meters per second, are indicated.

nominal rate of the reference frame. The variations in $\hat{\Omega}$ are largely confined to the convective core, although within the overshoot region there are still some weak gradients in $\hat{\Omega}$ evident. In the simulations of semiturbulent convection rotating at the solar rate (cases A, C, and E, with identical viscosities but increasing "stiffness" in the stratification of the radiative exterior), we obtain angular velocity contrasts $\Delta\hat{\Omega}/\Omega_0$ (from the equator to 60°) of order 60% (see also Table 2). These contrasts appear to be insensitive to the stratification of the radiative zone considered here; likewise, the character of the differential rotation throughout the convective core is similar in these three cases. In more laminar simulations at the same rotation rate (cases B and D, involving greater viscosities than their companion cases C and E), although the angular velocity contrast is lessened to about 25%, a central cylinder of slow rotation is still evident. At a fourfold higher rotation rate, considered as case C4, $\Delta\Omega$ increases by about a factor of 2, yielding a $\Delta\Omega/\Omega_0$ that is reduced to about 33%; a central column of slowness is retained. As we increased the rotation rate in going to case C4 from case C, we sought to maintain roughly the same degree of supercriticality in the convection, which required decreasing the effective viscosities to compensate for the stabilizing effects of rotation (e.g., Chandrasekhar 1961). Without such decreases, the angular velocity contrast was lessened to about 22% in the resulting more laminar flow.

Another assessment of the resulting differential rotation in these simulations is provided by examining the kinetic energies associated variously with the convection (CKE), meridional circulation (MCKE), and differential rotation (DRKE), together with their sum (KE), all relative to the rotating frame. As detailed in Table 2, the CKE is reasonably invariant across all our simulations rotating at the solar rate. In going from the more laminar flows of cases B and D to the semiturbulent flows in cases C and E, the stronger differential rotation that results is reflected in the greater DRKE and thus also in the total kinetic energy. The MCKE is likewise increased but remains a small fraction of KE. Thus, the more complex flows more effectively transfer energy—from the vast reservoirs of energy associated with the rotation of the frame and with the internal energy of the star—into KE, which nonetheless remains a small fraction of the total energy in these simulations.

From our limited sampling of rotation rates, we cannot reliably estimate how $\Delta\Omega/\Omega$ is likely to vary with Ω at the much higher rates typical of many A-type stars. However, we suspect that the strong differential rotation obtained in our simulations is likely to be realized even for core convection within more rapidly rotating stars with much stronger rotational constraints.

5. EVOLVING CONVECTION AND WAVE EXCITATION

The inherently time-dependent convection involves substantial pattern evolution and propagation within the bulk of the convective core and the excitation of gravity waves in the surrounding radiative envelope. Some large features in the convection appear, persist, and are sheared and advected by the mean flows that they drive. The radiative zone contains the rippling signature of unremitting gravity waves excited by the convection below, accompanied by weak circulations. We now consider such time variability.

5.1. *Propagation and Shearing of Convective Structures*

The flows in these simulations evolve in a complicated manner. This may be seen in Figure 8, which examines the radial velocity patterns within the convective core (at $r = 0.10R$) in case C at three instants each separated by 7 days in time. Large-scale features are recognizable in all three images but show evolution and propagation. Some orderly downflow structures within the convection persist for long periods of time. Yet they also clearly evolve over relatively short time intervals: major downflow lanes present in Figure 8*a*, for instance, are recognizable in Figure 8*c* but have changed in shape and intensity. They do not evolve in isolation: patterns merge, are sheared, and cleave into smaller patterns as they interact with surrounding flows. Such features are not simply advected by the mean motion of the region in which they are embedded but can additionally propagate relative to the differential rotation that they establish. The rate and sense of pattern propagation is most readily seen by turning to time-longitude mappings, such as in sampling the radial velocities at 65° north (Fig. 8*d*) and at the equator (Fig. 8*e*) over nearly 200 days. In these mappings, persistent strong downflow lanes are revealed as dark bands tilted to the right in Figure 8*e* and sheared to the left in Figure 8*d*. Such tilts reveal that patterns at this radius and near the equator propagate in a prograde sense, taking about 300 days to complete one revolution, and at the higher latitude their propagation is retrograde with a period of about 60 days. These mappings also emphasize that the convection possesses larger scales at the equator than at high latitudes, with a distinctive change in the sense of pattern propagation relative to the frame at midlatitudes.

5.2. *Internal Gravity Wave Responses*

The vigorous core convection extends upward into the stable stratification that bounds it, with such pummeling serving to excite internal gravity waves within the radiative envelope. Such wave responses are shown vividly in the upper panels of Figure 9, which displays the radial velocities at multiple depths in cases E and C4. These can appear either as localized ripples that are one signature of the waves (Fig. 9*a*), arising either from distinctive events or from the interference of many waves, or as striking large-scale global resonances (Fig. 9*d*) that persist (once established) for as many rotation

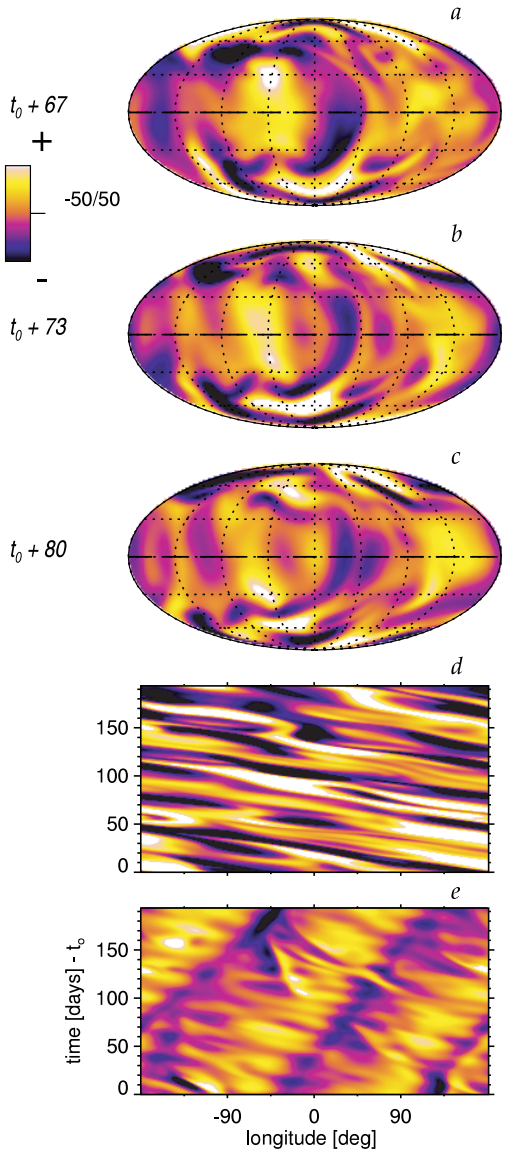

FIG. 8.—Evolution and propagation of the convective flows sampled for case C. (*a–c*) Global mappings of the radial velocity v_r within the convective core (at $r = 0.10R$) for three successive times each separated by 7 days, exhibiting shearing and cleaving of the convective structures. The propagation of those convective patterns is most evident in the time-longitude maps of v_r extracted at (*d*) a latitude of 65° and (*e*) the equator. The same color rendering is used in all panels.

periods as we continued the simulations. The latter response may be more easily realized in our simulations, with their artificially imposed outer boundary conditions that reflect gravity waves, than in real stars, where the radiative envelope is extensive and probably has no simple reflecting surfaces. However, they may also mimic gravity waves of moderate radial order n (such as $n = 8$ or 10) in a real star, although the stable stratifications in such stars are much stiffer than the ones we consider here.

The generation of gravity waves by the upward-directed plumes is fully expected. Waves with frequencies less than or equal to the Brunt-Väisälä frequency N (proportional to the square root of the local entropy gradient $d\bar{S}/dr$ of the stable stratification) are able to propagate in the radiative outer envelope and may be excited in abundance by the time-varying convection, as in case E at $r = 0.26R$ (Fig. 9*a*). This also implies that the spectrum will shift as the stiffness of the surrounding envelope is varied. More surprising is the large-scale global resonance of an internal gravity mode (of spherical harmonic degree $\ell = 3$ and azimuthal order $m = 2$) that is readily achieved within the more rapidly rotating case C4 and likewise within some of its more laminar relatives. This may come about because the rotating convection is likely to possess a range of inertial oscillations with frequencies less than $2\Omega_0$ (Greenspan 1969), which accompany the broad band of lower frequencies present in the time-dependent convection. When there is a suitable overlap between the temporal spectrum of the rotating convection and the admissible internal gravity wave frequencies that depend on ℓ and radial order n (e.g., Unno et al. 1979; Gough 1993; Dintrans, Rieutord, & Valdettaro 1999), a prominent wave response may result. In our models N varies somewhat with radius; for case C4 its representative value is 1.1×10^{-5} Hz, whereas Ω_0 is 1.04×10^{-5} Hz. It appears that a global gravity wave (with low ℓ) has been selected that propagates retrograde relative to the frame (with a period of about 40 days for a complete revolution), within a region that exhibits almost no differential rotation. In addition to the global mode, other gravity waves appear as ripples near the equator in Figure 9*d*.

6. CONVECTIVE PENETRATION AND RADIATIVE ENVELOPE

Convective motions do not stop abruptly at the interface between the convective core and the stable radiative envelope. Rather, outward-moving parcels of fluid possess momentum and therefore must travel some distance into the stable radiative zone before they come to a halt. There are two effects. First, if convective motions are sufficiently vigorous and possess a large enough filling factor, they can create a nearly adiabatic stratification within a portion of the overlying radiative zone that in a one-dimensional stellar structure model would be stably stratified. This may be termed a region of *penetration*, as discussed in Zahn (1991), Hurlburt et al. (1994), and Brummell, Clune, & Toomre (2002). Second, there will be a farther region of stable stratification into which convective motions extend but whose entropy gradient they fail to modify significantly. Within such a region of *overshooting*, outward-moving parcels of fluid are braked until they come to a halt. Throughout the domain of penetrative convection and the extended region of overshooting, the fluid motions should be effective in mixing the chemical composition.

6.1. *Shape of Convective Core*

In the one-dimensional stellar models used for our initial conditions, the region of unstable stratification is of course spherical. In the evolved simulations, penetrative convective motions have yielded a nearly adiabatically stratified core region (weakly superadiabatic) that is now prolate in shape

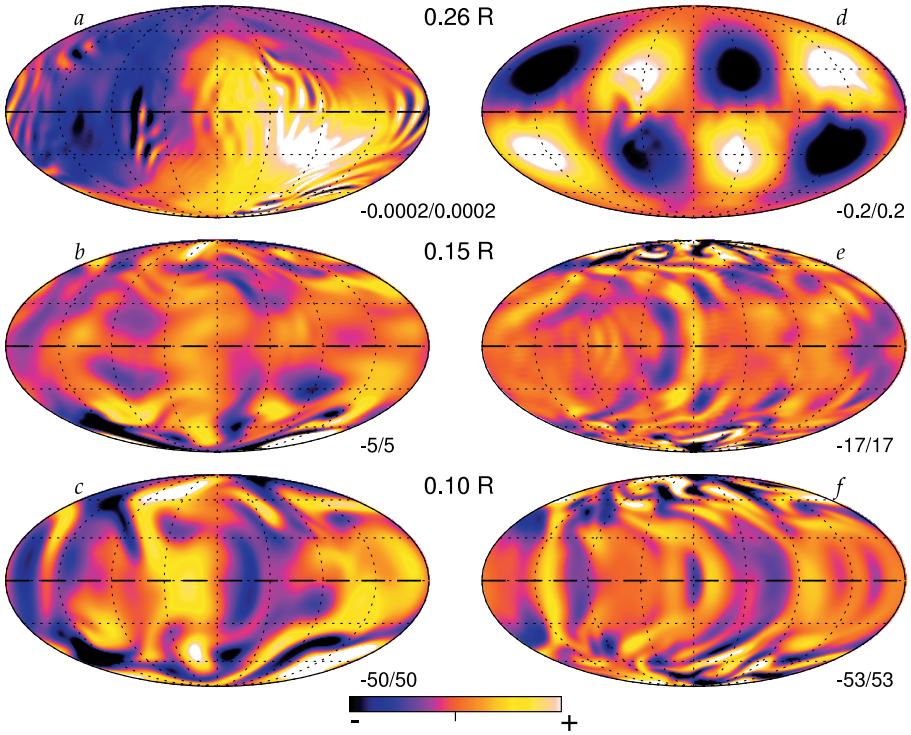

FIG. 9.—Excitation of gravity waves in the radiative envelope for cases E (*left*) and C4 (*right*), shown in global mappings of radial velocity v_r at one instant in time (*top*; sampling $r = 0.26R$). The associated convective flows are also shown within the overshoot region (*middle*; $r = 0.15R$) and in the convective core (*bottom*; $r = 0.10R$). For case E, gravity waves of small amplitude (scaling indicated) are visible in (*a*) as weak ripples in the largely quiescent radiative zone. For case C4, the waves appear in (*d*) as a prominent global resonance of greater amplitude.

and aligned with the rotation axis. The radius r_c of this core region thus varies with latitude, as sketched in Figure 10. The simulations further reveal that the overshooting motions extend outward to a radius r_o that is largely independent of latitude and thus roughly spherical in shape, as also sketched.

Such geometries for the penetrative core and the further region of overshooting are shown in Figure 11 for case C. These regions are delineated by turning to the time- and longitude-averaged enthalpy flux, given by

$$\hat{F}_e(r,\theta) = \bar{\rho} c_p \langle v_r T \rangle_{t,\phi}, \qquad (11)$$

where the angle brackets and their subscripts indicate the averaging. Within the convective core that includes the region of penetration, the enthalpy flux is typically positive, because of the positive correlations of radial velocity and temperature fluctuations that are largely realized there (see § 3.2). As the motions extend outward into the subadiabatic stratification of the region of overshoot, the enthalpy flux becomes negative, since the temperature fluctuations typically flip their sign almost immediately, becoming in the main anticorrelated with the radial velocity. Thus, the inner boundary of the region of overshoot is usefully also revealed by the radius at which $\hat{F}_e$ changes sign.

The outer boundary r_o of that overshooting region is taken to be the radius at which the enthalpy flux has attained an amplitude of 10% of its most negative value. We introduce this definition because small negative values of the enthalpy flux persist wherever any radial motions anticorrelated with temperature fluctuations exist, even if these radial motions are very weak. Our intent is to identify regions where overshooting motions are reasonably vigorous, recognizing that such a constraint on the amplitude of the enthalpy flux is somewhat arbitrary. For case C, r_o has a value of about $0.158R$, independent of latitude, whereas r_c ranges from about $0.131R$ at the equator to $0.148R$ at the poles (Fig. 11). The values for other cases are presented in Table 2. Since in all our cases the inner boundary r_c of the overshoot region is a function of latitude and the outer boundary r_o is largely not, the extent of the overshooting d_o varies with latitude, possessing the greatest spatial extent near the equator. Figure 11 also shows that the enthalpy flux $\hat{F}_e$ has prominent variations with latitude and radius within the convective core, with a greater flux at mid- and high latitudes than at the equator. As the convection evolves, the time-averaged $\hat{F}_e$ as determined over different epochs shows some changes in its structure and its symmetries with respect to the equator.

The prolate geometry of the convective core may result from the effects of rotation yielding convective flows that typically involve greater radial velocities at high latitudes than at the equator. Figure 12 shows the rms radial velocity in case C within both the convective core ($r = 0.10R$) and the region

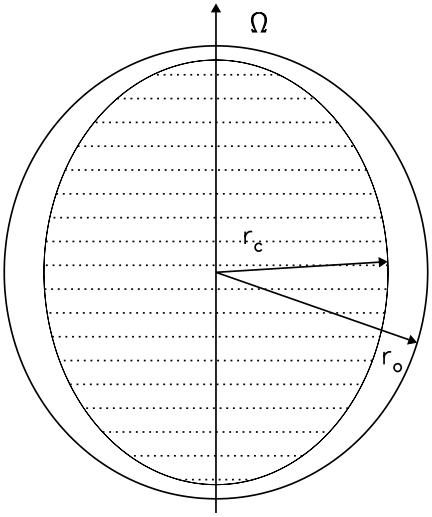

FIG. 10.—Schematic of the typical geometry of the prolate convective core of radius $r_c(\theta)$ and of the farther region of overshooting, which extends to radius r_o largely independent of latitude θ. The nearly adiabatic convective interior has greatest spatial extent along the axis of rotation (here vertical).

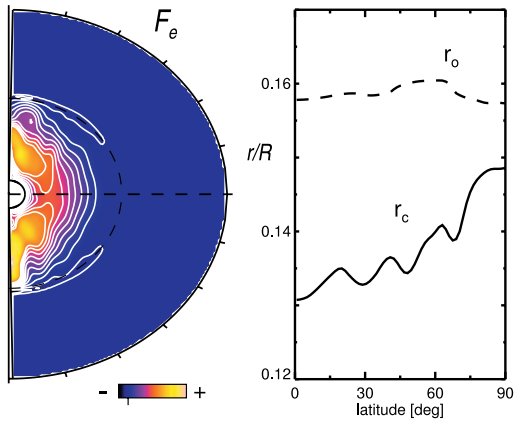

FIG. 11.—(*a*) Variation with radius and latitude of the radial enthalpy flux $\tilde{F}_e$ in case C, averaged over 180 days. This reveals the complex patterns to the transport achieved by the vigorous convection within the core (with positive flux denoted in yellow/red tones) and the weaker response in the overshooting region (with a negative flux). The equator is denoted by the dashed line. (*b*) Assessment of r_c and r_o for the same case, expressed in proportional radius as a function of latitude. Using $\tilde{F}_e$, r_c (*solid line*) measures the radius at the outer edge of the convective core at which the enthalpy flux becomes negative, and r_o the radius of overshooting at which that flux essentially vanishes.

of overshooting ($r = 0.15R$). It is evident that radial velocities are generally lowest near the equator and highest near the poles. Outward-directed motions at low latitudes are turned by the Coriolis forces, thus decreasing their radial velocity component; radial motions that are closely aligned with the rotation axis, such as at high latitudes, are deflected less and thus retain most of their radial velocity.

6.2. *Stable Stratification and Overshooting*

As convective motions enter the stable stratification of the radiative envelope, they are buoyantly braked (see § 3.2). The amount of braking they experience is controlled by the magnitude of the stable entropy gradient. By varying that gradient in our simulations, we have thus effectively altered the ability of flows to overshoot into the radiative envelope: a larger $d\bar{S}/dr$ implies stronger buoyancy braking and thus a smaller extent to the overshooting region. A larger $d\bar{S}/dr$ also leads to a smaller extent to the penetration as indicated by r_c. Both these effects are apparent in Figure 13, which displays $\tilde{F}_e(r)$ at several latitudes, for three simulations of varying $d\bar{S}/dr$. With increasing stiffness comes decreasing r_o and r_c.

For our stiffest and most complex case E, the latitude-averaged extent of overshoot, d_o, is 1.906×10^9 cm, or $0.208H_p$, where H_p is the local pressure scale height averaged over the region of overshoot. In the less stiff case C, a larger d_o is realized; such measures are quoted for all cases in Table 2. Increasingly complex flows, as achieved in our simulations by lowering the viscosity in going from case B to case C (or from case D to case E, at a different stiffness), yield smaller d_o than do their more laminar relatives. This seems at first paradoxical, given the larger rms velocities associated with the increased complexity of the convection. However, this trend is largely in keeping with nonlinear modeling of three-dimensional penetrative compressible convection in localized planar domains (see Brummell et al. 2002), which showed that a smaller filling factor for the plumes as realized in the more turbulent convection translates into a smaller extent to the overshooting.

Increasing Ω_0 without altering the viscosity leads to more laminar convection, because of the stabilizing effects of rotation. This in turn yields a greater overshooting. In devising case C4 with its fourfold greater rotation rate, we reduced the viscosity relative to case C in order to achieve comparable complexity in the convection as measured by the Reynolds numbers. In case C4, d_o is greater than that in the slower

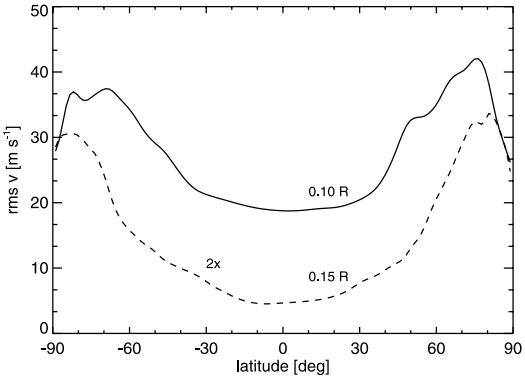

FIG. 12.—Variation with latitude of the rms of radial velocities $\tilde{v}_r$ in case C within both the convective core ($r = 0.10R$) and the region of overshooting ($r = 0.15R$), averaged over 180 days. The latter velocities have been multiplied by a factor of 2 for visibility. Radial velocities are highest near the poles and lowest near the equator, partly because of the deflection of outward motions by the Coriolis forces in these rotating domains. The prolate geometry of the convective core appears to arise from such latitudinal variation of v_r.

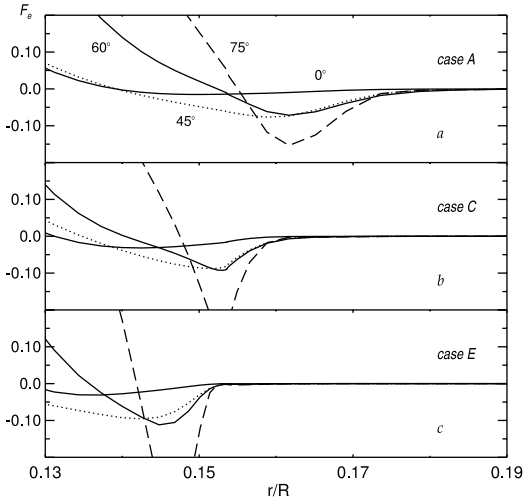

FIG. 13.—Variation of radial enthalpy flux $\hat{F}_e$ with radius at selected indicated latitudes for cases A, C, and E involving progressively stiffer stable stratifications in the radiative exterior. The radius r_c at which the enthalpy flux first becomes negative (providing an estimate of the boundary of the convective core) is a strong function of latitude, with higher latitudes having a core of greater spatial extent. In contrast, the radius r_o at which the negative enthalpy flux in the overshooting region essentially vanishes is largely insensitive to latitude. Increasing stiffness decreases the radii at which these transitions occur.

rotating case C, suggesting that increasing the rotation rate enhances somewhat the overshooting.

7. INDUCED MERIDIONAL CIRCULATIONS

Prominent meridional circulations are induced by the convection within the unstable core, accompanied by much weaker circulations in the radiative surroundings. Within the convective core, such mean meridional flows arise from a combination of buoyancy forces, Reynolds stresses, latitudinal pressure gradients, and Coriolis forces acting on the mean zonal flow (differential rotation). In the radiative exterior beyond the zone of overshooting, slow circulations can be driven both by viscous stresses that couple that region to the flows in the convective interior and by latitudinal temperature gradients arising from the nonuniform heating from below. Our simulations reveal that the resulting meridional circulations are complex in structure, possess multiple cells in both radius and latitude, and exhibit noticeable variations in time. Such multicellular patterns are in sharp contrast to the single monolithic cells often assumed in mean-field models of differential rotation (e.g., Rekowski & Rüdiger 1998; Durney 2000). On the other hand, our models include viscous stresses that may be largely absent in real stars, and thus our estimates of the meridional circulations in the immediate surroundings of the convective core are likely to be somewhat unrealistic.

7.1. *Patterns within Convective Core*

The time-averaged meridional circulations achieved in three of our simulations are shown in Figure 14 as stream functions of mass flux (see eq. [7] of Miesch et al. 2000). Within the convective core (Fig. 14, *left*), these flows have amplitudes of order 5 m s^{-1}; they are thus appreciably smaller than the instantaneous radial velocities in the same simulations (see Table 2). Indeed, the kinetic energy of these axisymmetric meridional flows (MCKE) is in all cases at least an order of magnitude smaller than that of the nonaxisymmetric convection (CKE) and of the differential rotation (DRKE). More rapid flows and more intricate cellular patterns are realized in the less viscous cases C and C4 than in case B.

The patterns of meridional flow are quite intricate, with multicelled structures achieved in radius and latitude. These structures exhibit some alignment with the rotation axis, particularly in the more rapidly rotating case C4. As the convection itself evolves (Fig. 8), so do the mean meridional circulations associated with it. Thus, Figure 14 represents

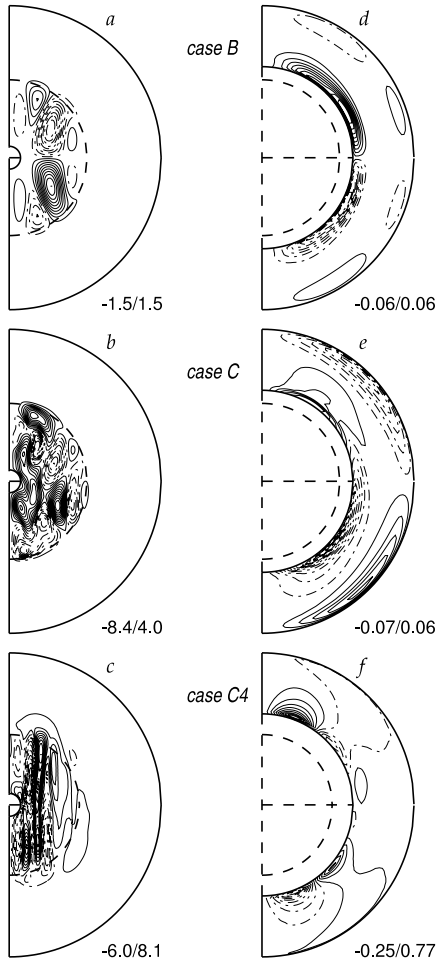

FIG. 14.—Time-averaged stream functions of meridional mass flux for cases B (*top*), C (*middle*), and C4 (*bottom*), displayed for the whole domain (*left*) and at much amplified scaling for the outer portion of the radiative zone only (*right*). The time intervals used in the averaging are all of order 110 days. Solid lines denote counterclockwise flow, dashed lines clockwise. The associated maximum and minimum velocities for $\tilde{v}_\theta$ (in meters per second) are indicated.

typical examples of these time-dependent circulations in a particular epoch. These circulations occupy most of the volume delineated by r_c and weaken in the region of overshooting. Thus, their extent varies with the stiffness of the exterior stratification.

7.2. *Weak External Circulations*

The meridional circulations achieved in the radiative envelope within our models are much weaker than those in the core. As shown in Figure 14 (*right*), these flows are of large scale and possess amplitudes that in cases B and C are about 0.06 m s^{-1}. The more rapidly rotating case C4 exhibits faster exterior circulations. Such flows evolve more slowly than do the meridional circulations within the core. They are driven by a combination of viscous stresses communicated across these domains (with a characteristic diffusion timescale across the radiative envelope of about 1.8 yr for case C) and by weak latitudinal thermal gradients resulting from the energy deposited by the latitudinally varying $\hat{F}_e$ (Fig. 11).

These mean flows within the radiative envelopes in our models are considerably greater in amplitude than estimates of Eddington-Sweet circulations. The latter, which arise from baroclinic effects due to the flattened shape of a rotating star, would involve flows of order 10^{-4} m s^{-1} in our A-type stars rotating at Ω_0 (see review in Pinsonneault 1997). Our modeling ignores centrifugal acceleration and thus such distortions and further imposes a spherical outer boundary upon which a uniform dS/dr is specified. Therefore, our model does not accurately address the very slow circulations of the Eddington-Sweet variety.

8. INTERPRETING THE ROTATION PROFILES

Our simplified model of rotating core convection coupled by penetration to a radiative envelope yields a nonlinear dynamical system with complex feedbacks. The rich variety of responses and marked time variability that is exhibited cannot now be predicted or explained from first principles. However, the numerical simulations have the great advantage that they provide full snapshots that can be assessed for the dynamical balances that are achieved. This can yield insights into the operation of these complicated dynamical systems. Such an approach is particularly useful in identifying the processes involved in continuously redistributing the angular momentum to establish the differential rotation. Because we have adopted stress-free boundary conditions at the top and bottom boundaries of our simulations, no net torque is applied to these rotating spheres of convection. Thus, total angular momentum within our simulations is conserved, and we now examine the manner in which it is redistributed.

8.1. *Redistributing the Angular Momentum*

We may assess the transport mechanisms of angular momentum in our simulations, which must combine to give rise to the observed differential rotation, in the manner of Elliott et al. (2000) and Brun & Toomre (2002). We consider the mean radial ($\mathcal{F}_r$) and latitudinal ($\mathcal{F}_\theta$) angular momentum fluxes and write the ϕ-component of the momentum equation, expressed in conservative form and averaged in time and longitude, as

$$\frac{1}{r^2}\frac{\partial(r^2\mathcal{F}_r)}{\partial r}+\frac{1}{r\sin\theta}\frac{\partial(\sin\theta\mathcal{F}_\theta)}{\partial\theta}=0, \tag{12}$$

involving the mean radial angular momentum flux

$$\mathcal{F}_r=\hat{\rho}r\sin\theta\left[-\nu r\frac{\partial}{\partial r}\left(\frac{\hat{v}_\phi}{r}\right)+\widehat{v_r'v_\phi'}+\hat{v}_r(\hat{v}_\phi+\Omega r\sin\theta)\right] \tag{13}$$

and the mean latitudinal angular momentum flux

$$\mathcal{F}_\theta=\hat{\rho}r\sin\theta\left[-\nu\frac{\sin\theta}{r}\frac{\partial}{\partial\theta}\left(\frac{\hat{v}_\phi}{\sin\theta}\right)+\widehat{v_\theta'v_\phi'}+\hat{v}_\theta(\hat{v}_\phi+\Omega r\sin\theta)\right]. \tag{14}$$

In equations (13) and (14), the first term in each pair of brackets is related to the angular momentum flux due to viscous transport (which we denote $\mathcal{F}_{r,V}$ and $\mathcal{F}_{\theta,V}$), the second term to the transport due to Reynolds stresses ($\mathcal{F}_{r,R}$ and $\mathcal{F}_{\theta,R}$), and the third term to the transport by the meridiona circulation ($\mathcal{F}_{r,M}$ and $\mathcal{F}_{\theta,M}$). The Reynolds stresses in the above expressions arise through correlations of the components of velocity.

In Figure 15, we show the components of $\mathcal{F}_r$ and $\mathcal{F}_\theta$ for cases D and E with a strong rotational influence, integrated along colatitude and radius, respectively, to deduce the net fluxes through shells at various radii and through cones at various latitudes, such that

$$I_{\mathcal{F}_r}(r)=\int_0^\pi\mathcal{F}_r(r,\theta)\,r^2\sin\theta\,d\theta,$$
$$I_{\mathcal{F}_\theta}(\theta)=\int_{r_{\rm bot}}^{r_{\rm top}}\mathcal{F}_\theta(r,\theta)\,r\sin\theta\,dr. \tag{15}$$

We have identified the contributions from viscous (V), Reynolds stress (R), and meridional circulation (M) terms. This representation is helpful in considering the sense and amplitude of the transport of angular momentum within the convective shells by each component of $\mathcal{F}_r$ and $\mathcal{F}_\theta$.

Turning first to the radial fluxes of angular momentum (Figs. 15*a* and 15*b*), we see that viscous forces act to transport angular momentum radially inward in both cases. In this they are opposed by a combination of the Reynolds stress and meridional circulation fluxes, to yield a total radial angular momentum flux that is nearly zero, as noted in Figure 15 by the solid line. While the systems here are highly variable in time, by allowing the system to evolve for extended periods of time (typically thousands of days) and performing long time averages, we appear to be sensing the equilibrated states reasonably well. In going from the more laminar flows of case D to the complex ones of case E, we see that the viscous flux has dropped and that the Reynolds stresses and meridional circulations have changed accordingly to maintain equilibrium. This includes the development of an appreciable integrated $\mathcal{F}_{r,M}$ that is directed radially inward, near the boundary of the radiative and convective zones; this is presumably a result of the stronger circulations and shear generated near that boundary by the more complex flows of case E.

Examining the latitudinal transport of angular momentum (Figs. 15*c* and 15*d*), we note that the effect of the Reynolds stresses in both cases is primarily to speed up the equator, since $\mathcal{F}_{\theta,R}$ is positive in the northern hemisphere and negative in the southern. It is opposed by the meridional circulation and viscous fluxes, which act to speed up the poles. The manner in which each of the different components of $\mathcal{F}_\theta$ acts does not appear to vary appreciably in going from case D to E. As the level of complexity is increased, however, we see a decrease in the magnitude of all components of $\mathcal{F}_\theta$.

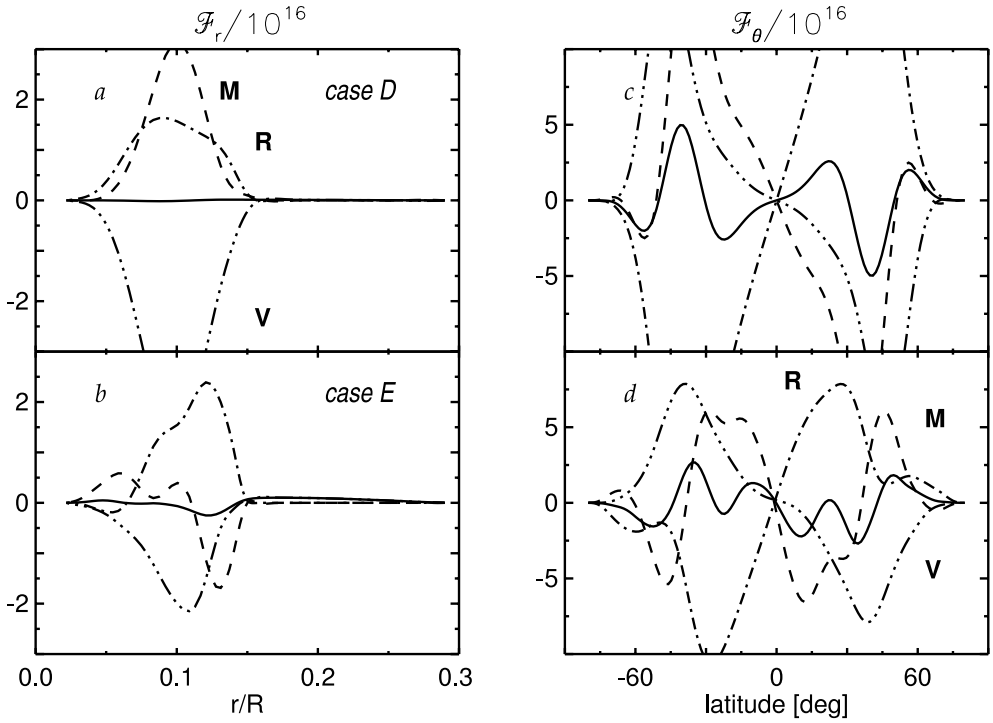

FIG. 15.—Time average of the latitudinal integral of the angular momentum flux $\mathcal{F}_r$ (*left*) and of the radial integral of the angular momentum flux $\mathcal{F}_\theta$ (*right*) for cases D (*top*) and E (*bottom*). The time intervals used in forming the averages were 670 days for case D and 620 days for case E. The fluxes have been decomposed into their viscous (V), Reynolds stress (R), and meridional circulation (M) components, and the solid curves represent the total fluxes. Positive quantities represent fluxes radially outward or latitudinally from north to south.

We conclude that for these cases involving a strong rotational constraint, the Reynolds stresses act latitudinally to speed up the equator and radially to slow down the convective core. These latitudinal fluxes are opposed by the meridional circulations and viscous effects, whereas the radial fluxes are aided somewhat by the meridional circulations. Examining these fluxes gives us a picture of how the angular momentum is continuously transported and which are the significant processes serving to speed up or slow down certain regions. However, it is difficult to infer from the fluxes alone what will be the detailed Ω profile that results.

8.2. *Baroclinicity and Thermal Winds*

Rotating convection involves both radial and latitudinal heat transport, with the likelihood that latitudinal gradients in temperature and entropy may result within the convective core. This implies that surfaces of mean pressure and density will not coincide, thereby yielding baroclinic terms in the vorticity equations (Pedlosky 1987; Zahn 1992). Under sufficiently strong rotational constraints, a "thermal wind balance" might be achieved in which departures of the angular velocity from being constant on cylinders (aligned with the rotation axis) are controlled by those baroclinic terms. Indeed, some mean-field approaches have invoked such a balance to obtain differential rotation profiles with bearing on the solar convection zone (e.g., Kichatinov & Rüdiger 1995). As discussed in Brun & Toomre (2002), such a balance effectively implies that

$$\frac{\partial \hat{v}_\phi}{\partial z} = \frac{1}{2\Omega_0 \hat{\rho} c_P} \nabla \hat{S} \times \nabla \hat{p}\Big|_\phi = \frac{g}{2\Omega_0 r c_P} \frac{\partial \hat{S}}{\partial \theta}, \qquad (16)$$

where z is parallel to the rotation axis. Thus, latitudinal entropy gradients could serve to break the Taylor-Proudman constraint, which would otherwise require the rotation to be constant on cylinders with $\partial \hat{v}_\phi/\partial z$ equal to zero. That constraint may also be broken by Reynolds and viscous stresses. We next show that these terms are at least as important as the baroclinic terms in establishing the differential rotation in the bulk of the convective core.

Figure 16 assesses for case E the extent to which latitudinal entropy gradients serve to drive the temporal mean zonal flows $\hat{v}_\phi$ seen as the differential rotation. Figure 16*b* displays the gradient $\partial \hat{v}_\phi/\partial z$ of those zonal flows, and Figure 16*c* the corresponding latitudinal entropy term on the right-hand side of equation (16), which in an exact thermal wind balance would be identical. Figure 16*d* shows the difference between this baroclinic term and the actual $\partial \hat{v}_\phi/\partial z$, thus providing a measure of departures from such a balance. Within the bulk of the convective core, Reynolds and viscous stresses lead to zonal flows that are not so balanced. At the interface between

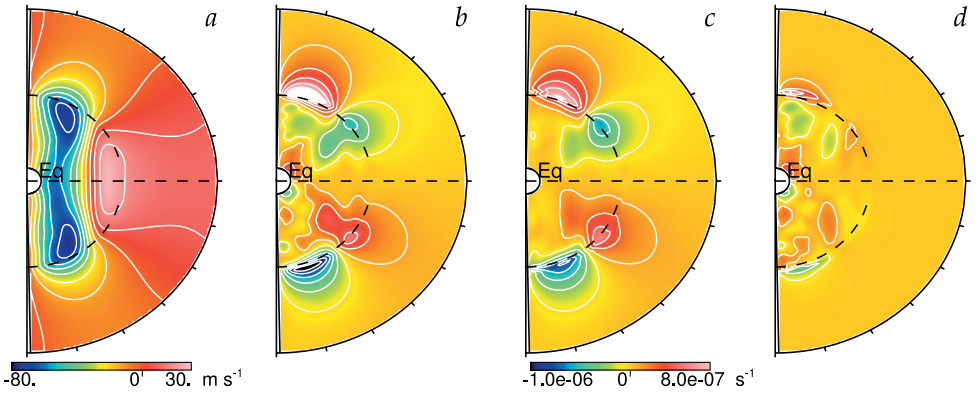

FIG. 16.—Temporal (640 day) and longitudinal averages for case E showing (*a*) the longitudinal velocity $\tilde{v}_\phi$, (*b*) $d\tilde{v}_\phi/dz$, (*c*) the baroclinic term in the meridional force balance, and (*d*) the difference between the latter two. The same color scale is used in (*b*), (*c*), and (*d*). Near the interface between the convective core and the radiative envelope, baroclinic effects account for much of the differential rotation. Within the bulk of the prolate convective core, Reynolds and viscous stresses have a significant role in driving those zonal flows.

the core and the radiative exterior, however, baroclinicity accounts for most of the differential rotation.

Thus, examining the nature of this thermal wind balance, combined with the assessment of fluxes of angular momentum, reveals that Reynolds and viscous stresses have a major role in establishing the differential rotation in the bulk of the core, with latitudinal thermal gradients influencing the profile near the interface between the convective region and the radiative envelope.

9. SUMMARY AND PERSPECTIVES

Our highly simplified treatment of core convection within A-type stars has begun to capture some of the complex dynamics that must be occurring when turbulent convection and rotation meet in a full spherical domain. The most severe simplifications in our models are that we are able to simulate only the central portions of these stars, that compositional gradients that must be present are ignored, and that the levels of turbulence studied here are only modest compared with what may be realized in real stars. The dynamics may well be influenced by each in turn and in ways that are difficult to predict at this stage. Although our work is thus quite preliminary, it has revealed several dynamical properties that may well turn out to be robust.

First, these convective cores rotate differentially. Prominent angular velocity contrasts are established in all cases studied here, with a central column of slow rotation realized in stars that are strongly influenced by rotation (with R_{oc} small). Within the bulk of the convection zone, this differential rotation is driven primarily by Reynolds and viscous stresses, whereas near the interface between the core and the radiative envelope, baroclinicity plays an important role.

Second, convective motions penetrate into the radiative envelope, yielding a prolate shape to the region of nearly adiabatic stratification. The surrounding region of overshooting, in which convective motions persist but do not appreciably modify the prevailing entropy gradient, is found to have an outer boundary that is largely independent of latitude, yielding a spherical shape to the domain experiencing convective stirring.

Third, small-amplitude circulations and gravity waves are excited within the radiative envelope. The latter appear in some simulations as a rippling patchwork of waves and in our more rapidly rotating case C4 as a striking global-scale resonance that, once established, appears to persist.

The simplifications we have made in our modeling are likely to impact the penetrative properties to some degree. In particular, the μ-gradients of chemical composition present in real stars should diminish the extent of penetrative and overshooting motions realized there (Zahn 1991). They also probably reduce the vigor of circulations within the radiative envelope (Lebreton & Maeder 1987). More turbulent flows are likely to yield smaller spatial filling factors for the convective plumes and hence probably also lessen the extent of overshooting (Brummell et al. 2002). Furthermore, real stars possess stiffer entropy stratifications in their radiative envelopes than those we have been able to consider. This too would lead to less overshooting. Thus, our estimates here provide upper limits for the extent of penetration and overshooting that may be achieved in real stars.

The strong regions of shear realized in all our simulations may contribute to the building of orderly magnetic fields by dynamo action. Poloidal fields can be converted into toroidal ones by such differential rotation (the Ω-effect), with regeneration of the poloidal fields perhaps accomplished by the helical turbulence (the α-effect; see Mestel 1999). Acting together, these processes may build well-organized fields that could, if subject to magnetic buoyancy instabilities, rise to the surfaces of these stars, where they might be observed (MacGregor & Cassinelli 2003). We are in the process of beginning to explore the generation of magnetic fields within these cores (see Browning, Brun, & Toomre 2004).

The penetrative convection and overshooting in our simulation may likewise have some observable consequences. Although we have not investigated in any detail the bringing of fresh fuel into the convective core by these motions, some replenishment of the hydrogen stockpile available for nuclear reactions must occur and thereby lead to a prolonged lifetime on the main sequence.

We thank Douglas Gough and Jean-Paul Zahn for very helpful discussions. J. T. thanks the Observatory of Paris, Meudon, and the CEA-Saclay for their hospitality during the interpretation of these simulations. This work was partly supported by NASA through SEC Theory Program grant NAG5-11879 and through the Graduate Student Researchers Program (NGT5-50416). Various phases of the simulations here were carried out with NSF PACI support of the San Diego Supercomputing Center, the National Center for Supercomputing Applications, and the Pittsburgh Supercomputing Center. Much of the analyses of the extensive data sets were conducted in the Laboratory for Computational Dynamics within JILA.

REFERENCES

Abt, H. A. 2000, ApJ, 544, 933
Adelberger, E., et al. 1998, Rev. Mod. Phys., 70(4), 1265
Browning, M., Brun, A. S., & Toomre, J. 2004, in Proc. IAU Symp. 215, Stellar Rotation, ed. A. Maeder & P. Eenens (San Francisco: ASP), in press
Brummell, N. H., Clune, T. L., & Toomre, J. 2002, ApJ, 570, 825
Brummell, N. H., Hurlburt, N. E., & Toomre, J. 1998, ApJ, 493, 955
Brun, A. S., Antia, H. M., Chitre, S. M., & Zahn, J.-P. 2002, A&A, 391, 725
Brun, A. S., & Toomre, J. 2002, ApJ, 570, 865
Carraro, G., Chiosi, C., Bressan, A., & Bertelli, G. 1994, A&AS, 103, 375
Chandrasekhar, S. 1961, Hydrodynamic and Hydromagnetic Stability (Oxford: Clarendon)
Charbonneau, P., & MacGregor, K. B. 2001, ApJ, 559, 1094
Clune, T. L., Elliott, J. R., Glatzmaier, G. A., Miesch, M. S., & Toomre, J. 1999, Parallel Comput., 25, 361
Cunha, M. S. 2002, in Radial and Nonradial Pulsations as Probes of Stellar Physics, ed. C. Aerts, T. R. Bedding, & J. Christensen-Dalsgaard (San Francisco: ASP), 272
Dintrans, B., & Rieutord, M., & Valdettaro, L. 1999, J. Fluid Mech., 398, 271
Durney, B. R. 2000, ApJ, 528, 486
Elliott, J. R., Miesch, M. S., & Toomre, J. 2000, ApJ, 533, 546
Gehren, T. 1988, Rev. Mod. Astron., 1, 52
Gilman, P. A. 1978, Geophys. Astrophys. Fluid Dyn., 11, 157
———. 1979, ApJ, 231, 284
Gough, D. O. 1993, in Astrophysical Fluid Dynamics, ed. J.-P. Zahn & J. Zinn-Justin (New York: North-Holland), 399
Gough, D. O., & Toomre, J. 1991, ARA&A, 29, 627
Greenspan, H. P. 1969, The Theory of Rotating Fluids (Cambridge: Cambridge Univ. Press)
Hurlburt, N. E., Toomre, J., Massaguer, J. M., & Zahn, J.-P. 1994, ApJ, 421, 245
Iglesias, C., & Rogers, F. J. 1996, ApJ, 464, 943
Kichatinov, L. L., & Rüdiger, G. 1995, A&A, 299, 446
Kurtz, D. W. 1990, ARA&A, 28, 607
Latour, J., Toomre, J., & Zahn, J.-P. 1981, ApJ, 248, 1081
Lebreton, Y., & Maeder, A. 1987, A&A, 175, 99
MacGregor, K. B., & Cassinelli, J. P. 2003, ApJ, 586, 480
Maeder, A., & Meynet, G. 1991, A&AS, 89, 451
Maeder, A., & Meynet, G. 2000, ARA&A, 38, 143
Matthews, J. 1991, PASP, 103, 5
Mestel, L. 1999, Stellar Magnetism (Oxford: Clarendon)
Meynet, G., Mermilliod, J.-C., & Maeder, A. 1993, A&AS, 98, 477 Michaud, G., Tarasick, D., Charland, Y., & Pelletier, C. 1983, ApJ, 269, 239
Miesch, M. S., Elliott, J. R., Toomre, J., Clune, T. L., Glatzmaier, G. A., & Gilman, P. A. 2000, ApJ, 532, 593
Mohanty, S., Basri, G., Shu, F., Allard, F., & Chabrier, G. 2002, ApJ, 571, 469
Morel, P. 1997, A&AS, 124, 597
Noyes, R. W., Hartmann, L. W., Baliunas, S. L., Duncan, D. K., & Vaughan, A. H. 1984, ApJ, 279, 763
Pedlosky, J. 1987, Geophysical Fluid Dynamics (New York: Springer)
Perryman, M. A. C., et al. 1998, A&A, 331, 81
Pinsonneault, M. 1997, ARA&A, 35, 557
Preston, G. W. 1974, ARA&A, 12, 257
Rekowski, B. V., & Rüdiger, G. 1998, A&A, 335, 679
Richard, O., Michaud, G., & Richer, J. 2001, ApJ, 558, 377
Richer, J., Michaud, G., & Turcotte, S. 2000, ApJ, 529, 338
Rogers, F. J., Swenson, J., & Iglesias, C. 1996, ApJ, 456, 902
Rosvick, J. M., & VandenBerg, D. A. 1998, AJ, 115, 1516
Roxburgh, I. W. 1965, MNRAS, 130, 223
———. 1978, A&A, 65, 281
———. 1989, A&A, 211, 361
———. 1992, A&A, 266, 291
———. 1998, Ap&SS, 261, 43
Schou, J., et al. 1998, ApJ, 505, 390
Thompson, M., et al. 2003, ARA&A, 41, 599
Unno, W., Osaki, Y., Ando, H., & Shibahashi, H. 1979, Nonradial Oscillations of Stars (Tokyo: Univ. Tokyo Press)
Vauclair, G., Vauclair, S., & Pamjatnikh, A. 1974, A&A, 31, 63
Vauclair, S. 2003, Ap&SS, 284, 205
Wolff, S. C. 1983, The A-Stars: Problems and Perspectives (Washington: NASA)
Woo, J.-H., & Demarque, P. 2001, AJ, 122, 1602
Zahn, J.-P. 1991, A&A, 252, 179
———. 1992, A&A, 265, 115

6.5.2 Simulations of core convection in rotating A-type stars: magnetic dynamo action

par Brun, Browning & Toomre 2005, ApJ, 629, 461-481

The Astrophysical Journal, 629:461–481, 2005 August 10

SIMULATIONS OF CORE CONVECTION IN ROTATING A-TYPE STARS: MAGNETIC DYNAMO ACTION

Allan Sacha Brun,[1,2] Matthew K. Browning,[2] and Juri Toomre[2]
Received 2004 September 24; accepted 2005 March 21

ABSTRACT

Core convection and dynamo activity deep within rotating A-type stars of 2 $M_\odot$ are studied with three-dimensional nonlinear simulations. Our modeling considers the inner 30% by radius of such stars, thus capturing within a spherical domain the convective core and a modest portion of the surrounding radiative envelope. The magnetohydrodynamic (MHD) equations are solved using the anelastic spherical harmonic (ASH) code to examine turbulent flows and magnetic fields, both of which exhibit intricate time dependence. By introducing small seed magnetic fields into our progenitor hydrodynamic models rotating at 1 and 4 times the solar rate, we assess here how the vigorous convection can amplify those fields and sustain them against ohmic decay. Dynamo action is indeed realized, ultimately yielding magnetic fields that possess energy densities comparable to that of the flows. Such magnetism reduces the differential rotation obtained in the progenitors, partly by Maxwell stresses that transport angular momentum poleward and oppose the Reynolds stresses in the latitudinal balance. In contrast, in the radial direction we find that the Maxwell and Reynolds stresses may act together to transport angular momentum. The central columns of slow rotation established in the progenitors are weakened, with the differential rotation waxing and waning in strength as the simulations evolve. We assess the morphology of the flows and magnetic fields, their complex temporal variations, and the manner in which dynamo action is sustained. Differential rotation and helical convection are both found to play roles in giving rise to the magnetic fields. The magnetism is dominated by strong fluctuating fields throughout the core, with the axisymmetric (mean) fields there relatively weak. The fluctuating magnetic fields decrease rapidly with radius in the region of overshooting, and the mean toroidal fields less so due to stretching by rotational shear.

Subject headings: convection — MHD — stars: evolution — stars: interiors — stars: magnetic fields

1. INTRODUCTION

1.1. *Surface Magnetism of A-Type Stars*

The magnetic Ap stars have been objects of intense scrutiny for much of the past century. These stars are broadly characterized by strong spectral lines of some elements (mainly Si and some rare earths), variability on timescales of days to decades, and surface magnetic fields as strong as tens of kG (see Wolff 1983 for a review). Extensive observations, ranging from the first analyses of the Ap star α^2CVn by Maury (1897) to recent surveys by Hubrig et al. (2000), have painted a fairly detailed picture of the many surface pathologies exhibited by these stars and have provided important clues about how the abundance features and surface magnetism may arise. Yet major puzzles remain. We begin here by outlining the major observational features of such stars that serve to motivate and guide the work described here.

Observations of the Zeeman effect in magnetic Ap stars suggest that the surface fields are variable in apparent strength, that most exhibit periodic reversals in polarity along the line of sight, and that they are of large spatial scale. The commonly accepted framework for the interpretation of these observations is the "rigid rotator" model, in which a global scale field is taken to have an axis of symmetry inclined at some angle with respect to the rotation axis (e.g., Stibbs 1950; Mestel & Moss 1977; Moss et al. 1990; Mestel 1999). In this model, variations in the apparent field strength are simply a consequence of the star's rotation, as the magnetic axis continually changes its orientation with respect to the line of sight. Likewise, variations in elemental abundance measurements are thought to result from viewing large patches of those elements as they rotate in and out of view.

The geometry of the surface magnetic field has been interpreted as being predominantly dipolar. Quadrupolar and higher order field components can have only a small influence on integrated Zeeman measurements of the longitudinal (line-of-sight) field component: thus, if the fields were mainly quadrupolar, the total field would have to be quite high (of order 20–40 kG) to yield commonly observed values for the longitudinal field component (1–2 kG). Such large values of the total field are ruled out for most Ap stars by measurements or nondetections of resolved Zeeman splitting, which is sensitive to the total surface field independent of direction. However, a field that is purely dipolar cannot account for the exact patterns of variation observed for the longitudinal and total field, suggesting that the surface magnetism does have some higher order component (e.g., Borra 1980). Very recently, extensive high-resolution spectropolarimetric observations have begun to yield more direct constraints on the geometry of the surface magnetic fields. Kochukhov et al. (2004) infer from line profiles in all four Stokes parameters that the surface magnetic field of 53 Cam is quite complex in structure, with high-order multipoles ($l = 10$ and greater) contributing strongly to the total field.

A few broad characterizations of the extensive observations of magnetic Ap star properties can be made. The most striking, as noted by many authors (e.g., Mestel 1999; Borra & Landstreet 1980), is the gross anticorrelation between rotation rate and magnetic field strength: the magnetic Ap stars are preferentially much slower rotators than A-type stars with no observed field. Some exhibit variations with periods of decades, which may imply very slow rotation rates indeed. However, there are some magnetic Ap stars that have rotational velocities well in excess of 100 km s^{-1}, so slow rotation does not appear to be an absolute prerequisite for surface magnetism. Within the class of magnetic

[1] DSM/DAPNIA/SAp, CEA Saclay, F-91191 Gif sur Yvette Cedex, France.
[2] JILA and Department of Astrophysical and Planetary Sciences, University of Colorado, Boulder, CO 80309-0440.

Ap stars, Hubrig et al. (2000) see some evidence for a weak correlation between rotation and magnetic flux, in that shorter period Ap stars exhibit marginally stronger fields. They also found that only Ap stars that have completed at least one-third of their main-sequence lifetimes show magnetism, though younger magnetic Ap stars have been observed by other authors (e.g., Bagnulo et al. 2003, who find that HD 66318 has completed only about 16% of its main-sequence lifetime). Finally, one of the most puzzling observational facts concerning these stars is their relative rarity: only about 10% of stars of the appropriate spectral type are observably magnetic (e.g., Moss 2001). There appears to be no set of stellar parameters that is a sufficient condition for the presence of magnetism in any given A-type star.

1.2. *Possible Origins of the Magnetism*

The central question raised by the extensive observational data is most simply, what is the origin of the magnetism? Two major theories have emerged that seek to account for the observed fields.

The "fossil" theory suggests that the fields are relics of the primordial field that threaded the interstellar gas out of which the stars formed. Ohmic decay times in the stable radiative envelopes of A stars are very long, so the primordial field, sufficiently concentrated by the star formation process, might well survive through most or all of such stars' main-sequence lifetimes. In the fossil theory, the slow rotation of most magnetic Ap stars relative to their nonmagnetic brethren is understood as a result of magnetic braking by the field threading the stars, through either magnetic coupling to a stellar wind or "accretion braking" (Mestel 1975). That not all A stars show magnetism is taken to be the result of the different initial conditions under which the stars formed. Probably the most pressing question concerning this theory is whether the primeval field can survive through the convective Hayashi phase of such stars' pre–main-sequence evolution. The Hayashi convection may expel the magnetic field from the outer layers of such a star, perhaps concentrating it in the initially radiative core (which forms rapidly during the star's descent of the Hayashi track). Alternatively, a sufficiently strong, concentrated field may be able to resist expulsion by the convection and later yield the observed global-scale fields (e.g., Moss 2001). A variant of the fossil theory suggests that the fields were generated by dynamo action driven by the Hayashi convection but are not presently being actively maintained against ohmic decay.

The second approach suggests that the surface magnetic fields may result from contemporary dynamo activity (e.g., Krause & Oetken 1976). A-type stars possess convective cores surrounded by extensive envelopes, which are radiative except for very thin shells of convection near the surface. Convection within the highly conductive plasma of the core, coupled with rotation, may serve to build strong magnetic fields. Yet those fields may well be forever buried from view: diffusion of the fields through the radiative envelope is thought simply to take too long. If the dynamo-generated fields are sufficiently strong, however, they may become subject to magnetic buoyancy instabilities that could allow them to rise to the surface where they could be observed (e.g., Moss 1989). Recent modeling (MacGregor & Cassinelli 2003) has provided tantalizing indications that this process might indeed be able to bring very strong fibril fields to the surface in a fraction of an A star's main-sequence lifetime. However, MacDonald & Mullan (2004) point out that realistic compositional gradients slow the rise of such buoyant flux tubes considerably. Whether the fields built by possible dynamo action within the core are actually strong enough for such buoyancy instabilities to play a role or are instead likely to remain hidden is thus one of the most pertinent questions regarding the dynamo approach to explaining the surface fields.

Recently, an alternative third explanation has emerged, which relies on the possibility that a radiative envelope could generate mean magnetic field via dynamo action involving shear layers and the instability of a large-scale mean toroidal field (Spruit 2002; MacDonald & Mullan 2004).

1.3. *Aspects of Core Convection*

Within the cores of A-type stars, the steep temperature gradient that arises from fusion via the CNO cycle drives vigorous convection. We have already examined that convection through extensive hydrodynamic three-dimensional nonlinear simulations (Browning et al. 2004, hereafter BBT04; Brun et al. 2005), in which we solved the compressible Navier-Stokes equations without magnetism within the anelastic approximation. Some of the dynamical properties revealed by such modeling of rotating convective cores using our ASH code are summarized in § 2.4.

In this paper, we turn to MHD simulations of the dynamo activity that may be occurring within the convective cores of A-type stars. Using our prior hydrodynamic simulations as a starting point, we examine here whether vigorous core convection coupled with rotation can amplify an initial seed magnetic field and sustain it indefinitely. Though we are motivated in part by the remarkable observations of surface magnetism in Ap stars, the work described here has little to say directly about such surface fields. As in the hydrodynamic simulations, we model only the inner regions of such stars, including the entire convective core but only a fraction of the overlying radiative zone. Our principal aim is simply to explore whether dynamo action occurs at all within such cores (Browning et al. 2005), and if so, to characterize the main properties of the resulting magnetic fields: their strength, their topology, and their variability. Although our work is thus quite preliminary, it should serve to illuminate some of the complex dynamical processes occurring within Ap stars.

In § 2 we describe our formulation of the problem and briefly summarize the computational techniques used to address it. In § 3 we summarize the flows and magnetic fields realized by dynamo action in our simulations and consider their evolution with time. In § 4 we examine the mean flows and transports of angular momentum and heat, and in § 5 the many spatial scales and the spectral distributions of the flows and fields. In § 6 we consider the evolution of the global-scale axisymmetric poloidal and toroidal magnetic fields, and in § 7 we briefly discuss the processes by which the magnetic fields are generated and sustained. We reflect on the main findings of this work and their implications in § 8.

2. FORMULATING THE PROBLEM

2.1. *Convective Core and Radiative Shell*

The simulations considered here are intended to be simplified descriptions of the inner 30% by radius of main-sequence A-type stars of 2 $M_\odot$, consisting of the convective core (approximately the inner 15% of the star) and a portion of the overlying radiative zone. Contact is made with a one-dimensional stellar model (at an age of 500 Myr) for the initial conditions, with realistic values for the radiative opacity, density, and temperature adopted. We have softened the steep entropy gradient contrast encountered in going from the convective core to the surrounding radiative zone, which would otherwise favor the driving of small-scale, high-frequency internal gravity waves that we cannot resolve

TABLE 1
PARAMETERS FOR MAGNETIC SIMULATIONS

Case	Em	C4m
Input Parameters		
N_r, N_θ, N_ϕ	82, 256, 512	82, 256, 512
Ω_0 (s^{-1})	2.6×10^{-6}	1.04×10^{-5}
R_a	3.1×10^5	1.3×10^7
P_m	5	5
R_c	0.33	0.12
ν ($cm^2\ s^{-1}$)	4.4×10^{11}	2.5×10^{11}
κ ($cm^2\ s^{-1}$)	1.7×10^{12}	9.9×10^{11}
η ($cm^2\ s^{-1}$)	8.7×10^{10}	5.0×10^{10}
τ_η (days)	3900	6800
Measured at Mid-Depth of Convective Core		
R_e	160	210
R_m	800	1050
Λ	23.2	17.8
P_e	40	52
R_o	3.5×10^{-2}	6.2×10^{-3}

NOTES.—The number of radial, latitudinal and longitudinal mesh points are N_r, N_θ, N_ϕ. All simulations have an inner radius $r_{\rm bot} = 3.0 \times 10^9$ cm and an outer radius $r_{\rm top} = 4.0 \times 10^{10}$ cm, with $L = 1.7 \times 10^{10}$ cm the approximate radial extent of the convective core. The overall radius R of the A-type star is 1.4×10^{11} cm. The effective viscosity ν, thermal diffusivity κ, and magnetic diffusivity η are quoted at the middle of the convective core ($r = 0.10R$), and likewise we evaluate there the Rayleigh number $R_a = (-\partial\bar{\rho}/\partial S)\Delta S g L^3/\rho\nu\kappa$ (with ΔS the entropy contrast across the core), the magnetic Prandtl number $P_m = \nu/\eta$, the convective Rossby number $R_c = (R_a/T_a P_r)^{1/2}$, the Reynolds number $R_e = \tilde{v}' L/\nu$, the magnetic Reynolds number $R_m = \tilde{v}' L/\eta$, the Elsasser number $\Lambda = \tilde{B}^2/4\pi\rho\eta\Omega_0$, the Péclet number $P_e = R_e P_r = \tilde{v}' L/\kappa$, the Rossby number $R_o = \tilde{v}'/2\Omega_0 L$, and the ohmic diffusion time $\tau_\eta = L^2/(\pi^2\eta)$, where $\tilde{v}'$ is the rms fluctuating convective velocity and $\tilde{B}$ is the rms magnetic field (see Table 2 and § 2.3). An R_e based on the peak velocity at mid-depth would be about a factor of 5 larger. The Prandtl number $P_r = \nu/\kappa = 0.25$ over the full depth range.

with reasonable computational resources. This lessened "stiffness" of the system has some impact on the extent to which convective motions may overshoot into the radiative region (see BBT04). The inner 2% of the star is excluded from our computational domain, for the coordinate systems employed in ASH possess both coordinate singularities at $r = 0$ and decreasing mesh size (and thus quite limited time steps) with decreasing radius. Though the exclusion of this central region might in principle give rise to some spurious physical responses, by projecting Taylor columns aligned with the rotation axis (e.g., Pedlosky 1987) or by giving rise to boundary layers, we have seen no evidence of such effects in our simulations. In trial computations with both smaller and larger excluded central regions, the developed mean flows were very similar to those described here.

The main parameters of our simulations are summarized in Table 1. These calculations with magnetism were begun by introducing small-amplitude seed magnetic fields into two statistically mature hydrodynamic simulations from BBT04. We then followed the evolution of those fields over multiple ohmic diffusion times. We have adopted here a magnetic Prandtl number $P_m = 5$, though P_m in the interiors of real A-type stars is close to unity, which allows us to achieve higher magnetic Reynolds numbers R_m at moderate resolution than would be attainable with lower P_m. A detailed description of the initial conditions and simulation parameters adopted in our modeling of A-star core convection are provided in BBT04. Our simulations are the magnetic analogs of cases E and C4 in that paper, using these as initial conditions and denoting the resulting models as Em and C4m. Thus, we consider here the central regions of 2 $M_\odot$ A-type stars at rotation rates of 1 and 4 times the solar mean angular velocity of $\Omega_0 = 2.6 \times 10^{-6}\ s^{-1} = 414$ nHz, corresponding to rotation periods of 28 and 7 days. Rotation acts to stabilize these systems against convection (Chandrasekhar 1961), so our more rapidly rotating case C4m was evolved at somewhat lower values of viscosity and diffusivity than case Em rotating at the solar rate. Cases Em and C4m involve different values of the maximum entropy gradient $d\bar{S}/dr$ in the radiative region, thus sampling the effects on penetration as the stiffness of the boundary between that region and the convective core is varied.

2.2. *Anelastic MHD Equations*

Our ASH code solves the three-dimensional MHD anelastic equations of motion in a rotating spherical geometry using a pseudospectral semi-implicit approach (e.g., Clune et al. 1999; Miesch et al. 2000; Brun et al. 2005). These equations are fully nonlinear in velocity and magnetic fields and linearized in thermodynamic variables with respect to a spherically symmetric mean state that is also allowed to evolve. We take this spherical mean state to have density $\bar{\rho}$, pressure $\bar{P}$, temperature $\bar{T}$, specific entropy $\bar{S}$; perturbations are denoted as ρ, P, T, and S. The equations being solved are

$$\nabla\cdot(\bar{\rho}\boldsymbol{v}) = 0, \tag{1}$$

$$\nabla\cdot\boldsymbol{B} = 0, \tag{2}$$

$$\bar{\rho}\left[\frac{\partial \boldsymbol{v}}{\partial t} + (\boldsymbol{v}\cdot\nabla)\boldsymbol{v} + 2\boldsymbol{\Omega}_0\times\boldsymbol{v}\right] = -\nabla P + \rho\boldsymbol{g} + \frac{1}{4\pi}(\nabla\times\boldsymbol{B})\times\boldsymbol{B} - \nabla\cdot\boldsymbol{\mathcal{D}} - [\nabla\bar{P} - \bar{\rho}\boldsymbol{g}], \tag{3}$$

$$\bar{\rho}\bar{T}\frac{\partial S}{\partial t} + \bar{\rho}\bar{T}\boldsymbol{v}\cdot\nabla(\bar{S}+S) = \nabla\cdot\left[\kappa_r\bar{\rho}c_p\nabla(\bar{T}+T) + \kappa\bar{\rho}\bar{T}\nabla(\bar{S}+S)\right] + \frac{4\pi\eta}{c^2}\boldsymbol{j}^2 + 2\bar{\rho}\nu\left[e_{ij}e_{ij} - \frac{1}{3}(\nabla\cdot\boldsymbol{v})^2\right] + \bar{\rho}\epsilon, \tag{4}$$

$$\frac{\partial \boldsymbol{B}}{\partial t} = \nabla\times(\boldsymbol{v}\times\boldsymbol{B}) - \nabla\times(\eta\nabla\times\boldsymbol{B}), \tag{5}$$

where $\boldsymbol{v} = (v_r,\ v_\theta,\ v_\phi)$ is the velocity in spherical coordinates in the frame rotating at constant angular velocity $\boldsymbol{\Omega}_0$, $\boldsymbol{g}$ is the gravitational acceleration, $\boldsymbol{B} = (B_r,\ B_\theta,\ B_\phi)$ is the magnetic field, $\boldsymbol{j} = c/4\pi(\nabla\times\boldsymbol{B})$ is the current density, c_p is the specific heat at constant pressure, κ_r is the radiative diffusivity, η is the effective magnetic diffusivity, and $\boldsymbol{\mathcal{D}}$ is the viscous stress tensor, with components

$$\mathcal{D}_{ij} = -2\bar{\rho}\nu\left[e_{ij} - \frac{1}{3}(\nabla\cdot\boldsymbol{v})\delta_{ij}\right], \tag{6}$$

where e_{ij} is the strain rate tensor, and ν and κ are effective eddy diffusivities. A volume heating term $\bar{\rho}\epsilon$ is included in these equations to represent energy generation by nuclear burning of the CNO cycle within the convective core. To close the set of equations, the thermodynamic fluctuations are taken to satisfy the linearized relations

$$\frac{\rho}{\bar{\rho}} = \frac{P}{\bar{P}} - \frac{T}{\bar{T}} = \frac{P}{\gamma\bar{P}} - \frac{S}{c_p}, \tag{7}$$

assuming the ideal gas law

$$\bar{P} = \mathcal{R}\bar{\rho}\bar{T}, \tag{8}$$

where $\mathcal{R}$ is the gas constant. The effects of compressibility on the convection are taken into account by means of the anelastic approximation, which filters out sound waves that would otherwise severely limit the time steps allowed by the simulation. In the MHD context here, the anelastic approximation filters out fast magneto-acoustic modes but retains the Alfven and slow magneto-acoustic modes. In order to ensure that the mass flux and the magnetic field remain divergence-free to machine precision throughout the simulation, we use a toroidal-poloidal decomposition

$$\bar{\rho}\boldsymbol{v} = \nabla\times\nabla\times(W\boldsymbol{e}_r) + \nabla\times(Z\boldsymbol{e}_r), \tag{9}$$

$$\boldsymbol{B} = \nabla\times\nabla\times(C\boldsymbol{e}_r) + \nabla\times(A\boldsymbol{e}_r), \tag{10}$$

with $\boldsymbol{e}$ a unit vector, and involving the stream functions W and Z and magnetic potentials C and A, which are functions of all three spatial coordinates plus time.

The full set of anelastic MHD equations solved by ASH is described in Brun et al. (2005), though they are dealing with solar dynamo processes in a deep convective shell. In order to be well posed, our system of equations for W, Z, C, and A, and for the fluctuating entropy S and pressure P, requires 12 boundary conditions and suitable initial conditions. Since we aim to assess the angular momentum redistribution in our simulations, we have opted for torque-free velocity and magnetic boundary conditions at the top and bottom of the deep spherical domain. These are symbolically

1. impenetrable top and bottom surfaces: $v_r = 0|_{r=r_{\rm bot}, r_{\rm top}}$,
2. stress-free top and bottom: $(\partial/\partial r)(v_\theta/r) = (\partial/\partial r)\,(v_\phi/r) = 0|_{r=r_{\rm bot}, r_{\rm top}}$,
3. constant entropy gradient at top and bottom: $\partial\bar{S}/\partial r = \text{constant}|_{r=r_{\rm bot}, r_{\rm top}}$,
4. purely radial magnetic field at top and bottom (match to a highly permeable external media; Jackson 1999): $B_\theta = B_\phi = 0|_{r=r_{\rm bot}, r_{\rm top}}$.

Requiring the magnetic field to be purely radial at the boundaries means that the Poynting flux vanishes there, with no magnetic energy leaking out of the domain.

2.3. *Numerical Approach*

Convection in stars occurs on many spatial scales. No numerical simulations can presently consider all these scales simultaneously. We choose to resolve the largest scales of the nonlinear flows and magnetic fields, which we think are likely to be the dominant players in establishing differential rotation and other mean properties of the core convection. Our large-eddy simulations (LESs) thus explicitly follow the larger scales, while employing sub–grid-scale (SGS) descriptions of the effects of unresolved motions. Those unresolved motions are manifested simply as enhancements to the kinematic viscosity and thermal and magnetic diffusivities (ν, κ, and η, respectively), which are thus effective eddy viscosities and diffusivities. For simplicity, we have taken these to be functions of radius alone, and chosen to scale them as the inverse of the square root of the mean density. We are encouraged by the relative successes that similar simulations (e.g., Miesch et al. 2000; Elliott et al. 2000; Brun & Toomre 2002) have achieved in matching the detailed observational constraints provided by helioseismology on differential rotation achieved by solar convection. However, we recognize that considerable refinements for SGS treatments are generally needed, and such work is under way.

Within ASH, the dynamic variables are expanded in spherical harmonics $Y_\ell^m(\theta, \phi)$ in the horizontal directions and in Chebyshev polynomials $T_n(r)$ in the radial. Thus, spatial resolution is uniform everywhere on a sphere when a complete set of spherical harmonics of degree ℓ is used, retaining all azimuthal orders m in what is known as a triangular truncation. We here limit our expansion to degree $\ell = \ell_{\rm max}$, which is related to the number of latitudinal mesh points N_θ [here $\ell_{\rm max} = (2N_\theta - 1)/3$], take $N_\phi = 2N_\theta$ latitudinal mesh points, and utilize N_r collocation points for the projection onto the Chebyshev polynomials. We employ a stacked Chebyshev representation, wherein the computational domain is split into two regions and separate Chebyshev expansions performed for each. We thus attain higher resolution at the interface between these two regions, here set as the approximate boundary between the convective and radiative zones, in order to capture better the penetrative convection occurring there. We have taken $N_r = 49 + 33 = 82$ and $\ell_{\rm max} = 170$ in the simulations considered here. The time evolution of the linear terms is determined using an implicit, second-order Crank-Nicholson scheme, whereas an explicit second-order Adams-Bashforth scheme is employed for the advective, Lorentz, and Coriolis terms. The ASH code has been optimized to run efficiently on massively parallel supercomputers, such as the IBM SP-4 and the Compaq TCS-1, using the message passing interface (MPI) and has demonstrated good scalability on such machines up to about 1000 processors. More details on the numerical implementation of ASH are provided in Clune et al. (1999) and in Brun et al. (2005).

The intricate and sustained time dependence typical of core convection requires extended simulation runs to assess the dynamical equilibration of such systems, spanning over 7000 days of physical time (or about 300 rotation periods) in one of our cases. The analysis of such dynamics requires forming various spatial and temporal averages of the evolving solutions. We will use the symbol $\tilde{a}$ to indicate temporal and longitudinal averaging of, say, the variable a, and the symbol $\langle a\rangle$ in denoting longitudinal averaging alone to obtain the axisymmetric component of the variable. The latter allows us to separate the fluctuating (denoted by the prime as a') from the axisymmetric (mean) parts of the variable. This is convenient, for instance, in defining fluctuating and mean velocity components (relative to the rotating frame). The symbol $\tilde{a}$ designates the rms average of the variable, carried out over a spherical surface for many realizations in time. Likewise, the combined symbols $\tilde{a}'$ represent similar rms averaging of the variable from which the axisymmetric portion has been subtracted.

2.4. *Progenitor Convection with Differential Rotation*

The simulations described here take as their starting point an evolved instant in the hydrodynamic simulations of core convection described in BBT04. We illustrate in Figure 1 some of the striking dynamical properties revealed by one of those progenitor simulations. Figure 1*a* shows a global mapping at one instant of the radial velocity deep within the core in case E, which is rotating at the solar rate. In this Mollweide projection, meridian lines are seen as curved arcs, and lines of constant latitude are indeed parallel. Convection within the core involves broad sweeping flows that span multiple scale heights, with little apparent asymmetry between upflows (*light features*) and downflows (*dark tones*). The convective flows in such global domains can readily plunge through the center, thus coupling widely

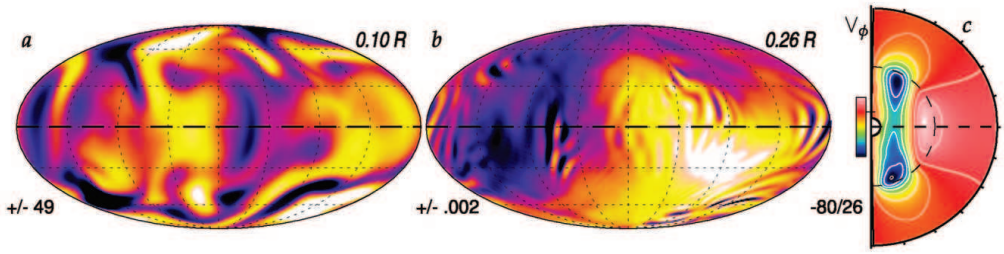

FIG. 1.—Flow properties of core convection in the progenitor hydrodynamic simulation case E from BBT04. (*a*) Radial velocity v_r at one instant in mid-core (at $r = 0.10R$), shown in a global view as a Mollweide projection. Broad regions of upflow are in light tones and downflows in dark tones, as indicated by color bar, with ranges in meters per second. (*b*) Companion view of v_r within surrounding radiative envelope (at $r = 0.26R$), showing signature of the relatively weak internal gravity waves excited by the plumes of penetration. (*c*) Resulting differential rotation established in the computational domain displayed in cross section of radius and latitude. Shown as a contour plot is the time and longitudinally averaged zonal velocity $\hat{v}_\phi$, which possesses a central column of particularly slow rotation (retrograde relative to the frame). The equator is denoted by the dashed line; the rotation axis is vertical, and the outer extent of the prolate core is indicated by the dotted curve.

separated sites. The flows are highly time dependent, with complex and intermittent features emerging as the simulations evolve. Such vigorous convection is able to penetrate into the overlying radiative zone, with that extent varying with latitude. The upward-directed penetrating plumes serve to excite gravity waves in the stable envelope, seen in Figure 1*b* as localized ripples on many scales.

The coupling of convection with rotation in these spherical geometries yields a prominent differential rotation exhibited in Figure 1*c*. The mean zonal flows shown there (relative to the rotating frame) are characterized by a central cylindrical column of slow rotation. Within the bulk of the convection zone, this differential rotation is driven primarily by the Reynolds stresses associated with the convection, helped by meridional circulation and opposed by viscous stresses. Near the interface between the core and the radiative envelope, baroclinicity also plays an important role.

The penetrative convection yields a nearly adiabatically stratified core region that is prolate in shape and aligned with the rotation axis (Fig. 1*c*, *dashed curve*). This is surrounded by a further region of overshooting in which the convective plumes can mix the chemical composition but do not appreciably modify the stable (subadiabatic) stratification. The outward extent of this zone is roughly spherical. Our progenitor simulations in BBT04 have thus revealed that core convection establishes angular velocity profiles with a distinctive central column of slowness, a prolate shape to the well-mixed core, and a broad spectrum of gravity waves in the radiative envelope.

3. DYNAMO ACTION REALIZED IN CORE

We have found that vigorous core convection coupled with rotation clearly admits magnetic dynamo action. The initial seed magnetic fields introduced into our two progenitor hydrodynamic simulations are amplified greatly by the convective and zonal flows, ultimately yielding magnetic fields that possess energy densities comparable to that in the convection itself. Here we begin by assessing the growth of the magnetic fields and their saturation, the morphology of the magnetism and the resulting modified convection, and the intricate time dependence of the sustained fields and flows.

3.1. *Growth and Saturation of Magnetic Fields*

The temporal evolution of the magnetic energy (ME) and kinetic energy (KE) densities (volume-integrated and relative to the rotating frame) in case C4m is displayed in Figure 2*a*. The magnetic field undergoes an initial phase of exponential growth from its very weak seed field, which lasts about 1000 days. In case Em (not shown), the initial phase of growth lasts about 1700 days. The seed dipole fields are in both simulations amplified by more than 8 orders of magnitude. The different growth rates for the magnetic field realized in the two simulations result from the differing Reynolds numbers and magnetic diffusivities adopted. Both have magnetic Reynolds numbers (see Table 1) well in excess of the threshold values that earlier studies of convection in spherical shells (e.g., Gilman 1983; Brun et al. 2005) have found necessary for dynamo action, typically $R_m \approx 300$. This exponential growth is followed by a nonlinear saturation

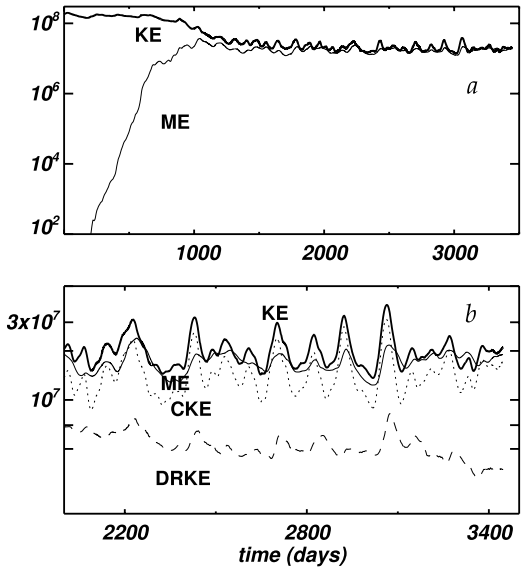

FIG. 2.—Temporal evolution in case C4m of the volume-averaged total kinetic energy density (KE) and the magnetic energy density (ME). (*a*) The initial seed magnetic field is amplified by many orders of magnitude. After an initial phase in which ME grows exponentially, it equilibrates to a level in which it becomes comparable to KE, which has been lessened by the feedback of the magnetism upon the flows. (*b*) Detailed view of fluctuations of energy densities once equilibration is approached, showing also energy densities of the convection (CKE) and the differential rotation (DRKE).

phase, during which the Lorentz forces acting upon the flows yield statistical equilibria in which induction is balanced in the large by ohmic dissipation. The magnetic field attains different saturation amplitudes in the two simulations. In case C4m, the energy density in the magnetic field (ME) is typically about 88% of the KE, whereas in case Em it is about 28% but fluctuates considerably in several phases of behavior. Such field amplitudes are sustained for longer than the magnetic diffusion time across the computational domain—here, $\tau \sim L^2/(\pi^2\eta) \sim$ 3900 days (Moffatt 1978)—implying that the magnetic field is being actively maintained against ohmic decay. Thus, sustained dynamo action has probably been realized. The different set of parameters used in the two simulations appear to account for the different saturation field strengths that are realized.

The strong magnetic fields established by dynamo action within the core are expected to interact with the convective and zonal flows. A clear indication of such feedback is provided by the reduction of KE visible in Figure 2*a* after about 1000 days. This first becomes apparent once ME grows to about 1% of KE, as the magnetic fields begin to significantly modify the flows through the Lorentz ($\boldsymbol{j}\times\boldsymbol{B}$) term in equation (3), much as in simulations of strong dynamo activity in the solar convection zone (Brun et al. 2005). The reduction in KE here is due primarily to a significant decline in the energy contained in the differential rotation (DRKE). In simulation C4m, DRKE decreases to only 3% of its value in the hydrodynamic progenitor simulation C4 (see also Table 3). In case Em, the decline is also appreciable, with DRKE dropping to 19% of its value in the hydrodynamic simulation. We consider issues of the resulting differential rotation and its linkage to temporal variations of ME in § 4.1.

Like the convective and zonal flows that build and sustain them, the magnetic fields in these simulations are highly variable in time. This variability is apparent in Figure 2*b*, which shows the evolution of various energy densities over an interval subsequent to the initial exponential growth of the magnetic field. Shown are the energies in the convection (CKE) together with KE, DRKE, and ME. Though no continuous growth or decline of the energy densities is evident, they show considerable variations for this case C4m. During this interval, KE fluctuates by about a factor of 3, with most of this variation reflecting that of CKE. The modulations in CKE have a temporal spacing of about 130–140 days, or roughly 20 rotation periods. Here ME likewise varies, as the convective and zonal flows serve to modify the magnetic fields through the production term in the induction equation (5). Indeed, during some intervals in the evolution of case C4m shown in Figure 2*b*, ME actually exceeds KE. It is interesting that the field strengths achieved in case C4m thus roughly represent equipartition between the flows relative to the rotating frame and the magnetism. Such values of ME represent typical rms field strengths in the core of about 67 kG, as compared to rms flow velocities that are about 30 m s^{-1} (Table 2).

TABLE 2
VELOCITY AND MAGNETIC FIELD AMPLITUDES

Case	Em	C4m	E	C4
$\tilde{v}_r$	20	15	26	19
$\tilde{v}_\theta$	22	16	23	16
$\tilde{v}_\phi$	22	21	43	72
$\tilde{v}'_\phi$	20	15	21	21
$\tilde{v}$	37	30	55	76
$\tilde{v}'$	36	26	38	32
$\tilde{B}_r$	28	33	...	...
$\tilde{B}_\theta$	30	36	...	...
$\tilde{B}_\phi$	28	45	...	...
$\tilde{B}'_\phi$	27	44	...	...
$\tilde{B}$	50	67	...	...
$\tilde{B}'$	49	65	...	...

NOTES.—Listed for both MHD simulations (cases Em, C4m) and their hydrodynamic progenitors (cases E, C4) are the rms amplitude of the velocity $\tilde{v}$ and each of its components, $\tilde{v}_r$, $\tilde{v}_\theta$, and $\tilde{v}_\phi$, averaged over time and over a spherical surface at mid-depth in the convective core (at $r = 0.10R$). Also listed are the rms amplitudes of the fluctuating velocity $\tilde{v}'$ and its zonal component $\tilde{v}'_\phi$, averaged in time and obtained after subtracting the longitudinal average. We also indicate (where appropriate) the corresponding rms amplitudes of the magnetic field and its components, $\tilde{B}$, $\tilde{B}_r$, $\tilde{B}_\theta$, $\tilde{B}_\phi$, $\tilde{B}'$, and $\tilde{B}'_\phi$. Velocities are expressed in m s^{-1} and magnetic fields in kG.

3.2. *Morphology of Flows and Magnetism*

Within the core, broad convective flows sweep through the spherical domain, with large-scale regions of upflow and downflow serving to couple widely separated regions. The global connectivity permitted in these full spheres, together with the fairly small density contrasts present, results in motions that can span large fractions of a hemisphere and extend radially through much of the convection zone.

Such global-scale convective flows are apparent in Figure 3*a*, which shows a volume rendering of a snapshot of the radial velocity v_r near the outer boundary of the convective core in case C4m. The region of vigorous convection is slightly prolate in shape, much as in the progenitor, extending farther in radius near the poles than near the equator. No obvious asymmetry between regions of upflow and downflow is visible. This stands in sharp contrast to the results of solar convection simulations that exhibit broad upflows together with narrow and fast downflows.

The magnetic fields sustained within the convection zone are characterized by smaller scale features than are present in the convective flows. The intricate nature of the field is most apparent in Figure 3*b*, which shows the radial component of magnetic field B_r. Here the field appears as a tangled collection of positive and negative polarity on many different scales. The finer structure present in the magnetic fields than in the convective flows comes about partly because we have taken the magnetic diffusivity to be smaller than the viscous diffusivity (with $\mathrm{P}_m = 5$).

The longitudinal fields B_ϕ shown in Figure 3*c* likewise possess small-scale structure, but they also exhibit organized bands of magnetism that wrap around much of the core. These broad ribbons of toroidal field may arise due to stretching by gradients of angular velocity near the interface between the core and the radiative envelope. Such stretching and amplification of toroidal field by differential rotation, described in mean-field theories as the ω-effect, mirrors what is thought to occur in the tachocline of rotational shear at the base of the solar convection zone. In the Sun, magnetic fields are thought to be pumped downward from the envelope convection zone into the radiative interior, with the tachocline at the interface producing strong toroidal fields that eventually rise by magnetic buoyancy through the convection zone (e.g., Charbonneau & MacGregor 1997). Here we may be seeing the reverse analog of such a process in stars with convective interiors surrounded by radiative envelopes.

The intricate networks of magnetic fields and convective flows are also revealed in Figure 4 (for case Em) and in Figure 5 (for case C4m) by global mappings of the radial velocity (v_r)

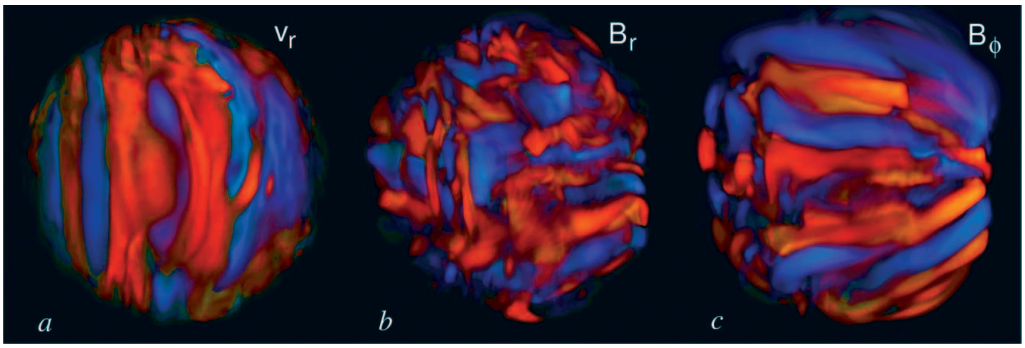

FIG. 3.—Volume renderings of flow and magnetic structures at one instant in case C4m near the outer boundary of the prolate convective core. (*a*) Radial velocity v_r exhibits columnar structures aligned with the rotation axis (here oriented vertically). Little asymmetry is apparent between upflows (*reddish*) and downflows (*bluish*). (*b*) Radial magnetic field B_r is more tangled, with field polarity shown in contrasting tones. (*c*) Longitudinal magnetic field B_ϕ possesses a distinctive ribbon-like morphology, with coherent bands that extend around much of the core.

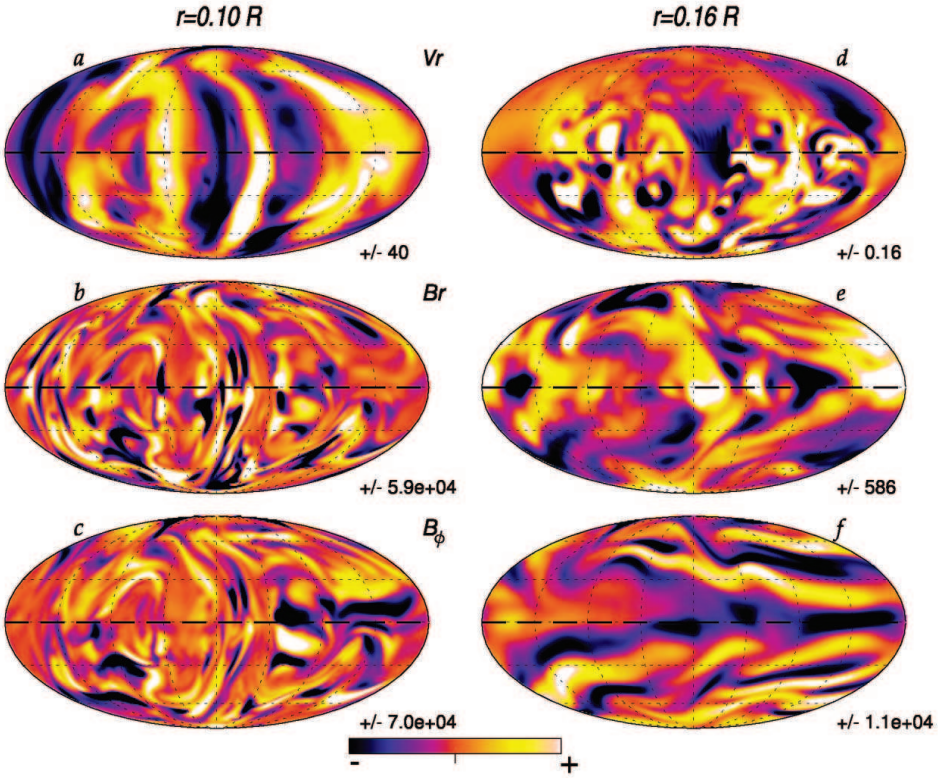

FIG. 4.—Global mappings at one instant in case Em of v_r, B_r, and B_ϕ sampled on two spherical surfaces, both at mid-core ($r = 0.10R$, *left*) and in the region of penetration and overshooting ($r = 0.16R$, *right*). Shown are Mollweide projections, with the dashed horizontal line denoting the equator. All fields share the same symmetric color table, with positive values in bright tones and negative ones in dark tones. The amplitude ranges are indicated adjacent to each panel, with magnetic fields in G and velocities in m s^{-1}.

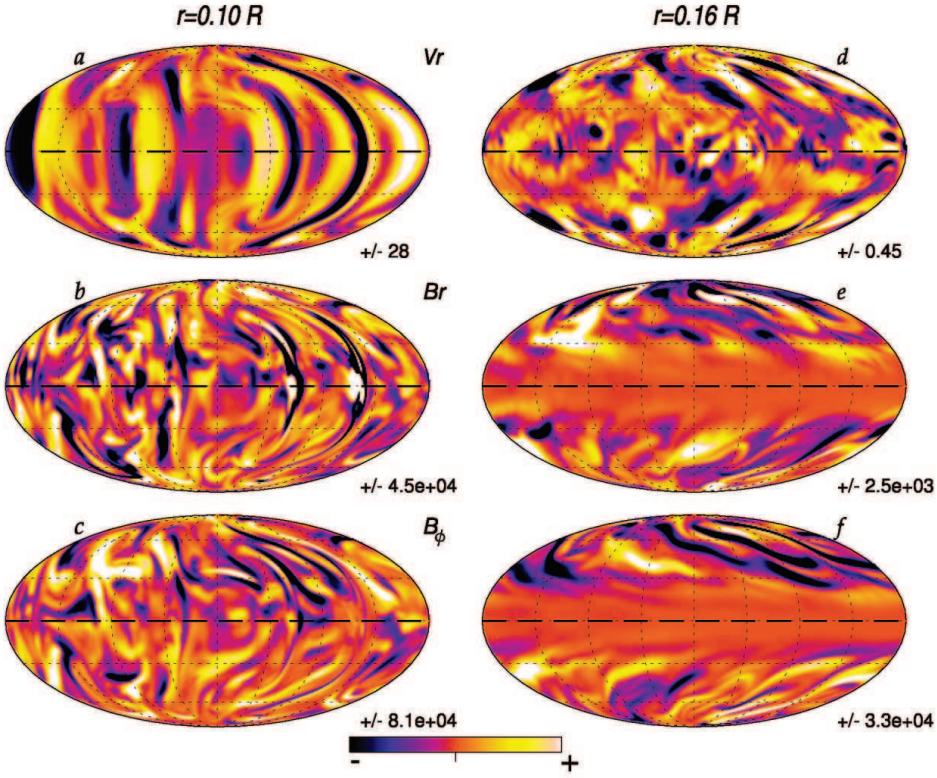

FIG. 5.—As in Fig. 4, global Mollweide projections of v_r, B_r, and B_ϕ, but for the more rapidly rotating case C4m at one instant in time.

together with the radial (B_r) and azimuthal (B_ϕ) magnetic fields at two depths. Deep within the convective core (at $r = 0.10R$, *left*), the finely threaded magnetic field coexists with the relatively broad patchwork of convective flows. Features in v_r and B_r possess evident links, with the convective downflow lanes containing strong radial magnetic field of both polarities. In contrast, upflows contain few strong magnetic structures. The azimuthal field B_ϕ within the core appears to be quite patchy, with little correlation to the radial velocity field v_r. Finer structure is present in all the fields displayed for case C4m (Fig. 5) relative to case Em, owing mostly to the slightly smaller viscosities and resistivities adopted for C4m.

Near the boundary of the convective core and the radiative envelope ($r = 0.16R$, *right*), v_r and B_r both possess considerably smaller amplitudes than in the deep interior, with v_r in case Em (Fig. 4) lessened by a factor of 240 and B_r by a factor of 100. This suggests that the spherical surface shown cuts through a region where only weak overshooting of the convection survives. In case C4m (Figs. 5*a* and 5*b*), the amplitudes of v_r and B_r are reduced by smaller factors (of 64 and 18, respectively) in going from $r = 0.10R$ to $0.16R$, most likely because one is sampling here the penetrative convection more directly, probably because of the weaker stable stratification in this case. In contrast, B_ϕ near the core boundary in both cases is only slightly diminished from its interior strength and may reflect the continuing production of toroidal field there by rotational shear. The overall magnetic fields at the core boundary are of larger physical scale than the fields deeper down, and B_ϕ (Figs. 4*f*, and 5*f*) shows the same broad and wavy, ribbon-like features evident in the volume renderings of Figure 3*c*. In case C4m (Fig. 5*f*), the magnetic field at this radius ($r = 0.16R$) is much stronger at high latitudes than at the equator, reflecting the prolate shape of the strongly magnetized core of convection. The spherical surface viewed here lies inside this prolate region near the poles, but outside it at the equator. Thus, the stronger influence of rotation in this case C4m has yielded greater departures from a spherical shape for the core with penetration than is realized in case Em, helped also by the reduced stiffness of the radiative envelope in case C4m.

Our global mappings (at $r = 0.16R$) also reveal that the pummeling of the base of the radiative envelope by the upward-directed convective plumes serves to excite a broad range of internal gravity waves. These waves are visible at the low latitudes in Figures 4*d* and 5*d* as low-amplitude ripples of small physical scales. Similar gravity waves were seen in the progenitor nonmagnetic simulations in BBT04.

3.3. *Time Dependence of Sustained Flows and Fields*

The convective flows and the magnetic fields that they generate in our two cases evolve in a complicated fashion. Throughout the convective core, we have observed the birth of magnetic structures, their advection and shearing by the flows, and their mergers with other features or cleaving into separate structures. Some flows and magnetic structures persist for many days, while

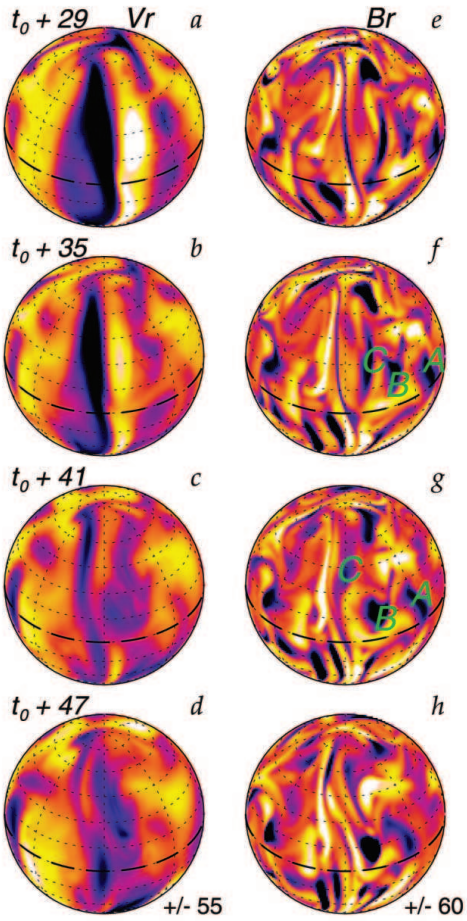

FIG. 6.—Rapid sampling in time of the evolution of structures seen in v_r (*left*) and B_r (*right*), as viewed on spherical surfaces at mid-core ($r = 0.10R$) for case Em. The four snapshots are separated by 6 days each, starting from a mature time t_0 within the simulation. Features (labeled A, B, and C) in the flows and magnetism persist but are advected and sheared, propagate relative to the frame, and can cleave into smaller structures. The color table is as in Fig. 4, and scaling is indicated.

others rapidly fade away. A brief sampling of such behavior in case Em is provided in Figure 6, showing a succession of spherical views of both v_r and B_r in midcore ($r = 0.10R$) at four closely spaced snapshots (each 6 days apart). Several features amid the magnetism, labeled *A*, *B*, and *C* in Figure 6, propagate in a slightly retrograde fashion (to the left) over the interval sampled. Features *A* and *B* remain confined to low latitudes, with feature *B* varying considerably in strength and size as the simulation evolves. In Figure 6*e*, this structure is visible as a weak patch of negative B_r at a latitude of about 20°; later it has become a much broader feature of greater amplitude (Fig. 6*h*), seen as a dark patch at a latitude of about 15°. Feature *C*, which at first appears as a narrow structure of negative polarity spanning latitudes from the equator to about 45°, then propagates toward higher latitudes and is sheared and weakened. The convective flows exhibit similar changes, with a coherent downflow lane

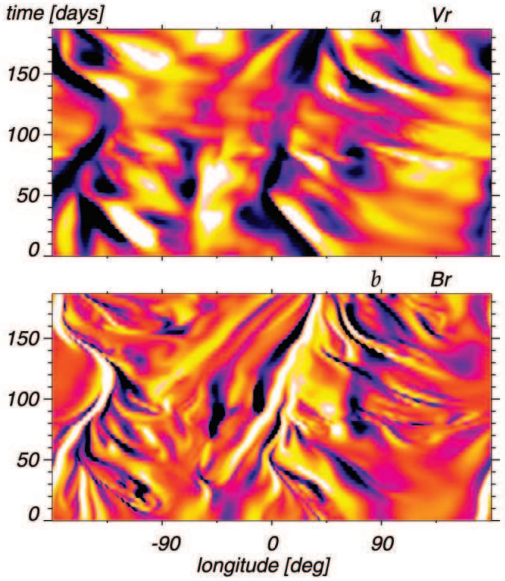

FIG. 7.—Extended evolution and propagation assessed by time-longitude sampling of (*a*) v_r and (*b*) B_r at mid-core ($r = 0.10R$) in case Em at the equator. At such low latitudes, persistent features in both v_r and B_r tend to propagate prograde (to the right) in longitude (relative to the frame). There is close correspondence in the structures evident in v_r and B_r. The color table and scaling is shared with Fig. 6, as is the sampling starting time t_0.

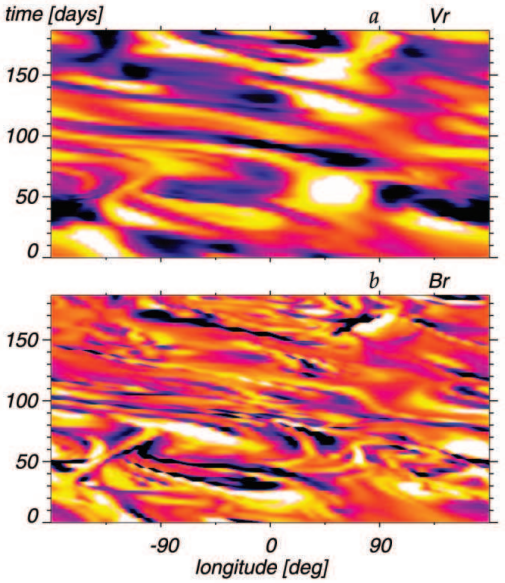

FIG. 8.—Same as Fig. 7, but at latitude 60°. Here the propagation of features in both fields is distinctly retrograde relative to the frame.

(Fig. 6*a*) spanning both hemispheres gradually breaking up into multiple structures.

Such rich time dependence is assessed over longer temporal intervals in case Em by turning to time-longitude mappings in Figures 7 and 8. These show the variation with time of v_r and B_r sampled (at $r = 0.10R$) for all longitudes either at the equator (Fig. 7) or at 60° latitude (Fig. 8). Coherent downflow lanes are visible in these time-longitude mappings of v_r as dark bands tilted to the right, indicating prograde propagation (relative to the frame), or to the left or retrograde, which often persist for multiple rotation periods. Similar evolution is observed in the companion mappings of B_r, with most major structures evident in both the flows and the magnetism. Much as in Figure 4, the persistent convective downflows contain magnetic fields of mixed polarities, whereas the upflows are largely devoid of strong magnetic structures. The propagation of these large-scale structures tends to be prograde at the equator (Fig. 7) and strongly retrograde at high latitudes (Fig. 8). There is also substantial evolution of the flows on short timescales, with some striking features of the convection rapidly emerging and then fading. Similarly, the magnetic field exhibits both rapid evolution of some structures and others that survive for extended periods of time. Identification of persistent features amid the magnetism is occasionally made more difficult by the finely threaded field topology. However, structures evident in B_r generally appear to be advected and to propagate in roughly the same fashion as features in v_r, with both tending to wax and wane as the simulations evolve.

4. MEAN FLOWS AND TRANSPORT

In the deep spherical domains studied here, the Coriolis forces associated with rotation can have major impacts on the structure of the convective flows and thus on the manner in which they redistribute angular momentum. When that influence is strong, as when the convective overturning time is at least as long as the rotation period (with the convective Rossby number R_c on the order of unity or smaller), a strong differential rotation may be achieved and maintained. This was realized in all the cases studied in BBT04. The dynamo action and consequent intense magnetic fields realized in our current simulations must feed back strongly on the convection through the Lorentz forces, probably reducing the differential rotation that can be maintained. Intuitively, one expects that the presence of magnetic fields will tend to diminish the differential rotation, with the field lines that thread the core acting like rubber bands to couple disparate regions and enforce more uniform rotation. Such an analogy is too simple given the tangled and intermittent nature of the magnetic fields in our simulations, yet the expectation that the presence of magnetism leads to reduced differential rotation turns out to be largely correct. We now consider the mean zonal flows of differential rotation that are realized in our cases Em and C4m, their variations in time, and the manner in which they are sustained.

4.1. *Nature of Accompanying Differential Rotation*

The differential rotation profiles achieved in our two cases Em and C4m are shown in Figure 9. These are displayed first as contour plots with radius and latitude of the longitudinal (or zonal) velocity $\hat{v}_\phi$, with the hat denoting an average in time and longitude. Shown also are plots of the radial variation of the associated angular velocity $\hat{\Omega}$ along three latitudinal cuts, contrasting the behavior in our magnetic simulations with that of their progenitors. The latter emphasize that in case Em the angular velocity contrasts have been lessened almost twofold from the

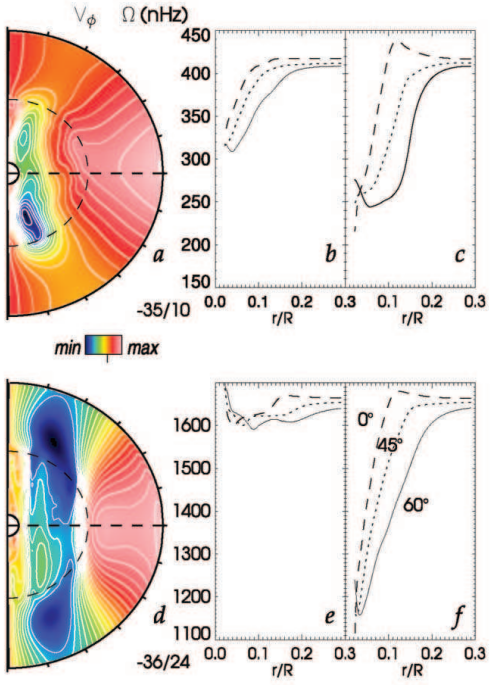

FIG. 9.—Differential rotation established in case Em (*top*) and *C4m* (*bottom*) and their progenitors. (*a* and *d*) Mean zonal velocity $\hat{v}_\phi$, averaged in time and longitude, shown as contour plots in radius and latitude, with color bar and ranges (in m s^{-1}) indicated. The equator is horizontal, the rotation axis vertical, and outer extent of convective core indicated by dashed curve. (*b* and *e*) Angular velocity $\hat{\Omega}$ with radius for latitudinal cuts at 0°, 45°, and 60°. (*c* and *f*) Value of $\hat{\Omega}$ achieved in progenitor nonmagnetic models. The magnetism acts to inhibit the strong angular velocity contrasts realized in the progenitor simulations.

hydrodynamic progenitor. In case C4m that contrast has been nearly eliminated. The contours of $\hat{v}_\phi$ emphasize that central columns of slow rotation are realized in both cases, as in their progenitors, but with reduced zonal flow amplitudes (see Fig. 1*c*). Both $\hat{v}_\phi$ profiles exhibit some asymmetry between the northern and southern hemisphere, with such behavior more pronounced for case Em (Fig. 9*a*). Noteworthy for case C4m is that the column of slowness in $\hat{v}_\phi$ extends well into the radiative envelope, owing in part to the stronger meridional circulations exterior to the core achieved with the faster frame rotation. The longitudinal velocity in C4m appears to be nearly constant on cylinders aligned with the rotation axis, somewhat akin to Taylor-Proudman columns achieved when rotational constraints are strong.

With the temporal changes seen in our convective flows and magnetism (Fig. 6) come also substantial variations in the differential rotation that they establish. This is most pronounced in case Em. Figure 10 shows a detailed view of temporal fluctuations in volume-averaged energy densities of the differential rotation (DRKE), convection (CKE), and magnetism (ME). These reveal that during extended intervals DRKE exceeds ME, but with moderate oscillations; such an interval was sampled in producing Figure 9. The fairly regular accompanying oscillations in CKE (and thus also KE) have periods of about 150–200 days, as contrasted to the rotation period of 28 days. There

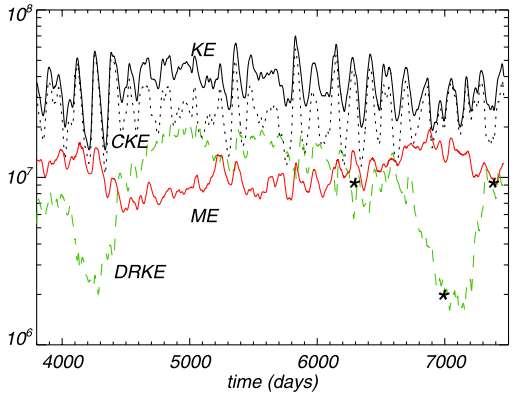

FIG. 10.—Detailed view in case Em of variations in the volume-averaged energy densities of the convection (CKE), differential rotation (DRKE), total kinetic energy density (KE), and magnetic energy (ME). Here DRKE undergoes two pronounced minima, the beginnings of which coincide with times at which ME climbs above $\sim 1.2 \times 10^7$ ergs cm^{-3}, or about 40% of KE. Indicated on the DRKE trace are the three times sampled for the differential rotation snapshots in Fig. 11.

are also remarkable brief intervals during which DRKE plummets by nearly an order of magnitude, with two such shown in Figure 10 at about 4200 and 7000 days in the simulation. The onset of those grand minima in DRKE coincide with times when ME has climbed to values greater than about 40% of KE. This suggests that strengthening magnetic fields can lead to abrupt collapses in the differential rotation established by the convection, followed by a recovery. This arises partly from the strong feedback of the Lorentz forces on the convection and on the differential rotation, both of which serve to build the fields through induction. With the consequent diminished flows, the field production is lessened, and so the magnetic fields weaken. Once below a given threshold (here ME less than 40% of KE), the convection regains its strength, leading to stronger Reynolds stresses (see § 4.2), which reestablish the differential rotation, with magnetic induction once again invigorated. Thus, the cycle lasting about 2000 days begins anew. Such intricate behavior seen in case Em is not realized in case C4m, where ME and KE are always comparable though moderately variable (see Fig. 2*b*). Since ME in this case is far stronger, cyclic behavior in which the Lorentz forces oscillate between being strong or weak is not realized. The complex changes in the differential rotation achieved in case Em are shown in Figure 11, which samples three short temporal averages of $\hat{v}_\phi$ and $\hat{\Omega}$. These examine intervals prior to, during, and after the second pronounced minimum of DRKE (Fig. 10). During that minimum the angular velocity contrast within the core (Fig. 11*b*) is modest, and the retrograde column of slowness in $\hat{v}_\phi$ is barely there. The samples before (Fig. 11*a*) and after (Fig. 11*c*) show zonal flows and angular velocity contrasts much as in Figures 9*a* and 9*b*, possessing central regions of slow rotation. In contrast, no comparable large variation in zonal flows are realized in case C4m, where angular velocity contrasts are modest at all times, much as in the long time average shown in Figures 9*d* and 9*e*.

4.2. *Redistributing the Angular Momentum*

The complex MHD systems studied here exhibit a rich variety of responses, with intricate time dependence seen in both

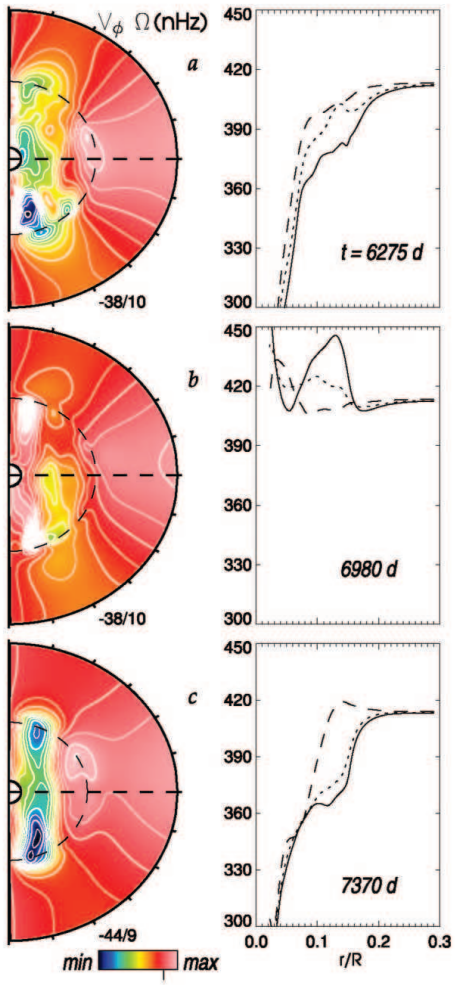

FIG. 11.—Differential rotation achieved in case Em at three different time-sampling intervals before (*a*), during (*b*), and after (*c*) a grand minimum in DRKE in Fig. 10. Shown as contour plots (*left*) are the longitudinal averaged zonal velocity $\hat{v}_\phi$ averaged over brief (20 day) intervals, accompanied by (*right*) angular velocity $\hat{\Omega}$ as radial cuts at the three latitudes indicated.

the flows and magnetic fields. How the zonal flows seen as differential rotation arise and are sustained, how they interact with the magnetism, and how they vary in time are thus all sensitive matters. This behavior cannot now be predicted from first principles, but the present simulations offer a unique opportunity to determine the roles played by different agents in transporting angular momentum and giving rise to the differential rotation. Since our case Em exhibits strong, albeit variable, angular velocity contrasts, we here examine how these are established.

Our simulations were conducted with stress-free and purely radial magnetic field boundary conditions, so no net external torque is applied to the computational domain. Thus, total angular momentum within the simulations is conserved. We can

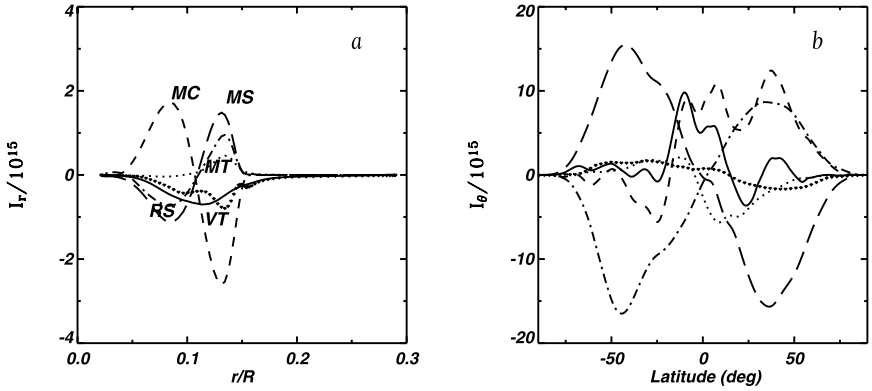

FIG. 12.—Temporal average in case Em of (*a*) the integrated vertical angular momentum flux I_r and (*b*) the integrated latitudinal angular momentum flux I_θ. These have been decomposed into components due to viscous transport (labeled VT), Reynolds stress (RS), meridional circulation (MC), Maxwell stress (MS), and large-scale magnetic torque (MT), and the solid curves represent the total fluxes. Positive quantities represent fluxes radially outward, or latitudinally from north to south. The interval chosen for the time averages spans 300 days late in the simulation.

assess the transport of angular momentum within these systems in the manner of Brun et al. (2005; see also Elliott et al. 2000). We consider the ϕ-component of the momentum equation expressed in conservative form and averaged in time and longitude:

$$\frac{1}{r^2}\frac{\partial(r^2\mathcal{F}_r)}{\partial r}+\frac{1}{r\sin\theta}\frac{\partial(\sin\theta\mathcal{F}_\theta)}{\partial\theta}=0, \tag{11}$$

involving the mean radial angular momentum flux,

$$\mathcal{F}_r=\bar{\rho}r\sin\theta\left[-\nu r\frac{\partial}{\partial r}\left(\frac{\hat{v}_\phi}{r}\right)+\widehat{v_r'v_\phi'}+\hat{v}_r(\hat{v}_\phi+\Omega r\sin\theta)-\frac{1}{4\pi\bar{\rho}}\widehat{B_r'B_\phi'}-\frac{1}{4\pi\bar{\rho}}\hat{B}_r\hat{B}_\phi\right], \tag{12}$$

and the mean latitudinal angular momentum flux,

$$\mathcal{F}_\theta=\bar{\rho}r\sin\theta\left[-\nu\frac{\sin\theta}{r}\frac{\partial}{\partial\theta}\left(\frac{\hat{v}_\phi}{\sin\theta}\right)+\widehat{v_\theta'v_\phi'}+\hat{v}_\theta(\hat{v}_\phi+\Omega r\sin\theta)-\frac{1}{4\pi\bar{\rho}}\widehat{B_\theta'B_\phi'}-\frac{1}{4\pi\bar{\rho}}\hat{B}_\theta\hat{B}_\phi\right]. \tag{13}$$

In the above expressions, the terms on both right-hand sides denote contributions, respectively, from viscous diffusion (which we denote as $\mathcal{F}_r^{\rm VD}$ and $\mathcal{F}_\theta^{\rm VD}$), Reynolds stresses ($\mathcal{F}_r^{\rm RS}$ and $\mathcal{F}_\theta^{\rm RS}$), meridional circulation ($\mathcal{F}_r^{\rm MC}$ and $\mathcal{F}_\theta^{\rm MC}$), Maxwell stresses ($\mathcal{F}_r^{\rm MS}$ and $\mathcal{F}_\theta^{\rm MS}$), and large-scale magnetic torques ($\mathcal{F}_r^{\rm MT}$ and $\mathcal{F}_\theta^{\rm MT}$). The Reynolds stresses are associated with correlations of the fluctuating velocity components (shown primed) that arise from organized tilts within the convective structures. Similarly, the Maxwell stresses are associated with correlations of the fluctuating magnetic field components that arise from tilt and twist within the magnetic structures.

Analyzing the components of $\mathcal{F}_r$ and $\mathcal{F}_\theta$ is aided by integrating over colatitude and radius to deduce the net fluxes through shells at various radii and through cones at various latitudes, such that

$$I_r(r)=\int_0^\pi \mathcal{F}_r(r,\theta)r^2\sin\theta\,d\theta,$$
$$I_\theta(\theta)=\int_{r_{\rm bot}}^{r_{top}}\mathcal{F}_\theta(r,\theta)r\sin\theta\,dr. \tag{14}$$

We then identify in turn the contributions from viscous diffusion (VD), Reynolds stresses (RSs), meridional circulation (MC), Maxwell stresses (MSs), and large-scale magnetic torques (MTs). This helps to assess the sense and amplitude of angular momentum transport within the convective core and the radiative exterior by each component of $\mathcal{F}_r$ and $\mathcal{F}_\theta$. We now examine the transports achieved within case Em by temporally averaging the fluxes over the interval spanning from 6700 to 7000 days, during which the system was undergoing changes (see Fig. 10).

Turning first to the integrated radial fluxes of angular momentum in Figure 12*a*, we see that the Maxwell stresses ($I_r^{\rm MS}$) are playing a major role in the radial transport, acting in the outer portions of the core to transport angular momentum radially outward and deeper down to transport it inward. In this they are opposed principally by meridional circulations ($I_r^{\rm MC}$) and aided by the Reynolds stresses ($I_r^{\rm RS}$) associated with the convective flows. The strong Maxwell stresses realized in our simulations are noteworthy, for they lead here to major departures from the angular momentum balance that was achieved in the progenitor hydrodynamic models. Over the evolution interval for case Em sampled in Figure 12*a*, the Maxwell stresses act in concert with the Reynolds stresses throughout much of the core, even though the corresponding terms in equation (12) carry opposite signs. This indicates that correlations between the radial and longitudinal components of the fluctuating magnetic field are reversed with respect to those of the fluctuating velocity field. Such behavior was not realized in the solar convection simulations of Brun et al. (2005) and is less pronounced in our companion case C4m. We also see that the torques provided by the axisymmetric magnetic fields ($I_r^{\rm MT}$) are small throughout most of the convective core, in keeping with the finding in § 6 that the mean axisymmetric fields are dwarfed in strength by the fluctuating ones. However, near the

outer boundary of the core these mean magnetic torques grow more significant, in keeping with the mean fields there becoming a significant contributor to the magnetic energy. There they act together with the Maxwell and Reynolds stresses to transport angular momentum outward. The viscous flux is everywhere negative and fairly small relative to the other components. All of the component fluxes decrease rapidly outside of the convective core, as both convective motions and magnetic fields vanish.

The net radial flux I_r (Fig. 12*a*) would be zero in a steady state but here is markedly negative. However, since in case Em the differential rotation shows prominent changes with time, there must be nonzero net fluxes of angular momentum to accomplish such changes. Over the interval sampled by Figure 12, the system is transitioning from a state of high DRKE—characterized by a strongly retrograde core—to one of low DRKE with only small angular velocity contrasts (see Fig. 10). Thus, the central regions of the convective core are being spun up, and so there must be a net angular momentum flux inward. Figure 12*a* confirms that this is indeed occurring during this interval.

The integrated latitudinal angular momentum fluxes in Figure 12*b* also reveal a complex interplay among the different transport mechanisms. Here the Maxwell stresses ($I_\theta^{\rm MS}$) act largely to slow down the equator (by transporting angular momentum toward the poles), opposing the strong Reynolds stresses ($I_\theta^{\rm RS}$) that seek to accelerate it. Thus, in contrast to the radial integrated fluxes, the Reynolds and Maxwell stresses transport angular momentum in opposite directions. Similar results for the respective role of the Reynolds and Maxwell stresses in transporting angular momentum latitudinally are found in the solar magnetic cases computed by Brun et al. (2005). Meridional circulations ($I_\theta^{\rm MC}$) also generally act to accelerate the equator, though the complicated multicelled nature of those circulations makes the angular momentum flux they provide decidedly nonuniform. The weak axisymmetric magnetic torques ($I_\theta^{\rm MT}$), like their strong fluctuating counterparts the Maxwell stresses, act to oppose the equatorial acceleration afforded by the Reynolds stresses. Viscous diffusion plays only a small role but also tends to transport angular momentum away from the equator.

Although Figure 12 assesses the angular momentum transports during an interesting interval marked by changes in the differential rotation, the character of the various contributing fluxes is much the same during other intervals. Examining these fluxes provides clues as to why the magnetic simulations exhibit much weaker differential rotation (or DRKE) than their progenitors. Whereas in the progenitor the Reynolds stresses $I_\theta^{\rm RS}$ that sought to accelerate the equator competed only against meridional circulations and viscous diffusion, here they must also counteract the poleward transport of angular momentum provided by the Maxwell stresses and large-scale magnetic torques (Fig. 12*b*). Though in principle the fluxes due to the Reynolds stresses and meridional circulations could adjust to compensate for such poleward transport, this was not realized in case Em. Thus, the speeding up of the equatorial regions of the outer core was lessened and so too the slowing down of the central column, with an overall decrease in the angular velocity contrast.

4.3. *Radial Transport of Energy*

Since convection in the core arises because of the need to move energy radially outward, we now assess the role of different agents in transporting the energy within our simulations. Figure 13 presents the radial energy fluxes provided by various physical processes, converted to luminosities and normalized to the stellar luminosity. The total luminosity $L(r)$ and its components are defined by

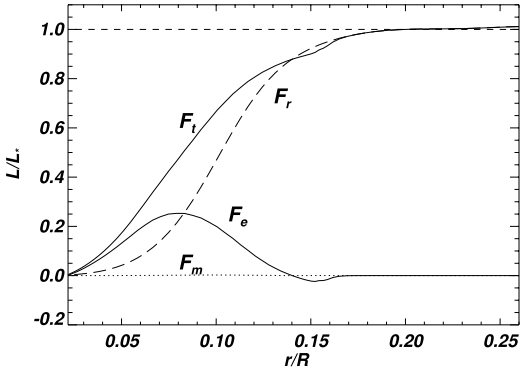

FIG. 13.—Variation with radius of the radial transport of energy in case C4m, as averaged over an interval of about 60 days. Shown are the enthalpy flux F_e, the radiative flux F_r, and the Poynting flux F_m, together with the total flux F_t; all quantities have been expressed as luminosities. The convective core extends here to about $r = 0.14R$, with the positive F_e there serving to carry as much as 80% of the total flux. The further region of overshooting involves a small negative (inward directed) enthalpy flux. Here F_m is small throughout the domain.

$$F_e + F_k + F_{\rm r} + F_u + F_v + F_m = \frac{L(r)}{4\pi r^2}, \tag{15}$$

with

$$F_e = \bar{\rho} c_p \overline{v_r T'}, \tag{16}$$

$$F_k = \frac{1}{2}\bar{\rho}\overline{v^2 v_r}, \tag{17}$$

$$F_r = -\kappa_r \bar{\rho} c_p \frac{d\bar{T}}{dr}, \tag{18}$$

$$F_u = -\kappa \bar{\rho} \bar{T} \frac{d\bar{S}}{dr}, \tag{19}$$

$$F_v = -\overline{\boldsymbol{v}\cdot\boldsymbol{\mathcal{D}}}, \tag{20}$$

$$F_m = \frac{c}{4\pi}\overline{E_\theta B_\phi - E_\phi B_\theta}, \tag{21}$$

where the overbar denotes an average over spherical surfaces and in time, $\boldsymbol{E} = 4\pi\eta \boldsymbol{j} c^{-2} - (\boldsymbol{v}\times\boldsymbol{B})c^{-1}$ is the electric field, F_e the enthalpy flux, F_k the kinetic energy flux, F_r the radiative flux, F_u the unresolved eddy flux, F_v the viscous flux, and F_m the Poynting flux. The unresolved eddy flux F_u is the enthalpy (heat) flux due to sub–grid-scale motions, which in our LES-SGS approach takes the form of a thermal diffusion operating on the mean entropy gradient. The kinetic energy flux, the viscous flux, the Poynting flux, and the flux carried by unresolved motions are here all small compared to F_e and F_r.

The balance of energy transport is much as in our progenitor models in BBT04. As shown in Figure 13, within case C4m the enthalpy flux is maximized near the middle of the convective core (at $r = 0.08R$), where it serves to carry about 50% of the stellar luminosity, with the remainder being transported by radiation. Within the nearly adiabatic stratification established in the convective core (with $\nabla - \nabla_{\rm ad} \sim 10^{-7}$), the associated temperature gradient serves to specify a radiative flux F_r that increases steadily with radius. Thus F_e is forced to decrease in

the outer half of the unstable core. Beyond the boundary of the convective core, the enthalpy flux becomes negative, owing to the anticorrelation of radial velocity and temperature fluctuations as penetrative motions are braked. This inward-directed enthalpy flux is also manifested as a small dip in the total luminosity in Figure 13. In real stars, or in fully relaxed simulations, the radiative flux in that region would compensate for the negative enthalpy flux. However, our simulations have not been evolved for a sufficiently long time to allow such adjustment to occur fully, since the relevant thermal relaxation time is very much longer than other dynamical timescales. The small amplitude of the Poynting flux F_m suggests that although magnetic processes significantly impact the dynamics, they do not actively transport enough energy to modify the radial energy flux balance within the core.

5. THE MANY SCALES OF FLOWS AND FIELDS

The complex operation of the dynamo within the convective core generates magnetic fields over a broad range of spatial scales, as is evident in Figures 4 and 5. The manner in which the energy in the fields and flows is distributed among these spatial scales, as well as between axisymmetric and fluctuating components, provides perspectives on the complicated nature of the magnetism. Thus, in addition to examining the breakdown of these fields into their poloidal and toroidal components, we also examine their spectral distributions and their probability density functions.

5.1. *Mean and Fluctuating Magnetic Energy*

The strong magnetism generated in these simulations consists of both mean (axisymmetric) and fluctuating fields. We assess the balance between these fluctuating and mean fields, defining various components of the magnetic energy as

$$\mathrm{MTE} = \frac{1}{8\pi}\langle B_\phi\rangle^2, \tag{22}$$

$$\mathrm{MPE} = \frac{1}{8\pi}\left(\langle B_r\rangle^2 + \langle B_\theta\rangle^2\right), \tag{23}$$

$$\mathrm{FTE} = \frac{1}{8\pi}\left[(B_\phi - \langle B_\phi\rangle)^2\right], \tag{24}$$

$$\mathrm{FPE} = \frac{1}{8\pi}\left[(B_r - \langle B_r\rangle)^2 + (B_\theta - \langle B_\theta\rangle)^2\right], \tag{25}$$

$$\mathrm{FME} = \frac{1}{8\pi}\left[(B_r - \langle B_r\rangle)^2 + (B_\theta - \langle B_\theta\rangle)^2 + (B_\phi - \langle B_\phi\rangle)^2\right], \tag{26}$$

where we recall that the angle brackets denote a longitudinal average. Here MTE denotes the energy in the mean toroidal magnetic field, MPE likewise that in the mean poloidal field, FTE the energy in the fluctuating toroidal component, FPE that in the fluctuating poloidal field, and FME the total energy in the fluctuating magnetic fields. In Figure 14, we illustrate for case Em how these components (further averaged in latitude) vary in strength with radius throughout the convective core and the surrounding radiative envelope. The ME, TME, and PME are there averaged over a temporal interval of about 100 days representative of the extended plateau of high DRKE in Figure 10.

The field within the core is mostly nonaxisymmetric, with that fluctuating field energy FME accounting for about 95% of the total ME at most radii within the convective core. The remaining

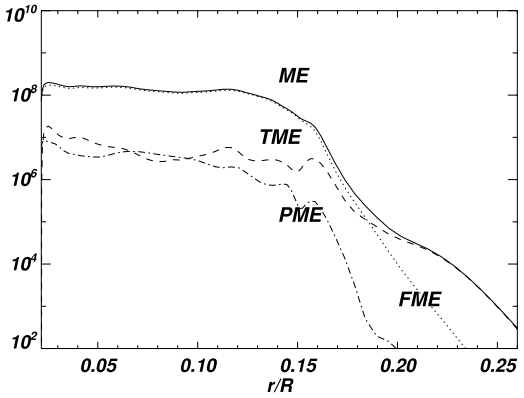

FIG. 14.—Radial variation of magnetic energy components in case C4m. Shown are the energy in the mean (axisymmetric) toroidal field (TME), the mean poloidal field (PME), and the fluctuating (nonaxisymmetric) fields (FME), together with their sum (ME), all averaged over radial surfaces and in time. In the convective core, FME accounts for most of ME. Outside the core, TME becomes the dominant component in the plummeting ME.

5% is distributed between the toroidal and poloidal mean fields, with the former stronger there by about a factor of 2 (Table 3). The FME is, in contrast, divided in roughly equal measure between FTE and FPE (not shown). The balance of magnetic field components changes rapidly near the edge of the radiative envelope (at about $r = 0.16R$). Throughout the region of overshooting, the toroidal mean field becomes a steadily larger fraction of ME, whereas the fluctuating field FME declines in proportional strength. By $r = 0.185R$, TME has become as large as FME, and exterior to that radius it is the dominant contributor to the magnetism. The $m = 0$ toroidal field energy MTE also remains much larger than MPE through the region of overshooting and the radiative envelope.

5.2. *Spectral Distributions of Flows and Magnetism*

The velocity and magnetic fields examined in Figures 4 and 5 for cases Em and C4m suggest that the magnetic field possesses relatively more small-scale structure than the flows. This is verified in Figure 15, where we display for case Em the magnetic and kinetic energy spectra computed at two depths in the convective core and within the region of overshooting. The slope of the magnetic energy spectrum (Fig. 15*b*) with degree ℓ is much shallower than the kinetic energy spectrum (Fig. 15*a*) and generally peaks at wavenumbers slightly higher. This means that the magnetic energy equals or exceeds the kinetic energy at both intermediate and small scales ($\ell \gtrsim 20$), even though when integrated over the volume, the magnetic energy is smaller than the kinetic energy. Given that our magnetic Prandtl number is greater than unity, such behavior is expected in the range of wavenumbers located between the viscous and ohmic dissipation scales, which here are in the range $\ell > 100$. More surprising is that the magnetic energy also exceeds the kinetic energy over a wide range of larger scales. Possibly some guidance is afforded by Grappin et al. (1983) in studying homogeneous isotropic MHD turbulent flows in which there was overall equipartition between ME and KE. They reported that the difference between magnetic and kinetic energy spectra should scale as ℓ^{-2} in the inertial range of the spectra, indicating a dominant role of the magnetic field over the flow at small values of ℓ. This ℓ^{-2} scaling is not realized in our two cases here

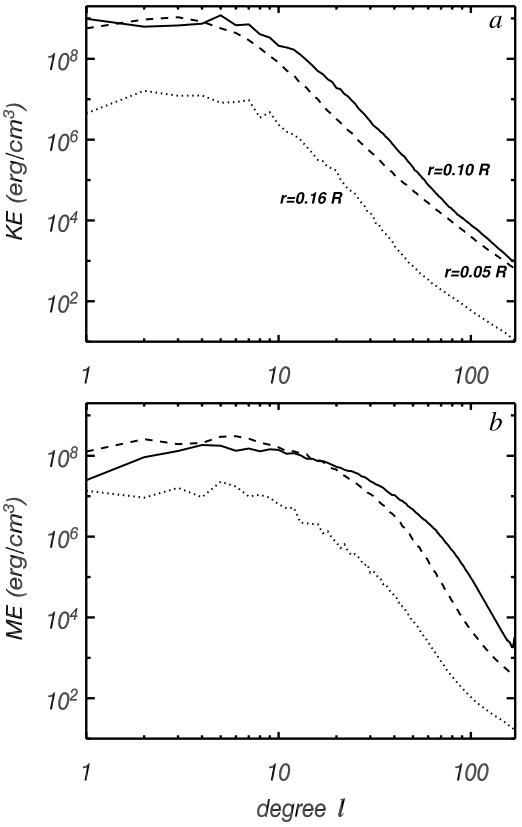

FIG. 15.—Time-averaged spectral distributions of (*a*) KE and (*b*) ME with degree ℓ for case Em, evaluated on three spheres with radii indicated.

(except over a small range of degrees in the overshooting layer), perhaps owing to the effects of rotation and stratification not included in the Grappin et al. (1983) analysis. Throughout most of the convective core, both spectra have broad plateaus at low wavenumbers, with shallow peaks near $\ell = 5$. For degrees $\ell \gtrsim 10$, the spectra suggest some power-law behavior, but it extends only over a decade in degree, so these simulations do not possess an extended inertial range. The slope of the kinetic energy spectrum (between ℓ^{-3} and ℓ^{-4}) is substantially steeper than that expected for homogeneous, isotropic, incompressible turbulence, either with magnetic fields ($l^{-3/2}$) or without ($l^{-5/3}$) (e.g., Biskamp 1993). The shallower magnetic energy spectra are somewhat closer to the $\ell^{-3/2}$ behavior.

The energy contained in the dipolar and quadrupolar magnetic fields (i.e., modes $\ell = 1$ and 2) is small when compared to the energy contained in all the other modes. In case Em we find that they constitute about 5% of the total magnetic energy in the core but contribute proportionately as much as 15% in the overshooting region. The quadrupolar field is generally stronger than the dipolar one in the convective core by about a factor of 2–3, but in the region of overshooting the dipole term comes to dominate the quadrupole one.

In considering the energy spectra for KE and ME as a function of azimuthal wavenumber m (not shown), within the convective core, the dominant wavenumbers between 1 and 7 contain more power than the axisymmetric mode $m = 0$, confirming the predominantly nonaxisymmetric nature of both the magnetic and velocity fields. Over the same temporal interval sampled by Figure 15, the axisymmetric $m = 0$ represents about 3% of the magnetic energy at $r = 0.10R$ and 5.5% at $r = 0.05R$. We find similar but slightly smaller percentages in case C4m. In the radiative zone, the axisymmetric mode becomes dominant for the toroidal field and contributes about 29% to the magnetic energy contained in that layer.

5.3. *Probability Density Functions*

The turbulent convective flows and magnetic fields in our simulations can be further characterized by their probability density functions (pdf's). In idealized isotropic, homogeneous turbulence the velocity fields possess Gaussian pdf's, yet departures from Gaussian statistics are known to be present in many real turbulent flows. In particular, velocity differences and derivatives generally have non-Gaussian pdf's that are often described by stretched exponentials $\exp[-\beta]$ with $0.5 \leq \beta \leq 2$ (e.g., Castaing et al. 1990; Vincent & Meneguzzi 1991). The tails of the distributions are often nearly exponential ($\beta \approx 1$) but can be even flatter, particularly in the viscous dissipation range. Furthermore, a flat slope ($\beta < 2$) indicates an excess of high-amplitude events relative to a Gaussian distribution, a consequence of spatial intermittency in the flow that may be associated with the presence of coherent structures (e.g., Vincent & Meneguzzi 1991; Lamballais et al. 1997).

Figure 16 shows pdf's for the radial and longitudinal components of the velocity and magnetic fields for case Em on a spherical surface within the convective core ($r = 0.10R$) and the region of overshooting ($r = 0.16R$). The pdf's have been averaged over a 50 day interval. In the convective core, the radial and longitudinal velocities are nearly Gaussian with departure toward an exponential distribution in their wings. By contrast, both components of the magnetic fields possess strong departures from a Gaussian distribution, with pdf's closer to an exponential distribution. In Figure 16*d*, the prominent hump in the left wing of the B_ϕ distribution indicates that the toroidal field is asymmetric and mostly negative over the temporal averaging interval. In the overshooting region, the radial velocity v_r (Fig. 16*e*) is much less Gaussian than in the convective core, which comes as a surprise, since in BBT04 this was not the case. We find here that the level of intermittency is higher than in our progenitor cases and that the developed flows are much less steady due to the complex interaction between convection and magnetic fields. This could perhaps partly justify why v_r is more intermittent at the convective core edge when magnetic fields are present. The longitudinal velocity v_ϕ is quite asymmetric, with a long tail for negative values, whereas the magnetic fields are still non-Gaussian, with a somewhat more intricate shape (less smooth) than in the core, possibly revealing some long-living magnetic structures in the overshooting layer. The pdf's within the core in case Em (Figs. 16*a*–16*d*) are qualitatively similar to those found by Brun et al. (2005) in the solar context and by Brandenburg et al. (1996) for compressible MHD convection in Cartesian geometries.

Higher order moments of the pdf, in particular the third and fourth moments, called, respectively, the skewness $\mathcal{S}$ and kurtosis (or flatness) $\mathcal{K}$, can be used to further quantify intermittency and asymmetry (see Frisch 1995; Brun et al. 2005). A large value for $\mathcal{S}$ indicates asymmetry in the pdf, whereas a large value of $\mathcal{K}$ indicates a high degree of spatial intermittency.

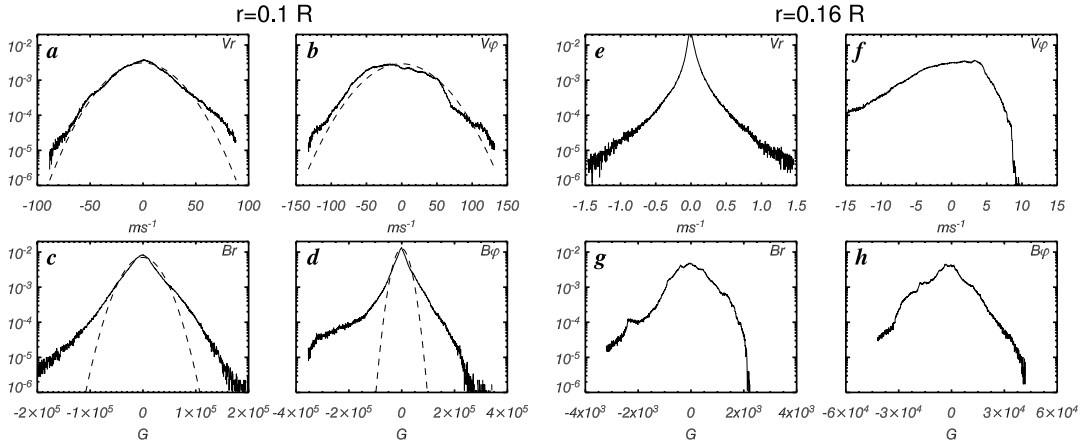

FIG. 16.—Time-averaged pdf's for case Em of velocities (v_r and v_ϕ) and magnetic fields (B_r and B_ϕ) sampled on two spherical surfaces ($r = 0.10R$ and $0.16R$). Some Gaussian fits to the distributions are indicated by dashed curves.

For Gaussian pdf's, $\mathcal{S} = 0$ and $\mathcal{K} = 3$, whereas for exponential distributions $\mathcal{S} = 0$ and $\mathcal{K} = 6$.

At $r = 0.10R$ the radial velocity is close to a Gaussian distribution with ($\mathcal{K} = 3.6$) and possesses a relatively small negative skewness ($\mathcal{S} = -0.10$); the fastest downflows and upflows are of the same amplitude $\sim$90 m s^{-1}, confirming the rather symmetric aspect of the convective cells. The longitudinal velocity v_ϕ is even more Gaussian ($\mathcal{K} = 3.1$) but rather asymmetric ($\mathcal{S} = 0.75$), reflecting the influence of the differential rotation. The radial and toroidal magnetic fields are more intermittent than the velocity field ($\mathcal{K} = 5.9$, 11.8). The radial magnetic field B_r appears to be quite symmetric ($\mathcal{S} = -0.10$), compared to B_ϕ, which possesses a relatively large skewness, $\mathcal{S} = -1.5$, mostly due to the presence of the prominent hump in the left wing. Maximum field strengths reach about 250 kG for the toroidal field and somewhat less (150 kG) for the radial field.

At $r = 0.16R$ the radial velocity shows the greatest departures from a Gaussian, with $\mathcal{K} = 19.5$, but is rather symmetric ($\mathcal{S} = 0.09$). The fastest downflows and upflows are of the same amplitude $\sim$1 m s^{-1} confirming the rather symmetric aspect of the convective patterns in the overshooting region. The zonal velocity is still Gaussian ($\mathcal{K} = 3.6$) but even more asymmetric than in the convective core ($\mathcal{S} = -1.7$), reflecting the rather intricate profile of differential rotation in that layer. The radial and toroidal magnetic fields are somewhat less intermittent than in the core ($\mathcal{K} = 4.4$, 3.7), confirming the greater importance of the axisymmetric part of the magnetic fields there. Both components are rather symmetric with $\mathcal{S} = -0.16$, -0.09, respectively. Maximum field strengths reach about 45 kG for the toroidal field and much less (3 kG) for the radial field.

Case C4m has pdf, skewness, and kurtosis values close to those for case Em. No clear trend due to a faster rotation rate is evident at this stage.

6. EVOLUTION OF GLOBAL-SCALE MAGNETIC FIELDS

We now turn to considering the structure and evolution of the mean fields realized in our simulations. We here take these to be the $m = 0$ (axisymmetric) component of the mostly nonaxisymmetric magnetism generated by dynamo action within the convective core. We recognize that in seeking to make contact with mean-field dynamo theories, other spatial and temporal averaging could be employed, such as general averaging over intermediate scales. However defined, such large-scale fields have particular significance in stellar dynamo theory. Our results provide insight into the generation of mean magnetic fields by turbulent core convection and might be used to evaluate and improve mean-field dynamo models that do not explicitly consider the turbulent field and flow components (e.g., Krause & Rädler 1980; Moss 1992; Ossendrijver 2003). We define the mean poloidal magnetic field to be the longitudinally averaged radial and latitudinal components, $\langle \boldsymbol{B_p} \rangle = \langle B_r \rangle \boldsymbol{e_r} + \langle B_\theta \rangle \boldsymbol{e_\theta}$, and the mean toroidal field in terms of the longitudinal component $\langle B_l \rangle \boldsymbol{e}_\phi = \langle B_\phi \rangle \boldsymbol{e}_\phi$.

The mean toroidal fields in our simulations can arise from the shearing, stretching, and twisting of mean and fluctuating poloidal fields by differential rotation (the ω-effect), or from helical convective motions (the α-effect). In contrast, mean poloidal fields are generated from fluctuating toroidal fields only via the α-effect. Thus, the mean and fluctuating magnetic fields, the differential rotation, and the convective flows are intimately linked.

6.1. *Axisymmetric Poloidal Fields*

The energy contained in the axisymmetric poloidal field throughout the shell is on the order of 5% of ME in the core and much less (<0.1%) in the radiative envelope. Typical poloidal field strengths are, respectively, on the order of 300 G and 0.1–1 G.

Figure 17 illustrates the structure and evolution of the axisymmetric poloidal field in case Em. The top row shows four snapshots of the magnetic lines of force of $\langle \boldsymbol{B_p} \rangle$ within the convective and radiative domains. Such a mean poloidal field within the core shows intricate morphology, with islands of positive and negative polarity that often intermix. During some intervals the field is dominated by a single polarity (Figs. 17*a* and 17*d*), whereas at other times both polarities are present in roughly equal measure (Figs. 17*b* and 17*c*). This complex evolution is connected to the nonaxisymmetric nature of the convective flows that have given rise to these fields from their initial weak dipole state. The evolution of $\langle \boldsymbol{B_p} \rangle$ in the radiative envelope is more passive and depends strongly on the properties of that field at the interface with the convective core and

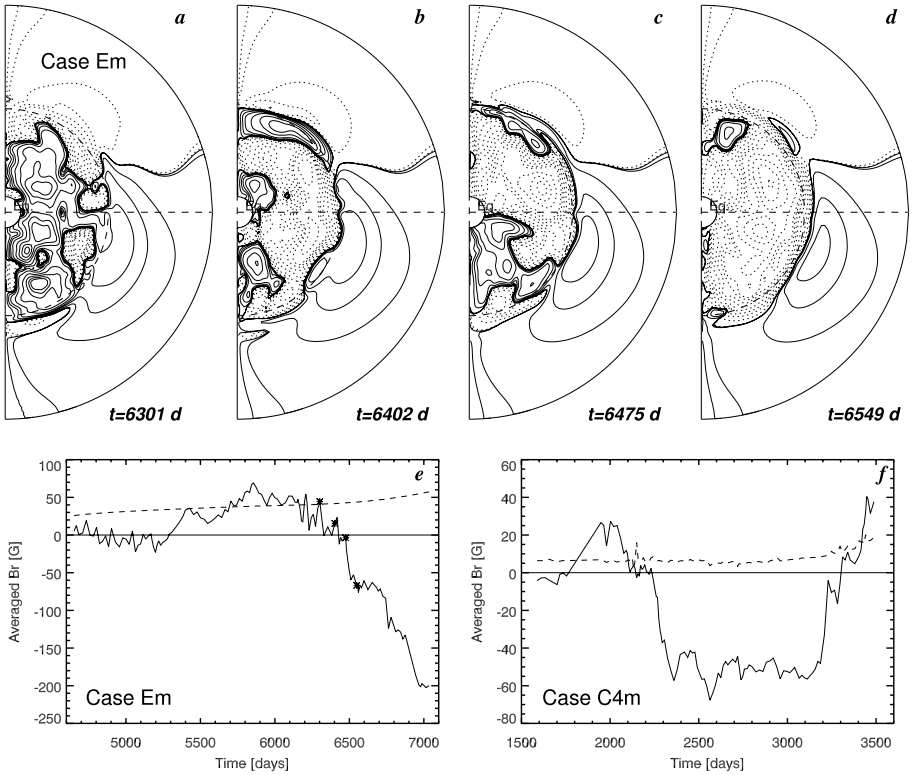

FIG. 17.—(*a*)–(*d*) Temporal evolution of the axisymmetric (mean) poloidal field $\langle \boldsymbol{B}_p \rangle$ for case Em, shown as meridional cross section at four selected times, as indicated. Solid contours denote positive polarity (field lines directed from north to south), and dotted contours denote negative polarity. (*e*) Accompanying radial field for case Em at the convective core boundary (*solid line*) and at the top of the domain (*dashed line*) as averaged over the northern hemisphere, shown over 2400 days late in the simulation with timings of upper snapshots denoted. (*f*) Temporal evolution of average polarity of B_r, as in (*e*), for case C4m.

their ability to diffuse outward, as evinced by $\langle \boldsymbol{B}_p \rangle$ now differing from its initial dipolar configuration. Within the core, the presence of strong magnetic field gradients and magnetic diffusion leads to continuous reconnection of the magnetic field lines. Such reconnection can be seen in the sequence in Figures 17*b*–17*d*, where in the northern hemisphere (at low latitudes near the core boundary) reconnection between fields of differing polarities occurs, resulting in a small isolated loop of positive polarity at mid latitudes that later rises slowly and diffuses away.

The regeneration of magnetic flux by the convection can lead to global reversals of the magnetic field polarity, as seen in Figures 17*a*–17*d*. Figure 17*e* shows the temporal evolution of the average polarity of the poloidal field in case Em, which we define in terms of the radial magnetic field B_r averaged over the northern hemisphere both at the convective core boundary (*solid line*) and at the top boundary (*dashed line*). Figure 17*f* is the equivalent plot for case C4m. This measures the total magnetic flux that passes through the northern hemisphere at those radial surfaces. Positive values indicate that the field is outward on average in the northern hemisphere, as in the dipolar seed field.

Figure 17*e* shows the evolution of the average field polarity in case Em between 4500 and 7000 days of computed physical time, corresponding to an interval in which the magnetic energy has reached a statistically stable phase. Two field reversals occur on a timescale of about 1000 days, but we cannot assess whether such polarity reversals are likely to be continued and regular. In the radiative envelope reversals could occur, but they would do so on a much slower timescale, as fields diffuse upward. The behavior in Figure 17*f* for case C4m is similar to that seen in case Em. Such changes in the magnetic polarity in the convective domain have also been seen in Brun et al. (2005) in the solar context. There also the convection generates rather weak axisymmetric fields and the fluctuating fields are the dominant players.

6.2. *Axisymmetric Toroidal Fields*

The axisymmetric toroidal field in the convective core contains about 6%–10% of the total magnetic energy, about a factor of 2 larger than the energy in the axisymmetric poloidal field. Figure 18 shows two snapshots of the radial and latitudinal variation of the longitudinally averaged toroidal magnetic field $\langle B_t \rangle$ for case Em at times coincident with Figures 17*a* and 17*d*. We can see that $\langle B_t \rangle$ possesses small-scale structure, with little correspondence apparent between the two time samples, indicating the complex evolution of the axisymmetric toroidal field. Mixed polarities and intricate topologies are present throughout the convective core. Varying symmetries may be evident at different instants but do not persist over extended intervals.

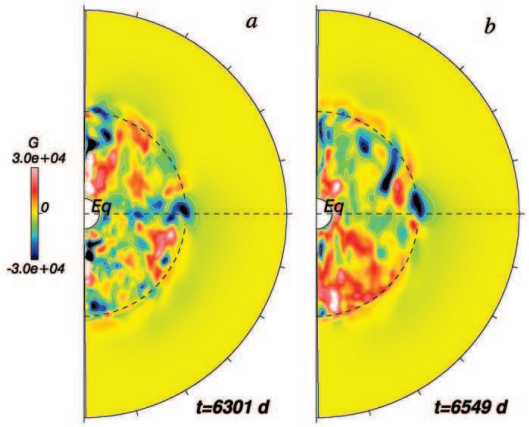

FIG. 18.—Variation of axisymmetric toroidal field $\langle B_t \rangle$ with radius and latitude for case Em at two instants coinciding with Figs. 17*a* and 17*d*. Red and blue tones denote in turn eastward (prograde) and westward (retrograde) field.

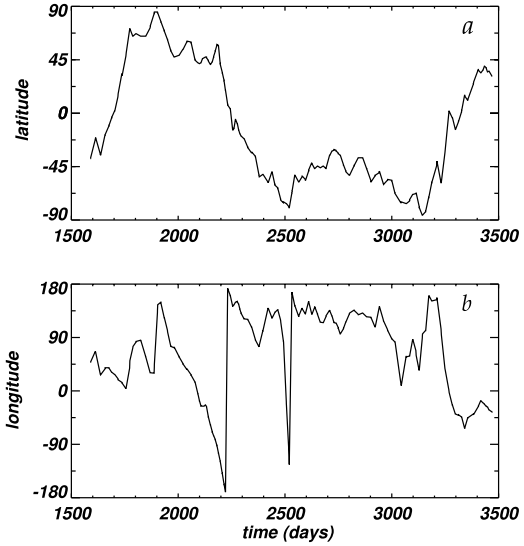

FIG. 19.—Wandering of the magnetic dipole axis in case C4m with time. (*a*) Position of the axis with latitude as the field swings between the northern and southern hemispheres. (*b*) Gradual drift in longitude of the positive pole.

Some hints regarding the interplay between the α-effect and the ω-effect in generating axisymmetric toroidal fields are afforded by comparing Figure 18 with the views of $\langle \boldsymbol{B}_p \rangle$ in Figure 17. If the ω-effect had a dominant role in the generation of $\langle B_t \rangle$, as may be realized at the core boundary where convective motions have waned, the evolution of the axisymmetric poloidal and toroidal fields would be clearly linked. The largely retrograde differential rotation acting on a negative poloidal field structure would generate a toroidal field with two opposite polarities: negative in the lower part of the structure and positive in the upper part. That the nonaxisymmetric convection also plays a role in generating $\langle B_t \rangle$ through the α-effect obscures the connection between structures in the two fields, though some links are indeed revealed by Figure 18. In Figure 17*a* the poloidal field possesses a counterclockwise (negative) polarity at mid latitudes along the convective core boundary in the northern hemisphere. The appearance in Figure 18*a* of both senses of toroidal fields at the same location may be indicative of the ω-effect at work. Similar linkages are apparent in Figure 18*b*, where the corresponding poloidal field was largely of negative polarity along the core interface, but $\langle B_t \rangle$ is largely of differing senses in the northern and southern hemispheres. Of course, some time lag should exist between the establishment of toroidal mean fields from a given mean poloidal field configuration via the ω-effect, further complicating the interpretation of links between the two fields. Furthermore, many departures from this idealized description of the generation of fields occur due to the major role played by the α-effect within the core in giving rise to the magnetism.

6.3. *Wandering of the Poles*

Like the axisymmetric poloidal and toroidal fields, the dipole component of the magnetism attracts interest despite its relatively small amplitude. Dipole magnetic fields have figured prominently in some theoretical efforts to construct simplified models of the interiors of A-type stars (e.g., Mestel & Moss 1977). In addition, the presence at the surface of largely dipolar fields further serves to motivate the examination of such fields in our simulations, though this interior magnetism may well be screened from view by the extensive radiative envelope. We here assess the temporal variations of the dipole field, which may differ appreciably from those of the rapidly evolving and intricate small-scale fields.

In our two simulations, the maximum amplitude of the dipole magnetic field (namely, the $\ell = 1$ component of B_r) is generally no greater than about 5% of the maximum total radial field, with variations in strength by a factor of 2 occurring as the fields evolve in time. Further, the low spherical harmonic degrees $\ell = 2$–12 typically possess somewhat greater amplitudes than the dipole. The evolution in case C4m of the dipole axis over a period of $\sim$1900 days (or about 270 rotations) is assessed in Figure 19, showing the position in latitude and longitude of the positive dipole axis with time. The orientation of the dipole, which is inclined with respect to the rotation axis, varies slowly: during the lengthy interval sampled, the pole completes only two full revolutions around the rotation axis, though there are brief periods during which its movement is more rapid. The wanderings from the northern hemisphere into the southern and back are similarly leisurely: only three such inversions of polarity, each separated by more than 500 days, are visible in Figure 19. The orientation of the dipole appears to correspond very well with the sign of the axisymmetric poloidal magnetic field when integrated over the northern hemisphere (Fig. 17*f*). As the dipole meanders from a northerly orientation to a southerly one, the sign of the integrated radial field at the edge of the convective core also flips from positive to negative. Similar slow wanderings are observed in case Em, though there the dipole axis lies close to the equatorial plane over the first 1500 days of the interval sampled in Figure 17*e*. Thus, the slow evolution of the dipole component of the magnetism stands in contrast to the far more rapid changes seen in the high-degree components.

7. SOME ASPECTS OF FIELD GENERATION

The detailed manner in which sustained dynamo action is achieved in our models is challenging to understand, since we have relatively few theoretical tools for predicting such behavior

short of carrying out nonlinear simulations. In mean-field dynamo theory (see, e.g., Moffatt 1978; Brandenburg & Subramanian 2004), one commonly speaks of the α-effect, by which helical turbulence in a resistive medium can produce mean toroidal magnetic fields from seed poloidal ones and vice versa, and of the ω-effect, in which stretching of field lines by contrasts in angular velocity can generate mean toroidal fields from poloidal ones. Although the ω and α effects strictly refer only to the generation of mean toroidal and poloidal fields from mean and fluctuating fields, their counterparts in the equation for the evolution of the fluctuating fields may be useful in looking at the generation of the strong fluctuating fields realized in our simulations.

Among these generation terms, what is commonly called the G-current (DeLuca & Gilman 1991), namely, $\boldsymbol{G} = \boldsymbol{v}' \times \boldsymbol{B}' - \langle \boldsymbol{v}' \times \boldsymbol{B}' \rangle$, plays a pivotal role. In the traditional first-order smoothing approximation of mean field dynamo theory (Krause & Rädler 1980; Ossendrijver 2003), this term is neglected, providing a simple closure procedure for the mean field induction equations. We find in our simulations that the G-current is by no means small, with $\langle \boldsymbol{v}' \times \boldsymbol{B}' \rangle$ considerably smaller (about only 5%) than $\boldsymbol{v}' \times \boldsymbol{B}'$. Furthermore, the nonlinear dynamo action realized in our simulations induces preferentially strong nonaxisymmetric fluctuating magnetic fields rather than axisymmetric ones, with the latter having only a very weak dynamical role. Our core convection dynamo simulations suggest that higher order mean field dynamo theories, which do not neglect the G-current, may be required to explain the dynamo operating in a stellar convective core.

A physical quantity of some interest in analyzing the properties of the magnetic field generated in our simulations is the kinetic helicity $\boldsymbol{v} \cdot (\nabla \times \boldsymbol{v})$. In Figure 20, we display the kinetic helicity both for case Em and for its hydrodynamical progenitor as a function of radius, averaged over the northern hemisphere and in time. It is negative in most of the domain except for a positive region near the center of the core. In contrast, the current helicity $\boldsymbol{j} \cdot \boldsymbol{B}$ in our simulations shows no comparable trends or sign preference in a given hemisphere, in agreement with the results obtained in the solar dynamo simulations of Brun et al. (2005). As a consequence, we see no evident relation between the kinetic and magnetic helicities in our modeling, though some links are implicit in certain mean field theories (e.g., Ossendrijver 2003). Turning back to Figure 20, we note that the kinetic helicity in case Em possesses a smaller amplitude than in its hydrodynamic progenitor. This suggests that the magnetic field acts to reduce local shear and stretching, in particular near sites of strong vorticity, leading to a reduced helicity in the convective region. Outside the core, in the region of overshooting and beyond, the kinetic helicity is very small, since only weak fluid motions persist. Thus, the generation of magnetic fields by helical convective motions must also basically vanish outside the core.

Conversely, angular velocity contrasts that are weak within the convective core grow stronger in the region of overshooting, particularly in case Em with its interface of strong shear. Thus, the balance of toroidal and poloidal field should vary with radius, as the relative importance of the helical motions grows smaller and the contribution of the large-scale shear becomes larger. The radial variation of the energy in the fluctuating and axisymmetric magnetic fields (§ 5.1) therefore provides clues about the mechanisms responsible for building the magnetism. Although the total ME declines sharply outside the convective core, the axisymmetric toroidal field $\hat{B}_\phi$ within the region of overshooting is still considerable. This, together with the longitudinally elongated topology of $\hat{B}_\phi$ (Fig. 3*c*), indicates that the large-scale

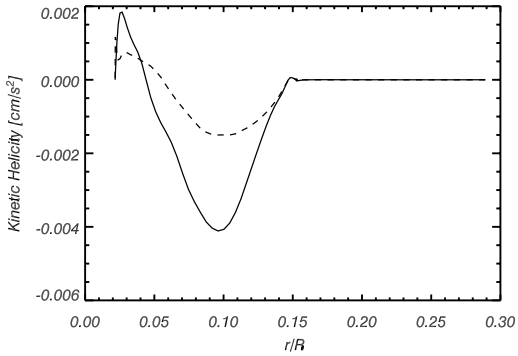

FIG. 20.—Kinetic helicity as a function of radius for case Em (*dashed line*) and its purely hydrodynamical progenitor (*solid line*), as averaged over the northern hemisphere and in time. The kinetic helicity is reduced in the presence of magnetism. The kinetic helicity has been averaged over 120 days in both cases given the large fluctuations that this quantity undergoes in the convective core.

shear helps generate the magnetism. That TME exceeds PME by a factor of 2 within the convective core suggests that the equivalent of an ω-effect plays a role there as well. These core convection dynamos thus generate magnetic fields through the joint effects of large-scale shear and helical motions acting on the axisymmetric and the nonaxisymmetric fields. The large-scale shear appears to dominate the generation of field near the convective core boundary, while the helical motions generate fields in a more distributed manner within the core.

8. CONCLUSIONS AND PERSPECTIVES

The simulations here reveal that vigorous convection within the cores of rotating A-type stars can serve to build strong magnetic fields through dynamo action. Small initial seed magnetic fields are amplified in strength by many orders of magnitude and sustained against ohmic decay, ultimately yielding fields that are nearly in equipartition with the flows. The resulting highly time-dependent magnetism possesses structure on many scales, with B_r mainly fibril and B_ϕ stretched by the zonal flows (differential rotation) into large-scale bands that extend around the core. Within the core, the magnetism is predominantly fluctuating, with such nonaxisymmetric fields accounting for about 90% of the total magnetic energy. The accompanying weak mean (axisymmetric) fields evolve comparatively slowly, undergoing flips in average polarity on timescales of hundreds of days. In the more distant region of overshooting and beyond, where the magnetic energy plummets from its interior value, the mean toroidal field becomes the dominant component of the surviving magnetism.

The differential rotation established in the hydrodynamic progenitors is lessened in latitude by the presence of magnetism, as the strong Maxwell stresses associated with the fluctuating fields transport angular momentum poleward, with the large-scale magnetic torques playing only a small role in the overall latitudinal balance. Conversely, the radial transport of angular momentum by the Maxwell stresses does not oppose that of the Reynolds stresses throughout much of the convective core. Thus, the Maxwell stresses are found to play a significant role in the angular momentum transport. In case Em, with ME about 40% of KE, central columns of slow rotation are still realized, with considerable variations in strength as the simulations evolve. Oscillations seen in the energy densities DRKE and ME (Fig. 10) hint

TABLE 3
ENERGY DENSITIES

Case	Em	C4m	E	C4
KE	4.54×10^7	1.76×10^7	7.58×10^7	1.67×10^8
DRKE/KE (%)	18.2	28.3	56.1	88.3
MCKE/KE (%)	1.9	0.2	1.8	0.2
CKE/KE (%)	79.9	71.5	42.2	11.5
ME/KE (%)	28.3	88.2	...	...
MTE/MEc (%)	3.4	2.7	...	...
MPE/MEc (%)	1.4	2.5	...	...
FME/MEc (%)	94.4	94.7	...	...
MEc	1.27×10^8	2.20×10^8	...	...
MTE/MEr (%)	91.3	98.1	...	...
MPE/MEr (%)	0.2	0.1	...	...
FME/MEr (%)	9.6	1.8	...	...
MEr	6.85×10^3	4.93×10^3	...	...

NOTES.—The kinetic energy density KE ($1/2\bar{\rho}v^2$), averaged over volume and time, is listed along with the relative contributions from the convection (CKE), the differential rotation (DRKE), and the meridional circulation (MCKE), together with the average magnetic energy density ME ($B^2/8\pi$) (where appropriate). The relative contributions from each of the components of ME, including the fluctuating field FME and the axisymmetric $m = 0$ toroidal and poloidal fields (MTE and MPE), are evaluated both within the radiative zone (at $r = 0.24R$, denoted by r) and the convective core (at $r = 0.10R$, denoted c), along with the values of ME at those two depths.

at the intimate connection between magnetic fields and flows, with intervals of high ME apparently acting to quench the differential rotation; the resulting weak angular velocity contrasts eventually lead to decreases in ME. In case C4m rotating at 4 times the solar rate, in which ME at times exceeds KE (Fig. 2), angular velocity contrasts are always weaker than in case Em, which rotates at the solar rate (Fig. 9). Similar damping of the differential rotation by the Lorentz forces is also realized to a lesser extent in three-dimensional MHD simulations of the solar convection zone (Brun et al. 2005; Brun 2004).

How the magnetism is built and sustained by the flows is an intricate matter. Both the helical convection and the differential rotation have significant roles, with axisymmetric fields generated in the core through processes somewhat akin to the α- and ω-effects of mean-field dynamo theory. It would appear that the two effects contribute in roughly equal measure to building axisymmetric toroidal fields within the core, as indicated by MTE sampled at mid-core exceeding MPE by a factor of about 2 in case Em (Table 3). The role of helical convection here in generating field is unlike that prescribed in the simpler variants of mean-field theory (i.e., the first-order smoothing approximation). In particular, the fluctuating field B' in our simulations is not proportional to the longitudinally averaged field $\langle B \rangle$, possibly because the G-current is not small. This may explain the absence of a linear relationship between the fluctuating and axisymmetric fields in our modeling. In the radiative envelope, convective motions do not persist and so cannot serve to build magnetism, but weak angular velocity contrasts continue to generate axisymmetric toroidal magnetic fields through stretching via the ω-effect. Thus, MTE with increasing radius comes to dominate over both FME and MPE, as seen in Figure 14.

We also find that the magnetic energy peaks slightly at the bottom of the convective domains due to the downward transport of magnetic fields by the convection. This is in sharp contrast with the much more peaked profile found in our simulation of the solar dynamo (Brun et al. 2005), where the asymmetry between weak upflows and strong downflows is more pronounced due to a stronger density contrast there.

The intense and rapidly evolving magnetism realized within the core is screened by the extensive radiative envelope, so assessing its possible impact at the stellar surface is difficult. The complex morphologies of the magnetic fields, their periodic reversals in mean polarity, and their intimate feedback upon the turbulent convection may all be hidden from view. If diffusion alone served to bring the magnetic fields outward from the core, the rapid temporal variations (and so too the intricate spatial structure) of the core fields would be obliterated by the characteristic diffusive timescales on the order of millions of years.

Whether the fields could migrate to the surface by means other than diffusion and thus perhaps contribute to the observed magnetism of Ap stars has been the subject of some debate. Magnetic buoyancy instabilities at the edge of the core could conceivably bring the fields to the surface much more rapidly than diffusion. We cannot address the rise of such buoyant flux tubes directly in our simulations, since we model only the interior portions of these stars at resolutions insufficient to capture the highly concentrated structures needed for these instabilities to act. However, MacGregor & Cassinelli (2003) have used simple models to consider how buoyant magnetic structures may traverse the radiative exterior. They deduce that magnetism from the core could arrive at the stellar surface in less than the main-sequence lifetime of an A-type stars if the interior fields were both very strong and highly fibril. Further modeling by MacDonald & Mullan (2004) suggests that the presence of compositional gradients would slow this process considerably. Furthermore, the field strengths likely to be realized at the surface from such buoyant flux tubes are only modest (MacGregor & Cassinelli 2003), in contrast with the kG fields that are observed in some Ap stars. The implications of these recent studies remain somewhat unclear because several effects that might modify the rise of buoyant core magnetic fields have yet to be included, among them global-scale circulations within the radiative envelope and the twist and writhe of the flux tubes that could modify their stability. The strong surface fields also appear to occupy large sectors, which might be very difficult to populate through the rise of individual elements. Invoking fossil origins for the observed surface magnetism, with predominate dipole structure surviving, is a favored explanation (e.g., Moss 2001), since strong fields could more easily be obtained. The interaction of the interior magnetism with such

possible large-scale fossil fields has also not yet been seriously studied. However, the alternative possibility that the radiative envelope could induce a magnetic field via dynamo action (Spruit 2002; MacDonald & Mullan 2004) may encourage reconsideration of that scenario. Also, the generation by the overshooting convection of internal waves could potentially play a role in the radiative zone, creating shear layers that could subsequently amplify a magnetic field (Kumar et al. 1999).

Future work will thus be required to explore in detail the possible role of the core convection dynamo in giving rise to the surface magnetism. Likewise, we have only briefly touched the possible variations with rotation of the dynamo action and differential rotation. Our limited sampling of two rotation rates provides some hints at that variation (i.e., the faster case C4m possesses a stronger magnetic field than case Em) but does not elucidate it, since we have explored only one avenue in the vast parameter space that could be relevant to real stars. Indeed, the detailed nature of the flows and magnetism in our simulations is surely affected by the many approximations we have made in considering these stars. How the far more turbulent flows attained in actual stars impact the generation of magnetic fields and differential rotation is quite uncertain. Yet some of the dominant features found here may well turn out to be robust. The conclusion that core convection drives some form of sustained dynamo action, producing very strong fields that feed back on the flows, appears to us to be inescapable.

This work was partly supported by NASA through SEC Theory Program grant NAG5-11879 and through the Graduate Student Researchers Program (NGT5-50416). The simulations were carried out with NSF PACI support of the San Diego Supercomputing Center (SDSC), the National Center for Supercomputing Applications (NCSA), and the Pittsburgh Supercomputing Center (PSC), as well as with the Centre de Calcul pour la Recherche et la Technologie (CCRT) of CEA at Bruyère-le-Chatel and in the CNRS supercomputers center IDRIS. Many of the analyses were conducted in the Laboratory for Computational Dynamics (LCD) at JILA. One of us (A. S. B.) is grateful to R. Grappin and J.-P. Zahn for interesting discussions and insights on turbulent MHD.

REFERENCES

Bagnulo, S., Landstreet, J. D., LoCurto, G., Szeifert, T., & Wade, G. A. 2003, A&A, 403, 645
Biskamp, D. 1993, Nonlinear Magnetohydrodynamics (Cambridge: Cambridge Univ. Press)
Borra, E. F. 1980, ApJ, 235, 915
Borra, E. F., & Landstreet, J. D. 1980, ApJS, 42, 421
Brandenburg, A., Jennings, R. L., Nordlund, Å., Rieutord, M., Stein, R. F., & Tuominen, I. 1996, J. Fluid Mech., 306, 325
Brandenburg, A., & Subramanian, K. 2004, Phys. Rep., submitted (astro-ph/0405052)
Browning, M. K., Brun, A. S., & Toomre, J. 2004, ApJ, 601, 512 (BBT04)
———. 2005, in IAU Symp. 215, Stellar Rotation, ed. A. Maeder & P. Eenens (San Francisco: ASP), 376
Brun, A. S. 2004, Solar Phys., 220, 333
Brun, A. S., Browning, M. K., & Toomre, J. 2005, in IAU Symp. 215, Stellar Rotation, ed. A. Maeder & P. Eenens (San Francisco: ASP), 388
Brun, A. S., Miesch, M. S., & Toomre, J. 2005, ApJ, 614, 1073
Brun, A. S., & Toomre, J. 2002, ApJ, 570, 865
Castaing, B., Gagne, Y., & Hopfinger, E. J. 1990, Physica D, 46, 177
Chandrasekhar, S. 1961, Hydrodynamic and Hydromagnetic Stability (Oxford: Clarendon)
Charbonneau, P., & MacGregor, K. B. 1997, ApJ, 486, 502
Clune, T. L., Elliott, J. R., Glatzmaier, G. A., Miesch, M. S., & Toomre, J. 1999, Parallel Computing, 25, 361
DeLuca, E. E., & Gilman, P. A. 1991, in Solar Interior and Atmosphere, ed. A. N. Cox, W. C. Livingston, & M. S. Matthews (Tucson: Univ. Arizona Press), 275
Elliott, J. R., Miesch, M. S., & Toomre, J. 2000, ApJ, 533, 546
Frisch, U. 1995, Turbulence: The Legacy of A. N. Kolmogorov (Cambridge: Cambridge Univ. Press)
Gilman, P. A. 1983, ApJS, 53, 243
Grappin, R., Léorat, J., & Pouquet, A. 1983, A&A, 126, 51
Hubrig, S., North, P., & Mathys, G. 2000, ApJ, 539, 352
Jackson, J. D. 1999, Classical Electrodynamics (3rd ed.; Wiley)
Kochukhov, O., Bagnulo, S., Wade, G., Sangalli, L., Piskunov, N., Landstreet, J. D., Petit, P., & Sigut, T. A. A. 2004, A&A, 414, 613
Krause, F., & Oetken, L. 1976, in Physics of Ap Star, ed. W. W. Weiss, H. Jenkner, & H. J. Wood (Vienna: Universitatssternwarte Wien), 29
Krause, F., & Rädler, K.-H. 1980, Mean-Field Magnetohydrodynamics and Dynamo Theory (Oxford: Oxford Univ. Press)
Kumar, P., Talon, S., & Zahn, J.-P. 1999, ApJ, 520, 859
Lamballais, E., Lesieur, M., & Métais, O. 1997, Phys. Rev. E, 56, 6761
MacDonald, J., & Mullan, D. J. 2004, MNRAS, 348, 702
MacGregor, K. B., & Cassinelli, J. P. 2003, ApJ, 586, 480
Maury, A. C. 1897, Harvard Ann., 28, 96
Mestel, L. 1975, Mem. Soc. R. Sci. Liège, 8, 79
———. 1999, Stellar Magnetism (Oxford: Clarendon)
Mestel, L., & Moss, D. L. 1977, MNRAS, 178, 27
Miesch, M. S., Elliott, J. R., Toomre, J., Clune, T. L., Glatzmaier, G. A., & Gilman, P. A. 2000, ApJ, 532, 593
Moffatt, H. K. 1978, Magnetic Field Generation in Electrically Conducting Fluids (Cambridge: Cambridge Univ. Press)
Moss, D. L. 1989, MNRAS, 236, 629
———. 1992, MNRAS, 257, 593
———. 2001, in ASP Conf. Ser. 248, Magnetic Fields Across the Hertzsprung-Russell Diagram, ed. G. Mathys, S. K. Solanki, & D. T. Wickramasinghe (San Francisco: ASP), 305
Moss, D. L., Mestel, L., & Tayler, R. J. 1990, MNRAS, 245, 550
Ossendrijver, M. 2003, A&A Rev., 11, 287
Pedlosky, J. 1987, Geophysical Fluid Dynamics (New York: Springer)
Spruit, H. C. 2002, A&A, 381, 923
Stibbs, D. W. N. 1950, MNRAS, 110, 395
Vincent, A., & Meneguzzi, M. 1991, J. Fluid Mech., 225, 1
Wolff, S. C. 1983, The A-Stars: Problems and Perspectives (Washington: NASA)

6.5.3 Turbulent convection and dynamo action in A- and G-type stars

par Brun 2005, semaine de la SF2A 2004

SF2A 2004
F. Combes, D. Barret, T. Contini, F. Meynadier and L. Pagani (eds)

TURBULENT CONVECTION AND DYNAMO ACTION IN A- AND G-TYPE STARS

Allan Sacha BRUN[1]

Abstract.
We present recent 3–D magnetohydrodynamic (MHD) simulations of the convective region of A- and G-type stars in spherical geometry using the ASH code. We discuss the nonlinear interactions between turbulent convection, rotation and magnetic fields and the possibility for such flows and fields to lead to dynamo action. We find that both core and envelope turbulent convective zones are efficient at inducing strong mostly non-axisymmetric fields near equipartition but at the expense of damping the differential rotation present in the purely hydrodynamic progenitor solutions. We discuss our findings in the light of recent X-ray observations and in term of the classical α and ω-effect of mean field theory.

1 Scientific Context and Model Description

For the last three decades or so, the study of stellar magnetic activity has been a field of fast development, due in part to excellent theoretical work, more accurate observations and better resolved MHD numerical simulations. X-ray emissions have been used to detect stellar magnetic activity as a function of spectral type, since the Sun is known to strongly emit in this frequency band during its maximum of activity. Interestingly enough a gap exists in the curve showing the normalised X-ray luminosity to bolometric luminosity as a function of stellar spectral type around the late B, A and early F-type stars, the so-called "A-gap" (Schmitt 2003). In turns out that stellar structure and evolution models predict that all those stars possess a core convection zone except for shallow surface convection zones in late A and early F-type stars. On the contrary late F, G and K-type stars exhibit high level of X-ray emissions in agreement with them having rather deep surface convection zones. It is thus tempting to relate the existence of magnetic activity in late type stars with the presence of a convection zone at their surface. The source of this activity being due to magnetic dynamo action driven by turbulent convective motions. However a lot more work remains to be done in order to draw a fully consistent picture (Mestel 2001). In particular explaining the 22 yr solar cyle of magnetic activity and the magnetic fields observed in Ap stars has been unexpectedly challenging. It is currently believe that the solar global dynamo is organized in a shear layer called the tachocline at the base of the convection zone (Ossendrijver 2003, Brun et al. 2004), where for Ap stars, a fossil magnetic field is thought to be at the origin of the observed magnetism (Moss 2001). We have thus decided to compute, as a first step, 3-D MHD numerical simulations of the solar

[1] DSM/DAPNIA/SAp, CEA Saclay, 91191 Gif-sur-Yvette Cedex, France

convection zone (Brun & Toomre 2002; Brun et al. 2004) and of the convective core of an A-type stars (Browning et al. 2004; Brun et al. 2005) using the anelastic spherical harmonic (ASH) code on massively parallel computers (Clune et al. 1999; Miesch et al. 2000; Brun et al. 2004). These simulations are part of a larger, long-term project that aims at understanding stellar dynamo and magnetic activity. We have chosen respectively the G and A-type stars as good proxy for envelope and core convection stars, thanks to the large quantity of observational constraints available, especially for the Sun.

Our models are intended to be simplified version of the convective region of a solar-type star (hereafter case G) and of an A-type star (case A).

- case G, possesses a solar luminosity, mass, radius, rotation rate and heat flux and a density contrast of 30; the computational domain extends from 0.7 to 0.97 $R_\odot$, with $R_\odot$ the solar radius. The following values for the Prandtl (Pr), magnetic Prandtl (Pm) and magnetic Reynolds (Rm) numbers have been respectively used, 0.125, 4 and 500.

- case A, possesses a luminosity ($L = 19\ L_\odot$), radius ($R = 45\ R_\odot$), mass ($M = 2\ M_\odot$) and heat flux typical of A-type star, rotates at the frame rate $\Omega_0 = \Omega_\odot$; the computational domain extends from 0.02 to 0.3 R, with the convective core edge located at $\sim 0.15\ R$; a heating source term is included in the energy equation to model the nuclear energy generated by the CNO cycle. The Pr, Pm and Rm numbers are respectively, 0.25, 5 and 800; the density contrast in the convective core is 2 and 20 over the entire domain.

Both models were started from mature purely hydrodynamic progenitor solutions, possessing strong differential rotations (Brun & Toomre 2002, Browning et al. 2004), in which we introduced a weak initial seed dipolar field. We then let the simulations evolve over several ohmic diffusion times.

2 Magnetic dynamo action

As the turbulent convective motions stretch, shear and fold the seed magnetic field (Moffatt 1978), dynamo action takes place, inducing a stronger magnetic field, whose energy rises by many orders of magnitude. Figure 1a and b show the temporal evolution (growth) of the magnetic energy (ME) densities for both cases.

We note that after a linear growth phase lasting 1200 days for case G and 2500 days for case A, ME saturates via the nonlinear feedback of the Lorentz forces on the convective flow. ME reaches about 7% of the total kinetic energy (KE) in case G and 40% in case A, but for the latter, large modulation on a longer time scale are observed as well (Brun et al. 2005). The fact that core convection can be as efficient as envelope convection (if not more) in generating strong fluctuating magnetic fields constitutes a very interesting result. Effectively, it indicates that massive stars certainly possess strong time dependent magnetic fields in their deep interior but that these fields are somewhat screened by the huge radiative envelope surrounding their convective core since such variability is not observed. Another interesting property of the dynamo simulations considered here is that most of the energy that channel to ME comes from the kinetic energy stored in the differential

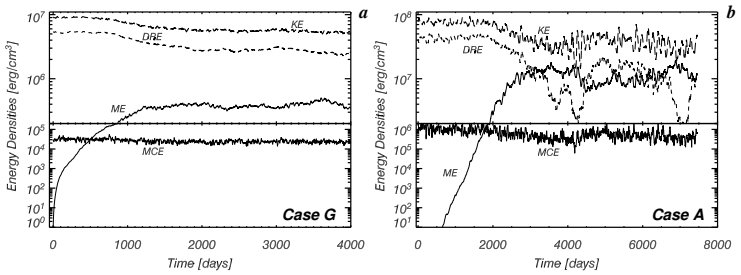

Fig. 1. Kinetic and magnetic energy densities as a function of time for a) case G and b) case A. Also shown are the kinetic energies contained in the differential rotation (DRE) and meridional circulation (MCE). Note the large reduction in amplitude of DRE.

rotation (DRE). In case A the interplay between differential rotation and magnetic field is so strong that each time ME becomes respectively greater (smaller) than 40% of KE, DRE drops (rises), resulting in highly time dependent angular velocity profile in the convective core. It seems that in convective rotating shells when ME is less than about 20% of KE, the kinetic energy is mainly store in differential motion whereas with ME above about 40% of KE the damping (or braking effect by Maxwell stresses) is so strong that the kinetic energy is mainly stored in non axisymmetric motions. Overall we find that the total energy ME+KE is smaller than KE in the progenitor hydrodynamic simulations.

3 Convective motions and magnetic fields

Figure 2 we represent the radial velocity, radial and longitudinal magnetic fields at midlayer depth in the convective zone for both cases. We clearly see that case A exhibits much larger spatial scales than case G, even though they have about the same level of turbulence. The convective motions in case A are slower and more symmetric between up and down motions due to a smaller density contrast. We see that Br tends to be concentrated in the downdrafts (after having been swept from the center of the convective eddies), whereas B_ϕ is more patchy and elongated due to the presence of a differential rotation or ω-effect (Moffatt 1978). The field strength is greater in case A than in case G, both because the energy content is larger and ME closer to equipartition. The mean axisymmetric magnetic fields are weak (less than 10% of ME). Some irregular reversals of the mean poloidal fields are seen but on too fast a time scale ($\sim 500 - 1000$ days) (Brun et al. 2004, 2005).

4 Conclusion

We have shown that dynamo action is realized in both type of convection zones (central or envelope) leading to field strength close to equipartition. The main

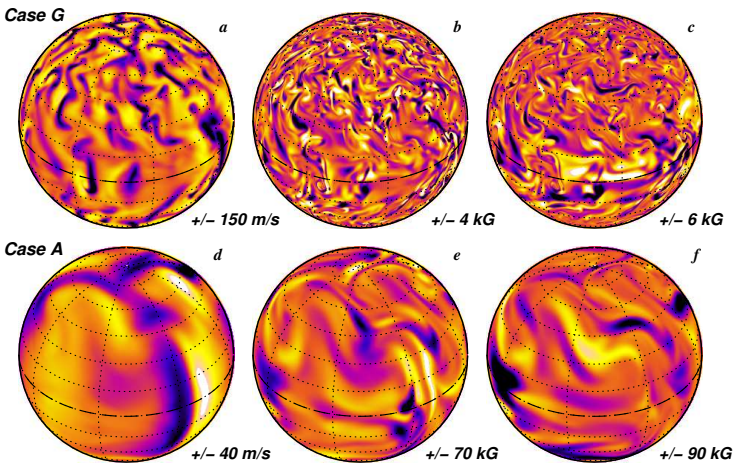

Fig. 2. Snapshot using an orthographic projection of the radial velocity (frame a and d), and radial (b and e) and longitudinal (c and f) magnetic fields for cases G and A. Downflows and negative polarities appears dark. The dashed line represents the equator.

effect of the Lorentz forces is to reduce the differential rotation contrast. In order to get the right timing for the solar cycle a stable shear layer (the tachocline) seems require, whereas in A-type stars whether or not the dynamo generated central fields are able to reach the surface remains a subject of debate.

References

Browning, M., Brun, A.S., & Toomre, J. 2004, ApJ, 601, 512

Brun, A.S., Browning, M., & Toomre, J. 2005, ApJ submitted

Brun, A.S., Miesch, M.S., & Toomre, J. 2004, ApJ, 614, 1073

Brun, A.S., & Toomre, J. 2002, ApJ, 570

Clune, T.L. et al. 1999, Parallel Computing, 25, 361

Mestel, L. 2001, in Magnetic Fields across the H-R diagram, ed. G. Mathys, S.K. Solanki, & D.T. Wickramasinghe, ASP Conf. Series, 248, 3

Miesch, M.S. et al. 2000, ApJ, 532, 593

Moffatt, H.K. 1978, Magnetic Field Generation in Electrically Conducting Fluids, (Cambridge: Cambridge University Press)

Moss, D.L. 2001, in Magnetic Fields Across the Hertzsprung-Russell Diagram, ed. G. Mathys, S.K. Solanki, & D.T. Wickramasinghe (San Francisco:ASP), 305

Ossendrijver, M. 2003, Astron. Astrophys. Rev., 11, 287

Schmitt, J. 2003, in Stars as Suns: Activity, Evolution and Planets, IAU Symp. 219, ed. A.K. Dupree, & A.O. Benz, in press

Chapitre 7

Perspectives

Les calculs MHD tridimensionnels à haute résolution numérique présentés dans ce manuscrit constituent une première étape vers une modélisation toujours plus réaliste des étoiles et du Soleil en particulier. Ils ne permettent aujourd'hui que de modéliser sur des temps relativement courts certains aspects (blocs) de leur dynamique, alors que le programme ambitieux que se sont fixé les physiciens stellaires et solaires, est de calculer l'évolution complète de l'étoile depuis sa formation jusqu'à sa mort en prenant en compte aussi bien la dynamique interne que l'interaction de l'étoile avec son milieu circumstellaire. Il est clair qu'un tel objectif mettra encore plusieurs décennies pour émerger. En attendant, la diversité et la richesse des résultats déjà obtenus aussi bien sur la convection, la rotation différentielle, l'effet dynamo et leur dépendance en fonction des paramètres stellaires tels que la masse, l'âge et le taux de rotation, que sur la description de la haute atmosphère (chromosphère, couronne, vent de particules) du Soleil et des étoiles, nous promettent encore de belles années de science fascinante en dynamique des fluides astrophysiques et en physique stellaire afin de préparer efficacement le développement d'un modèle général. Nous pensons que le moment est propice à ce que tous les chercheurs impliqués dans l'étude et la modélisation du Soleil, des étoiles et de leurs interactions avec leur environnement spatial, définissent un protocole/cadre physique et numérique dans lequel, tous pourraient développer, interfacer et coupler leurs codes. Ceci permettrait en effet de faciliter le développement d'un modèle global de la magnétohydrodynamique stellaire, un peu comme les météorologues ont récemment commencés à coupler les codes atmosphériques et océaniques. Le Soleil peut certainement jouer un rôle central dans cette construction car il fait le lien avec d'un coté l'évolution, la dynamique et l'activité stellaire et de l'autre avec l'environnement immédiat des étoiles via les interactions Soleil-Terre, impliquant la dynamique complexe de surface, le vent de particules et la dynamique de la magnétosphère. Un tel effort a déjà commencé pour les relations Soleil-Terre (voir par exemple le modèle du

Center for Space Environment Modeling de l'Université du Michigan), il est nécessaire de l'étendre aux autres types d'étoiles et à d'autres types codes, comme par exemple coupler un code comme ASH avec un code modélisant les disques d'accrétions afin de modéliser l'interaction d'une étoile jeune avec son disque. En attendant que de tels efforts d'unification (mutualisation) de moyens de simulations et de calculs, impliquant la communauté astrophysique au sens large se développent, il nous reste une multitude de problèmes très importants à résoudre en magnétohydrodynamique solaire et stellaires. Nous désirons ici présenter de manière synthétique ce que nous croyons être les enjeux de ce champ de recherche, quelle peut être la continuation naturelle de nos travaux dans les dix prochaines années pour contribuer à atteindre ces objectifs et comment nous pourrions commencer à mettre en place un cadre plus général pour modéliser les relations Soleil-Terre (étoiles-planètes) et les connections (au sens large) soleil-étoiles.

7.1 Convection, rotation et activité magnétique solaire

Les interactions non linéaires entre convection, rotation, cisaillement et champ magnétique restent au centre de la plupart des phénomènes dynamiques observés dans le Soleil. Pour améliorer notre compréhension de ces processus, les simulations de la convection turbulente solaire doivent atteindre une résolution numérique supérieure à celle accessible actuellement afin de pouvoir résoudre avec encore plus de précision et de fidélité le large intervalle d'échelles spatio-temporelles présentes. Actuellement la résolution maximale pour des runs cours est de l'ordre de 2000^3, ce qui ne permet pas encore de modéliser, avec les modèles globaux, la granulation. Il faudrait pour cela atteindre au moins une résolution de 10000^3 ou un $\ell_{max} \sim 5000$, ce qui n'est pas réalisable avant au mieux le milieu de la décennie prochaine. De plus, il sera également nécessaire d'intégrer les solutions sur des temps bien plus longs, ce qui pèsera également lourdement sur nos moyens de calculs et notre capacité à explorer systématiquement l'espace des paramètres. Parmi les sujets de la dynamique de surface du Soleil sur lesquels nous pensons apporter une contribution dans les années à venir, nous retenons:

– préparer et accompagner la nouvelle génération d'instruments comme ceux présents sur le satellite SDO, soit par le développement de modèles physiques 3D MHD et dépendant du temps de la surface (SSW), des échelles de convection intermédiaires (super ou mésogranulation), des ondes et des modes acoustiques, soit par la mise en place de programme informatique se servant des données pour faire de la prédiction d'évenement particulier (telles que les CMEs (ce qui se rap-

proche de la prédiction climatique). Les deux approches n'ayant pas le même but et domaine d'application.

- progresser sur la structure de la convection turbulente sous l'influence ou non de la rotation et/ou du champ magnétiques, en évaluant les différentes fonctions de structure et autres moments statistiques permettant de caractériser le processus physique. Vérifier l'existence d'un régime dur de convection turbulente à très hauts de nombre de Rayleigh (bien que pour les étoiles c'est la luminosité solaire qui est imposée et non pas une différence de température), ou celle d'une échelle de Bolgiano magnétique?
- Améliorer notre modèle de la rotation différentielle qui possède encore un profil trop cylindrique malgré les récents progrès effectués dans ce domaine par notre groupe. En particulier évaluer les rôles respectifs joués par la turbulence, les tenseurs de Reynolds et le transport anisotrope de moment cinétique et de chaleur, par les effets thermiques venant soit de la tachocline (Rempel 2005) soit du flux d'enthalpie en latitude associé aux mouvements convectifs et par le champ magnétiques et les tenseurs de Maxwell.
- Étudier non linéairement un à un puis de manière couplée, les différents blocs de la dynamo solaire, tels que: le stockage du champ toroidal moyen, les processus derrière l'amplification de ce dernier dans ou hors de la tachocline, l'émergence du flux magnétique sous la forme de structures allongées en fonction de la latitude (comme le diagramme papillon) et de la longitude (phénomène dit des longitudes actives (persistantes)), la pénétration et le pompage du champ magnétique par les panaches convectifs turbulents ainsi que leur distribution en latitude, la rétroaction du champ cyclique sur la convection et sa rotation différentielle (oscillations torsionnelles, plus faible amplitude), la forme (nombres de cellules en latitude et rayon) et l'amplitude de la circulation méridienne cruciale pour les modèle de dynamo Babcock-Leighton, etc...
- Améliorer les simulations 3-D, afin d'avoir une approche encore plus quantitative et fidèle des phénomènes dynamiques. Par exemple est-il possible de prédire (obtenir) le cycle de 11 ans de l'activité solaire à partir d'un modèle auto-consistant et non linéaire?
- Moderniser le code ASH, en lui permettant de suivre plusieurs espèces et leur degré d'ionisation, de traiter la singularité ($r = 0$), d'introduire un traitement sous maille plus adapté à la convection (projet STARS (Simulations de la Turbulence, de l'Activité et de la Rotation des étoilS), accepté par l'appel d'offre DEISA-DECI 2005). Considérer le développement d'un nouveau code basé sur

la méthode numérique des éléments spectraux (pour une meilleure flexibilité et adaptabilité vis à vis des problèmes considérés (Karniadakis et Sherwin 1998).

7.2 La tachocline et la zone radiative solaire

Cette couche limite à la base de la zone convective solaire, semble jouer un rôle important dans la dynamique globale du Soleil. Il est nécessaire de mieux en comprendre sa structure multidimensionnelle et sa dynamique sur des temps courts et longs. Il est aussi important de progresser dans la modélisation 2-D/3-D MHD des intérieurs radiatifs et en particulier de toutes les instabilités rotationnelles, magnétiques ou autres présentes dans ces zones. Nous pensons que les points suivants méritent une attention particulière:

- Modéliser le couplage entre zones convectives et radiatives, comme par exemple la redistribution du moment cinétique entre l'intérieur et la surface, où l'interaction d'un champ interne (fossile?) avec le champ dynamo.
- Caractériser les processus d'amplification et de génération du champ magnétique toroidal mais aussi poloidal dans une tachocline, en prenant en compte la sphéricité, la présence de plumes convectives, d'un cisaillement en rayon et latitude,
- Déterminer de manière non linéaire et 3-D, les configurations magnétiques stables dans les zones radiatives sous l'influence de la rotation et d'un cisaillement grande échelle. Il y a t il un effet dynamo? Ces instabilités engendrent t elles des circulations à grande échelle pouvant redistribuer le moment cinétique et modifier le profil de rotation interne?

7.3 Activité et dynamique des étoiles

On peut par simplicité classifier les étoiles en 3 catégories: les étoiles massives (cœur convectif et enveloppe radiative), les étoiles de type solaire (cœur radiatif et enveloppe convective) et les étoiles complètement convectives (que l'on trouve sur la PMS (TTauri) ou sur la ZAMS (naines M tardives)). Développer un modèle 3-D MHD capable de reproduire les différents types de magnétisme et leur manifestation à la surface des étoiles constitue une des priorités principales de la communauté. On pourra par exemple s'intéresser à:

- Prendre en compte le lien dynamique entre les différentes phases d'évolution des étoiles. En effet le champ magnétique est observé à certaines phases de la vie des

étoiles (comme dans les étoiles jeunes TTauri, les étoiles de type solaire ou plus tardif de la séquence principale et dans les étoiles dégénérées (naines blanches, étoiles à neutron)), mais pas à d'autres (phase géante, étoiles massives). Où est le champ B, que lui est il arrivé? Peut on suivre son évolution à travers une transition et faire le pont entre ces différentes phases?

- Dans les étoiles massives possédant une enveloppe radiative mais aussi dans l'intérieur radiatif des étoiles de type solaire, qu'elle est la nature des interactions entre le champ dynamo et un éventuel champ fossile? L'émergence de structures magnétiques depuis le cœur convectif des étoiles massives est-elle possible et si oui comment modifie t elle le champ de surface? Dans le Soleil, une variation temporelle ou spatiale du champ fossile est-elle ressentie par le champ dynamo?
- Caractériser les propriétés des tachoclines présentent dans d'autres étoiles possédant simultanément une zone convective et radiative. La présence d'une telle couche implique t elle systématiquement l'existence d'un champ cyclique et d'une dynamo globale?
- Quel type de profil de rotation et de magnétisme les étoiles complètement convective (jeunes ou de type tardif M3) possèdent-elles? L'absence d'une tachocline est-elle importante et résulte t elle en une activité irrégulière et un profil de rotation cylindrique?
- Quel rôle sur leur dynamique interne, un couplage entre 2 corps, soit par effets de marée, soit par interaction magnétique, exerce t il? Pouvons nous caractériser le transfert de moment cinétique interne et du système total l'un vers l'autre? Il y a t il synchronisation, modification forte de la dynamique interne (convection, rotation différentielle, etc..) des étoiles?
- faire le lien entre les codes du type de ASH résolvant les équations de la MHD sur des temps courts et la nouvelle génération de code d'évolution stellaire 2D (ESTER) et 3D (DJEHUTY), en fournissant par exemple différents moments caractérisant la turbulence en zone convective sans pour autant obliger le code d'évolution stellaire à suivre la dynamique aussi précisément que ASH. Ceci bien sur en attendant d'intégrer les codes dans un modèle global. Un couplage avec un code de transfert de rayonnement peut également être envisagé afin de reproduire plus fidèlement les quantités observées.

7.4 Effet dynamo dans les étoiles

Il est maintenant possible de parcourir le diagramme HR et de modéliser à partir de codes tridimensionnels comme ASH, les propriétés dynamiques des étoiles et en particulier leur effet dynamo. Il s'avère qu'une dynamo existe dans toutes les zones convectives modélisées jusqu'à présent (les chapitres 4 et 6 de ce manuscrit en sont une démonstration). Cependant le manque de réalisme de certains des paramètres, comme par exemple le nombre de Prandtl magnétique, invite à la prudence, pour une comparaison directe entre simulations et observations. Afin de progresser dans le réalisme de nos simulations, nous devons augmenter la résolution de celles-ci et construire le modèle le plus réaliste possible. Cela implique que les nombreux couplages non linéaires entre la convection, la rotation différentielle, la pénétration convective, le pompage du champ dans la tachocline par les panaches convectifs, l'amplification du champ par cisaillement, l'émergence de structures toroidales/poloidales à la surface, etc. . . , doivent être pris en compte.

- Il faut donc assembler les différents blocs dynamos dans un modèle plus intégré et évaluer leurs influences
- Caractériser l'influence du taux de rotation de l'étoile sur l'existence d'une dynamo et sur sa nature (petites ou grandes échelles, rapide, lente. . .).
- Étudier comment réduire la valeur trop élevée du nombre de Prandtl magnétique de la plupart des simulations de dynamo, en augmentant par exemple la résolution pour se permettre d'avoir des nombres Pm inférieur à 1 tout en conservant un Rm au dessus de sa valeur critique, où en développant une méthode LES-SGS spécifique comme Ponty et al. (2004).

7.5 Relations Soleil-Terre

Nous concluons ces perspectives par une discussion succincte de la problématique Soleil-Terre. La position centrale du Soleil entre la Terre et les étoiles est un atout indéniable car il permet de faire le lien entre différents aspects d'un problème complexe. De plus, l'influence du Soleil sur la Terre est un enjeux important pour notre société technologique car elle n'est pas toujours indolore. Afin de mieux comprendre les relations Soleil-Terre, il est nécessaire de faire un modèle physique des différents blocs et de les intégrer ultérieurement dans un modèle plus global. Cette approche a commencé aux États-Unis à l'Université du Michigan par exemple.

- Il serait donc très utile à notre communauté de créer un modèle des Relations

Soleil-Terre intégré à partir des codes français (et/ou européen) déjà existants, en partant de la dynamo interne, jusqu'à la magnétosphère terrestre, tout en passant par l'instabilité des boucles et le vent solaire. Dans le cadre du PNST, il faudrait définir un protocole pour le développement de codes interfaçables, car nous disposons déjà de tous les éléments nécessaires à la mise en place d'un tel modèle. On pourrait par exemple se mettre d'accord sur le jeu de variables utiles pour passer d'un code à l'autre ou sur la structure des données.

– Un autre aspect des relations Soleil-Terre important à étudier, est la problématique du réchauffement climatique et de l'augmentation de la constance solaire. Quel rôle le champ magnétique et les différents cycles solaires jouent t-ils dans l'augmentation de la constance solaire sur ce dernier siècle? Peut on bien séparer les effets anthropiques des effets naturels dans l'évolution actuelle du climat de la Terre.

Sur la Figure 7.1 nous rappelons la position centrale du Soleil, les enjeux scientifiques et le grand nombre de passerelles naturelles vers d'autres domaines scientifiques (figure non exhaustive).

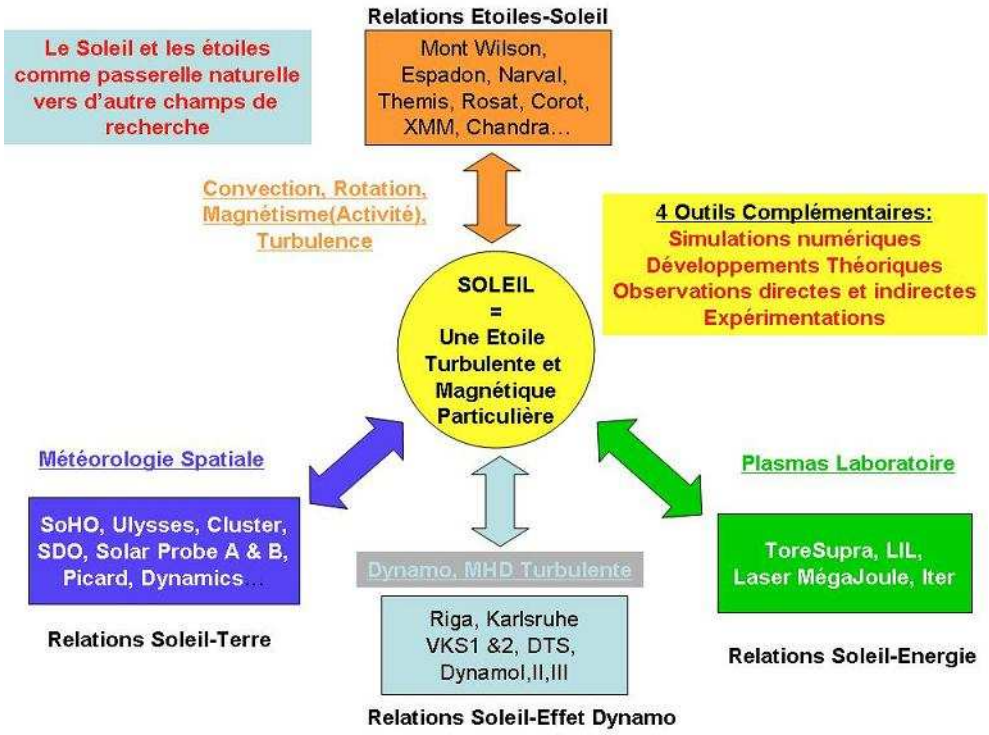

FIG. 7.1 – *Schéma représentant (figure non exhaustive) les intéractions naturelles de la physique solaire avec d'autres branches de la physique et les expériences et satellites directement ou indirectement concernés.*

Bibliographie

[1] Amari, T., Luciani, J. F. & Aly, J. J. 2004, ApJ, 615, L165

[2] Ambroz, P. 2002, in Solar variability: from core to outer frontiers, ed. A. Wilson. (Noordwijk: ESA SP), ESA SP-506, 827

[3] Ambroz, P. 2005, communication privée.

[4] André, P., Ward-Thompson, D. & Barsony , M. 1993, ApJ 406, 122

[5] Aurière, M. et al. 2003, A Peculiar Newsletter, 39

[6] Babcock, H. W. 1961, ApJ, 133, 572

[7] Babel, J. & Montmerle, T. 1997, A&A, 323, 121

[8] Baglin, A. 2003, AdSpR, 31 (2), 345

[9] Baliunas, S. L. et al. 1995, ApJ, 438, 269

[10] Baliunas, S. L. et al. 1996, ApJ, 460, 848

[11] Barnes et al. 2005, MNRAS, 357, L1

[12] Basri, G. 2003, in Stellar Rotation, IAU Symp. 215, eds. A. Maeder & P. Eenens, 248

[13] Battaner, E. 1996, Astrophysical Fluid Dynamics, (Cambridge: Cambridge Univ. Press)

[14] Bazán et al. 2003, in 3-D stellar evolution, ASP Conf. Series, 293, 1

[15] Beer, J., Tobias, S. M., & Weiss, N. O. 1998, Solar Phys., 181, 237

[16] Benzi, R., Toschi, M. & Tripiccione, R. 1998, Journal of Statistical Physics, 93, 901

[17] Biskamp, D. 1993, Nonlinear Magnetohydrodynamics (Cambridge: Cambridge Univ. Press)

[18] Bohm-Vitense, E. 1958, Z. Astrophys., 54, 114

[19] Bolgiano, R. 1959, J. Geophys. Res., 64, 2226

[20] Bonnazzola, B. S., Gougoulhon, E. & Marck, J. A. 1998, J. Comput. Appl. Math, 109, 433

[21] Bouvier, J. et al. 1997, A&A, 326, 1023

[22] Boyd, J. P. 1989, Chebyshev and Fourrier Spectral Methods (Berlin: Springer Verlag)

[23] Brainwaith, J. & Spruit, H. C. 2004, Nature, 431, 819

[24] Brandenburg, A., Jennings, R. L., Nordlund, Å., Rieutord, M., Stein, R. F., Tuominen, I. 1996, JFM, 306, 325

[25] Brandenburg, A. 2005, ApJ, 625, in press

[26] Beck, R., Brandenburg, A., Moss, D., Shukurov, A., & Sokoloff, D. 1996, Annual Review of Astronomy and Astrophysics, 34, 155

[27] Browning, M. K., Brun, A. S., & Toomre, J. 2004, ApJ, 601, 512

[28] Brummell, N. H., Hurlburt, N. E., & Toomre, J. 1996, ApJ, 473, 494

[29] Brummell, N. H., Hurlburt, N. E., & Toomre, J. 1998, ApJ, 493, 955

[30] Brun, A.S. voir page 287 pour une liste exhaustive de mes publications

[31] Busse, F. H. 1970, Phys. J. Fluid Mech., 44, 441

[32] Busse, F. H. & Cuong, P.G. 1977, Geophys. Astrophys. Fluid Dynam., 8, 17

[33] Busse, F. H. 1981, GAFD, 17, 215

[34] Busse, F. H. 1982, in Mantle Convection, ed R. Peltier, (Gordon & Breach: New York), 23

[35] Busse, F. H. 2000, Annu. Rev. Fluid Mech., 32, 383

[36] Castaing, B., Gagne, Y. & Hopfinger, E. J. 1990, Physica D, 46, 177

[37] Cattaneo, F. et al. 1991, ApJ, 370, 282

[38] Cattaneo, F. 1999, ApJ, 515, L39

[39] Cattaneo, F., Emonet, T. & Weiss, N. O. 2002, ApJ, 588, 1183

[40] Cattaneo, F. & Hughes, D. W. & Weiss, N. O. 1991, MNRAS, 253, 479

[41] Cattaneo, F. & Hughes, D. W. 1996, Phys Rev E, 54, 4532

[42] Cattaneo, F. & Hughes, D. W. 2001, Astron. & Geophys., 42, 3, 18

[43] Cayrel, R. 1998, Space Sci. Rev., 84, 145

[44] Chandrasekhar, S. 1939, An Introduction to the Study of Stellar Structure, (Chicago: Chicago University Press)

[45] Chandrasekhar, S. 1961, Hydrodynamic and Hydromagnetic Stability, (Oxford: Oxford University Press)

[46] Charbonneau, P. & MacGregor, K. B. 1997, ApJ, 486, 502

[47] Charbonneau, P. & MacGregor, K. B. 2001, ApJ, 559, 1094

[48] Charbonneau, P., Tomczyk, S., Schou, J., Thompson, M. J. 1998, ApJ, 496, 1015

[49] Charbonnel, C. & Talon, S. 2005, Science, vol 309, issue 5744, p2189

[50] Chillá, F. et al. 1993, Il Nuovo Cimento, 15D (9), 1229

[51] Childress, S. & Gilbert A. D. 1995, Stretch, Twist, Fold: The Fast Dynamo (Berlin: Springer)

[52] Christensen, U., Olson, P. & Glatzmaier, G. A. 1999, Geophys. J. Int., 138, 393

[53] Christensen-Daalsgaard, J. et al. 1996, Science, 272, 1286

[54] Chouduri, A. R., Schüssler, M. & Dikpati, M. 1995, A&A, 303, L29

[55] Chouduri, A. R. 1998, The Physics of Fluids and Plasmas, (Cambridge: Cambridge University Press)

[56] Clayton, D. D. 1968, Principles of Stellar Evolution and Nucleosynthesis (Chicago: Chicago University Press)

[57] Clune, T. L., Elliott, J. R., Glatzmaier, G. A., Miesch, M. S., & Toomre, J. 1999, Parallel Comput., 25, 361

[58] Corbard, T., Blanc-Féraud, L., Berthomieu, G. & Provost, J. 1999, A&A, 344, 696

[59] Couvidat, S., Garcia, R. A., Turck-Chièze, S., Corbard, T., Heney, C. J. & Jiménez-Reyes, S. 2003, 597, L77

[60] Couvidat, S., Turck-Chièze, S., & Kosovichev, A. 2003, ApJ, 599, 1434

[61] Cowling, T. G. 1957, Magnetohydrodynamics, (New York: Interscience Publishers Inc.)

[62] Cox, J. P. & Giuli, R. T. 1968, Principles of Stellar Structure (New York: Gordon & Breach)

[63] Cuong, P. G. & Busse, F. H. 1981, PEPI, 24, 272

[64] Davidson, P. A. 2001, An Introduction to Magnetohydrodynamics, (Cambridge: Cambridge University Press)

[65] DeRosa, M. L., Gilman, P. A. & Toomre, J. 2002, ApJ, 581, 1356

[66] Dikpati, M., Cally, P. S. & Gilman, P. A., 2004, ApJ, 610, 597

[67] Dikpati, M. & Charbonneau, P. 1999, ApJ, 518, 508

[68] Diu et al. 1989, Physique Statistique

[69] Donahue, R. A., Saar, S. H. & Baliunas, S. L. 1996, ApJ, 466, 384

[70] Donati, F. 2003, in Magnetism and Activity of the Sun and Stars, eds J. Arnaud & N. Meunier, EAS Pub. Series, 9, 169

[71] Donati, F. et al. 2003, MNRAS, 345, 1187

[72] Dorch, S. B. 2004, A&A, 423, 1101

[73] Dubrulle, B. & Valdetarro, L. 1992, A&A, 263, 387

[74] Dubrulle, B. 2002, Eur. Phys. J. B, 28(3), 361

[75] Dupree 2003, in The Future of Cool-Star Astrophysics, eds. A. Brown, G. M. Harper, & T. R. Ayres, Cool Stars Meeting XII, 1

[76] Durney, B. R., & Latour, J. 1978, Geophys. Astrophys. Fluid dynamics, 9, 241

[77] Durney, B. R. 1997, ApJ, 486, 1065

[78] Durney, B. R. 1999, ApJ, 511, 945

[79] Eddington, A.S. 1926, The Internal Constitution of the Stars, (Cambridge: Cambridge Univ. Press)

[80] Eddy, J. A., Gilman, P. A. & Trotter, D. E. 1976, Solar Phys., 46, 3

[81] Eggleton, P. et al. 2003, in 3-D stellar evolution, ASP Conf. Series, 293, 15

[82] Elliott, J.R. 1997, A&A, 327, 1222

[83] Elliott, J. R., Miesch, M. S. & Toomre, J. 2000, ApJ, 533, 546

[84] Elstner, D. 2005, in The Magnetized Plasma in Galaxy Evolution, Proceedings of the conference held in Kraków, Poland, Sept. 27th - Oct. 1st, 2004, Eds K. Chyzy, K. Otmianowska-Mazur, M. Soida, and R.-J. Dettmar, 117

[85] Fauve, S. 2004, contribution orale, programme MSI, Institut Newton, Cambridge.

[86] Fearn, D. S. 1998, Rep. on Progr. in Phys., 61, 175

[87] Feigelson et al. 2003, ApJ, 584, 911

[88] Fisher, G. H., Fan Y., Longcope, D. W., Linton, M. G. & Pevtsov, A. A. 2000, Solar Phys., 192, 119

[89] Forgacs-Dajka, E. 2004, A&A, 414, 1143

[90] Frisch, U. 1995, Turbulence: The Legacy of A.N. Kolmogorov, (Cambridge: Cambridge Univ. Press)

[91] Galloway, D. J. & Weiss, N. O. 1981, ApJ, 243, 945

[92] Garaud, P. 2002, MNRAS, 329, 1

[93] Gilman, P. A. 1975, Journ. Atmos. Sci., 32, 1331

[94] Gilman, P. A. 1979, ApJ, 231, 284

[95] Gilman, P. A. 1983, ApJS, 53, 243

[96] Gilman, P. A. 2000, Solar Phys., 192, 27

[97] Gilman, P. A., & Miller, J. 1981, ApJS, 46, 211

[98] Gilman, P. A., Morrow, C. A. & DeLuca, E. E. 1989, ApJ, 338, 528

[99] Glatzmaier, G. A. 1984, J. Comp. Phys., 55, 461

[100] Glatzmaier, G. A. 1985a, ApJ, 291, 300

[101] Glatzmaier, G. A. 1985b, Geophys. Astrophys. Fluid Dynam., 31, 137

[102] Glatzmaier, G. A. 1987, in The Internal Solar Angular Velocity, ed. B. R. Durney & S. Sofia (Dordrecht: D. Reidel), 263

[103] Glatzmaier, G. A., & Gilman, P. 1982, ApJ, 256, 316

[104] Glatzmaier, G. A., & Roberts, P. H. 1995, Nature, 377, 203

[105] Gough, D. O. & McIntyre, M. E. 1998, Nature, 394, 755

[106] Gough, D. O., & Toomre, J. 1991, Annu. Rev. Astron. Astrophys., 29, 627

[107] Grappin, R., Léorat, J. & Pouquet, A. 1983, A&A, 126, 51

[108] Haber, D. A., Hindman, B. W., Toomre, J., Bogart, R. S., Larsen, R. M., & Hill, F. 2002, ApJ, 570, 855

[109] Hansen, C.J. & Kawaler, S.D. 1995, Stellar Interiors: Physical Principles, Structure, and Evolution, (New York: Springer-Verlag)

[110] Hart et al. 1986, Science, 234, 61

[111] Harvey, J. W. et al. 1996, Science, 272, 1284

[112] Hathaway, D. H. et al. 1996, Science, 272, 1306

[113] Hawley, S. L. 1993, PASP, 105, 955

[114] Hawley, S. L. 2000, ASP Conf. Series, 212, 252

[115] Hubrig, S., North, P. & Mathys, G. 2000, ApJ, 539, 352

[116] Hurlburt, N.E., Toomre, J., Massaguer, J. 1986, ApJ, 311, 563

[117] Judge 2003, in The Future of Cool-Star Astrophysics, eds. A. Brown, G. M. Harper, & T. R. Ayres, Cool Stars Meeting XII, 158

[118] Karniadakis, G. E., & Sherwin, S. J. 1998, Spectral/hp Element Methods for Cfd (Oxford: Oxford Univ. Press)

[119] Kichatinov, L. L., & Rüdiger, G. 1995, A&A, 299, 446

[120] Kippenhahn, R. & Weigert, A. 1994, Stellar Structure and Evolution (Berlin: Springer-Verlag)

[121] Krause, F. & Rädler, K.-H. 1980, Mean-Field Magnetohydrodynamics and Dynamo Theory, (1st ed; Oxford: Pergamon Press)

[122] Kundu, P.J., Fluid Mechanics, (San Diego: Academic Press)

[123] Landstreet, J.D. 2003, in Magnetism and Activity of the Sun and Stars, eds J. Arnaud & N. Meunier, EAS Pub. Series, 9, 235

[124] Landstreet, J.D. & Mathys, G. 2000, A&A, 359, 213

[125] Leprovost, N. 2004, Thèse de l'Université de Paris 6.

[126] Lesieur, M. 1997, Turbulence in Fluid, (Dordrecht: Kluwer)

[127] Leighton, R. B. 1969, ApJ, 156, 1

[128] Libbrecht, K. G. 1989, ApJ, 336, 1092

[129] MacDonald, J. & Mullan, D.J. 2004, MNRAS, 348, 702

[130] MacGregor, K. B. & Cassinelli, J.P. 2003, ApJ, 586, 480

[131] MacGregor, K. B. & Charbonneau , P. 1999, ApJ, 519, 911

[132] Maeder, A. & Zahn, J. P. 1998, A&A, 334, 1000

[133] Maeder, A. & Meynet, G. 2003, A&A, 411, 543

[134] Mathis, S. & Zahn, J. P. 2004, A&A, 425, 229

[135] Mathis, S. & Zahn, J. P. 2005, A&A, sous presse

[136] Mathys, G. 2003, in Stellar Rotation, IAU Symp. 215, eds. A. Maeder & P. Eenens, 271

[137] McIntyre 2003, Stellar Astrophysical Fluid Dynamics, 111, (Cambridge: Cambridge Univ. Press)

[138] Meneguzzi, M., Frisch, U. et Pouquet, A. 1981, Phys. Rev. Letters, 47, Issue 15, 1060

[139] Markey, P. & Tayler, R. J. 1973, MNRAS, 163, 77

[140] Markey, P. & Tayler, R. J. 1974, MNRAS, 168, 505

[141] Mestel, L. & Moss, D. 1977, MNRAS, 178, 27

[142] Mestel, L. & Weiss, N. O. 1987, MNRAS, 226, 123

[143] Mestel, L. 1999, Stellar Magnetism, (Oxford: Clarendon)

[144] Mestel, L. 2001, "Magnetic Fields Across the HR Diagram", G. Mathys, S.K. Solanki & D.T. Wickramasinghe (eds), ASP Conf. Ser., 248, 3

[145] Meynet, G. & Maeder, A. 1997, A&A, 321, 465

[146] Miesch, M. S. 2003, ApJ, 586, 663

[147] Miesch, M. S., Elliott, J. R., Toomre, J., Clune, T. L., Glatzmaier, G. A., & Gilman, P. A., 2000, ApJ, 532, 593

[148] Mihalas, D. & Mihalas, B. 1984, Foundations of Radiation Hydrodynamics, (Oxford: Oxford Univ. Press)

[149] Moffatt, H. K. 1978, Magnetic Field Generation in Electrically Conducting Fluids, (Cambridge: Cambridge Univ. Press)

[150] Morel, P. 1997, A&AS, 124, 597

[151] Moss, D. 2001, "Magnetic Fields Across the HR Diagram", G. Mathys, S.K. Solanki & D.T. Wickramasinghe (eds), ASP Conf. Ser., 248, 305

[152] Moss, D. 2003, in Magnetism and Activity of the Sun and Stars, eds J. Arnaud & N. Meunier, EAS Pub. Series, 9, 21

[153] Nordlund, Ået al. 1992, ApJ, 392, 647

[154] Noyes, R.W., Weiss, N.O. & Vaughan, A.H. 1984, ApJ, 287, 769

[155] Ossendrijver, M. 2003, Astron. Astrophys. Rev., 11, 287

[156] Otmianowska-Mazur, K. & Elstner, D. 2003, Astrophysics and Space Science, v. 284, Issue 2, 761

[157] Parker, E. N. 1955, ApJ, 122, 293

[158] Parker, E. N. 1989, Cosmical Magnetic Fields: their Origin and their activity, ed. Clarendon Press.

[159] Parker, E. N. 1993, ApJ, 408, 707

[160] Pedlosky, J. 1987, Geophysical Fluid Dynamics, (New York: Springer-Verlag)

[161] Pinsonneault, M., ARA& A, 35, 557

[162] Pitts, E. & Tayler, R. J. 1985, MNRAS, 216, 139

[163] Pöhnl, H., Paunzen, E. & Maitzen, H. M. 2005, A&A, 441, 1111

[164] Ponty, Y. et al. 2004, voir preprint physics/1041004

[165] Pope, S. B. 2000, Turbulent Flows, (Cambridge: Cambridge University Press)

[166] Proctor, M. 2004, Astron. & Geophys., 45(4), 14

[167] Rast, M. 2003, ApJ, 597, 1200

[168] Reiners, A. 2005, A&A sous presse (astrop-ph/0509399)

[169] Reiners, A. & Schmitt, J.H.M.M. 2003, A&A, 398, 647

[170] Rempel, M. 2004, ApJ, 622, 1320

[171] Richard, O., Vauclair, S., Charbonnel, C. & Dziembowski, W. A. 1996, A&A, 312, 1000

[172] Richard, O., Michaud, G. & Richer, J. 2001, ApJ, 558, 377

[173] Rieutord, M. & Zahn, J.-P. 1995, A&A, 296, 127

[174] Rieutord, M. 1997, Une Introduction à la Dynamique des Fluide, (Paris: Masson)

[175] Rieutord, M. et al. 2000, A&A, 357, 1063

[176] Rieutord, M. et al. 2004, Projet ESTER, rapport CNRS-ASSNA

[177] Rincon, F. 2005, Thèse de Doctorat: Dynamique des grandes échelles de la convection dans la phtosphère solaire, Université de Toulouse III - Paul Sabatier.

[178] Rincon, F., Lignière, F. & Rieutord, M. 2005, A&A, 430, L57

[179] Roberts, P. H. 1968, Phil. Trans. R. Soc. Lond. A, 263, 93

[180] Roberts, P. H. 1972, Phil. Trans. R. Soc. Lond. A, 272, 663

[181] Roberts, P. H. & Glatzmaier 2000, Rev. Mod. Phys., 72, 1081

[182] Robinson, F. J 2004, in SoHO/GONG 2004, ESA SP-559,

[183] Robinson, F. J. & Chan, K. L. 2001, MNRAS, 321, 723

[184] Rogers, T. M. & Glatzmaier, G. A. 2005, MNRAS, 364, 1135

[185] Roudier et al. 2003, A&A, 409, 299

[186] Roxburgh, I. W. 1965, MNRAS, 130, 223

[187] Rüdiger, G. & Brandenburg, A. 1995, A&A, 296, 557

[188] Rüdiger & Kitchatinov 1997, Astron. Nach., 318, 273

[189] Rüdiger, G. & Hollerbach 2004, The Magnetic Universe, Wiley

[190] Rüdiger, G. et al. 2005, A&A, 431, 345

[191] Saar, S. H. & Brandenburg, A. 1999, ApJ, 524, 295

[192] Schatzman, E. & Praderie, F. 1990, Les Étoiles, (Paris: Éditions CNRS)

[193] Schmitt, J.H.M.M. 2004, in Stars as Suns: Activity, Evolution and Planets, IAU Symp. 219, ed. A.K. Dupree, & A.O. Benz, in press

[194] Schou, J. et al. 1998, ApJ, 505, 390

[195] Schrijver, C. J. & Title, A M. 2003, ApJ, 597, L165

[196] Skumanich, A. 1972, ApJ, 171, 565

[197] Spiegel, E. A. & Zahn, J.-P. 1992, A&A, 265, 106

[198] Spruit, H. C. 1999, A&A, 349, 189

[199] Spruit, H. C. 2002, A&A, 381, 923

[200] Spruit, H. C., Knobloch, E. & Roxburgh, I. W. 1983, Nature, 304, 520

[201] Starr, V. P. & Gilman, P. A. 1966, Pure and Applied Geophys., 64, 145

[202] Stein, R. F. & Nordlund Å. 1998, ApJ, 499, 914

[203] Stein, R. F. & Nordlund Å. 2000, Solar Phys., 192, 91

[204] Stix, M. 1975, A&A, 42, 85

[205] Stix, M. 1976, A&A, 47, 243

[206] Stix, M. 2002, The Sun: an introduction, 2nd ed, (Berlin: Springer-Verlag)

[207] Strassmaeir, K.G. 2004, in Stars as Suns: Activity, Evolution and Planets, eds A.K. Dupree & A.O. Benz, IAU Symp 219, 11

[208] Sturrock, P. A. 1994, Plasma Physics, (Cambridge: Cambridge University Press)

[209] Sun, Z.-P. & Schubert, G. 1995, Phys. Fluids, 7, 2686

[210] Sweet 1950, MNRAS, 110, 548

[211] Talon, S. 1997, Thèse de Doctorat: Hydrodynamique des Étoiles en Rotation, Université de Paris VII.

[212] Talon, S., Kumar, P. & Zahn, J.-P. 2002, ApJ, 574, L175

[213] Tayler, R. J. 1973, MNRAS, 161, 365

[214] Tayler, R. J. 1980, MNRAS, 191, 151

[215] Thompson, M. J. et al. 1996, Science, 272, 1300

[216] Thompson, M. J., Christensen-Dalsgaard, J., Miesch, M. S. & Toomre, J. 2003, Ann. Rev. Astron. Astrophys., 41, 599

[217] Tobias, S. M. 1996, A&A, 307, L21

[218] Tobias, S. M., Brummell, N. H., Clune, T.L. & Toomre, J. 2001, ApJ, 549, 1183

[219] Toomre, J. et al. 2002, Science, 296, 64

[220] Turck-Chièze et al. 1993, Phys. Rep., 230, 57

[221] Valdetarro 2005, Ecole d'Aussois no14, EAS Publication Series sous presse.

[222] Weiss, N. O. 1994, in Lectures on Solar and Planetary Dynamos, ed. M. R. E. Proctor & A. D. Gilbert (Cambridge: Cambridge Univ. Press), 59

[223] Weiss, N. O. 2002, Astronomy & Geophysics, 43, Issue 3, 3.09

[224] Wilson, O.C. 1978, ApJ, 226, 379

[225] Wolff, S. C. 1983, The A-stars: Problems and perspectives, (Washington, D.C.: NASA)

[226] Wong, V.C. & Lilly, D.K. 1994, Phys. Fluids, 6(2), 1016

[227] Wright, G. A. E. 1973, MNRAS, 162, 339

[228] Zahn, J.-P. 1983, in Astrophysical Processes in Upper Main Sequence Stars, p. 253, eds Cox, A.N., Vauclair, S. & Zahn J.-P., Swiss Soc. Astron. Astrophys., Geneva

[229] Zahn, J.-P. 1991, A&A, 252, 179

[230] Zahn, J.-P. 1992, A&A, 265, 115

[231] Zahn, J.-P., Talon, S., Matias, J. 1997, A&A, 322, 320

[232] Zahn, J.-P. 2004, in Evolution of Massive Stars, Mass Loss and Winds, held in Aussois, eds Heydari, M., Stee, Ph., & Zahn, J.-P., EAS Publication Series, 13, 63

[233] Zeldovich, Y. B., Ruzmaikin, A.A. & Sokoloff, D.D., Magnetic Fields in Astrophysics, (New York: Gordon & Breach)

Table des figures

Liste des tableaux

Troisième partie

Appendices

A-1 Le Code Anelastic Spherical Harmonics

Dans cet appendice nous présentons brièvement le code anelastic spherical harmonic (ASH). Ce code repose sur une méthode spectrale de résolution des équations de la MHD et sur l'approche dite LES (Large Eddy Simulation, cf. Lesieur 1999, Pope 2003) consistant à suivre fidèlement les grandes échelles dynamiques du système considéré et à paramétriser les petites échelles (SubGrid Scale modeling) inférieure à la résolution utilisée (voir plus loin).

Le code ASH est un code mûr, qui a produit plus de 6 années de publications scientifiques dans des revues majeures, aussi bien dans le contexte des applications parallèles qu'en AFD ou en astronomie solaire/stellaire. Il a été développé à l'Université du Colorado, vers la fin des années 90 en s'inspirant d'une version monoprocesseur Fortran77 écrite par G. Glatzmaier au NCAR dans les années 80 (Glatzmaier 1984, 1985). Il a été cependant écrit en partant de zéro dans une version moderne parallèle et Fortran90, notamment par T. Clune, M. Miesch et J. Elliott. Dans le cadre d'une collaboration franco-américaine impliquant entre autre J. Toomre, M. Miesch, moi-même (au travers de mon post-doc de 1999 à 2003 à Boulder) aux USA, et Jean-Paul Zahn, S. Turck-Chièze en France (avant mon retour), le code a été définitivement validé dans sa version hydrodynamique et étendu aux problèmes de MHD (par l'ajout de l'équation d'induction) ainsi qu'à d'autres étoiles que le Soleil (étoiles de type A, soleils jeunes). J'ai de plus récemment développé et validé une version 1.2 en France, entre autre sur les ordinateurs du CCRT au CEA et de l'IDRIS. Cette version plus complète vient d'être mise à la disposition de la collaboration dans le cadre du Memorandum of Understanding on Stellar Dynamics and Dynamos, signée entre les deux groupes.

A-1.1 Les Équations MHD anélastiques

Le code global ASH résout dans une coquille sphérique tridimensionnelle en rotation, les équations de Navier Stokes, de continuité, d'énergie et d'induction dans l'approximation anélastique (i.e. $\partial\rho/\partial t = 0$, Gough 1969), voir Clune et al. (1999), Miesch et al. (2000) et Brun et al. (2004). L'approximation anélastique est utilisée afin de conserver les importants effets de la stratification en densité sans avoir à résoudre les ondes sonores, ce qui permet de satisfaire le critère de Courant en considérant la vitesse du fluide et donc d'utiliser des pas de temps plus grands. En décomposant les variables thermodynamiques ρ, T, S et P entre une partie à symétrie sphérique (symbole $^-$) et une partie fluctuante, e.g.

$$\rho(r,\theta,\phi,t) \rightarrow \bar{\rho}(r,t) + \rho(r,\theta,\phi,t),$$

avec $\epsilon \simeq |\rho|/\bar{\rho}$, le paramètre d'expansion déterminant l'amplitude de la perturbation (proportionnel au nombre de Mach, $M = v/c$, au carré), on peut déduire des équations 3.8, après linéarisation, les équations MHD dans cette approche anélastique qui filtre les ondes sonores mais conserve les ondes Alfvén et magnétosonores lentes:

$$\begin{aligned}
\boldsymbol{\nabla} \cdot (\bar{\rho}\mathbf{v}) &= 0, && \text{(A-1)}\\
\boldsymbol{\nabla} \cdot \mathbf{B} &= 0, && \text{(A-2)}\\
\bar{\rho}\left(\frac{\partial \mathbf{v}}{\partial t} + (\mathbf{v}\cdot\boldsymbol{\nabla})\mathbf{v} + 2\boldsymbol{\Omega}_\mathbf{o} \times \mathbf{v}\right) &= -\boldsymbol{\nabla} P + \rho\mathbf{g} + \frac{1}{4\pi}(\boldsymbol{\nabla}\times\mathbf{B})\times\mathbf{B}\\
&- \boldsymbol{\nabla}\cdot\bar{\boldsymbol{\mathcal{D}}} - [\boldsymbol{\nabla}\bar{P} - \bar{\rho}\mathbf{g}], && \text{(A-3)}\\
\bar{\rho}\bar{T}\frac{\partial S}{\partial t} + \bar{\rho}\bar{T}\mathbf{v}\cdot\boldsymbol{\nabla}(\bar{S}+S) &= \boldsymbol{\nabla}\cdot[\kappa_r\bar{\rho}c_p\boldsymbol{\nabla}(\bar{T}+T) + \kappa\bar{\rho}\bar{T}\boldsymbol{\nabla}(\bar{S}+S)]\\
&+ \frac{4\pi\eta}{c^2}\mathbf{j}^2 + 2\bar{\rho}\nu\left[e_{ij}e_{ij} - 1/3(\boldsymbol{\nabla}\cdot\mathbf{v})^2\right] + \bar{\rho}\epsilon, && \text{(A-4)}\\
\frac{\partial \mathbf{B}}{\partial t} &= \boldsymbol{\nabla}\times(\mathbf{v}\times\mathbf{B}) - \boldsymbol{\nabla}\times(\eta\boldsymbol{\nabla}\times\mathbf{B}), && \text{(A-5)}
\end{aligned}$$

avec κ la diffusivité thermique effective intervenant dans le terme extra SGS de diffusion de l'entropie, $\bar{\rho}\epsilon$ le terme de chauffage et $\bar{\mathcal{D}}$ le tenseur des contraintes visqueuses linéarisés, ce dernier possédant les composantes suivantes:

$$\bar{\mathcal{D}}_{ij} = -2\bar{\rho}\nu[e_{ij} - 1/3(\boldsymbol{\nabla}\cdot\mathbf{v})\delta_{ij}], \tag{A-6}$$

Nous complétons le jeu d'équations, en utilisant une équation d'état linéarisée:

$$\frac{\rho}{\bar{\rho}} = \frac{P}{\bar{P}} - \frac{T}{\bar{T}} = \frac{P}{\gamma\bar{P}} - \frac{S}{c_p}, \tag{A-7}$$

où γ est l'exposant adiabatique, et en considérant l'équation d'état à l'ordre zéro:

$$\bar{P} = \mathcal{R}\bar{\rho}\bar{T}. \tag{A-8}$$

Pour des considérations de précision numérique, le flux de masse et le champ magnétique restent à divergence nulle à la précision machine près par l'utilisation d'une représentation " poloïdale/toroïdale ":

$$\begin{aligned}
\bar{\rho}\mathbf{v} &= \boldsymbol{\nabla}\times\boldsymbol{\nabla}\times(W\hat{\mathbf{e}}_r) + \boldsymbol{\nabla}\times(Z\hat{\mathbf{e}}_r), && \text{(A-9)}\\
\mathbf{B} &= \boldsymbol{\nabla}\times\boldsymbol{\nabla}\times(C\hat{\mathbf{e}}_r) + \boldsymbol{\nabla}\times(A\hat{\mathbf{e}}_r) \quad . && \text{(A-10)}
\end{aligned}$$

Les équations (A-1) et (A-2) sont donc réalisées par construction. En substituant cette décomposition dans les équations (A-3 - A-5) et en utilisant l'équation (A-7), pour éliminer ρ et T en faveur de S et P, on réduit le système à respectivement quatre (six) équations dans le cas hydrodynamique (MHD) pour les inconnues S, P, W et Z (et C et A) (voir Clune et al. 1999 et Brun et al. 2004).

A-1.2 La Méthode Numérique

Le code ASH repose sur une méthode numérique dite pseudo-spectrale (Boyd 1989, Glatzmaier 1984, Clune et al. 1999). Les variables thermodynamiques, les trois composantes du flux de masse $\bar{\rho}\mathbf{v}$ et du champ magnétique $\mathbf{B}$ (s'il est inclus) sont projetées sur les harmoniques sphériques $Y_{\ell m}(\theta,\phi)$ [20] pour leur structure horizontale, comme par exemple pour la fonction de courant poloidale W:

$$W(r,\theta_i,\phi_i,t) = \sum_{m=-m_{max}}^{m_{max}} \sum_{\ell=|m|}^{l_{max}(m)} W_\ell^m(r,t) Y_{\ell m}(\theta_i,\phi_i)\,,$$

où θ_i et ϕ_i représentent respectivement le i^{eme} et j^{eme} points de grille latitudinaux et longitudinaux. Cette décomposition en harmoniques sphériques a l'avantage qu'elle permet une résolution spatiale homogène (évitant ainsi le problème de la convergence des méridiens aux pôles) si tous les multiplets m pour un degré ℓ donné sont conservés (troncation dite triangulaire $\ell_{max}(m) = \ell_{max} = m_{max}$, Boyd 1989). La précision numérique est assurée en utilisant des points de maille vérifiant la quadrature de Gauss, c'est à dire les zéros de polynôme de Legendre pour la colatitude et des points équidistants en longitude pour Fourrier. Afin d'éviter les problèmes d'aliasing des termes non linéaires (comme ceux d'advection) calculés dans l'espace physique et ensuite transformés vers l'espace spectral (évitant ainsi de calculer des convolutions), on applique la relation $N_\theta \geq \frac{3\ell_{max}+1}{2}$, $N_\phi = 2N_\theta$.

Pour leur structure radiale nous décomposons les grandeurs physiques sur les polynômes de Chebyshev $T_n(r_k)$, ce qui donne (pour la W):

$$W_\ell^m(r_k,t) = \frac{2}{N_r - 1} {\sum_{n=1}^{N_r}}'' W_{\ell n}^m(t) T_n(r_k)\,, \text{ avec } 1 \leq k \leq N_r.$$

où ${\sum_{n=1}^{N_r}}''$ sous entend que le premiers et dernier points sont multipliés par 1/2. Nous réécrivons cette décomposition sous la forme matricielle suivante, utile pour la suite:

$$W_\ell^m(r_k,t) = \mathcal{T}_{kn} W_{\ell n}^m(t),$$

20. qui sont les fonctions propres du Laplacien horizontal $\Delta_\perp Y_{\ell m} = -\frac{\ell(\ell+1)}{r^2} Y_{\ell m}$

où la sommation pour répétition d'indices s'applique à n et r_k correspond au k^{eme} point de collocation Gauss-Lobatto, solution des polynômes de Chebyshev en rayon. Pour les mêmes raisons d'aliasing apparaissant lors du calcul des termes non linéaires, nous n'utilisons en pratique que $N_r' = N_r - 2$ points dans la direction radiale. Il est également possible d'utiliser deux domaines de Chebyshev avec le code ASH, ce qui nécessite d'imposer la continuité des fonctions et de leurs dérivées afin d'obtenir la continuité des variables thermodynamiques, des vitesses, des champs magnétiques ainsi que des contraintes visqueuses et du flux de chaleur diffusif (voir Clune et al 1999). Nous utilisons d'ailleurs cette option pour le calcul de nos modèles d'étoiles A (cf. chapitre 6).

L'évolution temporelle des équations peut alors s'écrire (en prenant encore ici W comme variable d'exemple):

$$\frac{\partial}{\partial t} W_\ell^m(r_k,t) = \mathcal{L}_{\ell mk}^W(t) + \mathcal{N}_{\ell mk}^W(t),$$

où $\mathcal{L}_{\ell mk}^W(t)$ et $\mathcal{N}_{\ell mk}^W(t)$ représentent respectivement les termes linéaires et non linéaires auxquels on a rajouté les forces de Coriolis et Laplace. Ceci implique qu'il n'y a pas dans les termes linéaires de couplage en ℓ et on peut alors écrire de façon formelle:

$$\mathcal{L}_{\ell mk}^W(t) = \mathcal{K}_{\ell;mk}^W W_{\ell n}^m(t),$$

ce qui sous entend qu'il n'y a pas de sommation sur ℓ et ce qui permet d'écrire l'évolution temporelle de l'équation par exemple pour W comme:

$$\frac{\partial}{\partial t} \mathcal{T}_{kn} W_{\ell n}^m(t) = \mathcal{K}_{\ell;mk}^W W_{\ell n}^m(t) + \mathcal{N}_{\ell mk}^W(t).$$

Comme des dérivées radiales interviennent dans ces équations temporelles, il est pratique de travailler dans l'espace de Chebyshev pour les variables S, P, W, et Z (et C et A).

Pour discrétiser dans le temps ces équations, nous utilisons un schéma numérique temporel dit semi-implicite, basé sur un algorithme Crank-Nicholson implicite d'ordre 2 pour les termes linaires et un algorithme Adams-Bashforth explicite d'ordre 2 pour les termes non linéaires, les forces de Coriolis et de Laplace (cf. Press et al. 1990) , c'est à dire:

$$\begin{aligned} \mathcal{T}_{kn}\left[\frac{W_{\ell n}^m(t_{\sigma+1}) - W_{\ell n}^m(t_\sigma)}{\Delta t}\right] &= \mathcal{K}_{\ell;mk}^W[\alpha_{CN} W_{\ell n}^m(t_{\sigma+1}) + (1-\alpha_{CN}) W_{\ell n}^m(t_\sigma)] \\ &+ \mathcal{N}_{\ell mk}^W(t_\sigma) + \frac{1}{2}\frac{\Delta t}{\Delta t_{old}}[\mathcal{N}_{\ell mk}^W(t_\sigma) - \mathcal{N}_{\ell mk}^W(t_{\sigma-1})], \end{aligned}$$

avec $\Delta t = t_{\sigma+1} - t_\sigma$, $\Delta t_{old} = t_\sigma - t_{\sigma-1}$ et α_{CN} un paramètre de contrôle caractérisant la méthode de Crank-Nicholson. En réarrangeant cette équation on obtient:

$$\begin{aligned}\left(\mathcal{T}_{kn} - \alpha_{CN}\Delta t\mathcal{K}^W_{\ell;mk}\right) W^m_{\ell n}(t_{\sigma+1}) &= \left(\mathcal{T}_{kn} + (1-\alpha_{CN})\Delta t\mathcal{K}^W_{\ell;mk}\right) W^m_{\ell n}(t_\sigma) \\ &+ \Delta t\mathcal{N}^W_{\ell mk}(t_\sigma) + \frac{1}{2}\frac{\Delta t^2}{\Delta t_{old}}[\mathcal{N}^W_{\ell mk}(t_\sigma) - \mathcal{N}^W_{\ell mk}(t_{\sigma-1})],\end{aligned} \tag{A-11}$$

ce qui sous forme matricielle donne:

$$\mathcal{A}^W_{\ell;kn} W^m_{\ell n}(t_{\sigma+1}) = \mathcal{B}^W_{\ell mk}.$$

Un cycle complet du code ASH procède alors en deux étapes. Premièrement nous calculons les termes de droite $\mathcal{B}^{S,P,W,Z,(C,A)}$, dont la partie faisant intervenir les termes de Adams-Bashforth du pas de temps précédent $t_{\sigma-1}$ est déjà connue. Cela consiste principalement à calculer les dérivées spatiales dans l'espace spectral approprié puis à passer dans l'espace physique pour évaluer $\mathcal{B}^{S,P,W,Z,(C,A)}$, et enfin à revenir par transformée inverse dans l'espace spectral. Deuxièmement, nous résolvons le système matriciel pour chaque membre de droite, grâce à une décomposition LU, étape dénommée solveur implicite. Finalement les solutions sont transformées depuis l'espace de Chebyshev vers l'espace physique dans la direction radiale (configuration dite primaire voir plus bas).

Avec le code ASH toutes les transformées spectrales sont appliquées à des données locales pour chaque processeur avec des transformations inter processeur quand nécessaire, ce qui nécessite en tout trois configurations de la distribution des données sur les $N_{cpus} - N_{I/O}$ processeurs utilisés pour le calculs:

- configuration primaire: ℓ en processeur et r et m distribués,
- configuration pour solveur implicite: r et m en processeur et ℓ distribué,
- configuration pour l'espace physique: r, θ distribués et ϕ en processeur.

La communication inter processeur utilise MPI (Message Passing Interface) et SHMEM (SHared MEMory). Bien qu'une bonne performance par processeur ait été atteinte pour les transformations (Fourier, Chebyshev, Legendre) ainsi que la partie implicite, la contrainte d'avoir les transformations locales et la représentation non triviale des données dans l'espace spectral empêchent toute distribution simple des données et de la charge par processeur (tel que Ncpus = Nrad x Nang + Ni/o, cf. Clune et al. 1999, pour une discussion plus complète). La stratégie a donc été d'utiliser des pointeurs, des tables d'accès et une allocation dynamique de la mémoire pour

morceler les données en blocs pouvant chacun être manipulés efficacement par un processeur et de distribuer ces blocs intelligemment à partir d'une évaluation préalable de la charge que chacun représente. Pour les gros problèmes, la transformée de Legendre domine le temps de calcul et un effort particulier a été fait pour en améliorer les performances (prise en compte de la symétrie équatoriale, bloc tenant dans la mémoire cache processeur et réutilisation des tableaux). L'utilisation de routines numériques spécifiques machine comme la librairie DXML sur Chrome au CCRT et les librairies numériques pour l'algèbre linéaire de types LAPACK maximise l'efficacité. Le code ASH a démontré une bonne portabilité et une bonne "scalabilité" (environ un facteur 1.75 d'accélération pour un doublement du nombre de processeurs sur les Cray T3E, avec des chiffres similaires sur IBM SP-3, SP-4 (comme Zahir à l'IDRIS ou Chrome au CCRT du CEA Bruyère le Chatel). Les performances peuvent atteindre plus de 900 MFlops/PE pour des problèmes allant jusqu'à un degré $\ell = 680$ & $Nr = 256$.

Finalement comme le code ASH utilise une approche de type LES avec comme traitement SGS, soit des diffusivités effectives turbulentes, soit une hyperviscosité (i.e Δ^{2n}, avec $n > 1$), avec la possibilité d'introduire des formulations plus complexes basées sur différentes méthodes de fermeture des équations du mouvement (modèles alpha-LANS, dynamique, cf. Wong & Lilly 1994, Lesieur 1997, Valdetarro 2005), il est nécessaire de préciser notre choix. Le code ASH utilise dans cette étude une approche très simple qui consiste à utiliser des diffusivités effectives (turbulentes) et d'introduire dans l'équation d'énergie, comme on l'a vu plus haut, un terme supplémentaire de diffusion de l'entropie. Des travaux sont en cours pour améliorer le traitement sous maille du code avec le groupe de N. Mansour du Center for Turbulence Research (CTR) de Palo Alto (USA).

A-1.3 perspectives

Le développement actuel de ASH consiste à en améliorer le contenu physique (nouvelles conditions initiales (hydro et MHD), équation d'état non idéale, conditions aux limites plus réalistes) ainsi que son fonctionnement numérique (ajout de nouveaux traitements sous maille, stratégie I/O basée sur plusieurs cpus, extension au traitement de la singularité géométrique à $r = 0$).

A-2 Équations de la Structure Interne des Étoiles

À partir des équations du mouvement (cas hydrodynamique) présentées chapitre 3, et en considérant plusieurs hypothèses simplificatrices, telles que la symétrie sphérique, l'équilibre hydrostatique et thermique (cf. Cox & Guili 1968, Kippenhahn & Weigert 1994 pour plus de détails), on peut dériver les équations de la structure interne des étoiles:

$$\begin{aligned}
\frac{\partial r}{\partial m} &= \frac{1}{4\pi\rho r^2} \\
\frac{\partial P}{\partial m} &= -\frac{Gm}{4\pi r^4} \\
\frac{\partial L}{\partial m} &= \epsilon_N - \epsilon_\nu - T\frac{\partial S}{\partial t} \\
\frac{\partial T}{\partial m} &= -\frac{GmT}{4\pi r^4 P}\nabla
\end{aligned}$$

avec r est le rayon normalisé, m la masse contenue dans la coquille de rayon r, G la constante de gravitation universelle, P la pression, T la température, S l'entropie, L la luminosité, $\nabla = (\ln T / \ln P)$ le gradient de température du milieu, ϵ_N la production d'énergie par les réactions nucléaires et ϵ_ν la perte par neutrino.

Pour résoudre ce système d'équations différentielles du 4 ème ordre, il est nécessaire d'introduire quatre conditions aux limites.

- Pour le centre:
  Dans ce système d'équations, le centre est un point singulier où les variables physiques telles que la pression P, la température T, la densité ρ et la composition chimique $\vec{X}$ doivent avoir une valeur finie. On pose également L=0 et r=0 en m=0.
- Pour la surface:
  Cette région est très sensible aux ingrédients physiques utilisés pour la décrire. La condition la plus simple consiste à considérer l'équilibre hydrostatique, une pression extérieure nulle $P_{ext} = 0$ pour une profondeur optique $\tau = 0$ et une température T égale à $T_{eff} = 5800K$ à un rayon solaire. Comme les modes de pression sont excités dans cette région et qu'ils y passent le plus de temps, des conditions plus réalistes, basées sur des modèles d'atmosphères stellaires ont été développées. Dans les modèles solaires, ils ne sont "restitués" qu'à travers une loi $T(\tau,T_{eff})$.

Le critère le plus souvent utilisé pour connaître le mode de transport de l'énergie est celui de Schwarzschild $\nabla > \nabla_{ad}$ caractérisant l'instabilité convective, où ∇ et

∇_{ad} sont respectivement le gradient radiatif et le gradient adiabatique. Le gradient de température est:

$$\begin{aligned}\frac{\partial T}{\partial m} &= -\frac{1}{4\pi\rho r^2}\frac{3}{4ac}\frac{\kappa\rho}{T^3}\frac{L}{4\pi r^2} \text{ , si le transport est radiatif} \\ &= \frac{\Gamma_2 - 1}{\Gamma_2}\frac{T}{P}\frac{\partial P}{\partial m} \text{ , si le transport est convectif et adiabatique}\end{aligned}$$

Pour pouvoir suivre l'évolution de la composition chimique de l'étoile, on couple les équations de la structure interne à l'équation différentielle caractérisant l'évolution de la concentration chimique X_i:

$$\frac{\partial X_i}{\partial t} = \frac{m_i}{\rho}\left(\sum_j r_{ji} - \sum_k r_{ik}\right) - \frac{\partial F_i}{\partial m}, i = 1,...,nchim \qquad \text{(A-12)}$$

où r_{ji} et r_{ik} sont respectivement les réactions nucléaires créant et détruisant l'espèce chimique X_i, $F_i(m,t) = -4\pi r^2\rho\left(4\pi r^2\rho\sum_j d_{i,j}\frac{\partial X_j}{\partial m} - v_i X_i\right)$ représente le flux de composition chimique dû à la diffusion, $nchim$ est le nombre d'espèces chimiques considérées, $d_{i,j}$ est le coefficient de diffusion atomique pour l'espèce chimique i par rapport à l'espèce j, la i-ème composante $d_{i,i}$ incluant un coefficient de diffusion turbulente D_T et finalement v_i est la vitesse de diffusion.

Durant ma thèse (1995-1998) j'ai utilisé, développé et modifié le code d'évolution stellaire CESAM (Morel 1997), résolvant les équations de la structure interne présentées plus haut. Plusieurs articles ont été écrits sur le modèle standard et non-standard du Soleil, allant de la prédiction de fréquences des modes acoustiques et de gravité, à la sensibilité du profil de vitesse du son solaire aux processus physiques (microscopiques et macroscopiques) et aux problèmes de sous abondances du Lithium (^{7}Li), voir entre autres Brun et al. (1998), (1999) et (2002).

A-3 Définitions des Symboles et Nombres sans Dimension

A-3.1 Symboles

Symbole	Unité	Définition
$\mathbf{B}(r,\theta,\phi,t)$	G	vecteur champ magnétique
$B_r(r,\theta,\phi,t)$	G	champ magnétique radial
$B_\theta(r,\theta,\phi,t)$	G	champ magnétique latitudinal
$B_\phi(r,\theta,\phi,t)$	G	champ magnétique longitudinal
$\tilde{B}(r)$	G	champ magnétique rms caractéristique
c_p	erg/g/K	chaleur spécifique à pression constante
$\mathcal{D}$		tenseur des contraintes visqueuses
e_{ij}	s^{-1}	tenseur du taux de déformation
g	cm/s^2	accélération gravitationnelle
η	cm^2/s	diffusivité magnétique
κ	cm^2/s	diffusivité thermique
κ_{rad}	cm^2/s	diffusivité radiative
ν	cm^2/s	viscosité cinématique
$\mathbf{\Omega_0}$	rad/s	vecteur de rotation du repère tournant
$\bar{P}(r,t)$ et $P(r,\theta,\phi,t)$	$dynes/cm^2$	pression moyenne et fluctuante (ou totale, chap 3)
$\bar{\rho}(r,t)$ et $\rho(r,\theta,\phi,t)$	g/cm^3	densité moyenne et fluctuante (ou totale, chap 3)
$\bar{S}(r,t)$ et $S(r,\theta,\phi,t)$	erg/K/g	entropie spécifique moyenne et fluctuante (ou totale, chap 3)
$\bar{T}(r,t)$ et $T(r,\theta,\phi,t)$	K	température moyenne et fluctuante (ou totale, chap 3)
$\mathbf{v}(r,\theta,\phi,t)$	cm/s	vecteur vitesse locale dans le repère tournant
$v_r(r,\theta,\phi,t)$	cm/s	vitesse radiale locale dans le repère tournant
$v_\theta(r,\theta,\phi,t)$	cm/s	vitesse latitudinale locale dans le repère tournant
$v_\phi(r,\theta,\phi,t)$	cm/s	vitesse longitudinale locale dans le repère tournant
$\tilde{v}(r)$	cm/s	vitesse rms locale caractéristique dans le repère tournant

TAB. A-1 – *Définition des symboles utilisés dans le manuscrit. Nous utilisons le système d'unité cgs sauf si autrement indiqué.*

A-3.2 Nombres sans dimension

Nombre	Formule	Définition (rapport des forces)
Ekman $\mathcal{E}_k$	$\nu/2\Omega_0 L^2$	forces visqueuses sur forces de Coriolis
Ekman magnétique $\mathcal{E}_m$	$\eta/2\Omega_0 L^2$	diffusivité magnétique sur forces de Coriolis
Elsasser (rms) Λ	$\tilde{B}'^2/4\pi\rho\eta\Omega_0$	forces de Laplace sur forces de Coriolis
Grashof G	$(-\partial\rho/\partial S)\Delta S g L^3/\rho\nu^2$	forces de flottaison sur forces visqueuses
Nusselt Nu	$F_{tot}L/\kappa\Delta T$	efficacité de la convection p/r au rayonnement
Péclet (rms) P_e	$R_e \times P_r = \tilde{v}' L/\kappa$	forces d'inertie sur diffusivité thermique
Rayleigh R_a	$(-\partial\rho/\partial S)\Delta S g L^3/\rho\nu\kappa$	force de flottaison sur forces dissipatives
Reynolds (rms) R_e	$\tilde{v}' L/\nu$	forces d'inertie sur forces visqueuses
Reynolds mag (rms) R_m	$\tilde{v}' L/\eta$	forces d'inertie sur diffusivité magnétique
Roberts Q	η/κ	diffusivité magnétique sur diffusivité thermique
Rossby R_o	$\tilde{\omega}'/2\Omega_0 \sim \tilde{v}'/2\Omega_0 L$	terme d'advection sur forces de Coriolis
Rossby stellaire R_{os}	P_{rot}/τ	période de rotation sur temps de retourn. conv.
Rossby convectif R_c	$\sqrt{R_a/T_a P_r}$	forces de flottaison sur forces de Coriolis
Prandtl P_r	ν/κ	viscosité cinématique sur diffusivité thermique
Prandtl magnétique P_m	ν/η	viscosité cinématique sur diffusivité magnétique
Taylor T_a	$4\ \Omega_0^2 L^4/\nu^2$	forces de Coriolis sur forces visqueuses
Temps diff. Ohmique τ_η	$L^2/(\pi^2\eta)$	cas d'une sphère

TAB. A-2 – *Définition des nombres sans dimension utilisés dans le manuscrit. Avec comme longueur, vitesse et champ magnétique caractéristiques $L = r_{top} - r_{bot}$, $\tilde{v}'$ et $\tilde{B}'$ où les deux dernières variables représentent respectivement la vitesse convective rms fluctuante et le champ magnétique rms fluctuant, $F_{tot} = F_{en} + F_{rad}$ est la somme du flux d'enthalpie (convectif) et du flux radiatif, ΔT représente ici la différence en température entre le haut et le bas du domaine (cf. Hansen & Kawaler 1995) et les autres variables ont leur signification habituelle (voir Table précédente).*

A-4 Vorticité et Vent Thermique dans le cas MHD

A-4.1 Équation de la Vorticité

Soit l'équation du mouvement dans l'approximation anélastique incluant les forces de gravité, Coriolis et Laplace, dans le repère tournant à $\mathbf{\Omega_0} = \Omega_0 \hat{\mathbf{e}}_{\boldsymbol{z}} = \Omega_0(\cos\theta \hat{\mathbf{e}}_{\boldsymbol{r}}, -\sin\theta \hat{\mathbf{e}}_{\boldsymbol{\theta}}, 0)$:

$$\begin{aligned} \bar{\rho}\left(\frac{\partial \mathbf{v}}{\partial t} + (\mathbf{v}\cdot\boldsymbol{\nabla})\mathbf{v}\right) &= -\boldsymbol{\nabla}P + \rho\mathbf{g} - 2\bar{\rho}\mathbf{\Omega_0}\times\mathbf{v} \\ &+ \frac{1}{4\pi}(\boldsymbol{\nabla}\times\mathbf{B})\times\mathbf{B} - \boldsymbol{\nabla}\cdot\boldsymbol{\mathcal{D}}, \end{aligned} \tag{A-13}$$

où $\boldsymbol{\mathcal{D}}$ le tenseur visqueux, est défini comme:

$$\mathcal{D}_{ij} = -2\bar{\rho}\nu[e_{ij} - 1/3(\boldsymbol{\nabla}\cdot\mathbf{v})\delta_{ij}]. \tag{A-14}$$

et toutes les autres variables ont leur signification usuelle. On peut réécrire l'équation du mouvement sous la forme:

$$\begin{aligned} \frac{\partial \mathbf{v}}{\partial t} &= \mathbf{v}\times(\boldsymbol{\nabla}\times\mathbf{v}) - \frac{1}{2}\boldsymbol{\nabla}\mathbf{v}^2 - \frac{1}{\bar{\rho}}\boldsymbol{\nabla}P - \frac{\rho g}{\bar{\rho}}\hat{\mathbf{e}}_{\boldsymbol{r}} - 2\mathbf{\Omega_0}\times\mathbf{v} \\ &+ \frac{1}{4\pi\bar{\rho}}(\boldsymbol{\nabla}\times\mathbf{B})\times\mathbf{B} - \frac{1}{\bar{\rho}}\boldsymbol{\nabla}\cdot\boldsymbol{\mathcal{D}}, \end{aligned} \tag{A-15}$$

en utilisant la relation $(\mathbf{v}\cdot\boldsymbol{\nabla})\mathbf{v} = \frac{1}{2}\boldsymbol{\nabla}\mathbf{v}^2 - \mathbf{v}\times(\boldsymbol{\nabla}\times\mathbf{v})$ et en divisant par $\bar{\rho}$. Appliquons l'operateur rotationel $\boldsymbol{\nabla}\times$ à l'équation précédente A-15 (nous rappelons que $\boldsymbol{\nabla}\times\boldsymbol{\nabla}f = 0$ et $\boldsymbol{\nabla}\cdot(\boldsymbol{\nabla}\times\mathbf{a}) = 0$):

$$\begin{aligned} \frac{\partial \boldsymbol{\omega}}{\partial t} &= -\boldsymbol{\nabla}\times(\boldsymbol{\omega}_a\times\mathbf{v}) + \frac{1}{\bar{\rho}^2}\boldsymbol{\nabla}\bar{\rho}\times\boldsymbol{\nabla}P - \boldsymbol{\nabla}\times\left(\frac{\rho g}{\bar{\rho}}\hat{\mathbf{e}}_{\boldsymbol{r}}\right) \\ &+ \frac{1}{4\pi}\boldsymbol{\nabla}\times(\frac{1}{\bar{\rho}}(\boldsymbol{\nabla}\times\mathbf{B})\times\mathbf{B}) - \boldsymbol{\nabla}\times(\frac{1}{\bar{\rho}}\boldsymbol{\nabla}\cdot\boldsymbol{\mathcal{D}}), \end{aligned} \tag{A-16}$$

avec $\boldsymbol{\omega} = \boldsymbol{\nabla}\times\mathbf{v}$ la vorticité relative (dans le repère tournant) et $\boldsymbol{\omega}_a = \boldsymbol{\nabla}\times\mathbf{v} + 2\mathbf{\Omega_0}$ la vorticité absolue. Explicitons tout d'abord le premier terme du membre de droite:

$$\begin{aligned} \frac{\partial \boldsymbol{\omega}}{\partial t} &= (\boldsymbol{\omega}_a\cdot\boldsymbol{\nabla})\mathbf{v} - (\mathbf{v}\cdot\boldsymbol{\nabla})\boldsymbol{\omega}_a - \boldsymbol{\omega}_a(\boldsymbol{\nabla}\cdot\mathbf{v}) \\ &+ \frac{1}{\bar{\rho}^2}\boldsymbol{\nabla}\bar{\rho}\times\boldsymbol{\nabla}P - \boldsymbol{\nabla}\times\left(\frac{\rho g}{\bar{\rho}}\hat{\mathbf{e}}_{\boldsymbol{r}}\right) \\ &+ \frac{1}{c}\boldsymbol{\nabla}\times(\frac{1}{\bar{\rho}}\mathbf{j}\times\mathbf{B}) - \boldsymbol{\nabla}\times(\frac{1}{\bar{\rho}}\boldsymbol{\nabla}\cdot\boldsymbol{\mathcal{D}}), \end{aligned} \tag{A-17}$$

avec $\mathbf{j} = \frac{c}{4\pi}\boldsymbol{\nabla}\times\mathbf{B}$ la densité de courant. Finalement en réarrangeant le terme magnétique on obtient, l'équation dans l'approximation anélastique pour la vorticité:

$$\begin{aligned}\frac{\partial\boldsymbol{\omega}}{\partial t} &= (\boldsymbol{\omega}_a\cdot\boldsymbol{\nabla})\mathbf{v} - (\mathbf{v}\cdot\boldsymbol{\nabla})\boldsymbol{\omega}_a - \boldsymbol{\omega}_a(\boldsymbol{\nabla}\cdot\mathbf{v}) \\ &+ \frac{1}{\bar{\rho}^2}\boldsymbol{\nabla}\bar{\rho}\times\boldsymbol{\nabla}P - \boldsymbol{\nabla}\times\left(\frac{\rho g}{\bar{\rho}}\hat{\mathbf{e}}_{\boldsymbol{r}}\right) - \boldsymbol{\nabla}\times(\frac{1}{\bar{\rho}}\boldsymbol{\nabla}\cdot\boldsymbol{\mathcal{D}}) \\ &+ \frac{1}{c}\left((\mathbf{B}\cdot\boldsymbol{\nabla})\frac{\mathbf{j}}{\bar{\rho}} - \frac{1}{\bar{\rho}}(\mathbf{j}\cdot\boldsymbol{\nabla})\mathbf{B} - \mathbf{B}\left[\mathbf{j}\cdot\boldsymbol{\nabla}\left(\frac{1}{\bar{\rho}}\right)\right]\right), \qquad \text{(A-18)}\end{aligned}$$

A-4.2 Vent Thermique

À partir de l'équation pour la vorticié A-18 et en considérant quelques hypothèses simplificatrices on peut déduire l'équation pour le vent thermique dans le cas MHD. Dans le cas stationnaire et en négligeant les termes d'advection faisant intervenir $\boldsymbol{\omega}$ mais pas $\boldsymbol{\Omega_0}$ (ce qui revient à dire que l'on considère le cas d'un petit nombre de Rossby $R_o = \omega/2\Omega_0 << 1$), l'équation A-18 devient:

$$\begin{aligned}-(2\boldsymbol{\Omega_0}\cdot\boldsymbol{\nabla})\mathbf{v} + 2\boldsymbol{\Omega_0}(\boldsymbol{\nabla}\cdot\mathbf{v}) &= \frac{1}{\bar{\rho}^2}\boldsymbol{\nabla}\bar{\rho}\times\boldsymbol{\nabla}P - \boldsymbol{\nabla}\times\left(\frac{\rho g}{\bar{\rho}}\hat{\mathbf{e}}_{\boldsymbol{r}}\right) - \boldsymbol{\nabla}\times(\frac{1}{\bar{\rho}}\boldsymbol{\nabla}\cdot\boldsymbol{\mathcal{D}}) \\ &+ \frac{1}{c}\left((\mathbf{B}\cdot\boldsymbol{\nabla})\frac{\mathbf{j}}{\bar{\rho}} - \frac{1}{\bar{\rho}}(\mathbf{j}\cdot\boldsymbol{\nabla})\mathbf{B} - \mathbf{B}\left[\mathbf{j}\cdot\boldsymbol{\nabla}\left(\frac{1}{\bar{\rho}}\right)\right]\right) \qquad \text{(A-19)}\end{aligned}$$

Considérons maintenant la composante ϕ de l'équation A-19 dans le cas axisymétrique $(\partial/\partial\phi = 0)$:

$$\begin{aligned}-2\Omega_0\frac{\partial v_\phi}{\partial z} &= \frac{1}{r\bar{\rho}^2}\left(\frac{d\bar{\rho}}{dr}\frac{\partial P}{\partial\theta}\right) + \frac{g}{r\bar{\rho}}\frac{\partial\rho}{\partial\theta} - \frac{1}{r}\frac{\partial(r\mathcal{A}_\theta)}{\partial r} + \frac{1}{r}\frac{\partial(\mathcal{A}_r)}{\partial\theta} + \frac{1}{c}\left((\mathbf{B}\cdot\boldsymbol{\nabla})\frac{j_\phi}{\bar{\rho}}\right. \\ &\left. + \frac{j_r B_\phi}{\bar{\rho}r} + \frac{j_\theta B_\phi cot\theta}{\bar{\rho}r} - \frac{1}{\bar{\rho}}(\mathbf{j}\cdot\boldsymbol{\nabla})B_\phi - \frac{B_r j_\phi}{\bar{\rho}r} - \frac{B_\theta j_\phi cot\theta}{\bar{\rho}r} - B_\phi\left[j_r\frac{d}{dr}\left(\frac{1}{\bar{\rho}}\right)\right]\right) \qquad \text{(A-20)}\end{aligned}$$

avec $\dfrac{\partial}{\partial z} = \cos\theta\dfrac{\partial}{\partial r} - \dfrac{\sin\theta}{r}\dfrac{\partial}{\partial\theta}$ et

$$\begin{aligned}\mathcal{A}_r &= \frac{1}{\bar{\rho}}\left[\frac{1}{r^2}\frac{\partial(r^2\mathcal{D}_{rr})}{\partial r} + \frac{1}{r\sin\theta}\frac{\partial(\sin\theta\mathcal{D}_{\theta r})}{\partial\theta} - \frac{\mathcal{D}_{\theta\theta}+\mathcal{D}_{\phi\phi}}{r}\right] \\ \mathcal{A}_\theta &= \frac{1}{\bar{\rho}}\left[\frac{1}{r^2}\frac{\partial(r^2\mathcal{D}_{r\theta})}{\partial r} + \frac{1}{r\sin\theta}\frac{\partial(\sin\theta\mathcal{D}_{\theta\theta})}{\partial\theta} + \frac{\mathcal{D}_{\theta r} - cot\theta\mathcal{D}_{\phi\phi}}{r}\right]\end{aligned}$$

ce qui légérement réarrangé et en négligeant les effets visqueux (justifié dans le Soleil si on prend la valeur moléculaire de la viscosité), donne l'équation pour le vent thermique dans le cas MHD et $R_o << 1$:

$$2\Omega_0\frac{\partial v_\phi}{\partial z} = -\frac{1}{r\bar{\rho}^2}\left(\frac{d\bar{\rho}}{dr}\frac{\partial P}{\partial\theta} - \frac{d\bar{P}}{dr}\frac{\partial\rho}{\partial\theta}\right) - \frac{1}{c}\left((\mathbf{B}\cdot\boldsymbol{\nabla})\frac{j_\phi}{\bar{\rho}} + \frac{j_r B_\phi}{\bar{\rho}r} + \frac{j_\theta B_\phi cot\theta}{\bar{\rho}r}\right.$$
$$\left. -\frac{1}{\bar{\rho}}(\mathbf{j}\cdot\boldsymbol{\nabla})B_\phi - \frac{B_r j_\phi}{\bar{\rho}r} - \frac{B_\theta j_\phi cot\theta}{\bar{\rho}r} - B_\phi j_r\frac{d}{dr}\left(\frac{1}{\bar{\rho}}\right)\right) \quad \text{(A-21)}$$

Considérons à présent quelques cas limites de cette équation, et commençons par le cas le plus simple:

- cas barotrope sans champ magnétique:

$$2\Omega_0\frac{\partial v_\phi}{\partial z} = 0$$

on retrouve le théorème de Taylor-Proudman, indiquant un fluide sous l'influence de la rotation tend à être aligné avec l'axe de rotation et ne variant pas le long de celui-ci, devenant ainsi quasi 2-D (e.g. colonnes de Taylor, rotation différentielle cylindrique) (cf. Pedloski 1987, Busse 1983).

- cas barocline sans champ magnétique:

afin de briser la cylindricité de la rotation différentielle sans invoquer la présence de champ magnétique on peut considérer des profils barocline (Zahn 1992):

$$\frac{\partial v_\phi}{\partial z} = -\frac{1}{2\Omega_0 r\bar{\rho}^2}\left(\frac{d\bar{\rho}}{dr}\frac{\partial P}{\partial\theta} - \frac{d\bar{P}}{dr}\frac{\partial\rho}{\partial\theta}\right) \quad \text{(A-22)}$$

Nous consirérons ici l'équation d'état linéarisée:

$$\frac{\rho}{\bar{\rho}} = \frac{P}{\bar{P}} - \frac{T}{\bar{T}} = \frac{P}{\gamma\bar{P}} - \frac{S}{c_p}, \quad \text{(A-23)}$$

avec γ l'exposant adiabatique, et l'équation des gaz parfaits:

$$\bar{P} = \mathcal{R}\bar{\rho}\bar{T} \quad \text{(A-24)}$$

Si de plus on considère que la stratification radiale est adiabatique (i.e. $\frac{d\bar{S}}{dr} = 0$), alors:

$$\frac{1}{\gamma\bar{P}}\frac{d\bar{P}}{dr} = \frac{1}{\bar{\rho}}\frac{d\bar{\rho}}{dr}$$

et on peut réécrire l'équation A-22:

$$\frac{\partial v_\phi}{\partial z} = -\frac{1}{2\Omega_0 r\bar{\rho}^2}\frac{d\bar{P}}{dr}\left(\frac{\bar{\rho}}{\gamma\bar{P}}\frac{\partial P}{\partial\theta} - \frac{\partial\rho}{\partial\theta}\right) \tag{A-25}$$

$$= \frac{g}{2\Omega_0 r c_p}\frac{\partial S}{\partial\theta} \tag{A-26}$$

où on a utilisé la relation de l'équilibre hydrostatique $\frac{d\bar{P}}{dr} = -\bar{\rho}g$. Cette relation implique que l'établissement d'un gradient latitudinal d'entropie (et de température) permet d'obtenir des profils de rotation différentielle autres que cylindriques via un vent thermique. Brun & Toomre (2002) et Browning, Brun & Toomre 2004, ont étudié la présence d'un tel vent dans des simulations de convection sous l'influence de rotation, et en ont déduit qu'il joue effectivement un rôle important mais pas toujours dominant comparer aux tenseurs de Reynolds (ici négligés, cf. equation A-18).

- cas barotrope avec champ magnétique:

Bien sur la présence d'un champ magnétique peut également suffire à contrer les effets de la rotation:

$$\frac{\partial v_\phi}{\partial z} = -\frac{1}{2\Omega_0 c}\left((B_r\frac{\partial}{\partial r} + \frac{B_\theta}{r}\frac{\partial}{\partial\theta})\frac{j_\phi}{\bar{\rho}} + \frac{j_r B_\phi}{\bar{\rho}r} + \frac{j_\theta B_\phi cot\theta}{\bar{\rho}r}\right.$$
$$\left. -\frac{1}{\bar{\rho}}(j_r\frac{\partial}{\partial r} + \frac{j_\theta}{r}\frac{\partial}{\partial\theta})B_\phi - \frac{B_r j_\phi}{\bar{\rho}r} - \frac{B_\theta j_\phi cot\theta}{\bar{\rho}r} - B_\phi j_r\frac{d}{dr}\left(\frac{1}{\bar{\rho}}\right)\right) \tag{A-27}$$

- Cas général (pour R_o quelconque):

Nous considérons toujours le cas stationnaire ($\partial/\partial t = 0$),

$$\begin{aligned} 0 &= (\boldsymbol{\omega}_a\cdot\boldsymbol{\nabla})\mathbf{v} - (\mathbf{v}\cdot\boldsymbol{\nabla})\boldsymbol{\omega}_a - \boldsymbol{\omega}_a(\boldsymbol{\nabla}\cdot\mathbf{v}) \\ &+ \frac{1}{\bar{\rho}^2}\boldsymbol{\nabla}\bar{\rho}\times\boldsymbol{\nabla}P - \boldsymbol{\nabla}\times\left(\frac{\rho g}{\bar{\rho}}\hat{\mathbf{e}}_{\boldsymbol{r}}\right) - \boldsymbol{\nabla}\times(\frac{1}{\bar{\rho}}\boldsymbol{\nabla}\cdot\boldsymbol{\mathcal{D}}) \\ &+ \frac{1}{c}\left((\mathbf{B}\cdot\boldsymbol{\nabla})\frac{\mathbf{j}}{\bar{\rho}} - \frac{1}{\bar{\rho}}(\mathbf{j}\cdot\boldsymbol{\nabla})\mathbf{B} - \mathbf{B}\left[\mathbf{j}\cdot\boldsymbol{\nabla}\left(\frac{1}{\bar{\rho}}\right)\right]\right), \end{aligned} \tag{A-28}$$

Explicitons les termes puis considérons leur composante azimuthale selon $\hat{\mathbf{e}}_{\boldsymbol{\phi}}$:

Terme d'étirement de la vorticité:

$$\begin{aligned} (\boldsymbol{\omega}_a\cdot\boldsymbol{\nabla})\mathbf{v} &= (\boldsymbol{\omega}\cdot\boldsymbol{\nabla})\mathbf{v} + (2\boldsymbol{\Omega_0}\cdot\boldsymbol{\nabla})\mathbf{v} \\ [(\boldsymbol{\omega}\cdot\boldsymbol{\nabla})\mathbf{v}]_\phi &= (\boldsymbol{\omega}\cdot\boldsymbol{\nabla})v_\phi + \frac{\omega_\phi v_r}{r} + \frac{\omega_\phi v_\theta\cot\theta}{r} \qquad \text{(A-29)} \\ [(2\boldsymbol{\Omega_0}\cdot\boldsymbol{\nabla})\mathbf{v}]_\phi &= (2\boldsymbol{\Omega_0}\cdot\boldsymbol{\nabla})v_\phi = 2\Omega_0\frac{\partial v_\phi}{\partial z} \qquad \text{(A-30)} \end{aligned}$$

Terme d'advection de la vorticité:

$$\begin{aligned} -(\mathbf{v}\cdot\boldsymbol{\nabla})\boldsymbol{\omega}_a &= -(\mathbf{v}\cdot\boldsymbol{\nabla})\boldsymbol{\omega} - 2(\mathbf{v}\cdot\boldsymbol{\nabla})\boldsymbol{\Omega_0} = -(\mathbf{v}\cdot\boldsymbol{\nabla})\boldsymbol{\omega} \\ -[(\mathbf{v}\cdot\boldsymbol{\nabla})\boldsymbol{\omega}]_\phi &= -(\mathbf{v}\cdot\boldsymbol{\nabla})\omega_\phi - \frac{v_\phi\omega_r}{r} - \frac{v_\phi\omega_\theta\cot\theta}{r} \end{aligned} \tag{A-31}$$

Terme de regroupement/séparation des tubes de vorticité:

$$\begin{aligned} -\boldsymbol{\omega}_a(\boldsymbol{\nabla}\cdot\mathbf{v}) &= -\boldsymbol{\omega}(\boldsymbol{\nabla}\cdot\mathbf{v}) - 2\boldsymbol{\Omega_0}(\boldsymbol{\nabla}\cdot\mathbf{v}) \\ -[\boldsymbol{\omega}_a(\boldsymbol{\nabla}\cdot\mathbf{v})]_\phi &= -\omega_\phi(\boldsymbol{\nabla}\cdot\mathbf{v}) = -\frac{\omega_\phi}{\bar\rho}(\bar\rho\boldsymbol{\nabla}\cdot\mathbf{v}) \\ &= \frac{\omega_\phi}{\bar\rho}[\mathbf{v}\cdot\boldsymbol{\nabla}\bar\rho] = \omega_\phi v_r\frac{d\ln\bar\rho}{dr} \end{aligned} \tag{A-32}$$

Terme barocline, $\frac{1}{\bar\rho^2}\boldsymbol{\nabla}\bar\rho\times\boldsymbol{\nabla}P$:

$$\left[\frac{1}{\bar\rho^2}\boldsymbol{\nabla}\bar\rho\times\boldsymbol{\nabla}P\right]_\phi = \frac{1}{r\bar\rho^2}\left(\frac{d\bar\rho}{dr}\frac{\partial P}{\partial\theta}\right) \tag{A-33}$$

Terme gravité, $-\boldsymbol{\nabla}\times\left(\frac{\rho g}{\bar\rho}\hat{\mathbf{e}}_{\boldsymbol{r}}\right)$:

$$-\left[\boldsymbol{\nabla}\times\left(\frac{\rho g}{\bar\rho}\hat{\mathbf{e}}_{\boldsymbol{r}}\right)\right]_\phi = +\frac{g}{r\bar\rho}\frac{\partial\rho}{\partial\theta} = -\frac{1}{r\bar\rho^2}\left(\frac{d\bar P}{dr}\frac{\partial\rho}{\partial\theta}\right) \tag{A-34}$$

En regroupant les deux termes précédents, et en ne considérant pas la stratification adiabatique (i.e $d\bar S/dr \neq 0$),

$$\frac{1}{c_p}\frac{d\bar S}{dr} = \frac{1}{\gamma\bar P}\frac{d\bar P}{dr} - \frac{1}{\bar\rho}\frac{d\bar\rho}{dr}$$

on obtient:

$$\begin{aligned} \frac{1}{r\bar\rho^2}\left[\frac{d\bar\rho}{dr}\frac{\partial P}{\partial\theta} - \frac{d\bar P}{dr}\frac{\partial\rho}{\partial\theta}\right] &= \frac{1}{r\bar\rho^2}\left[\frac{\bar\rho}{\gamma\bar P}\frac{d\bar P}{dr}\frac{\partial P}{\partial\theta} - \frac{\bar\rho}{c_p}\frac{d\bar S}{dr}\frac{\partial P}{\partial\theta} - \frac{d\bar P}{dr}\frac{\partial\rho}{\partial\theta}\right] \\ &= \frac{1}{r\bar\rho^2}\frac{d\bar P}{dr}\left[\frac{\bar\rho}{\gamma\bar P}\frac{\partial P}{\partial\theta} - \frac{\partial\rho}{\partial\theta}\right] - \frac{1}{r\bar\rho c_p}\frac{d\bar S}{dr}\frac{\partial P}{\partial\theta} \\ &= -\frac{g}{rc_p}\frac{\partial S}{\partial\theta} - \frac{1}{r\bar\rho c_p}\frac{d\bar S}{dr}\frac{\partial P}{\partial\theta} \end{aligned} \tag{A-35}$$

Terme visqueux, $-\boldsymbol{\nabla}\times(\frac{1}{\bar\rho}\boldsymbol{\nabla}\cdot\boldsymbol{\mathcal{D}})$:

$$-[\boldsymbol{\nabla}\times(\frac{1}{\bar\rho}\boldsymbol{\nabla}\cdot\boldsymbol{\mathcal{D}})]_\phi = -\frac{1}{r}\left[\frac{\partial}{\partial r}(r\mathcal{A}_\theta) - \frac{\partial}{\partial\theta}\mathcal{A}_r\right] \tag{A-36}$$

Dans le cas magnétique les termes supplémentaires sont:
$\frac{1}{c}(\mathbf{B}\cdot\boldsymbol{\nabla})\frac{\mathbf{j}}{\bar{\rho}}$:

$$\begin{aligned}\left[\frac{1}{c}(\mathbf{B}\cdot\boldsymbol{\nabla})\frac{\mathbf{j}}{\bar{\rho}}\right]_\phi &= \frac{1}{c}(\mathbf{B}\cdot\boldsymbol{\nabla})\frac{j_\phi}{\bar{\rho}}+\frac{j_r B_\phi}{c\bar{\rho}r}+\frac{j_\theta B_\phi\cot\theta}{c\bar{\rho}r}\\ &= \frac{1}{c\bar{\rho}}(\mathbf{B}\cdot\boldsymbol{\nabla})j_\phi+\frac{1}{c}B_r j_\phi\frac{d}{dr}\frac{1}{\bar{\rho}}+\frac{j_r B_\phi}{c\bar{\rho}r}+\frac{j_\theta B_\phi\cot\theta}{c\bar{\rho}r} \qquad \text{(A-37)}\\ &= \frac{1}{c\bar{\rho}}(\mathbf{B}\cdot\boldsymbol{\nabla})j_\phi-\frac{B_r j_\phi}{c\bar{\rho}}\frac{d}{dr}\ln\bar{\rho}+\frac{j_r B_\phi}{c\bar{\rho}r}+\frac{j_\theta B_\phi\cot\theta}{c\bar{\rho}r} \qquad \text{(A-38)}\end{aligned}$$

$-\frac{1}{\bar{\rho}c}(\mathbf{j}\cdot\boldsymbol{\nabla})\mathbf{B}$:

$$-\left[\frac{1}{c\bar{\rho}}(\mathbf{j}\cdot\boldsymbol{\nabla})\mathbf{B}\right]_\phi = -\frac{1}{c\bar{\rho}}(\mathbf{j}\cdot\boldsymbol{\nabla})B_\phi-\frac{B_r j_\phi}{c\bar{\rho}r}-\frac{B_\theta j_\phi\cot\theta}{c\bar{\rho}r} \qquad \text{(A-39)}$$

$-\frac{\mathbf{B}}{c}\left[\mathbf{j}\cdot\boldsymbol{\nabla}\left(\frac{1}{\bar{\rho}}\right)\right]$:

$$-\left[\mathbf{B}\left[\mathbf{j}\cdot\boldsymbol{\nabla}\left(\frac{1}{\bar{\rho}}\right)\right]\right]_\phi = -B_\phi\left[j_r\frac{d}{dr}\frac{1}{\bar{\rho}}\right]=\frac{B_\phi j_r}{c\bar{\rho}}\frac{d}{dr}\ln\bar{\rho} \qquad \text{(A-40)}$$

Donc finalement en regoupant tous les termes on obtient:

$$\begin{aligned}2\Omega_0\frac{\partial v_\phi}{\partial z} &= -(\boldsymbol{\omega}\cdot\boldsymbol{\nabla})v_\phi-\frac{\omega_\phi v_r}{r}-\frac{\omega_\phi v_\theta\cot\theta}{r}\\ &+ (\mathbf{v}\cdot\boldsymbol{\nabla})\omega_\phi+\frac{v_\phi\omega_r}{r}+\frac{v_\phi\omega_\theta\cot\theta}{r}-\omega_\phi v_r\frac{d\ln\bar{\rho}}{dr}\\ &+ \frac{g}{rc_p}\frac{\partial S}{\partial\theta}+\frac{1}{r\bar{\rho}c_p}\frac{d\bar{S}}{dr}\frac{\partial P}{\partial\theta}+\frac{1}{r}\left[\frac{\partial}{\partial r}(r\mathcal{A}_\theta)-\frac{\partial}{\partial\theta}\mathcal{A}_r\right]\\ &- \frac{1}{c\bar{\rho}}(\mathbf{B}\cdot\boldsymbol{\nabla})j_\phi+\frac{B_r j_\phi}{c\bar{\rho}}\frac{d}{dr}\ln\bar{\rho}-\frac{j_r B_\phi}{c\bar{\rho}r}-\frac{j_\theta B_\phi\cot\theta}{c\bar{\rho}r}\\ &+ \frac{1}{c\bar{\rho}}(\mathbf{j}\cdot\boldsymbol{\nabla})B_\phi+\frac{B_r j_\phi}{c\bar{\rho}r}+\frac{B_\theta j_\phi\cot\theta}{c\bar{\rho}r}-\frac{B_\phi j_r}{c\bar{\rho}}\frac{d}{dr}\ln\bar{\rho} \qquad \text{(A-41)}\end{aligned}$$

Quatrième partie

Annexes

B-1 Curriculum Vitae

ALLAN SACHA BRUN

DSM/DAPNIA/Service d'Astrophysique
CEA-Saclay, 91191 Gif-sur-Yvette, France
Téléphone: 01 69 08 76 60, Fax: 01 69 08 65 77
Courriel: sacha.brun@cea.fr
Page Personnelle: http://lcd-www.colorado.edu/sabrun

Éducation:

1998: Thèse d'Astrophysique et Techniques Spatiales de l'Université Paris 7-Denis Diderot co-dirigée par S. Turck-Chièze et J.-P. Zahn (mention très honorable avec félicitations du jury) sujet:"Étude théorique de la structure interne du Soleil: L'apport de l'héliosismologie avec le satellite SOHO."
1995: DEA d'Astrophysique et Techniques Spatiales de l'Université Paris 7-Denis Diderot (mention bien).
1994: Maîtrise de Physique fondamentale de l'Université Paris 7-Denis Diderot (mention bien).

Expériences de Recherche:

01/03-présent: *Chercheur Permanent*,
Service d'Astrophysique, CEA-Saclay, France.
01/03-présent: *Chercheur Associé*,
JILA, Université du Colorado à Boulder et LUTH, Observatoire de Paris-Meudon.
05/02-01/03: *Chercheur Assistant Sénior* (visa H1-B),
JILA et APS, Université du Colorado, Boulder, USA.
01/99-04/02: *Chercheur Assistant* (visa J1),
JILA et APS, Université du Colorado, Boulder, USA.
10/95-12/98: *Étudiant en Thèse*,
Service d'Astrophysique, CEA-Saclay et DASGAL, Observatoire de Paris, France.

Expériences d'Enseignement:

depuis 2004: *Enseignant*, cours d'introduction générale à l'astrophysique (module 12h

sur 24h), ENST Bretagne 1ere année
depuis 2004: *Enseignant*, cours Simulation en astrophysique, module champ magnétique et effet dynamo dans les corps célestes, master 2eme année Simulation et Modélisation, ENSTA
08/00-05/01: *Moniteur*, UFR de Physique, Université du Colorado, Boulder, USA.
- Cours niveau DEUG, Mécanique, Cinétique du point, Thermodynamique, statique des fluides
- salle de soutien, mécanique et électromagnétisme
- validation hebdomadaire quizz informatique en physique (DEUG), système CAPA
09/98-12/98: *Chargé de TD*,
École d'Ingénieur Française en Informatique et Électronique, Paris, France.

Expériences d'Encadrement au niveau supérieur:

- thèse J. Ballot (soutenue Nov 2004), partie simulations numériques hydrodynamiques (HD) (chapitres 7 & 8) sur la convection des jeunes soleils et l'influence de la rotation
- thèse M. Browning, (USA, soutenue Sept 2005), simulations numériques 3D HD & MHD des coeurs convectifs d'étoiles A et effet dynamo, simulations MHD + pénétration convective du Soleil actuel
- thèse B. Brown, (USA, début Nov 2003) simulations numériques hydrodynamiques (HD) sur la convection des étoiles de type solaire rapides
- stagiaire master 2eme année, L. Jouve (Jan 2005-Aout05), sur la dynamo solaire en théorie du champ moyen à l'aide d'un code 2-D éléments finis résolvant l'équation d'induction. Début de la Thèse en Octobre 2005 (financement CFR-CEA) sur l'étude du magnetisme stellaire à partir de simulations 3-D MHD utilisant ASH.

Diffusion des Connaissances (Public Outreach)

Conférences & Événements:
- Mediathèque de St Brieuc
- Mediathèque d'Ivry
- Mediathèque de Ville du Bois
- Fete de la Science 04 (Dijon)
- Cité des Sciences
- Emission de radio scientifique 2004
- Commentaires sur le film SolarMAx à la Géode et Remise de prix au concours Soleil du CEA
- Nombreuses fêtes des Sciences et portes ouvertes du SAp et de l'Observatoire de

Meudon
- Stand pendant 3 jours fête de la science sur le magnétisme et les interactions Soleil-Terre

Écris & Images Scientifiques:
- Fait Marquant Observatoire de Meudon (juillet 2003)
- National Geographic special Soleil (édition américaine et française juillet 2004)
- Lettre de l'IDRIS dec 2004 no 7 article sur les simulations 3-D des étoiles
- Clefs CEA no 49 , article sur les simulations MHD solaires
- Defis du CEA
- Envision no17
- Calendrier (SDSC 2003), (Pittsburg 2005), Poster, carte de voeux IDRIS 2005
- Chronique Scientifique dans les "Les Cahiers et Les Petits Matins de St Tropez"
- Entretien dans le numéro 393 (01/2006) de La Recherche, sur les calculs haute performance en astrophysique

Projets de Recherche:

• Calculs numériques 3–D non linéaires sur des machines à l'architecture massivement parallèle (IBM SP3-4, Compaq TCS-1) de la convection compressible sous l'influence de la rotation en coquille sphérique pour modéliser la zone convective solaire et le cœur convectif des étoiles A, avec le code (ASH) Anelastic Spherical Harmonic.
• Implémentation de la version MHD du code ASH. Calculs numériques 3–D non linéaires de la convection compressible sous l'influence de la rotation et du champ magnétique pour modéliser la dynamo solaire/stellaire avec le code (ASH).
• Interprétation du profil de rotation différentielle solaire et de circulation méridienne déduits par l'héliosismologie en termes de transport de moment cinétique et de vent thermique.
• Développement d'un code MHD 2–D axisymétrique pour étudier la magnéto hydrodynamique de la tachocline solaire avec une haute résolution utilisant la méthode des éléments finis, ainsi que l'adaptation de ASH pour étudier la tachocline et l'intérieur radiatif solaire.
• Amélioration du contenu physique (microscopique et macroscopique, tel que le mélange dans la tachocline) du code stellaire CESAM afin de parvenir à un meilleur accord entre le modèle solaire / stellaire standard 1–D et les contraintes d'abondances photosphériques, d'hélio- et astérosismologie ainsi qu'à une meilleure détermination du flux théorique de neutrinos solaires.

• Participation à la détection de modes solaires à partir des expériences sismiques du satellite SOHO et de prédiction théorique des modes acoustiques et de gravité.

Stages & Projets Numériques

- Compression adiabatique de mélanges de gaz quantiques, Observatoire de Meudon (DEA)
- Effet dynamo cinématique dans le Soleil en méthodes spectrales, Observatoire de Meudon (DEA)
- Etude de la trajectoire aérienne et impact à l'eau d'une torpille, DCN-ECAN (Maitrise)
- Vols spatiaux et système restreint à 3 corps, Université de Paris7 (Licence)

Connaissances Informatiques:

- Développement et webmestre des sites web APC (jusqu'en 2000), CESAM (depuis 2003) et GDR Dynamo (depuis 2003)
Langages: Fortran 77/90, C, C^{++}, HTML, PHP, PERL, MPI (programmation parallèle)
Logiciels: IDL, Matlab, LaTeX, VIZ/BOB/HVR/OpenDX, Microsoft Office, 3DSMax, Photoshop, Illustrator, Premiere, Macromedia Director
Systèmes: Unix, Linux, Windows+Cygwin, MacOS

B-2 Liste de Publications

– Brun, A. S. 1998, Thèse de Doctorat, (PhD Thesis) Université de Paris 7, 260 pp.

Papiers Comité de Lecture:

– Brun, A. S. & Zahn, J.-P. 2006, "Magnetic Confinement of the Solar Tachocline", A&A soumis

– Miesch, M.S., Brun, A.S. and Toomre, J. 2006, "Solar differential rotation influenced by latitudinal entropy variations in the tachocline", ApJ, 639, sous presse

– Brun, A. S., Browning, M. K. and Toomre, J. 2005, "Simulations of Core Convection in Rotating A-type Stars: Magnetic Dynamo Action", ApJ, 629, 461-481.

– Brun, A. S., Miesch, M. S. and Toomre, J. 2004, "Global-scale Turbulent Convection and Dynamo Action in the Solar Envelope", ApJ, 614, 1073-1098.

– Brun, A. S., 2004, "On the Interaction between Differential Rotation and Magnetic Fields in the Sun", Solar Physics, 220, 333-344.

– Turck-Chièze, S., Garcia, R. A.,..., Brun, A. S.,...(Golf Team) 2004, "Looking for Gravity Mode Multiplets with the Golf Experiment aboard SoHO", ApJ, 604, 455-468.

– Browning, M., Brun, A. S. and Toomre, J. 2004, "Simulations of Core Convection in Rotating A-type Stars: Differential Rotation and Overshooting", ApJ, 601, 512-529.

– Brun, A. S., Antia, H. M., Chitre, S. M. and Zahn, J.-P. 2002, "Seismic Test for Solar Models with Tachocline Mixing", A&A, 391, 725-739 .

– Brun, A. S. and Toomre, J. 2002, "Turbulent Convection Under the Influence of Rotation: Sustaining a Strong differential Rotation", ApJ, 570, 865-885.

– Turck-Chièze, S., Couvidat, S., Kosovichev, A. G., Gabriel, A. H., Berthomieu, G., Brun, A. S. et al. 2001, "Solar Neutrino Emission Deduced from Seismic Model", ApJ, 555, L69-L73.

– Garcia, R. A., C. Rgulo, Turck-Chièze, S., Bertollo, L., Kosovichev, A. G., Brun, A. S. et al. 2000, "Low-Degree Low-Order Solar P Modes as Seen by GOLF onboard SOHO", Solar Physics, 200, 361-379.

– Basu, S., Turck-Chièze, S., Berthomieu, G., Brun, A. S. et al. 2000, "Structure of the Solar Core: Effect of Asymmetry of Peak Profiles", ApJ, 535, 1078-1084.

– Turck-Chièze, S., Brun, A. S. and Garcia, R. A. 2000, "Solar modelling: Theory and Verification", Nuclear Physics B (TAUP99 Proc. Suppl.), 87, 162-171.

- Brun, A. S. and Zahn, J.-P. 2000, “Influence of the Tachocline on Solar Evolution”, Annals of the New York Academy of Sciences, 898, 113-121.
- Brun, A. S., Turck-Chièze, S. and Zahn, J.-P. 1999, “Standard Solar Models in the Light of New Helioseismic Constraints: II Mixing below the Convective Zone”, ApJ, 525, 1032-1041.
- Brun, A. S., Turck-Chièze, S. and Morel, P. 1998, “Standard Solar Models in the Light of New Helioseismic Constraints: I The Solar Core”, ApJ, 506, 913-925.
- Turck-Chièze, S., Basu, S., Brun, A. S., Christensen-Dalsgaard, J. et al 1997, “First View of the Solar Core from Golf Acoustic Modes”, Solar Physics, 175, 247-265, (Special volume: First SOHO results)

Compte-Rendus de Conférences et Talks Invités:

- Brun, A.S. 2005, “A Turbulent Magnetic Sun”, in “The Dynamic Sun: challenges for Theory and Observations”, SPM11 meeting, held in Leuven, ESA SP-600, sous presse
- Brun, A.S. 2005, ”On The Coupled Influence of Rotation and MAgnetism in convective Core of A-type Stars”, in “Element Stratification in Stars: 40 years of Atomic diffusion”, held in MONS, eds G. Alecian, O. Richerd et S. Vauclair, EAS Publication Series, 17, 203
- Jouve, L. and Brun, A.S. 2005, “The Influence of Multicellular Meridional Flows in Setting the Cycle Period in Solar Dynamo Models”, in Semaine de l’Astrophysique Francaise (SF2A05)
- Brun, A. S. 2004, ”3-D MHD Simulations of the Solar Convection Zone and Tachocline”, in Helio- and Asteroseismology: Towards a Golden Future, SOHO14/GONG04 Conference held in Yale, July 12-17, ESA SP-559, 271-282
- Brown, B., Browning, M. K., Brun, A.S. and Toomre, J. 2004, ”Differential Rotation When the Sun Spun Faster”, in Helio- and Asteroseismology: Towards a Golden Future, SOHO14/GONG04 Conference held in Yale, July 12-17, ESA SP-559, 341-344
- Brun, A. S. 2004, ”Turbulent Convection and Dynamo Action in A- and G-Type Stars”, in Semaine de l’Astrophysique Francaise (SF2A04), 207-211
- Ballot, J., Brun, A. S. and Turck-Chièze, S. 2004, ”Turbulent Convection in Young Solar-like Stars: Influence of Rotation”, in Semaine de l’Astrophysique Francaise (SF2A04), 197-201
- Brun, A. S. 2003, ”On Stellar Dynamo Processes and Differential Rotation”, in Workshop Magnetism and Activity of the Sun and Stars, eds J. Arnaud & N. Meunier, EAS Publication Series, 9, 179.

- Brun, A. S. and Toomre, J. 2003, "Solar Turbulence and Magnetism Studied Within a Rotating Convective Spherical Shell", in 3D Stellar Rotation, eds S. Turcotte, S. C. Keller & R. M. Cavallo, ASP Conference Series, 293, 134-146.
- Brun, A. S. 2002, "Mixing in the Solar Tachocline", in Highlights of Astronomy, 12, 282-285.
- Brun, A. S. 2000, "The Solar Tachocline: Where Do We Stand?", in Helio- and Asteroseismology at the Dawn of the Millennium, eds P. Palle & A. Wilson, (ESA: Noordwijk), ESA SP-464, 273-276.
- Brun, A. S. and Toomre, J. 2000, Mean Flows in Turbulent Rotating Convective Shells", in Helio- and Asteroseismology at the Dawn of the Millennium, eds P. Palle & A. Wilson, (ESA: Noordwijk), ESA SP-464, 619-624.
- Toomre, J., Brun, A. S., Derosa, M., Elliott, J. R. and Miesch, M. S. 2000, "Simulation of Turbulent Convection", in Recent Insights into Physics of the Sun and Heliosphere: Highlights from SOHO and other Space Missions, eds P. Brekke, B. Fleck and J. Gurman, IAU Symposium 203, 131-143.
- Turck-Chièze, S., Brun, A. S. and Garcia, R. A. 1999, "The Seismic Solar Core after Two Years of SOHO Mission", in Eight International Workshop on Neutrino Telescopes, ed M. Baldo Ceolin, 147-164.
- Brun, A. S., Turck-Chièze, S. and Zahn, J. P. 1999, "Mixing below the Solar Convective Zone", in Theory and Tests of Convective Energy Transport, eds A., Gimenez and B., Montesinos, ASP Conference Series, 173, 293-296.
- Brun, A. S. and Turck-Chièze, S. 1999, "The Helioseismic Constraints on 7Li and 9Be from SOHO", in LiBeB, Cosmic Rays and Related X- and Gamma-Rays, ASP Conference Series, 171, 64-71.
- Brun, A. S., Turck-Chièze, S. and Zahn, J. P. 1998, "Macroscopic Processes in the Solar Interior", in Structure and Dynamics of the Interior of the Sun and Sun-like Stars, eds S. G. Korzennik & A. Wilson, (ESA: Noordwijk), ESA SP-418, 1, 439-443.
- Turck-Chièze, S., Basu, S., Berthomieu, G., Bonanno, A., Brun, A. S., Christensen-Dalsgaard, J. et al. (GOLF Team E) 1998, "Sensitivity of the sound speed to the physical processes included in the standard solar model", in Structure and dynamics of the interior of the sun and sun-like stars, eds S. G. korzennik and A. Wilson, (ESA: Noordwijk), ESA SP-418, 1, 555-560.
- Turck-Chièze, S. and Brun, A. S. 1997, "Spatial Seismic Constraints on Solar Neutrino Prediction", in W. Hampel (ed.), Fourth International Neutrino Conference, 41-53.

– Brun, A. S., Lopès, I., Turck-Chièze, S. and Morel, P. 1997, "Sensitivity of p and g-modes on specified physical processes of solar modeling", in IAU Symposium 181: Sounding solar and stellar interior, eds F.-X. Schmider and J. Provost, 69-70.
– Turck-Chièze, S., Basu, S., Brun, A. S., Christensen-Dalsgaard, J. et al. (GOLF Team E) 1997, "Comparison of predicted acoustic mode frequencies with preliminary GOLF results", in IAU Symposium 181: Sounding solar and stellar interior, eds F.-X. Schmider and J. Provost, 131-132.

B-3 Conférences Internationales, Séminaires et Écoles

Conférences:

- European Fusion Theory Conference, Aix en Provence (talk invité, Oct 05)
- European SPM-11: The Dynamic Sun: Challenges for Theory and Observations, (talk invité), Leuvain (Belgique, Sept 05)
- Festival de Théorie, Aix en Provence (talk invité, Juil 05)
- Semaine de la SF2A 2005, (talk) Strasbourg (France, Juin 05)
- Astrophysical Fluid Dynamics, IPAM Workshop I, Los Angeles, (USA, Avril 05)
- Observations and Models of the Solar Cycle, ISSI (talk invité) Bern, (Suisse, Mars & Oct 05)
- Programme Théorique, "Magnetohydrdynamics of the Stellar Interior", Institut Newton, (talk invité) Cambridge (UK, Sept et Nov 04)
- GONG04-Soho14, Helio- and Aseroseismology: Towards a Golden Future, University of Yale, (revue invitée), New Haven (USA, Juil 04)
- Semaine de la SF2A 2004, (talk) Paris (France, Juin 04)
- Sub-grid scale Modelling in Turbulent Convection, University of Colorado, (talk invité) Boulder (USA, Avr 04)
- Mathematical Aspects of Dynamos, (talk) Caramulo, (Portugal, Sept 03)
- IAU XXVth General Assembly (S219, JD 03 & 12), (2 talks) Sydney (Australia, Juil 03)
- IAU Symposium 215 on Stellar Rotation, (talk) Cancun (Mexico, Nov 02)
- Workshop on Stellar and Solar Magnetism, (revue inviée) Toulouse (France, Sep 02)
- 3D Stellar Evolution Workshop, (revue inviée) Livermore (USA, Juil 02)
- AGU - Spring 2001 Meeting, (talk invité) Boston (USA, Juin 01)
- Helio- and Asteroseismology at the Dawn of the Millenium, SOHO10-GONG2000 workshop, (talk) Tenerife (Espagne, Oct 00)
- 24th IAU General Assembly, (talk invité) Manchester (UK, Aout 00)
- Helioseismic Diagnostic of Solar Convection and Activity, SOHO9 workshop, (poster) Stanford (USA, Jul 99)
- Astrophysical Convection and Turbulence, 14th Florida Workshop in Nonlinear Astronomy and Physics, (talk) Gainsville (USA, Fev 99)
- LIBEB, Cosmic Rays and Gamma-Ray line Astronomy, IAP Workshop, (talk) Paris (France, Dec 98)

- Theory and Tests of Convective Energy Transport, Workshop on Stellar Structure, (poster) Granada (Espagne, Oct 98)
- Structure and Dynamics of the Interior of the Sun and Sun-like Stars, SOHO6/GONG98 conference, (poster) Boston (USA, Jui 98)
- Fourth International Solar Neutrino Conference, (poster) Heidelberg (Germany, Avr 97)
- Sounding Stellar and Solar Interiors, IAU 181, (poster) Nice (France, Oct 96)

Séminaires:

- Cadarache, 12/04
- IAP, 07/03
- X, 12/00
- SAp, 05/00
- DASGAL 04/00
- CETP 03/00
- DASGAL 04/99

Écoles d'été:

- Ecole de Cargese en Dynamique des Fluides Astrophysiques, (Mai 05) (Conférencier)
- Ecole de structure interne d'Aussois no 14 (Sept 04) (Conférencier)
- Ecole de structure interne d'Aussois no 8 (Sept 97) (Élève)
- Ecole de structure interne d'Aussois no 6 (Sept 95) (Élève)
- EADN school no 8 (Juil 95) (Élève)